THE EFFECT OF ELASTOMERIC BEARING DEGRADATION ON BRIDGE DYNAMIC RESPONSE

Iain Peter Swan BEng (Hons)

A thesis submitted to Napier University,
in fulfilment of the requirements for the
Degree of Doctor of Philosophy

School of the Built Environment
Napier University
Edinburgh, U.K.
2006

This copy of the thesis has been supplied on condition that anyone who consults it is understood to recognise that the copyright rests with its author. No quotation from the thesis and no information derived from it may be published without the prior written consent of the author or the University (as may be appropriate).

Abstract

The dynamic response of highway bridges is a topic that has been thoroughly researched over many years. However, understanding of how the dynamic response of bridges is affected by the performance of their bearings over an extended period of time is, at present, not clearly defined. Although health monitoring of bridge structures is relatively advanced, the scope for further research is wide. The study presented in this thesis contains research on plate structures; ranging from a simple Euler-Bernoulli method to determine natural frequencies; modal analysis of a plate structure in the laboratory; FEA of the plate structure; modal analysis on a full-scale structure subjected to vehicle loading; and FEA of a simplified model representing the full-scale structure. A combination of these methods has allowed the conclusions presented herein to be drawn with respect to the effects of support degradation, and the consequent effect on structural performance.

In the laboratory, modal analysis of a small-scale, thin rectangular plate of Perspex® has been completed. A series of boundary conditions have been investigated through altering the support offered to the plate by a series of springs, each with a different stiffness, to simulate bearings with different stiffnesses. Vibrations of varying frequency have also been forced upon the plate, and its response recorded. Displacement values provided the clearest indication of the effect of bearing stiffness, with the least stiff spring resulting in the largest displacement. Alteration of support stiffness in the model can have a marked effect on the resonant frequency of the plate (approx. 23 % frequency change between spring 1 (1.22 Nmm^{-1}) and 5 (15.62 Nmm^{-1})).

Full-scale testing on a highway bridge at Berwick-upon-Tweed on the A1, over the River Tweed, was completed in May 2005. These data form the baseline for future dynamic testing and condition monitoring of the structure. To describe the dynamic properties of the structure, the force generated by each type of vehicle traversing the structure was determined using instrumentation already in place on the bridge. Statistics drawn from the data are presented, which indicate that the bearings are functioning as expected, but are subjected to forces of a much larger magnitude due to overloaded HGVs than in current design specifications. Larger HGVs made up a small percentage of overall vehicles recorded, but contribute a much higher proportion of damage caused to the bridge. Displacement and frequency were both valid measures of bearing performance and therefore state of degradation.

The method is offered as a condition monitoring test for bridges and their bearings.

Declaration

This thesis is submitted to Napier University for the Degree of Doctor of Philosophy. The work described in this thesis was carried out under the supervision of Dr David Reid and Dr Charles Fairfield. The work was undertaken in The School of the Built Environment, Napier University, Edinburgh.

In accordance with the Regulations of Napier University governing the requirements for the Degree of Doctor of Philosophy, the candidate submits that the work presented in this thesis is original unless otherwise referenced within the text.

The following papers were derived from the work in this thesis. Those papers published by the time this thesis is prepared are included in the Appendix. Full permission from the relevant publisher or copyright holder has been obtained.

1 Swan I.P. Degradation of elastomeric bridge bearings and their effect on bridge dynamic response. IStructE poster competition, 2004.

2 Swan I.P., Fairfield C.A. and Reid D.B. Modelling highway bridge vibrations: the effect of support conditions. *Insight*, 2005, **47(7)**, 409-413.

17/03/07

Iain Swan. [redacted]

Acknowledgement

The author is indebted to Dr David Reid and Dr Charles Fairfield for their vigorous supervision and encouragement throughout the course of this research at Napier University.

The facilities provided by The School of the Built Environment, Napier University, are hereby gratefully acknowledged. The author also thanks the Faculty's entire Technical Staff, especially Mr Willie Laing and Mr Alan Barber for their advice and patience during testing with the PULSE^{TM} system. The author also wishes to thank Mr Bill McTaggart, Mr Brian McMillan and Mr Barry Longbottom (Brüel & Kjær) for their assistance and technical support. Thanks also go to all the staff at RMP, especially Dr Sean Smith and Mr Tim Waters-Fuller, for their assistance and equipment. Special thanks go to my post-graduate colleagues for their support and encouragement throughout the tenure of this appointment.

The author would also like to thank: Mr Mike Brandrith (Structures Steward North, A-one Integrated Highway Services) for access to the River Tweed bridge for testing purposes, maintenance information and engineering drawings thereof, Mr Alan Cook (Managing Director, Applied Traffic) for access to weigh-in-motion sensor data, and The Highways Agency for permission to undertake the research under their agreed disclaimer as follows;

"The Highways Agency maintains and operates motorways and trunk roads in England on behalf of The Secretary of State for Transport. Whilst the Agency has cooperated with the authors in providing access for this study, and has read the report with interest, it does not vouch for the accuracy of the findings, nor does it necessarily subscribe to the conclusions drawn by the authors."

The author extends his gratitude to: Mr Paul Moss (Field Sales Manager, SK Bearings), Mr John Fabb (A. Proctor Group), and Industrial Springs Ltd.

Finally, the author wishes to thank his parents for their never-ending support and encouragement throughout.

CONTENTS

Abstract i

Declaration ii

Acknowledgement iii

Contents iv

List of Figures viii

List of Tables xv

Notation xvi

CHAPTER 1 Introduction

1 General introduction 1

1.1 Structural dynamics 2

1.2 Modal analysis 2

1.3 Euler-Bernoulli beam / Rayleigh-Ritz method 6

1.4 Finite element analysis 7

1.5 Research objectives 9

1.6 Outline of thesis 10

1.7 References 12

CHAPTER 2 Literature review

2 Introduction 26

2.1 Vibration of plates 26

2.1.1 Classic boundary conditions 27

2.1.2 Variable end conditions 35

2.1.3 Finite element analysis 40

2.2 Dynamic analysis 42

2.2.1 Modal analysis 42

2.2.1.1 The Fourier transform 43

2.2.1.2 Discrete Fourier transform 44

2.2.1.3 The fast Fourier transform 44

2.2.1.4 Sampling and aliasing 46
2.2.1.5 Leakage 46
2.2.1.6 Signal enhancement 47
2.2.1.7 Analysis 48
2.2.1.8 Time domain functions 48
2.2.1.9 Frequency domain analysis 49
2.2.1.10 Frequency response function 50
2.2.1.11 Coherence function 51

2.2.2 Damage detection 52
2.2.3 Wavelets 59
2.2.4 Genetic algorithms 62
2.2.5 Moving loads 65
2.2.6 Other NDT methods 69

2.3 Bridge bearings 72
2.4 Summary 88
2.5 References 91

CHAPTER 3 Small-scale model testing

3 Introduction 135
3.1 Static deflection of beams with spring end support 136
3.1.1 Euler-Bernoulli equation 136
3.1.2 Rayleigh-Ritz method 138
3.1.3 Forcing function 141
3.1.4 Response values 142

3.2 Small-scale model 143
3.2.1 Material property definition 143
3.2.1.1 PMMA plate 143
3.2.1.2 Springs 148

3.2.2 Method 149
3.2.2.1 Free-Free support 150
3.2.2.2 Fixed supports 151
3.2.2.3 Simply supported pin joints 152
3.2.2.4 Springs 152

3.2.3 Natural frequency analysis 153
3.2.4 Forced vibrations 159
3.2.4.1 Sinusoidal harmonic loading 160

3.3 Finite element analysis 161
3.3.1 Forced vibration testing 166

3.4 Results 168
3.4.1 Euler-Bernoulli analysis 168
3.4.2 Small-scale model 168
3.4.2.1 Experimental modal analysis 168
3.4.2.2 Finite element analysis 171

3.5 Discussion 172
3.6 Conclusions 179
3.7 References 182

CHAPTER 4 Full-scale testing at Berwick-upon-Tweed

4.1 Introduction 240
4.2 Bridge location and type 242
4.3 Test arrangement 244
4.3.1 Location of accelerometers 246

4.4 WIM classifier 248
4.4.1 WIM theory 249

4.5 Results 250
4.5.1 Principal inspection report 250
4.5.2 Traffic survey 250
4.5.3 NDT 251

4.6 Discussion 252
4.6.1 Principal inspection report 252
4.6.2 Traffic survey 254
4.6.3 NDT 257

4.7 Conclusions 265
4.8 References 267

CHAPTER 5 Conclusions and recommendations for future research

5.1 Executive summary 329
5.2 Conclusions 329
5.2.1 Chapter 2 329
5.2.2 Chapter 3 330
5.2.3 Chapter 4 332

5.3 Recommendations for future work 333
5.4 Summary 335

APPENDIX 1 Publications arising from the research 336
APPENDIX 2 Data CD

List of Figures

CHAPTER 1

Figure 1.1	Simple elastomeric bearing pad	12
Figure 1.2	Constrained pot bearing: *in situ*	13
Figure 1.3	Pot bearing - typical engineering drawing with general dimensions	13
Figure 1.4	Typical high-load rocker bearing with general dimensions	14
Figure 1.5	Typical high-load roller bearing	14
Figure 1.6 (a)	Loading regimes for standard elastomeric pad - sign convention	15
Figure 1.6 (b)	Loading regimes for standard elastomeric pad - deflected shapes due to loading	15
Figure 1.7	Shear stress distributions of corresponding loading applied in Figure 1.6 (b)	16
Figure 1.8	Undeformed plate geometry, elements, node points, mesh and spring support locations	17
Figure 1.9	Modeshape 3 - Perspex plate - spring stiffness 1	17
Figure 1.10	Contour plot - modeshape 3 - spring stiffness 1	18
Figure 1.11	Modeshape 3 - Perspex plate - spring stiffness 5	18
Figure 1.12	Contour plot - modeshape 3 - spring stiffness 5	19
Figure 1.13	Contour plot of bending strain - spring stiffness 1	19
Figure 1.14	Contour plot of bending strain - spring stiffness 5	20
Figure 1.15	Bending strain response - spring stiffness 1 at node 3635	20
Figure 1.16	Bending strain response - spring stiffness 5 at node 3635	21

CHAPTER 2

Figure 2.1	First three mode shapes of plate model used in experimental analysis with two opposite edges fully fixed and the two remaining sides free	109
Figure 2.2 (a)	Bending moment equations with parameters for simply supported plates of various length to breadth ratios	110

Figure 2.2 (b)	Bending moment equations with parameters for plates of various length to breadth ratios with two opposite edges fully fixed and the remaining two sides simply supported.	111
Figure 2.3	Chen's finite difference mesh and notation, with sign convention	112
Figure 2.4	Gorman's superposition method showing complete plate with central co-ordinate axes	112
Figure 2.5	Table of results comparing answers obtained using the DSC method with the three other methods outlined in the text	113
Figure 2.6	Experimental setup for Nieves *et al.* to detect out-of-plane movement.	113
Figure 2.7	Schematic representation of the eigenvalue matrix used by Gorman based on three-term functions	114
Figure 2.8	Schematic diagram of modal testing arrangement used by Teng *et al.*	114
Figure 2.9	Isoparametric Kirchhoff plate element used in the FEA	115
Figure 2.10	Window functions used in FFT analysis	116
Figure 2.11	Methods of excitation for modal testing	117
Figure 2.12	Schematic showing bridge monitoring procedure used by Lee *et al.*	118
Figure 2.13	Wavelet transform functions	119
Figure 2.14	Higher mode sensitivity due to increased slope	120
Figure 2.15	Historical GVW and speed limits for HGVs	120
Figure 2.16	Sample data from Brien *et al.* showing the effect of vehicle speed on DAF	121
Figure 2.17	Acceleration and strain plots against frequency	122
Figure 2.18	Sample data from Law and Zhu	123
Figure 2.19	Radar equipment and typical output	124
Figure 2.20	Typical SASW equipment	125
Figure 2.21	Typical acoustic emission equipment and output	126
Figure 2.22	Typical output from the photogrammetry method	127
Figure 2.23	Dynamic shear modulus *versus* temperature for elastomeric bearing material	127

Figure 2.24	Increase in shear modulus at three time exposure limits for nine bearing types at -10°C and -25°C	128
Figure 2.25	Typical durometer for measuring material hardness	128
Figure 2.26	Isotherms of minimum shade temperature in the UK	129
Figure 2.27	Constrained elastomeric pot bearing with simplified line diagram showing the effective support conditions provided	130

CHAPTER 3

Figure 3.1	Euler-Bernoulli beam deflection values due to forcing function	184
Figure 3.2	Euler-Bernoulli beam deflection values due to forcing function at 0.1 s time step intervals.	184
Figure 3.3	PMMA sample in four point bending test configuration	185
Figure 3.4	PMMA cyclical tests for E value determination	185
Figure 3.5	PMMA sample *in situ* during Poisson's ratio testing	186
Figure 3.6	Thickness measurements on PMMA plate	186
Figure 3.7	Springs used in experimental analysis	187
Figure 3.8	Centreline displacement versus rotation curve for PMMA plate	187
Figure 3.9	Load - displacement curve for spring diameter 2 mm	188
Figure 3.10	PMMA plate in freely suspended configuration	188
Figure 3.11	Guitar tuners for levelling PMMA plate in freely suspended configuration	189
Figure 3.12	PMMA plate in fully fixed arrangement	189
Figure 3.13	Simply supported configuration	190
Figure 3.14	Spring support configuration	190
Figure 3.15	Plate dimensions and grid	191
Figure 3.16	PULSE FFT analyser and laptop computer	191
Figure 3.17	FRF response slice at measurement point 4 against coherence values for ten excitations	192
Figure 3.18	FRF response slice at measurement point 4 against coherence values for one excitation	193
Figure 3.19	Accelerometer type 4508-B	194
Figure 3.20	Exploded view of ThetaShear accelerometer configuration	194
Figure 3.21	Impact hammer type 2301-10 showing typical dimensions	195

Figure 3.22	Schematic diagram of impact hammer apparatus configuration	195
Figure 3.23	Excitation frequency range of impact hammer tips	196
Figure 3.24	Mass shaker attached to plate with beeswax at excitation point 14	197
Figure 3.25	FEA plate geometry and mesh refinement	198
Figure 3.26	Effect of stiffness at V_L on resonance frequency (10 N load)	198
Figure 3.27	Effect of stiffness at V_L on resonance frequency (50 N load)	199
Figure 3.28	Mode shapes for free support condition	200
Figure 3.29	Mode shapes for simply supported condition	201
Figure 3.30	Mode shapes for fully fixed condition	202
Figure 3.31	Mode shapes for spring support condition 1	203
Figure 3.32	Mode shapes for spring support condition 2	204
Figure 3.33	Mode shapes for spring support condition 3	205
Figure 3.34	Mode shapes for spring support condition 4	206
Figure 3.35	Mode shapes for spring support condition 5	207
Figure 3.36	Mode shape slices in spring support condition 1	208
Figure 3.37	Forced vibration response of springs for first mode shape	209
Figure 3.38	Acceleration response at mid-span - test 1	210
Figure 3.39	Acceleration response at mid-span - test 2	210
Figure 3.40	Acceleration response at mid-span - test 3	211
Figure 3.41	Velocity response at mid-span	211
Figure 3.42	Displacement response at mid-span - test 1	212
Figure 3.43	Displacement response at mid-span - test 2	212
Figure 3.44	Displacement response at mid-span - test 3	213
Figure 3.45	First three FEA mode shapes of plate model used in experimental analysis in freely supported condition	214
Figure 3.46	First three FEA mode shapes of plate model used in experimental analysis in simply supported condition	215
Figure 3.47	First three FEA mode shapes of plate model used in experimental analysis in fully fixed support condition	216
Figure 3.48	First three FEA mode shapes of plate model used in experimental analysis in spring support 1 configuration	217

Figure 3.49	First three FEA mode shapes of plate model used in experimental analysis in spring support 2 configuration	218
Figure 3.50	First three FEA mode shapes of plate model used in experimental analysis in spring support 3 configuration	219
Figure 3.51	First three FEA mode shapes of plate model used in experimental analysis in spring support 4 configuration	220
Figure 3.52	First three FEA mode shapes of plate model used in experimental analysis in spring support 5 configuration	221
Figure 3.53	Displacement at mid-span	222
Figure 3.54	Vertical and rotational displacements	222
Figure 3.55	Displacement response against time at node 18	223
Figure 3.56	Acceleration response against time at node 18	223
Figure 3.57	Contour plot of displacement Dz in mm for spring stiffness 1	224
Figure 3.58	Contour plot of displacement Dz in mm for spring stiffness 2	224
Figure 3.59	Contour plot of displacement Dz in mm for spring stiffness 3	225
Figure 3.60	Contour plot of displacement Dz in mm for spring stiffness 4	225
Figure 3.61	Contour plot of displacement Dz in mm for spring stiffness 5	226
Figure 3.62	Bending strain about y axis	227
Figure 3.63	Maximum bending strain	228
Figure 3.64	Parametric study on plate response	228
Figure 3.65	Comparison of experimental and analytical data for frequency	229
Figure 3.66	Comparison of experimental and analytical data for Displacement	229
Figure 3.67	Alteration in modal response due to local damage effects	230
Figure 3.68	Van der Pol plot with *dx/dt* equal to zero times y	230
Figure 3.69	Van der Pol plot with *dx/dt* equal to 0.03 times y	231
Figure 3.70	Van der Pol plot with *dx/dt* equal to 0.1 times y	231
Figure 3.71	Van der Pol plot with *dx/dt* equal to one times y	232
Figure 3.72	Poincaré map of Figure 3.68	232
Figure 3.73	Poincaré map of Figure 3.69	233
Figure 3.74	Poincaré map of Figure 3.70	233
Figure 3.75	Poincaré map of Figure 3.71	234

CHAPTER 4

Figure 4.1	The A1 Bridge at Berwick-upon-Tweed	270
Figure 4.2	HA and HB loading diagrams	271
Figure 4.3	Expansion joint located at south abutment directly above bearings	272
Figure 4.4	Accelerometer locations: typical K-shaped bracing (Section 2 shown)	273
Figure 4.5	Access cage and walkway with access ladder *in situ*	274
Figure 4.6	Accelerometer *in situ* with mounting clips	275
Figure 4.7	Analyser lay out for initial testing	275
Figure 4.8	Accelerometer 5 mounted on bearing plinth	276
Figure 4.9	Accelerometer locations: South abutment, Section 1	276
Figure 4.10	Test section location plan (Scale 1:150)	277
Figure 4.11	Analyser in position for final testing regime, test 5	278
Figure 4.12	Typical instrumentation layout: weigh-in-motion sensors and induction loops	278
Figure 4.13	WIM data logger and housing	279
Figure 4.14	Highways Agency Area 14	280
Figure 4.15	Velocity histogram for vehicles in lane 1	281
Figure 4.16	Velocity histogram for vehicles in lane 2	281
Figure 4.17	Gross vehicle weight histogram lane 1	282
Figure 4.18	Gross vehicle weight histogram lane 2	282
Figure 4.19	Axle 1 weight histogram lane 1	283
Figure 4.20	Axle 2 weight histogram lane 1	283
Figure 4.21	Axle 3 weight histogram lane 1	284
Figure 4.22	Axle 4 weight histogram lane 1	284
Figure 4.23	Axle 5 weight histogram lane 1	285
Figure 4.24	Axle 6 weight histogram lane 1	285
Figure 4.25	Axle 1 weight histogram lane 2	286
Figure 4.26	Axle 2 weight histogram lane 2	286
Figure 4.27	Axle 3 weight histogram lane 2	287
Figure 4.28	Axle 4 weight histogram lane 2	287
Figure 4.29	Axle 5 weight histogram lane 2	288

Figure 4.30	Axle 6 weight histogram lane 2	288
Figure 4.31	Vehicle momentum histogram lane 1	289
Figure 4.32	Vehicle momentum histogram lane 2	289
Figure 4.33	Kinetic energy histogram lane 1	290
Figure 4.34	Kinetic energy histogram lane 2	290
Figure 4.35	Damage factor histogram lane 1	291
Figure 4.36	Damage factor histogram lane 2	291
Figure 4.37	Time trace of background noise level	292
Figure 4.38	Frequency domain plot of Figure 4.14	292
Figure 4.39	Frequency domain plot of Figure 4.14, 0 to 50 Hz shown	293
Figure 4.40	Time domain plot for test 2 (722s -729s)	294
Figure 4.41	Frequency domain plots of Figure 4.17	295
Figure 4.42	Time domain plot for test 2 (869s - 890s)	296
Figure 4.43	Frequency domain plot of Figure 4.19	296
Figure 4.44	Time domain plot for test 3 (610s - 630s)	297
Figure 4.45	Frequency domain plot of Figure 4.21	297
Figure 4.46	Time domain plot for test 3 (830s - 860s)	298
Figure 4.47	Frequency domain plot of Figure 4.23	298
Figure 4.48	Time domain plot for test 4 (205s - 245s)	299
Figure 4.49	Frequency domain plot of Figure 4.25	299
Figure 4.50	Time domain plot for test 4 (331s -337s)	300
Figure 4.51	Frequency domain plot of Figure 4.27	300
Figure 4.52	Time domain plot for test 5 (82s - 97s)	301
Figure 4.53	Time domain plot for test Figure 4.29	302
Figure 4.54	Time domain plot for test 5 (75s - 80s)	303
Figure 4.55	Frequency domain plot of Figure 4.31	304
Figure 4.56	Time domain plot for test 5 (630s - 710s)	305
Figure 4.57	Frequency domain plot of Figure 4.33	306
Figure 4.58	Inertance FRF under 92 kN HGV load of Figure 4.16	307
Figure 4.59	Inertance FRF under 92 kN HGV load of Figure 4.18	308
Figure 4.60	Admittance FRF under 92 kN HGV load of Figure 4.16	309
Figure 4.61	Admittance FRF under 92 kN HGV load of Figure 4.18	310
Figure 4.62	Dynamic stiffness FRF under 92 kN HGV load of Figure 4.16	311

Figure 4.63 Dynamic stiffness FRF under 92 kN HGV load of Figure 4.18 312
Figure 4.64 Rocker bearing with grease escaping from housing 313
Figure 4.65 Influence lines for a Type 56 vehicle 313
Figure 4.66 Effect of average GVW on dynamic stiffness 314
Figure 4.67 Effect of average axle weight on dynamic stiffness 314
Figure 4.68 Effect of Type 56 velocity on dynamic stiffness 315
Figure 4.69 Effect of bearing stiffness on primary resonance frequency 315
Figure 4.70 Effect of bearing stiffness on displacement 316

List of Tables

CHAPTER 2

Table 2.1 Finite strip results and comparison with other methods 131
Table 2.2 Frequency response functions 132
Table 2.3 Shi *et al.* results for damage detection in beams 132
Table 2.4 Bearing defects from Allot and Lomax survey 133
Table 2.5 Change in shear modulus for elastomeric bearings 134

CHAPTER 3

Table 3.1 Stiffness values for each individual spring diameter 235
Table 3.2 Average stiffness values for springs 235
Table 3.3 Plate frequencies for variable support displacements (10 kN load) 235
Table 3.4 Plate frequencies for variable support displacements (50 kN load) 236
Table 3.5 Displacement values relating to support stiffness values 236
Table 3.6 Material and geometric properties of PMMA plate 237
Table 3.7 Accelerometer and excitation point locations 237
Table 3.8 Resonant frequencies for modal analysis testing on PMMA plate 238
Table 3.9 Results of eigenvalue analysis in FEA for PMMA plate 239

CHAPTER 4

Table 4.1	Vehicle classifications	317
Table 4.2	Vehicle speed data for traffic in lane 1	318
Table 4.3	Vehicle speed data for traffic in lane 2	319
Table 4.4	Vehicle axle loading data for traffic in lane 1	320
Table 4.5	Vehicle axle loading data for traffic in lane 2	321
Table 4.6	Maximum and minimum axle weights for vehicles in lane	322
Table 4.7	Maximum and minimum axle weights for vehicles in lane 2	323
Table 4.8	Average axle weights for vehicles in lane 1	324
Table 4.9	Average axle weights for vehicles in lane 2	325
Table 4.10	Standard deviations of axle weights for vehicles in lane 1	326
Table 4.11	Standard deviations of axle weights for vehicles in lane 2	327
Table 4.12	Parametric study of FEA model for bridge structure	328
Table 4.13	Resonance frequencies of bridge structure	328

Notation

Unless otherwise stated in the text, the symbols used in this thesis are listed below in the order: Roman characters, Greek characters, and acronyms. The units used in this thesis are Système International (SI), or derived, units where possible. For verisimilitude, imperial units are quoted where originally used by a cited author. Approximate SI conversions are provided immediately afterwards in parentheses where appropriate.

Roman characters

$a(t)$	Input signal in time domain
A	Area
$A(f)$	Input signal in frequency domain
A_e	Effective plan area of bearing
A_l	Reduced effective plan area due to loading effects
b_e	Effective width
$B(f)$	Output signal in frequency domain
$b(t)$	Output signal in time domain
c_i	Constant for Rayleigh-Ritz method
E	Young's modulus
E_b	Bulk modulus
f	Frequency
F_0	Forcing function amplitude
$\mathbf{F}$	Force matrix
g	Acceleration due to gravity
G	Shear modulus
$G_{aa}(f)$	Input signal autospectrum
$G_{bb}(f)$	Output signal autospectrum
$G_{ab}(f)$	Cross-spectrum of input and output signals
h	plate thickness
$h(t)$	Impulse response function
$H(f)$	Frequency response function

H	Horizontal movement
I	Second moment of area
k	Set of discrete frequency components up to N-1
k_s	Spring stiffness
$\overline{k_s}$	Spring stiffness when subjected to rotational displacement
K	Stiffness matrix
l_p	Force-free perimeter of bearing
l_e	Effective length
L	Plate length
M_x	Moment at x
M	Mass matrix
n	Time sample index up to N-1
N	Number of samples
N_a	Number of averages
P	Load *per* unit area of surface
S	Shape factor
t	Time
t_e	Effective thickness of individual elastomer section in compression
t_q	Total thickness of elastomer in shear
t_i	Thickness of elastomeric sections
T	Record length
T	Potential energy
T	Boundary condition matrix
$\mathbf{T}^{\mathbf{T}}$	Transpose of **T**
$V_{0,}\ V_L$	Displacement at plate support
V	Kinetic energy
V_l	Vertical loading
V_W	Volume of water
V_{total}	Total displacement
$V_{(x,\ t)}$	Vibration displacement
V_{beam}	Static beam displacement
w	Transverse displacement

$\mathbf{w}_I$	Internal displacements
W_D	Dry weight
W_W	Wet weight
x	Displacement
$\dot{x}$	Velocity
$\ddot{x}$	Acceleration
$x(t)$	Periodic time signal
$X(f)$	Frequency spectrum
Y_x	Displacement at x
$z_i(x)$	Admissible function
Z	L/2

Greek characters

α_{xh}	
α_b	Angle of rotation across bearing width
α_l	Angle of rotation across bearing length
$\gamma^2(f)$	Coherence
δ_r	Maximum resultant horizontal displacement due to δ_b and δ_l
δ_b	Maximum horizontal displacement across bearing width
δ_l	Maximum horizontal displacement across bearing length
ε	Strain
ε_q	Shear strain due to translational movement
ε_c	Nominal strain due to compressive loads
ε_α	Nominal strain due to angular rotation
ε_t	Sum of nominal strains
λ	Eigenvalue
μ	Mass *per* unit area of plate surface
ρ	Mass density *per* unit area

υ	Poisson's ratio
ϕ_r	Mode shape function
σ	Direct stress
τ	Shear stress
ω	Angular frequency
Ω	Forcing function frequency
∇^4	Biharmonic operator

Acronyms

AE	Acoustic emission
CCLD	Constant current line drive
CWT	Continuous wavelet transform
DAF	Dynamic amplification factor
DfT	Department for Transport
DLV	Damage location vector
DQM	Differential quadrature method
DSC	Discrete singular convolution
DWT	Discrete wavelet transform
FD	Finite difference
FE(A)	Finite element (analysis)
FDD	Frequency domain decomposition
FRF	Frequency response function
HA	Highways Association
HGV	Heavy goods vehicle
NDT	Non-destructive testing
OMA	Operational modal analysis
PFM	Proportional flexibility matrix
PIR	Principal inspection report
PMMA	Polymethylmethacrylate

PSD	Power spectral density
SASW	Spectral analysis of surface waves
SSI	Stochastic subspace integration
TEDS	Transducer electronic data sheets
T(R)RL	Transport (& Road) Research Laboratory
WIM	Weigh-in-motion
WPT	Wavelet packet transform

CHAPTER 1

Introduction

1 General introduction

Vibrations caused by traffic loading are a major source of damage to highway bridges, especially in and around the area of support in single-span bridges. In highway bridges, elastomeric bearings are used to take the force actions from the superstructure into the substructure and to allow horizontal and vertical movement. The purpose of this research is to develop an understanding of the effect of traffic induced vibrations on critical elements at the deck slab/abutment interface.

Highway bridges are subjected to forced vibration due to moving vehicles of varying types throughout the duration of their service life. To transfer the loading generated by the vehicles passing over the bridge, a bearing is placed between the bridge super-structure and the bridge abutments. These bearings come in many different varieties, from simple pad bearings (Figure 1.1), pot bearings (Figures 1.2 and 1.3), rocker bearings (Figure 1.4), to large-scale roller bearings (Figure 1.5), and are designed specifically to cope with vertical and lateral movement of the structure. However, these types of bearings are not designed to withstand dynamic loading from vehicles, but primarily static loading. Figure 1.6 (b) shows the different types of loading an elastomeric pad can experience during its service life; (i) shear forces, (ii) rotational forces and (iii) compressive loading. Figure 1.7 provides the idealised stress distribution diagrams for the three loading cases shown in Figure 1.6 (b). Failure of bearings is a significant cause of damage to highway bridge structures. Providing a framework of

guidelines that allow early detection of bearing deterioration would result in large savings, in both a quantitative and qualitative sense.

1.1 Structural dynamics

Structural dynamics is the engineering discipline concerned with the behaviour of structures subjected to dynamic loading, or forced vibration, such as a sinusoidal harmonic excitation, impulse excitation or free vibration.

Modal testing allows experimental determination of the modal parameters of a structure, including resonant frequency, damping and mode shape. In most cases the first few modes of vibration are the most significant, as they result in larger displacements than those in the higher frequency range.

1.2 Modal analysis

There are two distinct separate types of modal analysis: operational modal analysis and classic modal analysis. Classic modal analysis determines the modal parameters of a structure as a relationship between the input and output of a system which are commonly referred to as frequency response functions (FRFs). Modal parameters are then extracted from the FRFs by curve-fitting algorithms. The most commonly used FRFs are compliance, mechanical mobility and dynamic stiffness. Choi *et al.*[1.1] use the compliance method to locate damage in structures which manifest themselves through a shift in frequency and alteration of modeshape. Other researchers have used this method of shifts in resonance frequency to locate and quantify damage in discrete systems[1.2].

To validate the initial hypothesis of bearing degradation affecting dynamic response, a small-scale model consisting of a Perspex® plate with variable support conditions was tested using classical modal analysis techniques[1.3]. The small-scale test is to be viewed as nothing more than a simplification of a bridge arrangement, and is not intended to model actual behaviour of a bridge, but simply to prove the concept of the effect of varying the stiffness of end supports. Figure 1.8 shows the original undeformed mesh and plate geometry, including support locations. Figures 1.9 to 1.12 show the effects of variable support conditions on the modeshape of the plate used during the small-scale testing. Figures 1.9 and 1.11 show the unscaled modeshape obtained for the third frequency of the arrangement with Spring 1 and Spring 5 as the support conditions, and Figures 1.10 and 1.12 show contour plots of displacement values in the vertical, Z-direction.

The problem can be reduced to a simple plate analysis. Research in this field is well advanced from initial investigations by Leissa[1.4] using the common Rayleigh-Ritz method[1.5] which listed all possible frequencies for the classical support conditions, to the more complex analysis involving elastic boundary conditions by the superposition method[1.6].

Operational modal analysis is a newer method and does not rely on an input signal, and is therefore known as "output only analysis". Rather than using a recorded force input, "output only analysis" determines the modal parameters of a structure using the ambient vibrations, caused in this case by vehicle movement. The full-scale experimental data presented relate to testing of a highway bridge currently in use on the A1 at Berwick-upon-Tweed. This chapter combines details of the Principal Inspection Report (PIR),

traffic count, vehicle speed, and axle weight data derived from *in situ* induction loops and weigh-in-motion sensors[1.7 & 1.8], followed by data arising from the non-destructive testing (NDT) of the bridge. The set of NDT results are intended to represent a baseline state of condition for further measurements. Brenner *et al.*[1.9] outline a method for bridge analysis and design based on the definition of a baseline model which reflects the behaviour of the structure as a whole rather than the elemental approach currently adopted.

Although the bridge tested here has been in use for over twenty years, the bearings should be functioning as intended. The accuracy of results for this portion of testing is of course reliant upon the correct parameter identification, modal data included in the identification analysis can affect the accuracy of results. One method of damage measurability was proposed[1.10], where damage is estimated quantitatively. The method is based on the sensitivity of a residual vector to the structural damage and the effect of noise on the measurements.

Two papers by Yang *et al.*[1.11 & 1.12] outline a method for determining the bridge frequencies using the dynamic response of a passing vehicle. The papers show an initial numerical treatment of the problem, followed by the experimental results obtained from testing on a structure. The method highlights the fundamental frequency only. The overall dynamic response of a bridge is affected by many parameters. Researchers have investigated the effects of bridge running surface texture, developing a three-dimensional analysis approach to define the response of the bridge structure[1.13]. What is apparent from data analysed from the experimental stage at Berwick-upon-Tweed is that the largest HGVs cause the highest proportion of damage to the bridge. Green and

Cebon[1.14] introduce the effects of HGVs on bridge structures, and recent research has also highlighted the effects of superloads on structures[1.15]. Superloads tend to be exceptionally rare and can range from large cranes to turbines.

Two methods of determining the modal parameters using operational modal analysis are available; frequency domain decomposition (FDD) and stochastic sub-space identification (SSI), in the time domain. Many papers outlining applications of the two methods are available[1.16 - 1.18], and the three cited herein highlight the key features of FDD and SSI methods. The two methods allow a graphical representation of mode shapes at each resonant frequency to be visualised. In general, the SSI technique will give the most accurate results, but a combination of the two is advisable to validate experimental results. Order estimation and the detection of spurious modes can often affect the accuracy of the two techniques. Zhang *et al.*[1.19] propose a method using component energy as an identifier rather than matrix values, and a stabilisation diagram utilising the Hankel matrix[1.20].

However, for this research, the mode shapes are not considered to be of any real importance. Rather the actual value of frequency and magnitude of acceleration, velocity and displacement are of interest as any changes in structural behaviour due to material properties will manifest themselves as a change in frequency or magnitude of acceleration, velocity or displacement. Similar research using this method, albeit applied to planar trusses as opposed to bridge structures, has been developed by Wang *et al.*[1.21].

Health monitoring is an important process in maintaining highway structures. Recent advances in transducer technology allow the early detection of deterioration in structural integrity and the prevention of catastrophic failure, especially when applied to large-scale structures[1.22]. One proposed method for health monitoring is based on a global fixity index, where any alteration in the structural modal flexibility matrix comes from a change in displacement of the structure[1.23].

1.3 Euler-Bernoulli beam / Rayleigh-Ritz method

Initial research into the effects of variable end conditions on the dynamic response of a plate structure incorporated a simple beam deflection equation analysis, combined with the Rayleigh-Ritz method for determining resonance frequencies. Varying the displacement of the supports, which is related to the support stiffness, allows a general value of the fundamental resonance frequency of a system to be established. The reason for undertaking this task was to apply end conditions which would mimic the characteristics of bridge bearings that would deflect when subjected to movement induced by traffic loading. The deflection is dependent on the stiffness of the bearings; therefore the effect of degradation in bearing performance could be simulated through the change in stiffness.

Similar methods to this have been employed by researchers investigating the effects of moving loads on bridges supported by elastomeric bearings. Methods outlined elsewhere[1.24 & 1.25] use essentially the same premise of setting the bearing stiffness, assuming a shape function based on beam theory and the flexural rigidity of the beam combined with the stiffness. In this case the method is applied to bridges subjected to moving train loads, but could simply be applied to highway bridges.

Research into bearing defects in the UK by Allot & Lomax[1.26] highlighted the fact that almost 94% of bearings had at least one defect. Each bearing type, and defect type, is listed with respect to age and other parameters such as temperature. The report shows that older bearings show an increased extent of damage, particularly in terms of bulging or splitting. Recent research carried out in the United States[1.27] on the condition of bearings after 40 years in service indicates that the pads tested still performed adequately. In addition to the visual inspection technique used by Allot & Lomax, shear and durometer testing were used to determine the effects of fatigue. These tests indicated that the bearings had increased in stiffness and also had an increased shear modulus, almost two times the specified value.

1.4 Finite element analysis

Finite element analysis (FEA) is a method for numerical solution of field problems, which requires that spatial distribution (in x, y, z coordinates) of one or more dependant variables (e.g. stress or strain) be determined. Mathematically, this can be described by a series of differential equations or an integral equation. The FEA method is a numerical analysis technique used to discretise a large problem, such as a bridge, into smaller sections, visualised through a mesh, which are simpler to analyse, thus reducing the computational power required. FEA lends itself to dynamic analysis, and as a result, recent advances from the original h-type analysis, which uses linear first-order functions to represent the field variables, to the p-type method, where the field variables are represented by higher-order polynomials, have resulted in researchers applying this method to vibration problems. Dalenbring and Zdunek[1.28] highlight the differences between the methods and the possible advantages of applying the p-version FEA. Combining the two types of FEA results in the hp-version which is based on shifted

Legendre orthogonal polynomials rather than the lower order polynomials of the h-version results in a more accurate solution as the polynomial order is increased simultaneously with mesh refinement. Houmat uses this method to analyse the three-dimensional behaviour of plates[1.29].

FEA is used to compare results obtained experimentally to those expected from analytical methods. In this thesis the FEA is used to compare frequency values obtained for each arrangement, modeshapes [Figures 1.9 to 1.12] and other parameters such as stress and strain behaviour due to harmonic loading, Figures 1.13 to 1.16. Figures 1.13 and 1.14 show contour plots of bending strain due to applied loading at time 0.1 s from the total analysis time of 0.4 s for Spring 1 and Spring 5. Figures 1.15 & 1.16 show graphs of the total duration of analysis for the two support conditions.

FEA is often used in conjunction with experimental data obtained to produce accurate solutions for dynamic analysis of complex problems. This technique is known as modal updating. Teughels and De Roeck use the technique to locate and quantify damage to a highway bridge currently in service in Switzerland[1.30]. Damage in the structure is represented by a change in the Young's and shear moduli, which are distributed over the model using linear piecewise approximation functions.

Other applications of FEA are to provide a damage indication and life-time estimate of structures. Kratzig develops this method[1.31] by applying it to three examples of damaged structures, then predicting the estimated life of the structure, which is effectively modal updating.

1.5 Research objectives

The main objective of this research is to determine the effects of a change in the dynamic response of highway bridges due to degradation of the bearings. In this regard, the following objectives will be considered:

1. It is intended that a set of guidelines be developed to predict optimum replacement times of bridge bearings before any serious damage be done to the structure as a whole.

2. The analysis of the system's dynamic behaviour will be developed through small-scale testing, using a Perspex® plate with variable support conditions.

3. The model will be used to describe the effects of varying the support stiffness.

4. The small-scale testing will be validated using the commercially available Finite Element Analysis package LUSAS v13[1.32].

5. Full-scale testing is to be used to determine a baseline level of condition for the A1 bypass bridge at Berwick-upon-Tweed.

6. The dynamic response due to traffic loading is to be shown through FRFs which describe the dynamic properties of the structure.

1.6 Outline of thesis

A method of determining the variation in dynamic response of a highway bridge due to degradation of the elastomeric bearing supports has been developed. The theoretical model has been tested, and response data obtained from a highway bridge in current service on a major trunk road over a river is presented as a baseline level of response for the structure. The information gathered has been presented graphically allowing detailed examination of the variation in response to be viewed accurately.

Chapter 2 presents a critical review of current relevant literature. Research involving modal analysis, finite element analysis, structural health monitoring, damage detection, analysis of plate sections and bridge bearings have all been considered.

Chapter 3 concentrates on the modal analysis and finite element analysis of the small-scale model tested in the laboratory. Initial investigations of plate behaviour in several common support conditions, with varying degrees of fixity, are presented. The effect of variation in support stiffness is shown, initially deriving the natural frequencies of each arrangement, and then performing a forced vibration test at a series of frequencies, by recording the difference in amplitude of acceleration at several locations on the plate. Finite element analysis of each support arrangement is presented, showing the eigenvalue analysis used to evaluate natural frequencies and mode shapes. A transient loading finite element analysis of the plate with variable end-conditions is also shown. Comparison of the modal analysis and finite element analysis results are made to illustrate the application of FEA on a larger scale.

Chapter 4 presents the data collected from large-scale testing performed on the highway bridge at Berwick-upon-Tweed. The modal analysis data recorded and post-processed is shown in graphical and tabular form to allow comparison between the series of data and individual events within those data. Data obtained from a weigh-in-motion (WIM) sensor located on the approach to the bridge is also displayed to allow specific events captured in the modal analysis to be attributed to a vehicle type and load, and FRFs be determined to describe the dynamic properties of the structure.

Chapter 5 presents the conclusions to be drawn from the research contained within this thesis. Recommendations for further research are presented.

References

1.1. Choi S. Park S and Stubbs N. Nondestructive damage detection in structures using changes in compliance. *Int. J. Solids Struct.*, 2005, **42(15)**, 4494-4513.

1.2. Dilena M. & Morassi A. Damage detection in discrete vibrating systems. *J. Sound Vib.,* 2006, **289(4)**, 830-850.

1.3. Swan I.P., Fairfield C.A. and Reid D.B. Modelling highway bridge vibrations: the effect of support conditions. *Insight*, 2005, **47(7)**, 409-413.

1.4. Leissa A.W. The free vibration of rectangular plates. *J. Sound Vib.*, 1973, **31(3)**, 257-293.

1.5. Ritz W. Theorie der Transversalschwingungen einer quadratischen Platte mit freien Rändern. *Annalen der Physik*, 1909, **28**, 737-786.

1.6. Gorman D.J. Free in-plane vibration analysis of rectangular plates with elastic support normal to the boundaries. *J. Sound Vib.,* 2005, **285(4)**, 941-966.

1.7. Wang T.-L., Liu C., Huang D. and Shahawy M. Truck loading and fatigue damage analysis for girder bridges based on weigh-in-motion data. *Proc. Am. Soc. Civ. Engnrs, J. Struct. Engng*, 2005, **10(1)**, 12-20.

1.8. Swan I.P., Fairfield C.A. and Reid D.B. The dynamic response of the Berwick-upon-Tweed bypass bridge. *Proc. Inst. Civ. Engnrs, J. Bridge Engng. Under Review*, 2006.

1.9. Brenner B., Sanayei M., Lattanzi D. and Bell E.S. Defining a baseline model for bridge analysis and design. *Proc. 85th TRB Annual Meeting,* January 22-26, Washington D.C., 2006.

1.10. Xia Y. & Hao H. Measurement selection for vibration-based structural damage identification. *J. Sound Vib.*, 2000, **236(1)**, 89-104.

1.11. Yang Y.B., Lin C.W. and Yau J.D. Extracting bridge frequencies from the dynamic response of a passing vehicle. *J. Sound Vib.*, 2004, **272(3)**, 471-493.

1.12. Lin C.W. and Yang Y.B. Use of a passing vehicle to scan the fundamental bridge frequencies: an experimental verification. *Engng Struct.*, 2005, **27**, 1865-1878.

1.13. Kim C.W., Kawatani M. and Kim K.B. Three-dimensional dynamic analysis for bridge-vehicle interaction with roadway roughness. *Comp. Struct.*, 2005, **83(20)**, 1627-1645.

1.14. Green M.F. & Cebon D. Dynamic response of highway bridges to heavy vehicle loads: theory and experimental validation. *J. Sound Vib.*, 1994, **170(1)**, 51-78.

1.15. Wood S., Akinci N.O., Liu J. and Bowman M.D. Analysis and instrumentation of a steel bridge for investigating the effects of superloads. *Proc. 85th TRB Annual Meeting,* January 22-26, Washington D.C., 2006.

1.16. Fragakis Y. and Papadrakakis M. The mosaic of high performance domain decomposition methods for structural mechanics: formulation, interrelation and numerical efficiency of primal and dual methods. *Comp. Methods Appl. Mech. Engng*, 2003, **192(35)**, 3799-3830.

1.17. Xiao H., Bruhns O.T., Waller H. and Meyers A. An input/output-based procedure for fully evaluating and monitoring dynamic properties of structural systems via a subspace identification method. *J. Sound Vib.*, 2001, **246(4)**, 601-623.

1.18. Cauberghe B., Guillaume P., Pintelon R. and Verboven P. Frequency-domain subspace identification using FRF data from arbitrary signals. *J. Sound Vib.*, 2006, **290(3)**, 555-571.

1.19. Zhang Y., Zhang Z., Xu X. and Hua H. Modal parameter identification using response data only. *J. Sound Vib.*, 2005, **282(2)**, 367-380.

1.20. Hankel H. Über eine besondere Classe der symmetrischen Determinanten. *Dr Phil. Thesis, Univ. Leipzig, Göttingen*, 1861.

1.21. Wang X., Hu N., Fukunaga H. and Yao Z.H. Structural damage identification using static test data and changes in frequencies. *Engng Struct.*, 2001, **23(6)**, 610-621.

1.22. Ko J.M. and Ni Y.Q. Technology developments in structural health monitoring of large-scale bridges. *Engng Struct.*, 2005, **27(12)**, 1715-1725.

1.23. Patjawit A. and Kanok-Nukulchai W. Health monitoring of highway bridges based on a Global Flexibility Index. *Engng Struct.*, 2005, **27(11)**, 1385-1391.

1.24. Li. W.L. Dynamic analysis of beams with arbitrary elastic supports at both ends. *J. Sound Vib.*, 2001, **246(4)**, 751-756.

1.25. Yau J.D., Wu Y.-S. and Yang Y.-B. Impact response of bridges with elastic bearings to moving loads. *J. Sound Vib.*, 2001, **248(1)**, 9-30.

1.26. Allot & Lomax, Consulting Engineers. Bridge bearing survey and problem assessment. *Transport & Road Research Laboratory, Contractor Report CR260, Crowthorne*, 1991.

1.27. Potter W., Ansley M. and Mtenga P. Condition of elastomeric bearing pads after 40 years of service. *Proc. 85th TRB Annual Meeting,* January 22-26, Washington D.C., 2006.

1.28. Dalenbring M. & Zdunek A. On the use of three-dimensional h- and p-version finite elements in solving vibration response problems. *J. Sound Vib.*, 2005, **288(5)**, 907-929.

1.29. Houmat A. Three-dimensional free vibration analysis of plates using the h-p version of the finite element method. *J. Sound Vib.*, 2006, **290(3)**, 690-704.

1.30. Teughels A. & De Roeck G. Structural damage identification of the highway bridge Z24 by FE model updating. *J. Sound Vib.*, 2004, **278(3)**, 589-610.

1.31. Krätzig W.B. & Petryna Y.S. Structural damage and life-time estimates by nonlinear FE simulation. *Engng Structs*, 2005, **27**, 1726-1740.

1.32. LUSAS v13 User Manual, *LUSAS for Windows*®. FEA Ltd, Kingston-upon-Thames, 1999.

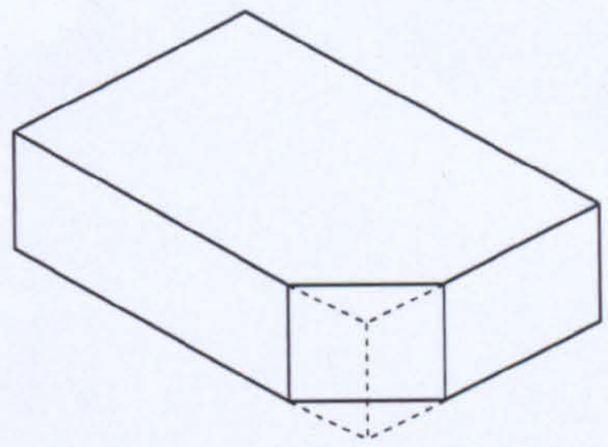

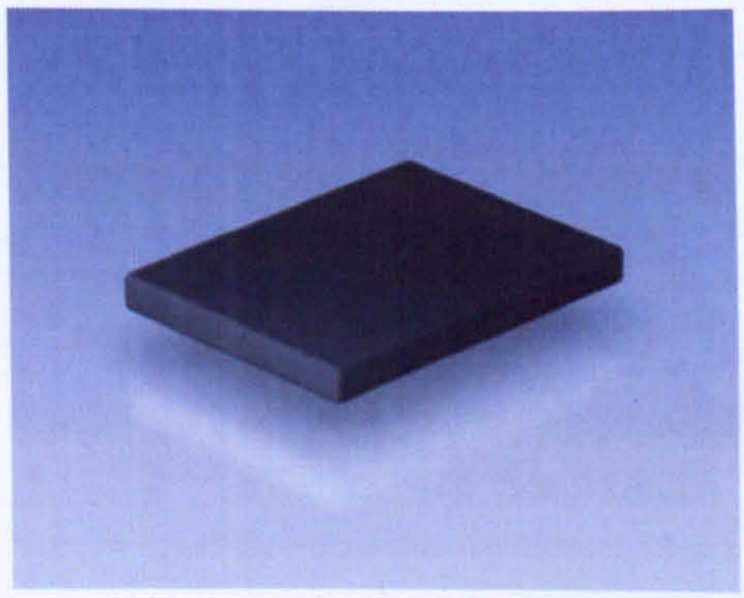

Plain rubber bearing

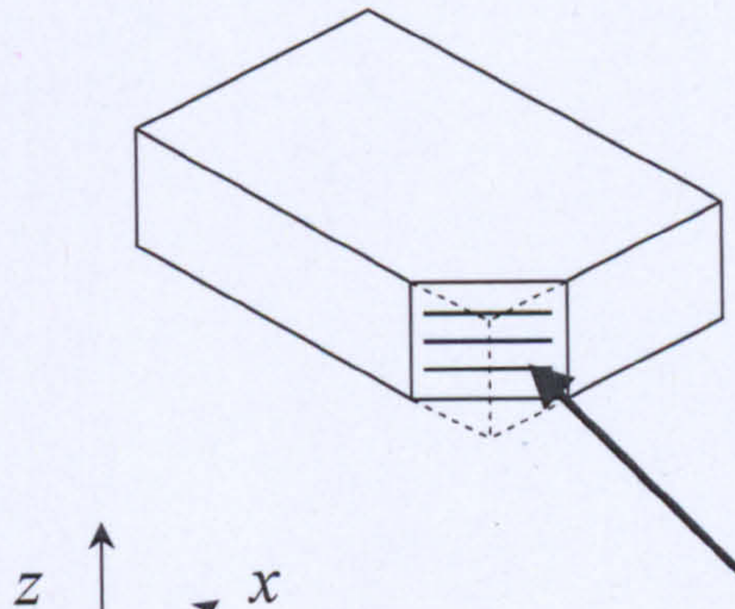

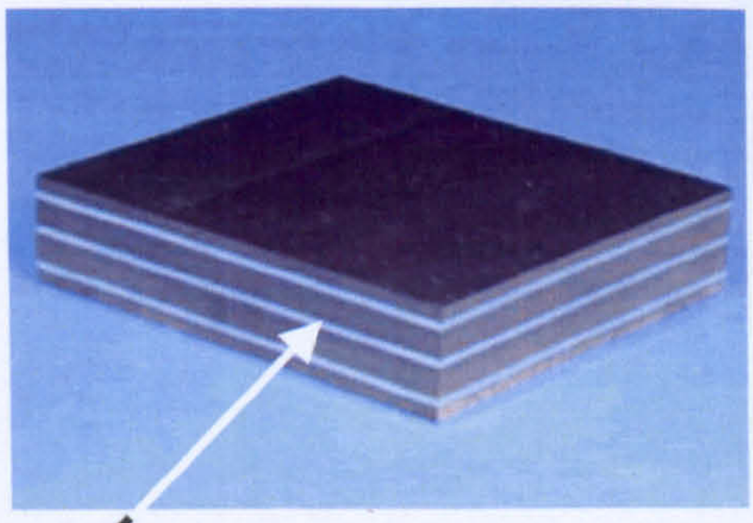

Reinforcement (steel plates)

Laminated rubber bearing

Figure 1.1 Simple elastomeric bearing pad

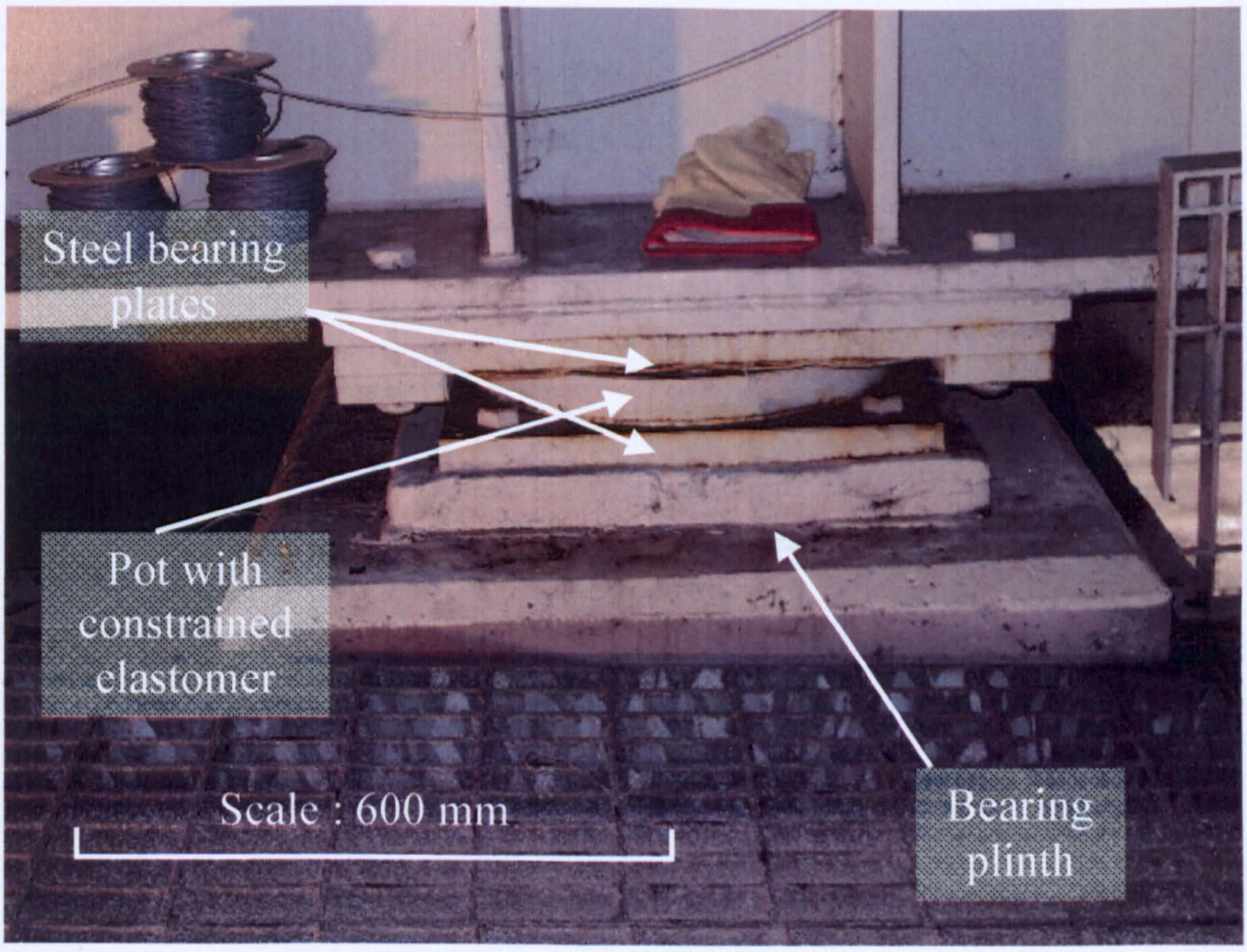

Figure 1.2 Constrained pot bearing: *in situ*

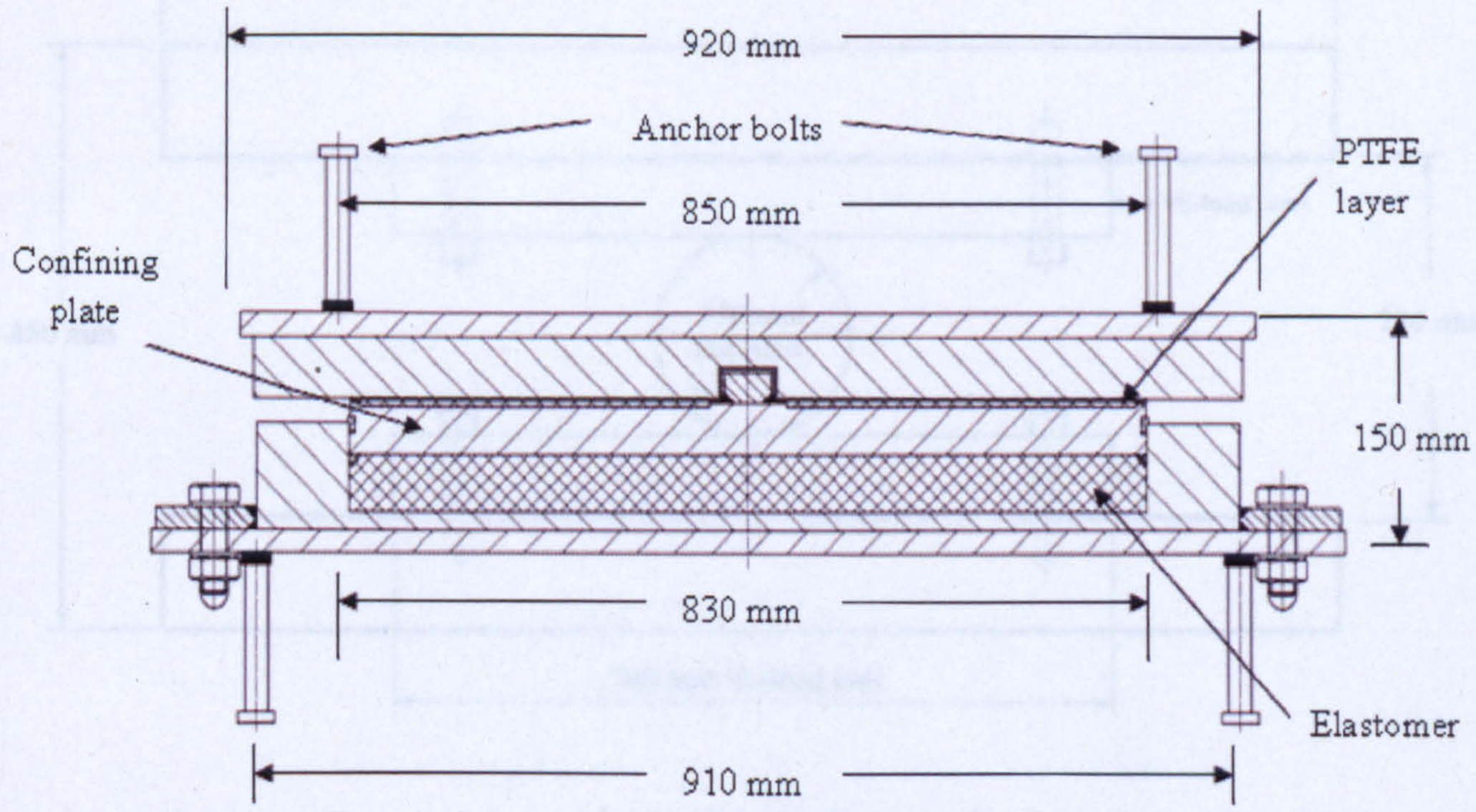

Figure 1.3 Pot bearing - typical engineering drawing with general dimensions

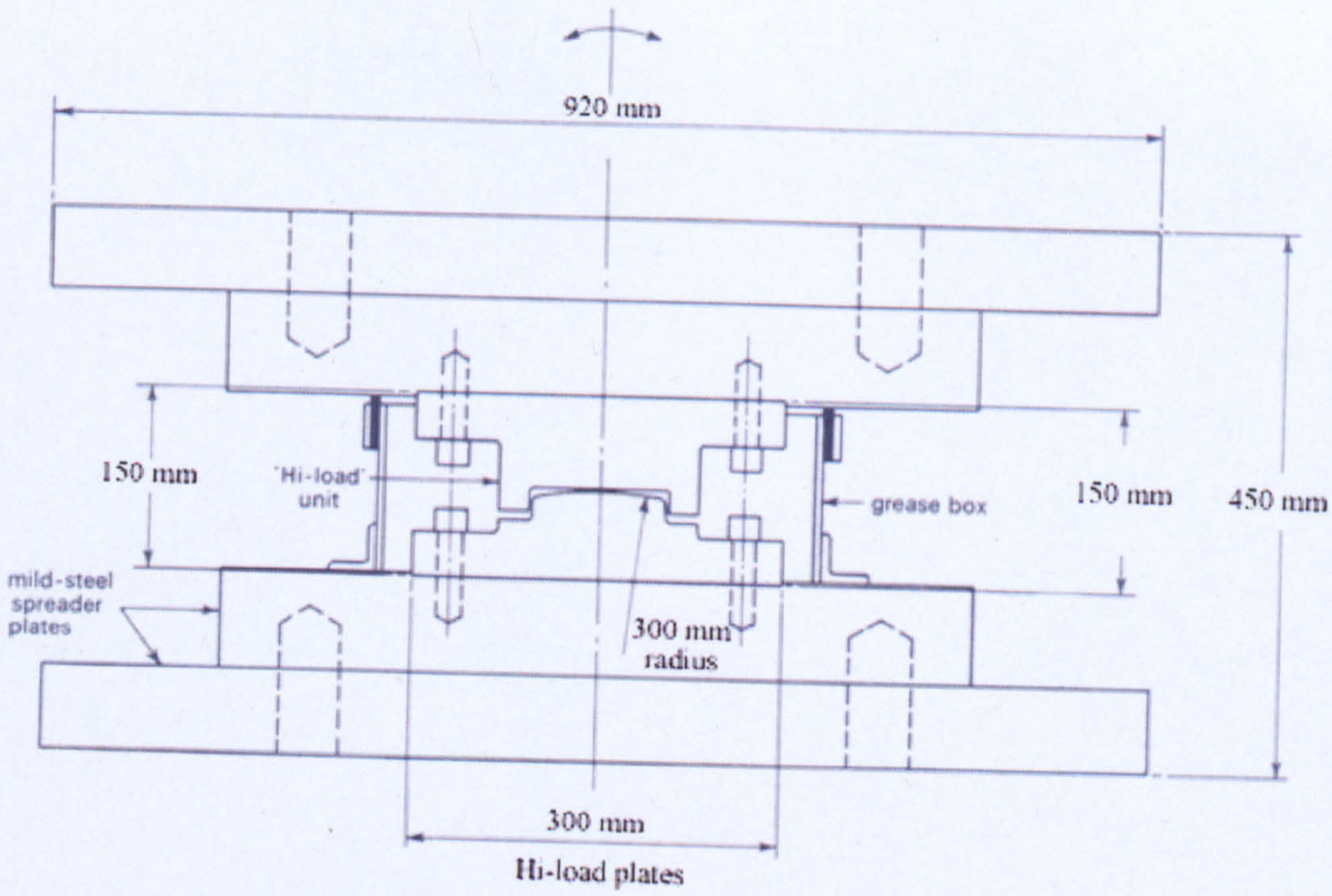

Figure 1.4 Typical high-load rocker bearing with general dimensions

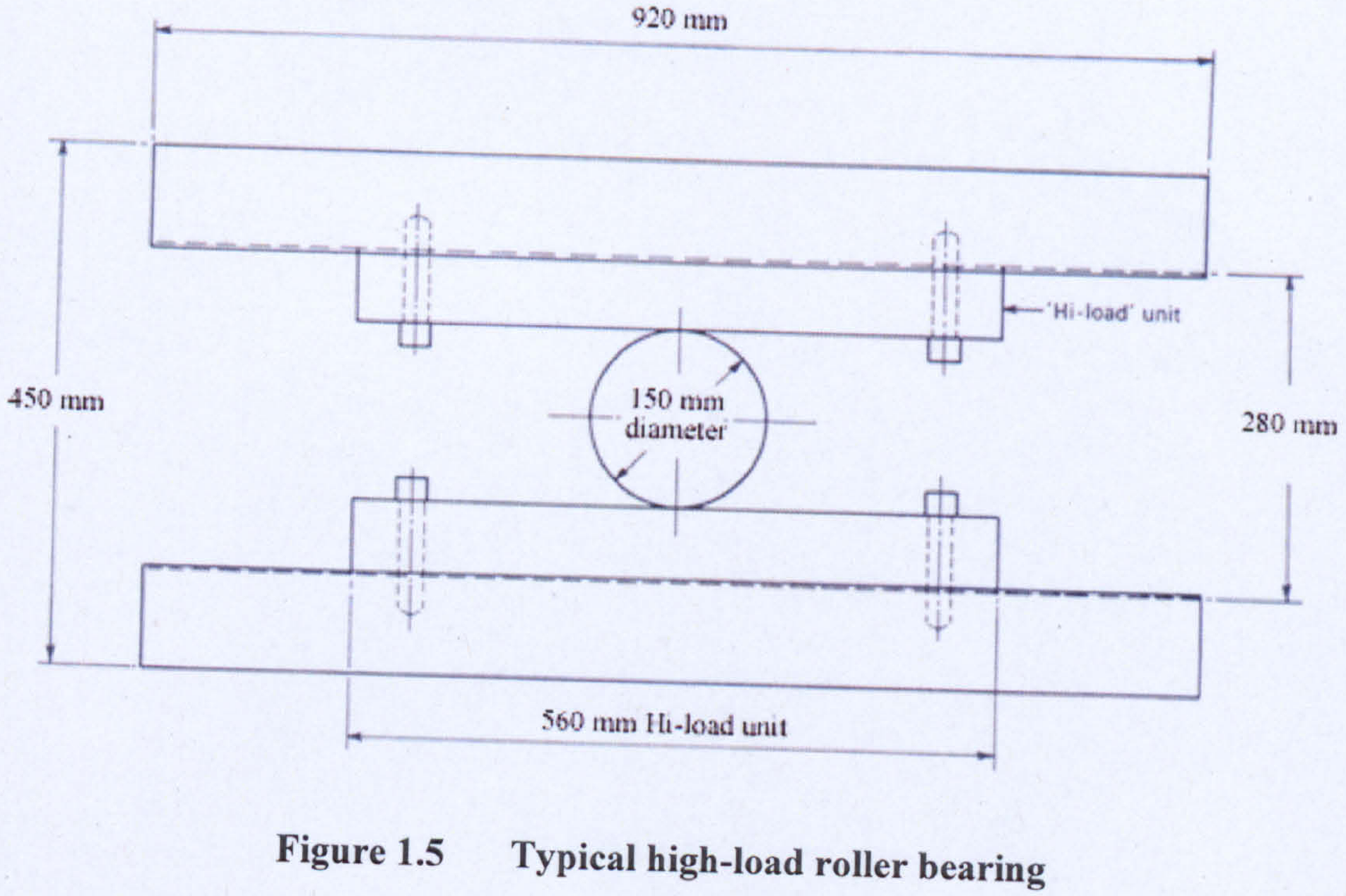

Figure 1.5 Typical high-load roller bearing

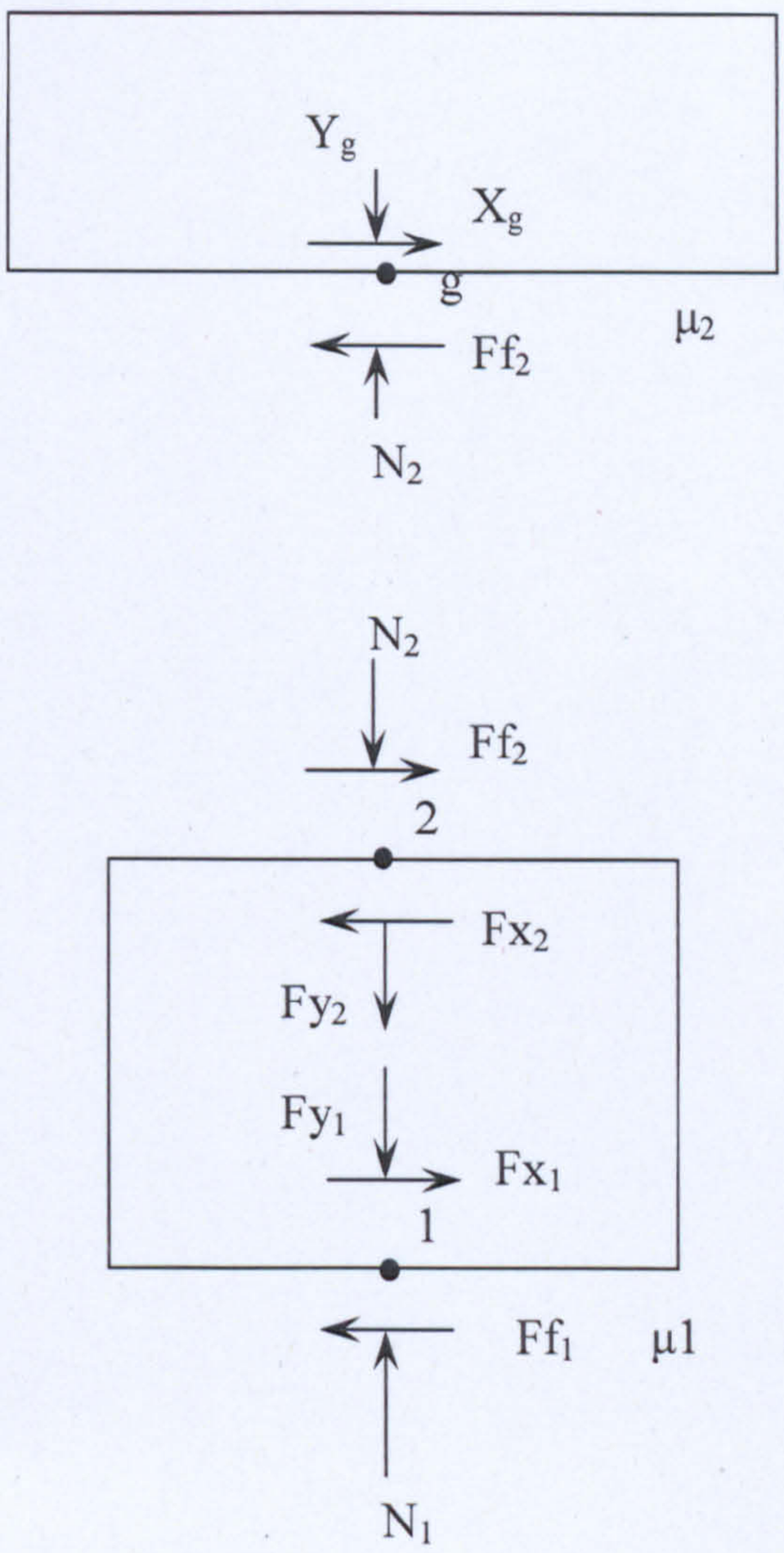

(a)

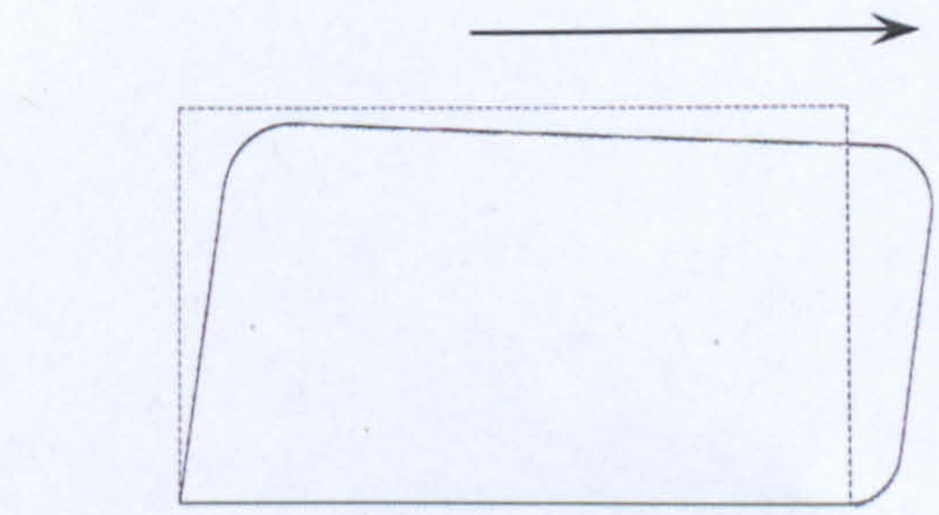

(i) Shear

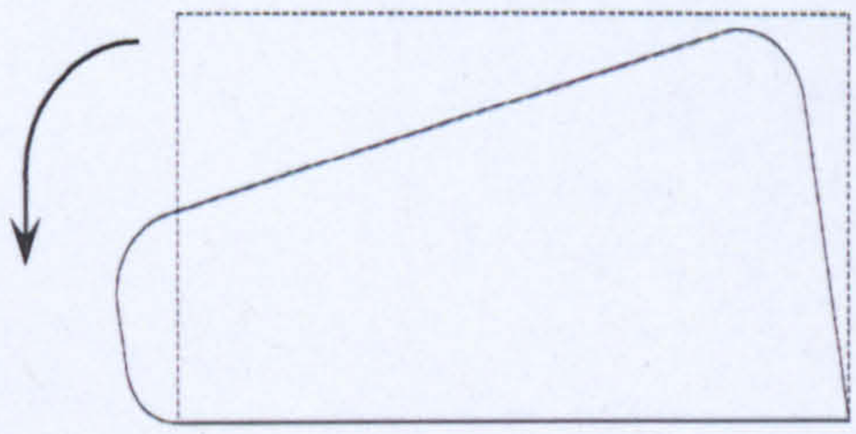

(ii) Flexure

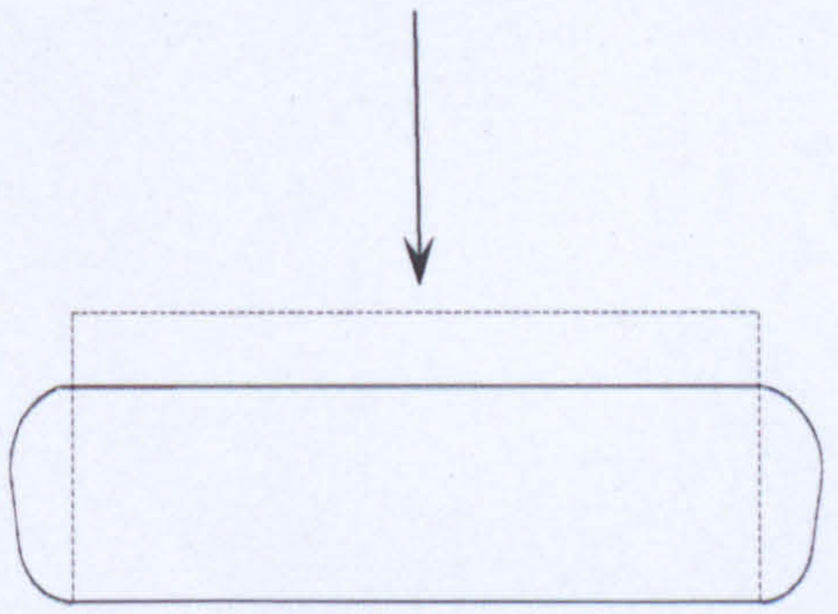

(iii) Compression

(b)

Figure 1.6 (a and b) Loading regimes for standard elastomeric pad.
Figure (a) shows the sign convention used throughout the remainder of the text. Point g is the contact point between girder and bearing, Points 1 and 2 are contact points between the bearing and girder, then bearing and concrete plinth. X_g and Y_g are the horizontal and vertical loads, Fx_1 and Fx_2 are shear forces, Fy_1 and Fy_2 are compressive forces, Ff_1 and Ff_2 are frictional forces calculated using the Coulomb friction law, N_1 and N_2 are the normal forces and μ_1 and μ_2 are the coefficients of friction at the two surfaces.

Figure (b) shows; (i) deflected shape due to applied shear force, (ii) deflected shape due to applied rotational moment and (iii) deflected shape due to compressive force.

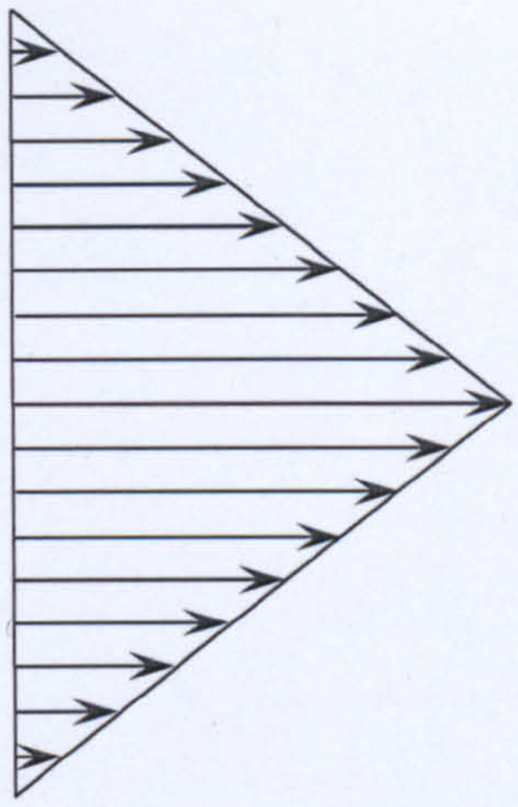

(i)

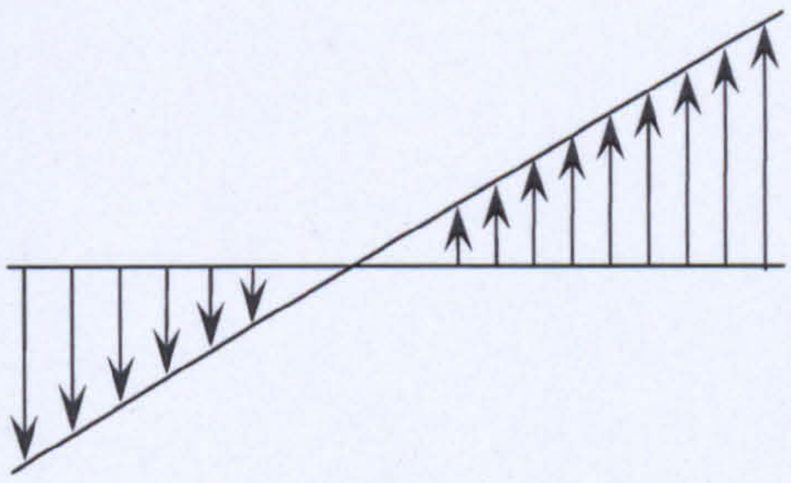

(ii)

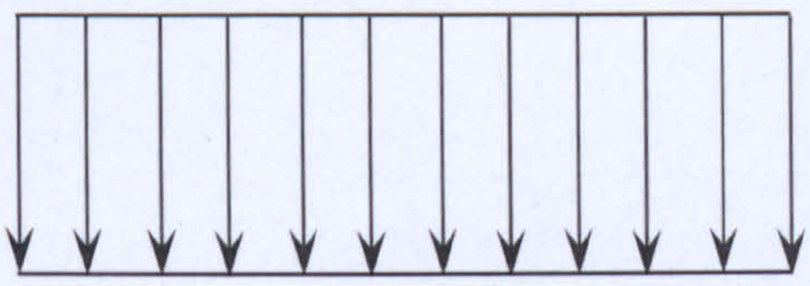

(iii)

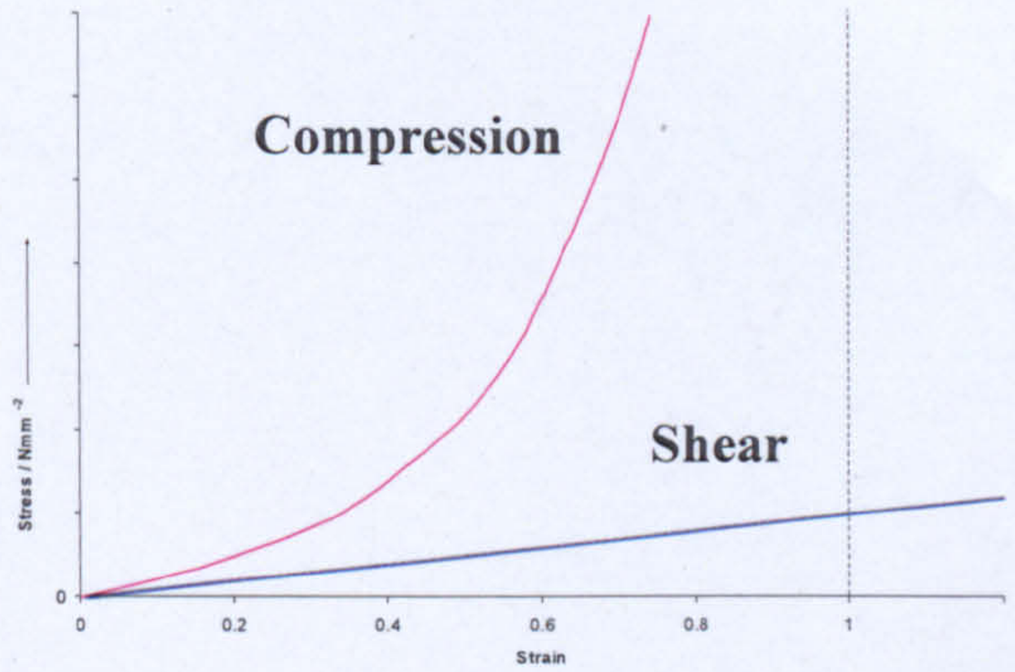

(iv)

Figure 1.7 Shear stress distributions of corresponding loading applied as in Figure 1.6 b (i, ii, iii).

Figure 1.7 (i) shows the stress distribution due to shear loading.
Figure 1.7 (ii) shows the distribution due to a rotational moment loading.
Figure 1.7 (iii) shows the distribution due to direct compressive loading.
Figure 1.7 (iv) shows a typical stress against strain curve for rubber materials.

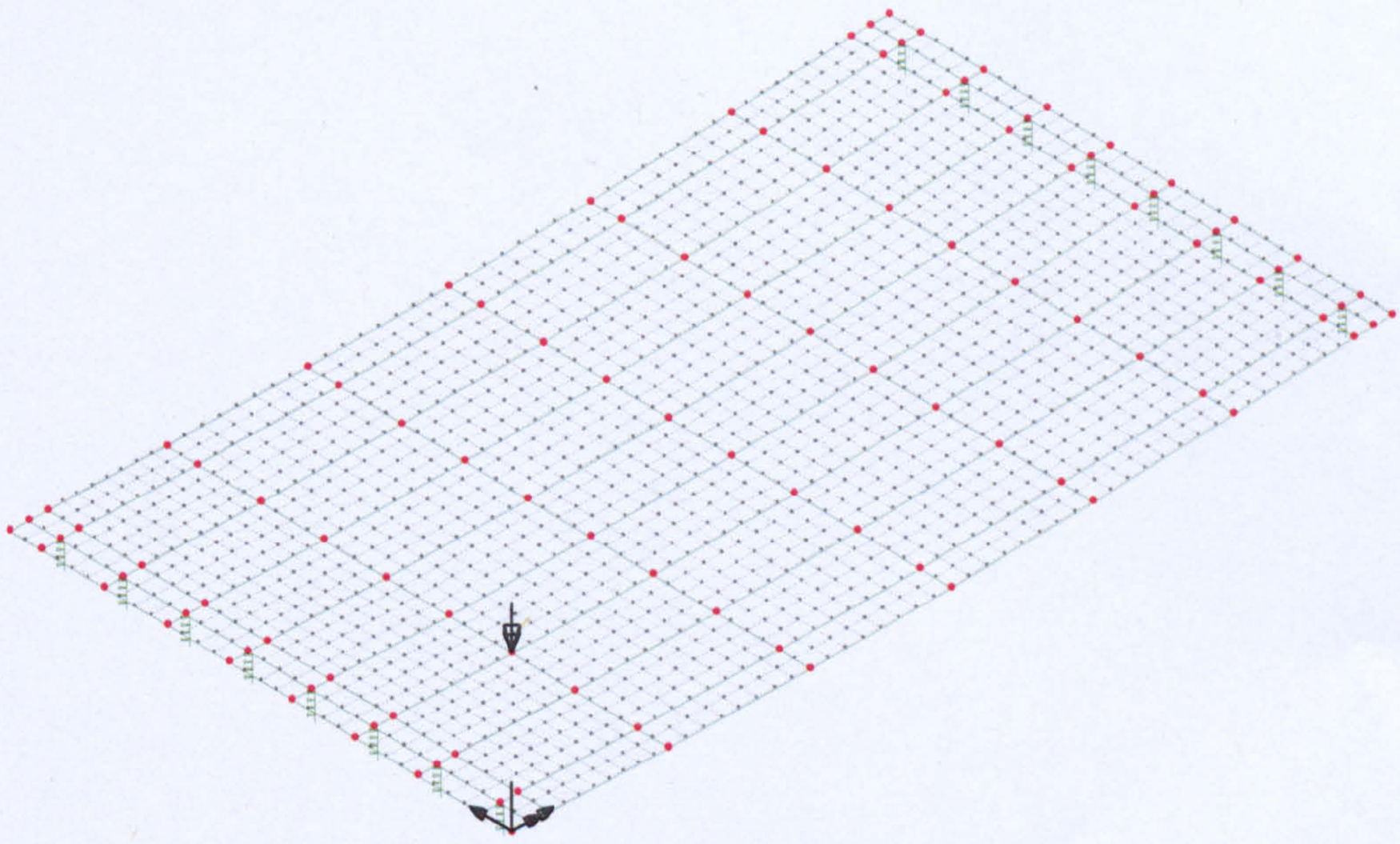

Figure 1.8 **Undeformed plate geometry, elements, node points, mesh and spring support locations. Location of loading for one transient test shown as black arrow (0.25, 0.25, -0.0111)**

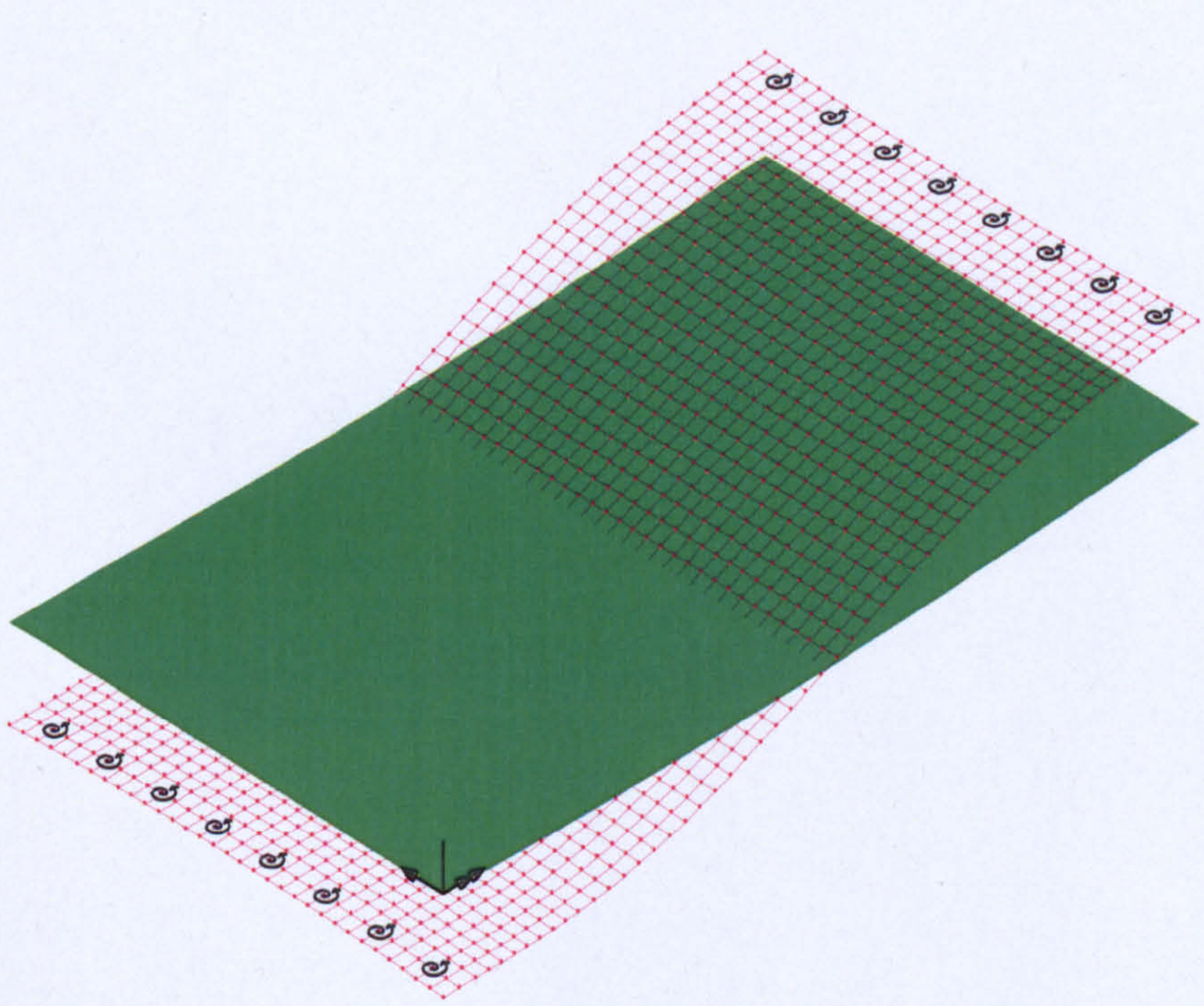

Figure 1.9 **Modeshape 3 - Perspex plate - spring stiffness 1. Black circles correspond to spring support location on deformed geometry.**

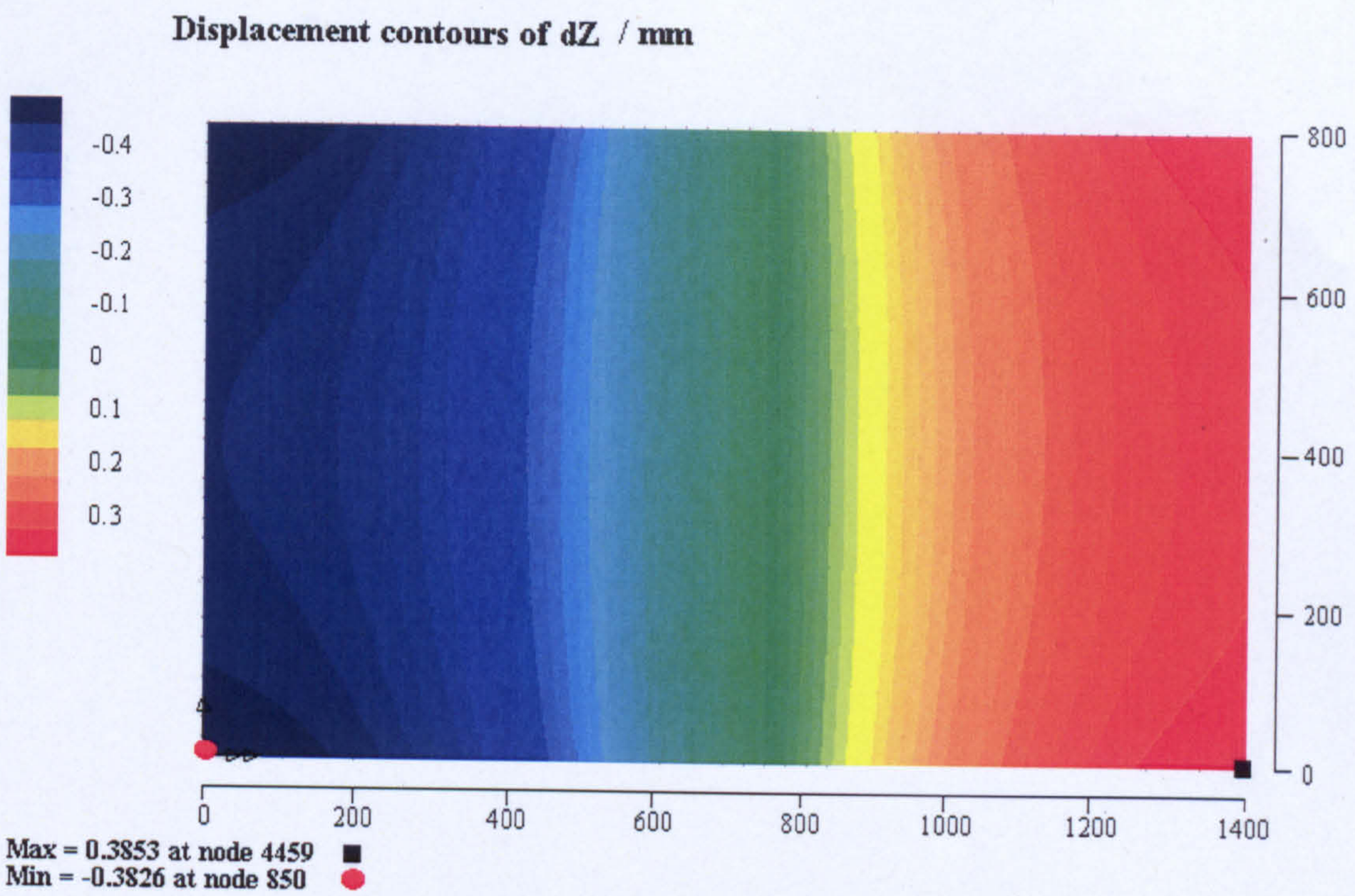

Figure 1.10 Contour plot - modeshape 3 - spring stiffness 1

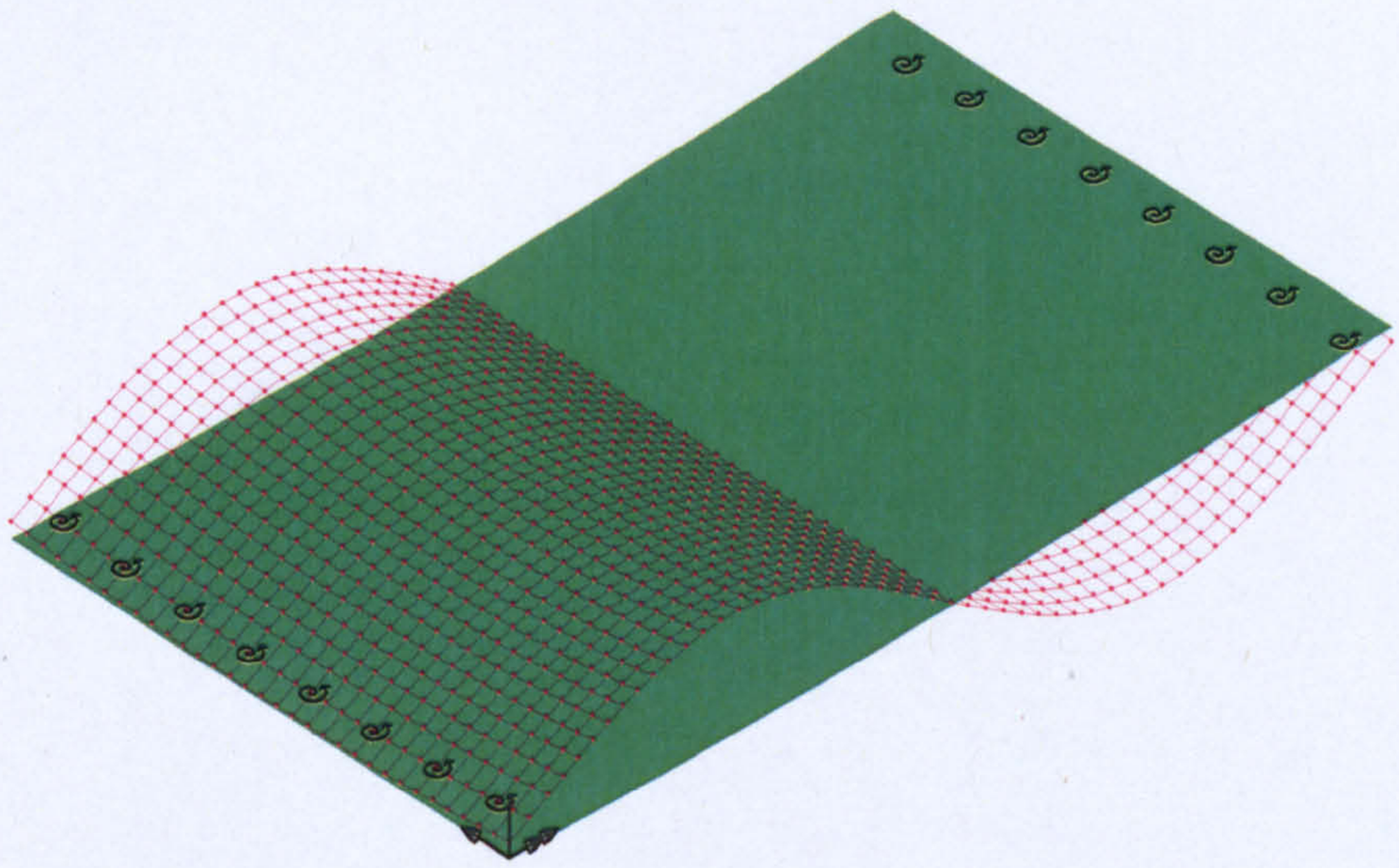

Figure 1.11 Modeshape 3 - Perspex plate - spring stiffness 5. Black circles correspond to spring support location on deformed geometry.

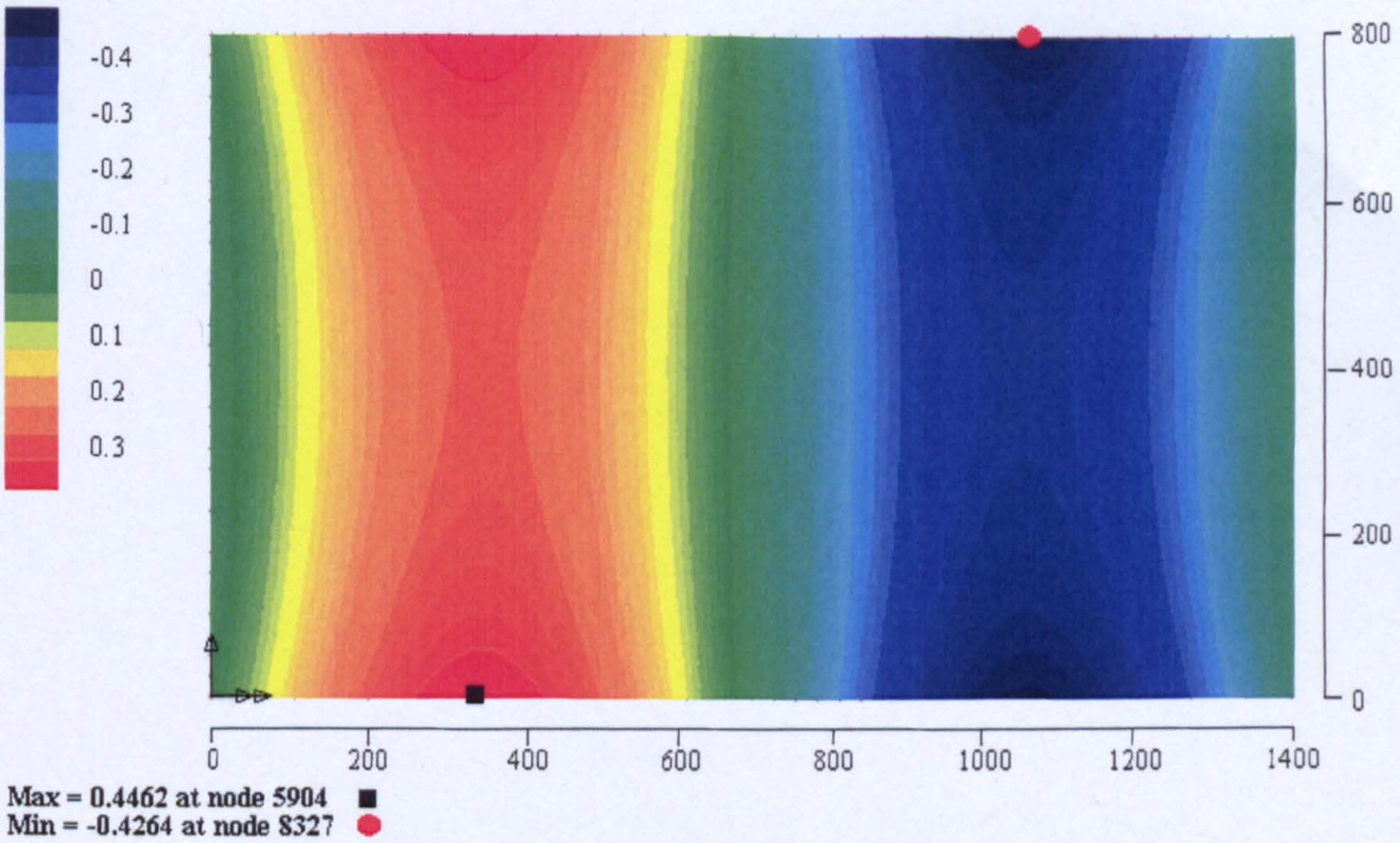

Figure 1.12 Contour plot - modeshape 3 - spring stiffness 5

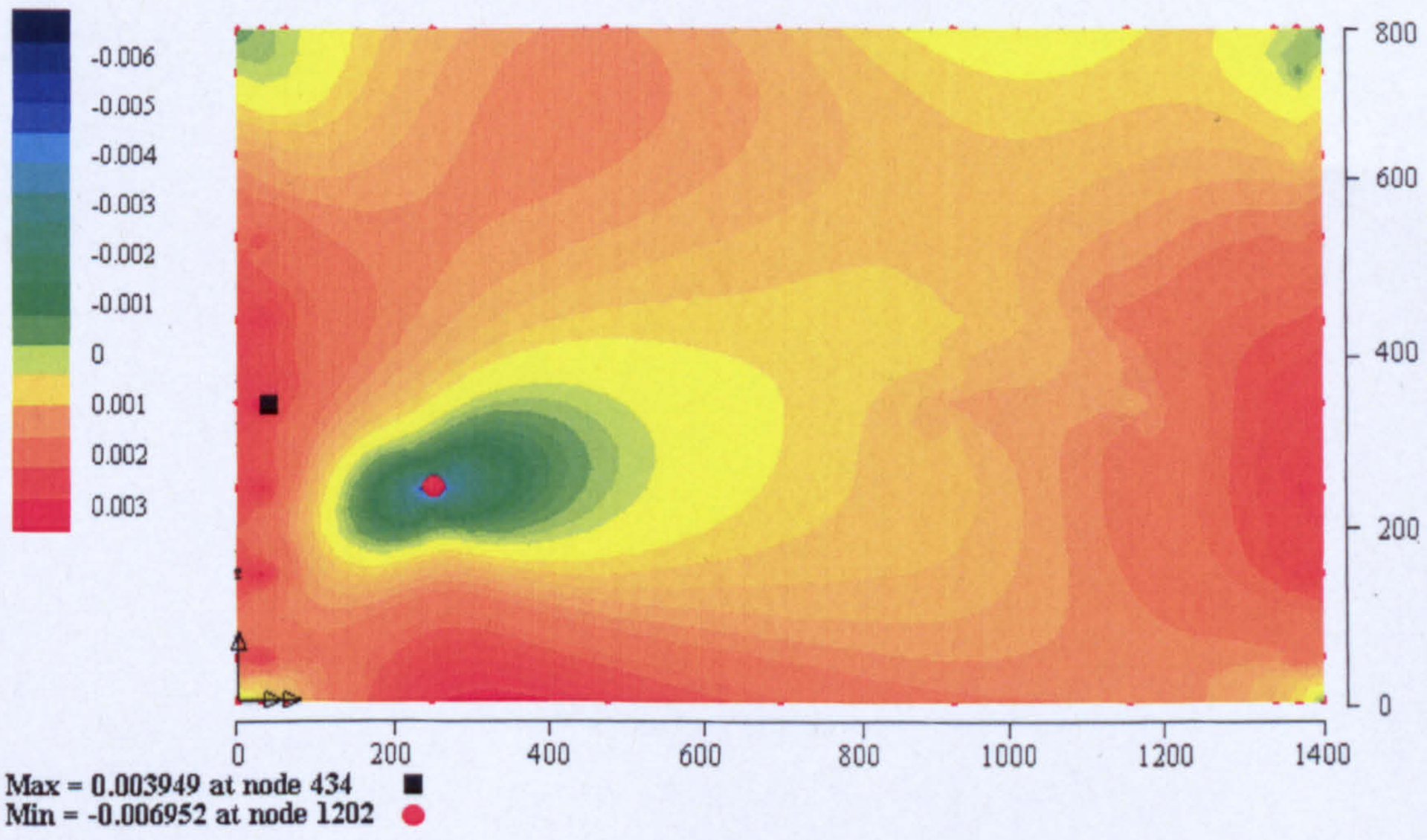

**Figure 1.13 Contour plot of bending strain - spring stiffness 1.
Time step 50 (0.1 s), input force location (0.25, 0.25, -0.0111).
Location of maximum and minimum values at node 434 (0.03, 0.35, -0.00094) and 1202 (0.25, 0.25, -0.0111).**

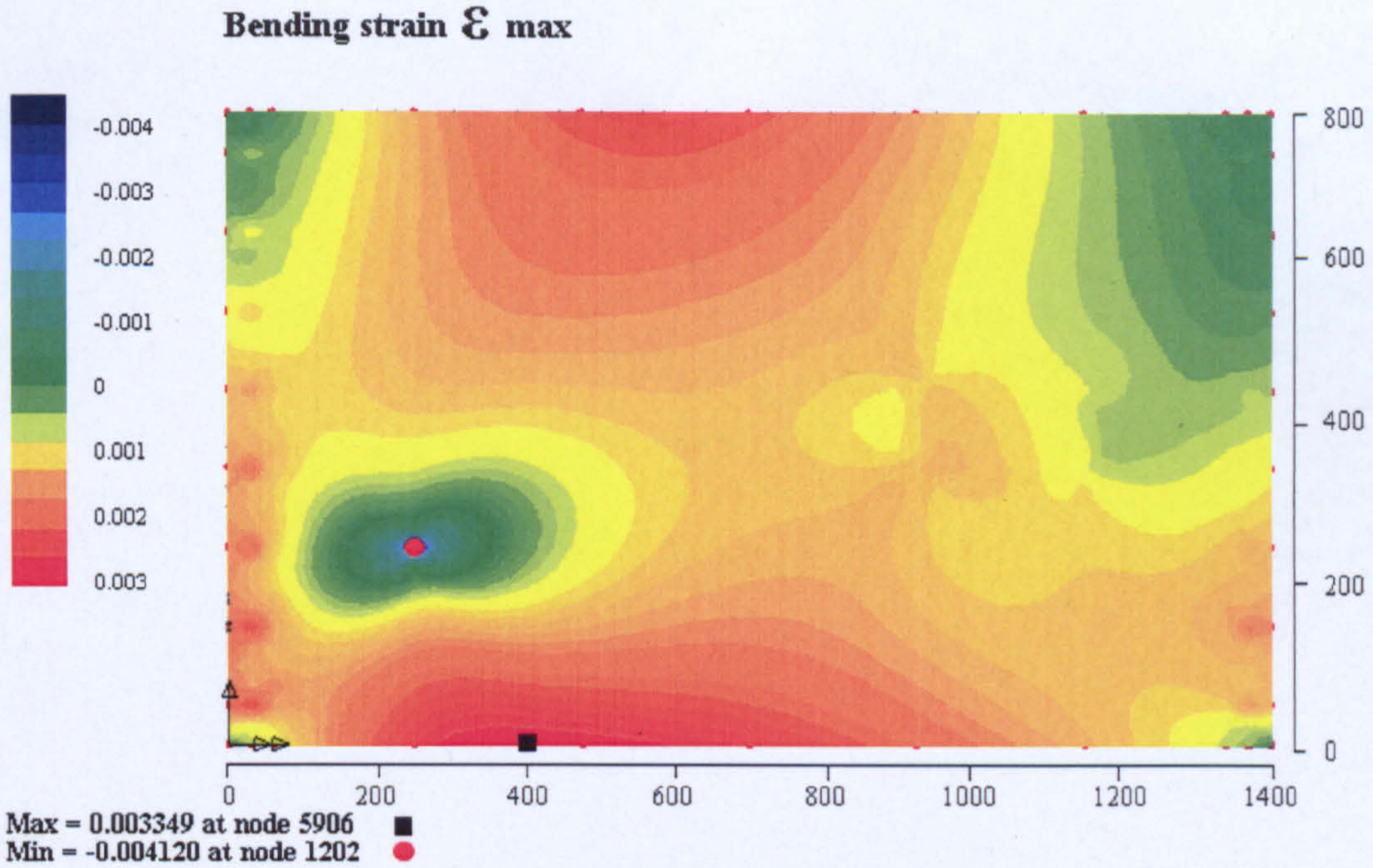

Figure 1.14 **Contour plot of bending strain - spring stiffness 5. Time step 200 (0.4 s), input force location (0.25, 0.25, -0.0111). Location of maximum and minimum values at node 5906 (0.4, 0, -0.01516) and 1202 (0.25, 0.25, -0.0111).**

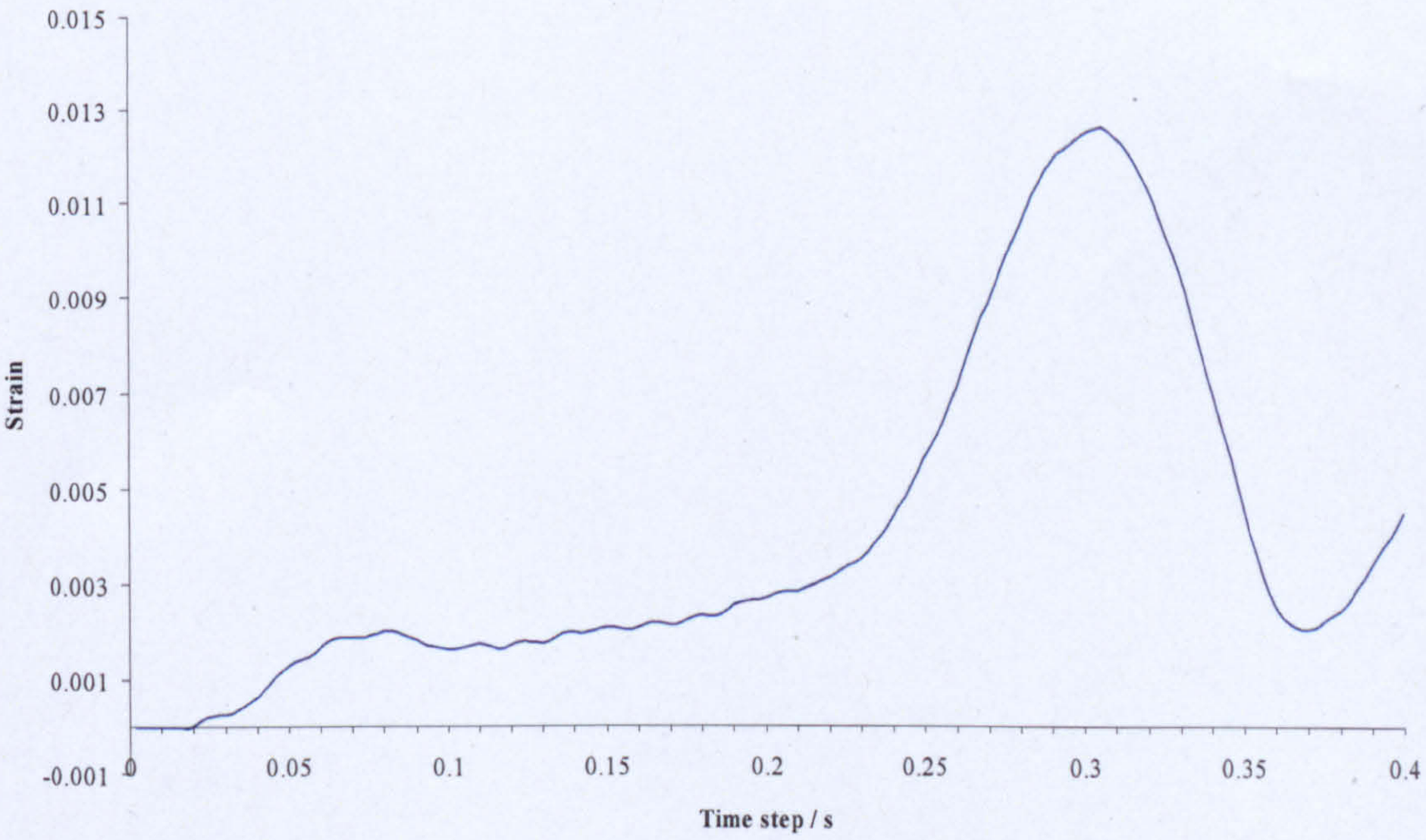

Figure 1.15 **Bending Strain response - spring stiffness 1 at node 3635 (1.37, 0.35, -0.00094), input force location (0.25, 0.25,-0.0111).**

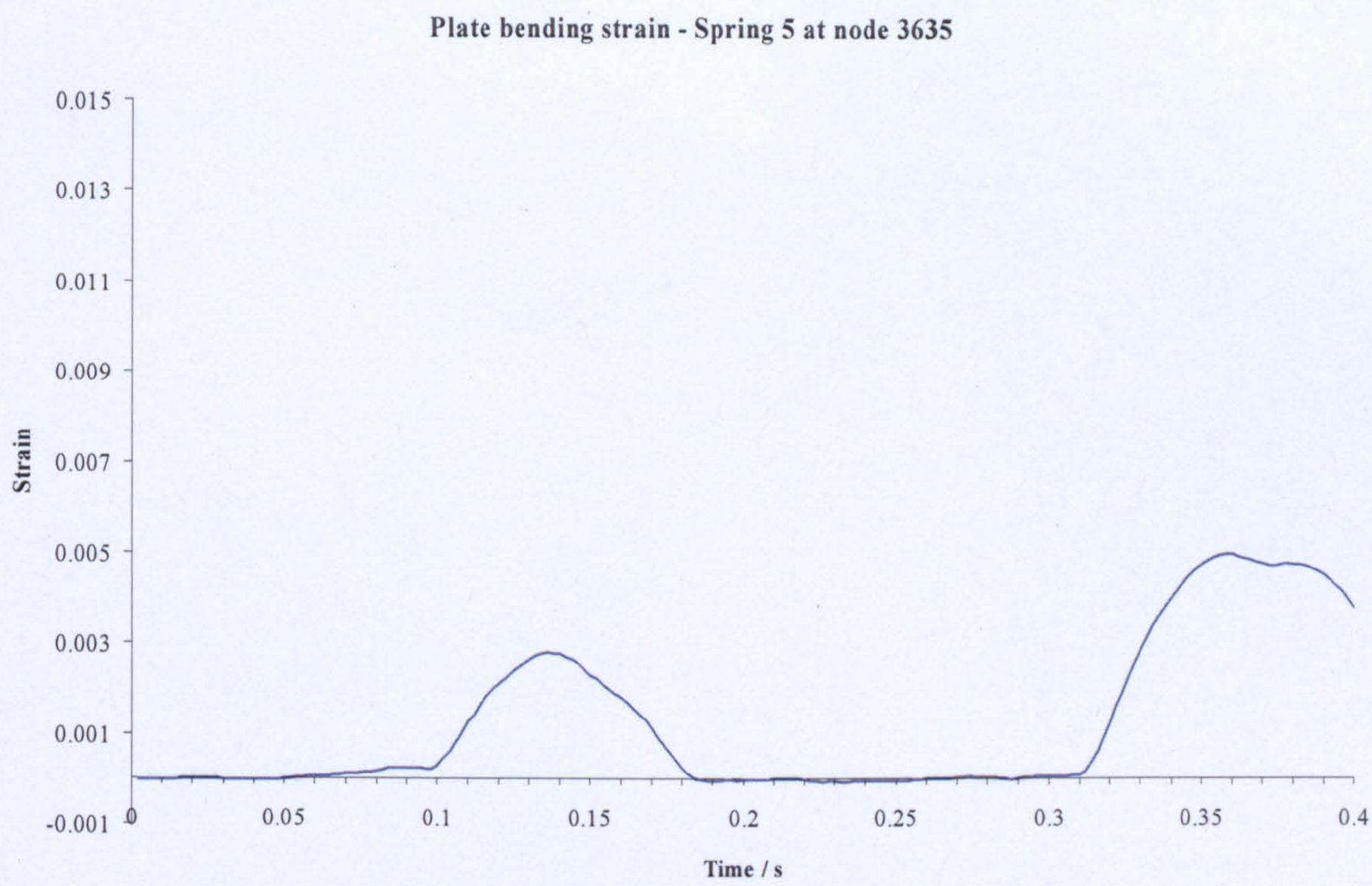

Figure 1.16 Bending Strain response - spring stiffness 5 at node 3635 (1.37, 0.35, -0.00094), input force location (0.25, 0.25,-0.0111).

CHAPTER 2

Literature Review

2 Introduction

This chapter presents the current extent of knowledge on the topics covered within the research presented in this thesis. The chapter is divided into three sections; vibration of plates, dynamic analysis and bridge bearings. The author's approach has been to cover the necessary background material from which this research stems and provide sufficient additional coverage for the interested reader / practitioner.

2.1 Vibration of plates

Plates of numerous geometries, *i.e.* rectangular, circular and polygonal *etc.*, material type such as orthotropic and isotropic are widely used in all engineering fields. Plates are used in modern aerospace, aircraft, naval engineering and civil engineering. An extensive body of literature exists for plates, especially on the free vibration of rectangular plates. Most of these papers use the classic theory for thin, isotropic plates of uniform thickness, using Eq. 2.1 to describe the vibrations of the plate.

$$\frac{Eh^3}{12\left(1-\nu^2\right)}\nabla^4 w+\mu\frac{\partial^2 w}{\partial t^2}=P \qquad \text{Eq. 2.1}$$

Where ∇^4 is known as the biharmonic differential operator, *i.e.* $\nabla^4=\nabla^2\nabla^2$, $\nabla^2=\frac{\partial^2 u}{\partial x^2}+\frac{\partial^2 u}{\partial y^2}$ when expressed in rectangular notation, w is the transverse

CHAPTER 2

Literature Review

2 Introduction

This chapter presents the current extent of knowledge on the topics covered within the research presented in this thesis. The chapter is divided into three sections; vibration of plates, dynamic analysis and bridge bearings. The author's approach has been to cover the necessary background material from which this research stems and provide sufficient additional coverage for the interested reader / practitioner.

2.1 Vibration of plates

Plates of numerous geometries, *i.e.* rectangular, circular and polygonal *etc.*, material type such as orthotropic and isotropic are widely used in all engineering fields. Plates are used in modern aerospace, aircraft, naval engineering and civil engineering. An extensive body of literature exists for plates, especially on the free vibration of rectangular plates. Most of these papers use the classic theory for thin, isotropic plates of uniform thickness, using Eq. 2.1 to describe the vibrations of the plate.

$$\frac{Eh^3}{12\left(1-\nu^2\right)}\nabla^4 w+\mu\frac{\partial^2 w}{\partial t^2}=P \qquad \text{Eq. 2.1}$$

Where ∇^4 is known as the biharmonic differential operator, *i.e.* $\nabla^4=\nabla^2\nabla^2$, $\nabla^2=\frac{\partial^2 u}{\partial x^2}+\frac{\partial^2 u}{\partial y^2}$ when expressed in rectangular notation, w is the transverse

displacement, $\frac{Eh^3}{12(1-\nu^2)}$ is the flexural rigidity; E is Young's Modulus; h is plate thickness; ν is Poisson's ratio; μ is mass per unit area of plate surface; P is the external load per unit area of plate surface; and t is time. Figure 2.1 shows the first three mode shapes for the plate equation using the Kirchhoff constraints.

2.1.1 Classic boundary conditions

Initial investigations into plate behaviour by Chladni[2.1] and Strutt (Third Baron Rayleigh a.k.a. Lord Rayleigh)[2.2] inspired many researchers to investigate the free vibration of plates in the late 19th and early 20th centuries with the increase in computational power now available, research involving more complex geometries and boundary conditions can be completed.

In his early research, Rayleigh assumes that plates and beams have the same waveforms, so a plate with fully fixed boundary conditions is comparable to a beam with each end fully fixed. This assumption is still used today by many researchers when determining the shape function applicable to plates in various boundary condition arrangements. Ritz[2.3] then adapted Rayleigh's formula to produce the Rayleigh-Ritz method, which is a faster, more direct method for solving the frequencies of plates requiring less calculation to resolve the general equation shown in Eq. 2.2.

$$z(x) = \sum_{i=1}^{n} C_i z_i(x) \qquad \text{Eq. 2.2}$$

Classic theory of plate vibration is based on research completed by Kirchhoff, whose theory states that plane sections remain plain and perpendicular to the mid-plane when

subjected to loading. Many approaches to the theory have been developed, with the most commonly used method developed by Mindlin[2.4], who's theory takes into consideration the shear and rotary inertia effects. Kirchhoff theory is generally applied to the analysis of thin plates as no consideration is given to the effects of transverse shear, whereas Mindlin theory is more applicable to thick plates as transverse shear and its effects are taken into consideration. A thorough review of research on thick plate vibration up to 1995 has been conducted by Liew *et al.*[2.5].

One of the most comprehensive studies of the theory of plates and shells was completed by Timoshenko and Woinowski-Kreiger[2.6] and initially published in 1936. They outline the basic theory of plates, deriving differential bending equations for thick and thin plates, the displacement of laterally loaded plates and finally outline the response of plates with various degrees of support condition to various types of loading (Figure 2.2).

The most common approach to determining the response of plates is to derive the governing equations of the plate using simplified beam functions. Warburton[2.7] highlights modeshapes and frequencies associated with fifteen separate configurations of support conditions using the Rayleigh-Ritz method for thin isotropic plates, all edges being free, simply-supported, clamped or a combination of these. Warburton assumed a modeshape for each arrangement that was a function of vibrating beam eigenfunctions. Young[2.8] and Hearmon[2.9] investigated vibrations in isotropic plates, and Hearmon then extends this treatment to plates that are "specially orthotropic", with the exception of free edges, and assumes the plate thickness and deflection to be small, therefore reducing the problem to a two-dimensional problem[2.10]. Other authors have evaluated the response of orthotropic plates, such as Biancolini *et al.*[2.11] who uses the Rayleigh

method applied to the simple general expression of the fundamental frequency of a plate to determine the higher value frequencies. Rossi *et al.*[2.12] compares values obtained through numerical and analytical methods for rectangular orthotropic plates with a free edge. Values are obtained using the Rayleigh-Ritz method and a Fourier expansion. The values obtained with these methods are in close agreement with those obtained with a finite element analysis.

Leissa[2.13 & 2.14] provides an excellent summary of the literature on the free vibration of plates up to 1973, highlighting the analytical results obtained for all twenty one cases of possible combinations of free, clamped or simply-supported edge conditions. Leissa compares values obtained using Warburton's approximate calculations, and makes note of the effects of a varying Poisson's ratio on the vibration response. Deobald and Gibson[2.15] used the Rayleigh-Ritz method to continue the solutions produced by Leissa with respect to orthotropic plates.

Thin plate theory has been extensively covered, and Leissa presented exact solutions by solving the differential governing equations for a thin plate with two opposite sides simply-supported. Hashemi and Arsanjani[2.16] present the exact solutions for thick plates using Mindlin theory, as these have not been determined previously. In this paper, six individual cases with differing boundary conditions are solved. The results presented can be taken as the benchmark values to be compared with other theories. Comparison with the values obtained by approximate solutions shows that the method is valid.

This method of using beam functions is used as the basis for research completed by Cheung and Zhou[2.17] on plates with elastic intermediate line-supports and edge constraints. The method outlined allows both the translational and rotational stiffness of supports to be altered, which are both considered simultaneously. The method is considered simple, with each beam function a third-order polynomial plus a sine function. The method is solvable with a computer program as a change in any of the boundary conditions of the plate can be altered by changing the coefficients of the polynomial beam functions. It is also noted that a small number of beam functions are considered sufficient to derive the response of the plates. The solutions presented are in close agreement with more established research.

The references cited above all derive the frequencies of plates by assuming a modeshape from beams as admissible functions for analysis methods. Dickinson[2.18] proposed an alternative method, obtaining modeshapes from the vibration of plates having two parallel edges simply-supported with the other two edges dependent on the edge conditions under consideration. The functions are similar to the beam functions used in previous research and exhibit similar characteristics, allowing the geometric boundary conditions to be satisfied, but are directly derived from the natural modes of a system and can be used to establish the higher modes, in addition to the fundamental modes of vibration for the plate in question. Dickinson[2.19] then compares results obtained using this method to those obtained by Leissa for several plates with different boundary conditions and edge aspect ratios. However, Dickinson states that neither method produces a solution of any great accuracy when considering a plate with a free boundary condition.

Several researchers have also applied the Rayleigh-Ritz method to the in-plane vibration of rectangular plates. In-plane vibrations tend to occur in the higher end of the frequency range than those in the transverse direction. Hyde *et al.*[2.20] uses the Rayleigh-Ritz method to determine the frequencies and modeshapes for the in-plane vibration of rectangular, isotropic plates subjected to plane stress deformation. Three boundary condition arrangements are investigated; free, a combination of fixed and free, and fully fixed, and plates with different aspect ratios have been analysed. This allows the method to be compared with solutions found using classical plate theories. Although the answers provided are in relatively close agreement in most cases, the method seems to overestimate the first few modes of vibration at the low end of the frequency spectrum. In recent years, the advent of computers with ever-increasing memory capacities and processor speeds mean it is now possible to solve previously labour intensive problems rapidly.

Bhat *et al.*[2.21] outline a method of determining the fundamental frequencies of plates using the Rayleigh-Ritz method which is ideal for solution by computer program. A numerical scheme to generate a two-dimensional boundary characteristic orthogonal polynomial using a recurrence relation is developed which satisfies the essential boundary conditions of the plate. The authors then compare the results with those obtained by performing an analysis using previous polynomials which have been orthogonalised.

One method of determining the response of plates is the finite difference method (FDM). Chen[2.22] uses the FDM to calculate the fundamental frequency of an orthotropic plate with clamped, simply-supported and free edge conditions. To derive

the constraints of the equations required to model the edge conditions stated the authors assumed a displacement at the outside nodes where the edge constraints are located. This method generates a three-dimensional problem which is computationally intensive, especially with respect to determination of the required stiffness matrices and depending on the mesh refinement chosen, a large matrix can be required. However, this method does produce an accurate solution for orthotropic plates. Figure 2.3 shows the mesh and sign convention chosen for this method.

Another simple method of analysis of plates is the finite strip method. The finite strip method effectively performs the same type of analysis as a finite element method, with the plate divided into several sections, or strips. Dawe[2.23] uses this method to investigate the vibration of Mindlin plates using four different models with varying degrees of interpolation of plate deflection and rotation. Numerical examples presented indicate that accuracy increases with more interpolations, as would be reasonable to assume. Results for the analysis are shown in Table 2.1. Lower order strip performance suffers accuracy problems when applied to thin plates as the bending effects are affected by poor representation of lateral displacement. (Refer to footnote on Table 2.1, p. 130)

Another method of determining the response of plates is the superposition method. Gorman is a prolific researcher in this particular field of analysis. He uses the technique to determine the response of rectangular plates with conventional boundary conditions[2.24] and extends this to a combined superposition-Galerkin method[2.25]. Figure 2.4 shows a schematic of the building blocks used. The Galerkin method produces answers of equal accuracy as the more traditional method, but requires less effort to calculate. However, the method has only been applied to symmetrical modes,

so further analysis would be required. The superposition method is also used to determine the free vibration response of completely free rectangular Mindlin plates[2.26], again extending this method to a combined superposition-Galerkin method[2.27].

Gorman also analyses Mindlin plates supported at four discrete points[2.28]. The superposition method satisfies the governing differential equations and boundary conditions by obtaining more terms in the solution series. The point supports can be located at any point on the plate, even along its edges. Gorman indicates that for the lower values of frequency for thick and thin plates, the superposition method provides answers in close agreement, to within three significant figures of the exact solution.

An alternative method of analysis of plates is the differential quadrature method (DQM). The DQM is similar to other methods of analysis such as the previously mentioned FD and FEA methods in that it solves the partial differential equations using a mesh of grid points. DQM is often used as the number of grid points required to solve the governing equations is smaller than for the other two methods. Depending on the type of problem being analysed, the governing equations are then reduced to either a set of algebraic time independent equations or a set of time dependent ordinary differential equations. Initial investigations into the method were based on a two-dimensional solution, and in recent years researchers have applied the method to three-dimensional elastic theory. Liew and Teo[2.29] highlights the history of the DQM and proposed a method for determining the response of rectangular plates with generic boundary conditions in three-dimensions. The method of solution, outlining the method of normalisation and discretisation of the governing equations, then constructing the eigenvalue equation from matrices derived from the equations. In the paper they

indicate that a cosine mesh pattern produces more reliable results which are then compared with other known solutions produced from classic theory and other two-dimensional solution methods. Results indicate a good correlation, indicating the method is valid, and could be extended into other possible boundary conditions.

An alternative method of analysis is called the Discrete Singular Convolution (DSC) method[2.30]. The DSC method uses singular convolutions, which are a special class of mathematical transformation used in the Hilbert and Radon transforms. The general governing equations are constructed, taking into consideration the equations for rotational stiffness. Comparisons are then drawn between the obtained data using the DSC method and data obtained from other methods, shown in Figure 2.5. The method produces answers in close agreement with other theories, but is only applied to either plates with edges simply-supported and elastically restrained in torsion, or clamped and elastically restrained.

A novel method of detection of the flexural vibration response of a plate is shown by Nieves *et al.*[2.31]. They use a method called laser-interferometry detection to obtain both the in-plane and out-of-plane components of vibration, most other methods simply detect the out-of-plane movement. Figure 2.6 shows a sketch of the experimental setup. It is considered that the classical methods of frequency analysis, perpendicular displacements, Kirchhoff theory and Mindlin theory, are not sufficient to describe the movement of the plate. Nieves uses the Ritz method to determine the modal response in three-dimensions using commercially available software for three different analyses; one where the Kirchhoff theory is used, another when Mindlin theory is used, and finally one method where the displacements are three-dimensional. The results obtained

using the experimental and theoretical methods are compared and are in close agreement for the first two modes of vibration. The third is not convergent with the experimental work, but with more terms in the three-dimensional series used in the Ritz method, the solution should become more accurate.

2.1.2 Variable end conditions

The main theme behind the research in this thesis is the effect of variable end conditions on the response of structures. An extensive survey of the present literature highlighted a number of interesting papers containing several different methods of analysis for both thick and thin plate vibration.

One such method is the Ritz method, used extensively in the determination of the vibration response in plates with classical boundary conditions such as free and simply-supported arrangements. Leissa *et al.*[2.32] analyses the response of rectangular plates with non-uniform elastic edge supports in various configurations. The displacements and frequencies of the plates are solved by deriving the exact solutions of the differential equations of motion, and by the Ritz method. The paper considers a support condition of parabolically varying stiffness, with two edges simply supported and symmetrical non-uniform elastic constraints in one case, and two edges simply supported with non-symmetrical non-uniform elastic constraints in another. The exact solutions converge rapidly, whereas the Ritz solution produces upper bounds on the frequencies, and is also sensitive to changes in the non-dimensional stiffness constraint or aspect ratio.

Warburton and Edney[2.33] investigates the vibrations of rectangular plates with elastically restrained edges, in terms of both translational and torsional stiffness. They use the general modeshapes of beams as the assumed functions, reducing the number of required functions. In contrast to many other researchers, they applied both rotational and translational elastic restraint to the plates. The accuracy of the answers obtained are compared with established baselines, their accuracy ranges from 0.5% to 2% depending upon the support configuration. The authors also state that the use of beam functions in place of polynomials should result in increased accuracy for higher modes.

Normally a two-dimensional method, Liew *et al.*[2.34] extend the method into three-dimensions for isotropic thick rectangular plates. The main focus of the research presented is to determine the effects of boundary conditions and the thickness ratio on the response of plates. To demonstrate the accuracy of the proposed approach, they carried out a convergence test, comparing values obtained with those calculated from classic theory, Mindlin theory and an exact solution. Once convergence has been established, the three-dimensional Ritz method is applied to two separate boundary condition configurations, SSSS and SFSF, with different aspect ratios and thickness ratios for each configuration. The results show that mode shapes can be switched or modal coupling can occur in plates with the simply-supported conditions. Meanwhile, in the SFSF condition, this switching can be seen in plates with a higher thickness ratio.

The Rayleigh-Ritz method is used by Li[2.35] to determine the response of plates with general elastic boundary conditions. Li stated that the admissible functions are composed of a trigonometric function supplemented by a polynomial function to ensure the smoothness of the residual displacement function used to describe the edge support

conditions. This method is also considered applicable to more complicated boundary conditions as the technique's polynomial functions used can be easily substituted with any other continuous function.

Gorman uses the superposition method to determine the free vibration response of rectangular plates with elastic edge supports[2.36], and analyses Mindlin plates resting on elastic supports[2.37]. Edge constraints can be applied with rotational and lateral stiffness in any distribution along the edge, and with any combination of edge supports. The Mindlin plate analysis allows a rotational stiffness to be added by a slight change to the eigenvalue matrix, adding or subtracting a stiffness value to the section of the main diagonal concerned with the building block used to generate the matrix, Figure 2.7.

Gorman also uses the superposition method to determine accurate solutions for plates resting on elastic edge supports both with a linear distribution of lateral and rotational stiffness[2.38], where stiffness is arbitrarily distributed[2.39], and in plates where the elastic support is normal to the boundaries[2.40]. The edge constraints are modelled using a series of building blocks with a separate equation to describe the distribution and location of support. It is also noted that where support is concentrated locally, or where discontinuities exist, more terms are required to represent accurately the support distributions for the building blocks. To determine the governing equations and boundary conditions, the in-plane stresses and support stiffness are calculated, where the support stiffness is related to the displacement normal to the plate boundary. The building blocks are then determined in the same manner as the previous papers[2.40], and solutions calculated. The method shown could be used to determine the response of

plates with opposite edges supported, with the other two edges free, by setting the edge constraints of one set of stiffness to zero.

Gorman applies the superposition method to obtain buckling loads and free vibration frequencies for a series of plates with elastic boundary conditions[2.41]. Two opposite edges are completely free, and the remaining two opposite edges are elastically restrained in rotation. Building blocks using the generalised equations of the plates are constructed, and the results for buckling and frequency analysis shown. The first four frequencies are shown with only one edge support elastically restrained, and with two opposite edges free. Both opposite edges are prescribed the same stiffness values from zero (simply-supported) to infinity (fully clamped).

Teng *et al.*[2.42] developed an analytical method to determine the realisation of boundary conditions in the vibration of plates. To determine the actual values of natural frequency, a series of modal tests was performed using a signal analyser detecting the response of plates subjected to a forced vibration. Plates with varying degrees of elastic edge restraint can then be simulated, and the closeness of experimental and theoretical tests can be compared. An analytical procedure was developed which enables the deflection to be computed, thus enabling the accuracy of the solution to be increased. Figure 2.8 provides a diagram of the apparatus used.

One new novel approach to the analysis of thin plates is the moving least square Ritz method, proposed by Zhou and Zheng[2.43]. The moving least square method is used to determine an unknown coefficient within the governing equations of the plate movement. Determining the value of theses coefficients than allows the Ritz function to

be displayed in terms of the displacement values of all the points used in the grid on the plate. The equation is then differentiated once and then again with respect to x and y, and the subsequent equations then inserted into the Lagrangian equation of the plate, then depending on the boundary conditions of the plate using a point substitution method, an equation comprising the stiffness matrix, the mass matrix and the nominal displacements for all grid points can be evaluated to produce the vibration frequency. The equations below are the key equations used to determine the resonant frequencies of the plates.

$$F = \frac{D}{2}\int_A \left\{ \left(\frac{\partial^2 w}{\partial x^2} + \frac{\partial^2 w}{\partial y^2} \right) - 2(1-\nu)\left[\frac{\partial^2 w}{\partial x^2}\frac{\partial^2 w}{\partial y^2} - \left(\frac{\partial^2 w}{\partial x \partial y} \right)^2 \right] \right\} dA - \frac{1}{2}\rho h \omega^2 \int_A w^2 dA \qquad \text{Eq. 2.3}$$

$$F = \frac{1}{2}\mathbf{W}_I^T \left(\overline{\mathbf{K}} - \omega^2 \overline{\mathbf{M}} \right) \mathbf{W}_I \qquad \text{Eq. 2.4}$$

$$\overline{\mathbf{K}} = \mathbf{T}^T \mathbf{K} \mathbf{T} \qquad \text{Eq. 2.5}$$

$$\overline{\mathbf{M}} = \mathbf{T}^T \mathbf{M} \mathbf{T} \qquad \text{Eq. 2.6}$$

$$\left(\overline{\mathbf{K}} - \omega^2 \overline{\mathbf{M}} \right) \mathbf{W}_I = 0 \qquad \text{Eq. 2.7}$$

Convergence studies have been completed, taking into consideration the effect of grid point size, the number of Gaussian integration points and the order of the polynomial function used in the general governing equations. Results obtained with this method applied to right-angled triangle slabs are compared with more established methods. The proposed method does show some agreement with the more established methods. However, no comparison is made for rectangular plates and as such, any validation for the method applied to rectangular plates cannot be made at the present time.

2.1.3 Finite Element Analysis

FEA is a method used to determine a numerical solution of field problems which require the determination of the spatial distribution of one or more variables, and is an extension of the commonly used Rayleigh-Ritz method of analysis. Such problems are defined by differential equations or an integral equation which may be used to formulate finite elements. FEA is one particular method which lends itself to the accurate analysis of plates due to the method's ability to analyse large, complex problems using vastly increased modern computational power currently available. The FE method is generally considered reliable. In recent years, many researchers have attempted to improve upon the accuracy of the method, which in certain cases can be time-consuming and computationally intensive. A small sample of recent literature proposing new or improved methods of solution for the FE method, and element types are highlighted in this section.

One common type of element used in FEA solutions is the four nodded isoparametric quadrilateral element available in computer analysis packages. Razaqpur *et al.*[2.44] proposed a new element based on a 9-noded Lagrangian isoparametric quadrilateral element called QUAD9 which has 27 degrees of freedom, 3 at each node. Figure 2.9 shows the element type with node numbering, gauss points and sign convention used in this thesis. W is the displacement, θy and θx are absolute rotations of the through-thickness normals after deformation based on Mindlin plate theory. These rotations include the transverse shear deformations. An element with thin plate performance is then produced by constraining the shear strains to zero at discrete points within the element. The element proposed is a four-noded element with 12 degrees of freedom, and element stiffness matrix is defined in the same manner as the classic discrete

Kirchhoff triangular element, and Kirchhoff thin plate constraints are applied. Following this procedure results in a more concise element formulation, as the QUAD9 element is often time consuming and has problems when connecting the element to other element types. The results obtained using the new element show a close agreement with the results obtained using classic Kirchhoff theory.

Commercially available FEA packages usually utilise the original h-version of the method. In this particular method, the displacements, stresses, strains, temperature and other physical quantities are represented by first order functions of spatial coordinates. Elements are flat-edged and faced, and the accuracy of solution is dependent on the mesh refinement; *i.e.* the mesh shape and element size.

Another method of FE is the p-method, which is a spectral version of the FE method. In this method, the field variables are represented by higher-order polynomials, meaning the method can fit physical data points more smoothly, and more accurately than the linear first-order functions of the h-version. The accuracy of the p-version is not dependent upon the mesh refinement as the element edges are curved, thus convergence is automatic.

Combining the two methods produces the h-p version of finite element analysis. The hp-version of the finite element method (hp-FEM) is a generalisation of the classical (h-version) FEM and the p-version FEM/spectral method in that convergence is achieved by simultaneously refining the mesh and increasing the approximation order. Houmat[2.45] uses this method based on a pentahedral element for the analysis of the free vibration of plates. The higher order polynomial functions are expressed as shifted

Legendre orthogonal polynomials, providing a solution that includes a full frequency spectrum: both in-plane and out-of-plane modes are detected. Comparisons of results obtained with the proposed method are made for a square plate with fixed edge conditions with classical two-dimensional plate theories. The results obtained are in close agreement for a thin plate, thickness of 0.01 m, but slightly overestimates the values compared with the Mindlin theory when applied to a thicker plate, 0.1 m. The Kirchhoff theory answers are not in agreement, but the explanation for such an occurrence lies in the fact that the Kirchhoff theory neglects the effects of thickness.

2.2 Dynamic analysis

Vibrations caused by traffic loading are one of the main causes of damage to highway bridges. The dynamic response of highway bridges to the applied random traffic excitation arising from day-to-day loading has been widely researched. Investigations into structural health monitoring and damage detection are also covered by existing research. The vast majority of dynamic analysis on large structures uses the principle of modal analysis. A brief outline of the theory behind the important procedures involved in modal analysis is highlighted in the following section, any further theory and applications of the method can be ascertained from existing literature on the subject as this is beyond the scope of this thesis[2.46-2.49].

2.2.1 Modal analysis

In non-destructive testing, the traditional way of observing signals is to view them in the time domain. However, it is also possible to view the signal in the frequency domain by a mathematical algorithm know as the Fourier transform. This type of analysis is commonly known as spectral analysis. Transforming the data signal from the time

domain into the frequency domain allows certain useful parameters describing the response of a structure or object to be extracted, and no information is lost or gained during this process. The transformation between time and frequency is carried out by using a digital analyser, which usually makes use of a more advanced form of the Fourier transform, the fast Fourier transform.

2.2.1.1 The Fourier transform

The transformation is based on the Fourier transform integral derived from a Fourier series. The integral transforms the infinite and continuous time signal into a continuous and infinite frequency spectrum using Eq. 2.8 and 2.9.

$$X(f) = \int_{-\infty}^{\infty} x(t)\, e^{-i2\pi\, ft}\, dt \qquad \text{Eq. 2.8}$$

And its inverse,

$$x(t) = \int_{-\infty}^{\infty} X(f)\, e^{i2\pi\, ft}\, df \qquad \text{Eq. 2.9}$$

Where $X(f)$ is the frequency spectrum,

$x(t)$ is the periodic time signal,

Eq. 2.8 and 2.9 show an idealised transform which can be applied to all time signals. In reality, not all of the required information will be available, normally only a small transient signal.

2.2.1.2 Discrete Fourier transform

Fourier analysis is not suitable for transforming a time limited non-periodic signal into the frequency domain. A waveform can be sampled and digitised using a spectrum analyser, and then transformed into the frequency domain using the DFT. The DFT transforms finite sequences of data by windowing and sampling the continuous time signal. Windowing the data, using one of several types available such as the Hann window, allows a short section of the data to be discretised using the sampling theorem. The modified equation for the DFT is shown in eqns 2.10 and 2.11.

$$X(k) = \sum_{n=0}^{N-1} x(n)\, e^{-i\,2\pi kn/N} \qquad \text{Eq. 2.10}$$

And its inverse,

$$x(n) = \frac{1}{N} \sum_{n=0}^{N-1} X(k)\, e^{i\,2\pi kn/N} \qquad \text{Eq. 2.11}$$

Where k is the set of discrete frequency components up to N-1,

n is the time sample index up to N-1,

N is the number of samples considered.

2.2.1.3 The fast Fourier transform

The DFT is the most straightforward mathematical procedure for transforming data the frequency domain from the time domain, but is considered inefficient. One method of improving the DFT's efficiency is known as the FFT, originally described by Cooley and Tukey[2.50] in 1965. The FFT is not a new transform, but simply a method used to

increase the efficiency of the transform. Most modern analysers use the FFT, although it should be pointed out that both methods produce the same answers, the FFT uses fewer computations to reach those answers. The FFT is a discrete Fourier transform algorithm which reduces the number of computations needed for N points from $2N^2$ to $2N\log_2 N$.

A discrete Fourier transform can be computed using an FFT by means of the Danielson-Lanczos lemma[2.51] if the number of points N is a power of two. If the number of points N is not a power of two, a transform can be performed on sets of points corresponding to the prime factors of N which is slightly degraded in speed. Base-4 and base-8 FFTs use optimised code, and can be 20-30% faster than base-2 FFTs. FFT algorithms generally fall into two classes: decimation in time, or decimation in frequency.

The Cooley-Tukey FFT algorithm first rearranges the input elements in bit-reversed order, then builds the output transform (decimation in time). The basic idea is to break up a transform of length N into two transforms of length N/2 using equation 2.12.

$$\sum_{n=0}^{N-1} a_n e^{-2\pi i n k / N} = \sum_{n=0}^{N/2-1} a_{2n} e^{-2\pi i (2n) k / N} + \sum_{n=0}^{N/2-1} a_{2n+1} e^{-2\pi i (2n+1) k / N}$$
$$= \sum_{n=0}^{N/2-1} a_n^{even} e^{-2\pi i n k / (N/2)} + e^{-2\pi i k / N} \sum_{n=0}^{N/2-1} a_n^{odd} e^{-2\pi i n k / (N/2)} \qquad \text{Eq. 2.12}$$

This is sometimes called the Danielson-Lanczos lemma. The easiest way to visualize this procedure is perhaps by the Fourier matrix. The Sande-Tukey algorithm[2.52] first transforms, then rearranges the output values (decimation in frequency).

2.2.1.4 Sampling and aliasing

To transform the time signal accurately, it is necessary to sample the signal at discrete points to represent the sinusoid transformed. A sampling rate that is too low will result in vital information about the signal being lost. This phenomenon is known as aliasing. To remove this error, the correct sampling rate must be determined, which is termed as the Nyquist sampling theorem[2.53]. In this paper, Nyquist presented a method for converting analogue waveforms into digital signals for more accurate transmission over phone lines. He presented a method whereby an analogue signal, if it were band-limited, could be captured and transmitted in digital values and then recreated in an analogue form on the receiving end. He presented the concept of sampling amplitudes at a specific rate, and most importantly determined that the sampling rate would need to be at least twice the highest frequency to be reproduced. If this is not the case, then aliasing occurs. Aliasing can be prevented by increasing the sampling rate and filtering the data before analysis. These filters are known as anti-aliasing filters and are designed to limit the high frequency content of the waveform.

2.2.1.5 Leakage

When performing an FFT analysis, the time history for the samples must be limited, discretising the continuous signal into smaller sections. However, truncation of a signal in the time domain will result in an error in the frequency domain, and vice versa. This error is called leakage. Leakage can be reduced by applying time weighting functions known as windows. Normally, the effect of the window in the frequency domain is understood as the convolution of the signal spectrum and the spectrum of the time window. This can lead to signal distortion in the frequency domain, as the signal is effectively changed. Several types of window exist, and each separate type is applicable

in different situations. The Hann window[2.54] is often used for continuous signals such as random excitation due to impacts. The Hann window reduces possible errors by setting the signal equal to zero at the start and end of the time record. Figure 2.10 shows the types of windowing available. It is also possible to use overlapping analysis for transients of a long time sample, effectively giving a flat overall analysis window, with the added advantage of reducing noise at the start and end of the record.

2.2.1.6 Signal enhancement

Measurements can often become contaminated with noise, which can result in signal degradation. Noise in a signal will still be analysed when present, which can lead to erroneous frequency spectra being displayed. In order to improve the process, time signals can be filtered and averaged. To reduce the noise element in a signal, a linear averaging technique can be employed which improves the signal to noise ratio by the square root of the number of repetitions of the figure. The technique of signal averaging is straightforward. A repetitive signal is acquired a number of times, each acquisition is added to the last, and the sum is then divided by the number of acquisitions. The more averages taken, the smoother the response curve will tend to be, as more extraneous noise is eliminated from the spectrum. It is mainly used for analysis of stationary signals and transients. In addition to linear averaging, analysers also offer exponential averaging and peak averaging. Exponential averaging places the emphasis on the latest sample. The contribution of each sample towards the average is weighted using an exponentially decaying curve with a time constant equal to the number of averages, N_a, times the record length, T. If a measurement is made with no overlap, $N_a \times T$ is equal to the time constant. Exponential averaging is a continuous process, and is useful for analysing continuous non-stationary signals. Peak averaging records the largest

amplitude of each spectral line. When a new sample is included, values are compared at each frequency and the largest retained. Averaging simply stops upon reaching the required number of averages.

2.2.1.7 Analysis

The main purpose of signal analysis here is to determine the dynamic behaviour of a structure. This is done by measuring the input-output relationship. Several methods can be used to describe the structural response, either in the time or frequency domains. Analysis in the time domain provides information on pulse reflection, whereas analysis in the frequency domain shows the vibration response of the structure. In general, the three parameters used in this type of structural analysis are acceleration, velocity and displacement. All three are related, and can be calculated using the following integrations (Eqns 2.13 to 2.15);

Acceleration $$\ddot{x} = \frac{\partial^2 x}{\partial t^2}$$ Eq. 2.13

Velocity $$\dot{x} = \frac{\partial x}{\partial t} \quad \text{or} \quad \dot{x} = \frac{\ddot{x}}{2\pi f}$$ Eq. 2.14

Displacement $$x = \frac{\ddot{x}}{4\pi^2 f^2}$$ Eq. 2.15

2.2.1.8 Time domain functions

The most common properties of interest can be obtained by the impulse response function $h(\tau)$. The output signal $b(t)$ is measured in terms of $a(t)$, with the relationship between the two signals given by Eq. 2.16.

$$b(t) = h(t) \times a(t) \qquad \text{Eq. 2.16}$$

For Eq. 2.10 to hold true, the system must be physically reliable, stable, linear and unchanging. Other time domain functions available include autocorrelation and cross-correlation. The autocorrelation expresses the correlation between a signal and a displaced version of itself. Autocorrelation is used for echo detection in signals and measurement of their strength and time delays, as well as the detection of periodicity buried in noise. This is possible because the autocorrelation of a periodic signal is also periodic whereas that of noise falls rapidly to zero with increasing time displacement. The cross-correlation expresses the correlation between the first signal and a displaced version of the other signal. Cross-correlation is used to measure time delays between signals or in systems, identifying transmission paths and to detect signals buried in extraneous noise.

2.2.1.9 Frequency domain analysis

A frequency spectrum is derived from an averaged time signal using an FFT analysis, and the resultant spectrum is often referred to as the autospectrum. The FFT of a correlation function, described in the previous section, results in the power spectrum. The FFT of the autocorrelation function is known as the autospectrum, whereas the FFT of the cross-correlation function is the cross-spectrum. Both of these spectra are required to construct the frequency response functions which describe the modal parameters of the structure.

2.2.1.10 Frequency response function

When a time signal is transformed into the frequency domain, the input $A(f)$ and output $B(f)$ are related by the following expression;

$$B(f) = H(f) \times A(f) \qquad \text{Eq. 2.17}$$

$$H(f) = \frac{B(f)}{A(f)} \qquad \text{Eq. 2.18}$$

Where $H(f)$ is known as the frequency response function (FRF) and can be described as the Fourier transform of the impulse response function $h(t)$. However, noise is often present in measurements in the input, output or both, which prevents this method form functioning. Therefore, modified equations are used as follows:

$$H_1(f) = \frac{G_{ab}(f)}{G_{aa}(f)} \quad \text{and} \quad H_2(f) = \frac{G_{bb}(f)}{G_{ba}(f)} \qquad \text{Eq. 2.19}$$

Where $G_{aa}(f)$ is the autospectrum of the input signal

$G_{ab}(f)$, $G_{ba}(f)$ is the cross-spectrum of the input and output signals

$G_{bb}(f)$ is the autospectrum of the output signal

In most cases, H_1 and H_2 will produce equal answers when used in impact testing. H_1 is used with noise-free measurements on non-linear systems and measurements with uncorrelated noise on the output signal, but no noise on the input signal. The latter is often the case at frequencies where the frequency response function shows anti-resonance. In these situations, the input autospectrum $G_{aa}(f)$ is measured correctly. If

the averaging number is sufficiently large, the non-linear contribution or the noise is averaged out in the cross-spectrum $G_{ab}(f)$. H_1 is also applicable to measurements with a flat input autospectrum and leakage in the output autospectrum. H_2 analyses measurements with uncorrelated noise on the input signal, but no noise on the output signal. (This can be the case at resonance frequencies for a mechanical system excited by a vibration exciter.) In this situation, the output spectrum $G_{bb}(f)$ is measured correctly. If the averaging number is sufficiently large the noise is averaged out in the cross-spectrum $G_{ba}(f)$. H_2 is applicable to measurements with a flat input autospectrum and leakage in the output autospectrum.

In this thesis, the H_1 method is used for the modal analysis section. In modal analysis, the input signal is measured in terms of force and the output signal is measured in terms of motion. This motion is typically acceleration, velocity or displacement. There are several different types of FRF, dependant on the parameter measured and the transducer type. Table 2.2 shows the range of structural FRFs available, dependant on the output parameter.

2.2.1.11 Coherence function

Coherence is a number between one and zero, and is a measure of the degree of linearity between two related signals, such as the input force of a structure related to the vibration response to that force.

$$\gamma^2(f) = \frac{H_1(f)}{H_2(f)} \qquad \text{Eq. 2.20}$$

Coherence, shown in Eq. 2.20, is thus a two-channel measurement, and does not apply to single-channel measurements of vibration signatures. In a frequency response

measurement of a mechanical structure, if the structure is linear, the coherence will be one, but if there is some non-linearly in the structure or if there is noise in a measurement channel, the coherence will be less than one. The FFT analyser is able to measure the coherence between channels, and it is a useful tool in determining good from noisy, or meaningless, data.

2.2.2 Damage detection

Full-scale dynamic testing of bridges can provide useful information on the performance of structures. By measuring the dynamic response due to loading, either ambient or impact loading, modal and system parameters can be determined. Salawu and Williams[2.55] highlight early research carried out on bridges, citing the reasons for the testing, as well as a general discussion of excitation devices used. Figure 2.11 shows two pieces of equipment used for exiting structures.

Researchers have used many different methods for the monitoring and damage detection of bridge structures, using both dynamic and static behaviour. Damage detection through changes in frequency have also been developed by researchers[2.56].

One dynamic method is the modal flexibility method which includes the influence of modeshapes and resonant frequencies. Usually this method uses the impact method, but in the case of Zhao and DeWolf[2.57], the approach is modified so that the excitation is provided by ambient vibration due to traffic loading.

One study by Nassif *et al.*[2.58] used data obtained from weigh-in-motion (WIM) sensors, incorporating axle load, gross vehicle weight and number of axles, to construct a three-dimensional model for the simulation of multiple truck loads on bridges. The results are

presented as a function of the static and dynamic stresses in each girder, and the intention is to provide an alternative method for the development of live-load models for design and evaluation.

Most bridges are designed using static analysis procedures, which can often produce inaccurate answers due to the inherently complex nature of vibration. Simplification of the problem into a beam yields accurate solutions for simple geometries, yet is not sufficiently rigorous for more complex structures such as skewed bridges. Memory *et al.*[2.59] developed a method for estimation of resonant frequency by applying Rayleigh's method to a grillage model which can provide results within ten percent accuracy. The paper also considers the effect of support stiffness, primarily through a change in bearing type from simply supported to resting on elastomeric bearings. This alteration of support condition is not considered to have an effect on the resonant frequency of the structure.

Damage detection in structures is a well researched topic, with many techniques available for the analysis of bridges. One such method of analysis is vibration based damage identification using ambient excitation from vehicles in the case of a bridge. Several methods of determining the modal parameters of the structure are available; mode shape curvature, change in flexibility, change in flexibility curvature and strain energy methods to name a few. Alvandi and Cremona[2.60] compare these techniques to detect damage in a beam structure. The results presented would tend to indicate that the strain energy method provides the most accurate results, especially when the signal being analysed contains a large proportion of noise.

Thyagarajan *et al.*[2.61] use the receptance version of an optimised FRF of a truss structure to determine damage location, which is then applied to an FEA model to predict structural integrity. However, this method does have a couple of deficiencies. The technique is computationally intensive making it more applicable to smaller structures. To apply this method on a larger scale would require the analysis of sections of the structure to be analysed sequentially, which could introduce possible errors into the analysis. The second limitation is that the variation in ambient temperature alters the elastic modulus of the structure to the extent that FRFs may not be repeatable.

The dynamic stiffness technique is used to locate damage in structures, with a particular emphasis on concrete or masonry structures, through an often small change in eigenfrequency values or magnitude. The dynamic stiffness shown is the force divided by the displacement and it is a dynamic measure (in Nm^{-1} units) of the ease with which a body may be deformed. Many researchers have applied this technique to locate damage in structures, with the most common application in civil engineering being the location of cracks in concrete beams[2.62 & 2.63].

In general, a variation in the primary natural frequency can be attributed to a cracking in the beam, a change in the deformation modulus of the beam or in bearing conditions[2.64]. It is often problematic to locate damage, or at least attribute it to a change in one single parameter. Therefore, it is necessary to record the change in more than one frequency. In addition to the application of the method for concrete damage, researchers have also used the method to determine the dynamic properties of masonry arches[2.65]. This particular investigation showed that the arch characteristics were related to the degree of restraint, fill material properties and any external loading on the

structure. These parameters are all possible considerations when considering the response of the highway bridge tested during this research.

Another dynamic descriptor for structures is the mechanical impedance method. Impedance is defined as the force divided by the velocity and is a dynamic measure of how much a structure resists motion when subjected to a given force, and it is the reciprocal of mobility. Tseng and Wang[2.66] use this method to determine the structural impedance response from the electrical admittance measurements of piezoelectric transducer patches bonded to the structure. The method highlighted does not involve any modal analysis, but the data are used to update an FEA model to locate damage and estimate its severity. Further research on the applicability of the method to larger structures is currently underway.

Lee and Shin introduce a method of damage detection in plates based on the partial differential equations of motion for damaged plates[2.67]. This method uses FRF data in the damaged state and can locate several different damage locations simultaneously. Two methods are compared, the full-domain and reduced-domain methods. In the reduced-domain method, the spatial domain of the problem is reduced based on prior knowledge of the damage location. In reality, this in an unlikely scenario, therefore a three step method of detection is outlined. The results showed that the best results are obtained using the reduced-domain method in conjunction with a multi-excitation frequency and multi-measurement point approach.

Green and Cebon[2.68] introduce the effects of HGVs on bridge structures, proving a potential method for predicting the behaviour of a bridge to a set of wheel loads. The

method uses the convolution of vehicle loads with the modal response of the structure. The convolution integral is then solved using the FFT. Experimental work is used to validate the method, where modal properties of a bridge obtained using an impact hammer test. Data obtained during single vehicle tests were then convolved with the impact testing data, and the results compared with the predicted response. The modal tests indicated that simple beam and plate models provide accurate predictions of mode shapes and natural frequencies of the bridge.

Boothby and Laman[2.69] investigated the extent of damage caused by vehicle loading on concrete bridge structures. An analytical model to evaluate the effects of loading on a bridge deck slab was developed. This analysis highlighted the importance of mechanical and environmental factors, but shows that due to the exceptionally high number of cycles required to failure, mechanical factors are less significant than environmental effects.

Petryna and Krätzig use the compliance method as the basis for a damage detection method[2.70]. The damage is based on the maximum compliance measurement from the structure's lowest eigenfrequencies and mode shapes. The method is therefore most applicable for determining damage which affects bending modes. Further research into a reduction of longitudinal stiffness and shear stiffness is currently underway. Results obtained using the method indicate that the method is relatively insensitive to possible uncertainty factors affecting the accuracy.

Model updating methods based on vibration data can often contain uncertainties that affect the accuracy of damage detection. Xia and Hao proposed a statistical method of

damage detection based on changes in frequency[2.71]. The stiffness matrices in the damaged and undamaged states are obtained, then the parameters are estimated by the perturbation method and then verified using the Monte Carlo method. The probability of damage is then determined based on these parameters in the damaged and undamaged states, and the higher the probability, the more likely damage is present.

Owolabi *et al.* use a technique of detection where accelerometers are attached to the damaged sample[2.72]. Measurements of frequency changes in the first three resonant frequencies are noted and the corresponding amplitudes of the FRFs are used to quantify the extent of the damage. The method provides accurate results and a simple procedure for determining structural alterations. However, this method has only been applied to small-scale structures, and the applicability to larger structures is uncertain as there are many more parameters that can affect the response.

FEA is often used in conjunction with experimental data obtained to produce accurate solutions for dynamic analysis of complex problems. This technique is known as modal updating. Teughels and De Roeck use the technique to locate and quantify damage to a highway bridge currently in service in Switzerland[2.73]. Damage in the structure is represented by a change in the Young's and shear moduli, which are distributed over the model using linear piecewise approximation functions.

Other applications of FEA are to provide a damage indication and life-time estimate of structures. Krätzig and Petryna develop this method[2.74] by applying it to three examples of damaged structures, then predicting the estimated life of the structure, which is effectively modal updating.

Operational modal analysis (OMA) is a newer method and does not rely on an input signal, and is therefore known as output only analysis. Rather than using a recorded force input, output only analysis determines the modal parameters of a structure using the ambient vibrations, caused in this case by vehicle movement. One example of OMA is presented by Lee *et al.*[2.75], who extract the modal parameters for the response data using the random decrement method. Once this data has been analysed, damage location is performed using a neural network using the ratios of pre-damaged resonant frequencies to post-damage as well as the mode shapes, Figure 2.12. Results indicate that the technique has some potential for locating cracks in the structure.

Two methods of determining the modal parameters using operational modal analysis are available; frequency domain decomposition (FDD) and stochastic sub-space identification (SSI), in the time domain. Many papers outlining applications of the two methods are available[2.76 - 2.78], and the three cited herein highlight the key features of FDD and SSI methods. The two methods allow a graphical representation of mode shapes at each resonant frequency to be visualised. In general, the SSI technique will give the most accurate results, but a combination of the two is advisable to validate experimental results. Order estimation and the detection of spurious modes can often affect the accuracy of the two techniques. Zhang *et al.*[2.79] propose a method using component energy as an identifier rather than matrix values, and a stabilisation diagram utilising the Hankel matrix[2.80].

Peeters and Ventura present a study comparing several different modal anlaysis techniques from forced, free to ambient vibration tests[2.81]. A highway structure in Switzerland was selected, and six separate different methods of system identification

were compared. The methods used ranged from simple peak picking methods, FDD methods, orthogonal polynomials, the Ibrahim time domain method, SSI methods and a two stage least squares method. The results obtained using the different methods indicate that certain methods of excitation are not applicable in every circumstance. What is clear is that ambient vibration techniques provide a method of exciting the full range of resonant frequencies in a large scale bridge structure when compared to a mass-shaker or simple impact testing.

2.2.3 Wavelets

In recent years, use of the wavelet transform as an analysis tool has become widespread. The wavelet transform (WT) is often compared with the Fourier transform, in which signals are represented as a sum of sinusoids. The main difference is that wavelets are localized in both time and frequency whereas the standard Fourier transform is only localized in frequency. Wavelet transforms are broadly classified into the discrete wavelet transform (DWT) and the continuous wavelet transform (CWT). Figure 2.13 shows three wavelet transforms and their equations. The principal difference between the two is the continuous transform operates over every possible scale and translation whereas the discrete uses a specific subset of all scale and translation values. The discrete wavelet transform is less computationally complex in comparison to the FFT, taking O(N) time as compared to O(N log N) for the FFT, where N is the data set size. Melhem and Kim[2.82] compare the two methods of analysis on a concrete pavement and simply supported pre-stressed concrete beams. Yin *et al.*[2.83] use the WT on FRFs from an FFT analysis to determine natural frequencies and damping estimates. This method provides a simple solution, but is not as accurate for closely spaced modes as multi-degree of freedom methods. Yan *et al.*[2.84] use a modified method of the WT

incorporating a bootstrap distribution theory to evaluate uncertainty effects. Data obtained experimentally is compared to data generated numerically, and an excellent correlation is achieved.

Kim and Melhem[2.85] provide an excellent review of structural damage detection using the wavelet transform. In this review, the methods for damage detection were arranged into three categories: variation of wavelet coefficients, local peturbation of wavelet coefficients in a space domain and reflected wave caused by local damage. The first method is used to find damage and its severity, usually by changes in the modal properties of the structure. The second method localises the damage by identifying any irregularities in the wavelet coefficients near the crack location. The final category measures the severity and location of damage, which identifies damage through reflected waves from cracks. However, it is noted that damage severity is often difficult to estimate accurately. One solution to this could be the application of artificial neural networks. Hou *et al.*[2.86] and Basu[2.87] use the WT to localise damage through a change in structural stiffness through spikes in the response data.

One possible drawback of the WT is that the resolution is poor in the high-frequency region. One method proposed to resolve this problem is the wavelet packet transform (WPT)[2.88]. In this method, dynamic signals measured from a structure are decomposed into wavelet packet components, then component energies are calculated and used as inputs for damage detection using neural network models. Results for a three span continuous bridge show that the method has some validity by locating changes in stiffness. Law *et al.*[2.89] also make use of this method, using the WPT sensitivity to locate and quantify damage. This method also has the advantage of not being sensitive

to noise in the measurements. Sun and Chang[2.90] apply a statistical damage threshold to data decomposed using the WPT. This method is particularly powerful for determination of damage location in noisy signals as components that have small signal energy are discarded.

Damage detection in plate structures is particularly applicable with respect to many engineering structures, especially civil engineering structures such as highway bridges. Loutridis *et al.*[2.91] use a two-dimensional WT to locate and quantify damage in plate structures using a method similar to that used for edge detection in images. Damage is identified by changes in the transform coefficients; spatial changes locate the damage, whilst the maximum value and energy content measured to investigate cracks of different length and depth. It should be noted that this method is only applicable to two-dimensional structures, and requires a fine spatial resolution as well as relying on the accuracy of response data. Sheen[2.92] proposes a three-dimensional analysis technique using a wavelet-based demodulating function by sweeping the filtering passband from a low-frequency band to a high-frequency band.

Rucka and Wilde[2.93] propose a method using wavelets on static deflection profiles as opposed to modeshape. The method relies on accurate digital pictures with a fine resolution which are not always available for standard visual inspections. It should be noted that due to noise in the measurements, in certain cases, it is awkward to locate damage due to false maxima being present in the responses. Only once the crack is of a significant depth can it be identified accurately. This could be a potential difficulty when trying to identify smaller instances of damage.

2.2.4 Genetic algorithms

Hu *et al.* use two algorithms applied to modal testing data to identify damage in structures which are based on the subspace rotation algorithm[2.94]. The first method uses the mass and stiffness matrices for damage identification purposes, whereas the second method only uses the mass matrix. The magnitude of damage is then estimated using a quadratic programming technique. Both methods can locate the damage, but only the second method using just the mass matrix can accurately predict the damage extent. Even then the second method cannot detect the extent in all of the presented cases, which is a weakness of this method.

One method of damage detection using FRFs obtained from vibration testing is the damage location vector (DLV) method. Huynh *et al.*[2.95] obtain damage location by comparing FEA models of the structure in its original undamaged state with an updated model using impact hammer testing which allows determination of the damaged structure's stiffness matrix. Test results showed that the method is capable of detecting damage in simple structures such as a truss or plate, although further investigation is required to determine applicability to larger, more complex structures.

Duan *et al.* use a proportional flexibility matrix (PFM) method from scaled mode shapes and frequencies to apply the DLV method to ambient vibration problems[2.96]. Instead of real flexibilities, the PFM is incorporated into the DLV method by determining PFMs for the undamaged and damaged states. This method is, however, reliant on the accuracy of the mode shapes and frequencies for determination of the PFM, and data used for the pre- and post-damaged PFMs must be comparable.

FEA is a powerful tool that can be used in the determination of damage location and extent. Dutta and Talukdar use an adapted version of FEA using the modal curvature technique to detect damage in simulated data for simply supported and continuous bridges[2.97]. Damage is located in multiple positions, and what is apparent is that damage is located more accurately using the lower modes in this case where the signal to noise ratio and sensitivity of measuring equipment is such that higher order modes may be swamped by noise in the signal. This is shown in Figure 2.14, which indicates that higher modes should have an increased sensitivity due to the increase in slope, but in practice, lower modes are better in the authors case due to the lower signal to noise ratio. This should come as no surprise, as these modes will tend to contain more dynamic energy than those in the higher end of the frequency spectrum, although more modes are required to increase the accuracy of the analysis.

The use of structural identification techniques has expanded in recent years due to the increase in computational power available and advances in signal processing techniques. Neural networks and genetic algorithms are one example of this improved technology, and are being used increasingly due to their ability to detect patterns in data. Early work in the 1990s by Masri *et al.*[2.98] highlights the methodology used for the genetic algorithm method, where data for a healthy structure is obtained and compared with data for varying stages of damage.

Lee *et al.* use a neural network to track damage present in a structure using modal properties applied to an FEA model this model is then compared with the original undamaged model by comparing the differences between mode shape coefficient ratios[2.99]. Two examples presented are a simple beam and a multi-girder highway

bridge. The method does provide accurate solutions but does present several false alarms when applied to the full scale multi-girder bridge. Chou and Ghaboussi[2.100] use a similar method, but identify alterations in static displacements to characterise structural parameters such as Young's modulus and cross-sectional area, as opposed to stiffness matrices.

Pothisiri and Hjelmstad use an algorithm to detect global damage parameter estimates using both an FEA model and the measured structural response[2.101]. An optimisation scheme is used to locate the damage, then the algorithm is used to determine the probability of these measurements being actual damage locations using Monte Carlo simulations. The method can produce results that are accurate, but does seem susceptible to noise in the measurements when the ratio of crack depth to sample thickness is above 10%.

Modal strain energy methods have also been used to locate and quantify damage where the technique relies on changes in mode shapes and the stiffness matrix. One method proposed by Shi *et al.*[2.102] only requires incomplete modal data to locate and quantify damage, such as the incomplete measured mode shapes, the analytical mode shapes and the element stiffness matrix. The damage detection procedure is shown with two examples, one numerical and one on a two storey steel frame. The results show that the method can locate damage, but the method is sensitive to noise in the measurements and cannot accurately determine the extent of damage when more than 5% noise is present in the data.

As a result, another paper by Shi *et al.* presents an improved method of detection using both the stiffness matrix and mass matrix of the system to quantify damage[2.103]. Using this method reduces errors present from modal truncation and improves the convergence properties of the previous algorithm. The same two tests are performed as in the previous paper, with vastly improved results (Table 2.3).

Sazonov and Klinkhachorn[2.104] attempt to determine an optimal time sampling interval that would reduce the effects of truncation and noise errors in the measurement.

2.2.5 Moving loads

The vibration of plate structures under moving loads is a topic that until recently was not researched to any great degree. Frýba and Pirner[2.105 & 2.106] provide an excellent initial background to the theory of moving loads on plate structures, as well as a comprehensive review of literature containing research on plate structures.

In bridge engineering, the loading on the structure comes in the form of a vehicle travelling at a certain velocity and imparting a force into the structure. The vehicles that cause the largest forces, and hence potentially most damage, are the largest vehicle types such as HGVs, which can impart forces up to four times greater than an average car. In recent years, the permissible loading for HGVs has increased to 44 tonnes, and may possibly be increased again to 48 tonnes in the near future. The distribution of loading in HGVs, and the type of vehicle configuration, *i.e.* number of axles and suspension type, can have a large influence on the transmission of loading into the structure. Figure 2.15 shows historic vehicle width limits, length restrictions and gross vehicle weight.

One method used to analyse moving loads is to use the orthotropic plate theory and apply the modal superposition principle, then using the Tikhonov regularisation procedure[2.107] to provide the boundary conditions for the loading in the time domain. Zhu and Law[2.108] use this method, and compare results obtained using a beam model with those for a plate model. Using actual measured strain and acceleration data from experimental work, the validity of the method is shown. What is apparent is that acceleration methods would appear to provide much clearer results than strain measurements, although it should be noted that forces moving down the centreline of the deck are more accurate than those measured on an eccentric path. This is only in the authors work, were more advanced sensors used, then strain based methods would be as accurate as acceleration methods. This is shown in Figure 2.17. It is also considered that the problem may be accurately analysed using a beam model when the longitudinal vibration modes are more prevalent. This method is also applied to continuous multi-lane bridges, and responses are considered with respect to the dynamic impact factor of the deck[2.109]. The study indicates that the road surface roughness is more important than the vehicle speed to the impact factors, as is the transverse position of the vehicle on the deck.

Two papers by Yang *et al.*[2.110 & 2.111] outline a method for determining the bridge frequencies using the dynamic response of a passing vehicle. The papers show an initial numerical treatment of the problem, followed by the experimental results obtained from testing on a structure. The method highlights the fundamental frequency only.

The overall dynamic response of a bridge is affected by many parameters. Researchers have investigated the effects of bridge running surface texture, developing a three-dimensional analysis approach to define the response of the bridge structure[2.112].

One method of parameter evaluation is highlighted by Chatterjee *et al.*[2.113] and Au *et al.*[2.114], where the response of a continuous bridge to a single sprung and unsprung mass is obtained by modelling the deck as a continuous system. The irregularity in pavement surface is modelled by a stationary random process characterised as a specific power spectral density (PSD) function. The response analysis is performed in the time domain by simulating the random profile of the deck. Effects of torsion due to eccentric loading and any non-linear response due to vehicle-pavement interaction are also considered. A parametric study highlights some interesting information with regard to the effect of pavement roughness, especially in terms of DAF which appears to be influenced by vehicle velocity and the type of idealisation applied[2.115]. Au *et al.* obtain the parameters through genetic algorithms which reduce the possible error in terms of parameter identification by comparing measured data with simulated data. Using this method, it is also possible to obtain information about the time varying vehicle contact forces between the vehicles and bridge surface (Figure 2.16).

The DAF is an important factor that can describe the response of structures to impact loading from vehicles. Pesterev *et al.*[2.116 & 2.117] proposed a method to assess the dynamic contact forces produced by vehicles passing over a discontinuity in the bridge running surface. Functions describing the road surface irregularity are used in conjunction with first-order complex differential equations that describe the moving vehicle, then the solutions to all equations are found and expressed in terms of a

complex variable, the pothole dynamic amplification factor. Each irregularity has a unique answer.

Law and Zhu investigate the influence of road surface roughness combined with the braking effects of a vehicle[2.118]. In this research, the structure is modelled as a multi-span Euler-Bernoulli beam with non-uniform cross-section resting on springs with a large stiffness. The vehicle is modelled as a series of moving loads at a fixed spacing. The braking effect of the vehicle generates excitation forces that cover a large frequency range, and as such this requires a large number of vibration modes for accurate solution. Figure 2.18 show the apparatus and results obtained. It is considered that the type of suspension has a significant effect on the dynamic response, particularly when braking on top of the structure. The pitching effect induced by the vehicle can generate large oscillatory forces in the deck structure.

Savin[2.119] uses an exact analytical solution for an Euler-Bernoulli beam traversed by a series of pointloads, analysing the dynamic amplifications for both the forced response and free vibrations. Based on the results derived, a set of simple formulae are obtained for the maximum expected dynamic amplifications. This method could be extended into plate vibration as all the required information regarding plate eigenmodes in most cases of boundary condition are currently available.

Zhu and Law[2.120] developed a method of determining the parameters of moving loads through a technique called regularisation and the superposition method. The method was applied to a continuous Euler-Bernoulli beam and uses measured strains and acceleration to identify and quantify interaction forces on the bridge structure. The

technique is best for single-span structures as multispan structures are more sensitive to noise in measurement data, and erroneous data are observed at the supports. It is apparent from the data presented that measured accelerations provide a much more accurate analysis than measured strain energy. Another paper by Zhu and Law[2.121] uses measured strains to identify moving loads by comparing the results obtained using two methods; one based on the exact solution method, the other based on FEM. The identified results are good for axle loads, but slightly poorer for individual loads, and both methods failed to identify loads with a large eccentricity.

2.2.6 Other NDT methods

Woodward[2.122] summarises a wide range of available techniques for NDT of concrete structures; pulse methods such as acoustic emission and ultra-sonics, electromagnetic methods, visual methods such as photogrammetry, infra-red methods, radar, electrical methods, magnetic methods and other methods such as surface hardness, pull out tests and permeability tests.

Forde outlines recent advances in NDT methods for concrete structures[2.123], outlining the possible advantages and applications of each particular type. The paper separates the methods into sonic, ultrasonic, electromagnetic, and electronic methods of NDT.

One method which is used extensively for the NDT of concrete structures is radar inspection, which falls into the electromagnetic category of analysis. Radar has been in use since its development during the Second World War, and with increasing computational power and advances in equipment technology, radar is used for a wide variety of applications. In terms of civil engineering structures, radar tends to be used to investigate the integrity of either concrete or masonry structures. Voids can be detected

by the reflections of signals, allowing the location to be determined due to wave velocity (Figure 2.19). Bungey and Millard use this method[2.124], and Bungey presents an update on the applications and limitations of radar testing such as the portability or the inherent cost of equipment[2.125]. One practical application of radar for highway structures was carried out in Virginia in the United States. Two methods of NDT were used, radar and impact-echo testing, and the results compared with concrete cores taken from the structure. The research found that the methods are in close agreement with the concrete cores taken, although the impact-echo method must be performed with great care and attention[2.126]. Consideration must also be given to the input parameters, namely the frequency in this case, as choosing the wrong frequency could result in data being lost or voids not being detected[2.127].

Advanced methods of NDT for concrete such as spectral analysis of surface waves (SASW) and ultrasonic pulse velocity testing are also used to determine material properties, shown in Figure 2.20. SASW is of particular use for bridges when attempting to determine the depth of weathering on the concrete[2.128]. Other applications of NDT methods are the determination of such parameters as the modulus of elasticity of concrete, which is not an easily definable variable once the structure has been constructed. Hassan *et al.*[2.129] apply the ultrasonic method of testing to determine this property.

Another method of determining structural integrity is the acoustic emission method[2.130 & 2.131]. Acoustic emission may be defined as a transient elastic wave generated by the rapid release of energy within a material. Small-scale damage is detectable long before failure, so AE can be used as a non-destructive technique to find defects during

structural proof tests. An typical transducer and output from AE tesing are shown in Figure 2.21.

Advances in technology in recent years have seen the development of new techniques for structural health monitoring. One example of this is fibre optic sensors. These sensors can provide high-resolution and measurement capabilities not possible with other types of system. Casas and Cruz[2.132] outline the possible applications for fibre optics in terms of structural assessment. The sensors are capable of monitoring strain, temperature, inclination, acceleration, load measurements, ice detection, vehicle speeds and weights as well as corrosion and cracking problems in concrete structures. This technology is currently in use on the Tsing Ma suspension bridge in Hong Kong[2.133]. Other structures, so called smart structures, have been monitored in the long-term using a combination of sensors such as strain gauges, deformation meters and WIM sensors. These structures have constantly updated information on the condition of the bridge which can be applied to an FEA model to analyse their dynamic response in a range of conditions.

A more recently developed technology called photgrammetry has been applied to the maintenance of bridge structures[2.134 & 2.135]. Photogrammetry is a non-contact technique used to determine the three-dimensional geometry of physical objects, with particular application to structures that are difficult to access (Figure 2.22).

2.3 Bridge bearings

Until the publication of BS 5400: Part 9[2.136] which deals with the design, manufacture, testing and installation of bearings for bridges, no British Standard had comprehensively covered bridge bearings. BS 5400: Part 9 is divided into two sections; Part 9.1 deals with the Code of Practice and outlines rules for the design of bearings, whereas Part 9.2 specifies the materials, method of manufacture and installation used for bearings. Bridge bearings fulfil a number of functions:

1. to transfer forces from one part of the bridge to another, usually from the superstructure to the substructure;
2. to allow movement (translation along, and/or rotation about any set of axes) of one part of a bridge in relation to another;
3. by allowing free movement in some directions but not in others, to constrain that part of the bridge supported by the bearings to defined positions and/or directions. Lee[2.137]

There are several types of bearing; roller bearings, rocker bearings, sliding bearings, pot bearings and elastomeric bearings (see figures 1.1 to 1.5). Elastomeric bearings come in two basic forms; the laminated bearings which consist of one or more sections of elastomer bonded to metal, usually though a process known as vulcanisation, a process of cross-linking the polymer chains of the rubber molecules invented in 1839 by Goodyear, and bearing pads which are simply un-reinforced sections of elastomer of relatively thin section, figure 1.1.

Elastomeric bearings have the capability to resist most types of movement to a certain extent. Translation can be accommodated by shear in the elastomer, and rotational movement by the difference in compressive strain within the elastomer. It is considered that elastomers should posses a high shearing flexibility to prevent the transmission of large horizontal loads as well as a high rotational capacity, thus avoiding the transmission of large moments to the supports. The vertical stiffness of the elastomer should be high enough so as to avoid large displacements under loads.

Tests reveal that the tolerance of layer thickness is of high consideration, as poor control can cause larger compression strains, deflections and can lead to early initiation of yield. The compression stiffness of an elastomeric bearing is dependent upon the shape factor S, defined as the ratio of one loaded area to the total force-free surface area.

$$S = \frac{A_e}{l_p t_e} \qquad \text{Eq. 2.21}$$

Where A_e is the effective plan area of the bearing, *i.e.* the plan area common to elastomer and steel plate; l_p is the force-free perimeter of the bearing; t_e is the effective thickness of an individual elastomer lamination in compression; this is taken as the actual thickness, t_i, for inner layers and $1.4t_i$ for outer layers.

When the bearing has no holes,

$$l_p = 2(l_e + b_e) \text{ and } A_e = l_e b_e \qquad \text{Eq. 2.22}$$

Where l_e is the effective length of the bearing which equates to the length of the reinforcing plates, and b_e is the effective width of the bearing, again equal to the width of the reinforcing plates[2.137].

The inclusion of steel plates in elastomeric plates has little effect on the shear stiffness, with shear strain limited to aid the prevention of fatigue problems. BS 5400: Part 9.1 states that the shear strain due to translational movement, ξ_q, is given by $\xi_q = \delta_r / t_q$. (Eq. 2.23)

BS 5400: Part 9.1 also states that the design pressure on elastomeric bearings should be limited to GS or 5G, where G is the shear modulus in terms of shear stress over shear strain. However, at sub-zero temperatures, elastomers are susceptible to stiffening, although the process is often reversible. Figure 2.23 shows typical shear modulus for an elastomeric bearing at varying temperatures. To accurately determine G, it must be multiplied by 1-T/25, where T is the recorded Celsius temperature. The frequency or rate of application must also be considered, and dynamic stiffness factors for different hardness and shear modulus are listed in BS 5400: Part 1.

BS 5400: Part 1 states that in order to provide a satisfactory margin against the effects of fatigue, the sum of the nominal strains should not exceed 5%.

$$\xi_t = k\,(\xi_c + \xi_q + \xi_\alpha) \qquad \text{Eq. 2.24}$$

Where k is equal to 1.5 for live loads; 1.0 for all other types of loading; ξ_c is the nominal strain due to compressive loads;

$$\xi_c = 1.5V / GA_1S; \qquad \text{Eq. 2.25}$$

ξ_q is the shear strain due to translational movement; ξ_α is the nominal strain due to angular rotation;

$$\xi_\alpha = (b_e^2\alpha_b + l_e^2\alpha_l) / 2t_i \sum t_i \qquad \text{Eq. 2.26}$$

V is the vertical load; A_1 is the reduced effective plan area due to the loading effects;

$$A_1 = A_e (1-(\delta_b / b_e) - (\delta_l / l_e)) \qquad \text{Eq. 2.27}$$

δ_b is the maximum horizontal relative displacement across its width; δ_l is the maximum horizontal relative displacement along its length; α_b is the angle of rotation across the width of the bearing; α_l is the angle of rotation along the length of the bearing; t_i is the thickness of individual layer of elastomer being checked; $\sum t_i$ is the total thickness of elastomer in the bearing.

This is an essential parameter to determine accurately as rotations incurred within the elastomer can lead to delamination of the steel plates, causing further degradation to occur. In general, the maximum rotational displacement is taken to not exceed the displacement due to vertical loading. The displacement can be determined using the following equation;

$$\delta = \frac{Vt_i}{5A_eGS^2} + \frac{Vt_i}{A_eE_b} \qquad \text{Eq. 2.28}$$

Where E_b is the bulk modulus of the elastomer.

The horizontal movement of bearings can be determined using the following expression;

$$H = \frac{AG\delta_r}{t_q} \qquad \text{Eq. 2.29}$$

Where A is the plane area of the elastomeric bearing; G is the shear modulus; δ_r is the maximum horizontal displacement; t_q is the total thickness of the elastomeric bearing.

Elastomeric bearings subject to long-term loads exhibit evidence of creep and stress relaxation which are dependent on temperature, stress history and formulation of elastomer. In certain cases, compressive creep to the order of 25% of the initial deformation due to loading has been identified though testing. In general, creep and stress relaxation need not be considered a severe problem (as far as elastomeric bearings are concerned) as a significant proportion of the creep has already occurred by the time joints and the final running surface are installed.

One particular special type of bearing is the pot bearing. Pot bearings are comprised of a circular, constrained non-reinforced natural rubber or neoprene pad, enclosed in a steel pot. The load is applied to the elastomer by a piston attached to the upper bearing plate, and the arrangement is sealed to prevent elastomer leakage between piston and pot. The elastomer is prevented from expanding, and as rubber is rendered incompressible, the elastomer behaves similarly to a fluid. The stress within the elastomer is limited by the effectiveness of the seal, but should be limited to 40 Nmm^{-2}. Pot bearings allow a rotation angle of up to 1/50, in the horizontal direction rotation should be limited so as the vertical strain experienced at the perimeter of the pad is not more than 15%, and in

combination with a sliding surface such as PTFE (Teflon®), can also allow horizontal movement.

As a general introduction to the research carried out up to the present time, a paper by Roeder[2.138] provides an extensive survey of research primarily carried out in the United States up to the early 1980s. Roeder presents a summary of the material behaviour of elastomers, combined with a review of theoretical and experimental work on bearings. From this survey, the main issues considered important for further research are; a better solution for the modes of failure of elastomeric bearings, with a particular emphasis on fatigue failure, and the provision of a set of guidelines for failure prevention; an enhanced understanding of rotation effects when combined with loading; and a fuller understanding of material behaviour with an emphasis on the effects of low temperature stiffening.

The University of Texas at Austin researches the behaviour and performance of elastomeric bearings. The main contributor is Yura, in conjunction with several other research staff and students, with many of the projects undertaken to provide guidelines for various national bodies and standards for bearings. Various reports[2.139 & 2.140] provide good background information regarding the behaviour of elastomeric bearings in the field, and test methods for bearings.

In the early 1970s the Transport Research Laboratory, TRL, investigated several different aspects of bearing behaviour. Taylor[2.141] investigated the effects of horizontal forces generated by bridge bearings by inputting a shearing force into the bearings using a test method developed, where the frictional forces generated by the elastomeric pad

are transmitted to a force transfer plate. The resultant forces were then recorded with force transducers. The results indicate that the method should be applicable to all types of bearing construction, and is particularly well suited to the monitoring of bearing performance over the long-term. Although the method produces errors, these are considered small, less than 2% for unidirectional loads and approximately 8% for multi-directional loads, and can be reduced if the accuracy of the transducers and stiffness of elastomer are factored into the equations.

Bridge bearings can also be used to mitigate translational movement caused by thermal expansion or by vehicle loading. Taylor[2.142] also investigates the behaviour of PTFE materials with respect to bearing movement. The research covers such phenomena as bearing stress, interface temperature, sliding speed, surface finish and lubrication, and their effects on bearing performance. What becomes apparent is that the sliding behaviour of the bearings is a function of the compressive stress, temperature, sliding speed, interface temperature and the previous loading history. Rather unsurprisingly, unlubricated surfaces generate a high frictional force during the first loading cycle which gradually decreases over time. The long term coefficient of friction can be calculate by an expression determined in the paper, and is related to the interface temperature as well as the applied compressive stress.

Material tests on elastomers were carried out in 1991 by Eyre and Stephenson[2.143] for the TRL. In addition to the tests performed to develop an understanding of the test methods, the effect of low temperature stiffening was evaluated on sample sheets, full-size samples and test pieces cut from bearings. From these tests, large increases in the modulus were measured in every case, although there were differences evident between

sample types (Figure 2.24). The testing showed that in certain cases, the modulus could increase by a factor of 4. Therefore, to obtain a more accurate value of modulus, it is recommended that tests be performed on samples of vulcanizates taken from the body of the bearing. It is considered that this will give a more accurate representation of the service performance. The testing was carried out on nine different vulcanizates supplied by bearing manufacturers, but only three were found to comply fully with BS 5400: Part 9. If the ageing resistance requirement is reduced from its current level then five of the samples would pass the tests, and would potentially last for up to 100 years.

Elastomeric bearings are often used to mitigate the effects of seismic activity due to the inherent properties, such as damping ratio, of the constituent elastomer. With elastomeric bearings as supports on a bridge structure, the dynamic response of the structure may be affected, and the natural frequencies of such an arrangement are required to determine overall response. Methods outlined[2.144 & 2.145] use the premise of setting the bearing stiffness, assuming a shape function based on beam theory and the flexural rigidity of the beam combined with the stiffness. In this case the method is applied to bridges subjected to moving train loads, but could simply be applied to highway bridges.

Monitoring of bridges with elastomeric bearings is not a common occurrence. One study on the feasibility of monitoring elastomeric bearing behaviour in a railway viaduct is presented by Wang and Chew[2.146]. A model to determine the relative displacement of bearings due to train loading is outlined, and the results indicate that the method could be applied to indicate the elasticity of the bearings over the long-term.

Maleki[2.147] investigates the effect of deck and support stiffness on the seismic response of bridges. The support stiffness was varied in the longitudinal and transverse directions, considering minimal stiffness to an infinite stiffness which is assumed to be pinned. The research indicates that an increase in the longitudinal stiffness value will result in a reduction in deck stress.

Kawatani *et al.*[2.148] investigate the effects of elastomeric bearings on the traffic-induced vibrations of highway bridges, when replacing steel bearings. Analytical three-dimensional studies are compared with numerical experimental data obtained on urban highway bridges. The results indicate that although the resonant frequencies or vertical displacements do not alter significantly, the horizontal displacements become larger. It is also noted that impact behaviour caused by vehicles striking the expansion joint is increased when elastomeric bearings are installed.

Research into bearing defects in the UK by Allot & Lomax[2.149] highlighted the fact that almost 94% of bearings had at least one defect. Each bearing type, and defect type, is listed with respect to age and other parameters such as temperature. The report shows that older bearings show an increased extent of damage, particularly in terms of bulging or splitting. Table 2.4 lists the bearing defects recorded.

Elastomeric bearing behaviour is often complex and provides a non-linear response. Haringx's theory is one method employed by researchers to determine certain parameters of laminated elastomeric bearings, as it considers lateral displacement and the rotational angle in the bearing as two separate variables. Chang[2.150] uses the Haringx method[2.151] to develop a finite element solution to the problem by obtaining a

4 × 4 analytical stiffness matrix. The matrix is then used in conjunction with another matrix for a rigid plate, and a stiffness summation procedure is used to construct the model. This model represents one individual layer of elastomer, and multi-layer bearings can be constructed using a number of elements. Chang investigates several distinct situations, such as the effect of compression forces, the effect of the total number of elastomer layers, the effect of the rubber layer thickness, the steel shim thickness, the effect of bearing diameter and rubber shear modulus. It is noted that the investigation into the behaviour of laminated bearings with varying layer thickness provides the most useful answer.

Testing elastomeric bearings is essential when attempting to determine the overall performance of bearings in service. One study in Florida by Potter *et al.*[2.152] determines the condition and strength of elastomeric bearings that have been in service for approximately 40 years. Durometer, Figure 2.25, and shear tests are used to determine the condition and strength. The tests revealed that although superficial damage to the bearings was evident through minor surface cracking, the bearings are still within acceptable limits for adequate working condition. The pads had shrunk slightly, and the stiffness of the pad had increased, but not to the extent that they would be considered faulty.

Bridge bearing specifications require the destructive testing of bearings to be performed. Othman[2.153] investigated the behaviour of elastomeric bearings, and discovered that thick rubber bearings exhibit a property profile, where the material properties of the bearing vary across its cross-section, when exposed to prolonged heating during the moulding process. The common accepted practice is to consider the outer layers of the

elastomer as being representative of the remainder of the bearing layers. However, certain properties show an increase closer to the centre of the bearings, such as modulus, tensile strength, hardness and compression set. This variation in behaviour does not adversely affect the performance of the bearing, as long as the change is relatively minor. If the change is large, it is noted that the compression and shear modulus may be affected, which could affect any design calculations performed. It is suggested that by improving the preparation and moulding techniques for bearings, any deterioration in the physical properties of the bearing can be reduced.

More recent research carried out in America investigated the performance of bearings at low temperatures[2.154 & 2.155]. Two separate types of bearing, each with a different shear modulus, were subjected to a series of tests to establish the effect of cyclic compression, shear, rate of loading, creep, temperature history, slip coefficient and the effect of the elastomer type. Tests were performed in an environmental chamber at four different temperatures; 23°C, -10°C, -20°C and -30°C over 21 days, and approximately 500 shear tests were performed during this time (Table 2.5). The results indicate that although creep rate is more significant at the low temperatures, the effect is much less than room temperature creep. However, cyclic compression forces and cyclic shear strain are not considered to have a large influence on the overall performance of the bearing. Recommendations are made with respect to values calculated from shear modulus tests. As this type of test is performed at a fast loading speed, it is considered that the results obtained be factored down to take this into consideration, and should also consider the crystallisation resistance and type of compound. Reductions of 30% and 20% are recommended for neoprene and natural rubber compounds respectively.

The research presented[2.156] forms the basis for a performance based test criteria for elastomeric bearings in cold temperatures. A variety of bearing types were tested at four separate locations with low temperature. A new evaluation criteria is proposed based on the expected bearing performance. Future performance is predicted based on a detailed analysis of regional temperature data to obtain test parameters. These results are then used to calculate the value of shear force and slip. Results obtained would tend to indicate that the current guidelines for cold-temperature testing are too severe as materials which perform adequately in service would be rejected based on test data. Figure 2.26 shows the minimum shade temperature for the UK, with Edinburgh and Berwick-upon-Tweed highlighted.

Yura furthers this research by suggesting a new method for defining shear modulus of bearings which does not rely on small samples of the bearing being removed. Testing by removing small samples can be costly and often do not accurately represent the actual in-service behaviour of the bearing, as well as being a destructive method. Research by the TRRL in the 1980s by Price and Fenn[2.157] highlights some of the factors to consider when proposed removal of bearings for testing is suggested. Yura's method is non-destructive, based on compression testing, and therefore only requires a compression test machine to apply the loading. Tests outlined in the AASHTO guidelines[2.158] involve inducing a shear force into the test sample. The inclined compression test proposed places two bearings between three wedge-shaped, or inclined, aluminium platens. Upon application of the compression force, a shearing force is introduced as a result of the inclined shape of the platens. The slope of the platens is factored into an equation used to calculate the shear modulus. The method outlined is only considered applicable to laminated bearings, plain bearings would be required to be bonded to steel

sole plates. The machine plates must be roughened to provide a surface to prevent slippage of the sample, and that slope should be restricted to a maximum value of 1:20. The values produced by this method are in close agreement with those obtained using the accepted methods outlined in the guidelines. The test method proposed can also be used to test sample sections of bearing removed from larger sections, but the test has the advantage of not destroying the bearing whilst proving its performance parameters.

The analysis of elastomeric bearings is often a complicated procedure as the response of bearings can be non-linear in certain cases, especially when considering laminated bearings containing steel reinforcing plates. FEA modelling of bearings can provide engineers with solutions to facilitate accurate design of structures, whether that is for base isolation or highway bridges. One such example of this type of analysis is shown by Herrmann *et al.*[2.159]. In a previous paper, Herrmann outlined a non-linear FE method for elastomeric bearings based on basic theory. Two computer codes, one in 2-dimensions based on plane strain analysis and another in 3-dimensions, have been constructed. At the time of submission of this thesis, the 3-dimensional analysis was simply considered a research tool, although initial comparisons with test results show that the model's accuracy is considered within acceptable limits. The intention was to develop a database of bearing response for a variety of bearing types and loading conditions. Several outcomes of the research warrant further investigation. It is proposed that a modified version of the shape factor is assumed to account for variations in bearing type and shape, and investigations into the effect of possible voids in the material on the overall response of the bearing. Other researchers[2.160] have applied a 3-dimensional FEA to high damping rubber bearings, with results that are in general agreement with experimental values obtained through testing.

More recent research involving FEA of bearings is presented in[2.161]. The research presented describes the effect of bearing pads on the performance of highway bridges, taking into consideration the pad-bridge interface which defines the support boundary conditions. FE was used to validate the bearing stiffness values set out in the AASHTO guidelines[2.158], varying the elastomer shear modulus, and subjecting the FE model of a bridge structure to static HGV loading. Bearings were simulated using vertical and horizontal spring elements. The research found that the effect of the bearing stiffness for new pads does not greatly influence the structural performance, and can actually be of benefit in certain cases. However, as the stiffness increases, the performance of the structure can be affected, although other effects caused by splitting and cracking of the neoprene are considered to be of greater influence to the overall performance of the structure. Other research using the finite element method has included investigations into large deformation behaviour of bearings [2.162 & 2.163] and a stress analysis under axial loading[2.164].

The stability of bearings is one of the major factors under consideration when designing highway bridges, in particular, the ability of bearings to cope with the increased horizontal loading now imparted onto structures by increasingly larger vehicles.

Gilstad[2.165] investigated the stability of three different bearing arrangements, a pot bearing, disc bearing and spherical bearing. Tests were based on two types of temporary loading events, one normal and one extraordinary. Conclusions drawn for the analysis of the three different types are: for pot bearings, the elastomer allows rotations therefore creating a pin support (Figure 2.27). The overturning moment depends on the distance from the applied force to the effective pin support. The disc support also allows rotations, and the overturning moment is dependent on the distance from the applied

force to the pin support. For the spherical bearing, the moment must take into consideration the effect of eccentricity of the vertical and horizontal loads. In general, an overturning load factor of safety of 3 for rectangular and 5 for circular surfaces are proposed under normal loading conditions. In the more extreme case of extraordinary loading, a factor of 1.5 for rectangular and 2 for circular surfaces is suggested.

The stability of elastomeric bearings is dependent on several factors. One such factor is the method of fixing the bridge superstructure to the bearing, and the bearing to the substructure. In most cases, simple pad bearings are held in place by frictional forces caused by the interaction between the rubber surface and either the steel beams or concrete abutments. However, in certain cases, pads can be tapered to carry inclined beams. Such pads can be prone to a phenomenon known as "walking", whereby the bearing slips from its position and can often lead to no bearing support under the inclined beam. The "walking" phenomenon has, in certain quarters, been attributed to shear forces in excess of the allowable frictional capacity of the interfaces. Hamzeh proposes another reason for this occurrence, namely viscosity-induced slippage, linked to the waxy substance which is added to the rubber as ozone protection which accumulates on the surfaces of the pad by secretion form the bearing. In the paper, Hamzeh *et al.*[2.166] describes an analytical model which makes use of Coulomb friction law by solving the equations of motion for the pad, noted in matrix form, as non-linear differential equations. The equations essentially represent an initial value problem solvable using the Newmark constant average acceleration method, and the resultant frictional forces can be determined.

McDonald *et al.*[2.167] investigates this phenomenon by compiling a large amount of information on neoprene bearings from DOTs in the United States, bearing manufacturers and respected researchers. A comprehensive field study attempted to capture slippage on video tape, and also girder thermal movements as well as pad relative to structure movements. From the data gathered, several conclusions can be drawn:

- Slippage occurs when girders undergo thermal movement, meaning slippage occurs on a daily basis, contrary to the currently accepted belief.
- The slope of the bottom of the girder at the bearing remains constant.
- Based on the survey of manufacturers, it is apparent that paraffin is added to bearings to account for ozone attack.

The paper concludes that bearing pads should not be ordered from companies who add paraffin to their bearings, and that the stringent ozone requirements be relaxed so that wax is not added to the bearing surface. In fact, no slippery substance should be present on the surface, which should be scraped clean to ensure no wax is present. Concrete surfaces should be roughened to promote a greater friction coefficient.

Fatigue is also an important design condition for elastomeric bearings, although understanding of this phenomenon seems limited as not much literature is readily available. One paper that does exist investigates the fatigue of steel-reinforced elastomeric bearings by Roeder *et al.*[2.168]. The paper examines what methods were used to control fatigue, performing twenty six tests in total to evaluate the design methods. All of the bearings were subjected to cyclical shear or compression testing. As a result, in certain cases, fatigue cracks formed in the rubber near the steel

reinforcement, often growing to a significant depth. It is noted that bearings subjected to breaking and acceleration forces from vehicles may experience more loading cycles, and therefore a faster strain rate. Fatigue is strongly influenced by the magnitude of the cyclic shear strain in the rubber. Extreme cracking is often accompanied by increasing temperature in the rubber, and an increasing load rate or hysterisis in the rubber could result in increased cracking and reduced fatigue life. It is noted that increasing the mean strain results in an increase in cracking, although this is less significant than the cyclic strain.

Lanzo investigates the instability phenomenon in laminated rubber bearings[2.169] using a Koiter perturbation method[2.170]. Two beam models are proposed and analysed, a linear-elastic model and a non-linear elastic model. The linear model analysis indicates that the load bearing capacity of the bearing is not affected by the post-critical behaviour. However, the non-linear analysis model shows a high variegated profile, due to strain induced discolouration, which affects the load carrying capacity. The author indicates that one difficulty with the method is the accurate definition of constitutive coefficients to take into account the actual geometry of a laminated bearing. This is deferred for future research.

2.4 Summary

Both theoretical and experimental works are still being carried out on plate structures, bearings and full-scale highway bridge structures. The analysis of plates is not new, but with advances in knowledge, older more established theories have been adapted and accuracy of solution has been improved in many cases. Plates with more conventional boundary conditions have been investigated thoroughly, and the current investigations

are concerned with the effects of moving loads or variable boundary conditions on the dynamic performance of plate structures.

Modal analysis is a widely used tool for structural analysis. In recent years, with the increase in computational power available, researchers have employed OMA techniques to extract natural frequencies and material properties from full-scale structures excited by ambient vibration. Various factors such as road surface roughness and the effects of cracking have all been investigated. Few researchers, in terms of damage location, have investigated the effect of support condition, and this is one area that provides further scope for research.

The available literature on bearings is mostly concerned with the material properties or performance of the bearings under loading, either compressive or shearing. Investigations into the performance of *in situ* bearings is restricted to the behaviour in cold temperatures, and the effects of bearing walking.

Although health monitoring of bridge structures is relatively advanced, the scope for further research is wide. This study contains a wide spectrum of research on plate structures; ranging from a simple Euler-Bernoulli method to determine natural frequencies; modal analysis of a plate structure in the laboratory; FEA of the plate structure; and modal analysis on a full-scale structure subjected to vehicle loading.

Further reference will be made to the possible applications of many of the techniques, such as wavelet transforms, modal updating of FEA models, Euler-Bernoulli equations

and compliance, impedance and dynamic stiffness, covered in this chapter throughout the remainder of this thesis.

2.5 References

2.1 Chladni E.F.F. Entdeckungen über die Theorie des Klanges. 1787, Leipzig.

2.2 Strutt J.W.S. (Lord Rayleigh) The theory of sound. 2nd edition, 1894-6. Re-issued; Dover Publications Inc., 1945, New York.

2.3 Ritz W. Theorie der Transversalschwingungen einer quadratischen Platte mit freien Rändern. *Annalen der Physik*, 1909, **28**, 737-786.

2.4 Mindlin R.D. Influence of rotary inertia and shear on flexural motions of isotropic elastic plates. *Proc. Am. Soc. Mech. Engnrs,* **18(1)**, 1951, 31-38.

2.5 Liew K.M., Xiang Y. and Kitipornchai S. Research on thick plate vibration: a literature survey. *J. Sound Vib.*, **180(1)**, 1995, 163-176.

2.6 Timoshenko S.P. and Woinowski-Kreiger S. Theory of plates and shells. 1972, London, McGraw-Hill International.

2.7 Warburton G.B. The vibration of rectangular plates. *Proc. Inst. Mech. Engnrs*, **168**, 1954, 371-384.

2.8 Young D. Vibration of rectangular plates by the Ritz method. *J. Appl. Mech.*, **17**, 1950, 448-453.

2.9 Hearmon R.F.S. The frequency of flexural vibration of rectangular orthotropic plates with clamped or supported edges. *J. Appl. Mech.,* **26**, 1959, 537-540.

2.10 Hearmon R.F.S. and Adams E.H. The bending and twisting of anisotropic plates. *J. Appl. Phys.*, **3**, 1952, 150-156

2.11 Biancolini M.E., Brutti C. and Reccia L. Approximate solution for free vibrations of thin orthotropic rectangular plates. *J. Sound Vib.,* **288(1-2)**, 2005, 321-344.

2.12 Rossi R.E., Bambilli D.V. and Laura PAA. Vibrations of a rectangular orthotropic plate with a free edge: a comparison of analytical and numerical results. *Ocean Engng,* **25(7)**, 1998, 521-527.

2.13 Leissa A.W. Vibration of plates. NASA SP-160, Office of Technology Utilization, Washington D.C., National Aero. Space Administration, 1969.

2.14 Leissa A.W. The free vibration of rectangular plates. *J. Sound Vib.*, **31**, 1973, 257-293.

2.15 Deobald L.R. and Gibson R.F. Determination of elastic constants of orthotropic plates by a modal analysis/Rayleigh-Ritz technique. *J. Sound Vib.*, **124(2)**, 1988, 269-283.

2.16 Hashemi S.H. and Arsanjani M. Exact characteristic equations for some of classical boundary conditions of vibrating moderately thick rectangular plates. *Int. J. Solids Structs*, **42(3-4)**, 2005, 819-853.

2.17 Cheung Y.K. and Zhou D. Vibrations of rectangular plates with elastic intermediate line-supports and edge constraints. *Thin-walled Structs*, **37(4)**, 2000, 305-331.

2.18 Dickenson S.M. On the use of simply supported plate functions in Rayleigh's method applied to the flexural vibration of rectangular plates. *J. Sound Vib.*, **59(1)**, 1978, 143-146.

2.19 Dickenson SM. On the use of simply supported plate functions in the Rayleigh-Ritz method applied to the flexural vibration of rectangular plates. *J. Sound Vib.*, **80(2)**, 1982, 292-297.

2.20 Hyde K., Chang J.Y., Bacca C. and Wickert J.A. Parameter studies for plane stress in-plane vibration of rectangular plates. *J. Sound Vib.*, **247(3)**, 471-487.

2.21 Bhat R.B., Chakraverty S. and Stiharu I. Recurrence scheme for the generation of two-dimensional boundary characteristic orthogonal polynomials to study vibration of plates. *J. Sound Vib.*, **216(2)**, 1998, 321-327.

2.22 Chen Y.Z. Evaluation of fundamental vibration frequency of an orthotropic bending plate by using an iterative approach. *Comp. Methods Appl. Mech. Engng*, **161(3-4)**, 1998, 289-296.

2.23 Dawe D.J. Finite strip models for vibration of Mindlin plates. *J. Sound Vib.*, **59(3)**, 1978, 441-452.

2.24 Gorman D.J. Free in-plane vibration analysis of rectangular plates by the method of superposition. *J. Sound Vib.*, **272(3-5)**, 2004, 831-851.

2.25 Gorman D.J. Free vibration analysis of completely free rectangular plates by the superposition-Galerkin method. *J. Sound Vib.*, **273(5)**, 2000, 901-914.

2.26 Gorman D.J. and Ding W. Accurate free vibration analysis of the completely free rectangular Mindlin plate. *J. Sound Vib.*, **189(3)**, 1996, 341-353.

2.27 Gorman D.J. and Ding W. The superposition-Galerkin method for free vibration analysis of rectangular plates. *J. Sound Vib.*, **194(2)**, 1996, 187-198.

2.28 Gorman D.J. Accurate free vibration analysis of point supported Mindlin plates by the superposition method. *J. Sound Vib.*, **219(2)**, 1999, 265-277.

2.29 Liew K.M. and Teo T.M. Three-dimensional vibration analysis of rectangular plates based on differential quadrature method. *J. Sound Vib.*, **220(4)**, 1999, 577-599.

2.30 Zhao Y.B. and Wei G.W. DSC analysis of rectangular plates with non-uniform boundary conditions. *J. Sound Vib.*, **255(2)**, 2002, 203-228.

2.31 Nieves F.J., Gascón F. and Bayón A. Natural frequencies and mode shapes of flexural vibration of plates: laser-interferometry detection and solutions by Ritz's method. *J. Sound Vib.*, **278(3)**, 2004, 637-655.

2.32 Leissa A.W., Laura P.A.A. and Gutierrez R.H. Vibrations of rectangular plates with nonuniform elastic edge supports. *J. App. Mech.*, **47**, 1980, 891-895.

2.33 Warburton G.B. and Edney S.L. Vibrations of rectangular plates with elastically restrained edges. *J. Sound Vib.*, **95(4)**, 1984, 537-552.

2.34 Liew K.M., Hung K.C. and Lim M.K. Three-dimensional vibration of rectangular plates: effects of thickness and edge constraints. *J. Sound Vib.*, **182(5)**, 1995, 709-727.

2.35 Li W.L. Vibration analysis of rectangular plates with general boundary supports. *J. Sound Vib.*, **273(3)**, 2004, 619-635.

2.36 Gorman D.J. A general solution for the free vibration of rectangular plates resting on uniform elastic edge supports. *J. Sound Vib.*, **139(2)**, 1990, 325-335.

2.37 Gorman D.J. Free vibration analysis of Mindlin plates with uniform elastic edge support by the superposition method. *J. Sound Vib.*, **207(3)**, 1997, 335-350.

2.38 Gorman D.J. The superposition method for free vibration analysis of rectangular plates with elastic edge support. *Finite Elements in Analy. & Des.*, **18(1-3)**, 1994, 155-168.

2.39 Gorman D.J. A general solution for the free vibration of rectangular plates with arbitrarily distributed lateral and rotational elastic edge support. *J. Sound Vib.*, **174(4)**, 1994, 451-459.

2.40 Gorman D.J. Free in-plane vibration analysis of rectangular plates with elastic support normal to the boundaries. *J. Sound Vib.*, 2005, **285(4)**, 941-966.

2.41 Gorman D.J. Free vibration and buckling of in-plane loaded plates with rotational elastic edge support. *J. Sound Vib.*, **229(4)**, 2000, 755-773.

2.42 Teng T.-L., Chang F.-A. and Liang C.-C. The realization of boundary conditions in the vibration analysis of plates. *J. Franklin Inst.*, **335B(5)**, 1998, 799-812.

2.43 Zhou L. and Zheng W.X. Moving least square Ritz method for vibration analysis of plates. *J. Sound Vib.*, **290(3-5)**, 2006, 968-990.

2.44 Razaqpur A.G., Nofal M. and Vasilescu A. An improved quadrilateral finite element for analysis of thin plates. *Finite Elements in Analy. & Des.*, **40(1)**, 2003, 1-23.

2.45 Houmat A. Three-dimensional free vibration analysis of plates using the h-p version of the finite element method. *J. Sound Vib.*, 2006, **290(3)**, 690-704.

2.46 Ewins D.J. Modal Testing: Theory, practice and application. J. Wliey & Sons, New York, 1995.

2.47 Newland D.E. Random vibrations, spectral and wavelet analysis. Longman Publishers Ltd., Harlow, 1993.

2.48 Ramirez R.W. The FFT fundamentals and concepts. Prentice-Hall Inc., New Jersey, 1985.

2.49 Brüel and Kjær. Introduction to modal analysis. Nærum offset, Nærum, Denmark, 1987.

2.50 Cooley J.W. and Tukey J.W. An algorithm for the machine calculation of complex Fourier series. Digital Signal Processing, ed. Rabiner L.R and Rader C.M., *IEEE Press*, 1972, 223-227.

2.51 Davidson G.C. and Lanczos C. Some improvements in practical Fourier analysis and their applications to X-ray scattering in liquids. *J. Franklin Inst.*, 1942, 297.

2.52 Gentleman W.M. and Sande G. Fast-Fourier transforms - for fun and profit. *Proc. Am. Fed. Info. Process. Soc.*, **29**, 1966, 563-578.

2.53 Nyquist H. Certain topics in telegraph transmission theory. *Trans. Am. Inst. Elec. Engnrs*, **47**, 1928, 617-644.

2.54 Blackman R.B. and Tukey J.W. Particular pairs of windows. The measurement of power spectra, from the point of view of communications engineering. Dover Inc., New York, 1959, 98-99.

2.55 Salawu O.S. And Williams C. Review of full-scale dynamic testing of bridge structures. *Engng Structs*, **17(2)**, 1995, 113-121.

2.56 Salawu O.S. Detection of structural damage through changes in frequency: a review. *Engng Structs*, **19(9)**, 1997, 718-723.

2.57 Zhao J. and DeWolf J.T. Dynamic monitoring of steel girder highway bridge. *Proc. Am. Soc. Civ. Engnrs, J. Bridge Engng*, **7(6)**, 2002, 350-356.

2.58 Nassif H.H., Liu M. and Ertekin O. Model validation for bridge-road-vehicle dynamic interaction system. *Proc. Am. Soc. Civ. Engnrs, J. Bridge Engng*, **8(2)**, 2003, 112-120.

2.59 Memory T.J., Thambiratnam D.P. and Brameld G.H. Free vibration analysis of bridges. *Engng Structs*, **17(10)**, 1995, 705-713.

2.60 Alvandi A and Cremona C. Assessment of vibration-based damage identification techniques. *J. Sound Vib*. **292(1-2)**, 2006, 179-202.

2.61 Thyagarajan S.K., Schultz M.J., Pai P.F. and Chung J. Detecting structural damage using frequency response functions. *J. Sound Vib.*, **210(1)**, 1998, 162-170.

2.62 Maeck J., Wahab M.A., Peeters B., De Roeck G., De Visscher J., De Wilde W.P., Ndambi J.-M. and Vantomme J. Damage identification in reinforced concrete structures by dynamic stiffness determination. *Engng Structs*, **22(10)**, 2000, 1339-1349.

2.63 Maguire J.R. and Severn R.T. Assessing the dynamic properties of prototype structures by hammer testing. *Proc. Instn Civ. Engrs, Part 2*, **83**, 1987, 769-784.

2.64 Casas J.R. and Aparicio A.C. Structural damage identification from dynamic test data. *Proc. Am. Soc. Civ. Engnrs, J. Struct. Engng*, **120(8)**, 1994, 2437-2450.

2.65 Armstrong D.M., Sibbald A. and Forde MC. Integrity assessment of masonry arch bridges using the dynamic stiffness technique. *NDT & E Int.*, **28(6)**, 1995, 367-375.

2.66 Tseng K.K. and Wang L. Impedance-based method for nondestructive damage identification. . *Proc. Am. Soc. Civ. Engnrs, J. Engng Mech.*, **131(1)**, 2005, 58-64.

2.67 Lee U., and Shin J. A structural damage identification method for plate structures. *Engng Structs*, **24(9)**, 2002, 1177-1188.

2.68 Green M.F. & Cebon D. Dynamic response of highway bridges to heavy vehicle loads: theory and experimental validation. *J. Sound Vib.*, 1994, **170(1)**, 51-78.

2.69 Boothby T.E. and Laman J.A. Cumulative damage to bridge concrete deck slabs due to vehicle loading. . *Proc. Am. Soc. Civ. Engnrs, J. Bridge Engng*, **4(1)**, 1999, 80-82.

2.70 Petryna Y.S. and Krätzig W.B. Compliance based structural damage measure and its sensitivity to uncertainties. *Comp. & Struct.*, **83(14)**, 2005, 1113-1133.

2.71 Xia Y. and Hao H. Statistical damage identification of structures with frequency changes. *J. Sound Vib.*, **263(4)**, 2003, 853-870.

2.72 Owalabi G.M., Swamidas A.S.J. and Seshadri R. Crack detection in beams using changes in frequencies and amplitudes of frequency response functions. *J. Sound Vib.*, **265(1)**, 2003, 1-22.

2.73 Teughels A. and De Roeck G. Structural damage identification of the highway bridge Z24 by FE model updating. *J. Sound Vib.*, 2004, **278(3)**, 589-610.

2.74 Krätzig W.B. and Petryna Y.S. Structural damage and life-time estimates by nonlinear FE simulation. *Engng Structs*, 2005, **27(12)**, 1726-1740.

2.75 Lee J.W., Kim J.D., Yun C.B., Yi J.H. and Shim J.M. Health-monitoring method for bridges under ordinary traffic loadings. *J. Sound Vib.*, **257(2)**, 2002, 247-264.

2.76 Fragakis Y. and Papadrakakis M. The mosaic of high performance domain decomposition methods for structural mechanics: formulation, interrelation and numerical efficiency of primal and dual methods. *Comp. Methods Appl. Mech. Engng*, 2003, **192(35)**, 3799-3830.

2.77 Xiao H., Bruhns O.T., Waller H. and Meyers A. An input/output-based procedure for fully evaluating and monitoring dynamic properties of structural systems via a subspace identification method. *J. Sound Vib.*, 2001, **246(4)**, 601-623.

2.78 Cauberghe B., Guillaume P., Pintelon R. and Verboven P. Frequency-domain subspace identification using FRF data from arbitrary signals. *J. Sound Vib.*, 2006, **290(3)**, 555-571.

2.79 Zhang Y., Zhang Z., Xu X. and Hua H. Modal parameter identification using response data only. *J. Sound Vib.*, 2005, **282(2)**, 367-380.

2.80 Hankel H. Über eine besondere Classe der symmetrischen Determinanten. *Dr Phil. Thesis, Univ. Leipzig, Göttingen*, 1861.

2.81 Peeters B. and Ventura C.E. Comparitive studies of modal analysis techniques for bridge dynamic characteristics. *Mech. Sys. Signal Processing*, **17(5)**, 2003, 965-988.

2.82 Melhem H. and Kim H. Damage detection in concrete by Fourier and wavelet analysis. . *Proc. Am. Soc. Civ. Engnrs, J. Engng Mech.*, **129(5)**, 2003, 571-577.

2.83 Yin H.P., Duhamel D., and Argoul P. Natural frequencies and damping estimation using wavelet transform of a frequency response function. *J. Sound Vib.*, **271(3-5)**, 2004, 999-1014.

2.84 Yan B.F., Miyamoto A. and Bruhwiler E. Wavelet transform-based modal parameter identification considering uncertainty. *J. Sound Vib.*, **291(1-2)**, 2006, 285-301.

2.85 Kim H. and Melhem H. Damage detection of structures by wavelet analysis. *Engng Struct.*, **26(3)**, 2004, 347-362.

2.86 Hou Z., Noori M. and St Amand R. Wavelet-based approach for structural damage detection. *Proc. Am. Soc. Civ. Engnrs, J. Engng Mech.*, **127(7)**, 2000, 677-683.

2.87 Basu B. Identification of stiffness degradation in structures using wavelet analysis. *Const. Build. Materials*, **19(9)**, 2005, 713-721.

2.88 Sun Z. and Chang C.C. Structural damage assessment based on wavelet packet transform. *Proc. Am. Soc. Civ. Engnrs, J. Struct. Engng*, **128(10)**, 2002, 1354-1361.

2.89 Law S.S., Li X.Y., Zhu X.Q. and Chan S.L. Structural damage detection from wavelet packet sensitivity. *Engng Struct.*, **27(9)**, 2005, 1339-1348.

2.90 Sun Z. and Chang C.C. Statistical wavelet-based method for structural health monitoring. *Proc. Am. Soc. Civ. Engnrs, J. Struct. Engng*, **130(7)**, 2004, 1055-1062.

2.91 Loutridis S., Douka E., Hadjileontiadis L.J. and Trchidis A. A two-dimensional wavelet transform for detection of cracks in plates. *Engng Struct.*, **27(12)**, 2005, 1327-1338.

2.92 Sheen Y-T. 3D spectral analysis for vibration signals by wavelet-based demodulation. *Mech. Sys. Signal Processing*, **20(4)**, 2006, 843-853.

2.93 Rucka M. and Wilde K. Crack identification using wavelets on experimental static deflection profiles. *Engng Structs*, **28(2)**, 2006, 279-288.

2.94 Hu N., Wang X., Fukunaga H., Yao Z.H., Zhang H.X. and Wu Z.S. Damage assessment of structures using modal test data. *Int. J. Solids Structs*, **38(18)**, 2002, 3111-3126.

2.95 Huynh D., He J. and Tran D. Damage location vector: a non-destructive structural damage detection technique. *Comp. & Struct.*, **83(28-30)**, 2005, 2353-2367.

2.96 Duan Z., Yan G., Ou J. and Spencer BF. Damage localisation in ambient vibration by constructing proportional flexibility matrix. *J. Sound Vib.*, **284(1-2)**, 2005, 455-466.

2.97 Dutta A. and Taukdar S. Damage detection in bridges using accurate modal parameters. *Finite Elements in Analysis & Des.*, **40(3)**, 2004, 287-304.

2.98 Masri S.F., Nakamura M., Chassiakos A.G. and Caughey T.K. Neural network approach to detection of changes in structural parameters. *Proc. Am. Soc. Civ. Engnrs, J. Engng Mech.*, **122(4)**, 1996, 350-360.

2.99 Lee J.J., Lee J.W., Yi J.H., Yun C.B. and Jung H.Y. Neural networks-based damage detection for bridges considering errors in baseline finite element models. *J. Sound Vib.*, **280(3-5)**, 2005, 555-578.

2.100 Chou J.-H. and Ghaboussi J. Genetic algorithm in structural damage detection. *Comp. Struct.*, **79(14)**, 2001, 1335-1353.

2.101 Pothisiri T. and Hjelmstad K.D. Structural damage detection and assessment from modal response. *Proc. Am. Soc. Civ. Engnrs, J. Engng Mech.*, **129(2)**, 2003, 135-145.

2.102 Shi Z.Y., Law S.S. and Zhang L.M. Structural damage detection from modal strain energy change. *Proc. Am. Soc. Civ. Engnrs, J. Engng Mech.*, **126(12)**, 2000, 1216-1223.

2.103 Shi Z.Y., Law S.S. and Zhang L.M. Improved damage quantification from elemental modal strain energy change. *Proc. Am. Soc. Civ. Engnrs, J. Engng Mech.*, **128(5)**, 2002, 521-529.

2.104 Sazonov E. and Klinkhachorn P. Optimal spatial sampling interval for damage detection by curvature or strain energy mode shapes. *J. Sound Vib.*, **285(4-5)**, 2005, 783-801.

2.105 Frýba L. Vibration of solids and structures to moving loads. Thomas Telford, London, 1999.

2.106 Frýba L. and Pirner M. Load tests and modal analysis of bridges. *Engng Struct.*, **23(1)**, 2001, 102-109.

2.107 Tikhonov A.N. Solution of incorrectly formulated problems and the regularization method. *Soviet Math. Dokl.*, **4**, 1963, 1035-1038. (English translation of *Dokl. Akad. Nauk (CCCP)*, **151**, 1963, 501-504.

2.108 Zhu X.Q. and Law S.S. Moving loads identification through regularization. *Proc. Am. Soc. Civ. Engnrs, J. Engng Mech.*, **128(9)**, 2002, 989-1000.

2.109 Zhu X.Q. and Law S.S. Dynamic load on continuous multi-lane bridge deck from moving vehicles. *J. Sound Vib.*, **251(4)**, 2002, 697-716.

2.110 Yang Y.B., Lin C.W. and Yau J.D. Extracting bridge frequencies from the dynamic response of a passing vehicle. *J. Sound Vib.*, 2004, **272(3)**, 471-493.

2.111 Lin C.W. and Yang Y.B. Use of a passing vehicle to scan the fundamental bridge frequencies: an experimental verification. *Engng Struct.*, 2005, **27(13)**, 1865-1878.

2.112 Kim C.W., Kawatani M. and Kim K.B. Three-dimensional dynamic analysis for bridge-vehicle interaction with roadway roughness. *Comp. & Struct.*, 2005, **83(20)**, 1627-1645.

2.113 Chaterjee P.K., Datta T.K. and Surana C.S. Vibration of continuous bridges under moving vehicles. *J. Sound Vib.*, **169(5)**, 1994, 619-632.

2.114 Au F.T.K., Jiang R.J. and Cheung Y.K. Parameter identification of vehicles moving on continuous bridges. *J. Sound Vib.*, **269(1-2)**, 2004, 91-111.

2.115 O'brien E., Li Y. and Gonzalez A. Bridge roughness as an indicator of bridge dynamic amplification. *Comp. & Struct.*, **84(12)**, 2006, 759-769.

2.116 Pesterev A.V., Bergman L.A., Tan C.A. and Yang B. Application of the pothole DAF method to vehicles traversing periodic roadway irregularities. *J. Sound Vib.*, **279(3-5)**, 2005, 843-855.

2.117 Pesterev AV., Bergman LA., Tan CA. and Yang B. Assessing tire forces due to roadway unevenness by the pothole dynamic amplification factor method. *J. Sound Vib.*, **279(3-5)**, 2005, 817-841.

2.118 Law S.S. and Zhu X.Q. Bridge dynamic responses due to road surface roughness and braking of vehicle. *J. Sound Vib.*, **285(5)**, 2005, 805-830.

2.119 Savin E. Dynamic amplification factor and response spectrum for the evaluation of vibrations of beams under successive moving loads. *J. Sound Vib.*, **248(2)**, 2001, 267-288.

2.120 Zhu X.Q. and Law S.S. Identification of vehicle axle loads from bridge dynamic responses. *J. Sound Vib.*, **236(4)**, 2000, 705-724.

2.121 Zhu X.Q. and Law S.S. Dynamic axle and wheel loads identification: laboratory studies. *J. Sound Vib.*, **268(5)**, 2003, 855-879.

2.122 Woodward R. Non-destructive testing methods for concrete bridges. *Transport & Roads Research Laboratory*, *Research Report RR250*, Crowthorne, 1989.

2.123 McCann D.M., and Forde M.C. Review of NDT methods in the assessment of concrete and masonry structures. *NDT & E Int.*, **34(2)**, 2001, 71-84.

2.124 Bungey J.H. and Millard S.G. Radar inspection of structures. *Proc. Inst. Civ. Engng, Structs & Bldngs*, **99**, 1993, 173-186.

2.125 Bungey J.H. Sub-surface radar testing of concrete: a review. *Const. Build. Materials*, **18(1)**, 2004, 1-8.

2.126 Scott M., Rezaizadeh A., Delahaza A., Santos C.G., Moore M., Graybeal B. and Washer G. A comparison of nondestructive evaluation methods for bridge deck assessment. *NDT & E Int.*, **36(4)**, 2003, 245-255.

2.127 Colla C. and Lausch R. Influence of source frequency on impact-echo data quality for testing concrete structures. *NDT & E Int.*, **36(4)**, 2003, 203-213.

2.128 Sack D.A. and Olson L.D. Advanced NDT methods for evaluating concrete bridges and other structures. *NDT & E Int.*, **28(6)**, 1995, 349-357.

2.129 Hassan M., Burdet O. and Favre R. Ultrasonic measurements and static load tests in bridge evaluation. *NDT & E Int.*, **28(6)**, 1995, 331-337.

2.130 Shigieshi M., Colombo S., Broughton K.J., Batchelor A.J. and Forde M.C. Acoustic emission to assess and monitor the integrity of bridges. *Const. Build. Materials*, **15(1)**, 2001, 35-49.

2.131 Grosse C.U., Finck F., Kurz J.H. and Reinhardt H.W. Improvements of AE technique using wavelet algorithms, coherence functions and automatic data analysis. *Const. Build. Materials*, **18(3)**, 2004, 203-213.

2.132 Casa J.R and Cruz P.J.S. Fibre optic sensors for bridge monitoring. *Proc. Am. Soc. Civ. Engnrs, J. Bridge Engng*, **8(6)**, 2003, 362-373.

2.133 Chan T.H.T., Yu L., Tam H.Y., Ni Y.Q., Liu S.Y., Chung W.H. and Cheng L.K. Fiber Bragg grating sensors for structural health monitoring of Tsing Ma bridge: background and experimental observation. *Engng Struct.*, **28(5)**, 2006, 648-659.

2.134 Jiang R., Jauregui D.V. and White K.R. Review of close range photogrammetry applications in bridge engineering. *Proc. 85th TRB Annual Meeting*, January 22-26, Washington D.C., 2006.

2.135 Jauregui D.V., Tian Y. and Jiang R. Photogrammetry applications in routine bridge inspection and historic bridge documentation. *Proc. 85th TRB Annual Meeting,* January 22-26, Washington D.C., 2006.

2.136 British Standards Institution. *BS 5400-1:1988 Steel, concrete and composite bridges – Part 9:Bridge bearings*. BSI, London, 1983.

2.137 Lee D.J. Bridge bearings and expansion joints. Spon Press, London, 1994.

2.138 Roeder C.W. And Stanton J.F. Elastomeric bearings: state-of-the-art. *Proc. Am. Soc. Civ. Engnrs, J. Struct. Engng*, **109(12)**, 1983, 2853-2871.

2.139 English B.A, Klingner R.E. and Yura J.A. Elastomeric bearings: background information and field study. *Texas Department of Transport*, Research Report 1304-1, Austin, Texas, 1994.

2.140 Artitzoglou Y.J., Yura J.A. and Haines A.H. Test methods for elastomeric bearings on bridges. *Texas Department of Transport*, Research Report 1304-2, Austin, Texas, 1995.

2.141 Taylor M.E. A method of measuring the horizontal forces generated by bridge bearings. *Transport & Road Research Laboratory, Laboratory Report LR532*, Crowthorne, 1973.

2.142 Taylor M.E. PTFE in highway bridge bearings. *Transport & Road Research Laboratory, Laboratory Report LR491*, Crowthorne, 1972.

2.143 Eyre R. and Stephenson A. Characterisation of rubber vulcanisates for bridge bearings. *Transport & Road Research Laboratory, Research Report RR299*, Crowthorne, 1991.

2.144 Li. W.L. Dynamic analysis of beams with arbitrary elastic supports at both ends. *J. Sound Vib.*, 2001, **246(4)**, 751-756.

2.145 Yau J.D., Wu Y.-S. and Yang Y.-B. Impact response of bridges with elastic bearings to moving loads. *J. Sound Vib.*, 2001, **248(1)**, 9-30.

2.146 Wang J. and Chew C.H. Feasibility of condition monitoring of bearings used in a viaduct. *Applied Acoustics*, **48(3)**, 1996, 237-247.

2.147 Maleki S. Effect of deck and support stiffness on seismic response of slab-girder bridges. *Engng Struct.*, **24(2)**, 2002, 219-226.

2.148 Kawatani M., Kobayashi Y. and Kawaki H. Influence of elastomeric bearings traffic-induced vibration of highway bridges. TRB Research Record 1696, Washington D.C., 2000.

2.149 Allot & Lomax, Consulting Engineers. Bridge bearing survey and problem assessment. *Transport & Road Research Laboratory, Contractor Report CR260*, Crowthorne, 1991.

2.150 Chang C.-H. Modeling of laminated rubber bearings using an analytical stiffness matrix. *Int. J. Solids and Structs*, **39(24)**, 2002, 6055-6078.

2.151 Haringx J.A. On the buckling and lateral rigidity of helical springs. *Proc. Konink. Ned. Akad. Wetenschap*, **45**, 1942, 533.

2.152 Potter W., Ansley M. and Mtenga P. Condition of elastomeric bearing pads after 40 years of service. *Proc. 85th TRB Annual Meeting,* January 22-26, Washington D.C., 2006.

2.153 Othman AB. Property profile of a laminated rubber bearing. *Polymer Testing*, **20(2)**, 2001, 159-166.

2.154 Yakut A. and Yura J.A. Evaluation of elastomeric bearing performance at low temperatures. *Proc. Am. Soc. Civ. Engnrs, J. Struct. Engng*, **128(8)**, 2002, 995-1002.

2.155 Yakut A. and Yura J.A. Parameters influencing performance of elastomeric bearings at low temperatures. *Proc. Am. Soc. Civ. Engnrs, J. Struct. Engng*, **128(8)**, 2002, 986-994.

2.156 Topkaya C. and Yura J.A. Test method for determining the shear modulus of elastomeric bearings. *Proc. Am. Soc. Civ. Engnrs, J. Struct. Engng*, **128(6)**, 2002, 797-805.

2.157 Price A.R. and Fenn M.A. Removal and testing of elastomeric bridge bearings. *Transport and Roads Research Laboratory, Supplementary Report SR812*, 1983.

2.158 AASHTO. Standard specification for highway bridges. 17th Edn, AASHTO, Washington D.C., rev. 2005.

2.159 Herrmann L.R., Ramaswamy A. and Hamidi R. Analytical parameter study for class of elastomeric bearings. *Proc. Am. Soc. Civ. Engnrs, J. Struct. Engng*, **115(10)**, 1989, 2415-2434.

2.160 Yoshida J., Abe M., Fujino Y. and Watanabe H. Three-dimensional finite element analysis of high damping rubber bearings. *Proc. Am. Soc. Civ. Engnrs, J. Engng Mech.*, **130(5)**, 2004, 607-620.

2.161 Yazdani N., Eddy S. and Cai C.S. Effect of bearing pads on precast prestressed concrete bridges. *Proc. Am. Soc. Civ. Engnrs, J Bridge Engng*, **5(3)**, 2000, 224-232.

2.162 Lizuka M. A macroscopic model for predicting large-deformation behaviours of laminated rubber bearings. *Engng Structs*, **22(4)**, 2000, 323-334.

2.163 Hamzeh O.N., Tassoulas J.L. and Becker EB. Behaviour of elastomeric bridge bearings: computational results. *Proc. Am. Soc. Civ. Engnrs, J. Bridge Engng*, **3(3)**, 1998, 140-146.

2.164 Imbimbo I. and DeLuca A. F.E. stress analysis of rubber bearings under axial loads. *Comp. Structs*, **68(1-3)**, 1998, 31-39.

2.165 Gilstad D.E. Bridge bearings and stability. *J. Struct. Engng*, **116(5)**, 1990, 1269-1277.

2.166 Hamzeh O., Becker E.B. and Tassoulas J.L. Model for viscous "walking" of elastomeric bridge bearings. *Proc. Am. Soc. Civ. Engnrs, J. Engng Mech.*, **124(2)**, 1998, 240-242.

2.167 McDonald J., Heymsfield E. and Avent R.R. Slippage of neoprene bridge bearings. *Proc. Am. Soc. Civ. Engnrs, J. Bridge Engng*, **5(3)**, 2000, 216-223.

2.168 Roeder C.W., Stanton J.F. and Taylor A.W. Fatigue of steel reinforced elastomeric bearings. *Proc. Am. Soc. Civ. Engnrs, J. Struct. Engng*, **116(2)**, 1990, 407-426.

2.169 Lanzo A.D. On elastic beam models for stability analysis of multilayered rubber bearings. *Int. J. Solids Structs*, **41(20)**, 2004, 5733-5757.

2.170 Koiter W.T. Over de stabiliteit van het elastisch evenwicht. PhD thesis, Delft Univ. of Technology, H.J. Paris, Amsterdam, 1945. (English translation; *USAF Flight Dynamics Lab. Tech. Rep.*, AFFDL-TR-70-25, Stanford Univ., Stanford, 1970.

2.171 Gade S. and Herlufsen H. Use of weighting functions in DFT / FFT analysis: part 1.Technical review no. 3, Windows to FFT analysis: part 1, Nærum offset, Nærum, Denmark, 1987.

2.172 Brüel and Kjær. Transducer catalogue. Nærum offset, Nærum, Denmark, 2005.

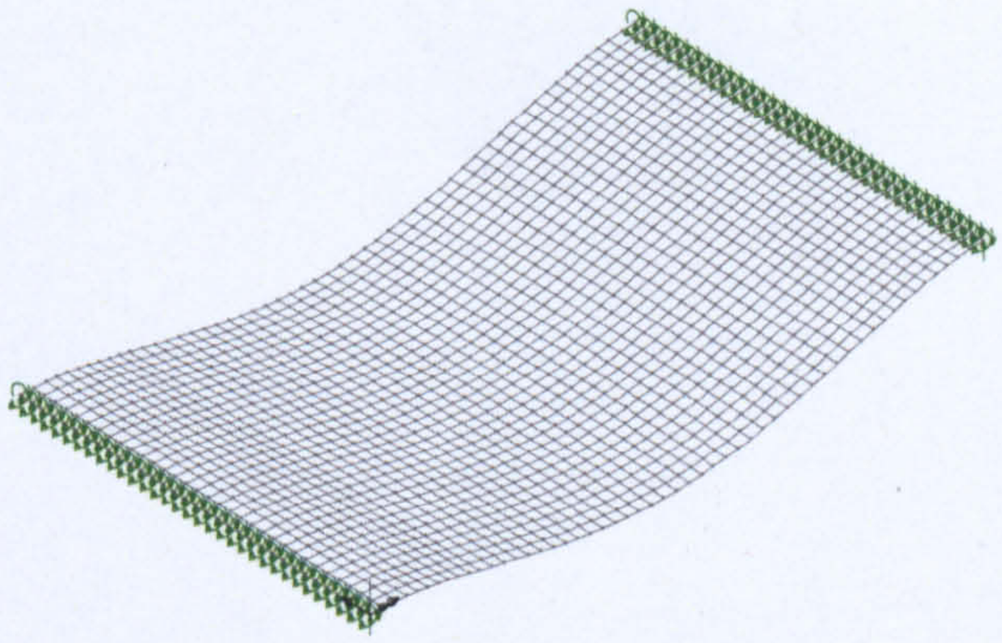

Primary bending mode

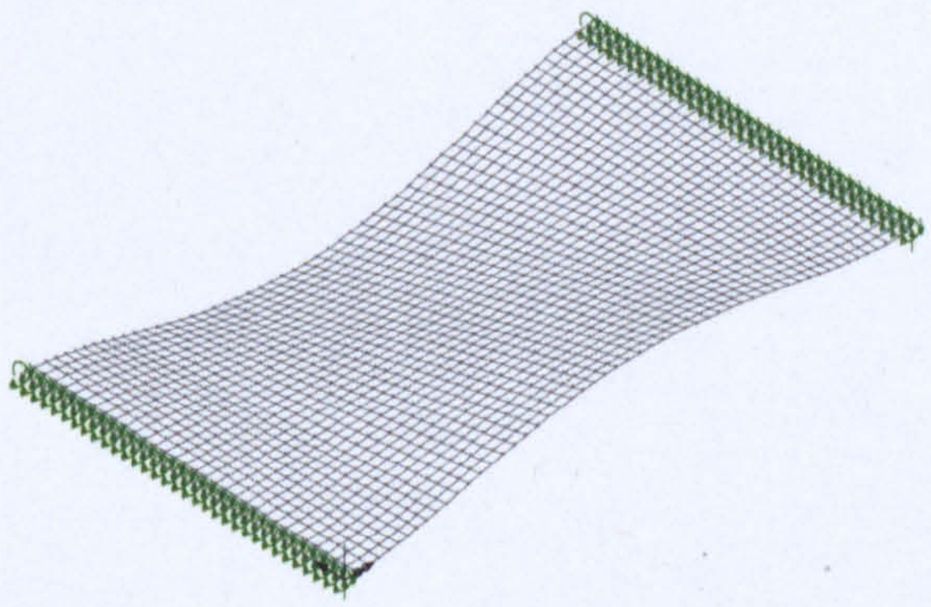

Primary torsional mode

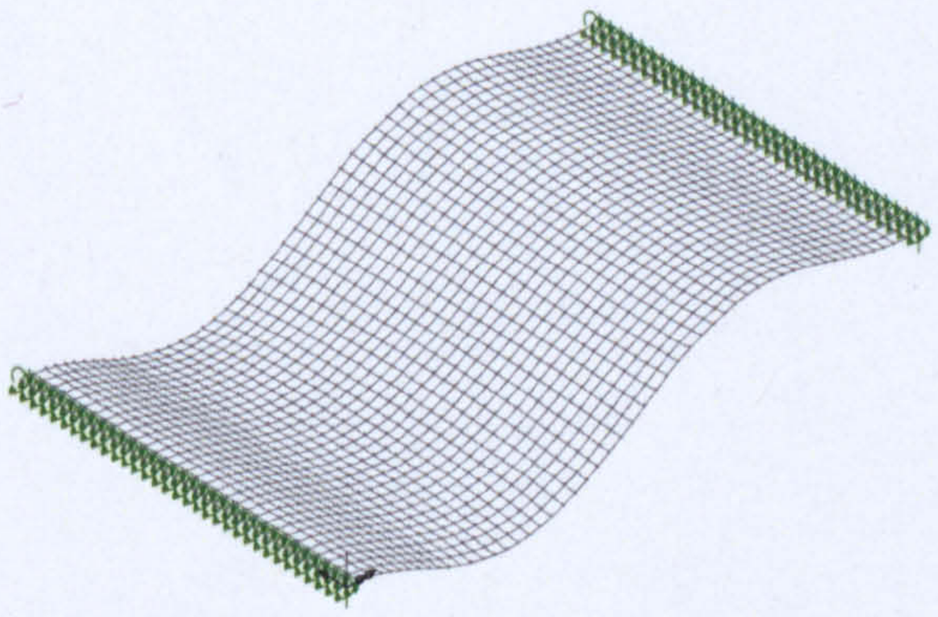

Second bending mode

Figure 2.1 First three mode shapes of plate model used in experimental analysis with two opposite edges fully fixed and the two remaining sides free.

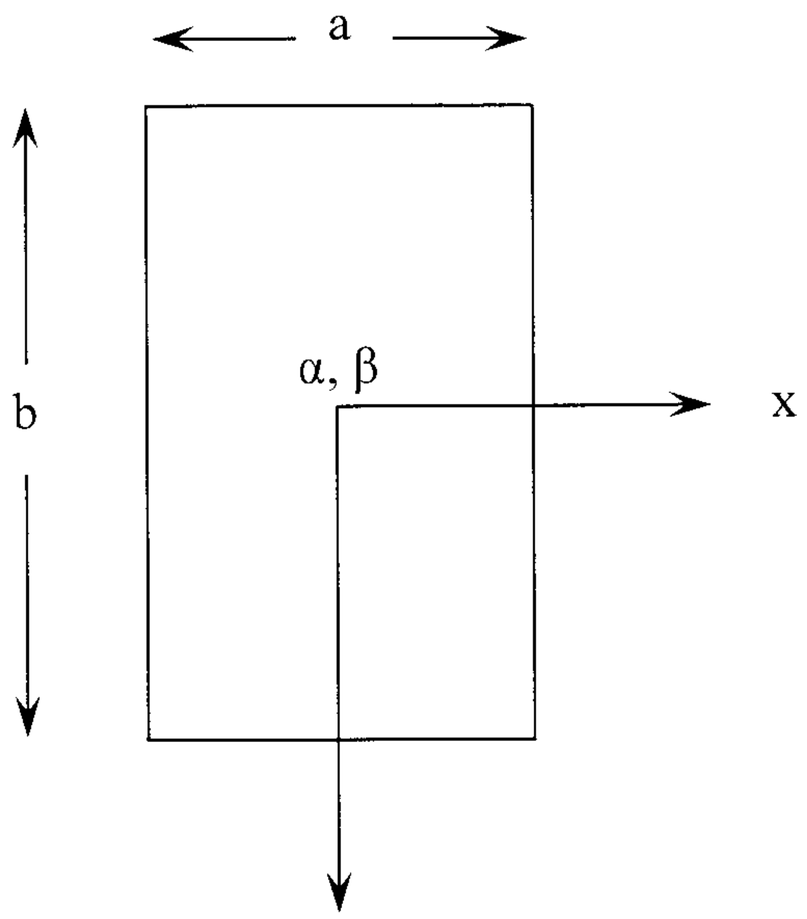

b/a	Centre of plate		Factor
	$M_x = \alpha_1 q l^2$	$M_y = \beta_1 q l^2$	
	α_1	β_1	
0	0.0250	0.1250	
0.5	0.0367	0.0999	
0.6	0.0406	0.0868	
0.7	0.0436	0.0742	qb^2
0.8	0.0446	0.0627	
0.9	0.0449	0.0526	
1.0	0.0442	0.0442	
1.1	0.0517	0.0449	
1.2	0.0592	0.0449	
1.3	0.0660	0.0444	
1.4	0.0723	0.0439	
1.5	0.0784	0.0426	
1.6	0.0836	0.0414	qa^2
1.7	0.0885	0.0402	
1.8	0.0972	0.0391	
1.9	0.0966	0.0378	
2.0	0.0999	0.0367	
∞	0.1250	0.0250	

Figure 2.2 (a) Bending moment equations with parameters for simply supported plates of various length to breadth ratios.

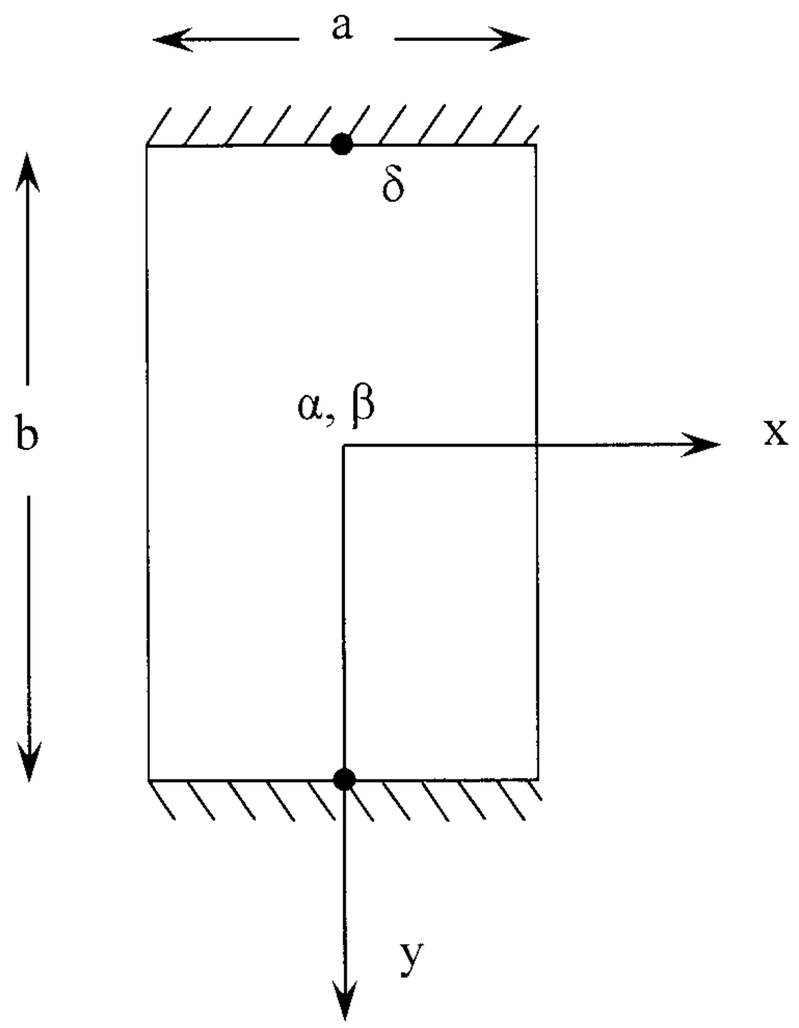

b/a	Centre of plate		Middle of fixed edge	Factor
	$M_x = \alpha_3 q l^2$ α_3	$M_y = \beta_3 q l^2$ β_3	$\overline{M}_y = \delta_3 q l^2$ δ_3	
0	0.0083	0.0417	-0.0833	qb^2
0.5	0.0100	0.0418	-0.0842	
0.6	0.0121	0.0410	-0.0834	
0.7	0.0151	0.0393	-0.0814	
0.8	0.0173	0.0371	-0.0783	
0.9	0.0196	0.0344	-0.0743	
1.0	0.0216	0.0316	-0.0697	
1.1	0.0276	0.0349	-0.0787	qa^2
1.2	0.0344	0.0372	-0.0868	
1.3	0.0414	0.0391	-0.0938	
1.4	0.0482	0.0405	-0.0998	
1.5	0.0554	0.0411	-0.1049	
1.6	0.0620	0.0413	-0.1099	
1.7	0.0683	0.0412	-0.1122	
1.8	0.0741	0.0408	-0.1152	
1.9	0.0795	0.0401	-0.1174	
2.0	0.0846	0.0394	-0.1191	
∞	0.1250	0.0250	-0.1250	

Figure 2.2 (b) Bending moment equations with parameters for plates of various length to breadth ratios with two opposite edges fully fixed and the remaining two sides simply supported.

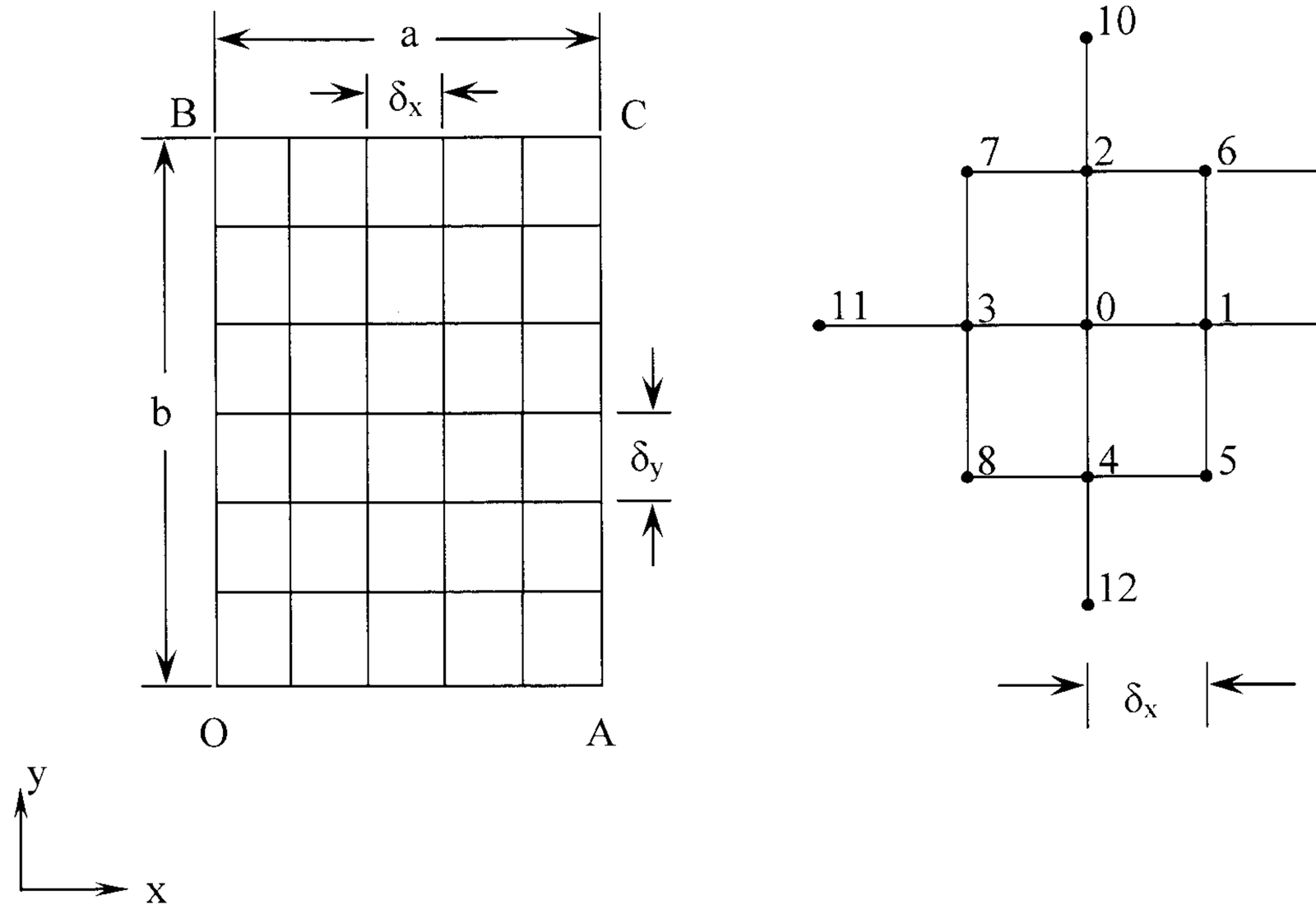

Figure 2.3 Chen's finite difference mesh and notation, with sign convention[2.22].

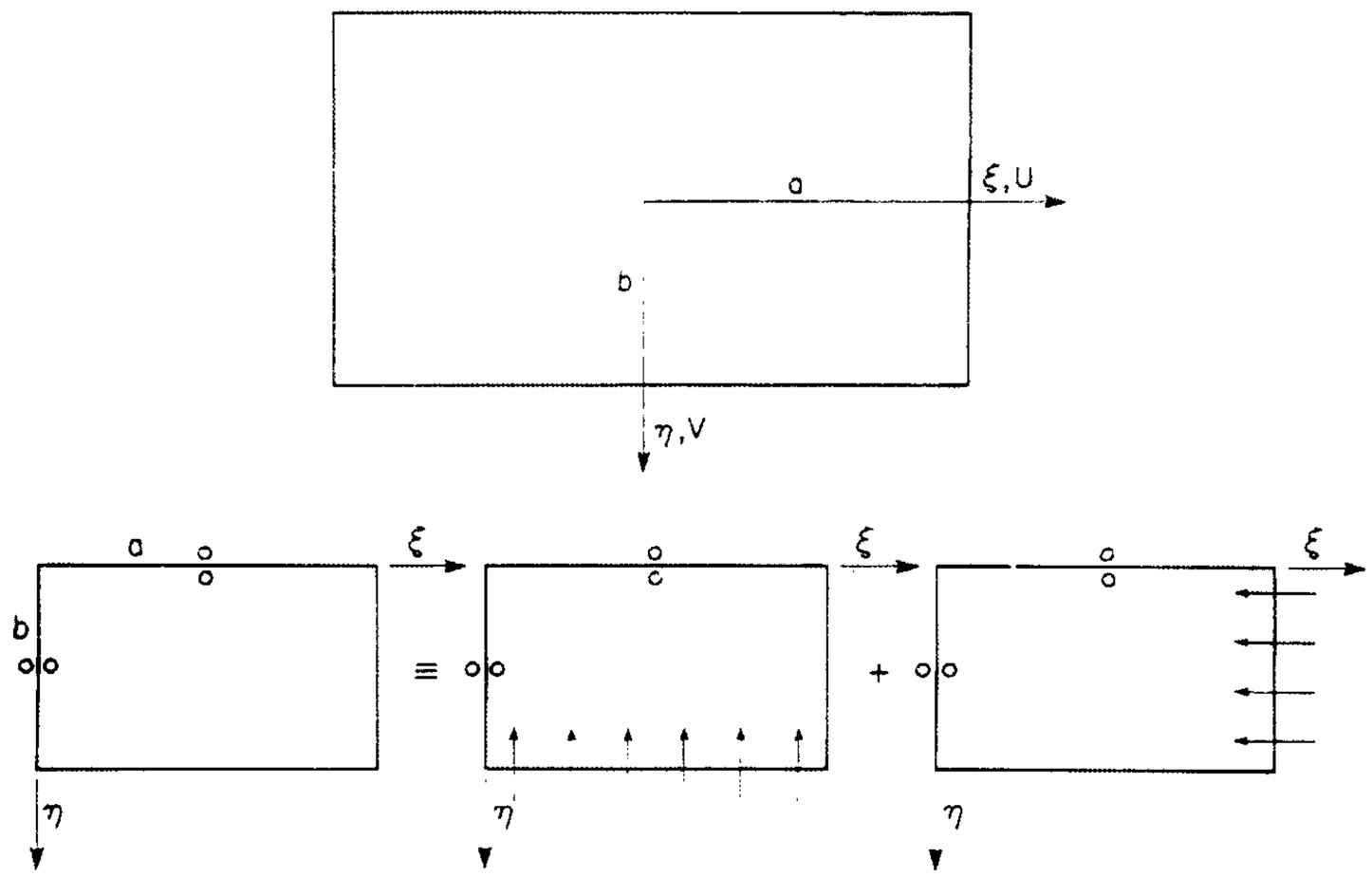

Figure 2.4 The superposition method used by Gorman[2.24] showing complete plate with central co-ordinate axes, and quarter plate section showing building blocks used in the superposition method.

Comparison of frequency parameters Ω of rectangular plates with all edges transversely supported with uniform elastic rotational restraint

λ	K		Ω_1	Ω_2	Ω_3	Ω_4	Ω_5	Ω_6	Ω_7	Ω_8
1	0·1	DSC	19·968	49·580	49·580	79·190	98·931	98·931	128·541	128·541
		a	19·937	49·546	49·546	79·155	—	—	—	—
		b	19·936	49·533	49·546	79·142	—	—	—	—
		c	19·937	49·549	49·556	79·164	98·938	99·036	—	—
	1	DSC	21·748	51·474	51·474	81·130	100·900	100·910	130·535	130·535
		a	21·502	51·191	51·191	80·828	—	—	—	—
		b	21·501	51·177	51·191	80·814	—	—	—	—
		c	21·502	51·196	51·202	80·838	100·633	100·736	—	—
	100	DSC	34·758	70·990	79·990	104·804	127·460	128·038	159·995	159·995
		a	34·671	70·781	70·781	104·450	—	—	—	—
		b	34·666	70·746	70·784	104·480	—	—	—	—
		c	34·675	70·801	70·819	104·509	127·236	127·862	—	—
2·5	0·1	DSC	72·815	102·13	151·24	220·18	258·01	287·50	308·01	336·70
		a	72·64	101·99	151·14	220·09	—	—	—	—
		b	72·636	101·99	151·13	220·09	—	—	—	—
		c	72·64	101·99	151·12	220·28	257·88	287·38	—	—
	1	DSC	82·31	109·69	157·13	224·96	269·39	297·99	312·99	346·04
		a	81·03	108·63	156·26	224·21	—	—	—	—
		b	81·03	108·62	156·26	224·20	—	—	—	—
		c	81·04	108·63	156·29	224·40	267·79	296·49	—	—
	100	DSC	142·66	167·97	214·28	282·82	373·22	381·19	407·52	452·69
		a	143·30	167·50	213·50	281·70	—	—	—	—
		b	142·29	167·59	213·68	282·04	—	—	—	—
		c	142·34	167·54	213·69	282·18	372·99	380·38	—	—

Figure 2.5 **Table of results comparing answers obtained using the DSC method with the three other methods outlined in the text[2.30].**

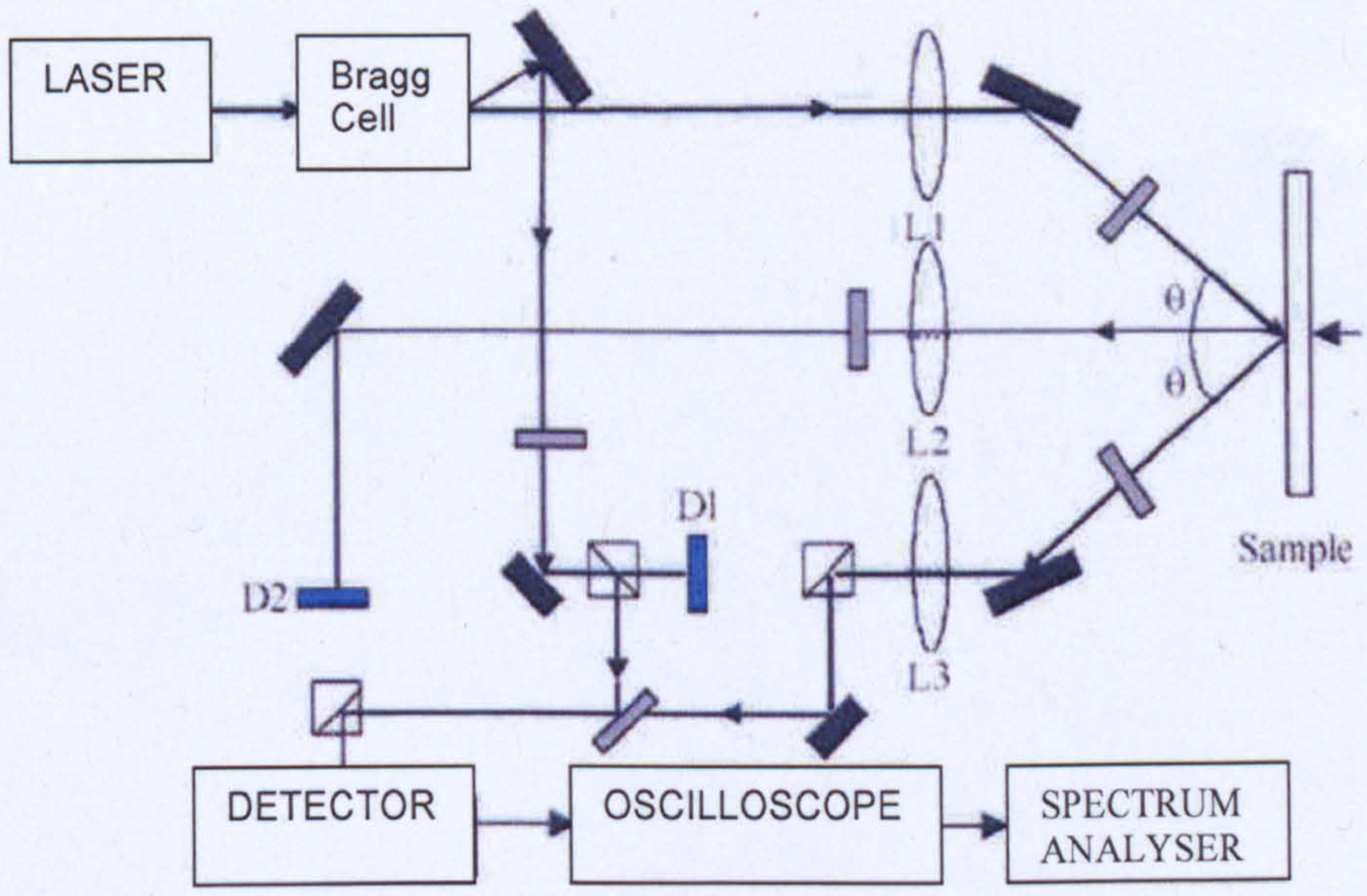

Figure 2.6 **Experimental setup for Nieves *et al.*[2.31] to detect out-of-plane movement. Mirrors are drawn in black and the shutters are in blue.**

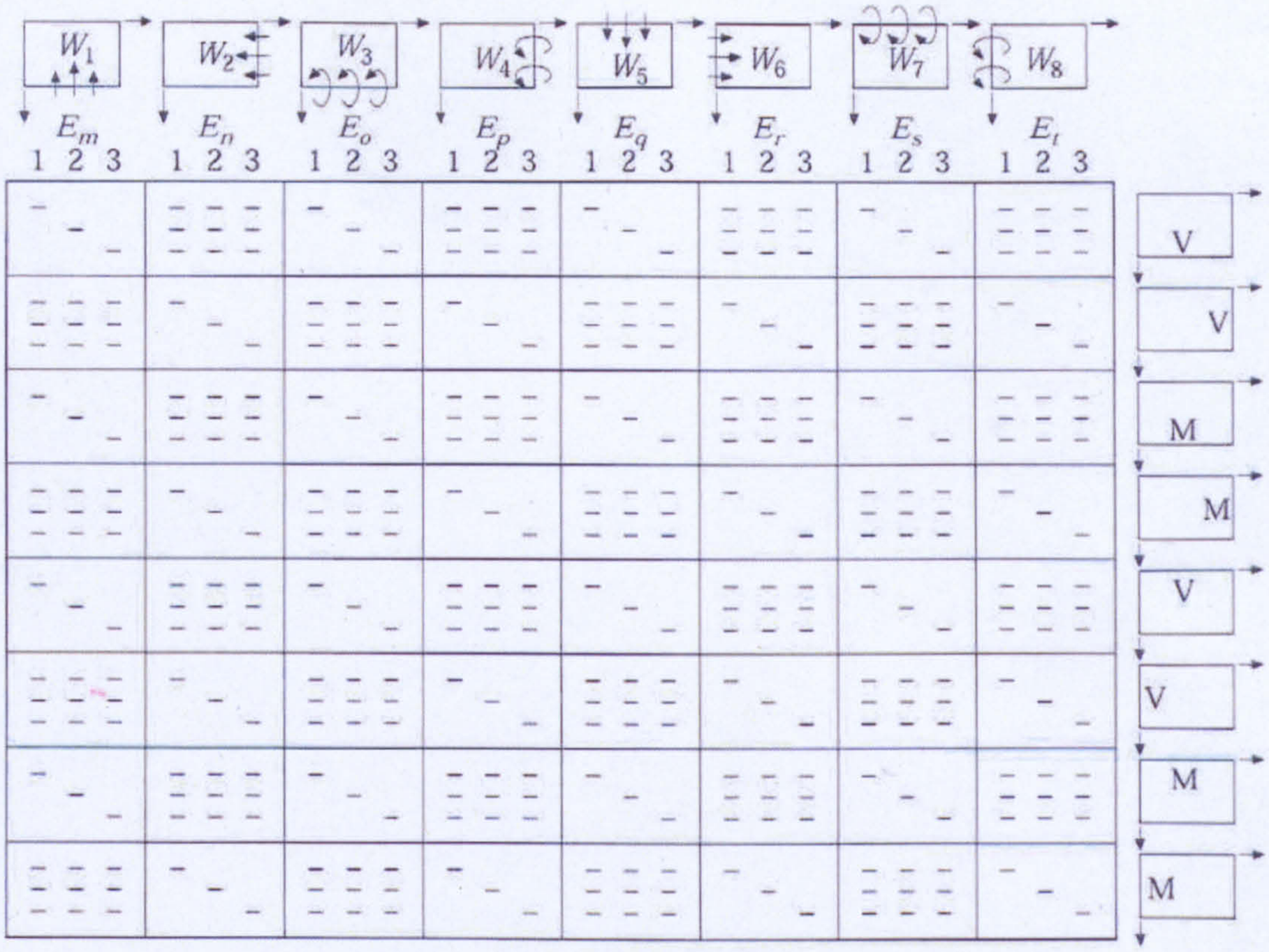

Figure 2.7 **Schematic representation of the eigenvalue matrix used by Gorman[2.36] based on three-term functions. The short bars indicate non-zero elements, and the M and V notation indicates the edges along which moments or lateral force equilibrium is enforced.**

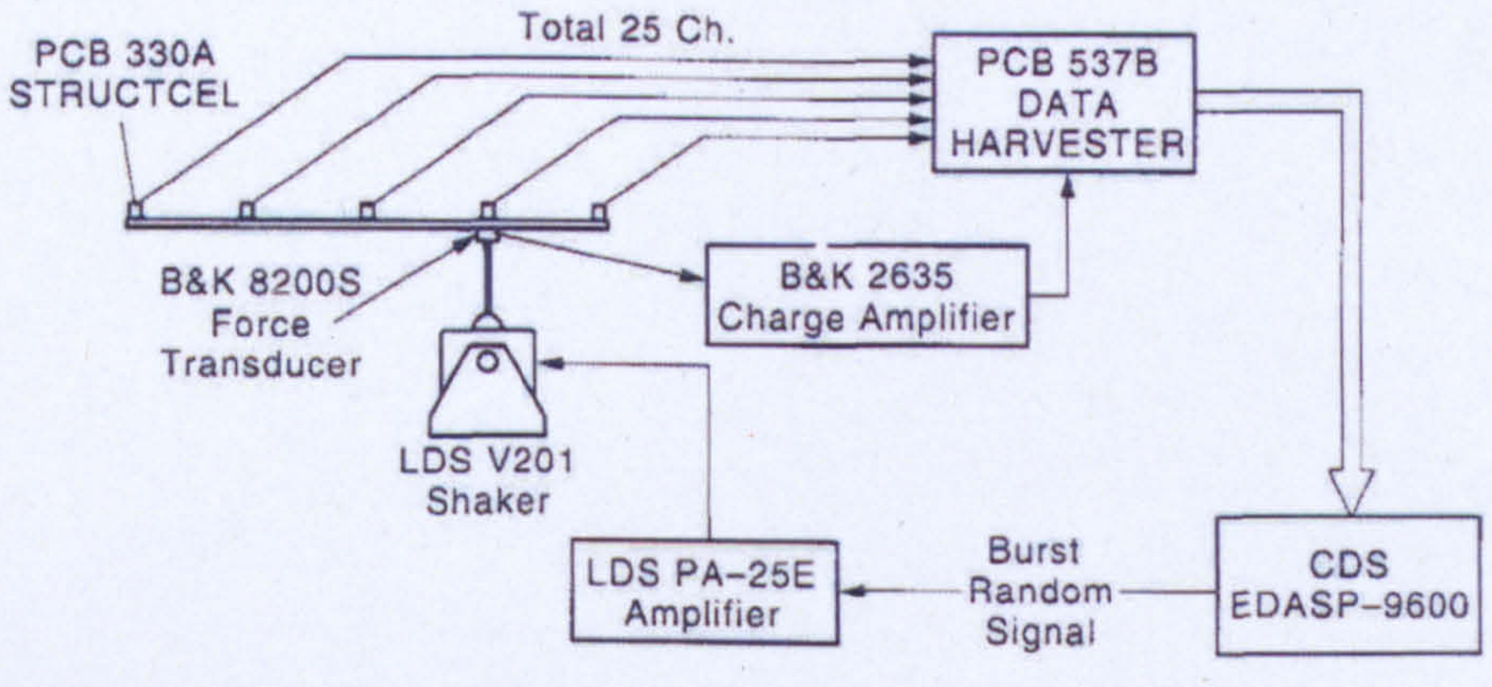

Figure 2.8 **Schematic diagram of modal testing arrangement used by Teng *et al.*[2.42].**

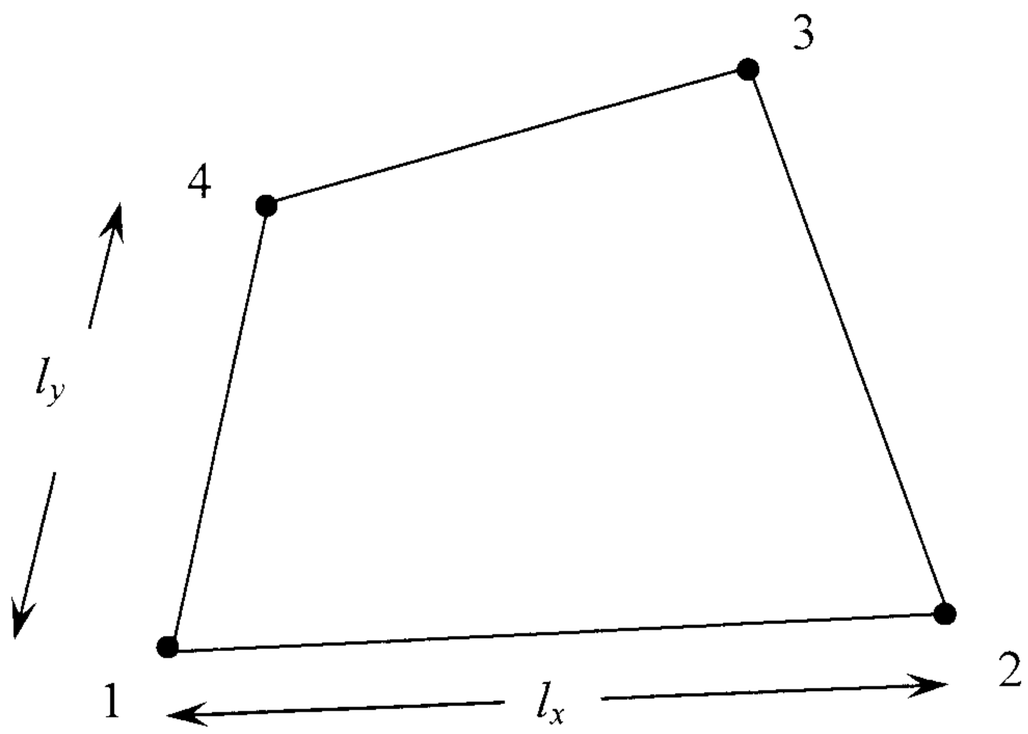

(a)

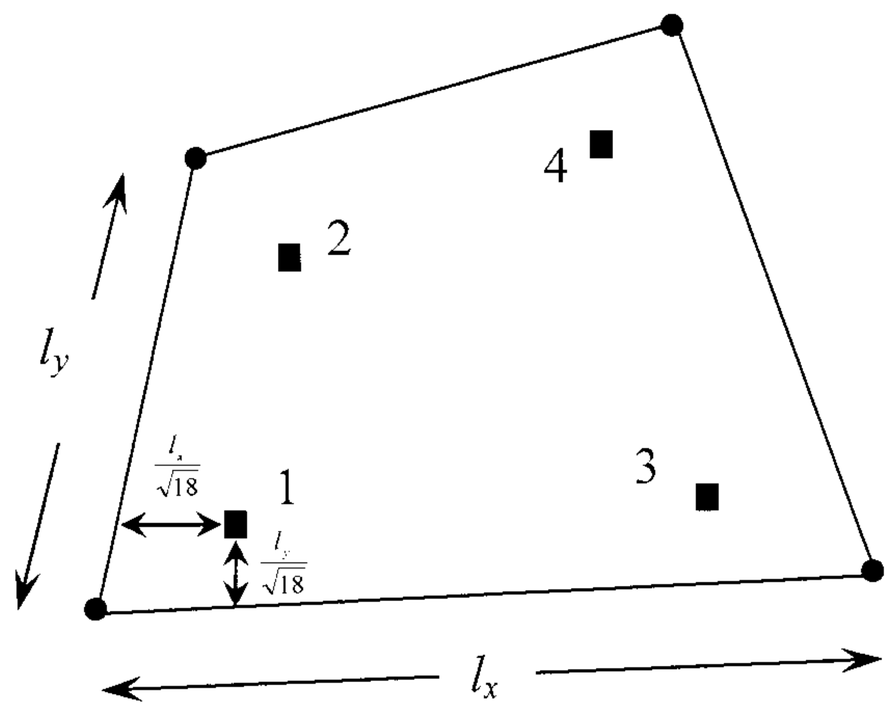

(b)

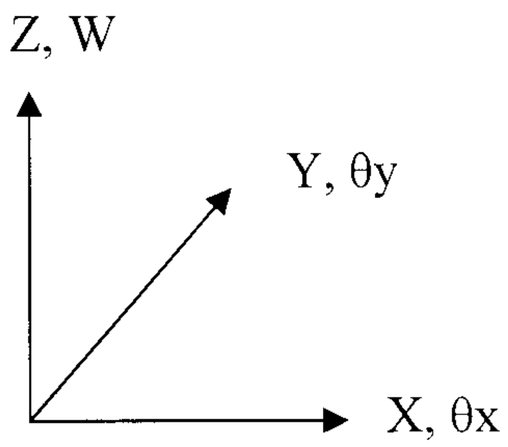

(c)

Figure 2.9 **Isoparametric Kirchhoff plate element used in the FEA anlysis of plate structure used in experimental analysis. Figure 2.9 (a) shows the node numbering convention adopted; Figure 2.9 (b) shows the location of Gauss points in each element; and Figure 2.9 (c) shows the degrees of freedom used for this element type.**

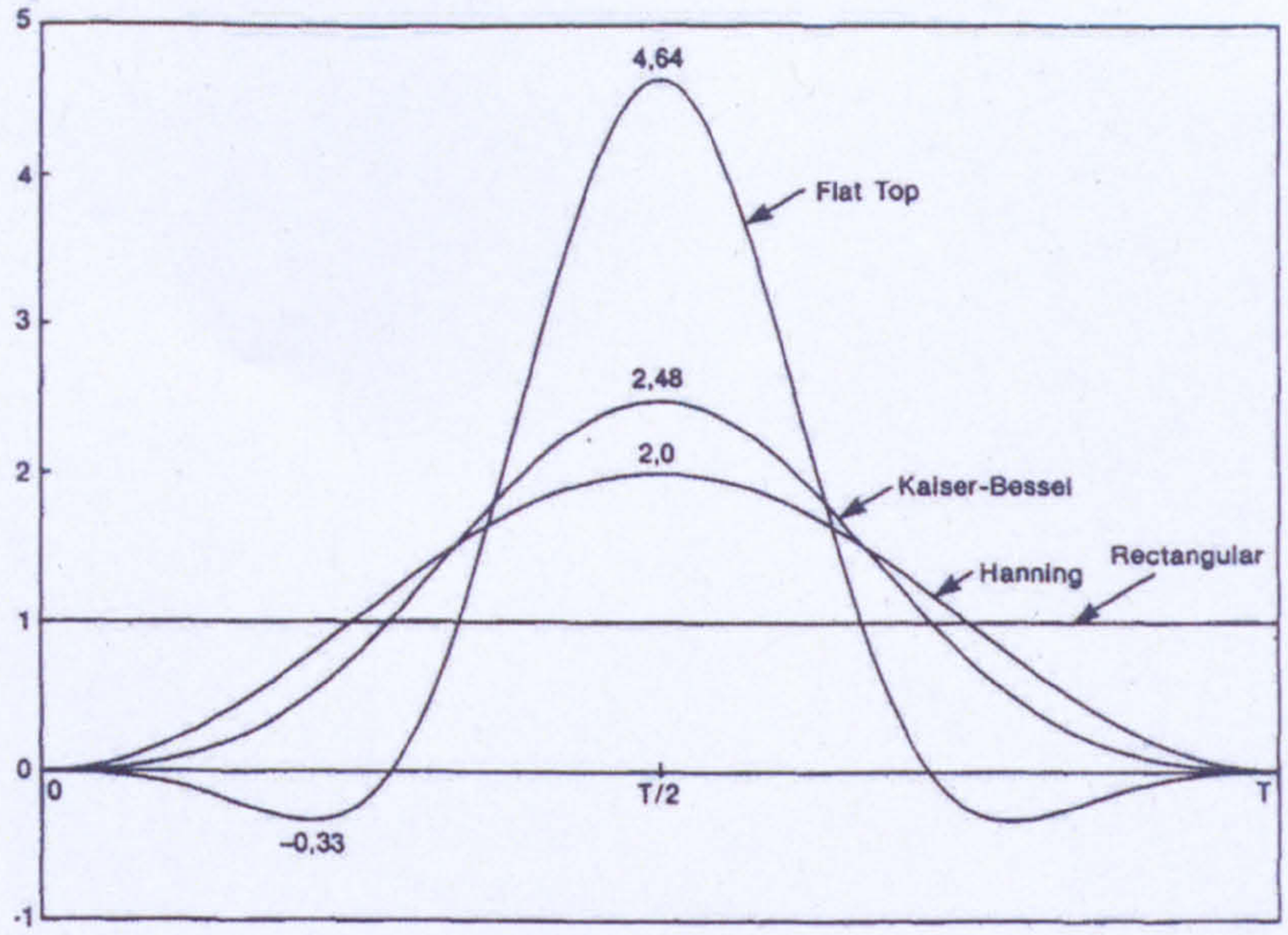

Rectangular window

$$w(t)=1 \qquad \text{for} \qquad 0\le t<T$$

$$w(t)=0 \qquad \text{elsewhere}$$

Hann window

$$w(t)=1-\cos\frac{2\pi t}{T}$$

for $0\le t<T$

$$w(t)=2\sin^2\frac{2\pi t}{T}$$

$$w(t)=0 \qquad \text{elsewhere}$$

Kaiser-Bessel window

$$w(t)=1-1.24\cos\frac{2\pi t}{T}+0.244\cos\frac{4\pi t}{T}-0.00305\cos\frac{6\pi t}{T} \qquad \text{for} \qquad 0\le t<T$$

$$w(t)=0 \qquad \text{elsewhere}$$

Flat top

$$w(t)=1-1.93\cos\frac{2\pi t}{T}+1.29\cos\frac{4\pi t}{T}-0.0388\cos\frac{6\pi t}{T}+0.0322\cos\frac{8\pi t}{T}$$

for $0\le t<T$

$$w(t)=0 \qquad \text{elsewhere}$$

Figure 2.10 Window functions used in FFT analysis. Window shape and governing equations are shown[2.171].

(a)

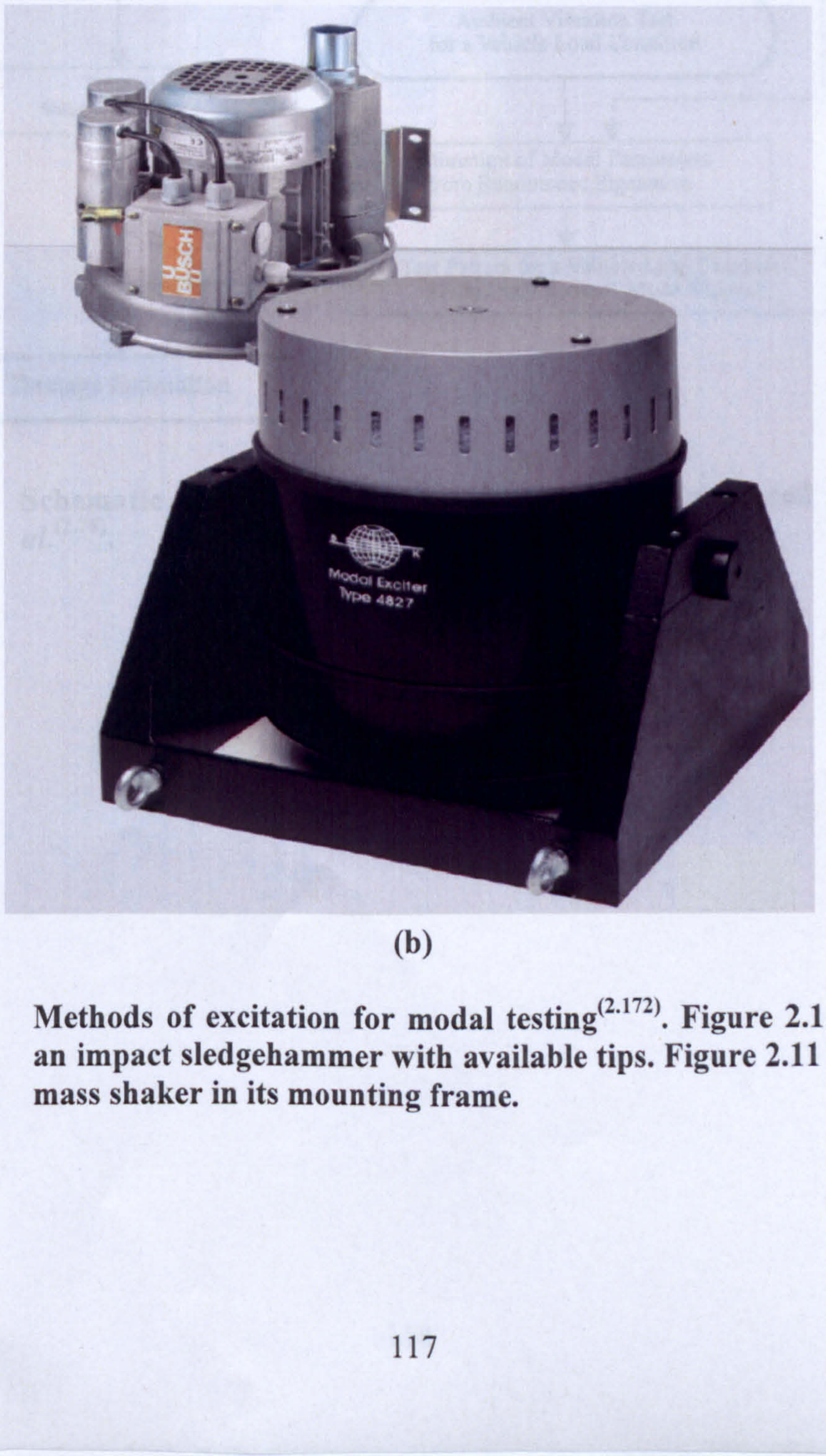

(b)

Figure 2.11 **Methods of excitation for modal testing[2.172]. Figure 2.11 (a) shows an impact sledgehammer with available tips. Figure 2.11 (b) shows a mass shaker in its mounting frame.**

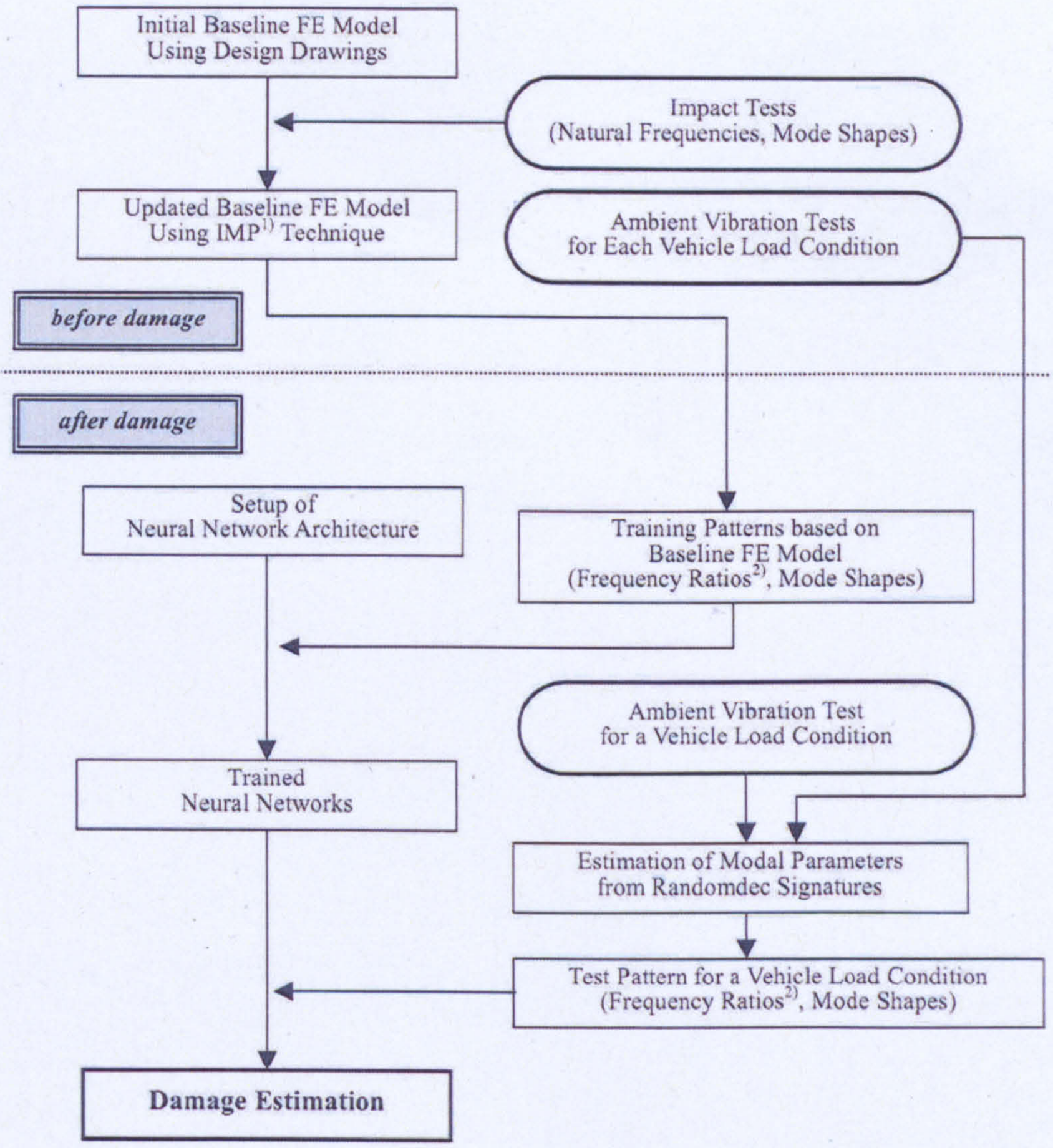

Figure 2.12 Schematic showing bridge monitoring procedure used by Lee *et al.*[(2.75)].

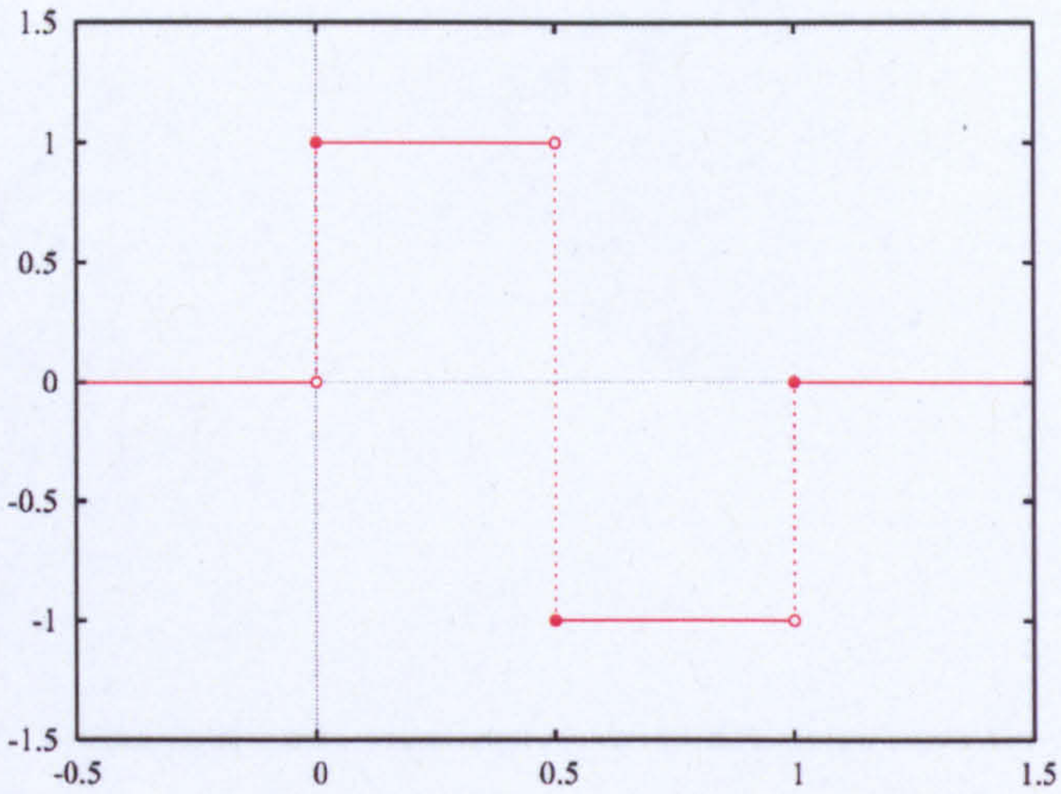

(a)

$$f(x)=\begin{cases}1 & 0\le x<1/2,\\ -1 & 1/2\le x<1,\\ 0 & otherwise\end{cases}$$

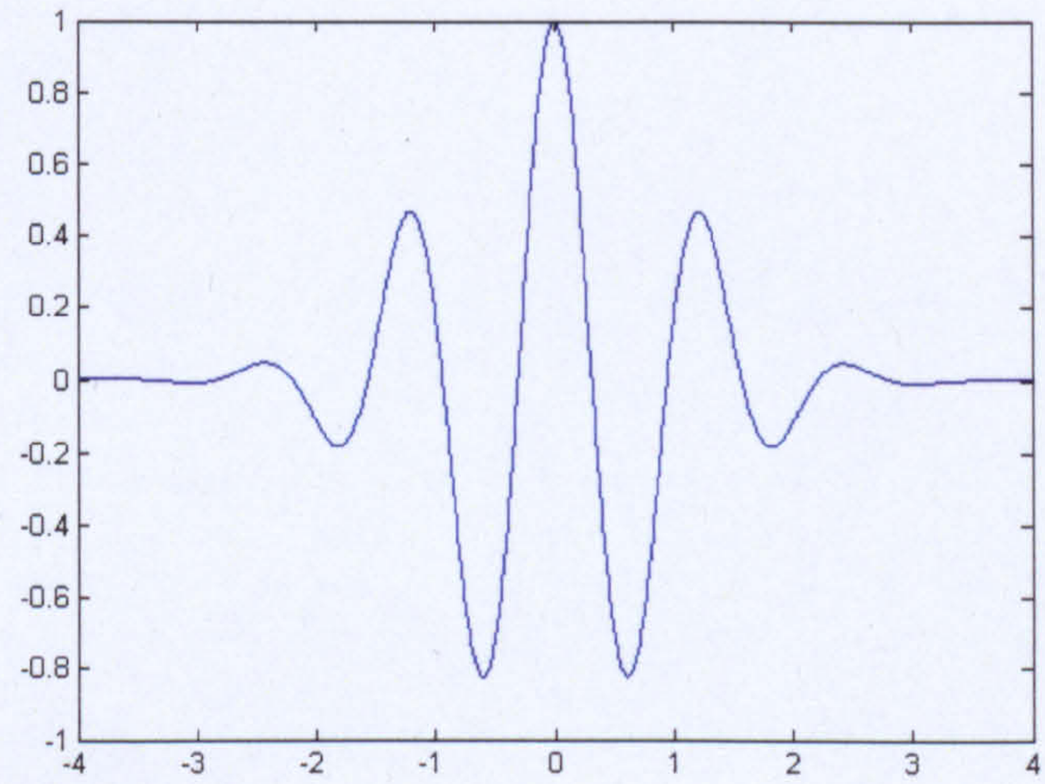

$$\Psi_\sigma(t)=c_\sigma\pi^{-\frac{1}{4}}e^{-\frac{1}{2}t^2}\left(e^{i\sigma t}-\kappa_\sigma\right)$$

(b)

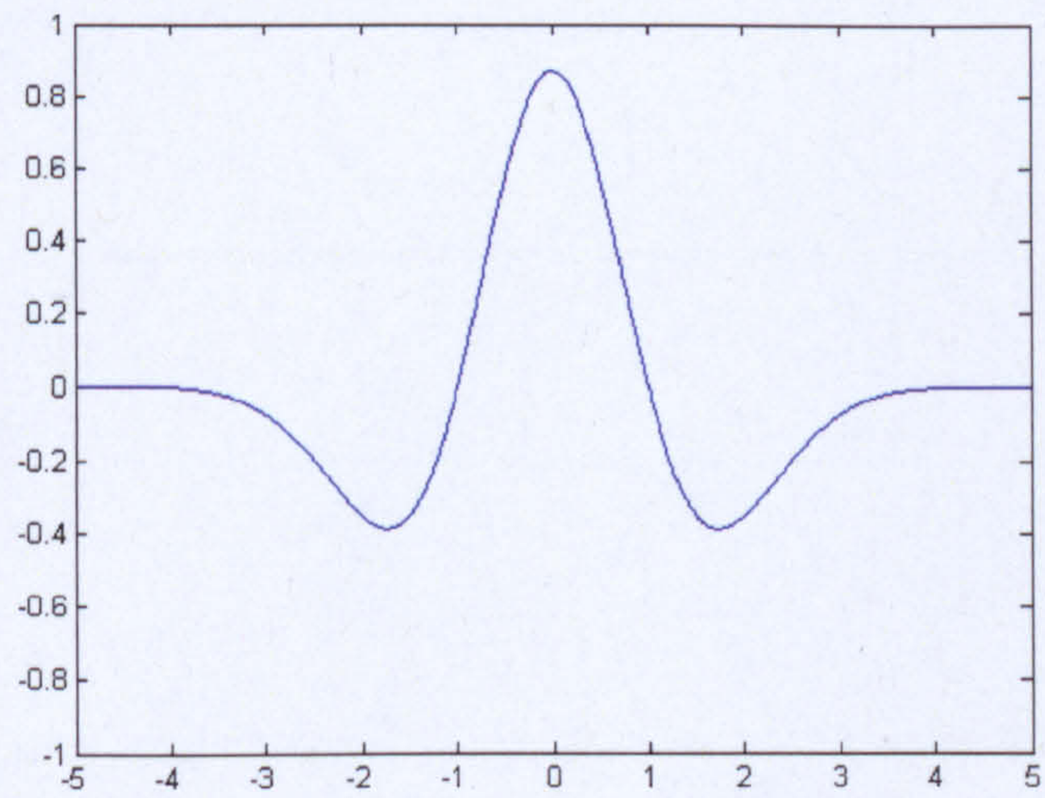

$$\Psi(t)=\left(\frac{2}{\sqrt{3}}\pi^{-\frac{1}{4}}\right)\left(1-t^2\right)e^{\frac{-t^2}{2}}$$

(c)

Figure 2.13 Wavelet transform functions.
Figure 2.13 (a) shows the Haan transform and constituent equation.
Figure 2.13 (b) shows the Morlet transform and its equation.
Figure 2.13 (c) shows the Mexican Hat transform with its equation.

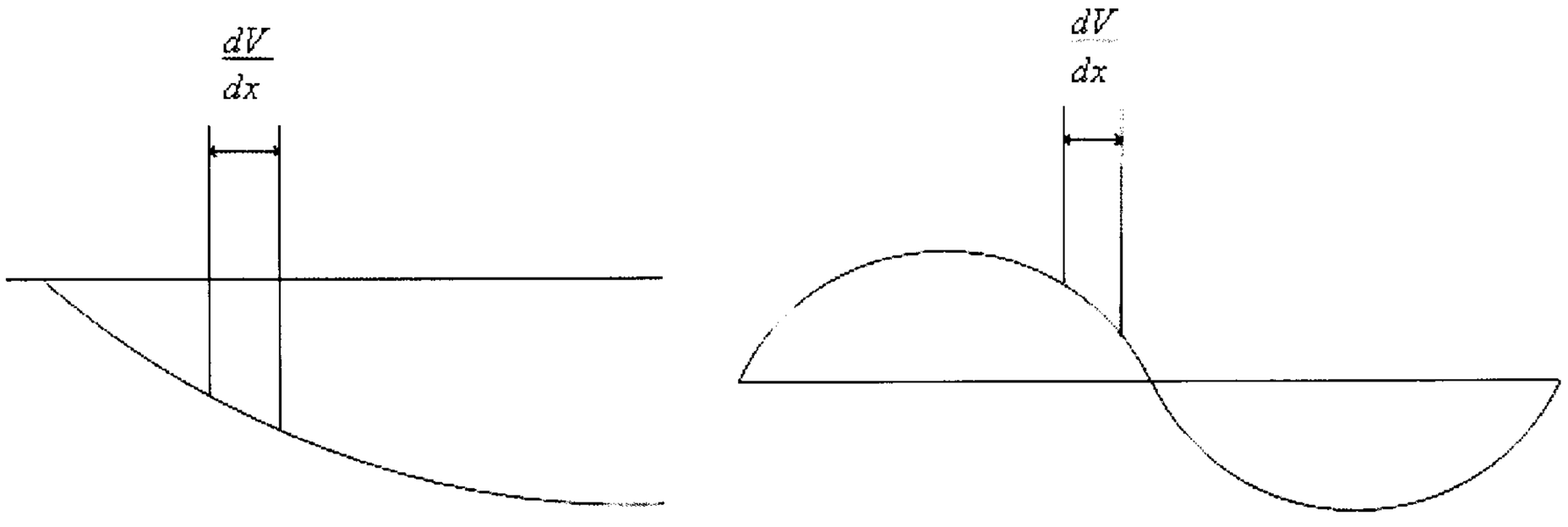

Figure 2.14 Higher mode sensitivity due to increased slope.

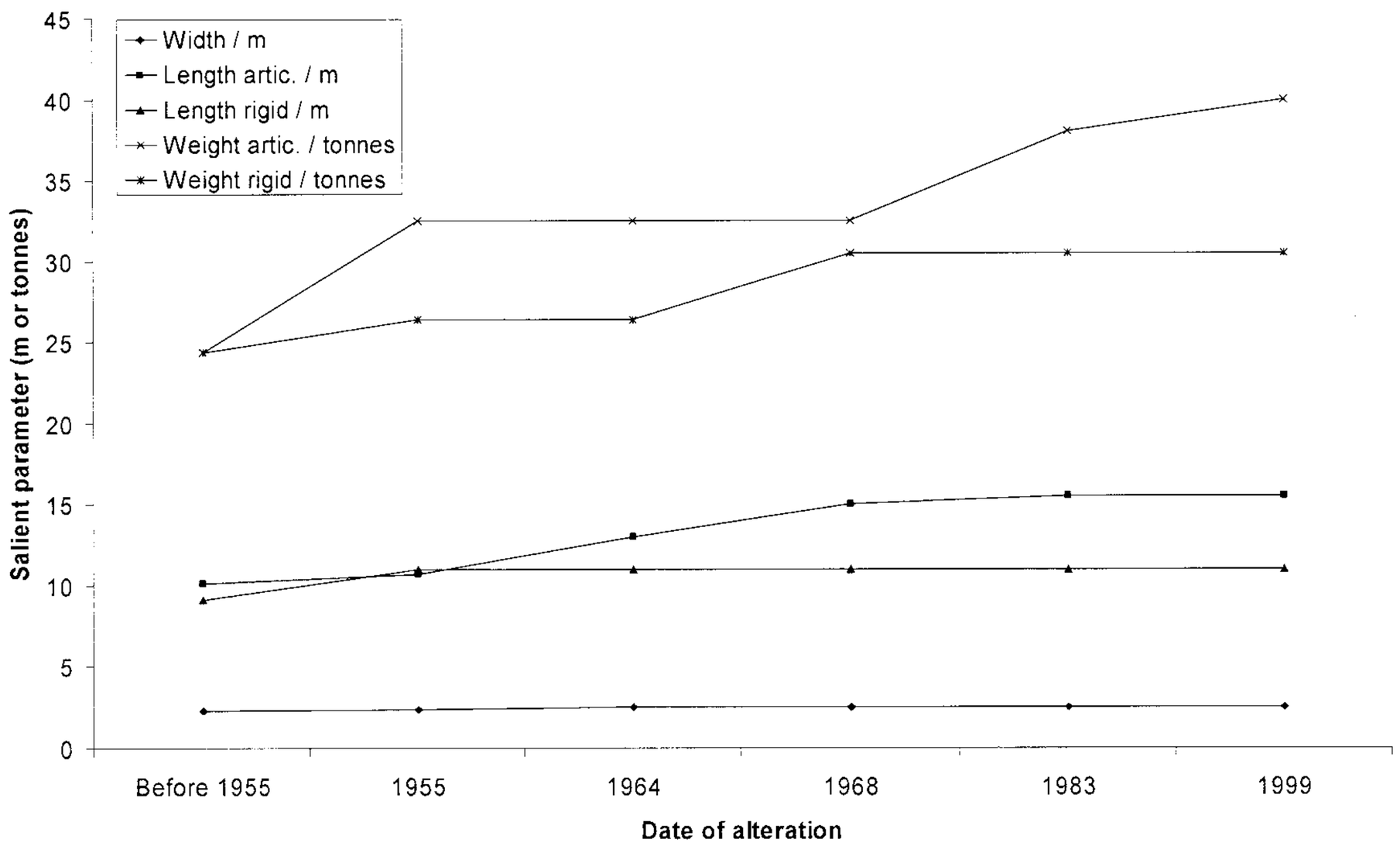

Figure 2.15 Axle weights and vehicle lengths and width alterations in the last 50 years.

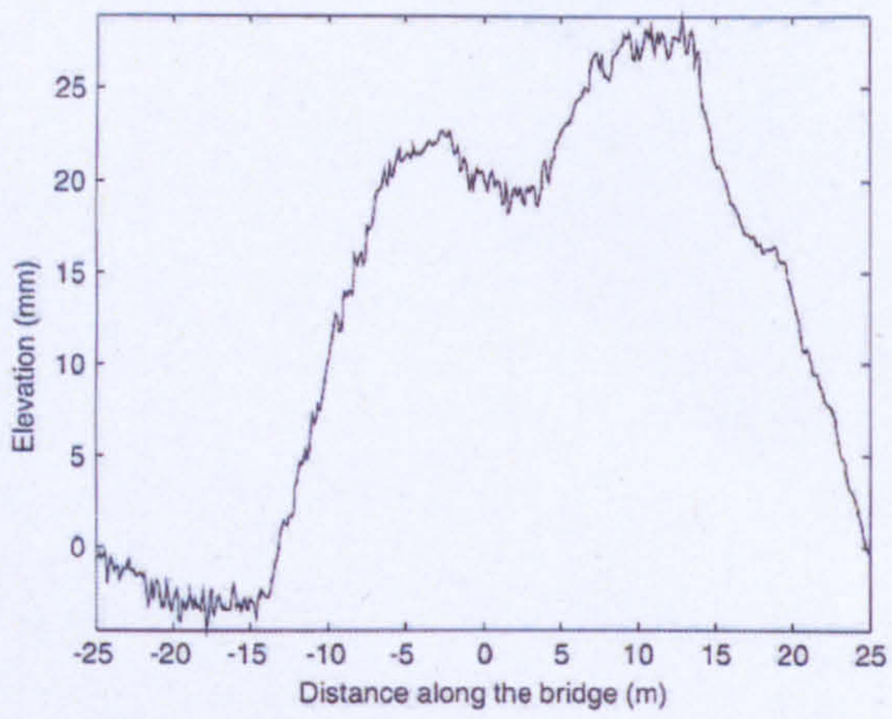

(a)

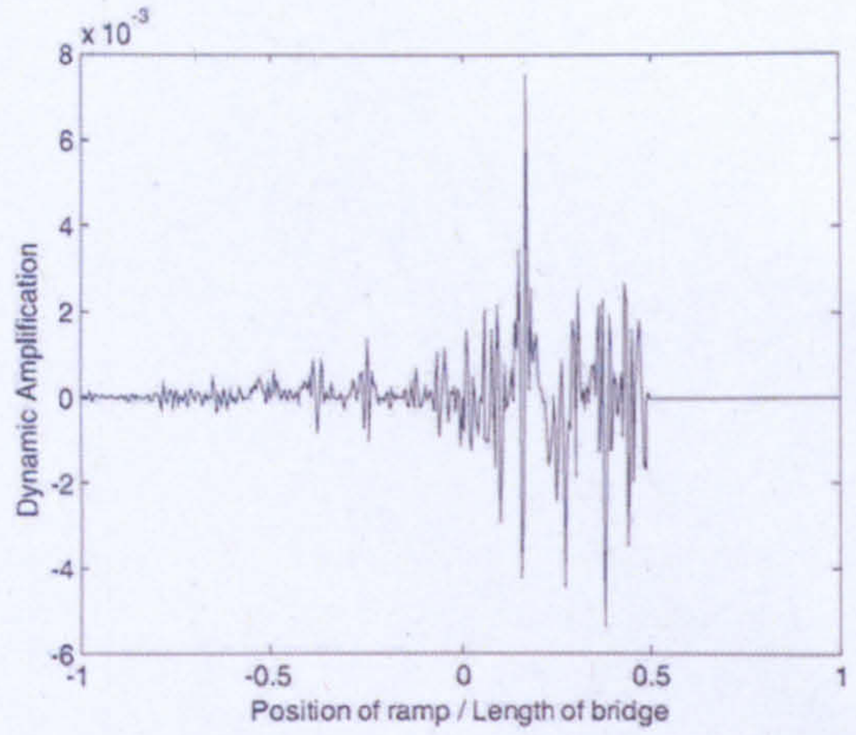

(b)

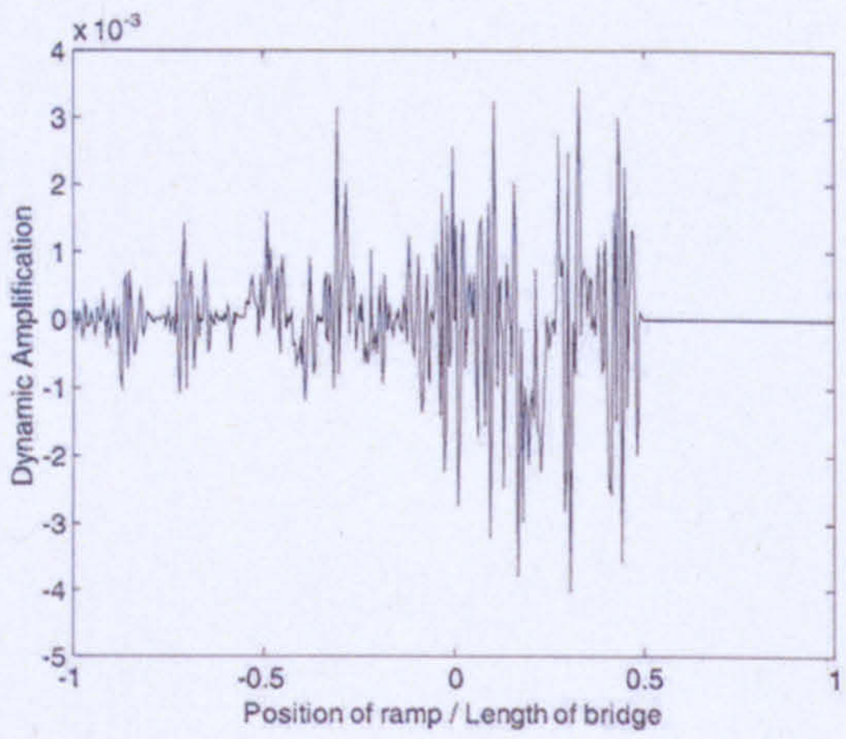

(c)

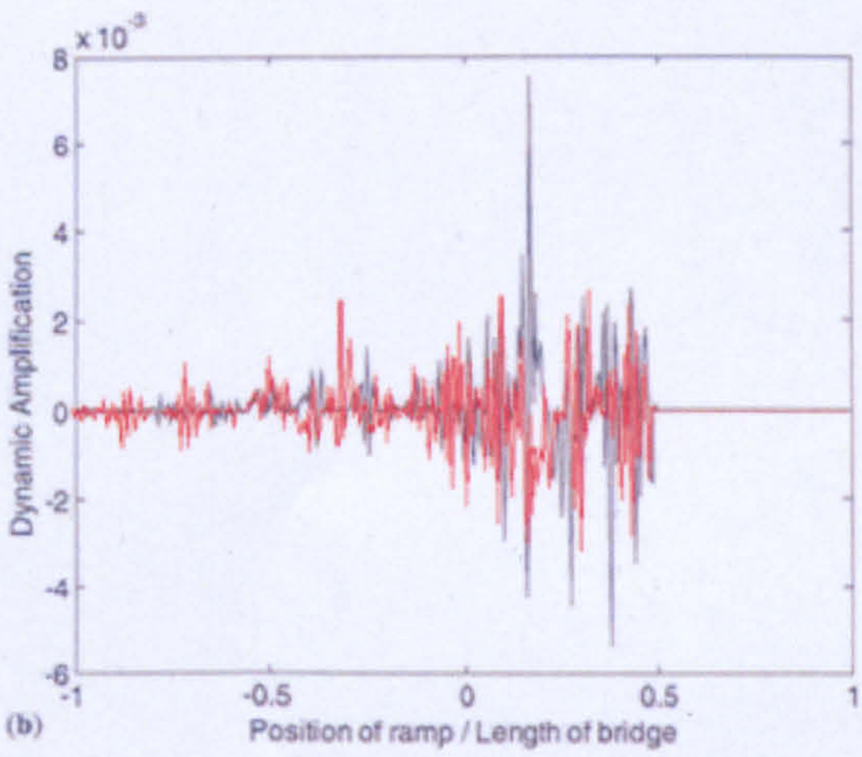

(d)

Figure 2.16 **Sample data from O'brien *et al.*[2.115] showing the effect of vehicle speed on DAF. Figure 2.15 (a) shows the road roughness profile; Figure 2.15 (b) shows the DAF caused by a vehicle travelling at 80 kph across the bridge; Figure 2.15 (c) shows the DAF caused by a vehicle travelling at 120 kph; Figure 2.15 (d) shows (c) superimposed on (b).**

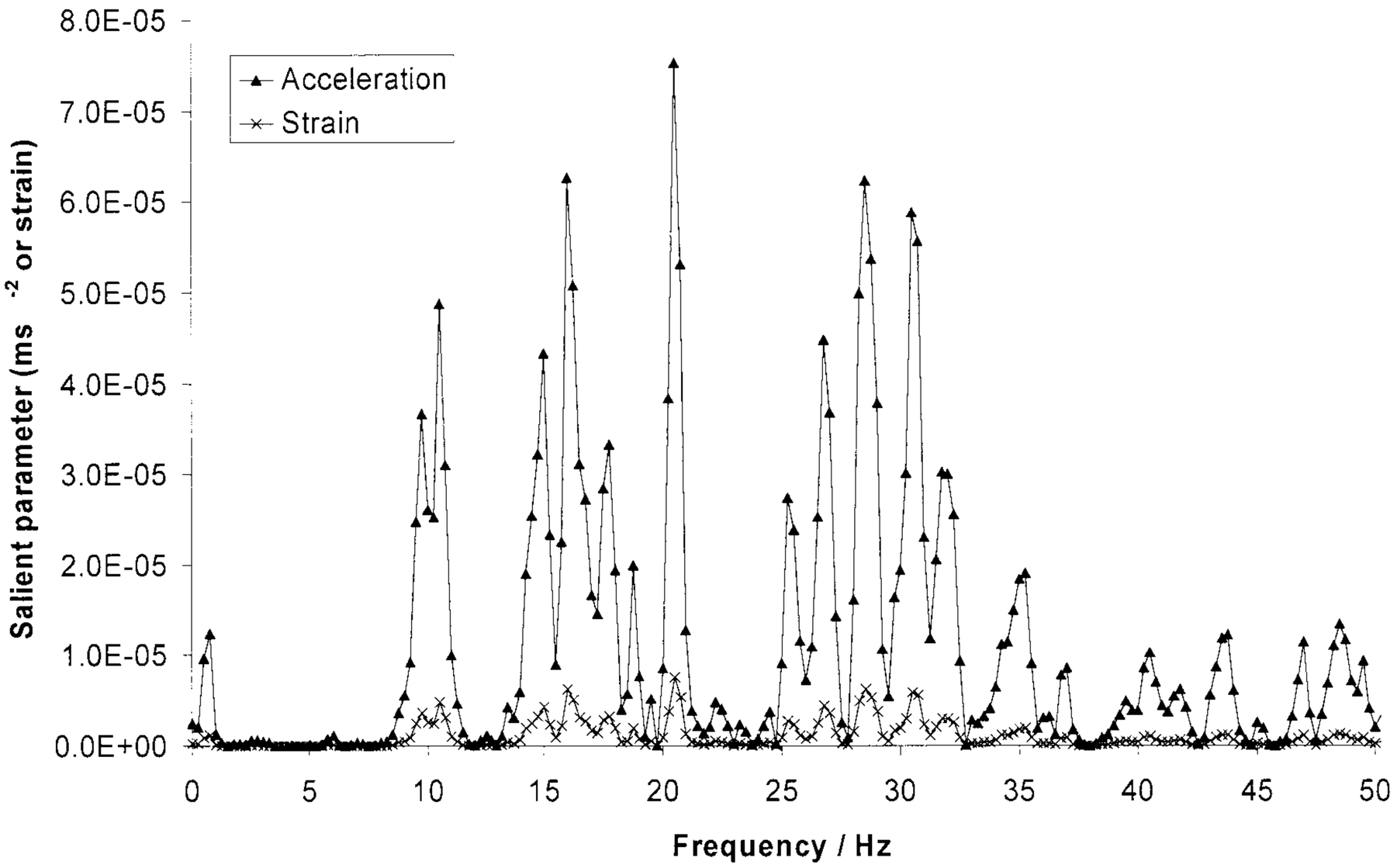

Figure 2.17 Acceleration and strain plots against frequency value.

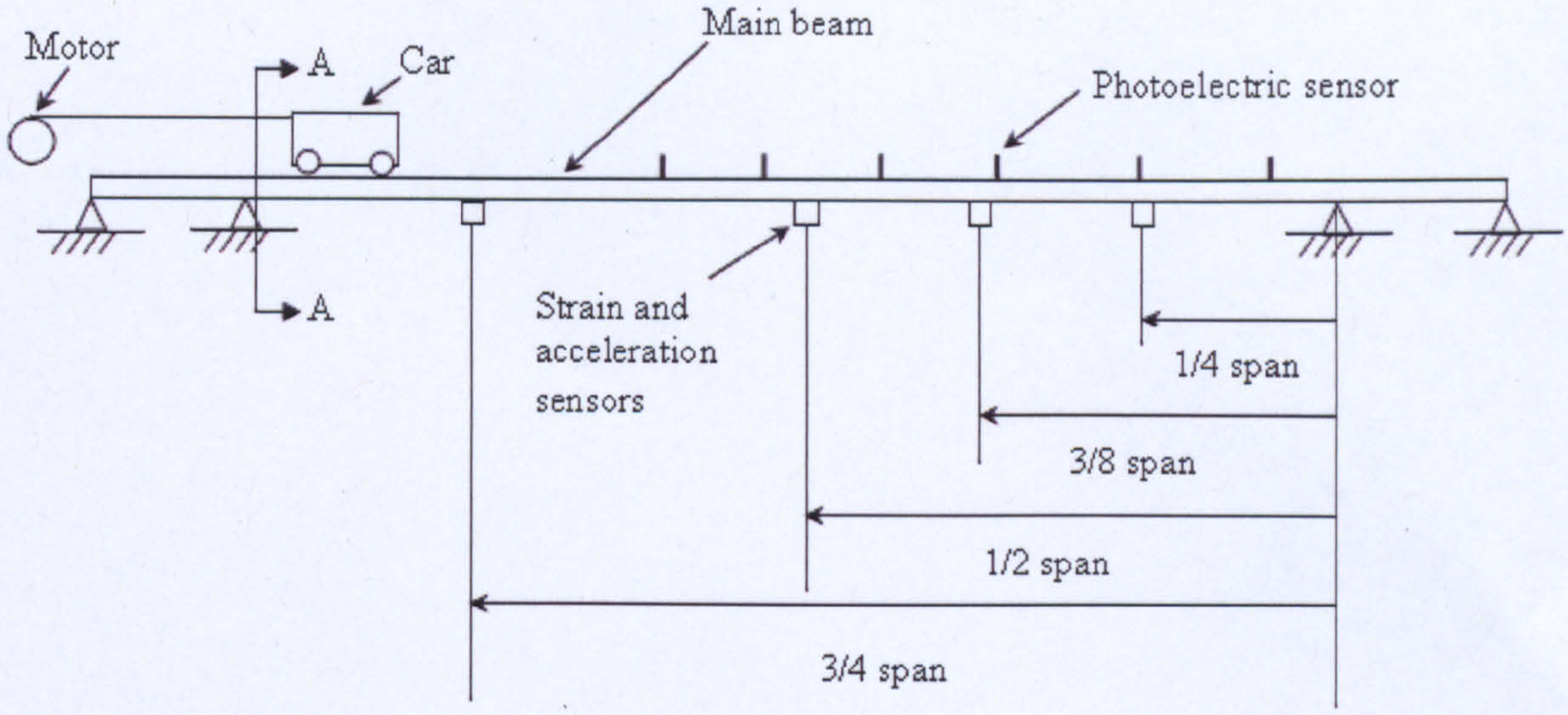

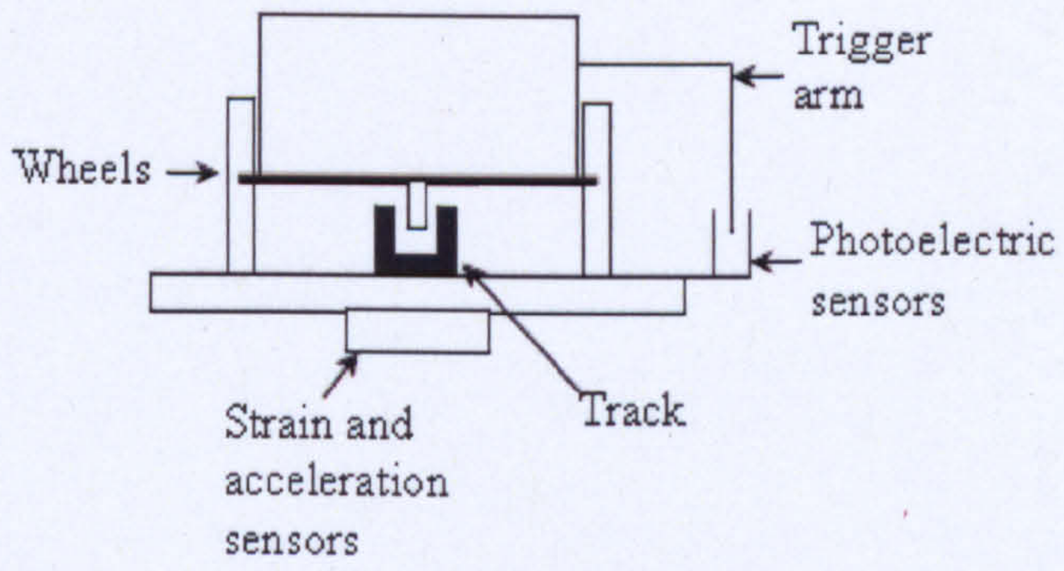

(a)

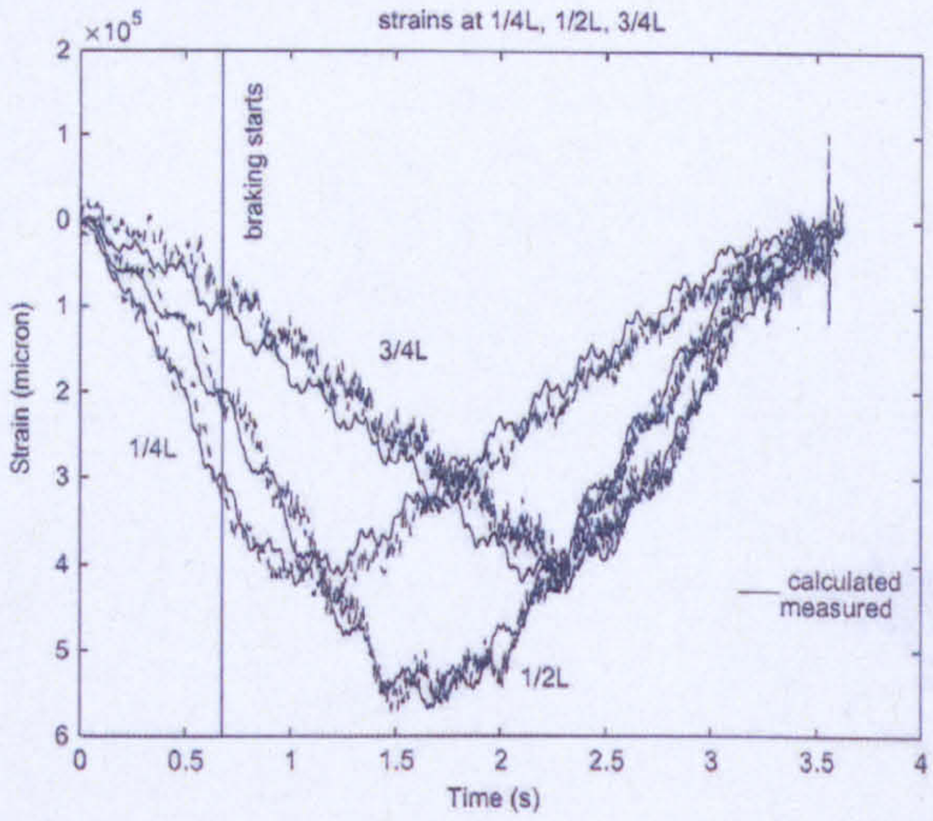

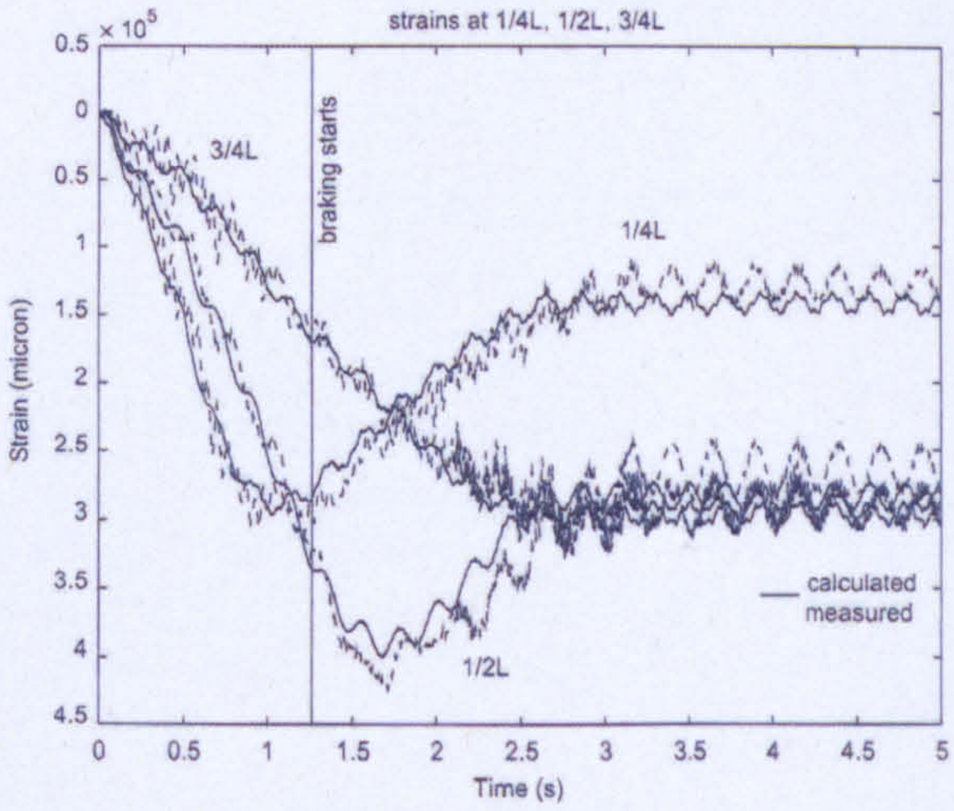

(b) (c)

Figure 2.18 **Sample data from Law and Zhu[2.118]. Figure 2.16 (a) shows the experimental setup; Figure 2.16 (b) shows measured and calculated strains from gentle braking on the system; and Figure 2.16 (c) shows strains from hard braking.**

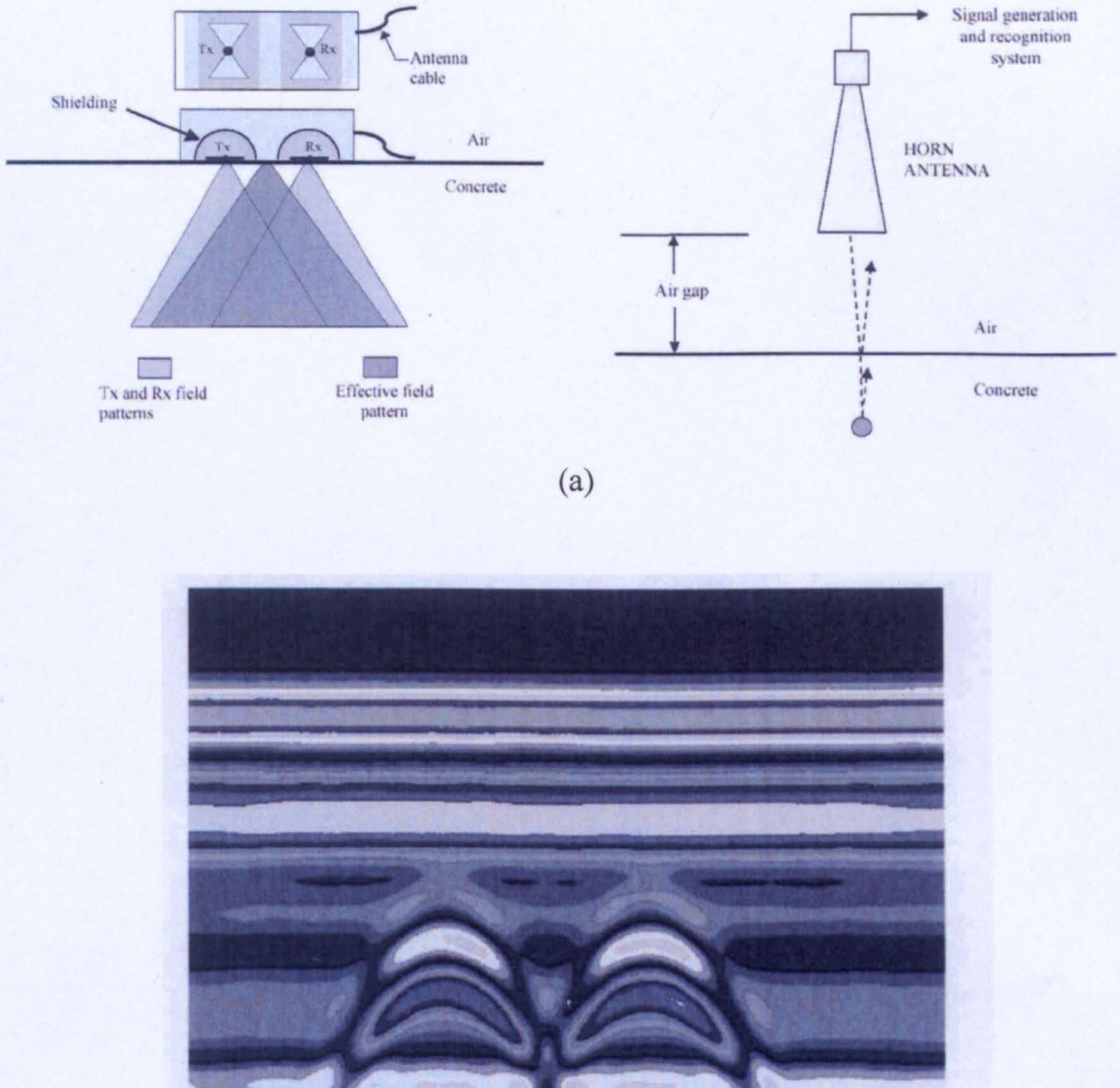

(a)

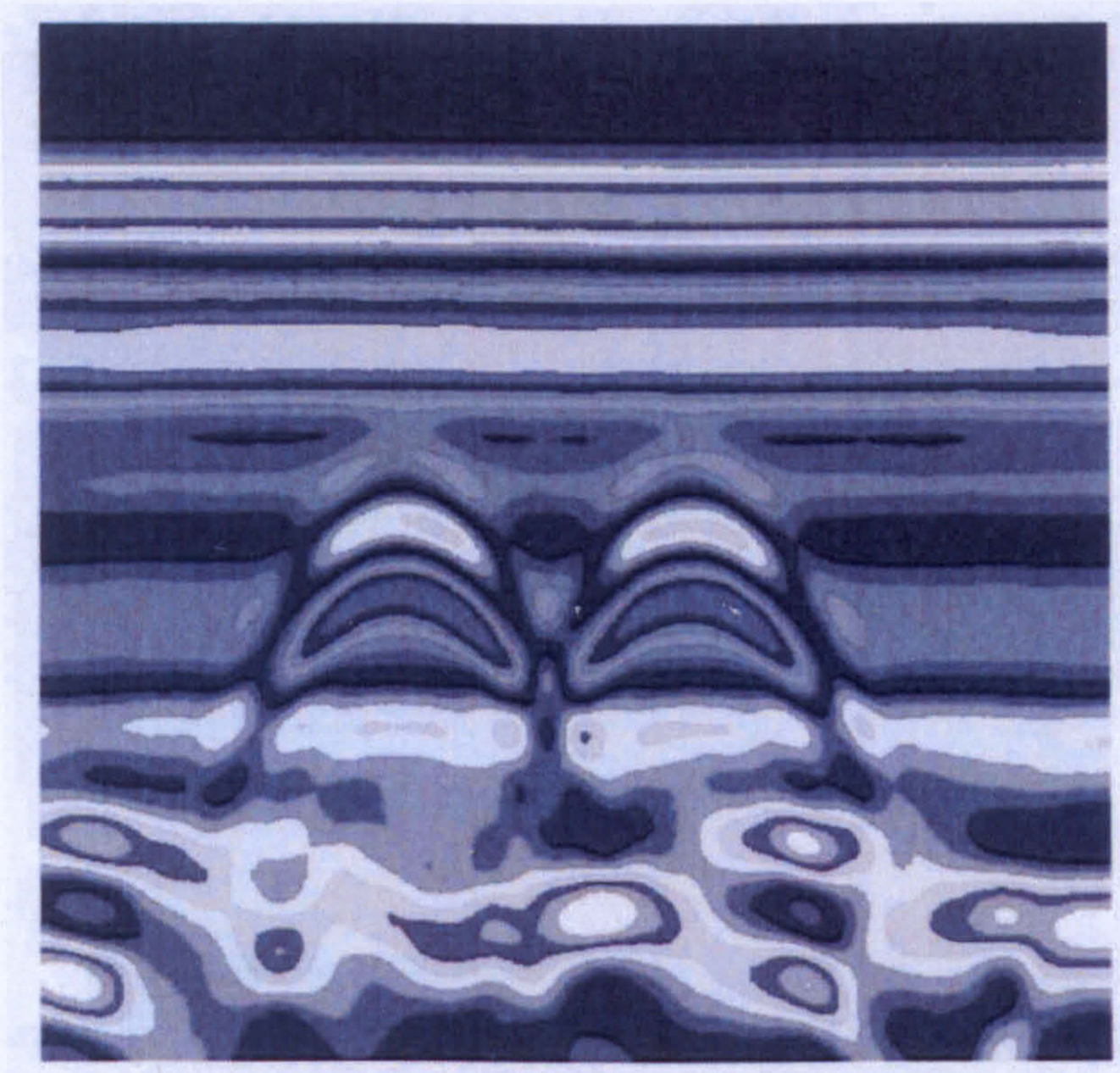

(b)

Figure 2.19 **Radar equipment and typical output[2.125]. Figure 2.17 (a) shows two types of radar equipment; and Figure 2.17 (b) shows a typical output obtained on a reinforced concrete beam.**

Figure 2.20 Typical SASW equipment.

(a)

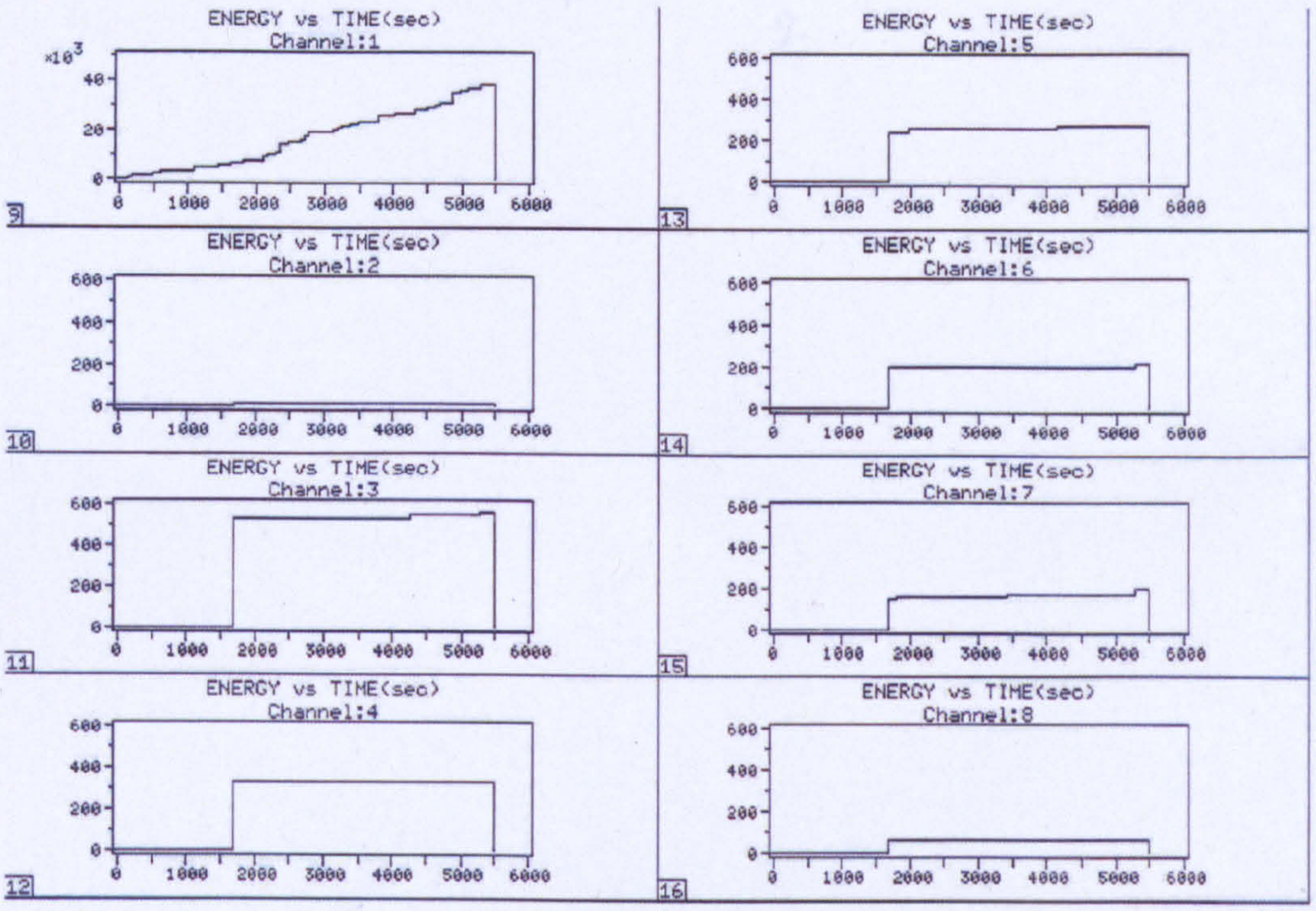

(b)

Figure 2.21 Typical acoustic emission equipment and output[(2.130)].
Figure 2.19 (a) shows the transducers *in situ*.
Figure 2.19 (b) shows typical output spectra for a beam with eight transducers attached.

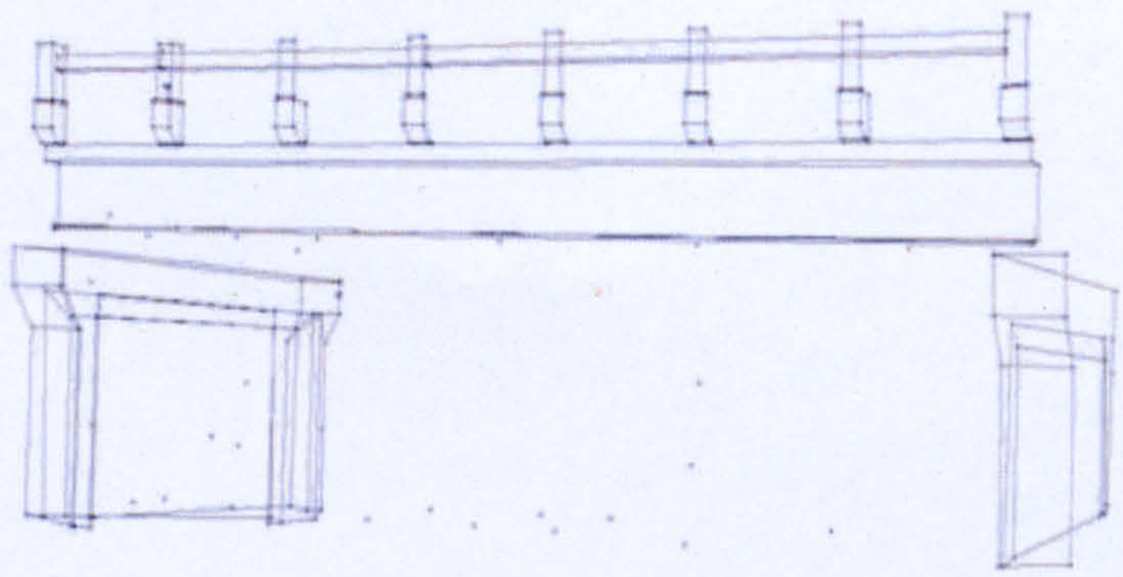

(a)

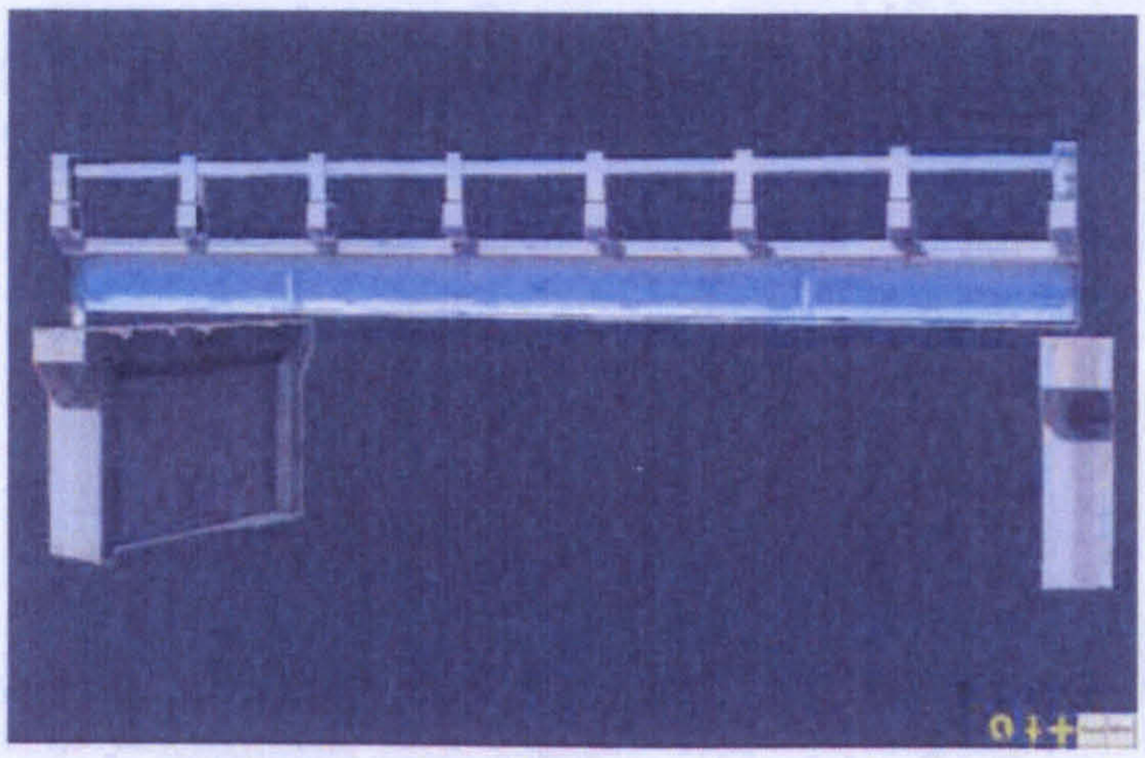

(b)

Figure 2.22 Typical output from the photogrammetry method[2.135]. Figure 2.20 (a) shows the sampling points; and Figure 2.20 (b) shows the final rendered version of the structure.

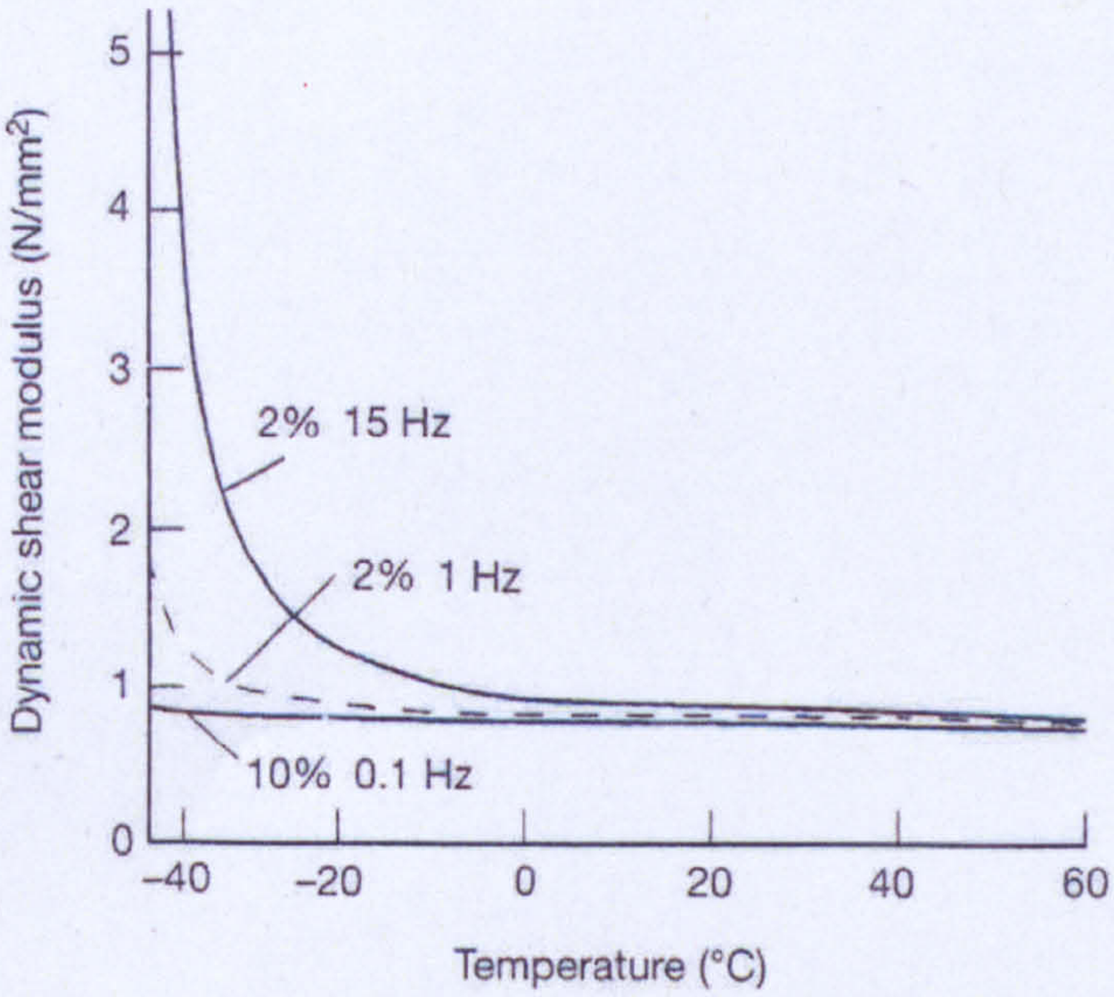

Figure 2.23 Dynamic shear modulus *versus* temperature for elastomeric bearing material.

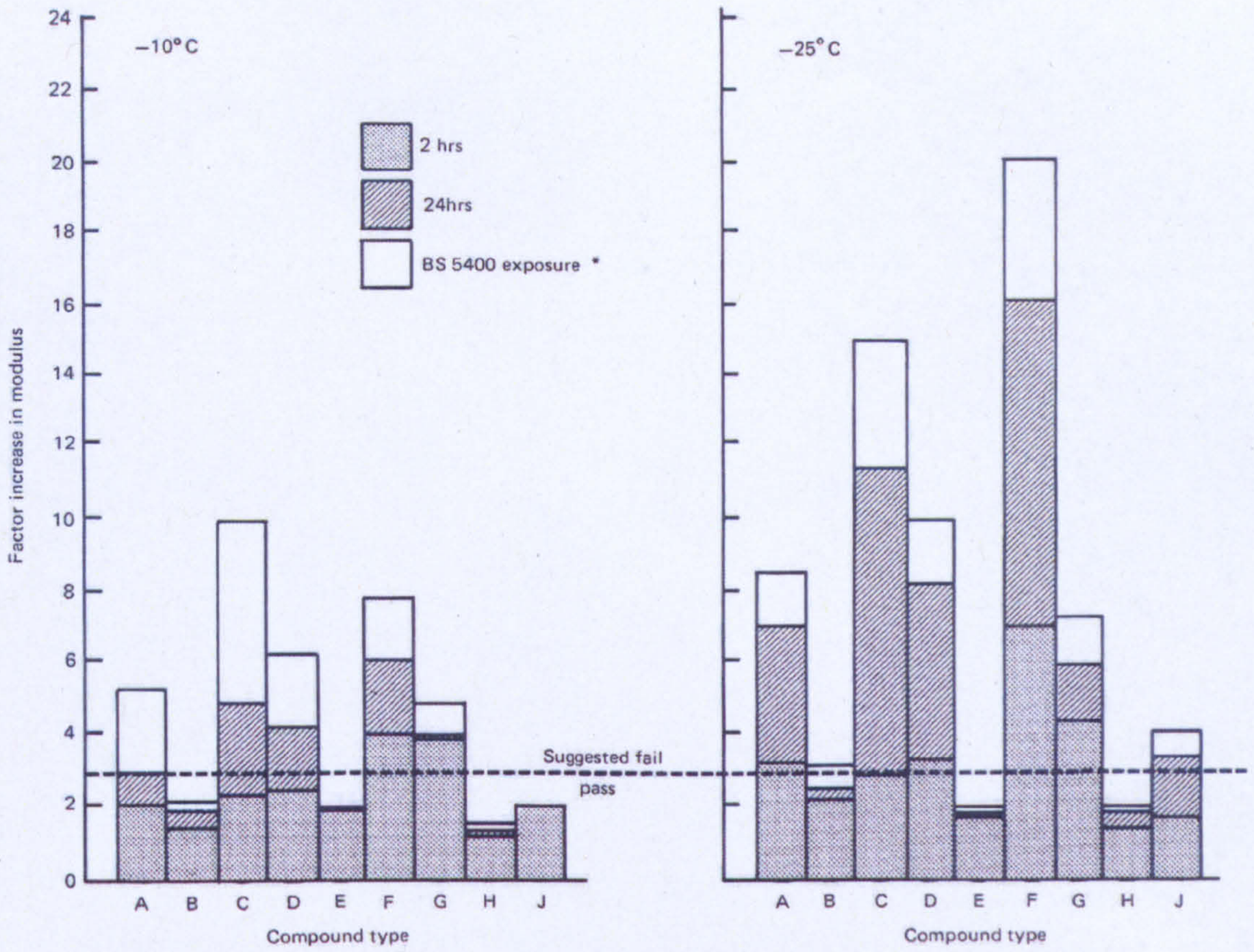

Figure 2.24 Increase in shear modulus at three time exposure limits for nine bearing types at -10°C and -25°C.

Figure 2.25 Typical durometer for measuring material harness showing typical output values on LED screen. (after www.zwick.com)

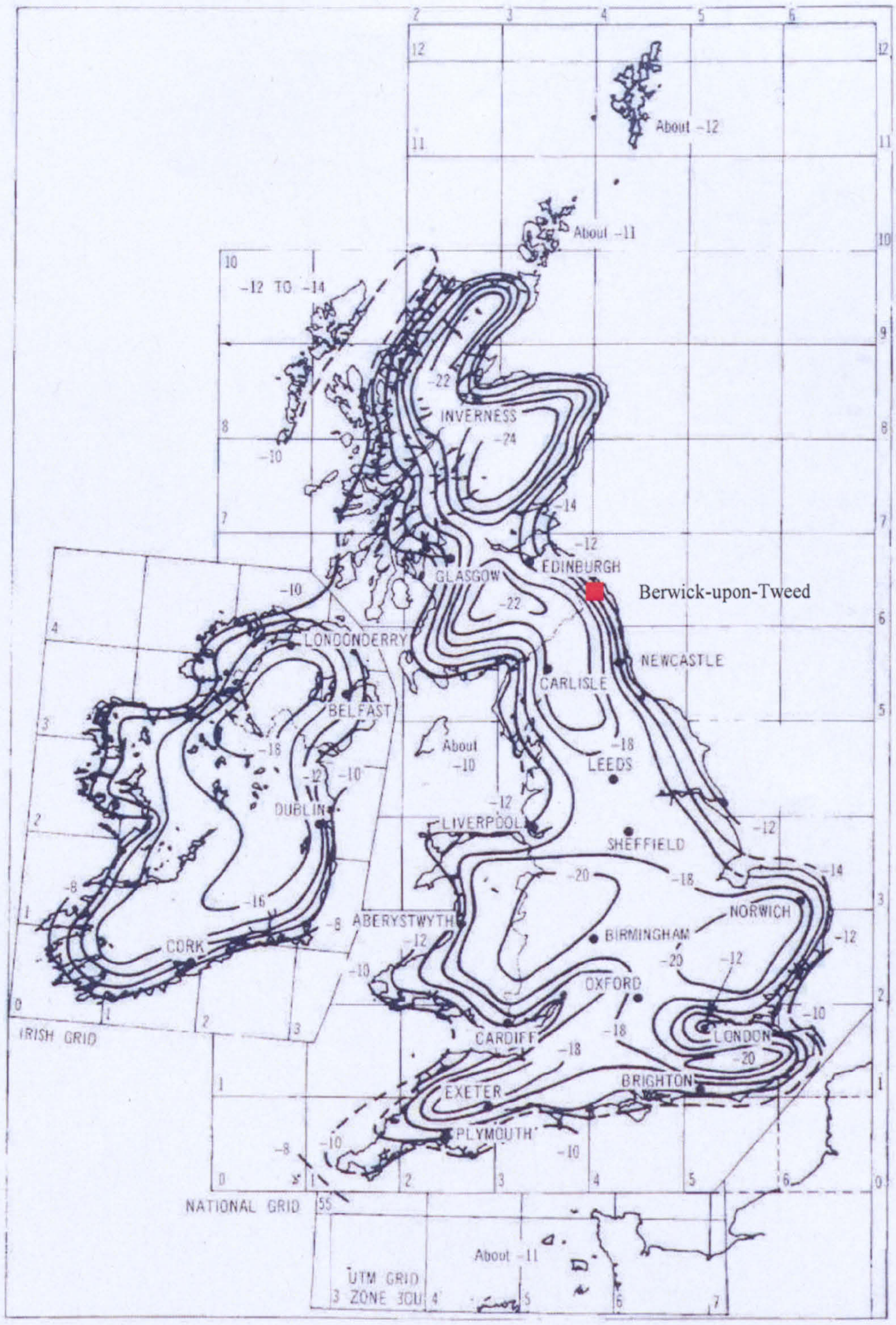

Figure 2.26 **Isotherms of minimum shade air temperature (in °C) in the UK[2.136]. Shown are Edinburgh and Berwick-upon-Tweed, where full-scale experimental testing was completed. The value for Berwick-upon-Tweed is taken as 12 °C.**

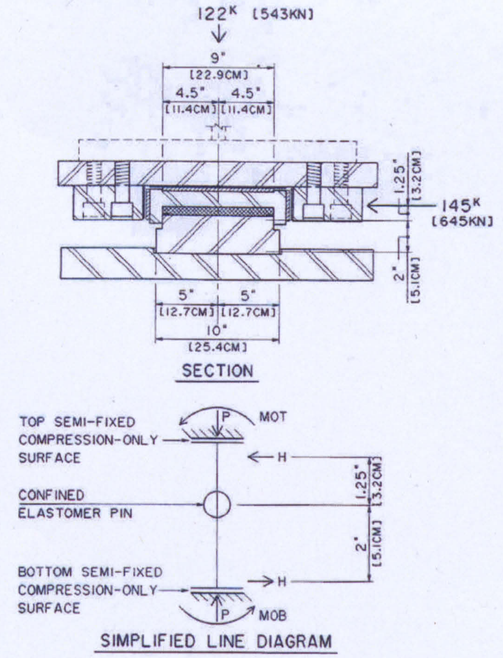

Figure 2.27 **Constrained elastomeric pot bearing with simplified line diagram showing the effective support conditions provided[2.165].**

Table 2.1 Finite strip results and comparison with other methods[2.23].

Values of % error in strip solutions, based on converged strip solution							
	Model C (Quartic)			Model D (Quintic)		Values of Ω	
Mode	1 strip	2 strips	3 strips	1 strip	2 strips	Converged strip solution	Thin plate solution
1, 1	0.001	0.00	0.00	0.01	0.00	0.1413	0.1412
1, 2	0.22	0.08	0.02	0.22	0.01	0.2668	0.2671
2, 1	908*	0.07	0.08	1.23	0.05	0.3376	0.3383
2, 2	641*	0.05	0.03	0.26	0.01	0.4604	0.4615
1, 3	0.37	0.14	0.03	0.36	0.02	0.4977	0.4988
3, 1	1224*	3.43	0.11	496*	0.83	0.6279	0.6299

* High errors are due to poor representation of the lateral deflection in circumstances where bending effects are predominant. Increased order of interpolation, from Quartic to Quintic, leads to improved accuracy when combined with an increasing number of strips.

Table 2.2 Frequency response functions, equations and units.

Frequency response function (H_1 or H_2)	Notation	Quantity	Units	S.I. unit
$\frac{\text{Acceleration}}{\text{Force}}$	$\frac{\ddot{x}}{F}$	Inertance	$\frac{ms^{-2}}{N}$	kg^{-1}
$\frac{\text{Velocity}}{\text{Force}}$	$\frac{\dot{x}}{F}$	Mobility or mechanical admittance	$\frac{ms^{-1}}{N}$	$kg^{-1}s$
$\frac{\text{Displacement}}{\text{Force}}$	$\frac{x}{F}$	Dynamic compliance	$\frac{m}{N}$	$kg^{-1}s^{2}$
$\frac{\text{Force}}{\text{Acceleration}}$	$\frac{F}{\ddot{x}}$	Dynamic mass	$\frac{N}{ms^{-2}}$	kg
$\frac{\text{Force}}{\text{Velocity}}$	$\frac{F}{\dot{x}}$	Mechanical impedance	$\frac{N}{ms^{-1}}$	kgs^{-1}
$\frac{\text{Force}}{\text{Displacement}}$	$\frac{F}{x}$	Dynamic stiffness	$\frac{N}{m}$	kgs^{-2}

Table 2.3 Shi *et al.*: results for damage detection in beams in percentage change[2.102]. Columns marked a correspond to data obtained with the previous method, and b contain data obtained with the improved method.

	Iteration no.	**1**		**2**		**3**	
		a	b	a	b	a	b
Damage at element 16	Damage at node 4	9.30	8.55	7.00	5.03	5.10	4.52
	Damage at node 7	-57.10	-58.09	-54.70	-55.02	-53.80	-55.82
Damage at elements 15 and 16	Damage at node 11	-24.90	-24.38	-29.60	-31.88	-31.80	-33.09
	Damage at node 7	-61.00	-62.11	-56.80	-57.23	-56.00	-56.94

Table 2.4 Bearing defects from Allot and Lomax survey[2.149].

Bearing types	Number of groups inspected	Fault code (% of each type)									Percentage of groups without any fault
		1	2	3	4	5	6	7	8	9	
Roller	34	-	-	-	94	-	-	41	18	50	3 %
Rocker	40	-	-	-	88	-	-	45	25	48	10 %
Knuckle	27	-	-	93	96	-	-	37	11	30	4 %
Plane sliding	2	-	-	50	50	-	-	0	50	50	50 %
Pot	20	-	-	75	80	-	-	25	30	10	15 %
Elastomeric laminated	46	65	-	-	-	-	-	43	24	33	7 %
Elastomeric plain	32	91	-	97	-	-	-	63	28	66	0 %
*Fabreeka®	21	-	52	-	-	-	-	0	5	43	14 %
Others	31	93	-	0	0	84	90	58	0	52	0 %
Total	253										

1 Elastomeric bearing faults
2 Fabreeka bearing faults
3 PTFE / stainless sliding interface faults
4 Metal bearing faults
5 Mortar and concrete bearing faults
6 Sheet bearing faults
7 Bedding mortar faults
8 Bearing related structure faults
9 General faults (independent of bearing type)

* Fabreeka® Structural Bearing with a stainless steel upper unit mating with a PTFE (Teflon)-surfaced elastomeric pad lower unit. The smooth, mirror-finished stainless steel of the upper unit slides with low friction over the PTFE-surfaced pad of the lower unit to allow the beam to freely expand and contract.

Due to differing ages, the 0 % elastomeric plain bearing faults are not considered as significant as thought, as this category of bearings have been in service for a longer duration than elastomeric laminated bearings.

Table 2.5 **Change in shear modulus for elastomeric bearings. NEO150 and NR150 relate to neoprene and natural rubber bearings with a compressive strength of 150 psi (1.03 MPa); NEO100 and NR100 correspond to neoprene and natural rubber bearings with a compressive strength of 100 psi (0.69 MPa).**

Shear modulus at 30% strain, MPa (% change)									
Compound		Room temperature		-10°C		-20°C		-30°C	
		Fast	Slow	Fast	Slow	Fast	Slow	Fast	Slow
NEO150	G / MPa Δ G (%)	1.57 (16)	1.35 (0)	5.47 (50)	3.65 (0)	-	-	-	-
	G / MPa Δ G (%)	-	-	6.55 (31)	5.01 (0)	-	-	-	-
NR150	G / MPa Δ G (%)	0.88 (13)	0.78 (0)	1.23 (27)	0.97 (0)	-	-	3.64 (24)	2.93 (0)
	G / MPa Δ G (%)	-	-	1.34 (30)	1.03 (0)	-	-	3.74 (19)	3.15 (0)
	G / MPa Δ G (%)	-	-	1.34 (22)	1.10 (0)	-	-	1.90 (33)	1.43 (0)
NEO100	G / MPa Δ G (%)	0.72 (16)	0.62 (0)	1.54 (21)	1.28 (0)	1.07 (35)	0.79 (0)	2.28 (46)	1.56 (0)
	G / MPa Δ G (%)	0.66 (23)	0.54 (0)	1.85 (19)	1.56 (0)	3.38 (19)	2.83 (0)	2.33 (36)	1.71 (0)
	G / MPa Δ G (%)	-	-	2.17 (26)	1.72 (0)	-	-	-	-
	G / MPa Δ G (%)	-	-	2.31 (25)	1.84 (0)	-	-	-	-
NR100	G / MPa Δ G (%)	0.68 (15)	0.59 (0)	0.85 (15)	0.74 (0)	0.95 (16)	0.82 (0)	-	-
	G / MPa Δ G (%)	-	-	0.85 (15)	0.74 (0)	1.00 (14)	0.88 (0)	-	-

CHAPTER 3

Small scale model testing

3 Introduction

Bridge bearings are designed to withstand a maximum loading and to allow a certain amount of movement in a prescribed direction, often laterally or in certain cases, rotationally. However, bridge bearings are prone to damage as they are traversed by motor vehicles of varying sizes and speeds. As a consequence, bearing replacement is time consuming and requires specialist installation. If the response of bridge bearings to vibrations could be better understood this could potentially save both time and capital expenditure.

Initial research yielded a simple method for determining the fundamental natural frequency of a plate structure using the Euler-Bernoulli and Rayleigh-Ritz methods. The derivation of the method is highlighted herein, and several examples of answers obtained with the method are shown.

To validate the initial hypothesis of bearing degradation affecting dynamic response, a small-scale model consisting of a PMMA plate with variable support conditions was tested. The small-scale test is to be viewed as nothing more than a simplification of a bridge arrangement, and is not intended to model actual behaviour of a bridge, but simply to prove the concept of the effect of varying the stiffness of the end supports. Finally, the FEA included within this chapter is intended to show the degree of concurrence between measured data from testing and analytical methods to determine the pattern and wave propagation of response due to support stiffness changes.

3.1 Static deflection of beams with spring end support

In addition to the modal analysis and FEA performed on the plate shown later in this chapter, a quick and simple solution for determining the primary resonance frequency in the various end condition arrangements used in experimental work was developed using the Euler-Bernoulli beam equation[3.1] and the Rayleigh-Ritz principle[3.2].

The rationale was to evaluate a plate with variable end conditions, where the deflection, displacement and bending moment can be different at either end of the beam, and be totally independent of each other, using established methods. The reason for undertaking this task was to apply end conditions which would mimic the characteristics of bridge bearings which compress when subjected to movement induced by traffic loading. The degree of compression is dependent on the stiffness of the bearings; therefore the effect of degradation in bearing performance is simulated through the change in stiffness.

Other researchers have investigated the effects of support stiffness on the response of plate structures. Methods outlined by Li and Yau *et al*[3.3 & 3.4] use the same premise of setting the bearing stiffness, assuming a shape function based on beam theory and the flexural rigidity of the beam combined with this stiffness. In this case the method is applied to bridges subjected to moving train loads, but could simply be applied to highway bridges.

3.1.1 Euler-Bernoulli equation

The Euler-Bernoulli method, often called classical beam theory or the engineering beam theory, is the methodology covered in elementary treatments of mechanics of materials.

This model accounts for bending moment effects on stresses and deformations. Its fundamental assumption is that beam cross-sections remain plane and normal to the deformed longitudinal axis. Any rotation which occurs does so about a neutral axis that passes through the centroid of the beam cross-section.

Initially, the general Euler-Bernoulli equation for beam flexure was used to determine an equation for a beam with flexible supports, where the end conditions of the beam are independent of each other, *i.e.*, V_0 and V_L are potentially different values.

$$V = C_1 + C_2 x + C_3 x^2 + C_4 x^3 - \left(\frac{\rho A g}{24 E I}\right) x^4 \qquad \text{Eq. 3.1}$$

This equation is then differentiated once with respect to x to give an equation for the deflection of the beam:

$$\frac{dV}{dx} = C_2 + 2C_3 x + 3C_4 x^2 - \left(\frac{\rho A g}{6 E I}\right) x^3 \qquad \text{Eq. 3.2}$$

That equation is then differentiated once more with respect to x to give an equation for the moment in the beam:

$$\frac{d^2 V}{dx^2} = 2C_3 + 6C_4 x - \left(\frac{\rho A g}{2 E I}\right) x^2 \qquad \text{Eq. 3.3}$$

The end conditions:

At $x = 0$, $V = V_0$ and $\frac{d^2V}{dx^2} = 0$; At $x = L$, $V = V_L$ and $\frac{d^2V}{dx^2} = 0$

are then applied to Eqns 3.1 to 3.3 to determine values for the constants which are given below as Eqns 3.4 to 3.8.

$$C_1 = V_0 \qquad \text{Eq. 3.4}$$

$$C_2 = \left(\frac{V_L - V_0}{L}\right) - \frac{\rho A g L^3}{24EI} \qquad \text{Eq. 3.5}$$

$$C_3 = 0 \qquad \text{Eq. 3.6}$$

$$C_4 = \left(\frac{\rho A g L}{12EI}\right) \qquad \text{Eq. 3.7}$$

$$C_5 = \left(\frac{\rho A g}{24EI}\right) \qquad \text{Eq. 3.8}$$

Once the above calculations had been carried out, it was then possible to evaluate values of deflection, V, for different values of V_0.

3.1.2 Rayleigh-Ritz method

A complete analysis of the natural frequencies of a beam is a complicated problem, especially if the geometry is complex, and is best solved with the aid of FEA software. It is also possible to perform a modal analysis on a finite element model of even complex geometries. Executing such an analysis will result in a large number of natural frequencies being determined, all in three-dimensional space. This is the preferred and frequently used approach when analysing a completed or mature design in detail. However, in the early stages of design, when the part geometries are still not fully defined, a quick and easily applied method for finding at least an approximate

fundamental frequency for a proposed design is useful. The Rayleigh-Ritz method, which is an energy-based method that gives results within a few percent of the true natural frequency, serves that purpose.

The Rayleigh-Ritz method equates the potential and kinetic energies in the system. The potential energy is in the form of strain energy in the deflected beam and is at a maximum value at the largest deflection. The kinetic energy is a maximum when the vibrating beam passes through the undeflected position with maximum velocity. This method assumes that the lateral vibrating motion of the beam is sinusoidal and that some external excitation, or forcing function, is present to force the lateral vibration.

$$V_\delta = \left(C_1 + C_2 x + C_4 x^3 - C_5 x^4\right) \sin \omega t \qquad \text{Eq. 3.9}$$

Using the Rayleigh-Ritz method on the above equation derived from the Euler-Bernoulli equation, it is possible to derive an equation for the natural frequency of the beam. It is then necessary to calculate the period and frequency from Eqns 3.10 to 3.14.

$$2T = \rho A \int_0^L \left(\frac{\partial V_\delta}{\partial t} \right)^2 dx \qquad \text{Eq. 3.10}$$

$$2T = \rho A \omega^2 \int_0^L \left(C_1 + C_2 x + C_4 x^3 - C_5 x^4\right)^2 dx \qquad \text{Eq. 3.11}$$

$$= \rho A \omega^2 \int_0^L \left(\begin{array}{l} C_1{}^2 + 2C_1C_2x + C_2{}^2x^2 + 2C_1C_4x^3 - 2C_1C_5x^4 + 2C_2C_4x^4 \\ -2C_2C_5x^5 + C_4{}^2x^6 - 2C_4C_5x^7 + C_5{}^2x^8 \end{array} \right) dx$$

$$= \rho A \omega^2 \left[\begin{array}{l} C_1{}^2 x + C_1C_2x^2 + \frac{C_2{}^2x^3}{3} + \frac{C_1C_4x^4}{2} - \frac{2C_1C_5x^5}{5} + \frac{2C_2C_4x^5}{5} \\ -3C_2C_5x^6 + \frac{C_4{}^2x^7}{7} - \frac{C_4C_5x^8}{4} + \frac{C_5{}^2x^9}{9} \end{array} \right]_0^L$$

$$= \rho A \omega^2 \left(\begin{array}{l} C_1{}^2 L + C_1C_2L^2 + \frac{C_2{}^2L^3}{3} + \frac{C_1C_4L^4}{2} - \frac{2C_1C_5L^5}{5} + \frac{2C_2C_4L^5}{5} \\ -3C_2C_5L^6 + \frac{C_4{}^2L^7}{7} - \frac{C_4C_5L^8}{4} + \frac{C_5{}^2L^9}{9} \end{array} \right)$$

Eq. 3.12

$$2V = EI \int_0^L \left(\frac{\partial^2 V_\delta}{\partial x^2} \right)^2 dx$$

Eq. 3.13

$$= EI \int_0^L \left(6C_4x - 12C_5x^2 \right)^2 dx$$

$$= EI \int_0^L \left(36C_4{}^2x^2 - 144C_4C_5x^3 + 144C_5{}^2x^4 \right) dx$$

$$= EI \left[12C_4{}^2x^3 - 36C_4C_5x^4 + \frac{144C_5{}^2x^5}{5} \right]_0^L$$

$$= EI \left(12C_4{}^2L^3 - 36C_4C_5L^4 + \frac{144C_5{}^2L^5}{5} \right)$$

Eq. 3.14

Upon completion of the calculations, Eq. 3.15 below is obtained by combining Eqns 3.12 and 3.14, with the constants remaining as stated previously.

$$\omega = \left(\frac{EI}{\rho A} \frac{\left(12C_4{}^2L^3 - 36C_4C_5L^4 + \frac{144C_5{}^2L^5}{5} \right)}{\left(C_1{}^2L + C_1C_2L^2 + \frac{C_2{}^2L^3}{3} + \frac{C_1C_4L^4}{2} - \frac{2C_1C_5L^5}{5} + \frac{2C_2C_4L^5}{5} - \frac{C_2C_5L^6}{3} + \frac{C_4{}^2L^7}{7} - \frac{C_4C_5L^8}{4} + \frac{C_5{}^2L^9}{9} \right)} \right)^{1/2}$$

Eq. 3.15

The natural frequency of the beam will change when V_0 and V_L are altered, due to the C_1 term on the bottom line of Eq. 3.15.

3.1.3 Forcing function

In order to evaluate the overall deflection of the beam in a realistic and useful way, it is necessary to introduce a forcing function which will simulate loading from traffic on the bridge. To calculate the overall deflection, Eqns 3.16 and 3.17 are used to determine the vibration amplitude.

$$V(x,t) = \alpha_{xh} F_0 \sin \Omega t \qquad \text{Eq. 3.16}$$

$$\alpha_{xh} = \frac{1}{\rho A Z} \sum_{r=1}^{\infty} \frac{\phi_r(h)\phi_r(x)}{\omega^2 - \Omega^2} \qquad \text{Eq. 3.17}$$

Then one calculates mode shapes from Eqns 3.18 and 3.19 below:

$$\phi_r(x) = \sin \pi \frac{x}{L}, \qquad \phi_r(h) = \sin \pi \frac{h}{L} \qquad \text{Eq. 3.18}$$

$$Z = \frac{L}{2} \qquad \text{Eq. 3.19}$$

Where Ω is the input frequency of the forcing function,

ω is the natural frequency of the beam as calculated from Rayleigh-Ritz,

x is the position of interest on the beam, and

h is the input position of the forcing frequency.

The first step is to calculate the mode shapes and then apply Eq. 3.17 to calculate the α_{xh} parameter. The value calculated for α_{xh} can then be substituted into the main equation, and the deflection due to vibration on a certain point of the beam can be calculated. Once the deflection due to the vibration has been determined, it can be added

to the deflection due to Eqns 3.1 to 3.8 calculated by using Euler-Bernoulli. It can be seen that the closer the value the input frequency is to the natural frequency, the greater the deflection of the beam.

3.1.4 Response values

Figure 3.1 shows typical displacement values obtained using the Rayleigh-Ritz method. The dashed line shown indicates the vibration deflection, *i.e.* how much the beam will deflect due to the input frequency forcing function and the solid line shown determines the value of V_{total}. V_{total} is simply V_{beam} and $V_{(x,t)}$ added together. The beam deflection values change when V_0 is varied as a result of the different natural frequency obtained.

The derived equations for the natural frequency of the beam were all inserted into an MS-Excel spreadsheet. This allows all of the variables, such as the input frequency and the end conditions, to be changed easily by altering the values in the spreadsheet cell. This simply means that the graphs can be generated instantaneously and a picture of the beam movement can be established without having to do separate calculations for each input frequency. Calculating the beam deflection for each 0.1 s time increment produces the graph shown in Figure 3.2.

3.2 Small-scale model

3.2.1 Material property definition

Before performing the modal analysis on the small-scale model, it was necessary to determine the material properties of all materials used in the model to input the data required by the FEA package to complete the analysis accurately. Of primary concern are the elastic properties of the Perspex® and the compression stiffness of the series of springs to be used as support conditions.

3.2.1.1 PMMA plate

Perspex®, or polymethylmethacrylate (PMMA), is a vinyl polymer made using the process known as free-radical (addition) vinyl polymerisation from the monomer methylmethacrylate. There are two manufacturing methods for PMMA, the extrusion method and the casting method. The PMMA plate used in the small-scale testing was produced using the extrusion method.

The most significant material property to define is Young's modulus of elasticity[3.5]. If the extension or compression in a member due to a load disappears on removal of the load, then the material is said to be elastic. Elastic materials obey Hooke's law[3.6], which shows that the strain is directly proportional to the applied stress as shown by Eq. 3.20.

$$E = \frac{\text{stress}}{\text{strain}} = \frac{\sigma}{\varepsilon} \qquad \text{Eq. 3.20}$$

However, in this particular instance, a four point bending test was required to determine the E value of the PMMA plate as the flexural E value is required in this case. To calculate this modulus, a series of five, four-point bending tests using a Lloyd

compression-testing machine were completed (Figure 3.3). Each specimen of PMMA used was 400 mm in length, 30 mm wide and nominally 10 mm thick. Load was applied at two locations situated 100 mm from the centre point of the sample, and the sample was supported at 50 mm in from each end. Each sample was then cycled through ten loading and unloading sequences, up to a maximum displacement of 11 mm, to determine if any hysteresis existed within the material, and to demonstrate the repeatability of the tests. Little hysteresis was evident whilst performing the tests and each sample returned, within a relatively close envelope, to the position it was in at the commencement of testing. Figure 3.4 shows an example of five cycles from test specimen number 1, note that the cycles are very close together with the exception of the initial loading curve.

Simple elastic beam bending theory to determine the E value, initially constructing the equation of the bending moments generated by the loading on the sample, is then performed.

$$M_x = P_x - P_{(x-0.05)} - P_{(x-0.25)} \qquad \text{Eq. 3.21}$$

Eq. 3.21 is then integrated once to determine the slope θ_x, and again to obtain the displacement Y_x.

$$\theta_x = \frac{1}{EI}\int M_x dx = \frac{1}{EI}\left(\frac{P_x^{\,2}}{2} - \frac{P_{(x-0.05)}^{\,2}}{2} - \frac{P_{(x-0.25)}^{\,2}}{2} + C\right) \qquad \text{Eq. 3.22}$$

$$Y_x = \int \theta_x dx = \frac{1}{EI}\left(\frac{P_x^{\,3}}{6} - \frac{P_{(x-0.05)}^{\,3}}{6} - \frac{P_{(x-0.25)}^{\,3}}{6} + Cx + D\right) \qquad \text{Eq. 3.23}$$

When $x = 0$, $Y_x = 0$ so that $D = 0$

Eq. 3.23 is then rearranged to calculate C. This value for C is then substituted into the following rearranged equation for E:

$$E = \frac{\frac{P_x^{\,3}}{6} + Cx}{Y_x I} \qquad \text{Eq. 3.24}$$

where P is the loading on the sample in N,

C is a constant that varies from sample to sample,

Y_x is the sample displacement directly under the applied load in m,

I is the second moment of area of the sample in m^4, see Eq. 3.25.

$$I = \frac{bd^3}{12} \qquad \text{Eq. 3.25}$$

where b is the width of the sample in m,

d is the depth of the sample in m.

Taking an average of the values calculated from the five tests, $E_{Bending}$ was taken as 3.15 GPa.

To determine the uniformity of the plate in terms of thickness, a series of 2600 ultrasound thickness measurements were taken over the entire plate using an EPOCH4 ultrasonic flow detector and a 2 MHz transducer coupled to the plate with glycerine. This data was downloaded to a PC and imported into a spreadsheet, then post-processed (see footnote on Table 3.9). In order to determine the thickness, the EPOCH4 requires

the wave speed (V_c) of compression wave through the material, which in this case is the PMMA plate. To establish the wave speed, Eq. 3.26 was used.

$$V_c = \sqrt{\frac{\left(1\times10^9 E(1-\nu)\right)}{\left(\rho(1+\nu)(1-2\nu)\right)}} \qquad \text{Eq. 3.26}$$

where ρ is the density (1194 kgm^{-3}),

ν is Poisson's ratio (0.34),

E is the Young's modulus (3.15 GPa).

Notice that to ascertain the wave speed in PMMA, it was essential to determine a value for Poisson's ratio[3.7]. Poisson's ratio can simply be described as a strain ratio and is the negative ratio of lateral strain against uniaxial strain, in axial loading. Its value can range from –1, for some sponges, to 0.5 for incompressible materials such as elastomers. Poisson's ratio is dimensionless although it does exhibit some stress and strain dependency.

$$\nu = -\frac{\varepsilon_1}{\varepsilon_3} \qquad \text{Eq. 3.27}$$

where ε_1 is the strain normal to loading,

ε_3 is the strain parallel to loading.

The Poisson's ratio of the PMMA was calculated by performing a tensile test using the Lloyd machine. A sample of PMMA (Figure 3.5) was placed into the rig and a rosette

of strain gauges were mounted on the sample to read strain in the required x and y direction. The rig outputs the data from the strain gauges in the form of a graph, whose values can then be imported into a spreadsheet. Using this data, the Poisson's ratio for the PMMA was found to be 0.34 ± 0.005.

The density, ρ, was calculated by performing an immersion weighing of five samples in water and in air, obtaining the volume of water displaced, then dividing the dry weight by the volume of water displaced. In this case the average value determined for the samples was 1194 kgm^{-3}. Conventional density measurement techniques would have been as simple and would have resulted also have given a value close to the manufacturers density of 1.15 to 1.19 kgm^{-3}. Substituting these values into Eq. 3.26, the wave speed in this particular blend of PMMA was 2027 ms^{-1}.

Inputting this value for wave speed into the EPOCH4, approximately 2600 thickness measurements were taken. Figure 3.6 shows the variation in thickness across the plate. The change of thickness in this case is not a particular concern, but can be used to explain any variation between the numerical solutions, such as FEA, and the experimental modal analysis. The plate was rotated regularly and stored horizontally to minimise the effects of creep. Between tests, the plate was covered to prevent ultraviolet radiation induced changes to E and ρ in particular. All tests were undertaken at temperatures between 19°C and 23°C and at 65 % relative humidity.

The parameters determined for the Perspex plate used for small scale modal analysis are, of course, not directly relatable to full scale bridges by simply multiplying the values obtained for frequency by a scaling factor. As a result, a dimensional analysis

technique called Buckingham Π Theorem was used to develop a series of equations using known parameters, such as ρ, E, ω, F, b and d. In this case, ρ, E and ω are taken as the core parameters that occur in each equation, and F, b, d and L are the remaining parameters. Equation 3.28 Shows the series of equations derived.

$$\frac{\omega^2 \rho F}{E^2} = \phi\left(\frac{\omega \rho^{\frac{1}{2}} b}{E^{\frac{1}{2}}}, \frac{\omega \rho^{\frac{1}{2}} d}{E^{\frac{1}{2}}}, \frac{\omega \rho^{\frac{1}{2}} L}{E^{\frac{1}{2}}}\right) \qquad \text{Eq. 3.28}$$

3.2.1.2 Springs

To vary the stiffness of support offered to the plate it was necessary to manufacture a series of five springs, from Industrial Springs Ltd, each with its own particular stiffness. Each spring was 38 mm in diameter and 90 mm in length, but each set of springs has a different nominal diameter of wire; 2 mm, 2.5 mm, 3 mm, 3.5 mm and 4 mm (see Figure 3.7). The stiffness of each spring was determined through a series of cyclic compression tests, as with the evaluation of E_{Bending} for the Perspex plate. To determine the repeatability, and reproducibility, of the compression testing, three springs from each stiffness set were tested. In this series of tests, with the machine loading heads parallel to the machined ends of the springs, each spring was subjected to a load sufficient to induce a 30 mm displacement. Twenty loading and unloading cycles were performed to determine what hysteresis, if any, there was in the material. Figure 3.9 shows the linearity of the material, which exhibits little deviation in stiffness, or hysteresis, from cycle to cycle. The springs were held in place by two specifically machined plastic holders, Figure 3.7, which were machined slightly larger than the diameter of the springs but still tight enough to stop slippage, and to resist any lateral movement induced by loading of the springs.

The range of stiffness values obtained are shown in Tables 3.1 and 3.2. The values shown in the final two columns of Table 3.1 relate to an additional series of tests performed on the same sets of springs. Observing the sag of the Perspex plate when supported by a set of springs, it became apparent that the springs would never be in an idealised state where the springs were parallel to the plate. As a result, a series of tests where the machine platens are loaded onto the spring holders as before, but to mimic the effect of the plate curvature, wedges of various thicknesses were inserted below the lower holder. From inspection, the maximum displacement of the plate at its centre point was taken as 22 mm; therefore, the worst possible case scenario would be an angle of approximately 2° for this span of plate. Figure 3.8 shows a range of rotations versus displacement at midspan.

To test the ability of the springs to function within acceptable parameters, two angles of 10° and 20° were imparted onto two separate spring samples. The resulting data indicated that, although there is a large reduction in stiffness at 20°, the springs will never be subjected to a rotation of this magnitude during any of the tests. The reduction in stiffness at 10° is, on average, only 5 % to 10 %, although again it should be noted that the springs would never be subjected to rotations of this magnitude. Values for all stiffness tests are shown in Table 3.4.

3.2.2 Method

Small-scale modelling in structural analysis is normally used with a view to determining how a scaled down version of a structure reacts to either a type of prescribed loading, such as an impact load or a moving load on the structure, or environmental effects, such as temperature, wind loading or in the case of bridges traversing a river, scour caused at

pier bases by river currents. In this particular case, of most interest was the effect of changing the support conditions and the effect such changes had on the dynamic response of the structure. It should be noted that the plate model used is not intended to simulate an actual bridge deck in any way, but should merely be viewed as method of facilitating valid response spectra using modal analysis techniques by using establishing a series of base readings with the plate constrained at its edges in more a conventional manner. The end conditions were then altered, and the analysis with the variable support conditions was completed and compared.

3.2.2.1 Free-free support

Initially, to establish a baseline series of readings to be used in order to validate the FEA used, the simplest type of support condition of a freely suspended plate, in effect having no support, was tested. In reality, arranging a set-up with no support is virtually impossible as, even if supported by wires, some portion of the plate must be in contact with a wire. To try and simulate this set-up as best possible, an arrangement whereby the plate was suspended on four wires from each corner, shown in Figure 3.10, was constructed. The wires were attached to a frame, independent of the suspended plate, by a guitar tuner, as shown in Figure 3.11. Using the guitar tuners allowed the length of each wire to be altered until the plate was level to a tolerance of 0.5 mm per m length (0.7 mm over 1.4 m, which results in $\theta = \tan^{-1}(0.7\,\text{mm}/1400\,\text{mm}) = 0.029°$). To dampen out any extraneous vibrations that could be imparted upon the plate by equipment located in the heavy structures laboratory where the testing was completed, a foam-like material called Sylomer® was placed between the floor and the frame. A Sylomer® section was also placed between the plate holding the guitar tuners in place and the frame, as well as on the end of the wires, pressing against the underside of the

plate. The reason for using the Sylomer® in such a way was to reduce the possibility of scratches occurring from the wire, and to try and reduce any external vibrations. The wires were prevented from coming back through the hole in the plate using an arrangement similar to that used on a bicycle breaking system. The wire is passed through a bolt with a hole drilled through it. The wire is then bent over, and passed back through the hole and then clamped in place using a nut, shown as a callout in Figure 3.11.

3.2.2.2 Fixed supports

The second arrangement in the baseline readings was a fully fixed arrangement. This arrangement is a common one in structural engineering, where many bridges are described as having fixed supports. A fixed support will not allow any rotation or translation in the x and y directions, therefore resisting moments. In reality, this type of arrangement, as with the freely suspended set-up, is very difficult to achieve as some rotation will inevitably be allowed by the support. This rotation can be ignored, as it is relatively small in most cases.

Using the same frame as used previously for the freely suspended tests, the PMMA plate was clamped between two sections of timber at either end (Figure 3.12). The timber sections were clamped together using two lengths of screwed rod located either side of the extremities of the plate, with a locking nut at one end of the rod, then tightened with a nut until the plate was secured. Once the plate was clamped between the timber sections, these were then attached to the frame by another section of timber, two for each end of the plate. This section had two pieces of timber with four sections of threaded rod holding the timber sections together, shown in closer detail in Figure

3.12. To reduce the vibrations transmitted through the steel frame, Sylomer® sections were placed either side of the steel frame, between one side of the timber, plate clamp, and one of the two pieces of timber used to hold the plate in place. Sylomer® sections were also placed between the other piece of timber used to hold the plate in place, and the timber clamp. Having this particular arrangement of clamps facilitated easier manipulation of plate location, allowing the plate to be levelled more accurately.

3.2.2.3 Simply supported pin joints

The final arrangement for the initial base readings was a simply supported arrangement. A simple support allows rotation in one direction, usually about the x-axis, but will not allow translation in the x or y directions. Many joints are assumed to be pinned, even though in some cases they do resist moments, because the actual value of the moment is insignificant. To simulate a simple support, two sections of steel tubing were placed underneath the PMMA plate at either end, thus allowing the plate to rotate about those points in the x-axis (Figure 3.13).

3.2.2.4 Springs

Once the initial testing had been completed, a series of variable support conditions were investigated. To facilitate easy alteration of the support conditions by changing the springs, a set-up similar to the one used for the fully fixed arrangement was employed.

Initially, the lower section of the arrangement was secured to the steel frame in the same manner as used in the fully-fixed arrangement. However; in this case, the piece of timber used to hold the plate was shallower and had an attachment made from plastic fastened to it, as shown in Figure 3.14. This piece of plastic, the same length as the

width of the plate, 800 mm long by 50 mm wide, had eight holes, each of 38 mm diameter, along its length. The centres of the first and last holes were located 50 mm in from either end, with each subsequent hole located at 100 mm centres therein. Care was then taken to ensure that the two sections were level with each other, and then sixteen springs, eight at either end, were placed in the holes. An identical plastic section was secured to the plate, both top and bottom, and the plate was then carefully placed on to the springs. Once the plate was in place, sixteen more springs, again eight at either end of the plate, were placed into the plastic holding section on the top surface of the plate. The arrangement was completed by placing the second timber section, with plastic holding section as before, on to the springs. The timber section was secured to the steel frame, imparting a small compressive force on the springs, as in the fully-fixed arrangement.

As the springs are all of a uniform length and diameter, only the diameter of the wire differs, once the arrangement has been set up, the springs can simply be changed over without having to remove the wooden holding sections.

3.2.3 Natural frequency analysis

Modal analysis is the process of experimentally determining the modal parameters of a structure, such as vibration mode shape and material damping. There are two methods of modal analysis, the classical method and the operational modal analysis method. The classical method is when the structure being tested is stimulated by a known force, usually an impact hammer or mass shaker, and the response to this force is determined using a fast Fourier transform (FFT) analyser.

To determine the modal parameters, several methods can be employed; a roving hammer test, a roving accelerometer test, a swept sine test or a pseudo-random excitation test with a mass shaker. In this instance for the baseline tests on the plate, a roving hammer test was carried out on each arrangement. A roving hammer test, described in this case as a single input-multiple output test (SIMO), is when several accelerometers are fixed to the plate and are not moved during the tests. To maintain consistency throughout the series of tests performed, the accelerometers were left *in situ* on the plate, and not removed, to eliminate the possibility of modal shift which can be caused by adding mass to different sections of the plate. With the accelerometers fixed in place, the force hammer was used to excite the plate in several different locations, down a line of points taken over the whole length of the plate. Moving the hammer to different locations, in this case down two lines of points in the longitudinal and transverse directions, will excite all of the modes the plate is capable of producing. Figure 3.15 shows the grid of points relating to all future results presented. Using the FFT analyser (Figure 3.16) the imaginary part of a series of frequency response functions (FRFs) can be taken after each excitation of the plate and displayed as a waterfall plot graph. The imaginary part of the spectrum displays the direction of the vibration rather than the actual value of vibration, which is shown in the magnitude graph that combines the real and imaginary parts of the spectrum. This allows the mode shapes at each resonant frequency, in both longitudinal and transverse directions, to be displayed by taking a slice through the waterfall plot at the desired frequency.

When performing a modal analysis, it is standard practice to view the coherence function when displaying the FRF of a signal. Coherence is a number between zero and one, and is a measure of the degree of linearity between two related signals such as the

input force of a structure related to the vibration response to that force. In a frequency response measurement of a mechanical structure, if the structure is linear, the coherence will be one, but if there is some non-linearity in the structure, or if there is noise in a measurement channel, the coherence will be less than one. The multi-channel FFT analyzer is able to measure the coherence between channels. Coherence is a useful tool in determining good from noisy or meaningless data.

In the case of the mobility measurements taken on the plate using the roving hammer test, only one exponential average hammer strike *per* recorded measurement was captured. As a result, the coherence is one over the whole frequency range. To show the linearity of the material, and the quality of measurements taken, a separate set of tests in each arrangement were completed. Five points located on the line of points used during the roving hammer test were excited in turn.

A single measurement with the hammer set up in the exponential averaging mode was taken, as in the roving hammer test, to act as a baseline for the subsequent readings. A total of ten linear averages were taken for each measurement point, recording each of the accelerometer's FRF and coherence functions. The results in Figures 3.17 and 3.18 showed that the material was not susceptible to hysteresis, and the signals imparted upon the plate can be assumed to be good as the coherence function graph is at a constantly high value throughout. Any drop in the coherence function graph can be explained as noise or signal leakage in the measurements.

It should, however, be noted that due to certain material properties of the PMMA which have resulted in high modal coupling, it is often problematic to identify the actual peaks

that correspond to natural frequencies of the plate for any given arrangement. This also results in difficulty obtaining accurate damping ratios for each frequency. To identify the value of each resonant frequency of the plate, the autospectrum graphs generated for each accelerometer were used as a reference. By curve fitting the autospectra, each frequency can be identified clearly, and then a slice at this frequency can be taken through the waterfall plot of FRFs taken for the same reading.

The accelerometer type used for this modal analysis was a Type 4508-B DeltaTron transducer electronic data sheet (TEDS) accelerometer[3.8] (see Figure 3.19). This type of accelerometer is specifically designed to withstand the harsh environment of the automotive industry, and as a result, should be more than adequate for this set of tests. The 4508-B is a ThetaShear accelerometer coupled with a DeltaTron preamplifier within a lightweight titanium housing. The shear accelerometer works by having a central seismic mass flanked by two piezoelectric plates. This assembly is then clamped together with a titanium ring, meaning the parts are held firmly together without the use of any bonding agent, solely relying on frictional forces. This assembly is then hermetically sealed within the titanium shell. An exploded schematic diagram of this type of accelerometer is shown in Figure 3.20. The DeltaTron accelerometer removes the requirement for an external charge amplifier to boost the signal in the accelerometer, and also removes the requirement for expensive cables. The TEDS allow the inherent parameters of the accelerometer to be detected automatically by the PULSE system, effectively making the transducer a "plug and play" device.

Care must be taken when attaching the accelerometers to the plate. Placing the accelerometers at locations which are considered to be node points will result in various

frequencies not being detected. As a result, several measurement points are chosen to reduce the likelihood of such an occurrence.

Placing accelerometers on to a surface can result in the modal parameters of the structure, in this case the PMMA plate, being altered[3.9]. Adding the extra mass of the accelerometers can result in modal shift, meaning the vibration modes occur at slightly different frequencies than would otherwise be the case. However; this phenomenon only occurs when the mass of the accelerometer is significantly large as a proportion of the mass of the plate. Typically, the accelerometer used should not be more that one tenth of the mass of the structure. In this case, the mass of the Perspex plate is 13 kg and the mass of the accelerometers used is only 0.004 kg, so each accelerometer added 0.03 % mass.

In addition to modal shift, consideration should also be given to phase deviation between accelerometers and base strain sensitivity. To remove the possibility of phase deviation, an accelerometer with no phase shift within the frequency range of interest should be selected. Direct current (DC) coupled designs are the best choice in this particular case. The type chosen for the tests is a constant current line drive (CCLD) accelerometer, which has no phase deviation. Base strain occurs when the structure being excited imparts a force onto the accelerometer due to the structure's movement during vibration. Base strain sensitivity can be reduced by using an accelerometer with a thick base, or by using a DeltaShear accelerometer such as the 4508-B, as the internal elements are not connected directly to the base.

The impact hammer used for the initial modal parameter testing was an 8202 hammer, incorporating a type 8200 force transducer. The type 8200 transducer is a piezoelectric transducer, as the accelerometers are, but produces the outputs in a different manner. In the force transducer, forces are focused directly onto the piezoelectric elements, squeezing the element thus generating a charge across the element. This charge was then converted to a force in the same manner as the charge was converted to an acceleration in an accelerometer.

The type of hammer initially used for the experiments is an old piece of equipment designed to be used with a dual channel analyser, type 2034. The transducer requires an external charge amplifier, or pre-amplifier, in order to function. The pre-amplifier available was not compatible with the PULSE system. As a result, the charge amplifier type 2635 was used whilst a new hammer was obtained. A major difficulty with using the 2635 amplifier is that it introduces another possible error to the readings. Initial tests showed that the transducer was producing a noisy signal on the analyser display. This problem was remedied by altering the sensitivity and upper frequency bounds on the charge amplifier, and by windowing the data in the time domain to remove any noise either side of the signal. Another difficulty using the hammer with a charge amplifier is that it inverts the signal from the transducer by 180°. As a result, when setting up a trigger for the measurements using the initial hammer strike, the slope of the hammer must be set to a negative slope, otherwise the incorrect starting point of the measurement will be detected.

After completing the initial testing in the four baseline reading arrangements, a new hammer, fully compatible with the analyser was obtained. As a result, it was decided to

redo the original testing with the new impact hammer, Type 2302-10. Figure 3.201shows a diagram of the hammer and Figure 3.22 shows how the hammer is connected to the analyser, bypassing the need for a signal conditioner. As with the previous hammer, the 2302-10 comes with three different tip materials; rubber, plastic and steel. Each tip excites a different range of frequencies (Figure 3.23) and after several trial runs with the different hammer tips, the plastic tip was chosen for the testing as it resulted in the cleanest response spectra.

Having the new hammer resulted in the time taken to perform the tests being reduced dramatically. Instead of having to activate each measurement manually, triggering the measurements with the hammer became possible. This meant that the analyser could be set up to record each individual hammer strike above a certain trigger level making the measurement clearer with a much higher coherence value. Average coherence improved from 0.90 to 0.98. The window used from this set of tests was the rectangular window, for both the output and input channels. This window was chosen as it is a general-purpose window and gives clean responses in relatively noise-free environments. Most impact hammer testing tends to be performed using exponential and transient windows[3.10].

3.2.4 Forced vibrations

After determining the modal parameters of the plate using the impact hammer test, the next stage of testing was to determine the effect of varying stiffness of support conditions on the propagation of waves across the plate.

The PULSE system contains a generator output in one of the modules located in the front end. The generator function can then be used to power a mass shaker, which is attached to the plate. The generator function, once activated in the analyser software, can generate a wide range of signal types to power the mass shaker, or whichever type of device is attached. The signals the generator can produce are: a single fixed sine (either continuous or burst), a single swept sine wave, a dual fixed sine, a dual swept sine, a fixed sine plus swept sine, a stepped sine wave, a multi-sine wave, a random excitation (again continuous or burst), a pseudo-random excitation, a pulse excitation, a periodic random, and a user-defined excitation.

3.2.4.1 Sinusoidal harmonic loading

The main purpose of the forced vibration testing is to determine what effect, if any, the variation in support stiffness has on vibration amplitude. To test this theory, a single sinusoidal loading generated by the analyser was forced into the plate at five separate locations. The points chosen to excite the plate were five of those used in the roving hammer test, with the accelerometer locations remaining consistent with earlier tests. A second set of points, all located at the centre point of the plate, were chosen after analysis of the results obtained from the primary set of tests.

Each of the five location points was excited at each of the natural frequencies obtained through the impact hammer testing for each of the five spring arrangements, as well as one common frequency, in this case 39.1 Hz, which is not considered a resonance in any of the test arrangements.

To force the vibrations into the plate successfully, the mass shaker must be securely attached to the plate. Most shakers are attached to objects using a "stinger" which is simply a metal rod, or piece of wire, which is then attached to the plate through a force transducer. The force transducer is then either glued or cemented on to the structure. However, in this case a force transducer is not required as the mode shapes have already been determined using the impact hammer testing. Therefore, a bolt of 60 mm in length was screwed into the mass shaker and then stuck to the underside of the PMMA plate with a small portion of beeswax at every excitation point (Figure 3.24). A nominal precompression was applied and manually tested to ensure continuity of contact between stinger and plate, therefore eliminating the possibility of chatter.

To test the ability of the arrangement to transmit vibrations into the plate, two accelerometers were used, one on the diaphragm of the mass shaker and the other on the plate directly above the bolt. Results indicated that although there was an average 10 % decrease in magnitude, the values were sufficiently close to assume that there was no problem with transmission. The Hann[3.11] window is used in this case as it is applicable to continuous or random excitation signals as it reduces the noise in the spectrum at the beginning and end of the recorded data.

3.3 Finite element analysis

FEA is a well-known and well-understood method of engineering analysis of complex structures. To investigate further changes in support stiffness for plate vibrations, an FEA model has been constructed using a commercially available package. Initially, the FEA is used to predict the response of the PMMA plate in the laboratory for all the test arrangements used in the modal analysis section of the research.

The model generated for the analysis was a simple plate. To construct the model, there are several steps to perform. To begin with, the structure geometry must be established and entered into the model. Each individual point's coordinates are entered, then the points are linked together in turn by selecting the points to be joined, then selecting the line drawing command. Figure 3.25 shows the completed geometry and mesh refinement used for all FEA simulations.

Once the structure's geometrical shape is outlined it is necessary to generate surfaces to be analysed. Each line that is to make up the boundary of the surface is selected in turn, then the surface drawing command is utilised, and the surface generated.

Once the geometry properties are completed, the next step is to assign the model attributes. The first attribute to define is the mesh definition. A mesh can be defined for a point, line, surface or volume, but in this case, a mesh for a line and surface are defined. The line mesh simply indicates how refined the mesh is, depending on how many divisions are defined within that mesh, but it can be used to model beams or bars. The surface mesh is defined by selecting the element type from a menu, in this case a thin plate element, as well as the element shape, either quadrilateral or triangular, and the interpolation order, either linear or quadratic, are assigned in a similar manner. In this menu it is also possible to change the meshing pattern between regular and irregular meshing. As the model is a simple rectangle, the meshing pattern was left as the default regular pattern. After defining the surface mesh, the surface thickness is assigned by selecting the geometric properties menu, then the surface section. For each of the model tests the plate thickness was 10 mm.

Assigning the material properties to the model was done through the materials section of the attributes menu. In this menu there were several sections that can be chosen to input the material properties of the model, such as a general materials library in which materials such as concrete and mild steel are located, isotropic material sets can be generated as well as orthotropic and anisotropic material definitions. The PMMA used for the model plate is considered to be isotropic. Selecting the isotropic material tab in the menu allows various parameters to be entered into the model, such as elastic, plastic, creep and damage properties. For this model, only the elastic properties have been entered as the plate is not taken to the plastic limit during the testing regime. The flexural Young's modulus (3.15 GPa), Poisson's ratio (0.34) and the mass density (1194 kgm^{-3}) determined through the materials testing were entered for all models.

The final section of model definition is the support conditions. The FEA package comes with the most common support conditions pre-programmed into the model templates, such as pinned supports, fully fixed and a range of degrees of fixity in the x, y and z directions, with respect to translation and rotation. In addition to the pre-programmed support conditions it is possible to define conditions using the attributes menu, selecting the support tab, and then selecting the structural tab. Within this menu the various degrees of movement can be defined by selecting the required tab. There are three degrees of fixity that can be selected, free, fully fixed and spring stiffness, which allows the spring stiffness to be entered in either absolute stiffness, stiffness *per* unit length or stiffness *per* unit area.

The initial set of tests carried out in the laboratory had the plate effectively freely suspended on wires. To imitate this circumstance in the support conditions in the model,

all of the tabs were set to free with the exception of translation in the z direction, which was set to fixed to prevent rigid body movement under load.

Similarly, the second set of tests were carried out with the plate in a simply supported arrangement, where all the tabs are set to fixed with the exception of rotation about the y axis. The final test in the initial baseline readings was an arrangement with a fully fixed support condition, with no translation or rotation allowed at the edge of the plate.

To imitate the spring support conditions, each stiffness *per* unit length was entered into the model parameters and assigned to a node point at the exact location of the centre point of each spring on the actual plate.

Initial FE testing was intended to determine the natural frequencies of the plate in the various support conditions. This particular type of analysis is known as an eigenvalue analysis, where eigenvalues are the roots of the equations of the matrices generated in the FEA. The eigenvalue analysis output gives the eigenvector, the frequency in hertz and the error normalisation. The solution is completed by calculating error estimates on the precision with which the eigenvalues and eigenvectors have been evaluated, and normalising the eigenvectors according to a user-specified criterion. The computer package is capable of displaying the mode shapes for each frequency determined in the analysis. However, it should be noted that absolute displacement is not available from any eigenvalue analysis, and as a result the mode shapes shown are un-scaled mode shapes that accurately represent the deformations, but do not quantitatively define the displacements as there is no forcing function or load from which to derive the required information.

It is necessary to complete an eigenvalue analysis in order to force a sinusoidal loading in to the model, and simulate the testing completed using the mass shaker in the laboratory testing.

The type of element chosen for the model is an 8 noded quadratic isoparametric thin plate element with 2×2 Gaussian quadrature within the software package. The bending properties of a plate depend on its thickness as compared to its other dimensions. In the case of the PMMA plate used for the model presented, it was considered to be thin with a small deflection. It was possible to make several assumptions when developing the analytical model;

1. There was no deformation in the middle plane of the plate. This plane remains neutral during bending.
2. Points of the plate lying initially on a normal-to-the-middle surface of the plate remain on the normal-to-the-middle surface of the plate after bending.
3. The normal stresses in a direction transverse to the plate can be disregarded[3.12].

The element is therefore formed by applying Kirchhoff constraints to elements formulated using Mindlin[3.13] plate theory. Kirchhoff theory[3.14], in recognition of Kirchhoff's research on plate theory in 1850, excludes transverse shearing effects which are included in Mindlin theory, also known as Mindlin-Reissner[3.15] theory. Transverse shear becomes negligible in a plate whose span is much greater than its thickness. Both theories provide a model that can be solved using FEA, and in both models normal stress in the thickness direction is taken to be zero. The FEA package formulates the Mindlin plates using general isoparametric elements, elements where the two shape

function matrices are identical, then applies the Kirchhoff constraints to exclude the transverse shearing strains by forcing them to zero value at discrete locations in the element[3.16].

The evaluation of stresses and strains are determined using 2×2 Gaussian quadrature, as these are generally more accurate than the nodal values. The nodal values are then determined using a procedure known as nodal extrapolation from the Gauss points. A fictitious element with nodes at the element Gauss points is defined, and the stresses and strains are then extrapolated out to the nodal points of the real element by using the shape functions of the fictitious element[3.13].

3.3.1 Forced vibration testing

To validate the modal analysis testing of the plate, the FE method was used to simulate a forced vibration of the plate. Once the eigenvalue analysis had been performed on the model and the natural frequencies recorded, a transient analysis was performed. The transient analysis was set up by selecting the model properties from the file menu, then selecting the solution tab on the next menu. In the solution tab the box marked "Load Curve" is selected, and set to a transient problem. Selecting the "set control" button then allows the type of transient analysis to be determined, and in this case a dynamic analysis is selected. The various parameters such as the initial time step, the overall analysis time and the number of increments *per* analysis are then defined. For the analysis performed on the plate, a time step of 0.002 s was chosen, and the overall analysis record time was determined by the frequency of forcing function to allow at least one full cycle of vibration to be completed.

After completing the initial transient set-up, the type of waveform to be forced into the model, the peak value, frequency and the phase offset were all determined in the loadcase parameter section. For each test the forcing function was a sine wave with a peak value of one and an offset value of zero. The only parameter that changed was the input frequency, which was the natural frequency value recorded from the eigenvalue analysis for each arrangement.

3.4 Results

3.4.1 Euler-Bernoulli analysis

The results from the Euler-Bernoulli method adopted for plate analysis are shown in Tables 3.3 and 3.4. All input variables used in the method are shown in Table 3.5, and the material and geometric properties used are shown in Table 3.6. Figures 3.26 and 3.27 show the effect of support stiffness and loading on the fundamental resonance frequency. The range of values shown for stiffness relate to the values obtained for the springs used in the modal analysis, from the stiffest at 15.6 Nmm^{-1} to 1.22 Nmm^{-1}. Also included are values relating to infinite support stiffness, where the displacement was assumed to be zero.

3.4.2 Small-scale model

3.4.2.1 Experimental modal analysis

Figures 3.28 to 3.35 show the resonance frequency outputs from the laboratory modal analysis carried out on the PMMA plate. Figures 3.28 to 3.30 are the baseline readings taken for the plate in more conventional support conditions; free, simply supported and fully fixed. These figures show the response at three locations, shown in Table 3.7 and Figure 3.15, in both the longitudinal and transverse directions. The purpose of this was to allow the mode shapes to be determined in three dimensions, thus making it clearer as to the alterations in plate behaviour with varying support conditions. Figures 3.31 to 3.35 are the waterfall plots for spring support stiffnesses 1 to 5. These figures show the effect of altering support stiffness on the resonant frequencies, where the resonant frequencies become more evenly spread as stiffness of support increases. The resonant frequency values are shown in Table 3.8 for each experimental set-up used. It should be noted that in the higher range of frequencies shown in Table 3.8, the modal analysis

missed several frequencies. In this case, the first three modes were considered to be the most important, and as a result, only the first three modes were considered when making comparisons between data. The first three modes generally tended to contain the most energy, and would be considered to be the most important from a structural engineering viewpoint in any case. Figure 3.36 shows mode shapes, both transverse and longitudinal, for the various support conditions in spring support configuration 1. This figure shows that the first mode was a bending mode; the second mode was torsional: and the third mode was bending. The higher modes were generally a combination of bending and torsion. These modes tended not to have the same energy as the lower modes (3.3×10^{-8} J at 240 Hz compared to 5.0×10^{-6} J at 5.63 Hz), and result in infinitesimally small displacements (47.1 nm compared to 24.9 μm). As a result, only data for the first mode was considered in the analysis. The energy required to excite the higher modes in a full-scale structure to a destructive degree would be unlikely to occur. This logically follows as a corollary to the fact that they contained less energy in the first place. Other methods of representing data in plane and vector space exist. Van der Pol and Poincaré plots derived using a Java applet are presented in Figures 3.67 to 3.74. Figure 3.67 shows the expected result for the Perspex plate, as lateral displacement is assumed to be zero times the vertical displacement. Figures 3.68 to 3.70 illustrate the effect of increasing the lateral displacement relative to the vertical displacement. Data obtained through testing of the plate could not be used to derive either type of graph as only data in two dimensions, x and t, were recorded. Analysis of the data by integrating the data obtained and using the Van der Pol equation, indicated that the system is not a Van der Pol oscillator as the right hand side of the equation, Eq. 3.29, did not equal zero at any time step. The Van der Pol oscillator (named for Dutch physicist Balthasar van der Pol) is a type of non-conservative oscillator with nonlinear damping.

It evolves in time according to the second order differential equation shown in equation 3.29 below.

$$\frac{dx^2}{d^2y} - \mu\left(1 - x^2\right)\frac{dx}{dy} + x = 0 \qquad \text{Eq. 3.29}$$

where x is the position coordinate — which is a function of the time t, and μ is a scalar parameter indicating the strength of the nonlinear damping that affects how non-linear the system is. For μ equal to zero, the system is actually just a linear oscillator.

Taking a slice through the x axis of a Van der Pol plot produces a Poincaré map. In mathematics, particularly in dynamical systems, a Poincaré map is the intersection of a trajectory which moves periodically (or quasi-periodically, or chaotically), in a space of at least three dimensions, *x*, *y* and *t*, with a transversal hypersurface of one fewer dimension. More precisely, one considers a trajectory with initial conditions on the hyperplane and observes the point at which this trajectory returns to the hyperplane. The Poincaré map refers to the map of points in the hyperplane induced by the intersections. These are shown in Figures 3.71 to 3.74.

Figures 3.37 to 3.44 present data obtained from the forced vibration testing. Figure 3.37 shows the effect of support condition at the three accelerometer points for the first modeshape at each of the five forced vibration input locations. Figures 3.38 to 3.44 show the response at the plate mid-span due to forced vibration at the five excitation locations for each spring stiffness in terms of velocity, displacement and acceleration. The data presented are not the absolute values of acceleration, but a ratio of output to input acceleration. The data is presented this way as the force generated by the mass shaker was not consistent, especially as the frequency altered for each spring within

each modeshape boundary. This method of presenting data allows comparison between data obtained for the same mode shape with different frequency values.

3.4.2.2 Finite element analysis

The FEA performed on the small-scale model yielded the eigenvalue analysis which determined all of the possible resonant frequencies for the plate. Figures 3.45 to 3.47 show the three dimensional mode shapes obtained for initial, baseline, boundary conditions for the first three modes. Figures 3.48 to 3.52 show the mode shapes obtained with the variable spring support conditions. Resonant frequency values obtained from the FEA are shown in Table 3.9. The input variables used for the FEA were previously shown in Table 3.6.

In addition to the eigenvalue analysis, the results obtained from forced vibration loading are also presented. Figure 3.53 shows the effect of support condition on vertical displacement for the first mode shape at all five forced vibration input locations. Figure 3.54 shows the effect of support condition on vertical and rotational displacements for the first mode shape displacements for the first mode shape at forced vibration input location point 4. Figures 3.55 and 3.56 show the acceleration and displacement response at node point 18. Figures 3.57 to 3.61 show the displacement contour plots of the plate in each of the five spring stiffness configurations in the first mode of vibration. These figures also show the location of maximum and minimum displacements.

The stress response of the plate at each of the support nodes, with variable end conditions for the excitation loading points is also considered, and the results obtained are shown in Figure 3.62. This figure shows strain about the y-axis for node point 18 in

contour plot form and graphical representation. Figure 3.63 shows the maximum bending strain response at node 18 for each support stiffness value at input location 4. Figure 3.64 shows the results obtained from a parametric study on the plate model and Figures 3.65 to 3.66 compare the values obtained by modal analysis with those from FEA for frequency and displacement (see footnote on Table 3.9 for effect of variation in thickness).

3.5 Discussion

The initial simple Euler-Bernoulli method for beams has been adapted for use with plates having variable end conditions. The main aim of this method was to provide a simple method of analysis when component geometry is in its infancy, before more complex designs are done, to indicate the primary resonance frequency. Allowing either end to displace by a value proportional to the stiffness of the support means this method can be used to simulate the effects of degradation in bearings. The method outlined allows either end of the plate to be altered independently, meaning the degree of support can be altered separately.

The results showed that an alteration in the support stiffness can have a marked effect on the resonant frequency of the plate. Using the stiffness values obtained for the springs in the model yielded results which, when compared to the modal and FEA results, underestimated the recorded values of resonance frequency. However, the method was not intended to provide the exact numerical answer, merely a general baseline frequency for use in calculations. The apparent underestimation need not be a problem, thereby building in a factor of safety as far as design calculations are concerned.

The major weakness in the method outlined was that it only takes the first mode of vibration into consideration, whereas in reality there will be more than one mode. However, the first mode of vibration was generally the worst case, providing the largest amplitude oscillations and stresses on the plate. Further adaptation of the method could yield further frequencies if the assumed plate mode shapes were altered. The method could also be modified to take more conventional support conditions into consideration at one end of the plate, leaving the other end supported on the spring. This would further mimic actual bridge structures, many of which are not supported by elastomeric pads at each end. The method could also be modified to take rotational and transverse restraint into consideration. Increasing the complexity of the model, and therefore calculations, may result in a more accurate answer.

Determining the modal parameters of the plate using the impact hammer test provides the first indication of the effect of variable support conditions on the plate response. Figures 3.31 to 3.35 showed a gradual alteration of spacing between frequency peaks as the support stiffness increases. The spacing became more regular over the frequency range shown, with some frequencies at the higher end of the range in spring 5 configuration, disappearing from the graph altogether. This was shown in the data presented in Table 3.9, where the final two columns contained no data relating to specific mode shapes.

The forced vibration testing results shown in Figure 3.37 indicated that an increase in support stiffness affected the dissipation of each vibration as it traversed the plate. Each point on the graphs indicated the plate's response at the given accelerometer location. Each graph for the individual input points for the forced vibration show the same trends,

with differences between the values depending on input location ranging from -25 to +13 %. However, as the frequency was altered to become the natural frequency for the plate in each arrangement, the measurement is effectively reset with the new frequency resulting in a new base reading being set. This made it impossible to compare sets of data obtained for each mode-shape recorded as the frequencies changed from set-up to set-up. Therefore, the ratio of output response to input excitation was recorded and used as the diagnostic tool, whether that is in terms of acceleration, velocity or displacement.

The purpose of deliberately inputting the natural frequencies as a forced vibration spectrum for the plate was to find which mode shapes were most affected by the prescribed changes in support stiffness. What became apparent was that the bending modes were affected in a more recognisable way.

The data in Figures 3.38 to 3.44 were those obtained for the first resonance frequency at each excitation location for each spring stiffness. The figures indicated that as the stiffness increased, the acceleration, velocity and displacement level recorded change at the centre point of the plate. However, the velocity plot did not follow the expected pattern as values for springs 2 and 3 are considered to be in the wrong order. The values obtained for spring 3 in Figure 3.41 would appear to be erroneous, removing (or indeed negating) velocity as a means of identification for bearing stiffness. Acceleration and displacement plots shown in Figures 3.38 to 3.40 and 3.42 to 3.44 indicated that either would have been an appropriate method of detection of change in support stiffness. What was interesting from these plots was the apparent effect of forcing the vibration in at the plate edges compared to at the mid-span. In fact, the order in which the springs occurred was reversed in this case, with one point of interest being the apparent location

where each spring exhibited the exact same response, located between points 7 and 14 and points 14 and 17. The results suggested that as the springs became stiffer (springs 4 and 5) the support conditions tended towards being simply supported. This was confirmed by the values of resonant frequency shown in Table 3.8.

FEA results indicated that all possible mode shapes have not been detected by the modal analysis method. However, the first three modes were the same, and were identical mode shapes to those in the modal analysis, shown in Figures 3.48 to 3.52. The frequency values obtained and presented in Table 3.9 are lower than the experimental values obtained, ranging between 20 % to 30 % from spring 1 to spring 5. This was not considered to be of great significance, as it was the mode shapes and method of detection rather than the absolute values of frequency that are being considered here.

A parametric study, in which the values of Young's modulus, density and Poisson's ratio were reduced by half of their original value, indicated that a change in density would significantly alter the frequency values obtained, for reference: $\frac{\partial f}{\partial E} = -9\,\%, \frac{\partial f}{\partial \rho} = +14\,\%, \frac{\partial f}{\partial \nu} = +77\,\%$.

Initially, data were obtained for strains, acceleration, velocity and displacement at node point 18, shown in Figures 3.53 to 3.56. Analysis of these data allowed the selection of displacement as the method of detection for a change in support stiffness. The strain values in Figure 3.62 and 3.63, and therefore stresses, in the plate at the node points did not provide a clear pattern with which to determine overall response of the plate. In each case, in terms of bending strains in the x, y and xy directions, maximum and minimum

principal bending strain (σ_1 and σ_3), the maximum bending strain, and the equivalent bending strain for node point 18 were notably the same values for each spring configuration. The acceleration response of the node points was unclear and although a pattern did exist, it was problematic to separate the information within Figure 3.61. The displacement values were shown for the vertical and rotational directions. In this case, as the point of interest was the effect of support stiffness, greater importance was placed upon the vertical response as although rotations will occur, bearings are designed to allow a certain amount of rotation. What the response from the FEA showed was the rotations about the x-axis changed whereas those about the y-axis did not. This would tend to infer that the transverse stiffness of a support can affect the response. This could provide further scope for investigation at a later date.

Displacement data shown in Figures 3.57 to 3.61 showed how the variation in support stiffness altered the recorded displacement and wave propagation across the plate. As would be expected, the stiffest support (spring 5), produces the smallest displacement values and the least stiff (spring 1), resulted in the largest displacements at each location. Comparing results obtained from both methods, Figures 3.65 and 3.66, indicated that the FEA underestimated the resonant frequencies obtained for each arrangement, but over-estimated the displacements at the mid-span.

One minor reason for the difference in values obtained was the geometric properties used in the FEA analysis may not be accurate, especially as the plate thickness varied over its entire area. This variation in thickness means that certain areas will be less prone to oscillate than others, illustrated schematically in Figure 3.66, and also referred to in FEA of the plate with varying thickness (see Table 3.9). As the variability arose

from normal manufacturing tolerances on thickness during extrusion processes, this was unlikely to alter E, ν or ρ. There may be minute variations in E, ν or ρ due to thermal or manufacturing effects. Referring back to Figure 3.64, it was apparent how sensitive the model was to changes in these parameters. The only way of accurately modelling the plate is to ascribe a different thickness to several sections of the plate to match the ultrasonic thickness measurements, as attempted in Table 3.9. In terms of practicality, this is not always possible, and an assumption of uniform thickness over the whole plate seemed reasonable in this case.

One other source of error could be the support conditions. In FEA, the support conditions were idealised, whereas in experimental modal analysis, defects in materials can affect the overall response, but these were dwarfed by differences in support restraint. The major difference between the methods was that in the modal analysis, springs were placed on either side of the plate. In the FEA however, the plate was only supported on the bottom surface. The FEA also assumed the springs were linear in their behaviour. It should also be noted that the springs are effectively acting as a point support with varying degrees of stiffness in the FEA, whereas in the modal analysis, the springs support an area equivalent to their wire diameter over their circumference.

Although a method of highlighting the effects of support stiffness has been developed, several issues relating to the analysis should be noted. NDT is not a panacea, but simply a tool used in conjunction with more traditional visual inspection methods and must be corroborated. In NDT, the main principal, in terms of probability of detection, should be to determine the biggest defect that may be missed, not the smallest detectable as is often the case.

As the method is based on small-scale model testing, the difficulty with scale effects when applying the method to a full-scale structure can be problematic. The simplification of a plate model in this case when related to a bridge structure does not take into consideration the more complex geometries and composition of constituent parts of a bridge structure.

In addition to the scale effects, the material properties can also present a problem in large scale structures. Bridge structures are often in a poor state of repair, and as such, contain numerous defects ranging from hairline cracks to reinforcement corrosion or running surface degradation. All of these defects will affect the response of the structure, making it problematic to detect the alteration in the desired parameter. For example, has the method detected the change in response due to bearing stiffness, or has the structure moved clear of the bearings and is resting on the superstructure? This example highlights the requirement for visual inspection in conjunction with any proposed NDT method.

3.6 Conclusions

- The modified Euler-Bernoulli method for plate structures provides a simple method to determine the fundamental resonant frequency when support conditions are variable at either end of the plate.

- Alteration of support stiffness in the model can have a marked effect on the resonant frequency of the plate (approx. 23 % between spring 1 and 5).

- The proposed method underestimated the exact resonant frequency value by almost 13 %. This difference is due to idealised conditions assumed for the analytical models, compared to the actual conditions for modal testing.

- Improvement of the method is possible if consideration is given to rotational and translational restraint.

- The method only produced the first resonant frequency, but could be extended to higher order modes with application of higher order polynomial assumed mode shape functions in the general equation.

- Simple modal analysis testing protocols, such as the single input-multiple output test used herein, were adequate for routine inspection purposes.

- Modal analysis allowed the effect of stiffness to be visualised through waterfall plots of FRFs.

- Forced vibration testing indicated that bending modes were of more use for detection of the effect of alteration in bearing support stiffness. Torsional modes provide no real discernable pattern in *this* case, but conceivably with different measurement locations, damage could be identified in these modes.

- Identification of the mode shapes was essential if accelerometer locations are not to coincide with nodal points. Finite element analyses may offer some useful guidance, albeit at some cost (both direct and time-based), as to the mode shapes likely in a deck slab.

- Considering individual resonant frequency values was not considered to be a viable option, rather the mode shapes relating to each frequency which can be matched were of significance.

- Excitation data relating to a non-resonant frequency did not provide any insight into the effects of support stiffness, although data presented from modal analysis testing showed the effect of approaching or receding from a resonant frequency in the higher spring stiffnesses.

- The baseline frequency used in any full-scale condition assessment should be chosen to avoid proximity to a natural frequency of the bridge deck.

- The structural support conditions, with reference to their stiffness in particular, were effective in influencing the FRF measured on a model bridge deck.

Continual monitoring over time would be required if this method were to have any basis as a condition monitoring, or degradation assessment, tool.

- The FRF may be used as an accurate general indication of the overall state of a bridge deck's stiffness. Support changes affected wave propagation across the model deck slab.

- Displacement and acceleration values in the vertical direction provided accurate information as to the response of the plate when subjected to forced vibration with variable support stiffness.

- Velocity response was not a viable diagnostic tool in this case. Integration will flip the amplitudes of vibration from acceleration, to velocity, then again to displacement. In this set of results, this integration appeared to affect the velocity response.

- Relative displacements at the mid-span due to loading at plate edges were higher than those subjected to loading at the centre nodes.

- Strain values provided no indication of the effect of support stiffness on wave propagation or dynamic response.

- The plate response and propagation of waves was dependent on the location of excitation.

3.7 References

3.1 Bernoulli D. De vibrationibus et sono laminarum elasticarum commentationes physico-geometricae. Commentari Acad. Sci. Imperialis Petropolitanae, St Petersburg, **13**, 1751, 105-120.

3.2 Ritz W. Theorie der Transversalschwingungen einer quadratischen Platte mit freien Rändern. *Annalen der Physik*, 1909, **28**, 737-786.

3.3 Li. W.L. Dynamic analysis of beams with arbitrary elastic supports at both ends. *J. Sound Vib.*, 2001, **246(4)**, 751-756.

3.4 Yau J.D., Wu Y.-S. and Yang Y.-B. Impact response of bridges with elastic bearings to moving loads. *J. Sound Vib.*, 2001, **248(1)**, 9-30.

3.5 Young T. A course of lectures on natural philosophy on the mechanical arts. J. Johnson, London, 1807.

3.6 Hooke R. Lectures de potentia restitutiva. Printed for John Martin, London, 1678.

3.7 Poisson S.D. Traité de mécanique. École Polytechnique, Courcier, Vol. 1, Paris, 1811.

3.8 Brüel and Kjær. Transducer catalogue. Nærum Offset, Nærum, Denmark, 2005.

3.9 Brüel and Kjær. Introduction to modal analysis. Nærum Offset, Nærum, Denmark, 1987.

3.10 Gade S. and Herlufsen H. Use of weighting functions in DFT / FFT analysis: part 1. Technical Review No. 3, Nærum Offset, Nærum, Denmark, 1987.

3.11 Blackman R.B. and Tukey J.W. Particular pairs of windows. The measurement of power spectra, from the point of view of communications engineering. Dover Inc., New York, 1959, 98-99.

3.12 Cook R.D., Malkus D.S., Plesha M.E. and Witt R.J. Concepts and applications of finite element analysis. J Wiley & Sons, New York, 2002.

3.13 Mindlin R.D. Influence of rotary inertia and shear on flexural motions of isotropic elastic plates. *Proc. Am. Soc. Mech. Engnrs,* **18(1)**, 1951, 31-38.

3.14 Kirchhoff G.R. Vorlesungen über mathematische Physik. Mechanik, Vols 1-3, Leipzig, 1874-1876.

3.15 Reissner E. On bending of elastic plates. *Quarterly J. Appl. Math.*, **5(1)**, 1947, 55-68.

3.16 LUSAS v13 User Manual, *LUSAS for Windows®*. FEA Ltd, Kingston-upon-Thames, 1999.

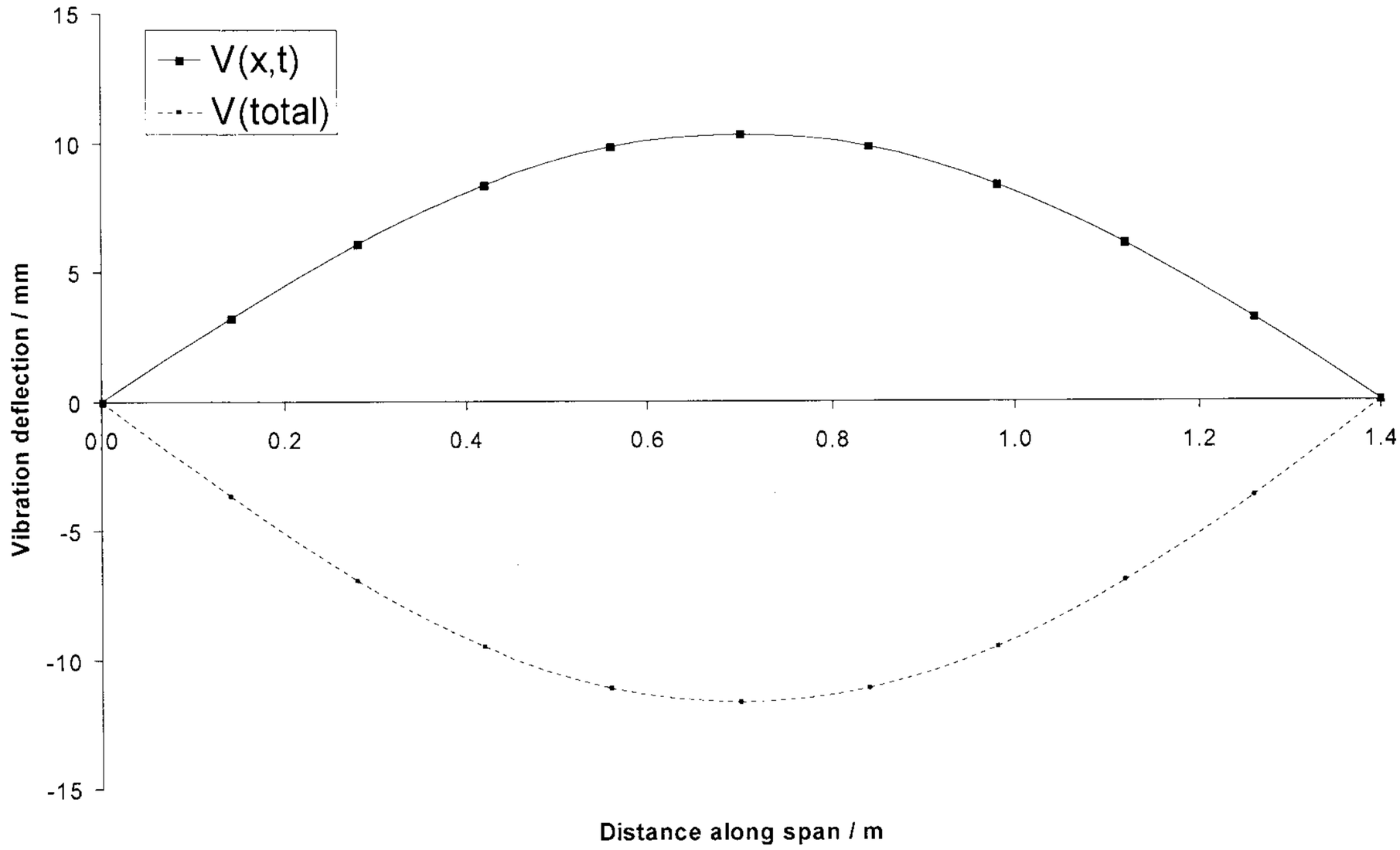

Figure 3.1 **Euler-Bernoulli beam deflection values due to forcing function at t = 0.1 s**

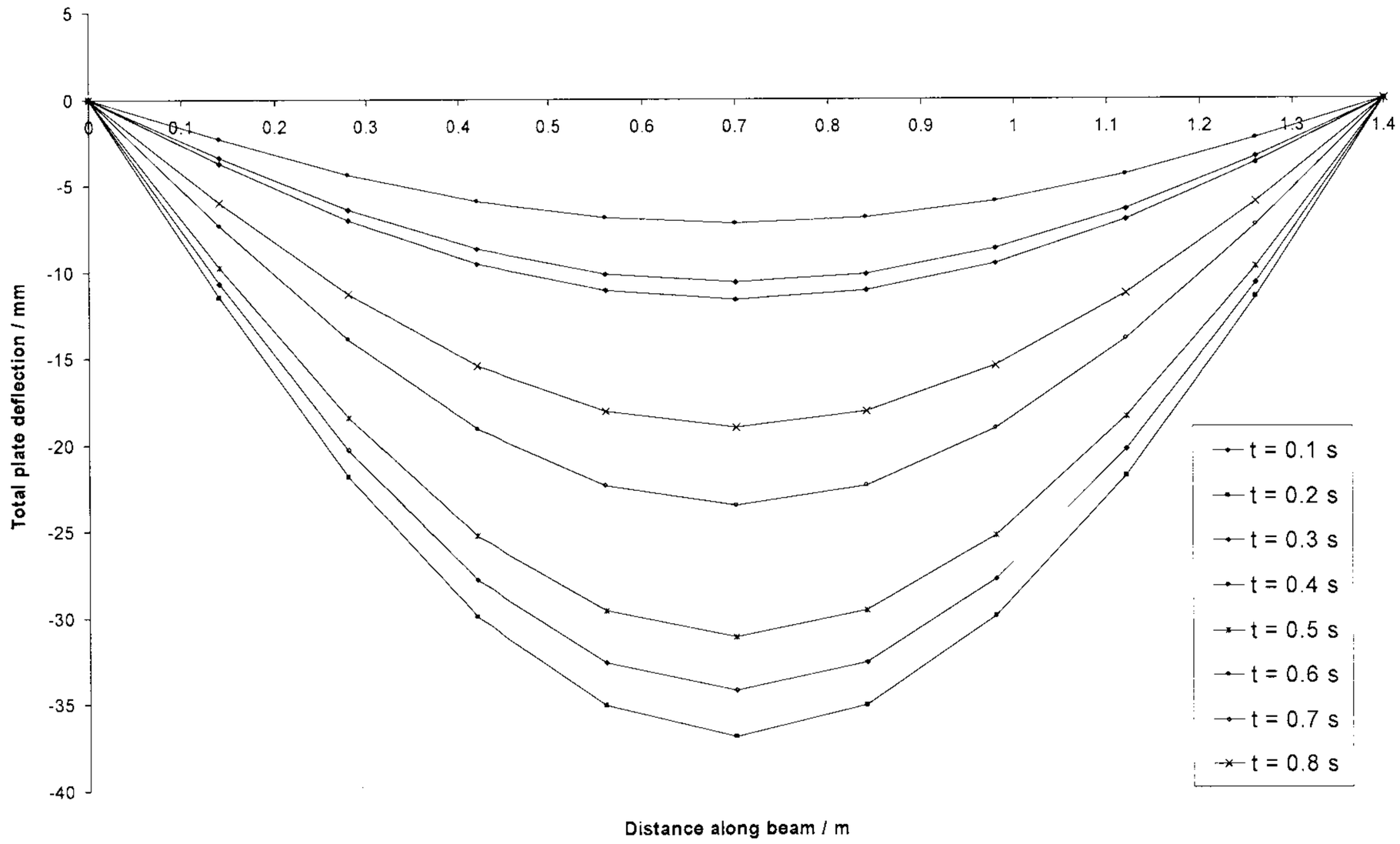

Figure 3.2 **Euler-Bernoulli beam deflection values due to forcing function at 0.1 s time step intervals**

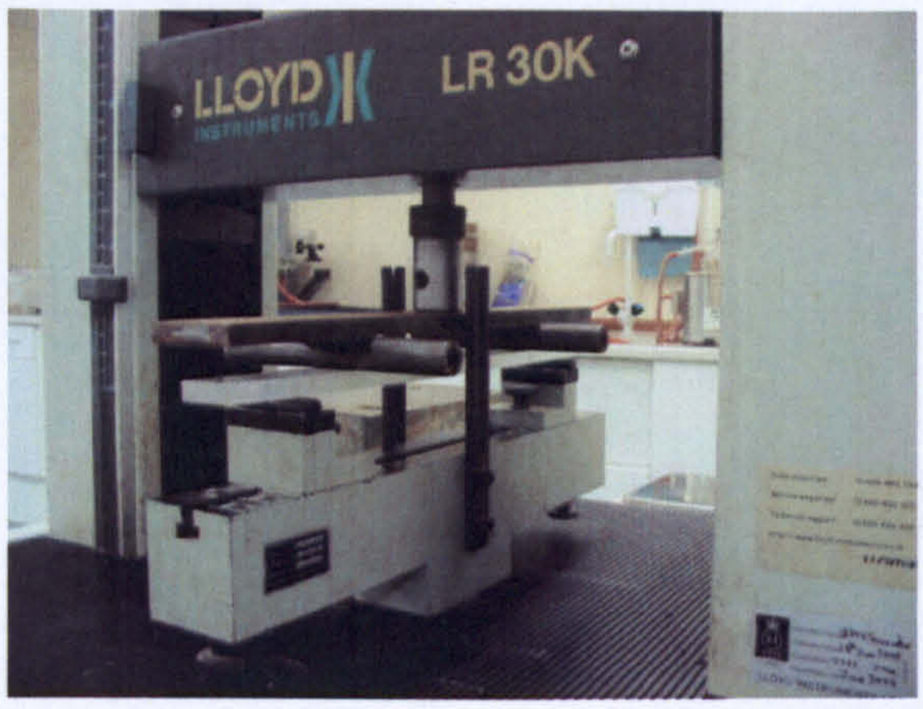

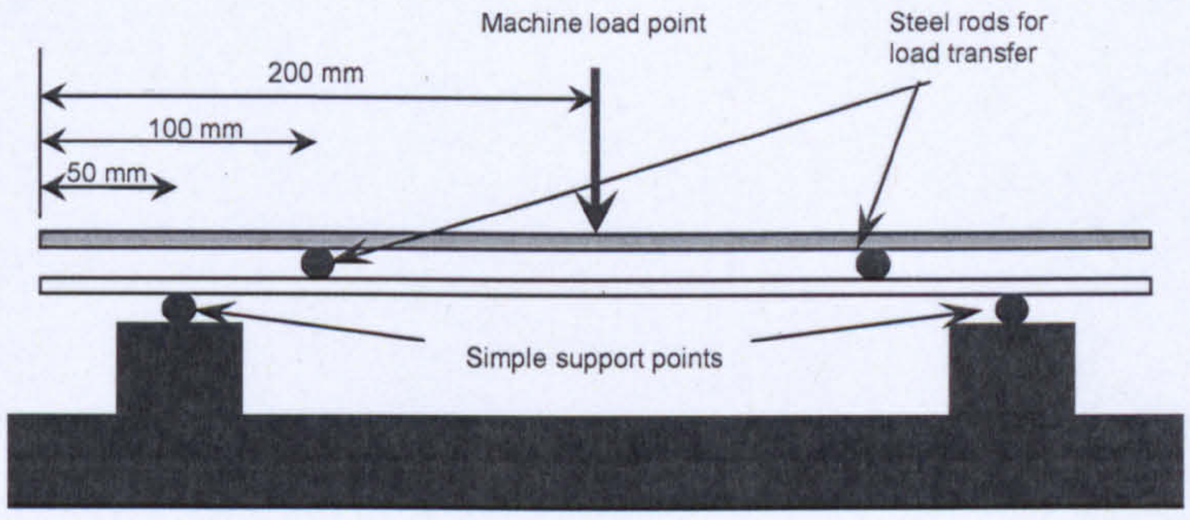

Figure 3.3 PMMA sample in four point bending test configuration

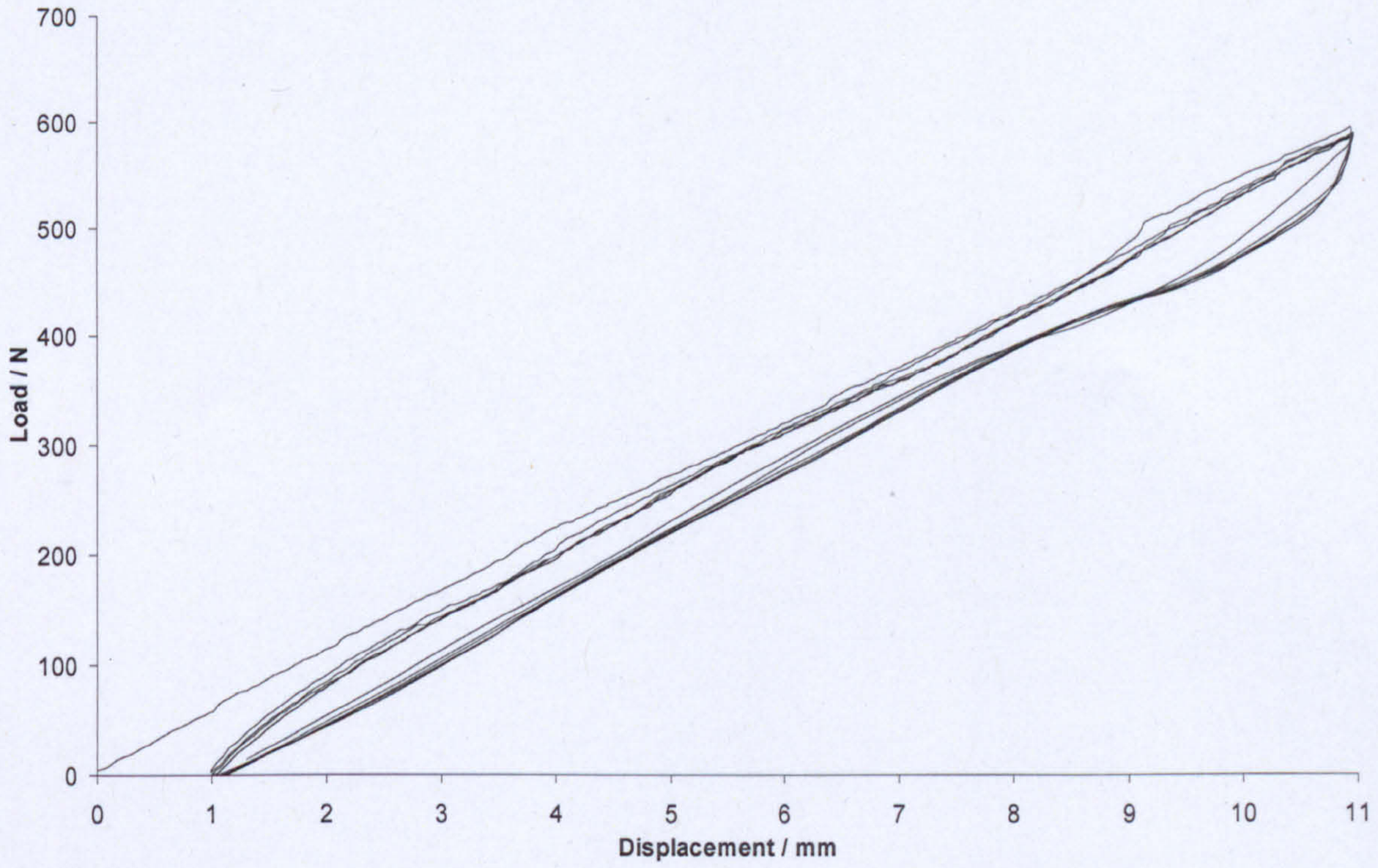

Figure 3.4 PMMA cyclical tests for E value determination. Five loading and unloading cycles are shown, at a loading rate of 2 mm *per* minute

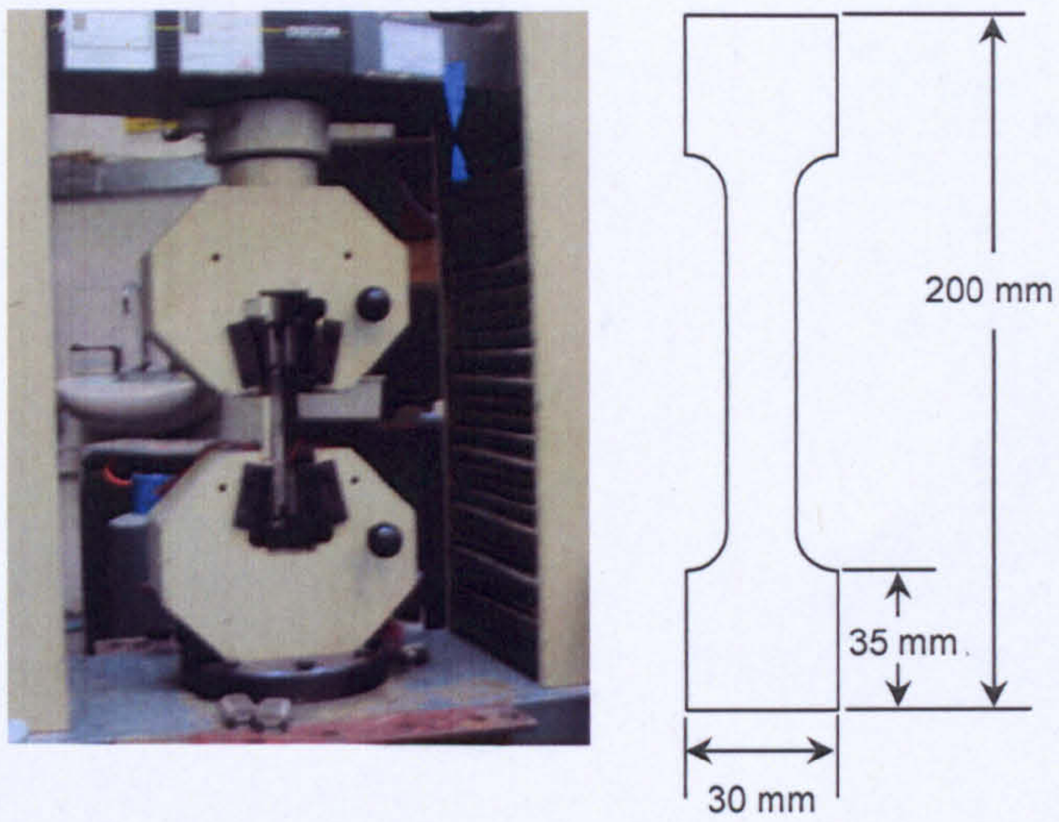

Figure 3.5 **PMMA sample *in situ* during Poisson's ratio testing at loading rate of 25 N *per* second;** $\frac{\partial \varepsilon_x}{\partial t} = 62\ \mathrm{s}^{-1}$

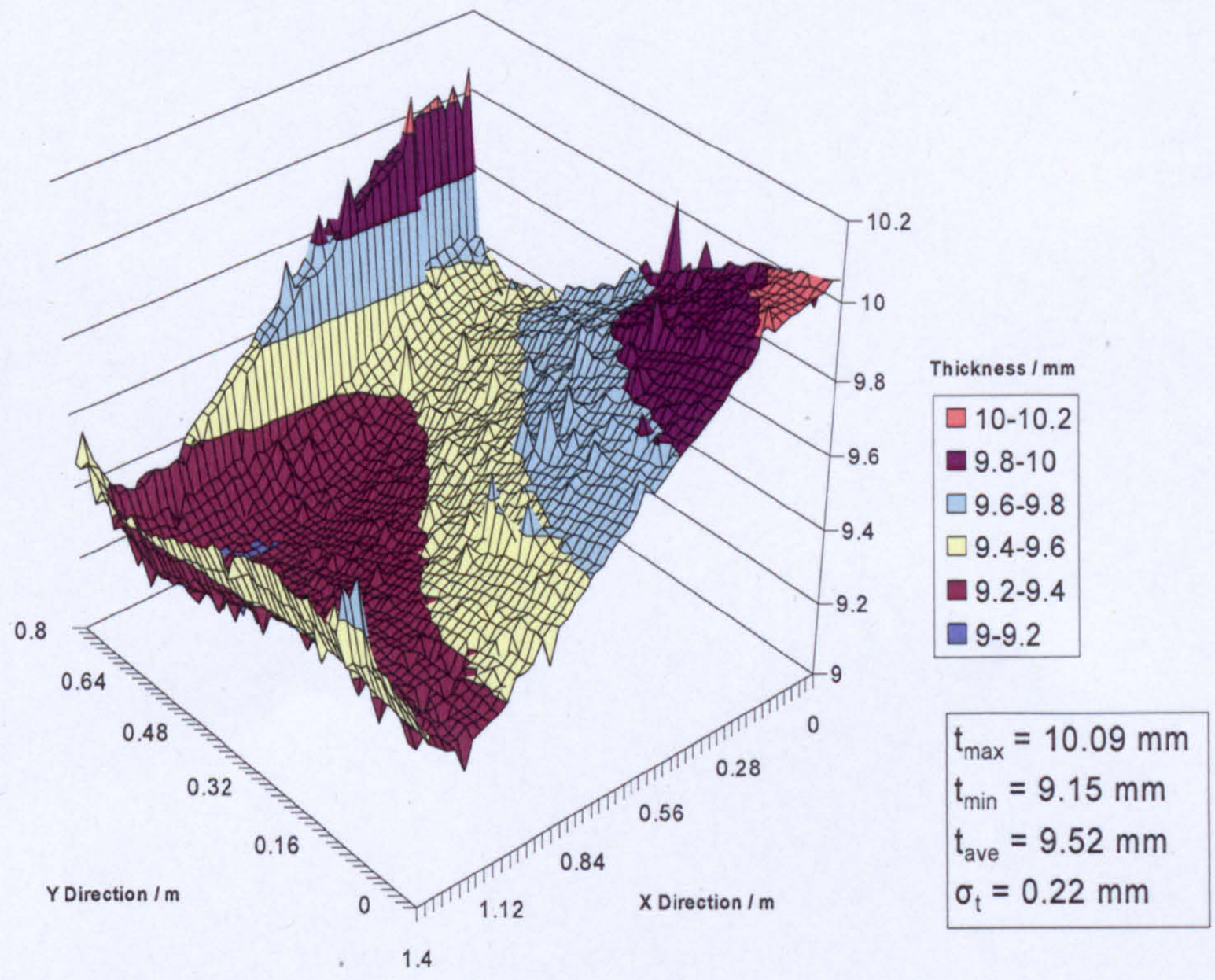

Figure 3.6 **Thickness measurements on PMMA plate**

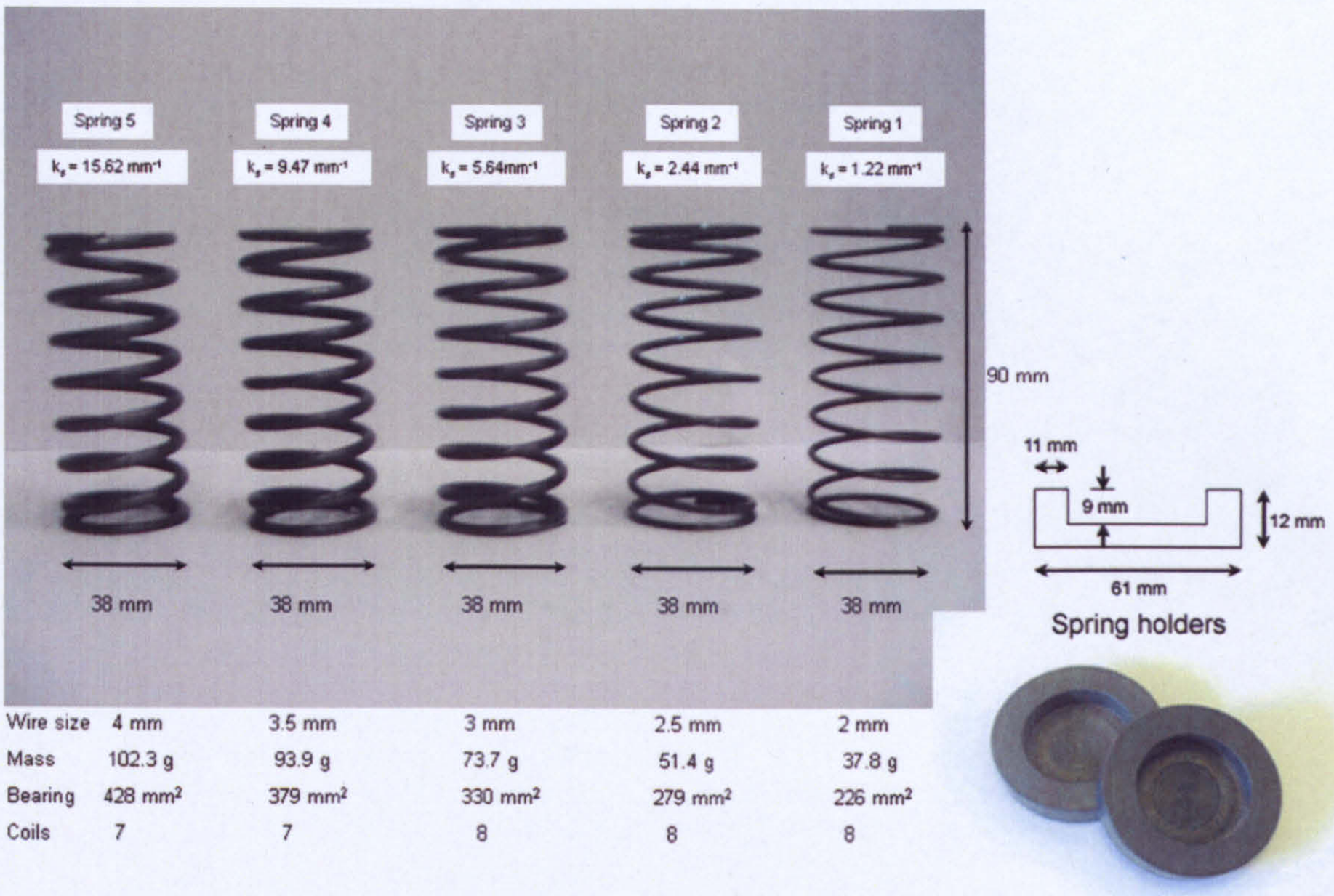

Wire size	4 mm	3.5 mm	3 mm	2.5 mm	2 mm
Mass	102.3 g	93.9 g	73.7 g	51.4 g	37.8 g
Bearing	428 mm^2	379 mm^2	330 mm^2	279 mm^2	226 mm^2
Coils	7	7	8	8	8

Figure 3.7 Springs used in experimental analysis and holders. Each spring is nominally 1 m in free length

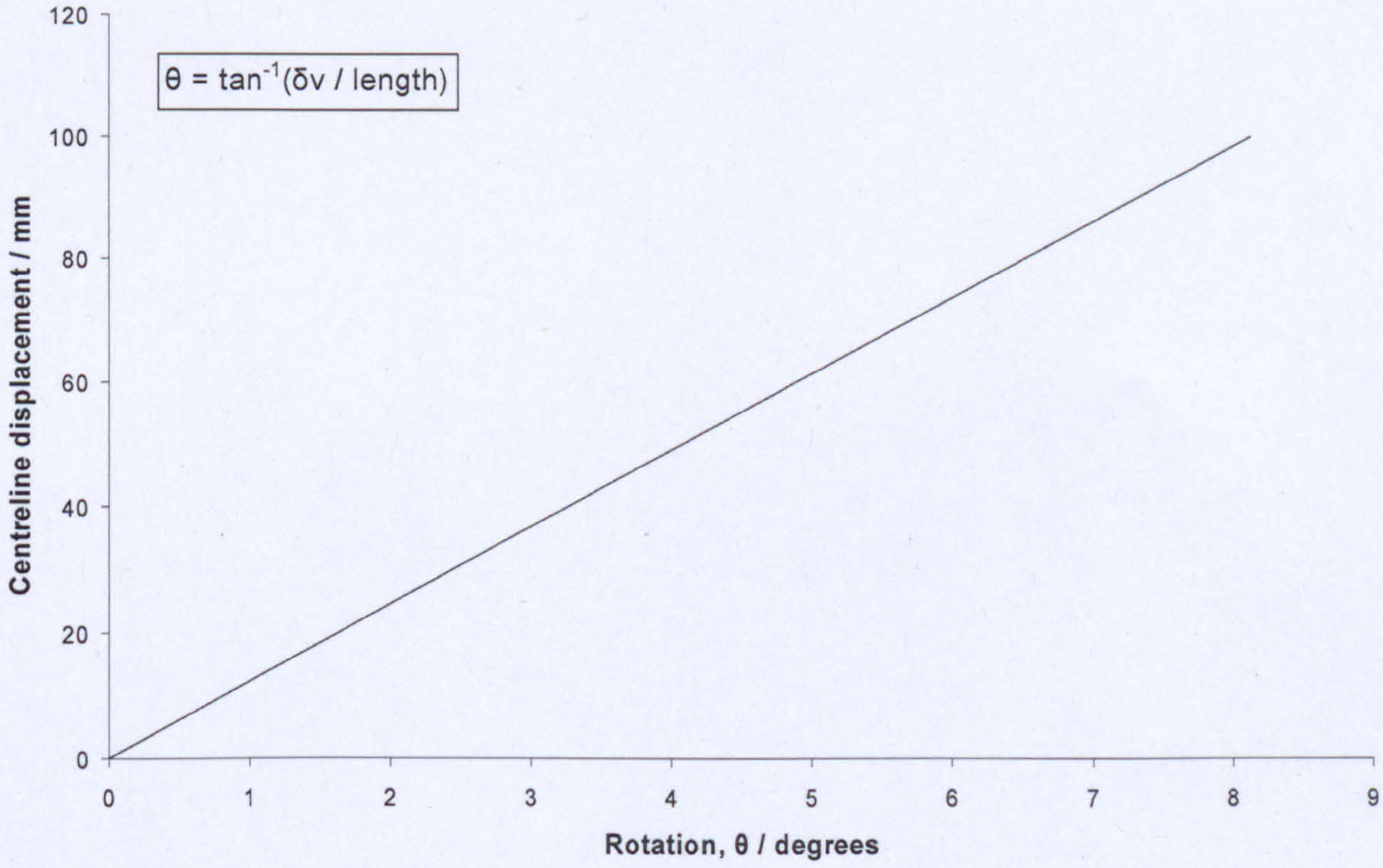

Figure 3.8 Centreline displacement versus rotation curve for PMMA plate.

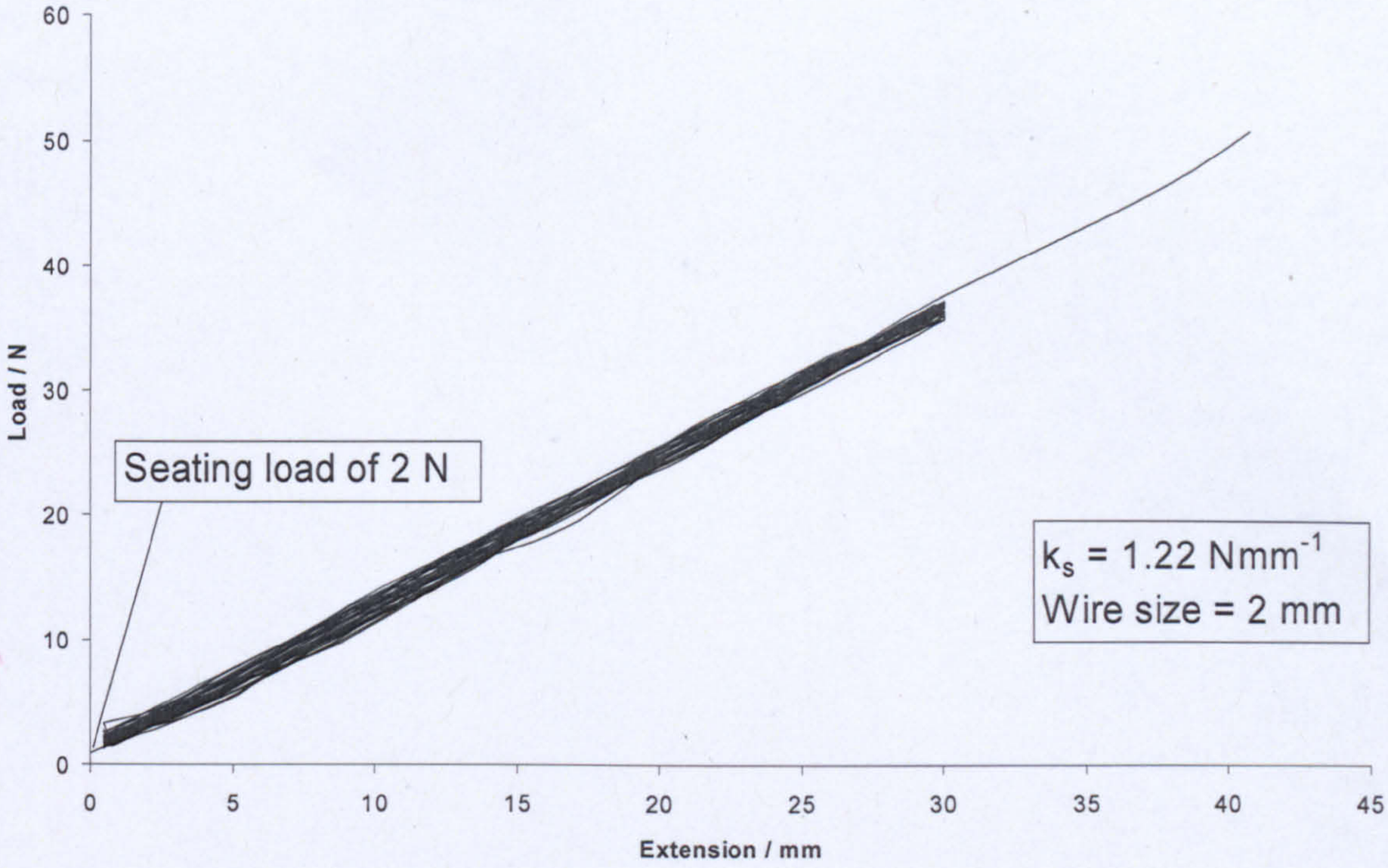

Figure 3.9 **Load - displacement curve for spring 1.**
Loading rate of 2 mm *per* minute, all tests performed at 20°C.

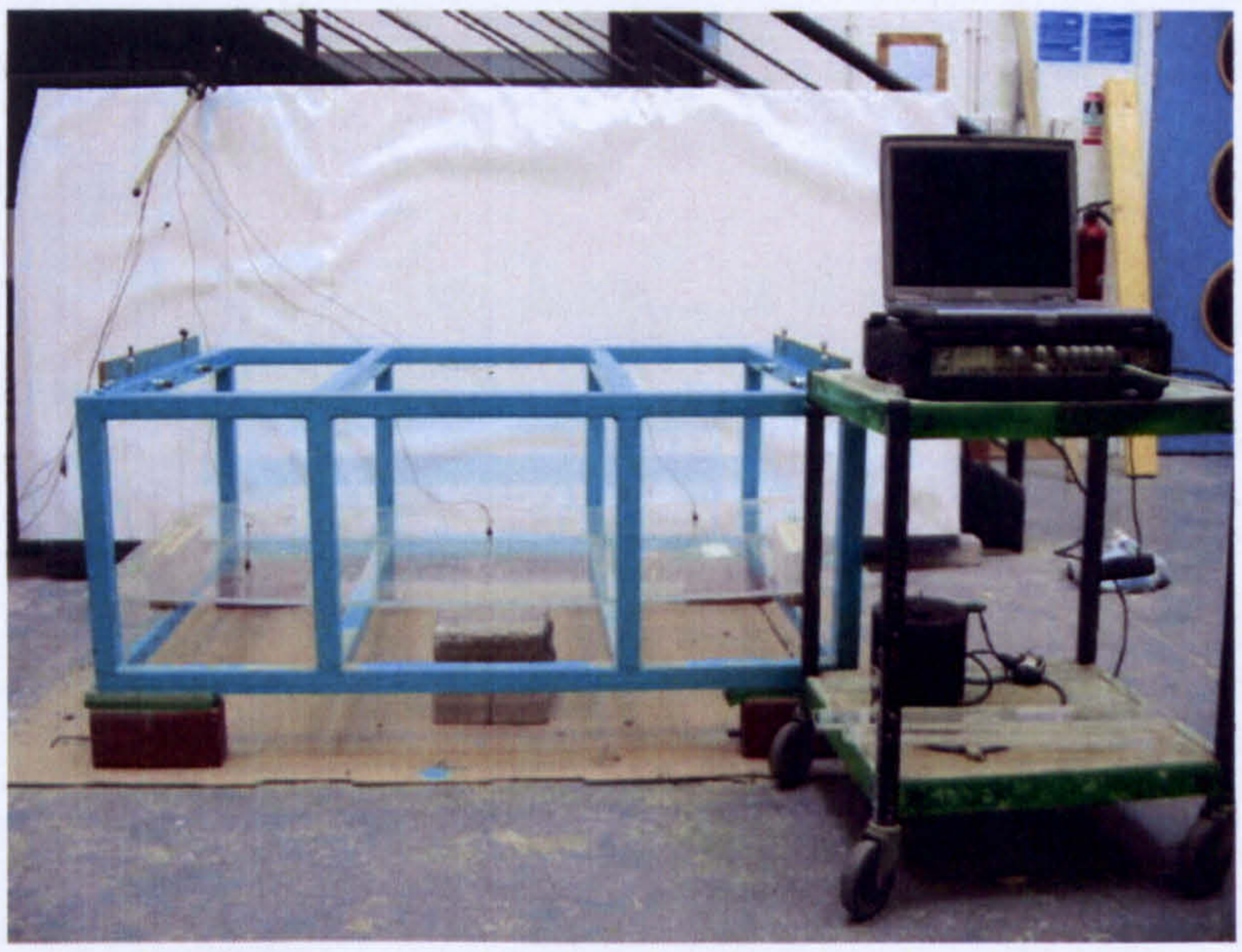

Figure 3.10 **PMMA plate in freely suspended configuration.**

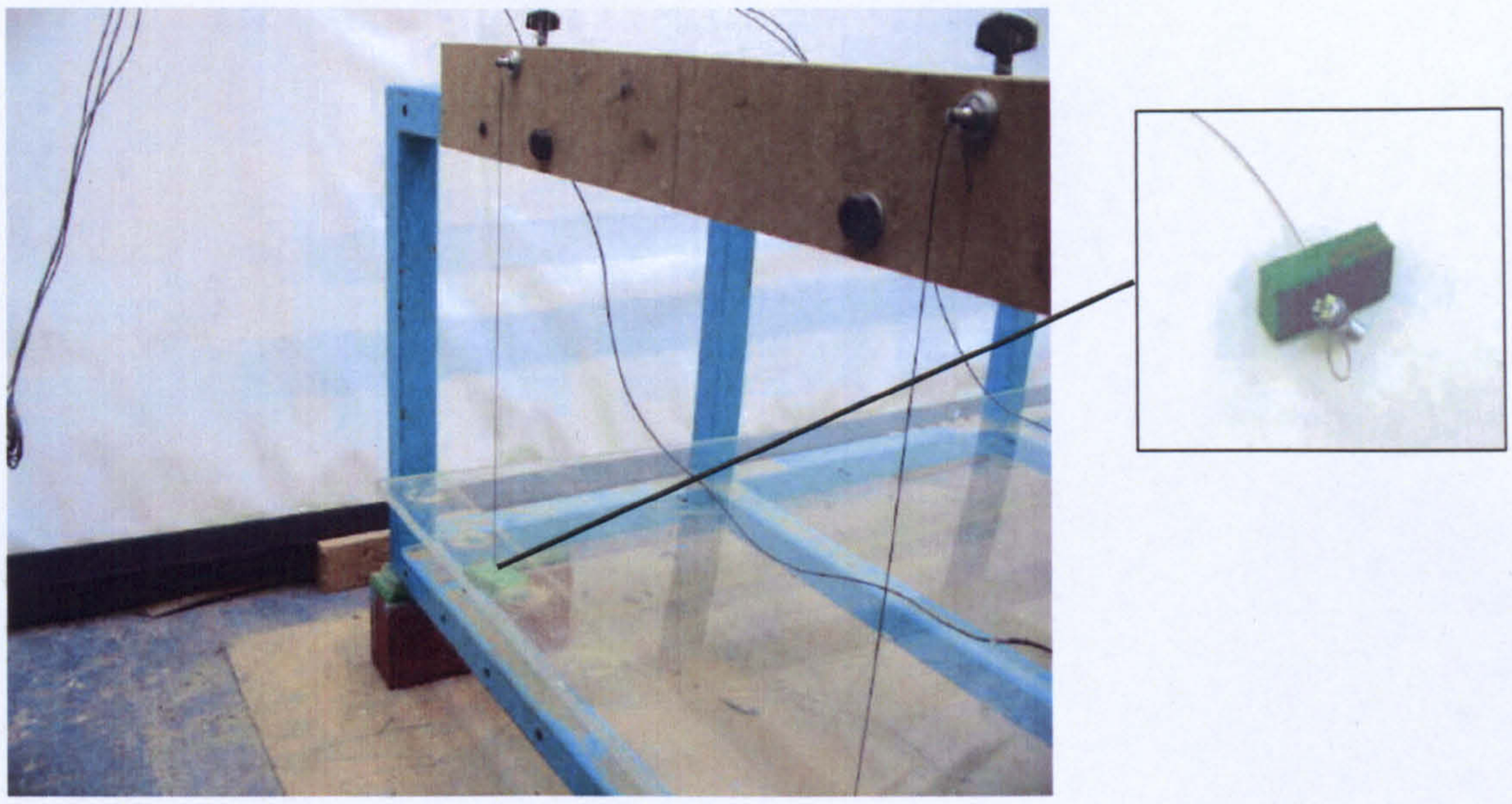

Figure 3.11 Guitar tuners for levelling PMMA plate in freely suspended configuration.

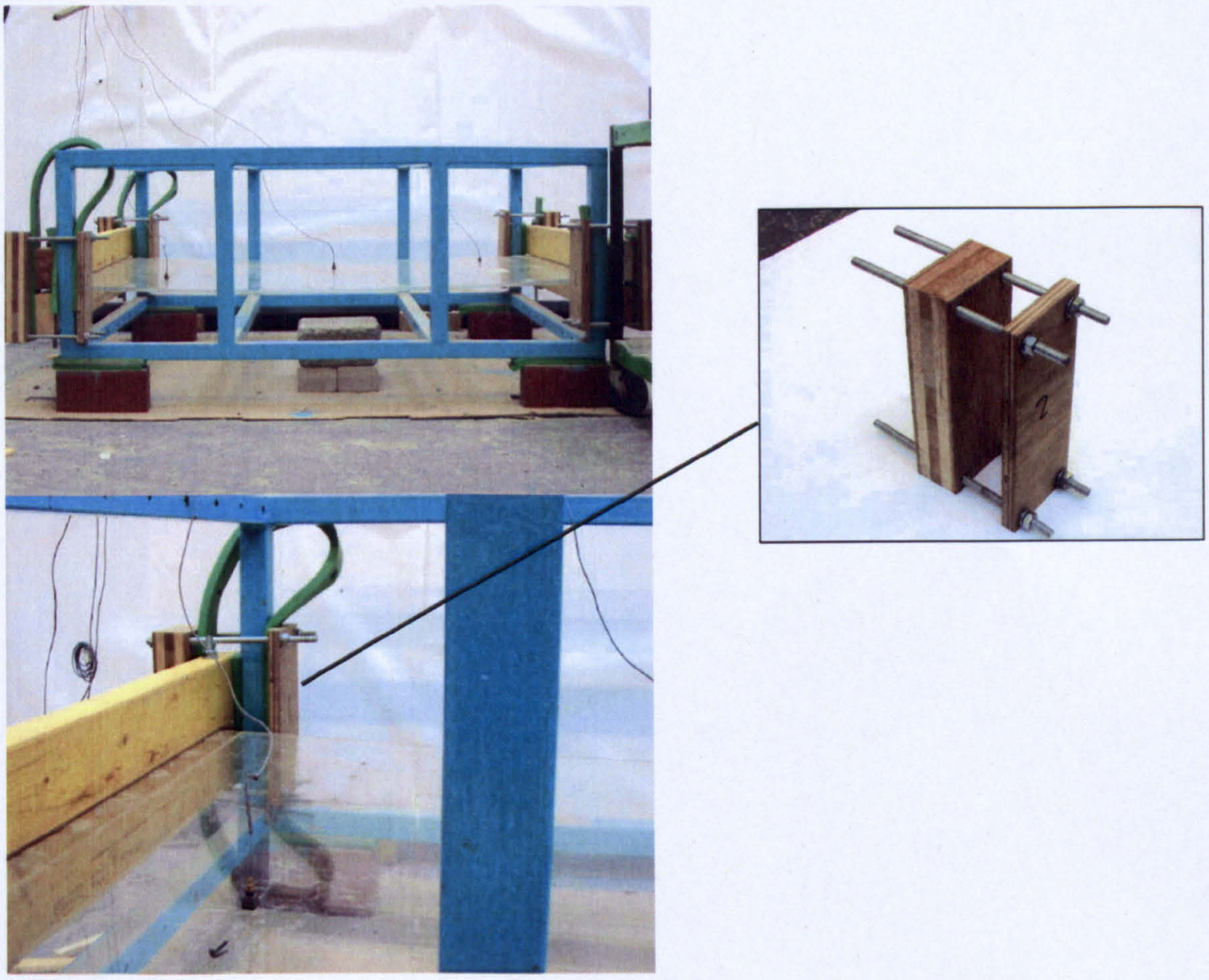

Figure 3.12 PMMA plate in fully fixed arrangement.

Figure 3.13 Simply supported configuration.

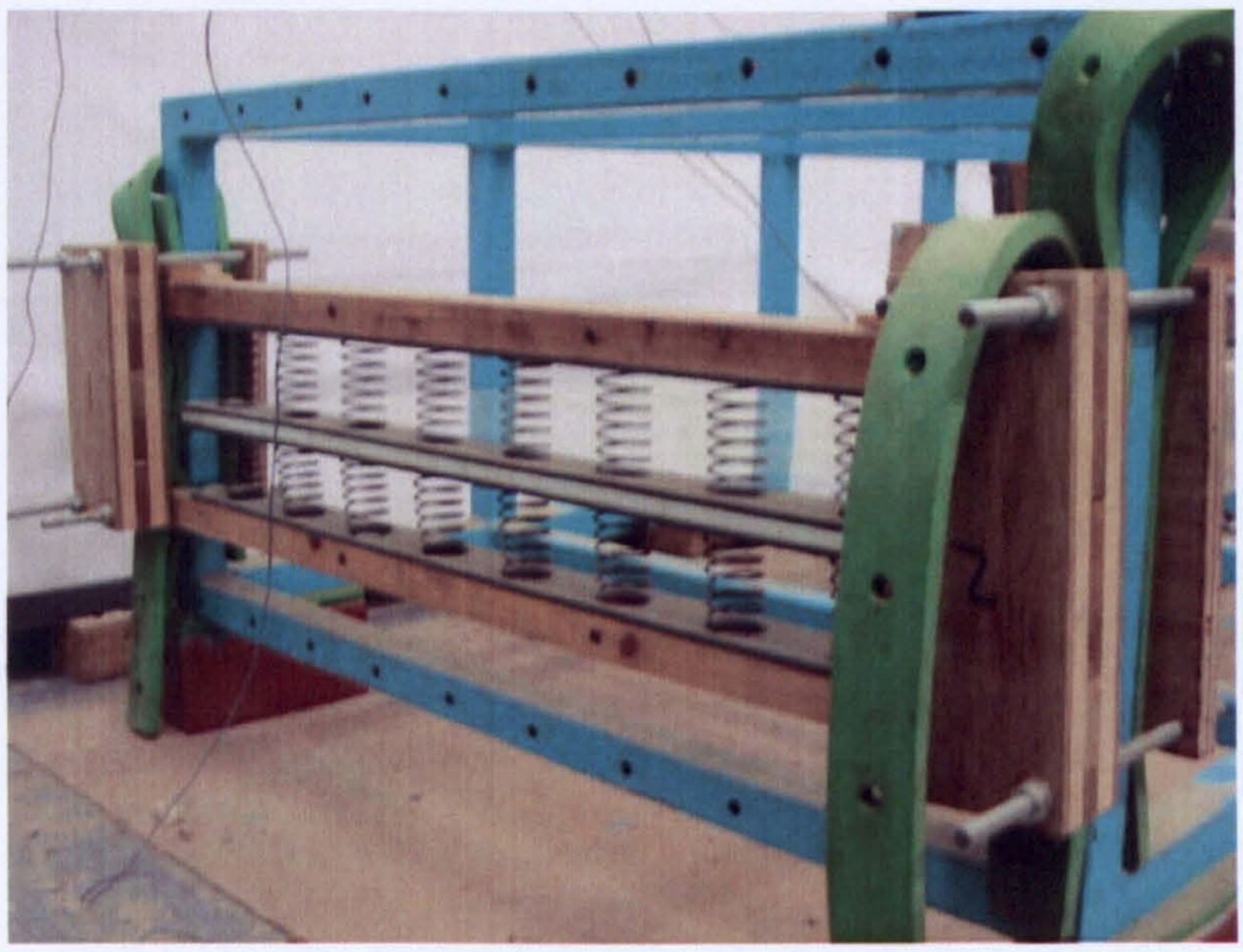

Figure 3.14 Spring support configuration.

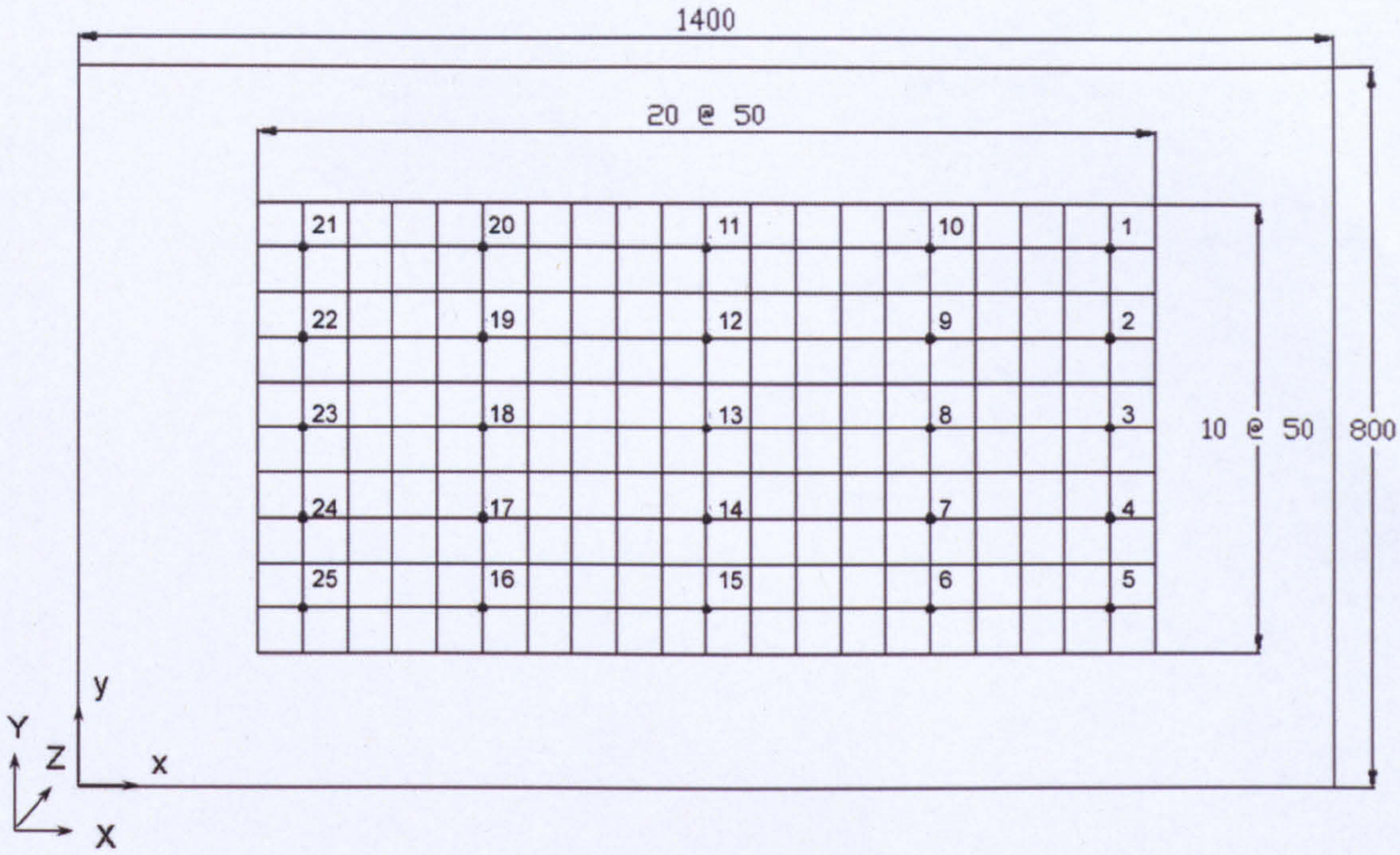

Figure 3.15 PMMA plate with dimensions, grid and point locations numbered (all dimensions in mm)

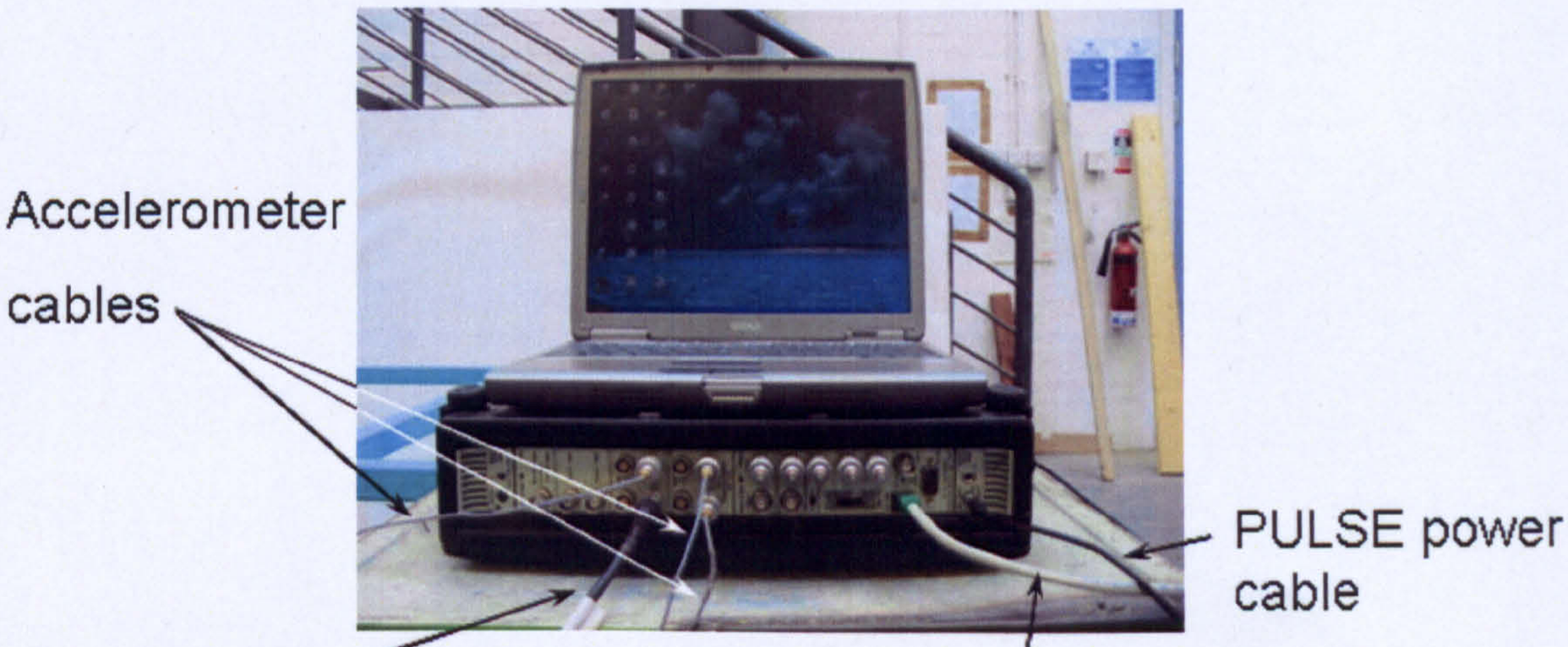

Minimum PC requirements are: Pentium® 3, 750 MHz processor, 256 RAM.
Software requirements are: Windows® XP Professional and Microsoft® Office 2003.

Figure 3.16 PULSE FFT analyser and laptop computer

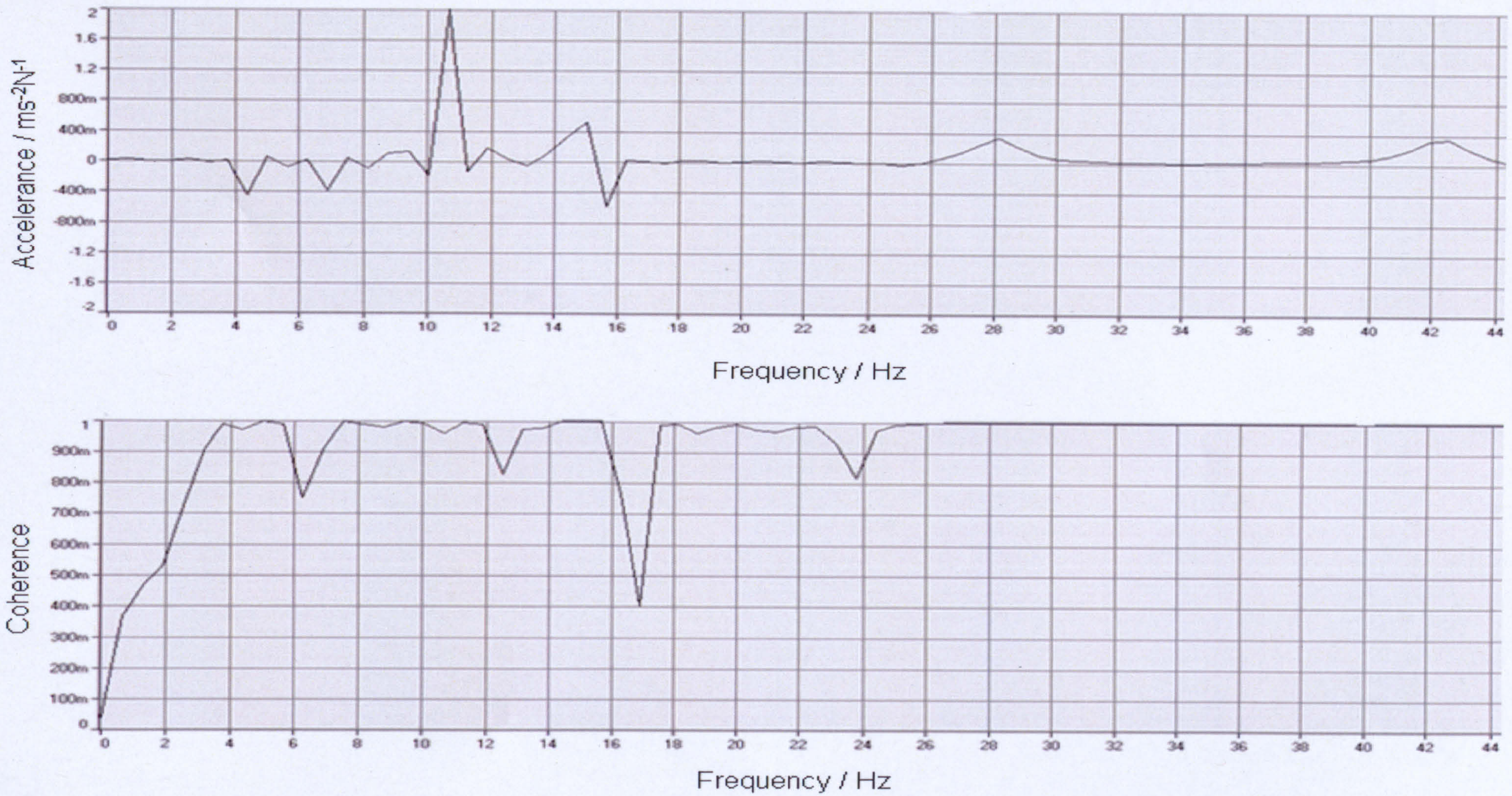

Figure 3.17 FRF response slice at measurement point 4 against coherence values for ten excitations

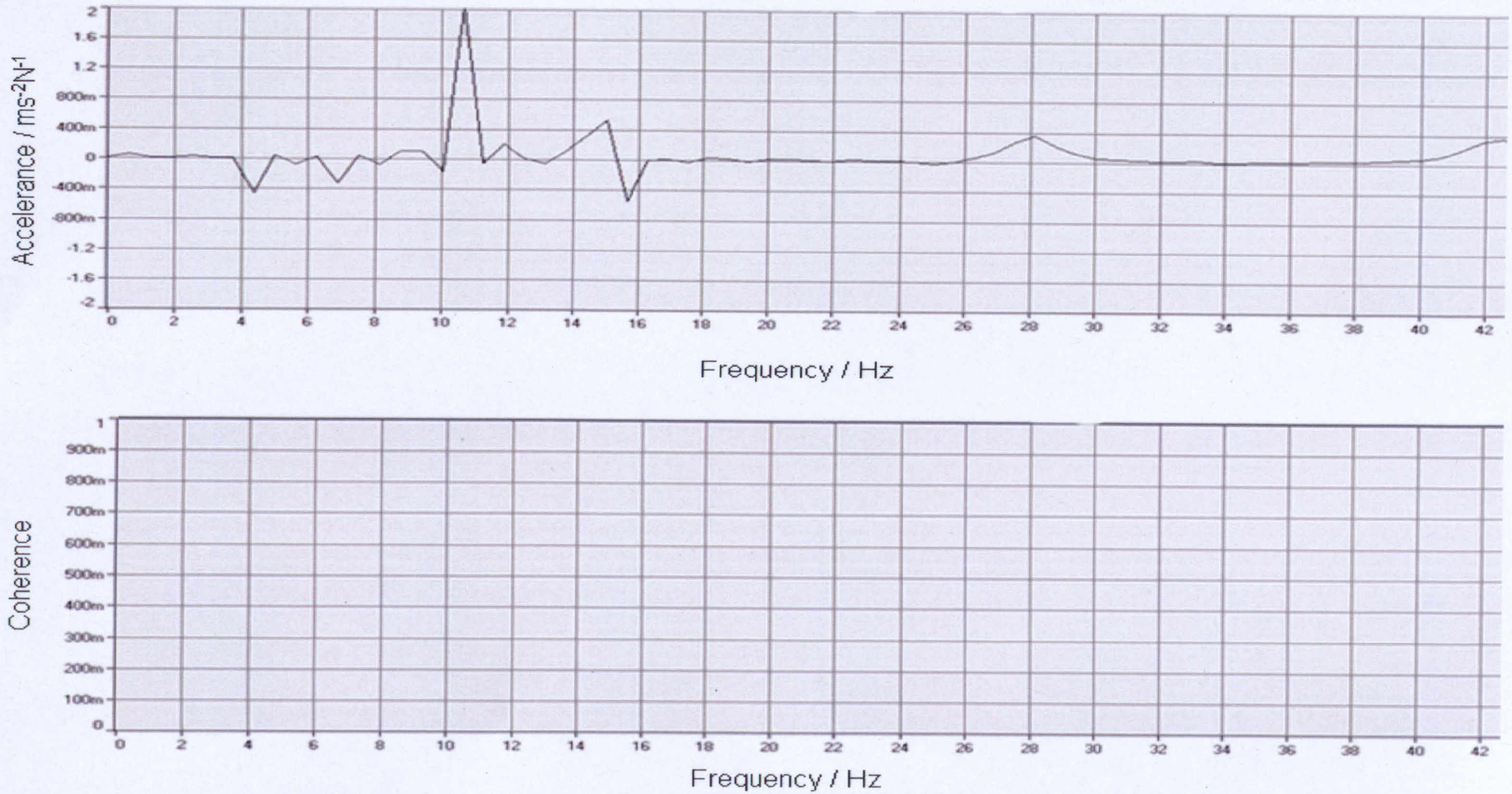

Figure 3.18 FRF response slice at measurement point 4 against coherence values for one excitation.

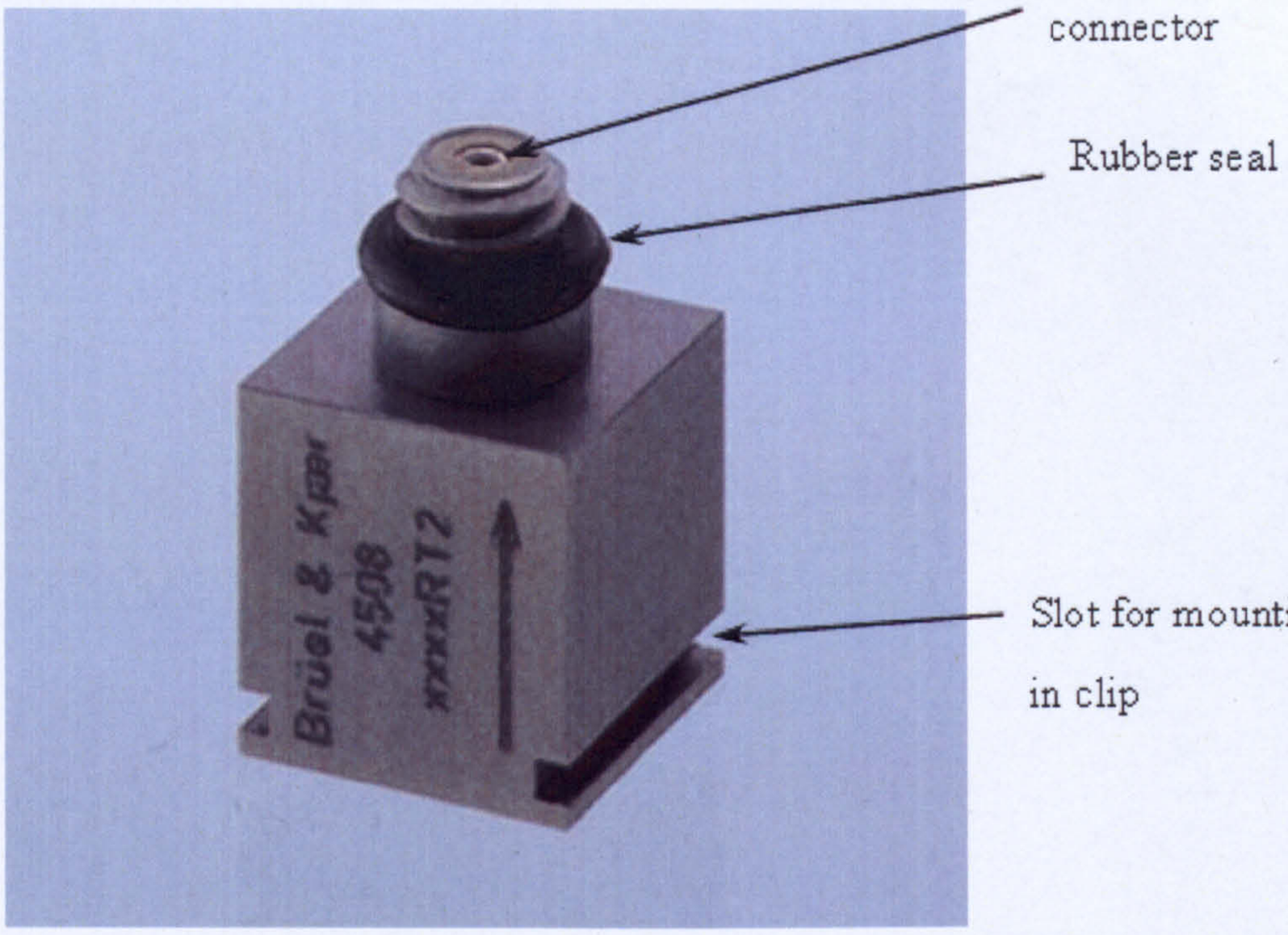

Sensitivity: 10 mV / ms^{-2}; Measuring range: 700 ms^{-2}; Frequency range: 0.3 - 8 kHz ± 10 %; Bias voltage: 13 V ± 1V; Inherent noise: < 35 μV; Weight: 4.8 g; Temperature range: -54°C to 100°C.

Figure 3.19 Accelerometer type 4508-B. Arrow indicates direction of measurement

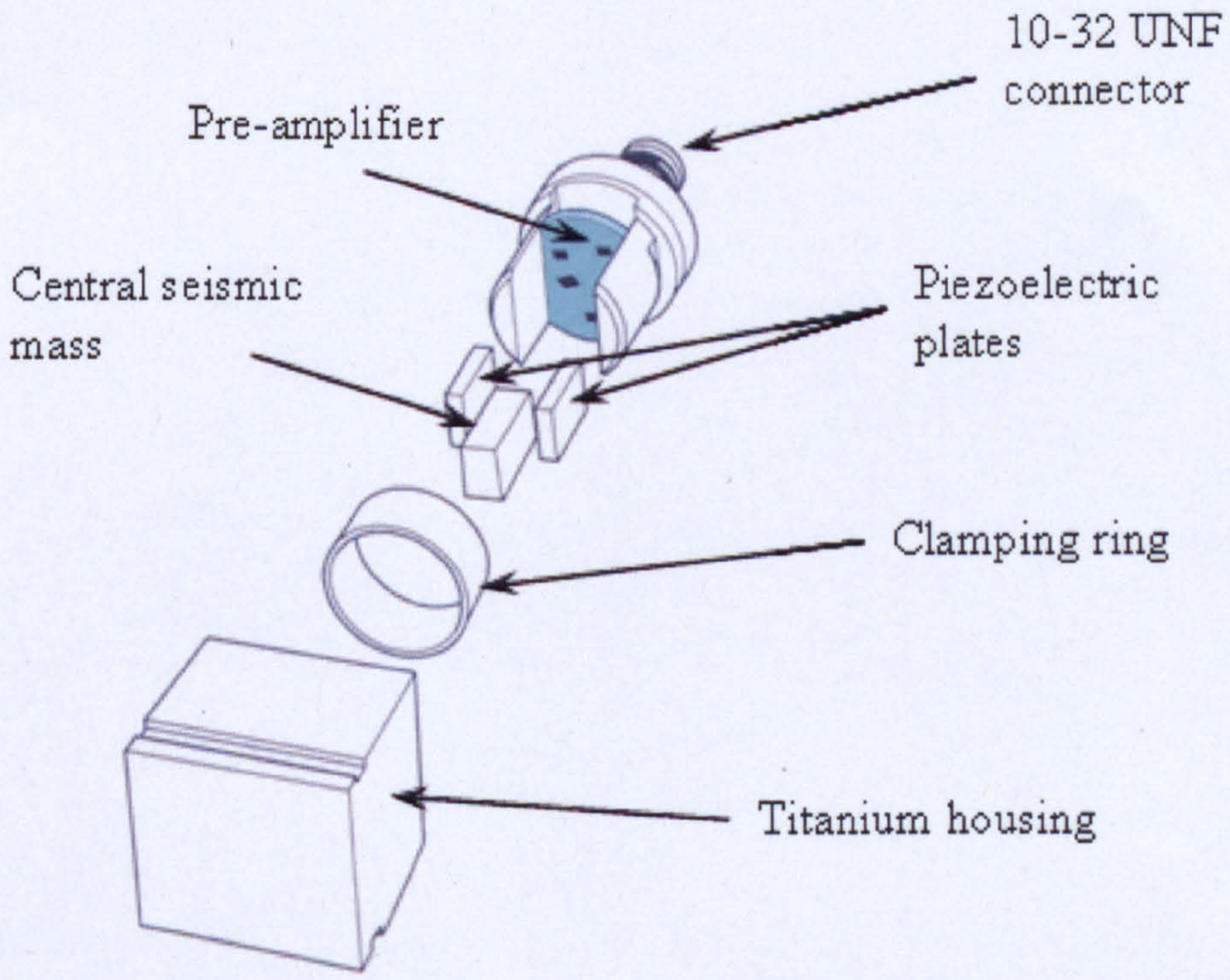

Figure 3.20 Exploded view of ThetaShear accelerometer configuration

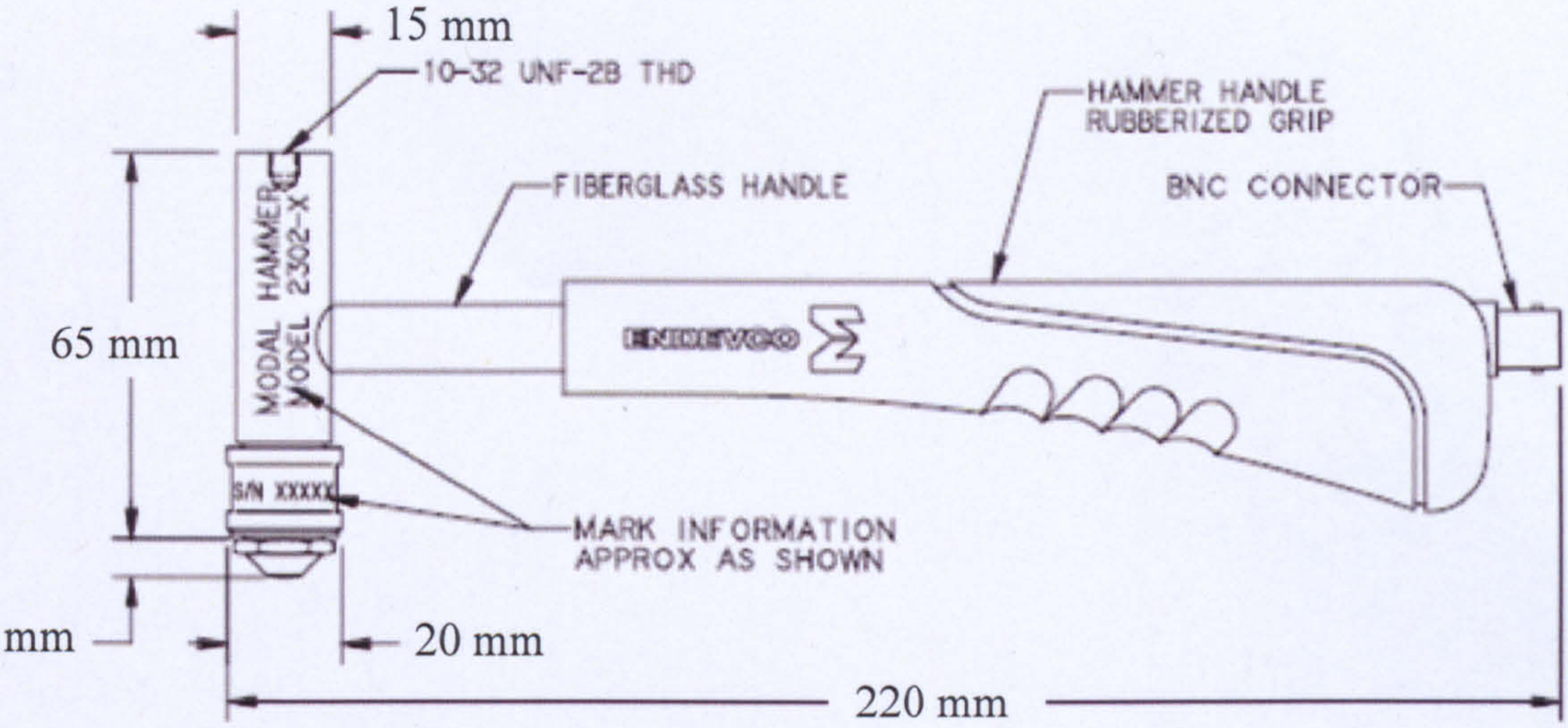

Figure 3.21 Impact hammer Type 2301-10 showing typical dimensions.

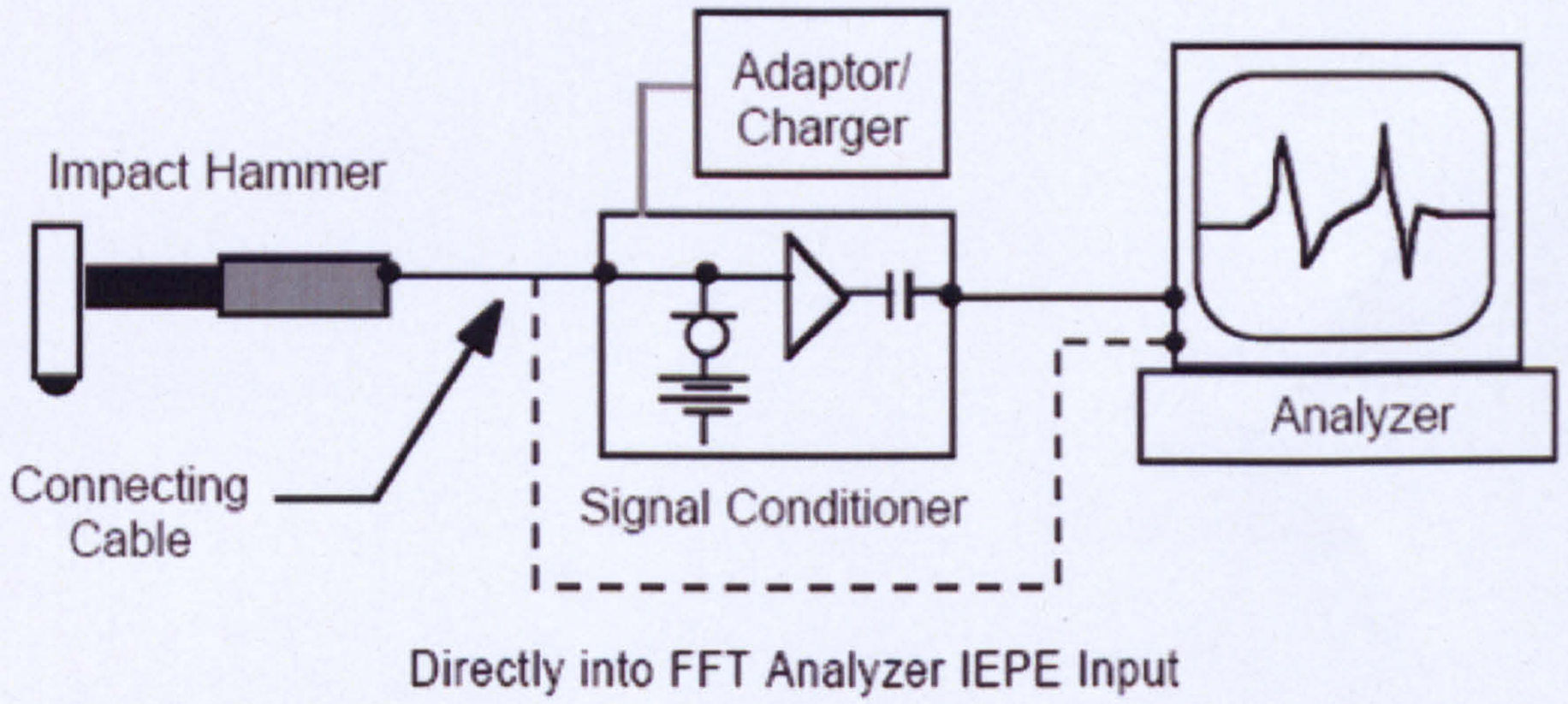

Figure 3.22 Schematic diagram of impact hammer apparatus configuration.

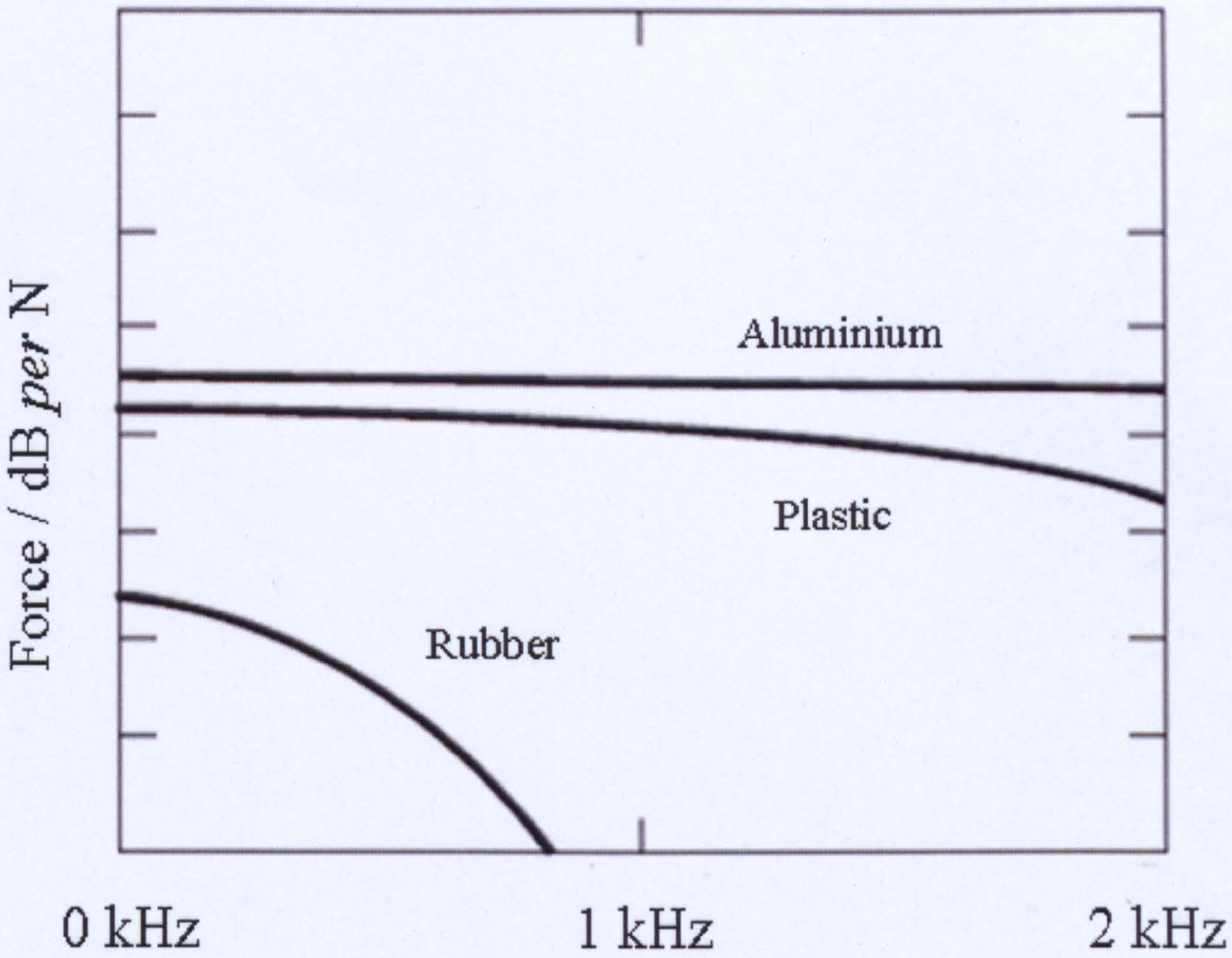

Figure 3.23 Excitation frequency range of impact hammer tips

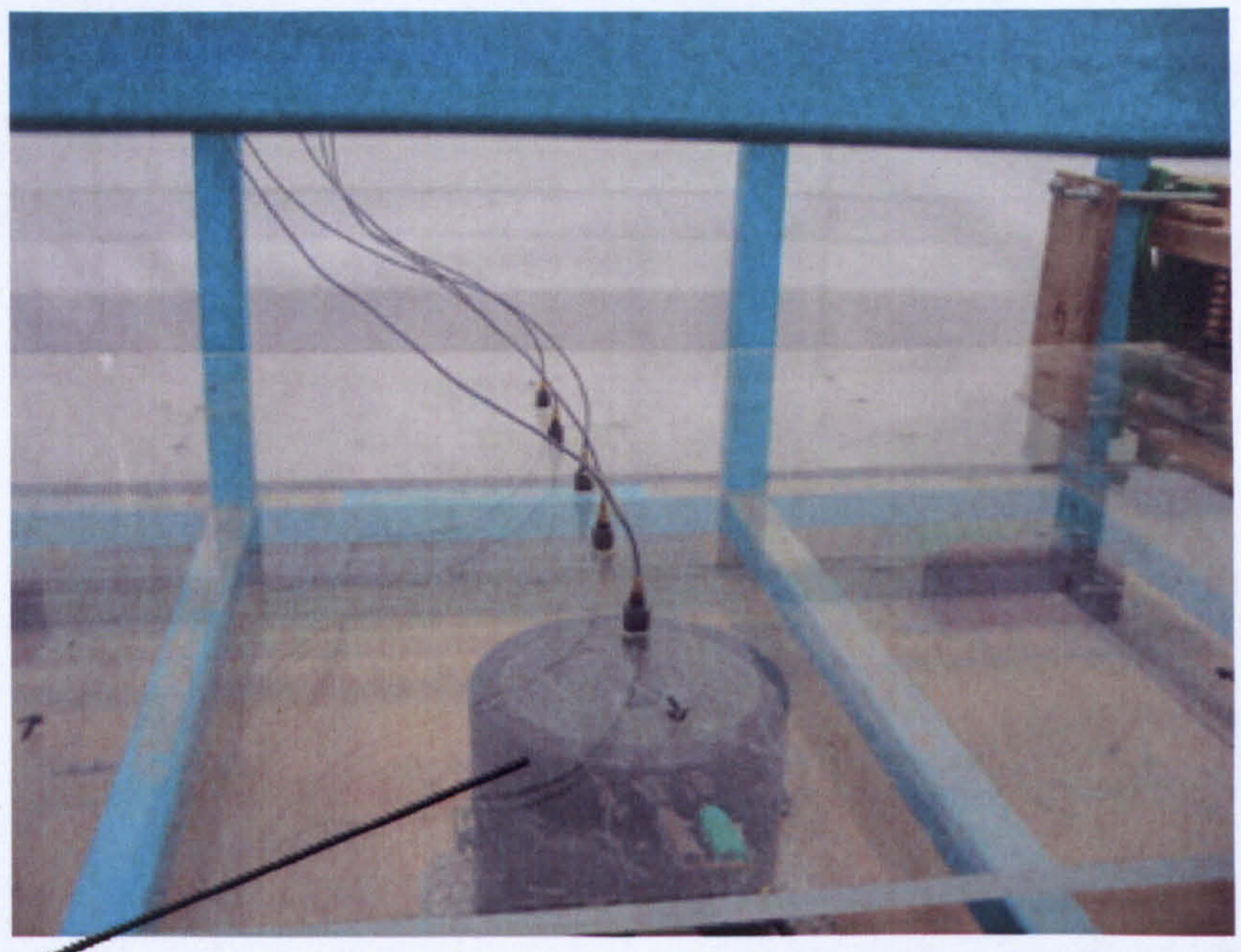

The mass shaker is an electromagnetic shaker, and essentially works in the same way as a speaker. A coil of wire is wrapped around a piece of metal, and an electrical current passed through the wire creates a magnetic field around the coil, magnetizing the metal it is wrapped around. The field acts just like the magnetic field around a permanent magnet: It has a polar orientation, a "north" end and a "south" end, and it is attracted to iron objects. Unlike a permanent magnet, in an electromagnet you can alter the orientation of the poles. If the flow of the current were reversed, the north and south ends of the electromagnet switch, hence the oscillatory movement of the mass shaker.

Figure 3.24 Mass shaker attached to plate with beeswax at excitation point 14

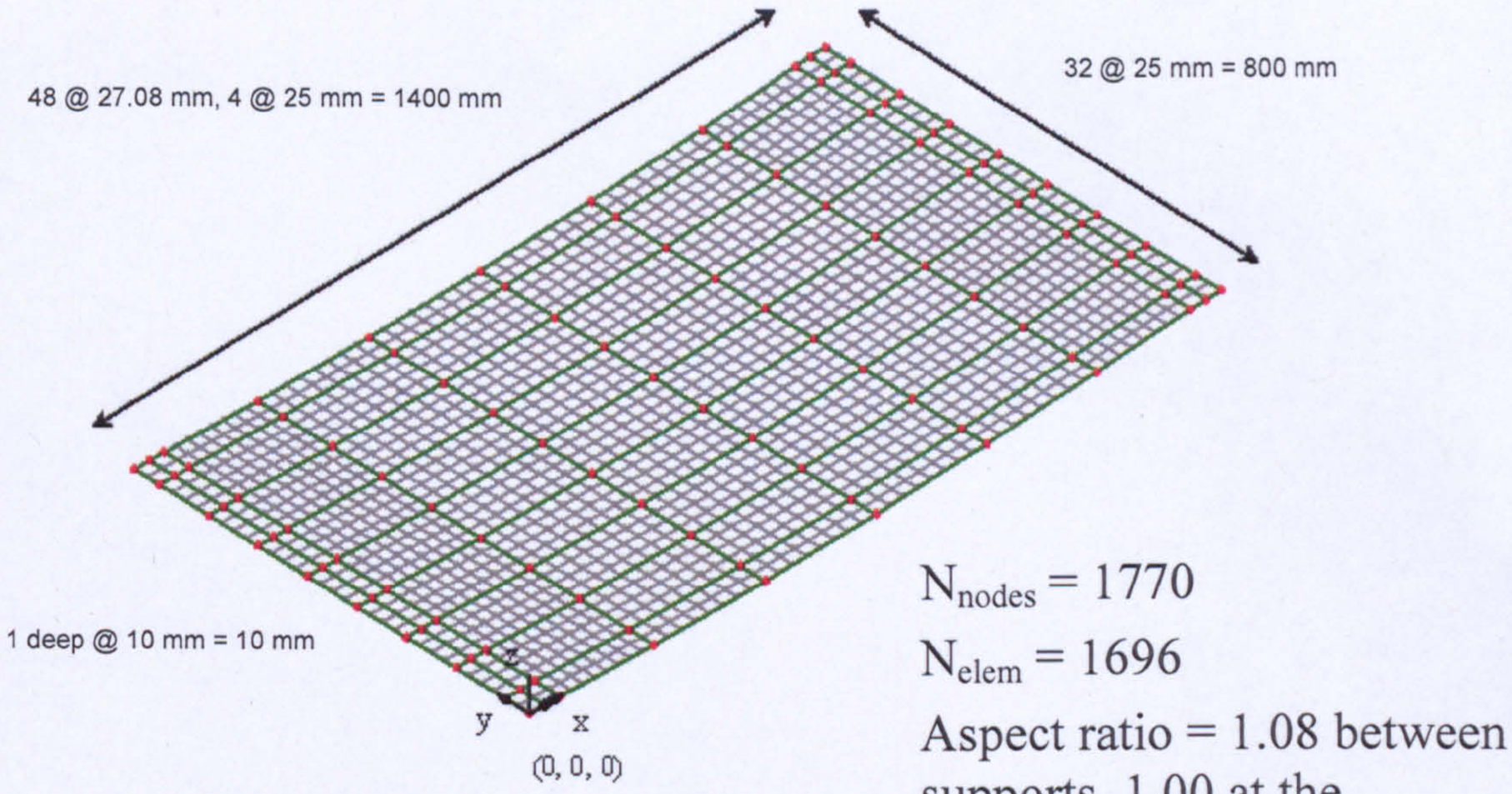

Figure 3.25 FEA model geometry and mesh refinement

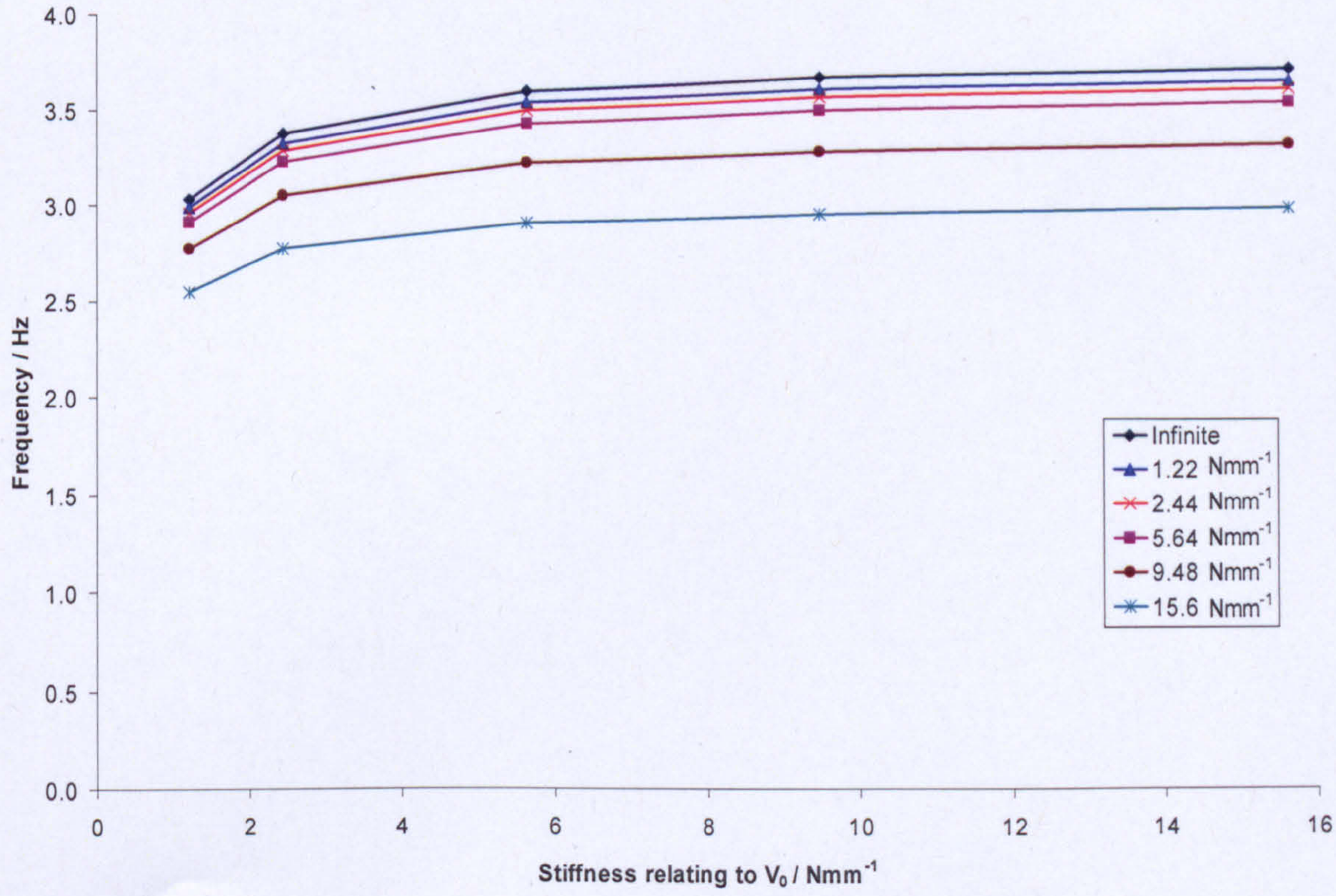

Figure 3.26 Effect of stiffness at V_L on resonance frequency due to 10 N loading

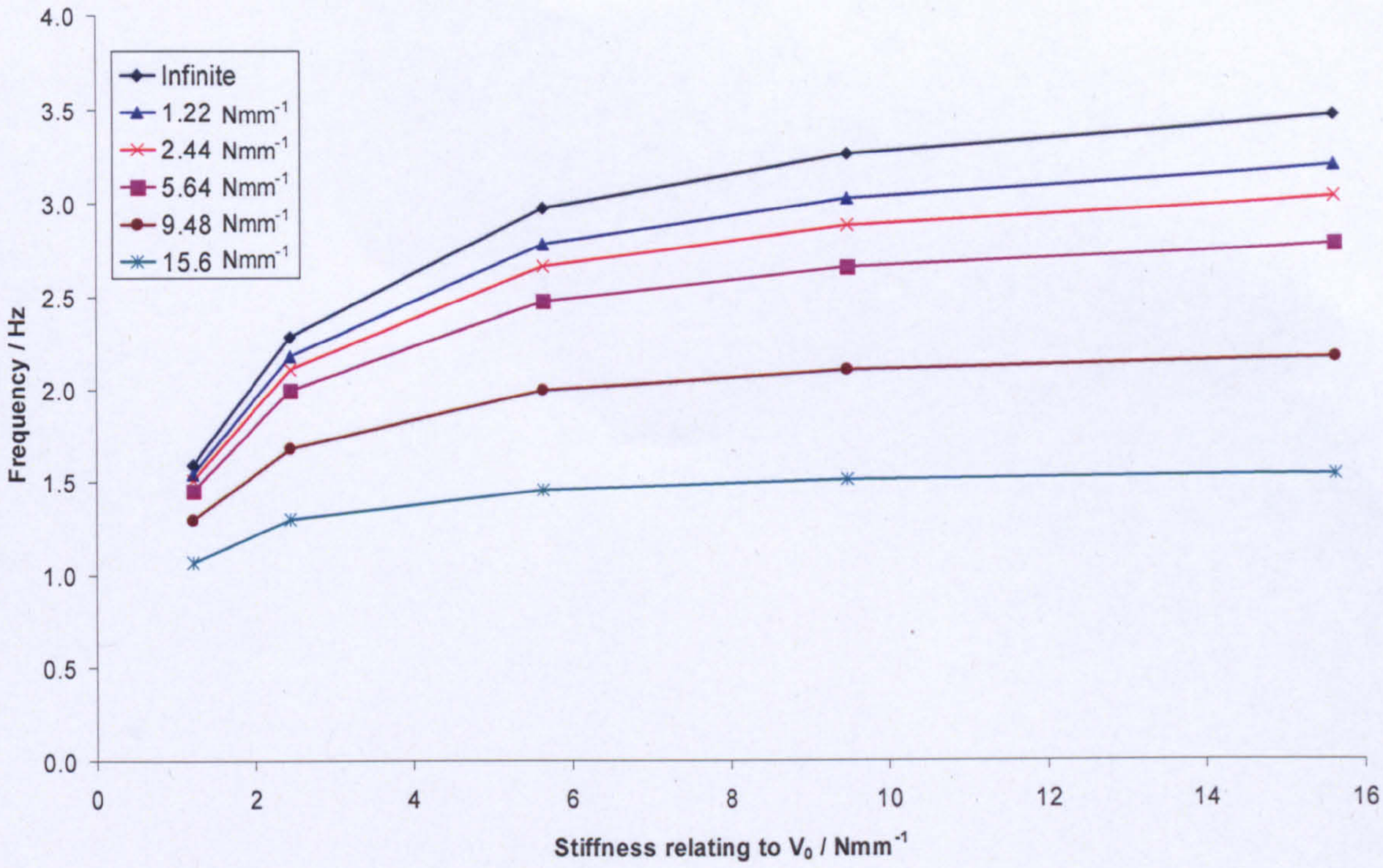

Figure 3.27 Effect of stiffness at V_L on resonance frequency due to 50 N loading.

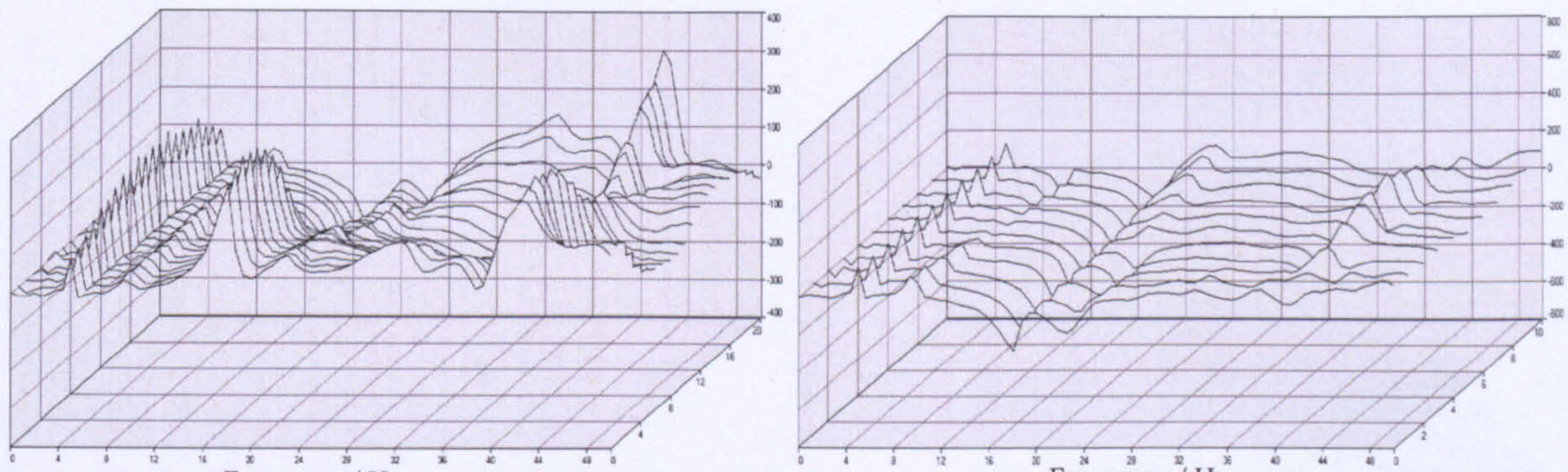

Accelerometer point 1 (250, 200)

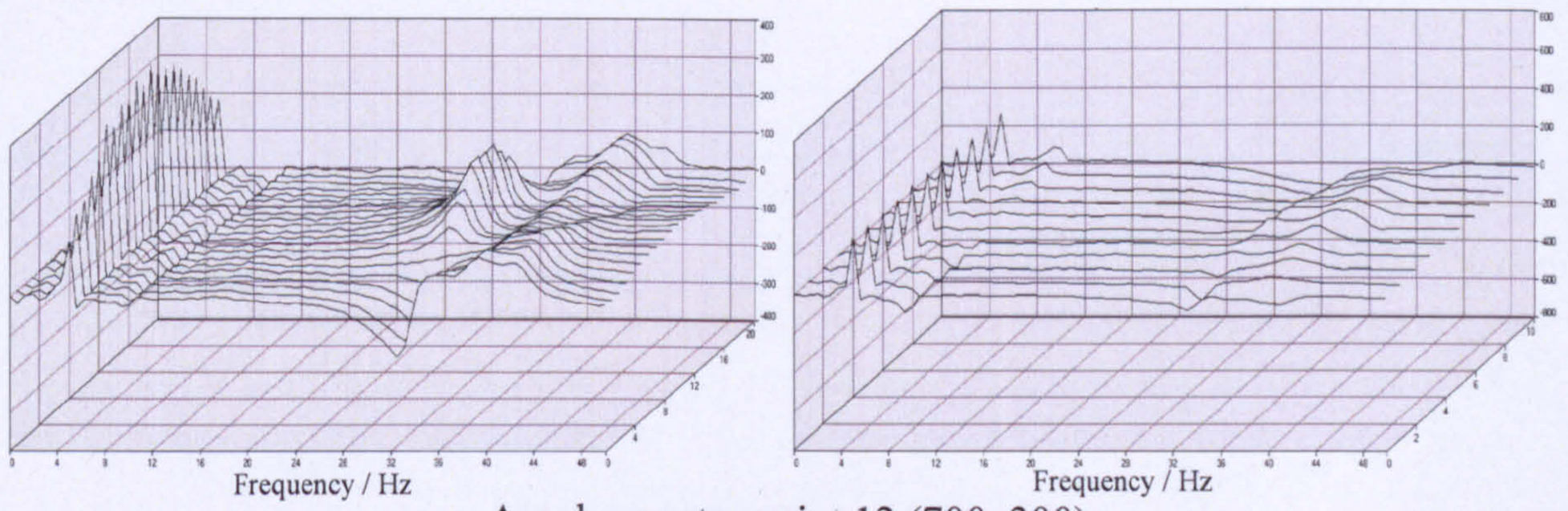

Accelerometer point 12 (700, 300)

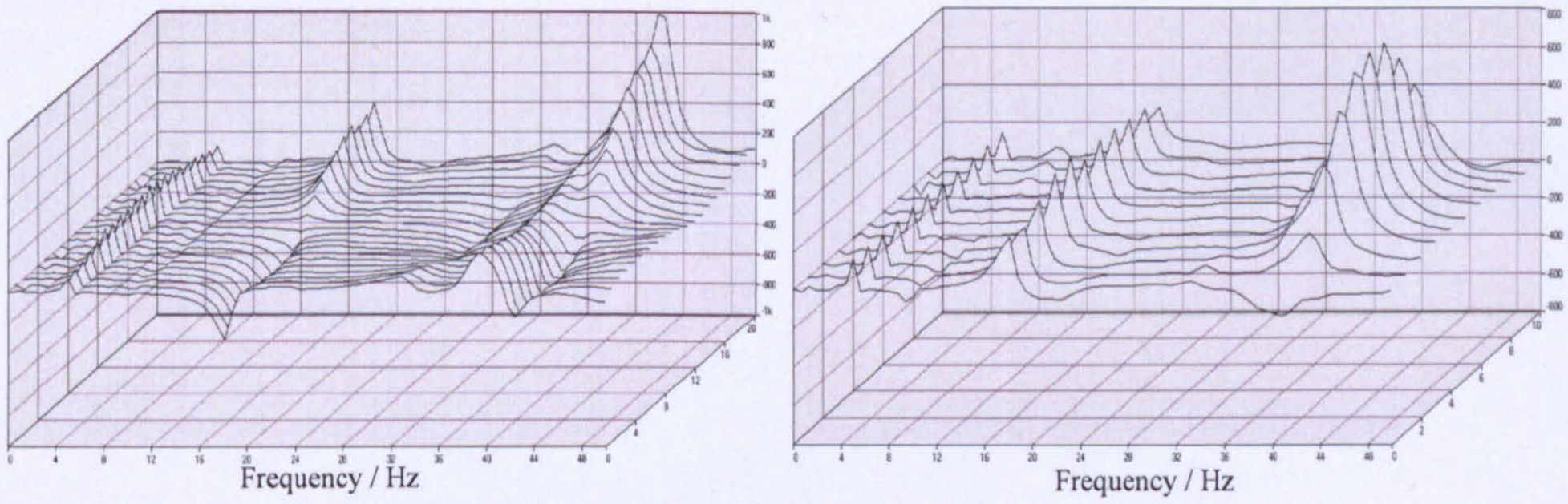

Accelerometer point 25 (1250, 700)

Longitudinal mode shapes

Transverse mode shapes

Figure 3.28 Mode shapes in free support condition

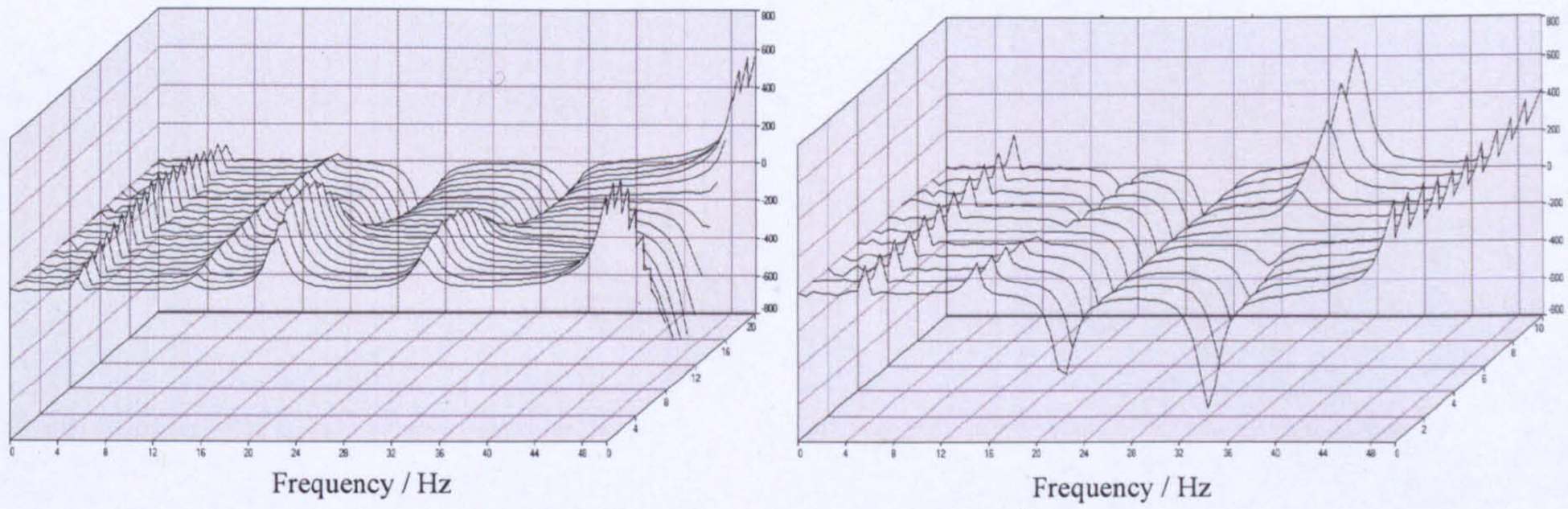

Accelerometer point 1 (250, 200)

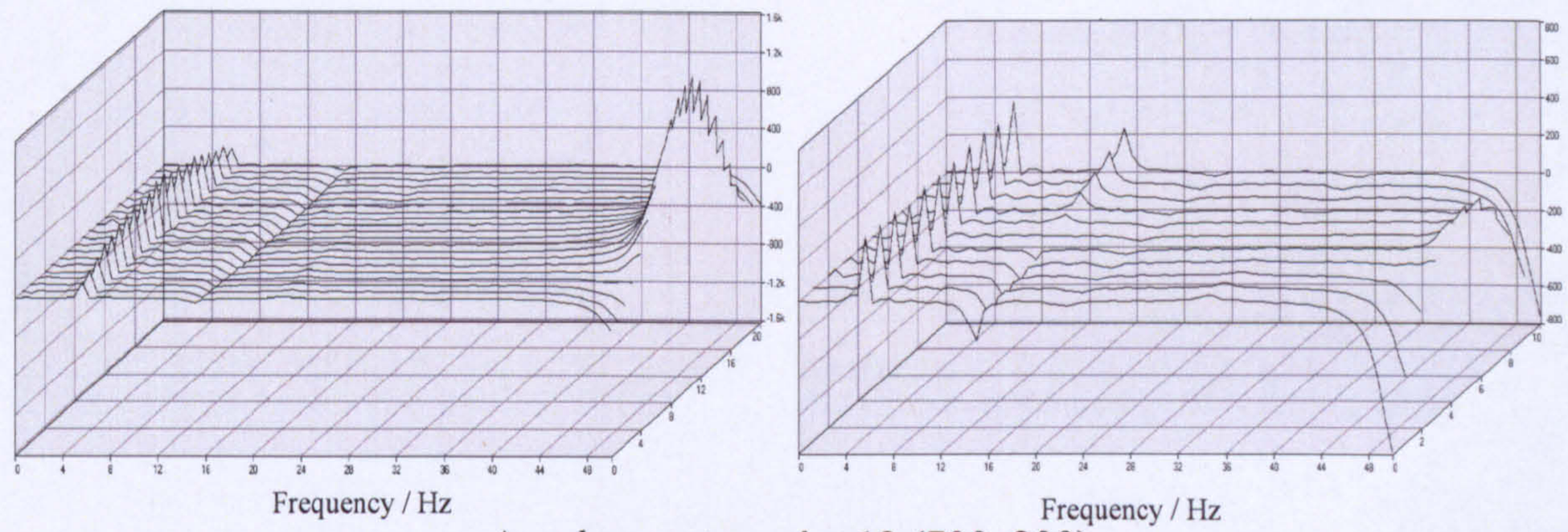

Accelerometer point 12 (700, 300)

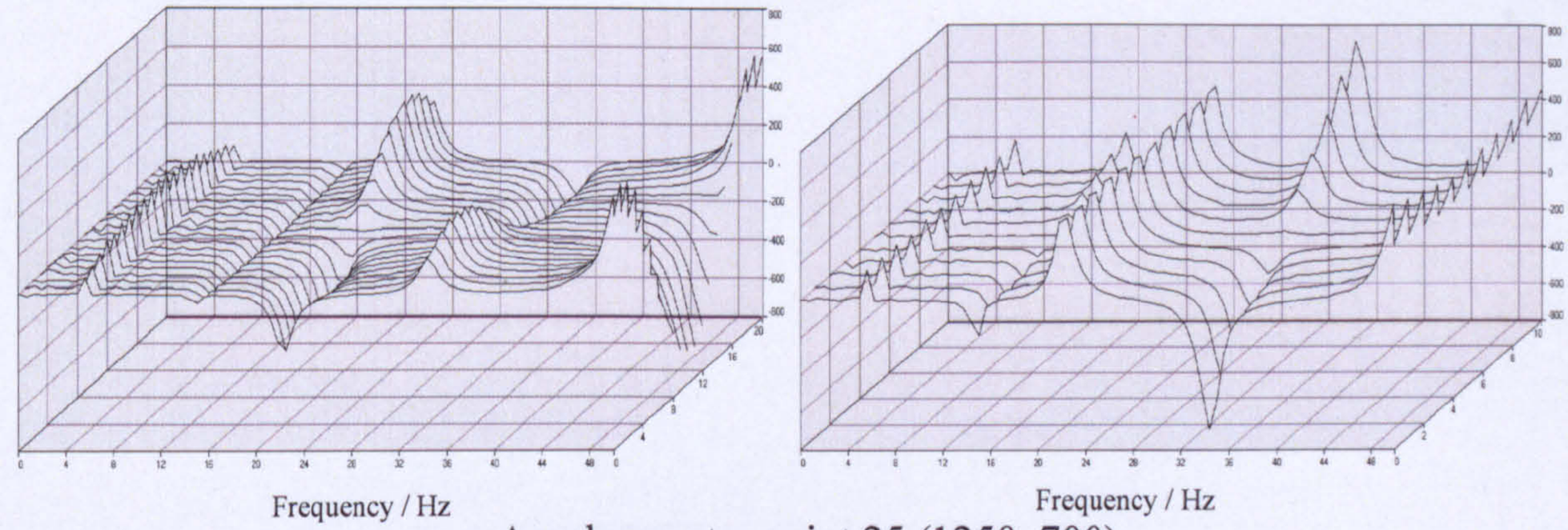

Accelerometer point 25 (1250, 700)

Longitudinal mode shapes

Transverse mode shapes

Figure 3.29 Mode shapes in simply supported condition

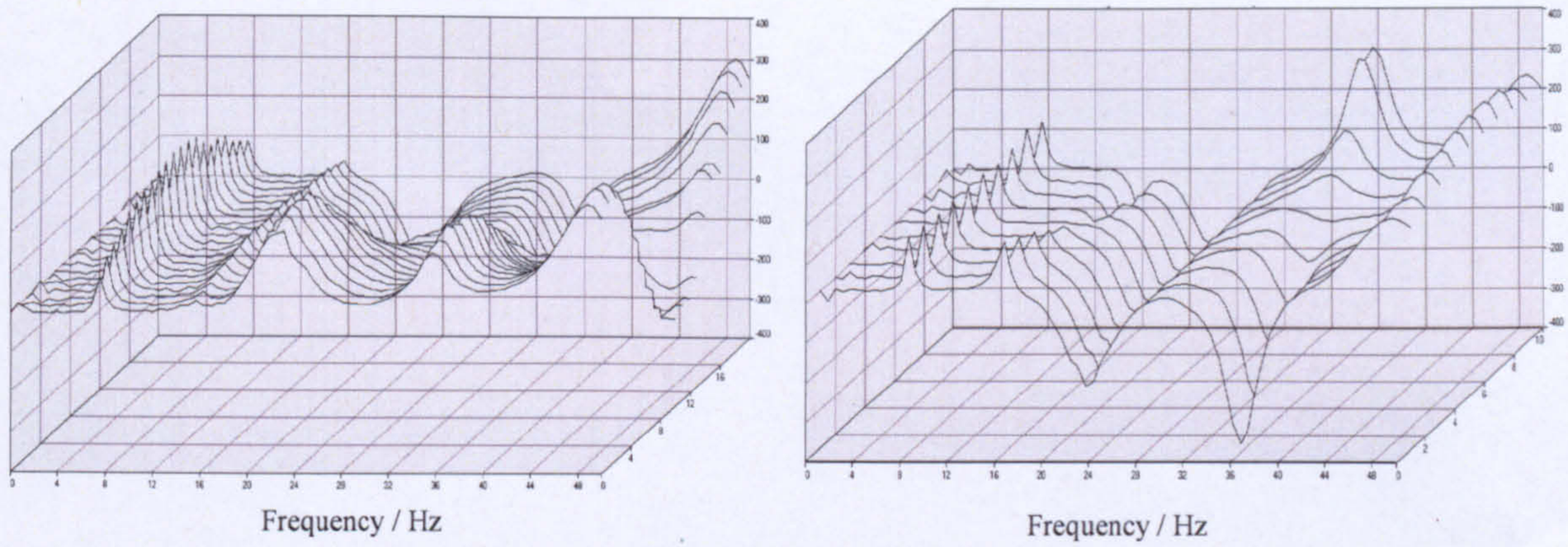

Figure 3.30 Mode shapes in fully fixed condition

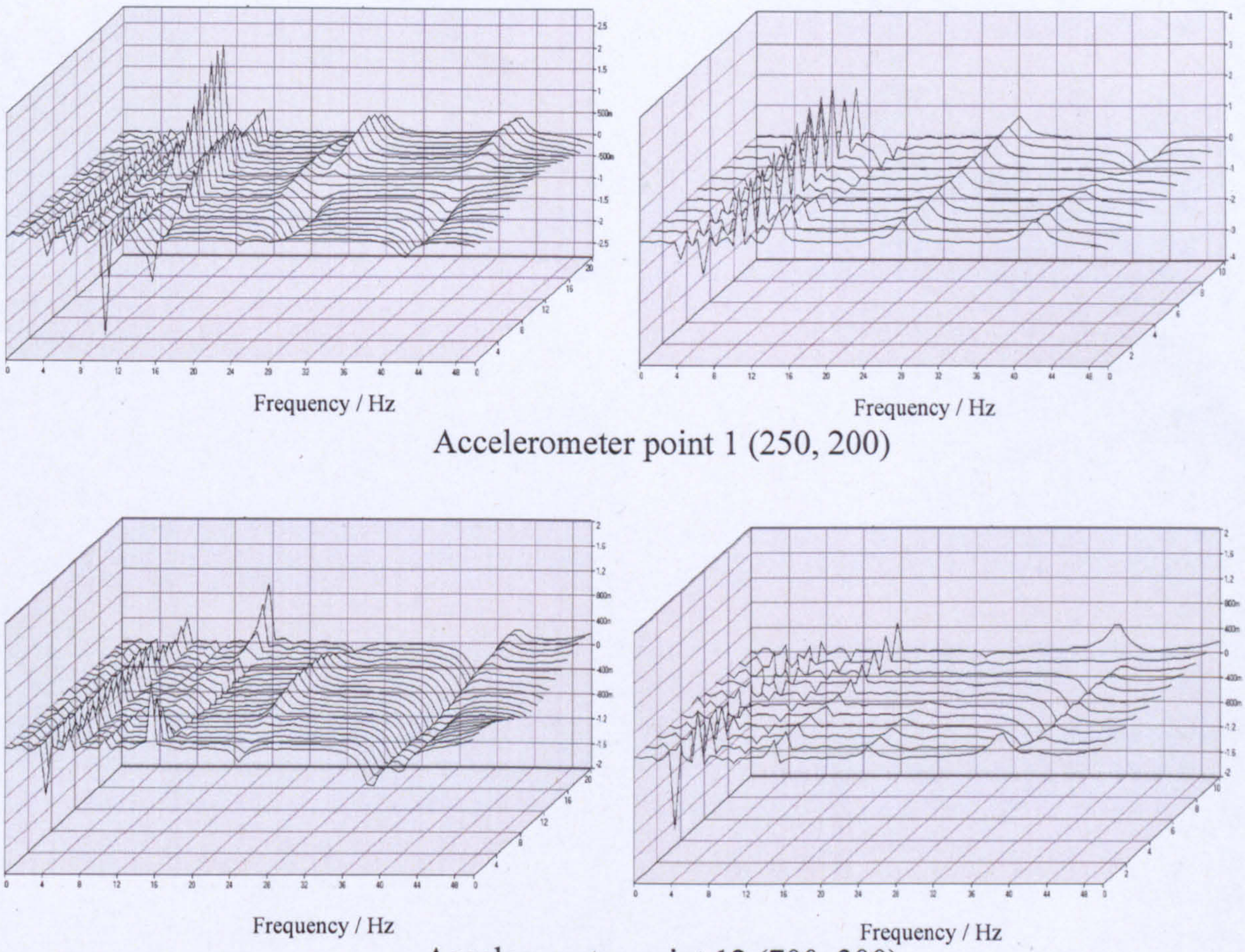

Figure 3.31 Mode shapes in spring support condition 1

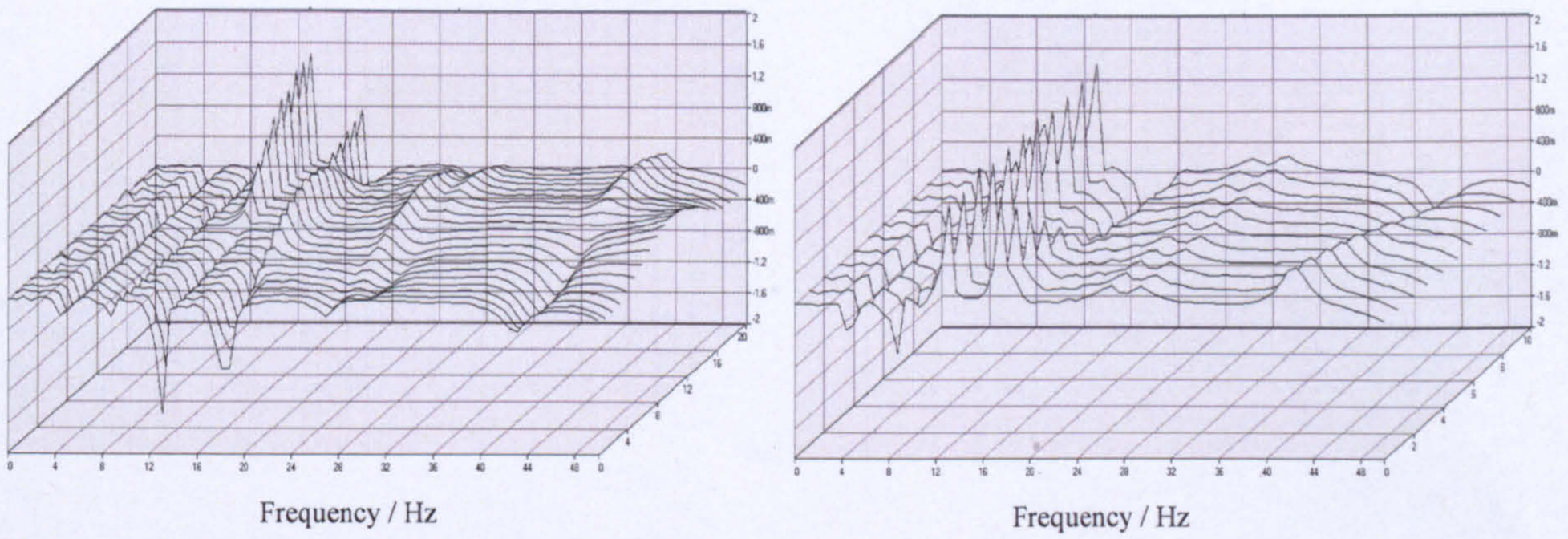

Accelerometer point 1 (250, 200)

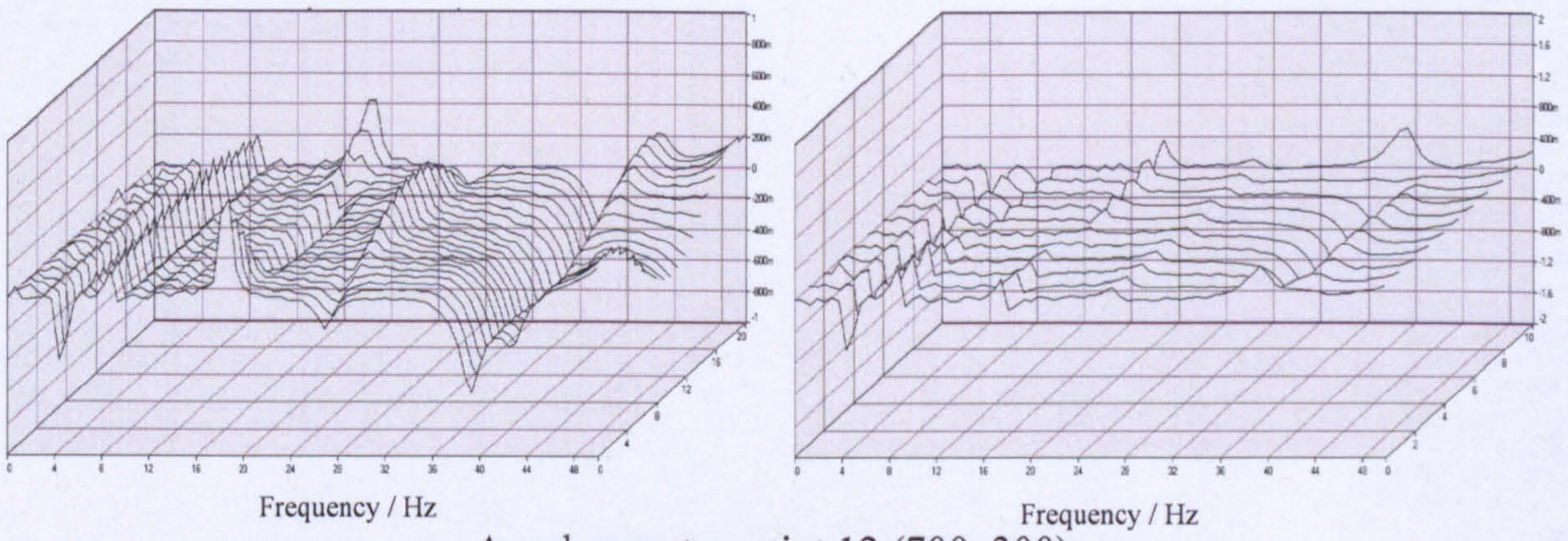

Accelerometer point 12 (700, 300)

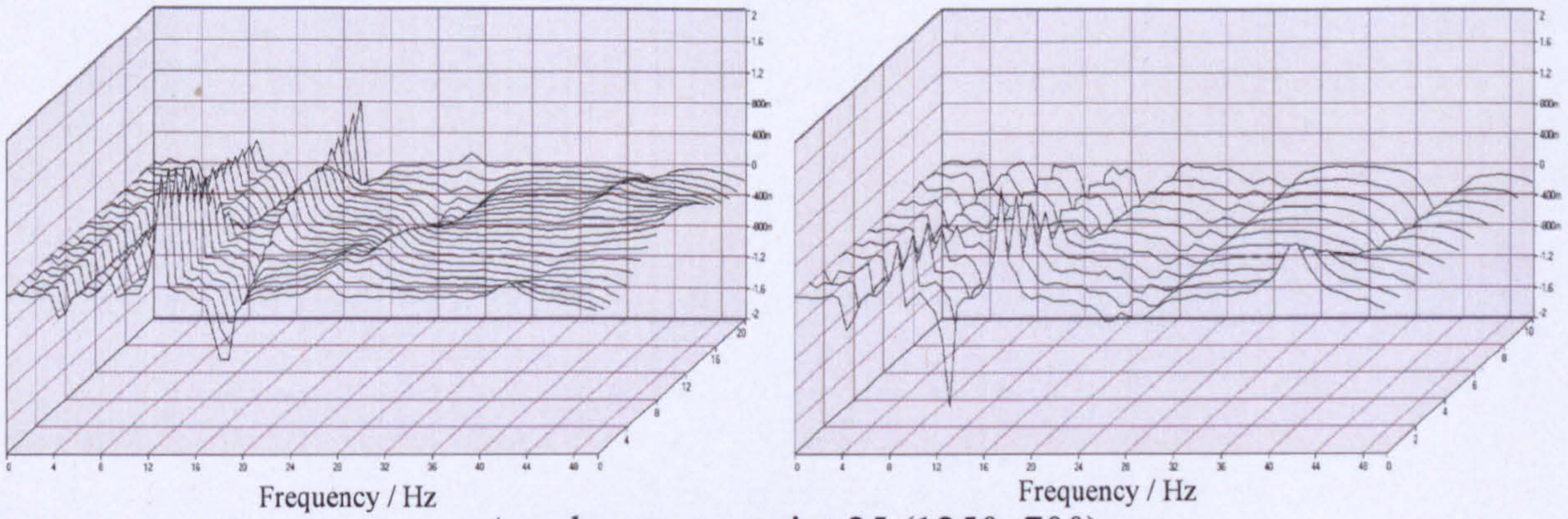

Accelerometer point 25 (1250, 700)

Longitudinal mode shapes

Transverse mode shapes

Figure 3.32 Mode shapes in spring support condition 2

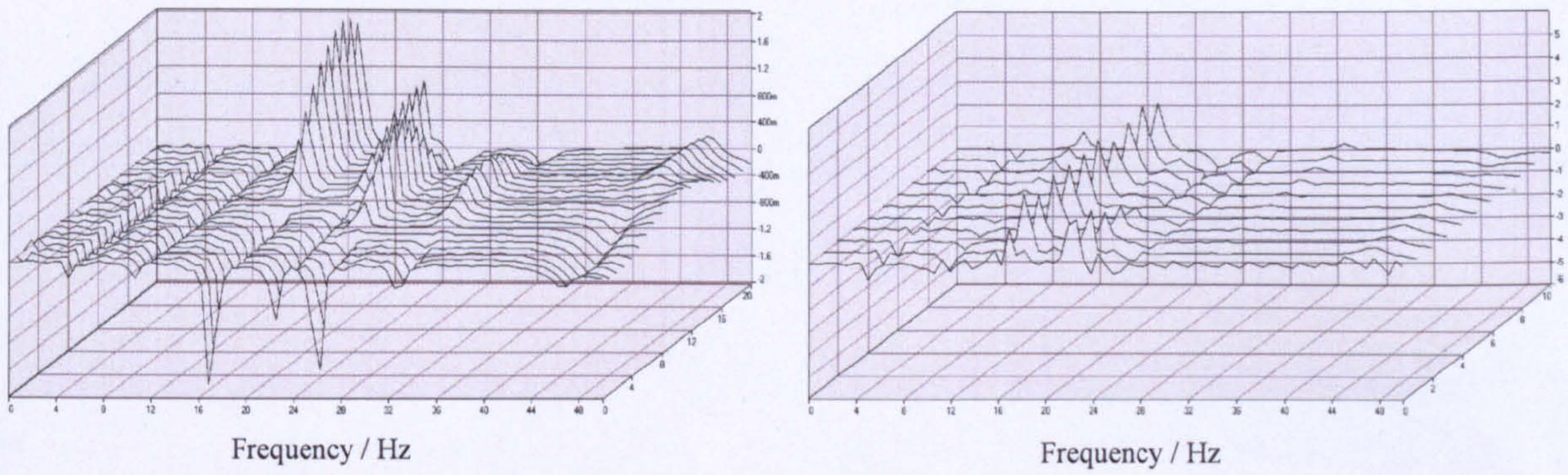

Accelerometer point 1 (250, 200)

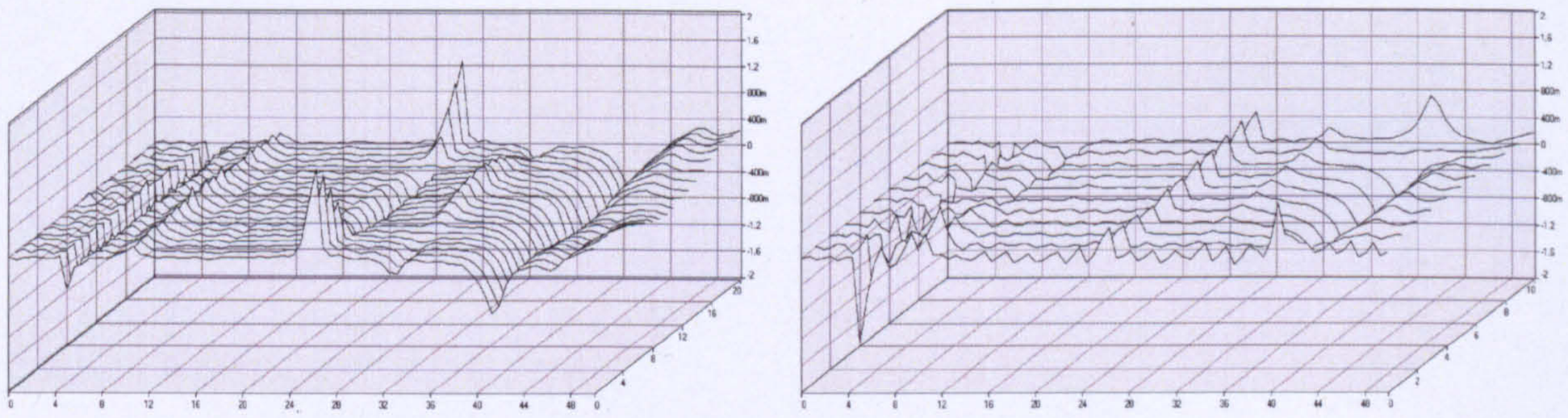

Accelerometer point 12 (700, 300)

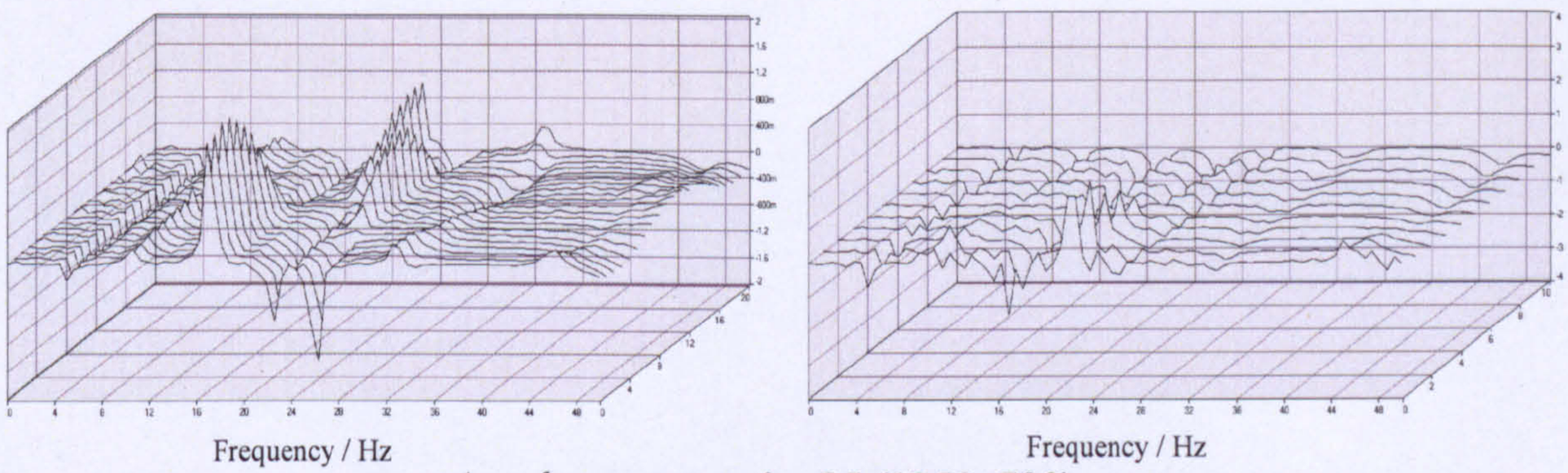

Accelerometer point 25 (1250, 700)

Longitudinal mode shapes

Transverse mode shapes

Figure 3.33 Mode shapes in spring support condition 3

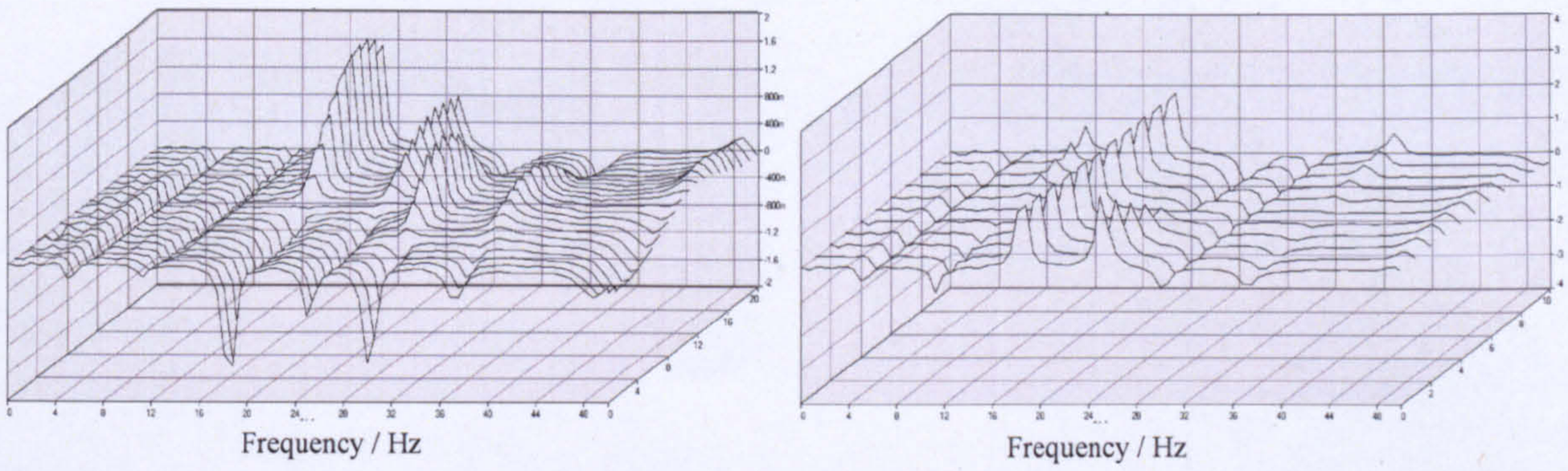

Accelerometer point 1 (250, 200)

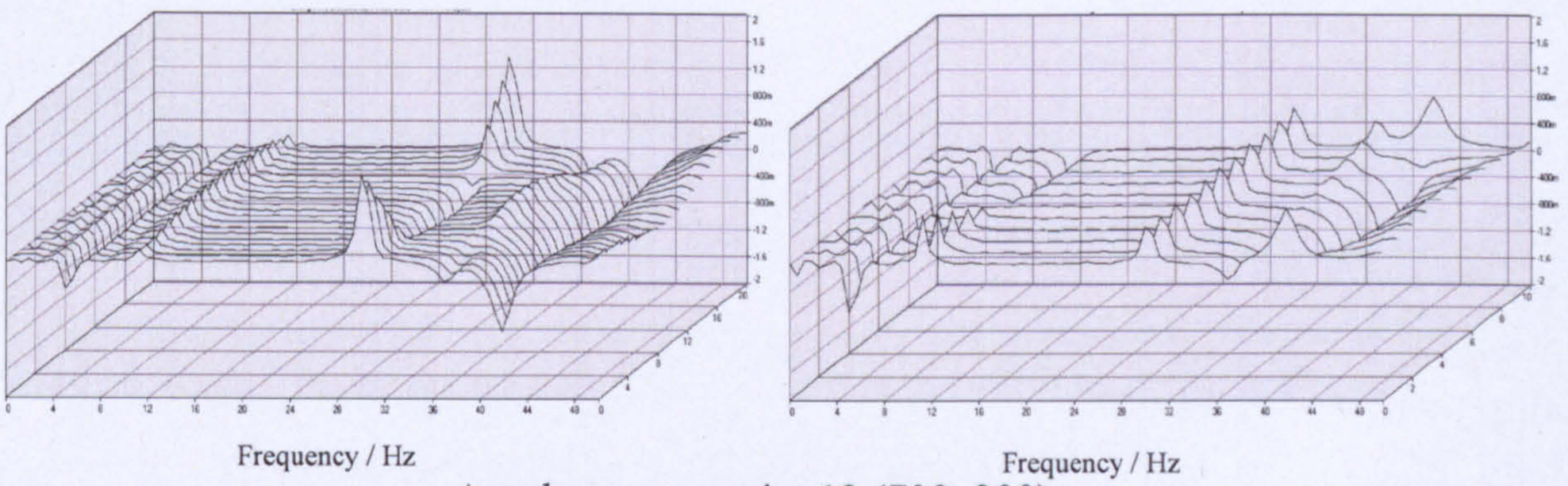

Accelerometer point 12 (700, 300)

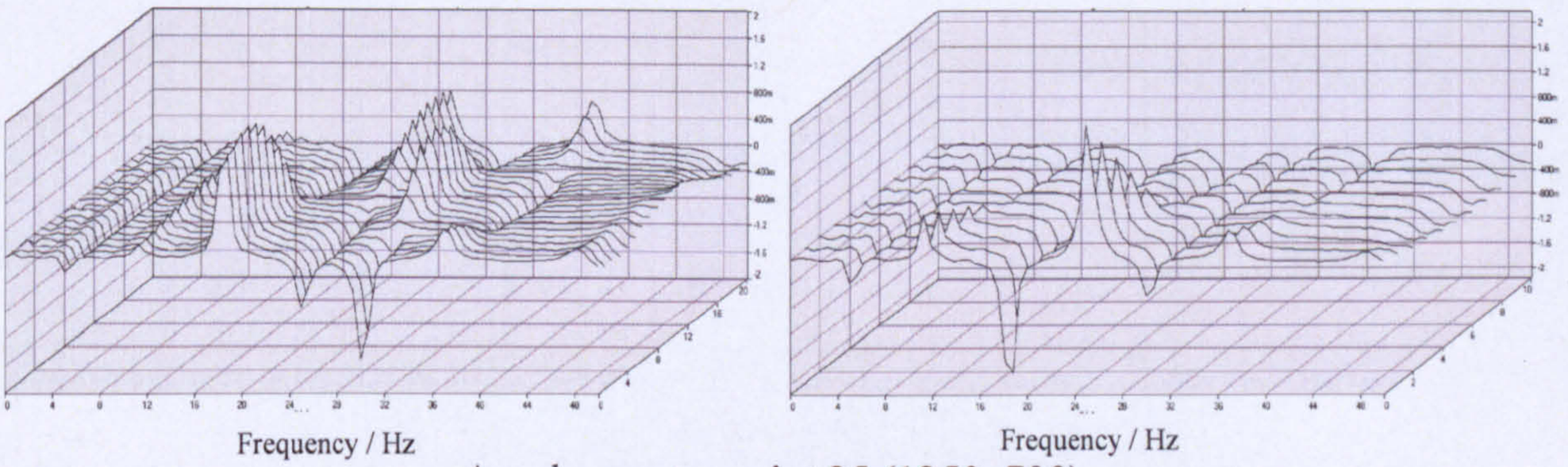

Accelerometer point 25 (1250, 700)

Longitudinal mode shapes

Transverse mode shapes

Figure 3.34 Mode shapes in spring support condition 4

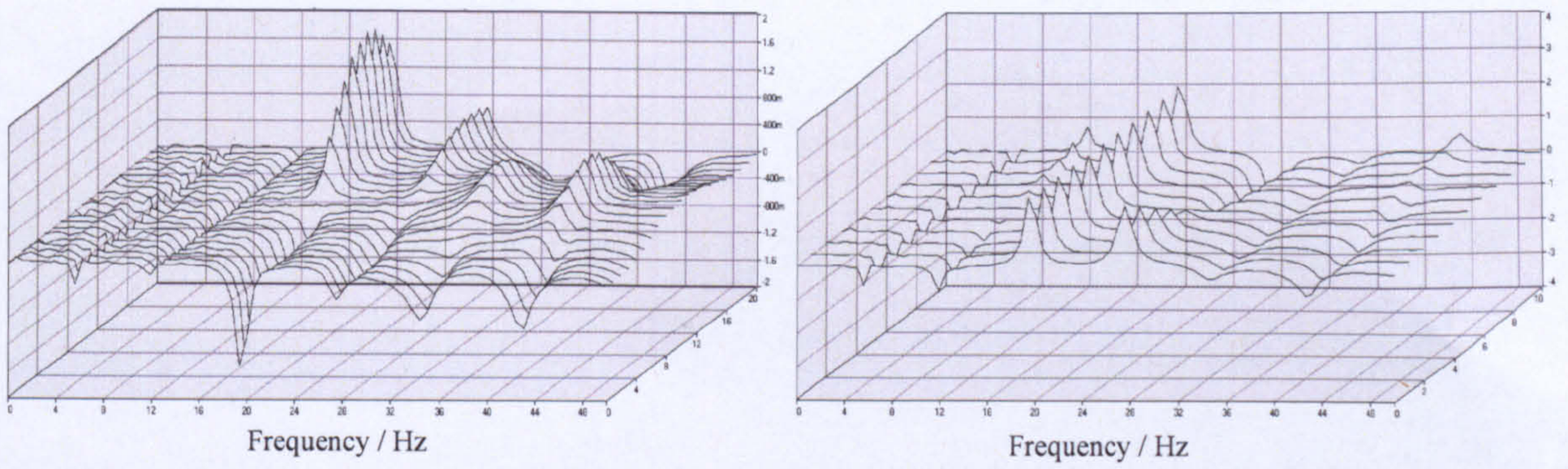

Accelerometer point 1 (250, 200)

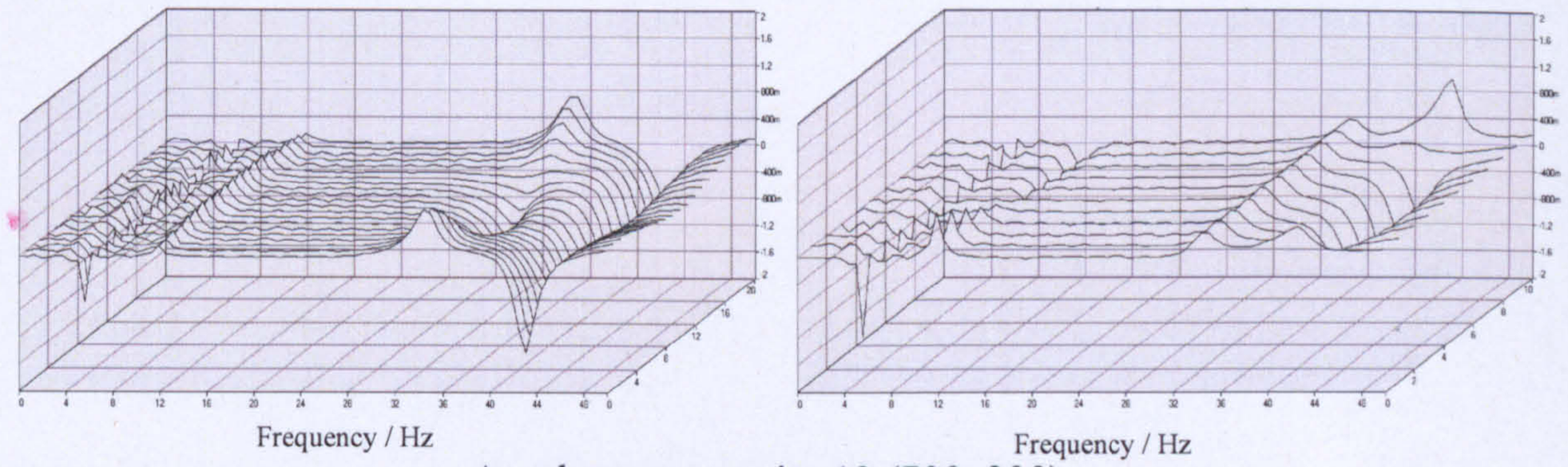

Accelerometer point 12 (700, 300)

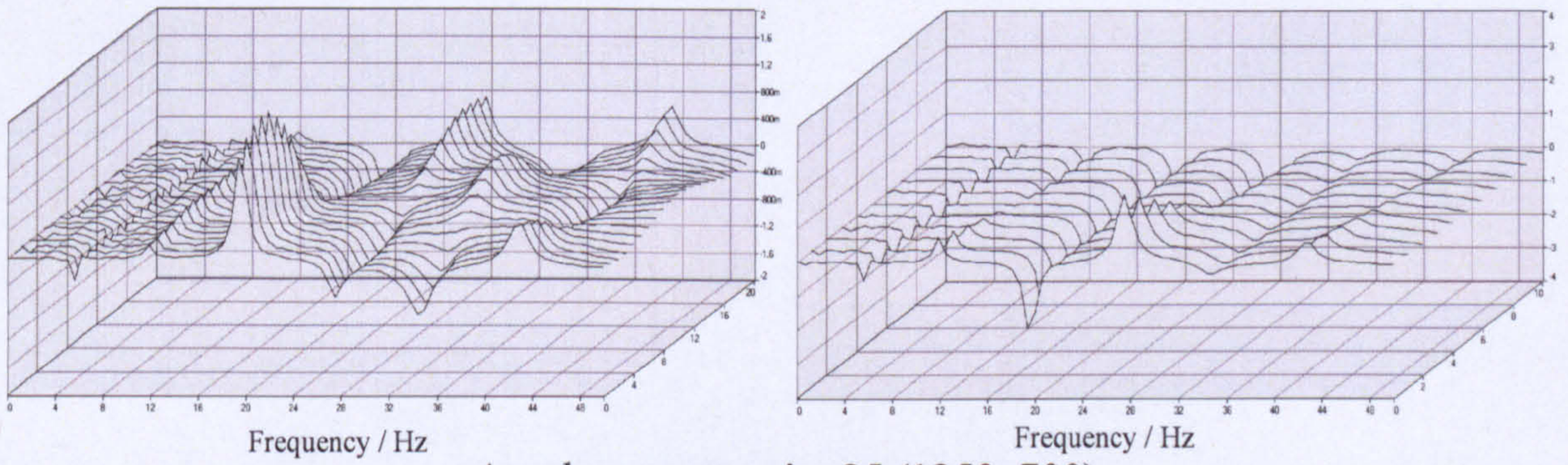

Accelerometer point 25 (1250, 700)

Longitudinal mode shapes Transverse mode shapes

Figure 3.35 Mode shapes in spring support condition 5

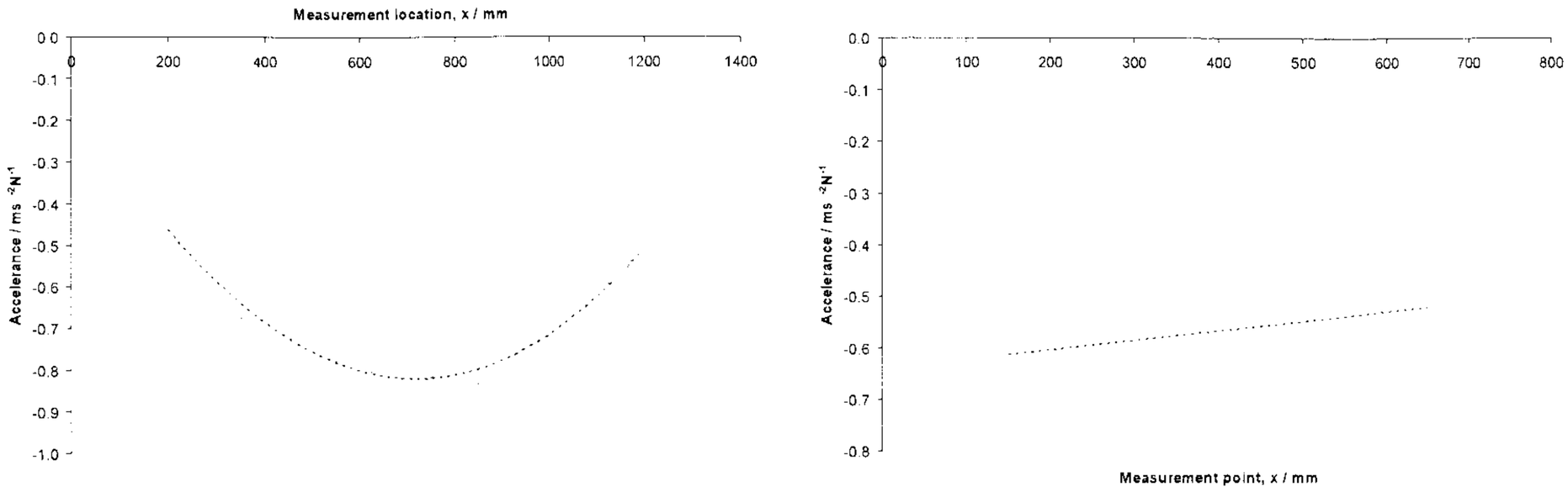

$f_0 = 4.375$ Hz

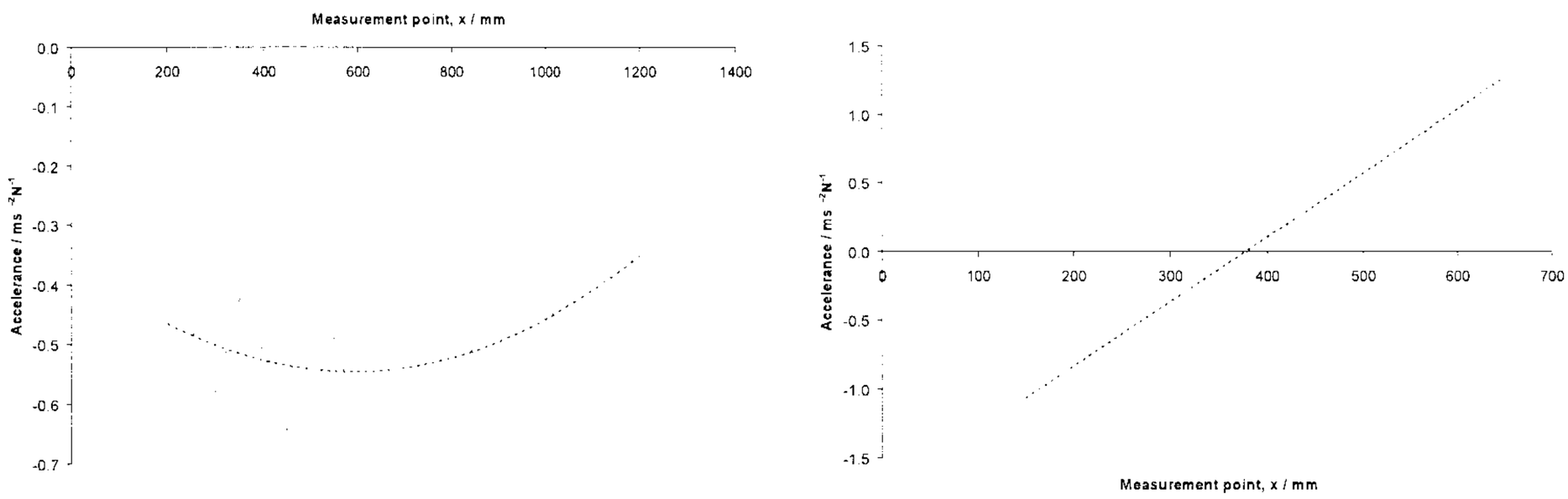

$f_1 = 6.875$ Hz

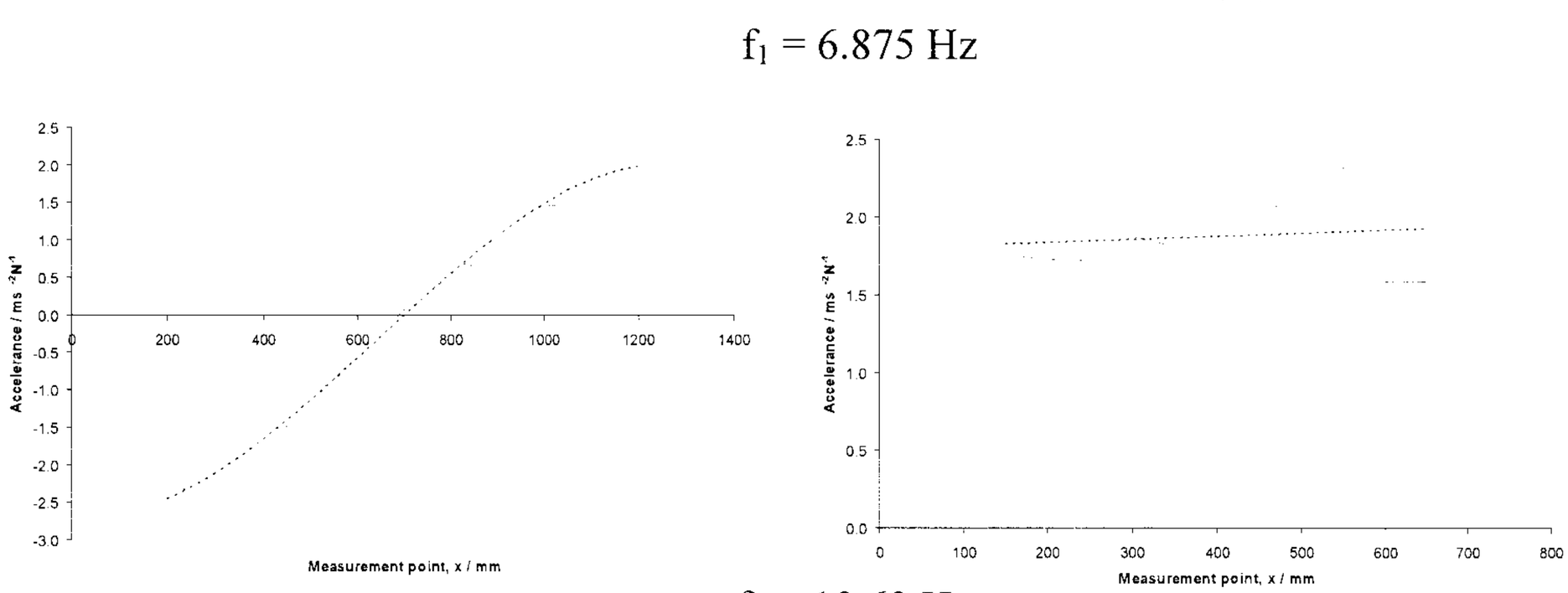

$f_2 = 10.63$ Hz

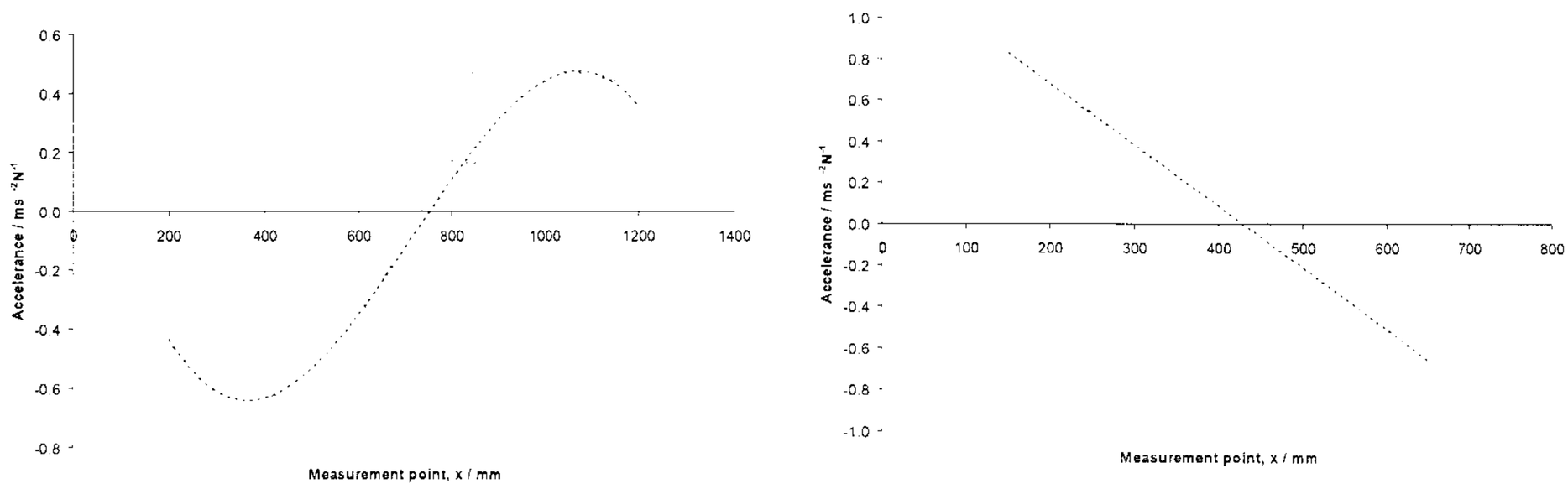

$f_8 = 42.5$ Hz

Figure 3.36 Mode shape slices in spring support condition 1

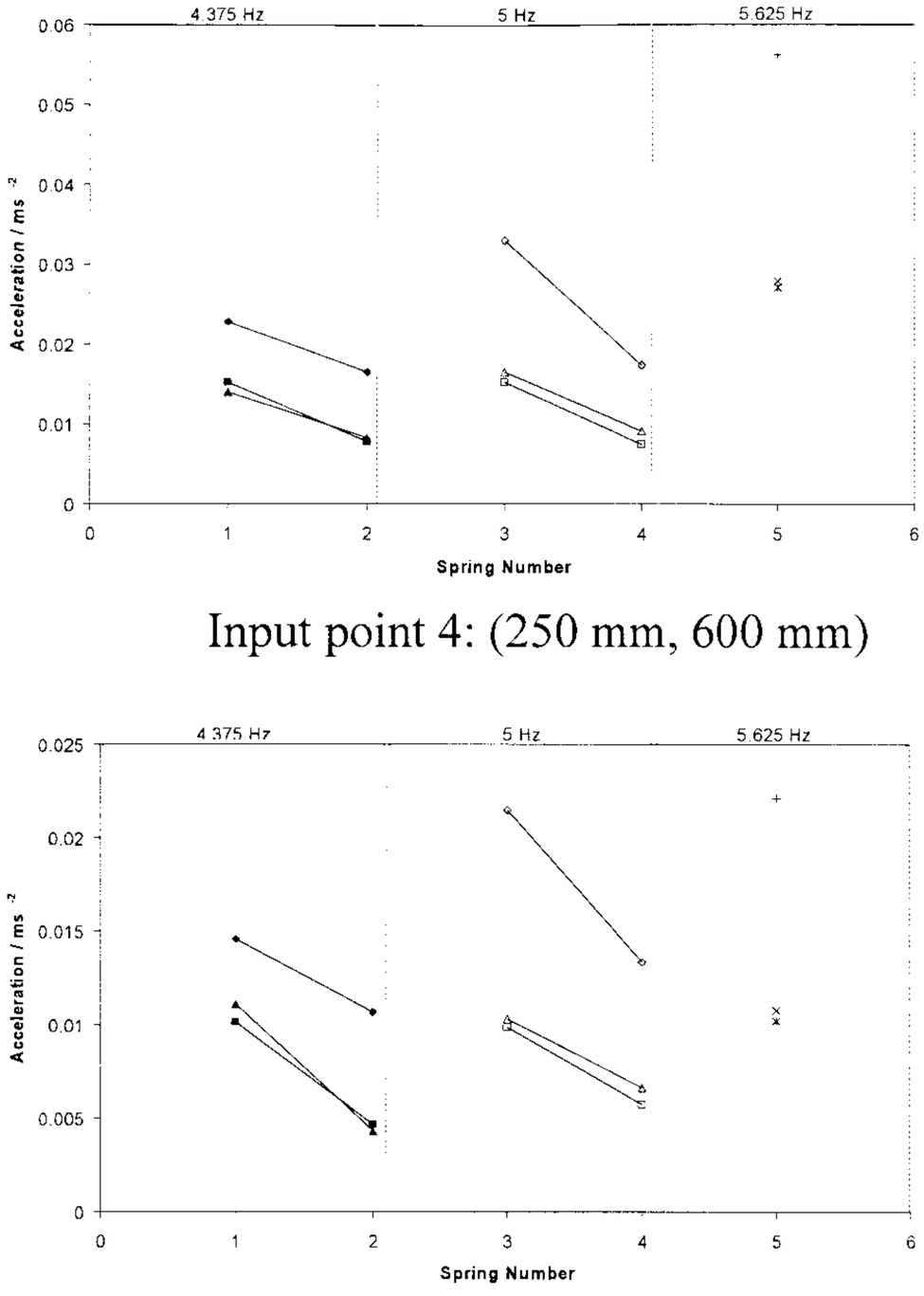

Input point 4: (250 mm, 600 mm)

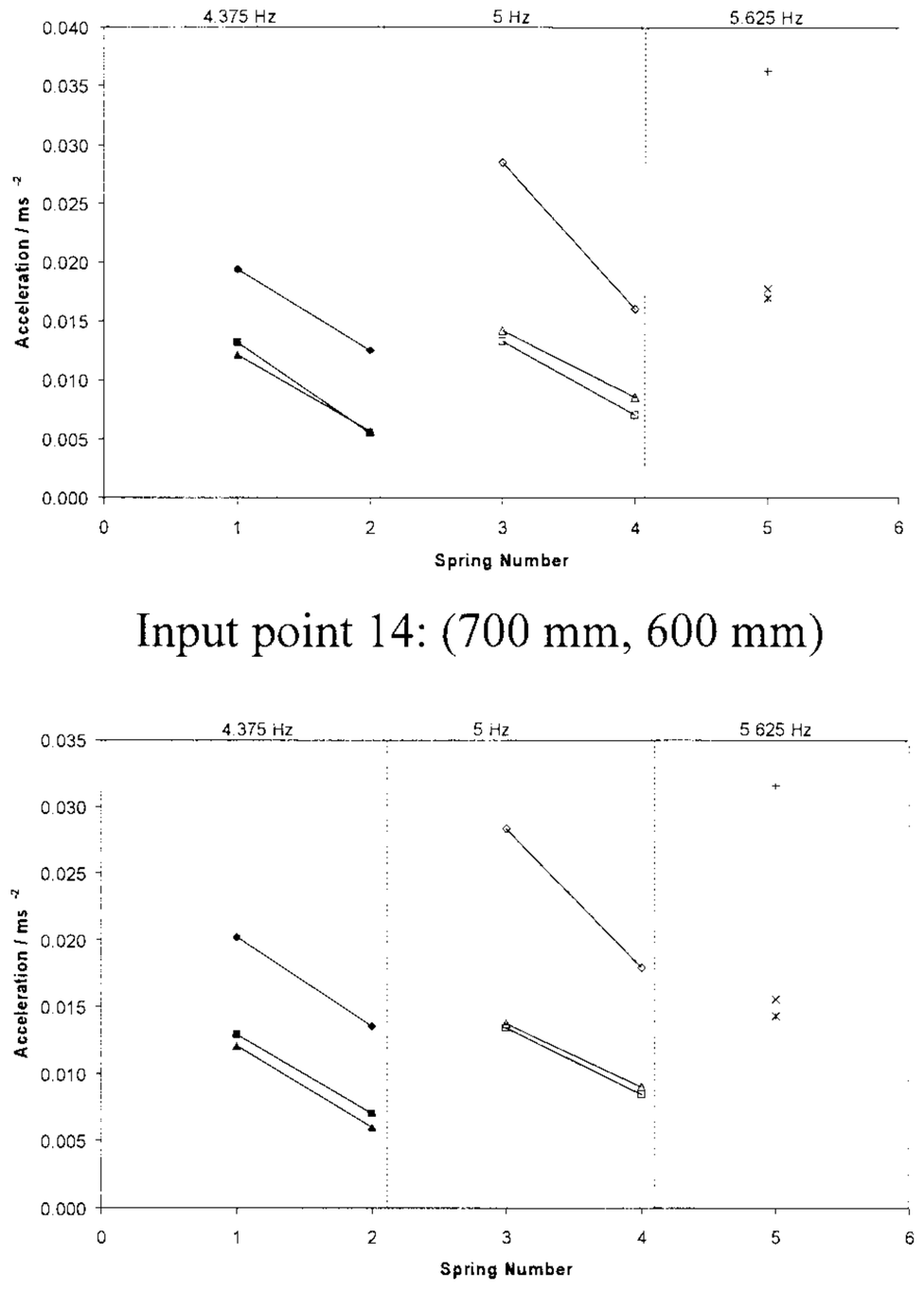

Input point 14: (700 mm, 600 mm)

Input point 7: (450 mm, 600 mm)

Input point 17: (950 mm, 600 mm)

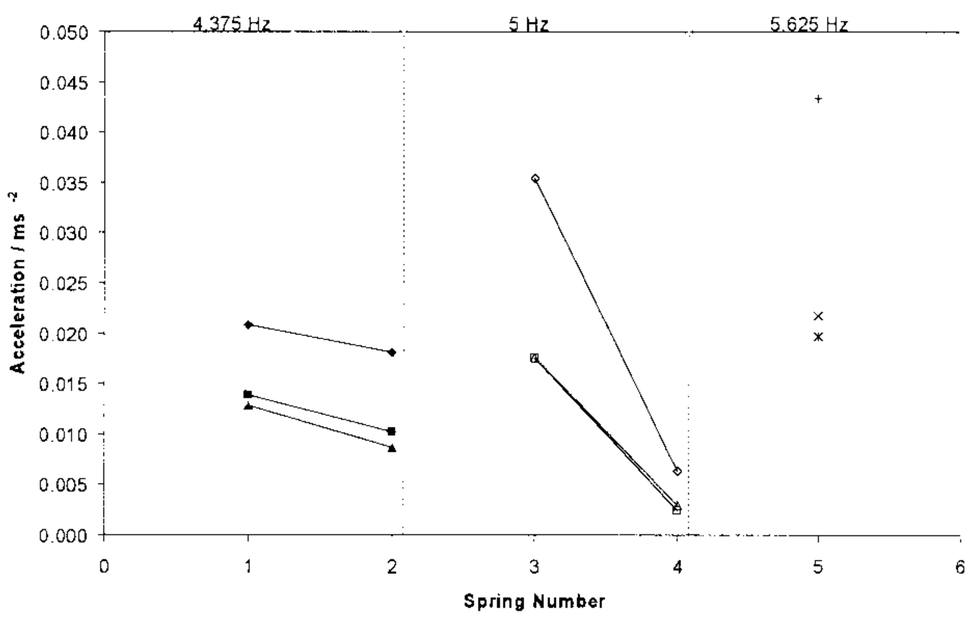

Input point 24: (1250 mm, 600 mm)

Accelerometer 25	(1250, 700)
Accelerometer 12	(700, 300)
Accelerometer 1	(250, 200)
Accelerometer 25	(1250, 700)
Accelerometer 12	(700, 300)
Accelerometer 1	(250, 200)
Accelerometer 25	(1250, 700)
Accelerometer 12	(700, 300)
Accelerometer 1	(250, 200)

Figure 3.37 Forced vibration response of springs for first mode shape

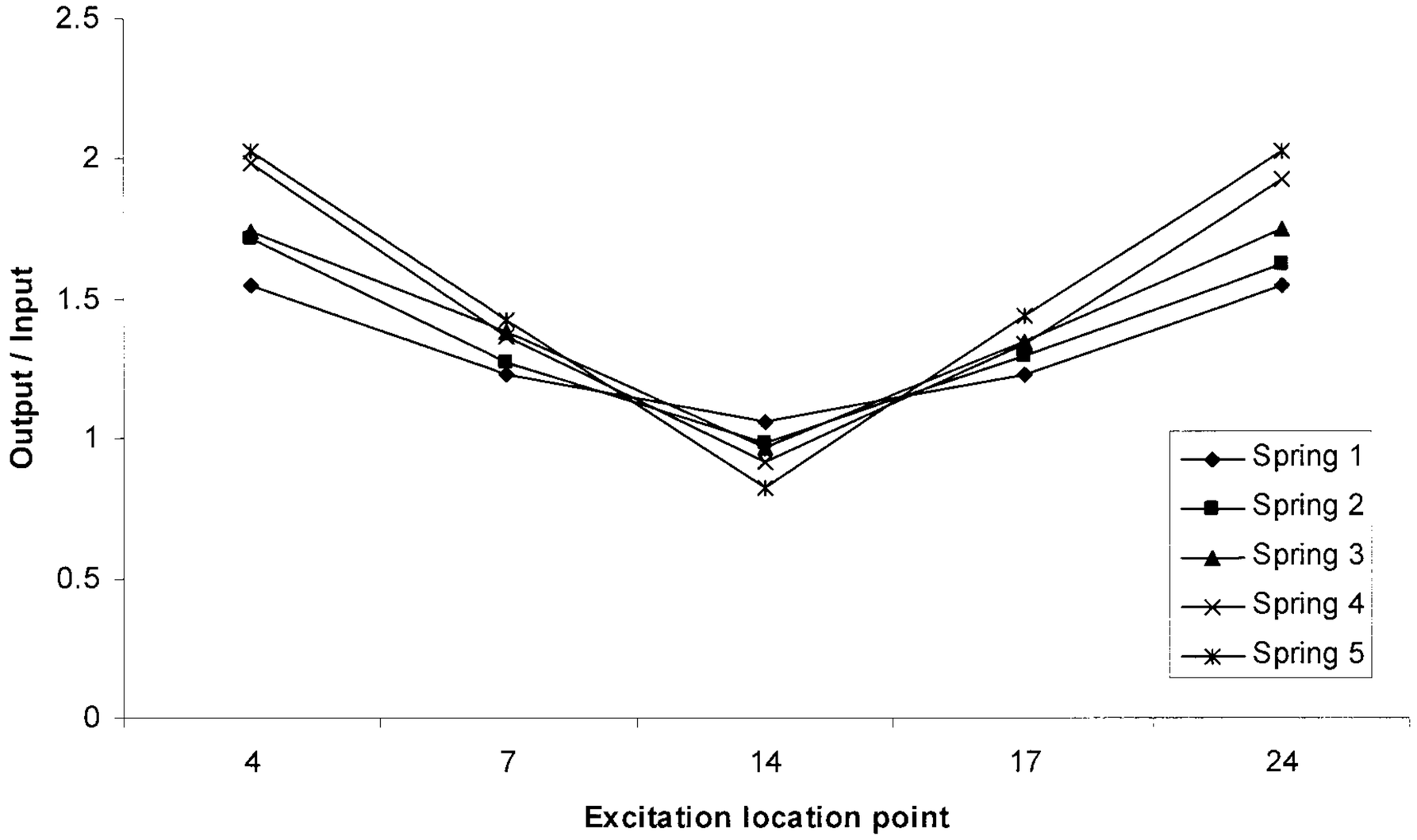

Figure 3.38 Acceleration response at mid-span – test 1

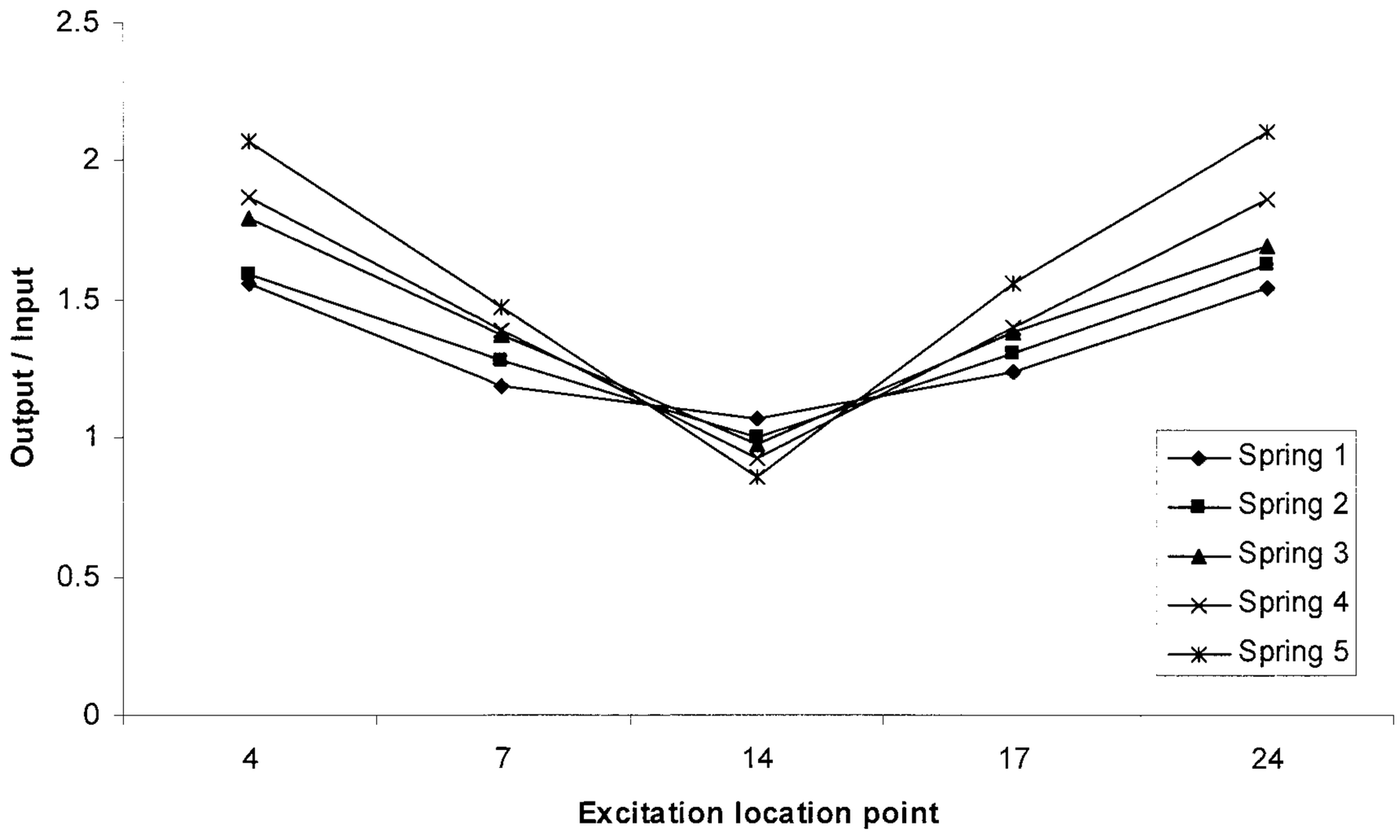

Figure 3.39 Acceleration response at mid-span – test 2

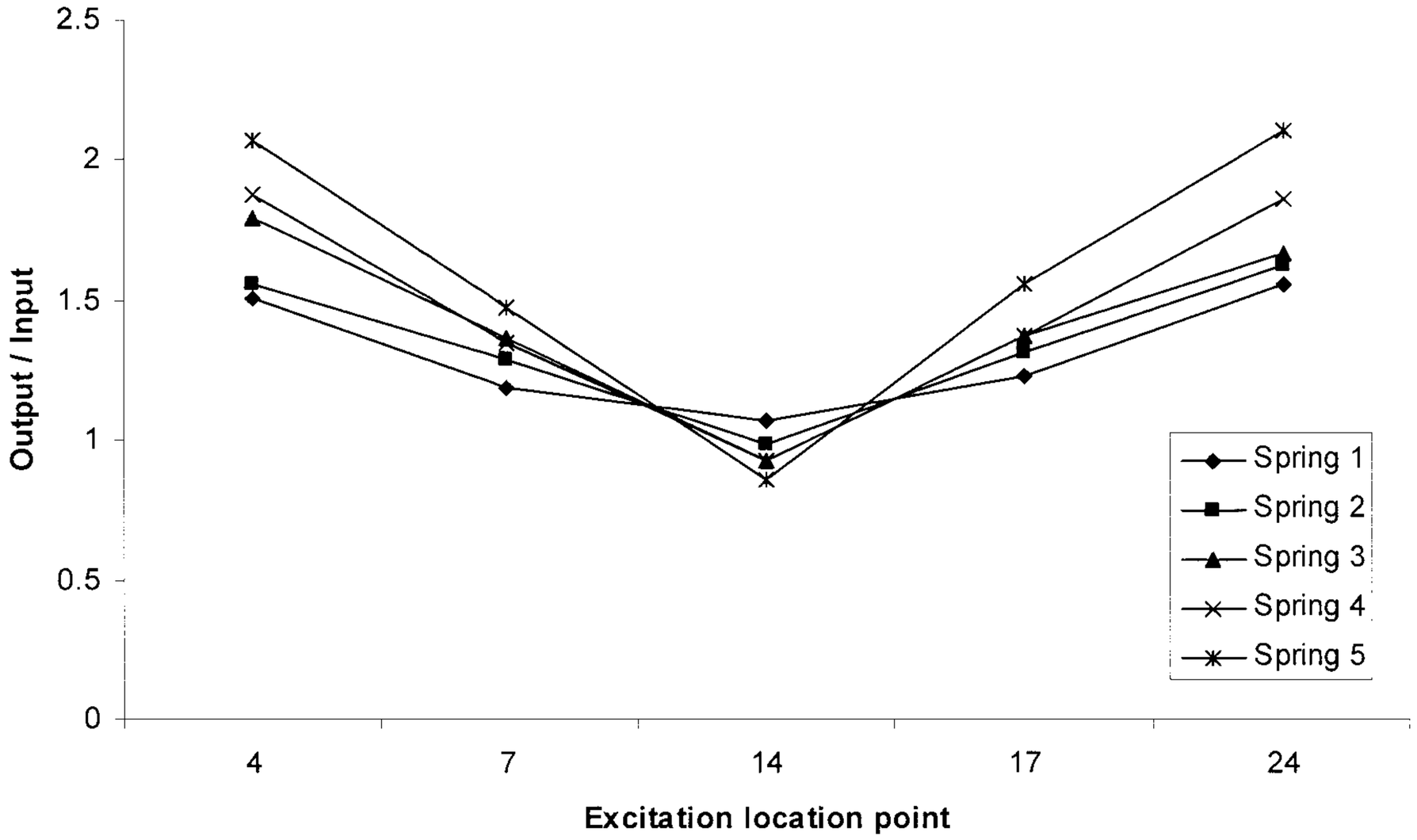

Figure 3.40 Acceleration response at mid-span – test 3

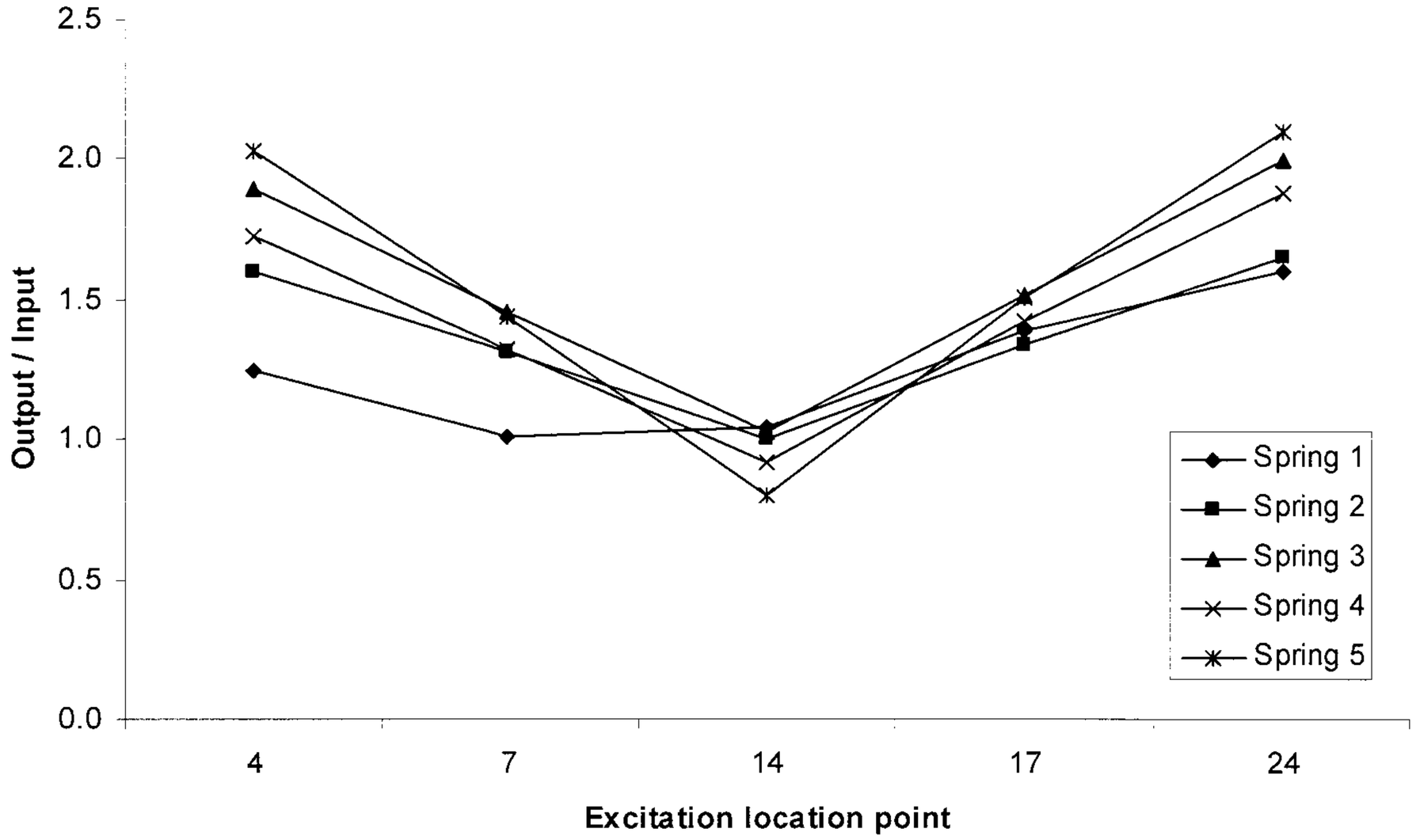

Figure 3.41 Velocity response at mid-span

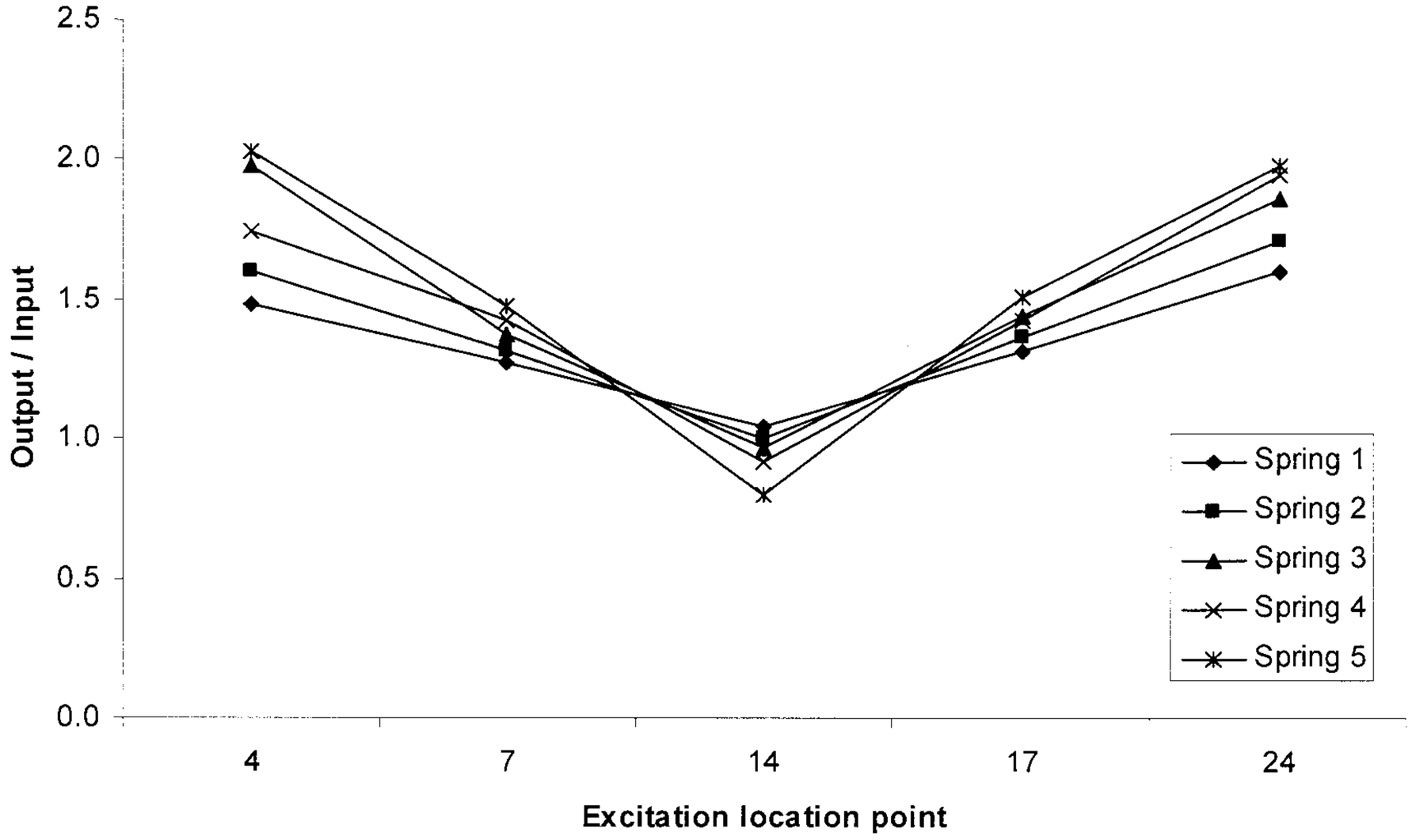

Figure 3.42 Displacement response at mid-span – test 1

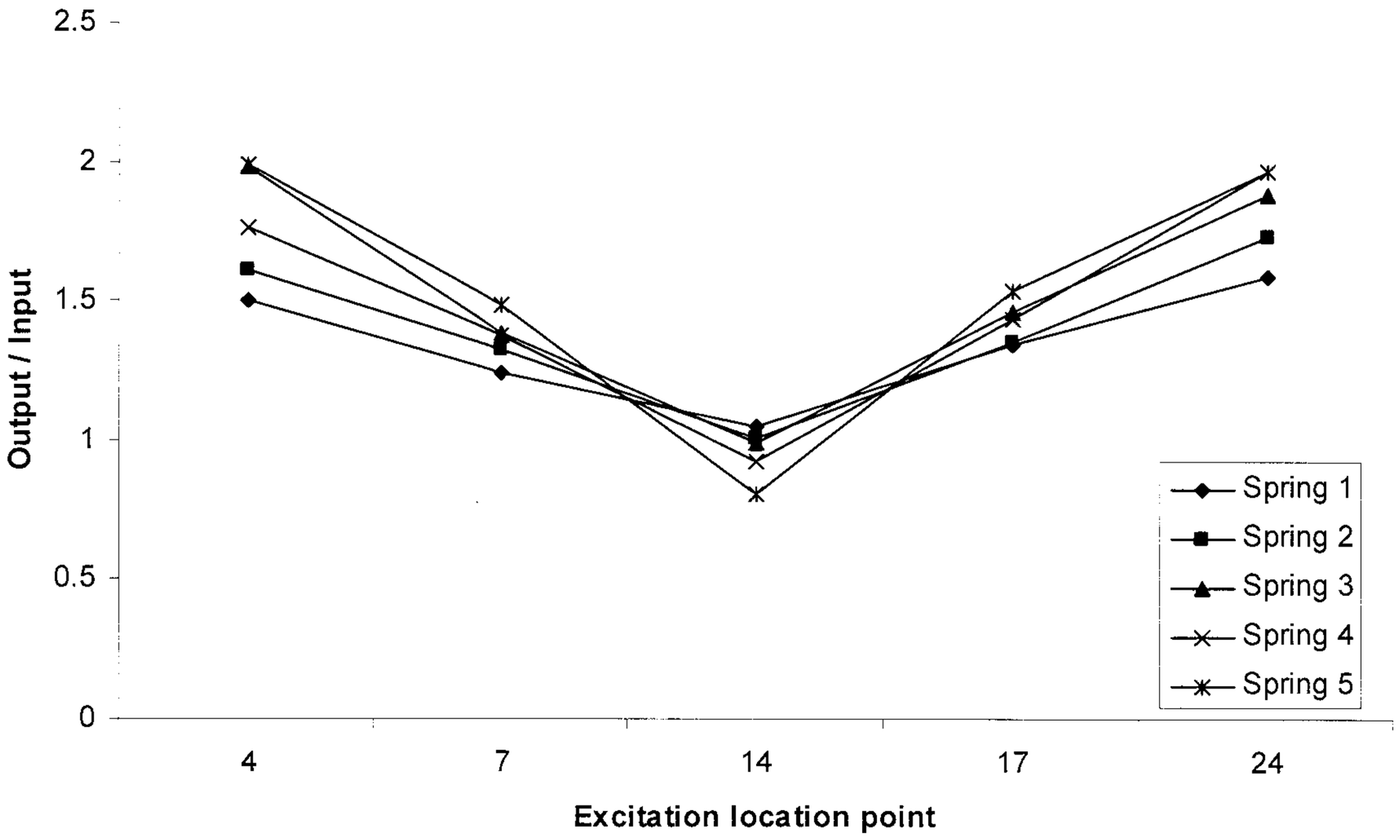

Figure 3.43 Displacement response at mid-span – test 2

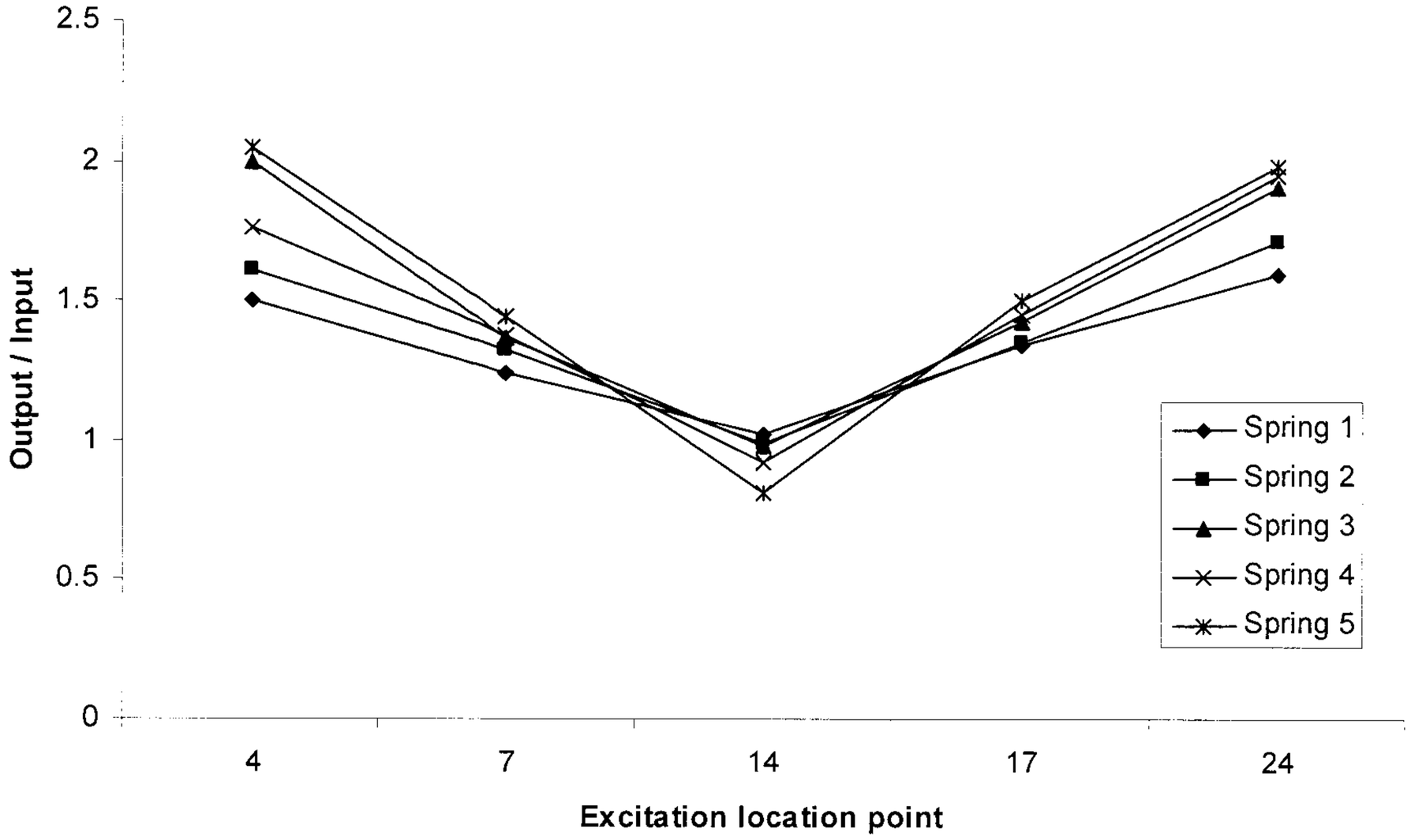

Figure 3.44 Displacement response at mid-span – test 3

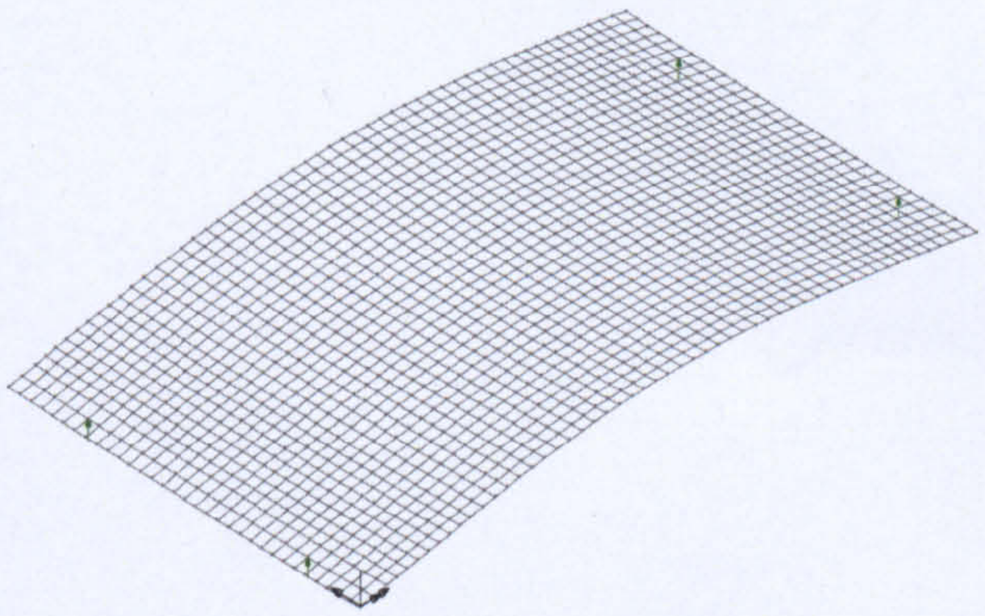

Figure 3.45 **First three FEA mode shapes of plate model used in experimental analysis in freely supported condition. (Displacements exaggerated to 15 mm for clarity)**

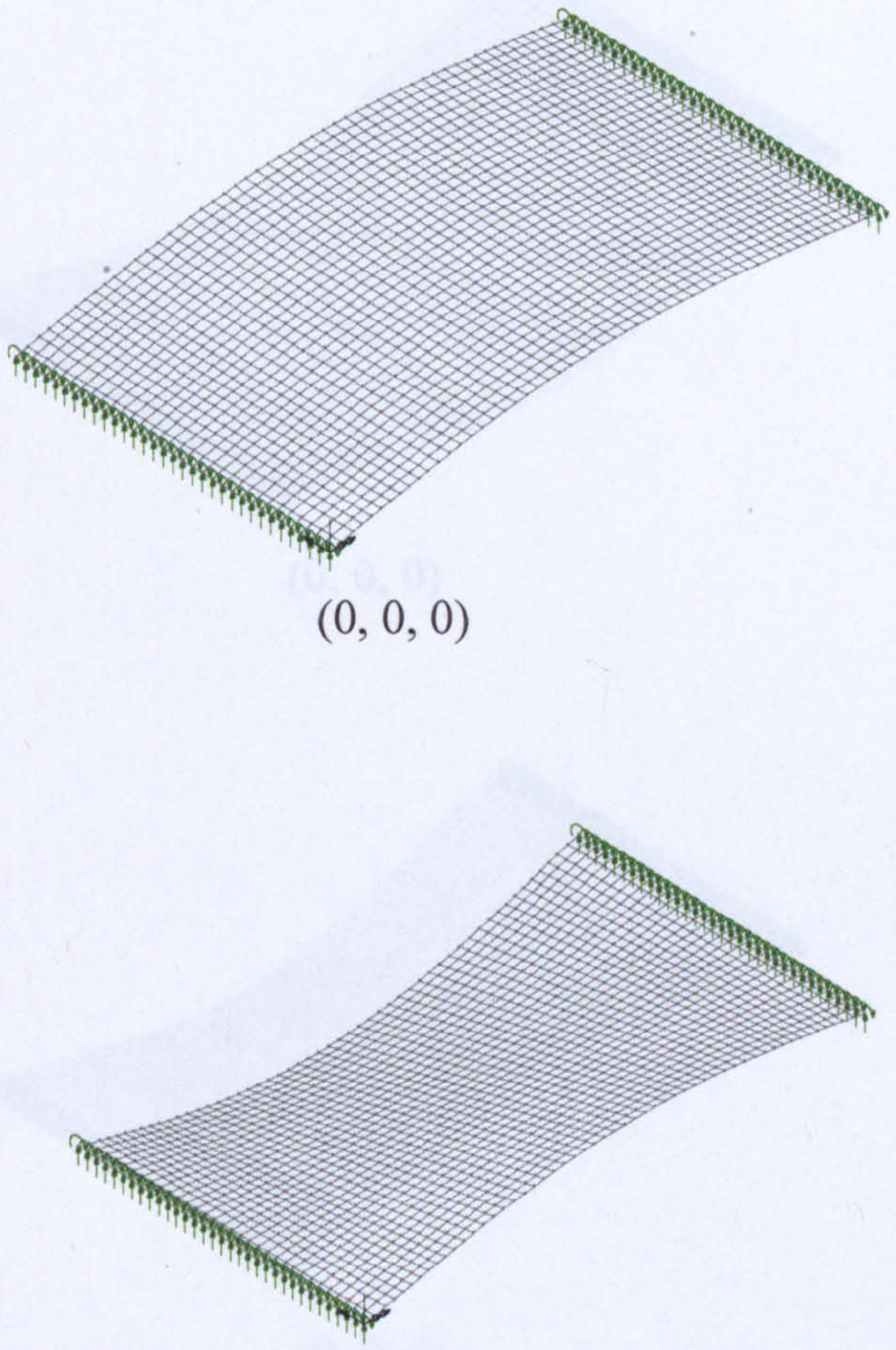

Figure 3.46 First three FEA mode shapes of plate model used in experimental analysis in simply supported condition. (Displacements exaggerated to 15 mm for clarity)

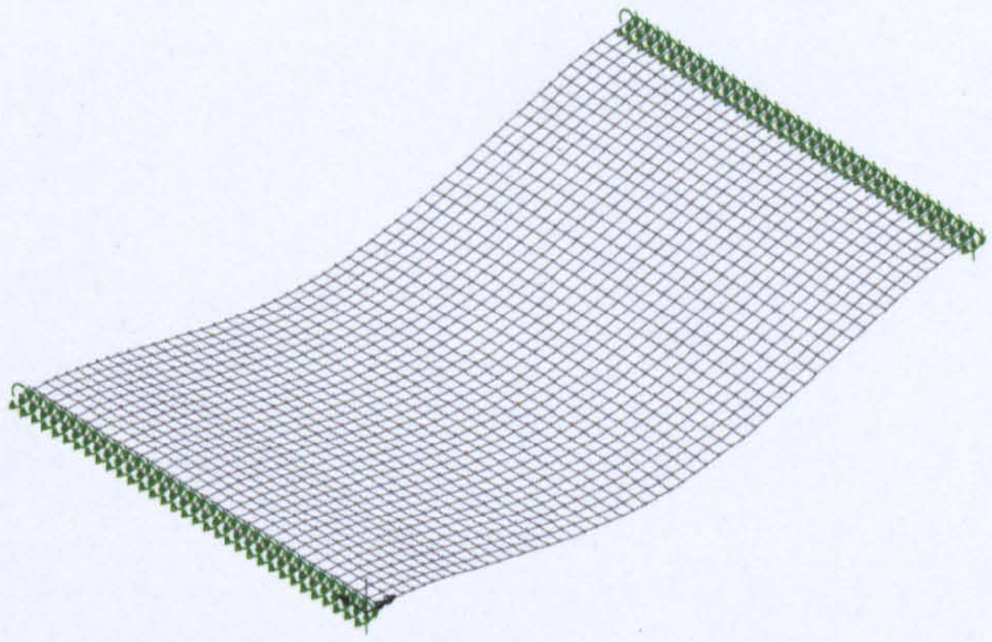

Figure 3.47 First three FEA mode shapes of plate model used in experimental analysis in fully fixed support condition. (Displacements exaggerated to 15 mm for clarity)

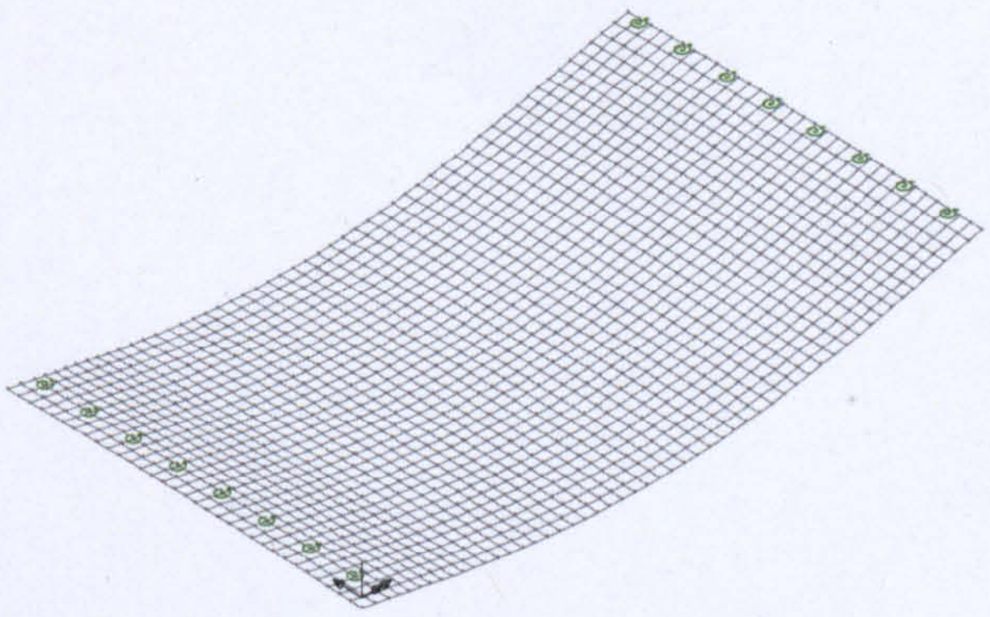

Primary bending mode

(0, 0, 0)

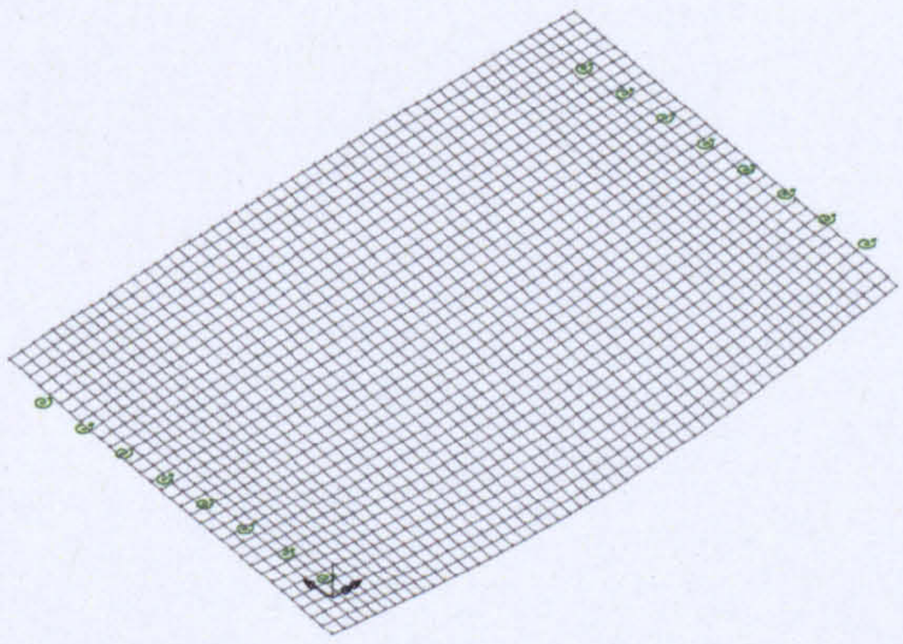

Primary torsional mode

(0, 0, 0)

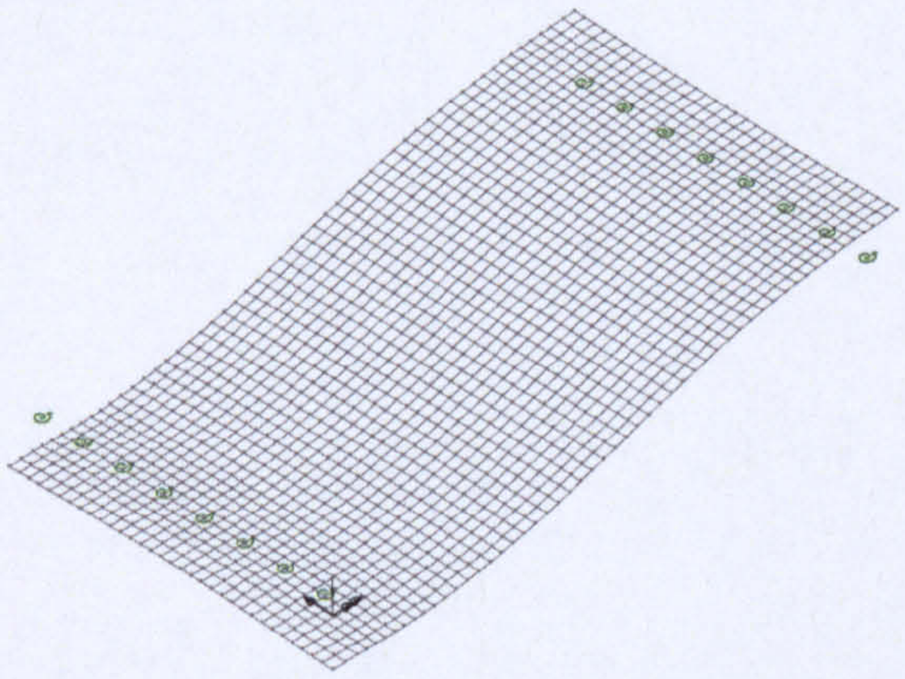

Second bending mode

(0, 0, 0)

Figure 3.48 First three FEA mode shapes of plate model used in experimental analysis in spring support 1 configuration. (Displacements exaggerated to 15 mm for clarity)

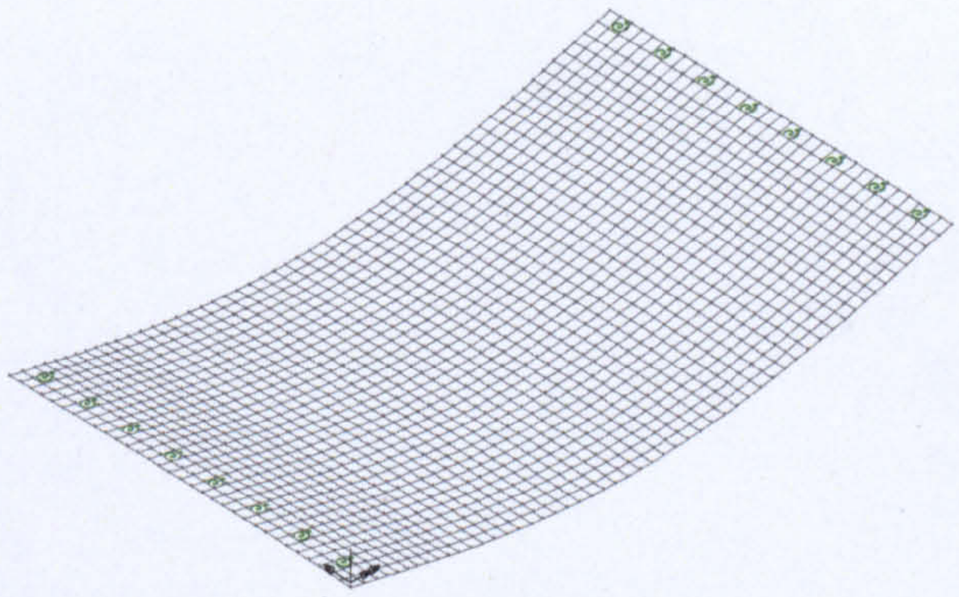

Primary bending mode

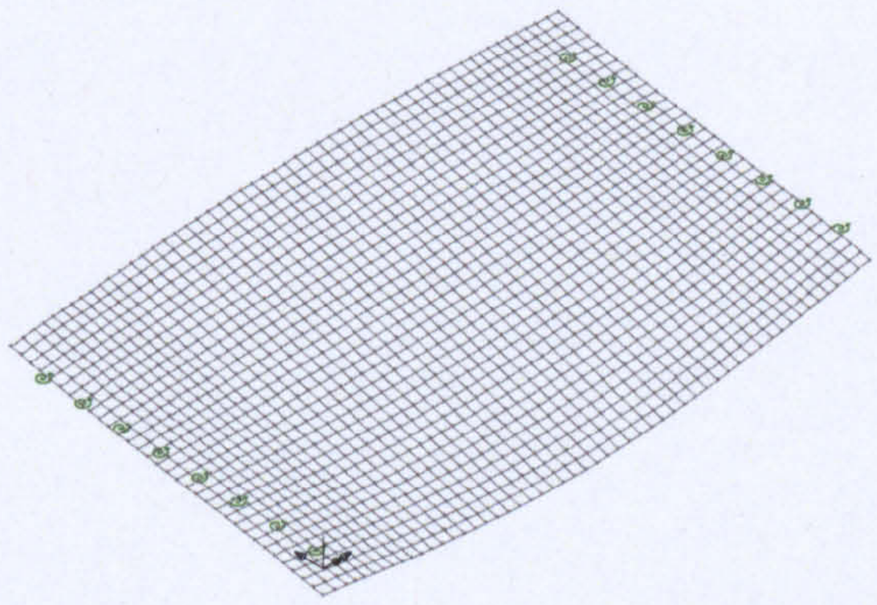

Primary torsional mode

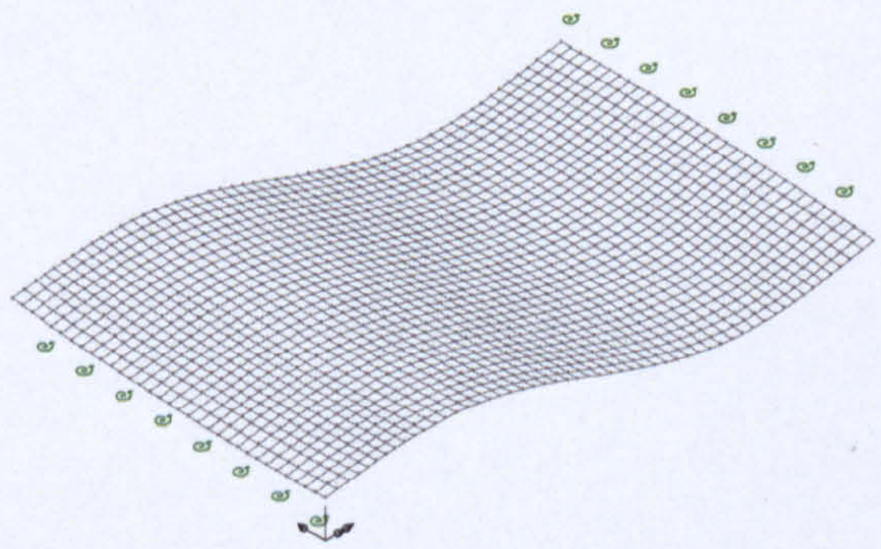

Second bending mode

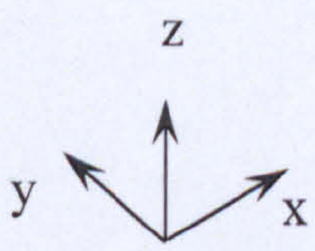

Figure 3.49 First three FEA mode shapes of plate model used in experimental analysis in spring support 2 configuration. (Displacements exaggerated to 15 mm for clarity)

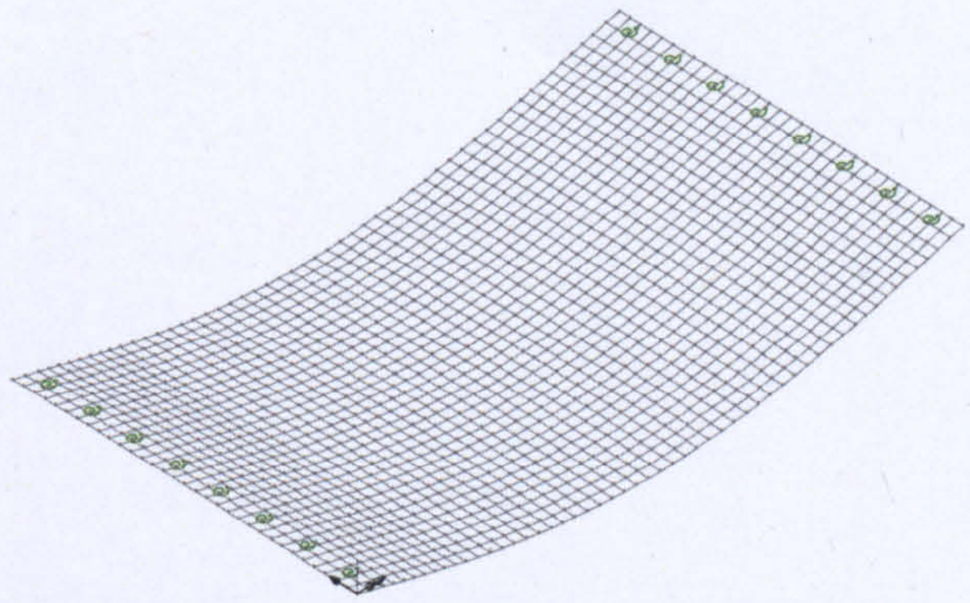

Figure 3.50 **First three FEA mode shapes of plate model used in experimental analysis in spring support 3 configuration. (Displacements exaggerated to 15 mm for clarity)**

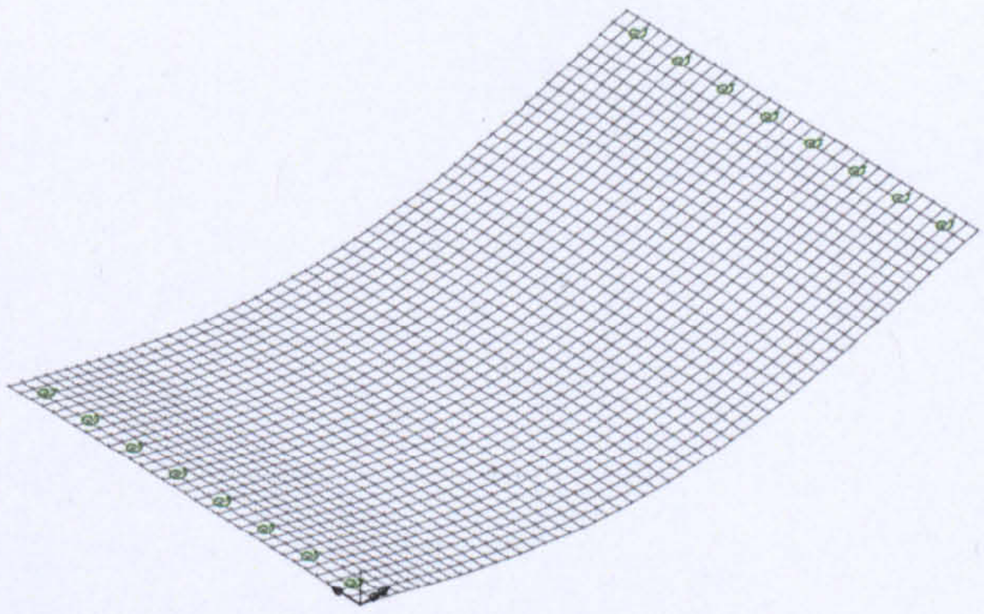

Figure 3.51 First three FEA mode shapes of plate model used in experimental analysis in spring support 4 configuration. (Displacements exaggerated to 15 mm for clarity)

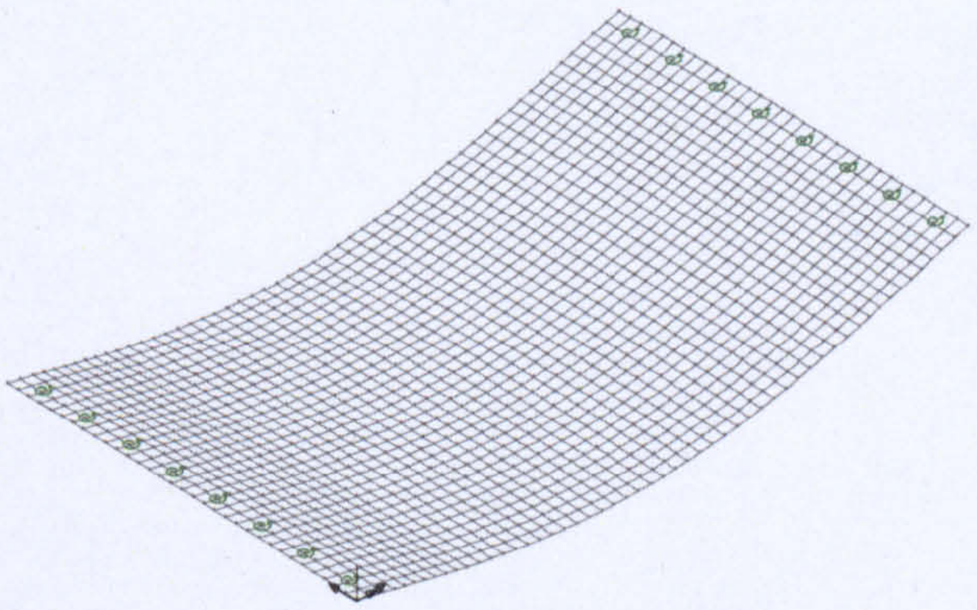

Primary bending mode

(0, 0, 0)

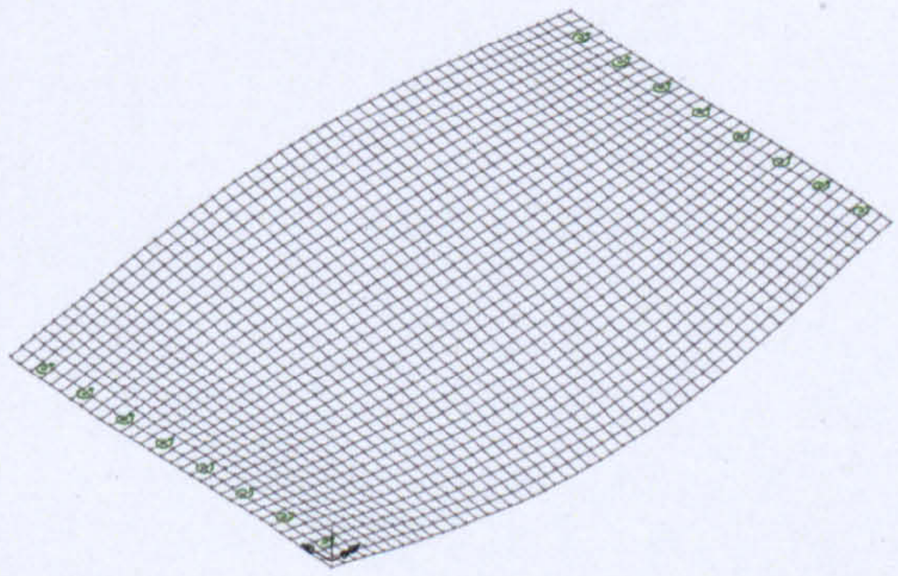

Primary torsional mode

(0, 0, 0)

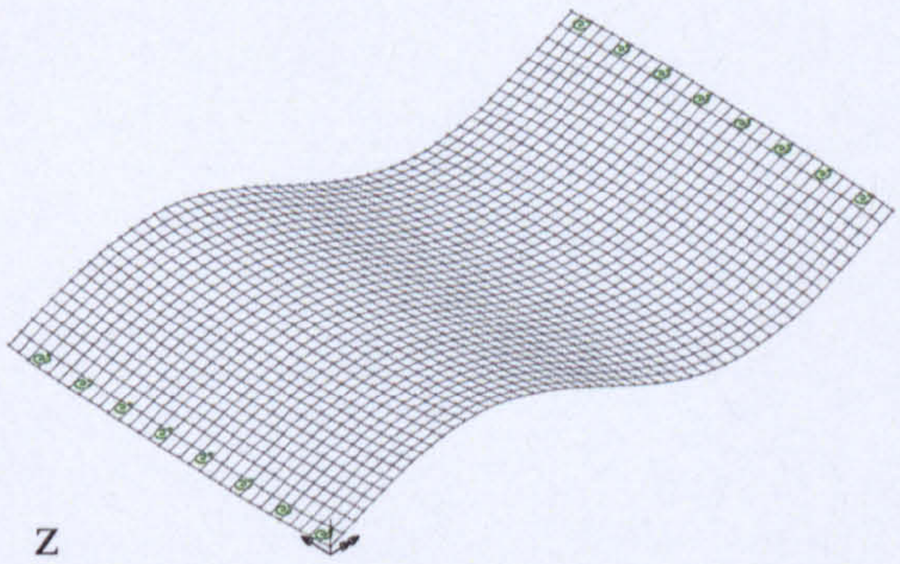

Second bending mode

(0, 0, 0)

Figure 3.52 First three FEA mode shapes of plate model used in experimental analysis in spring support 5 configuration. (Displacements exaggerated to 15 mm for clarity)

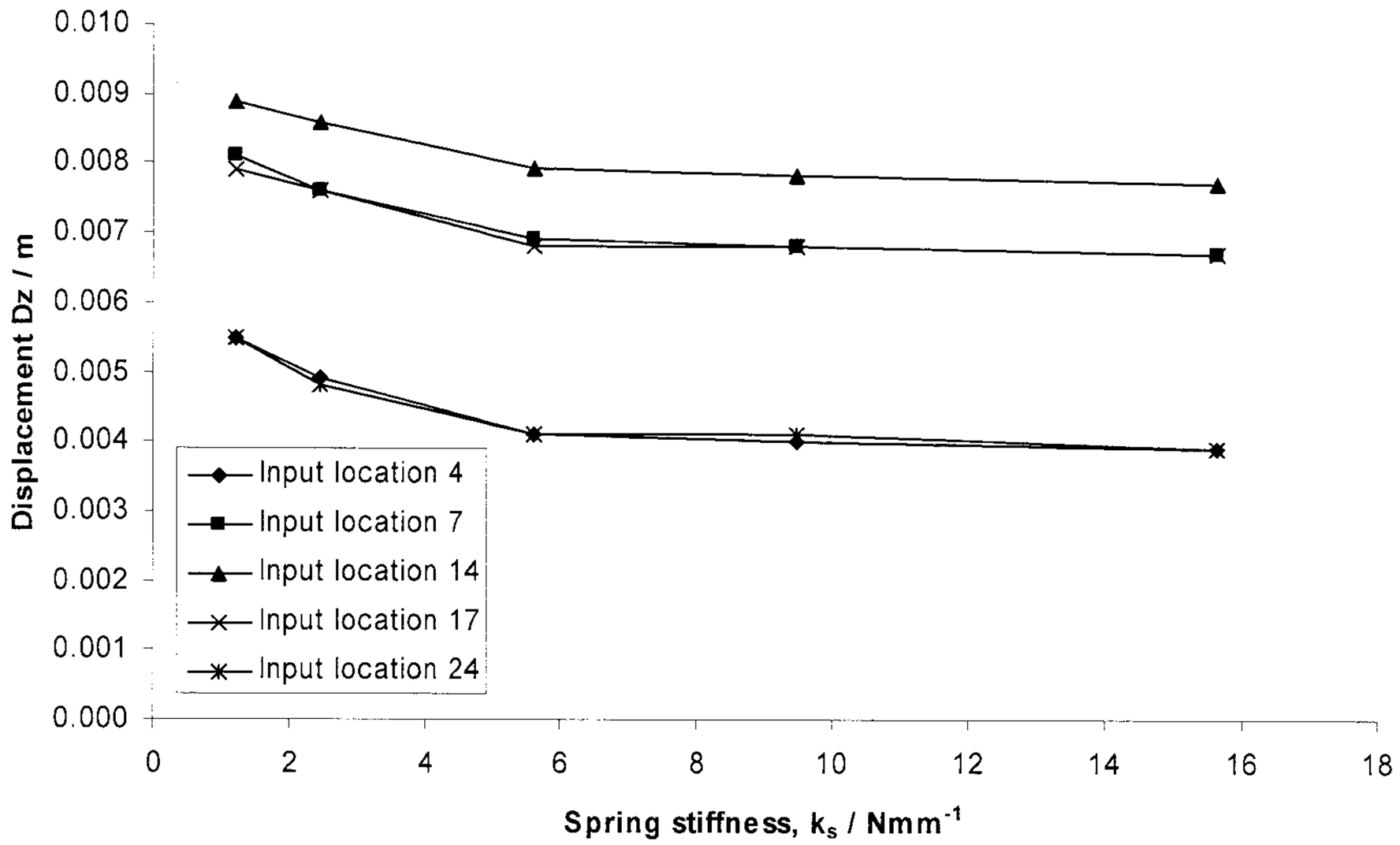

Figure 3.53 Displacement at mid-span

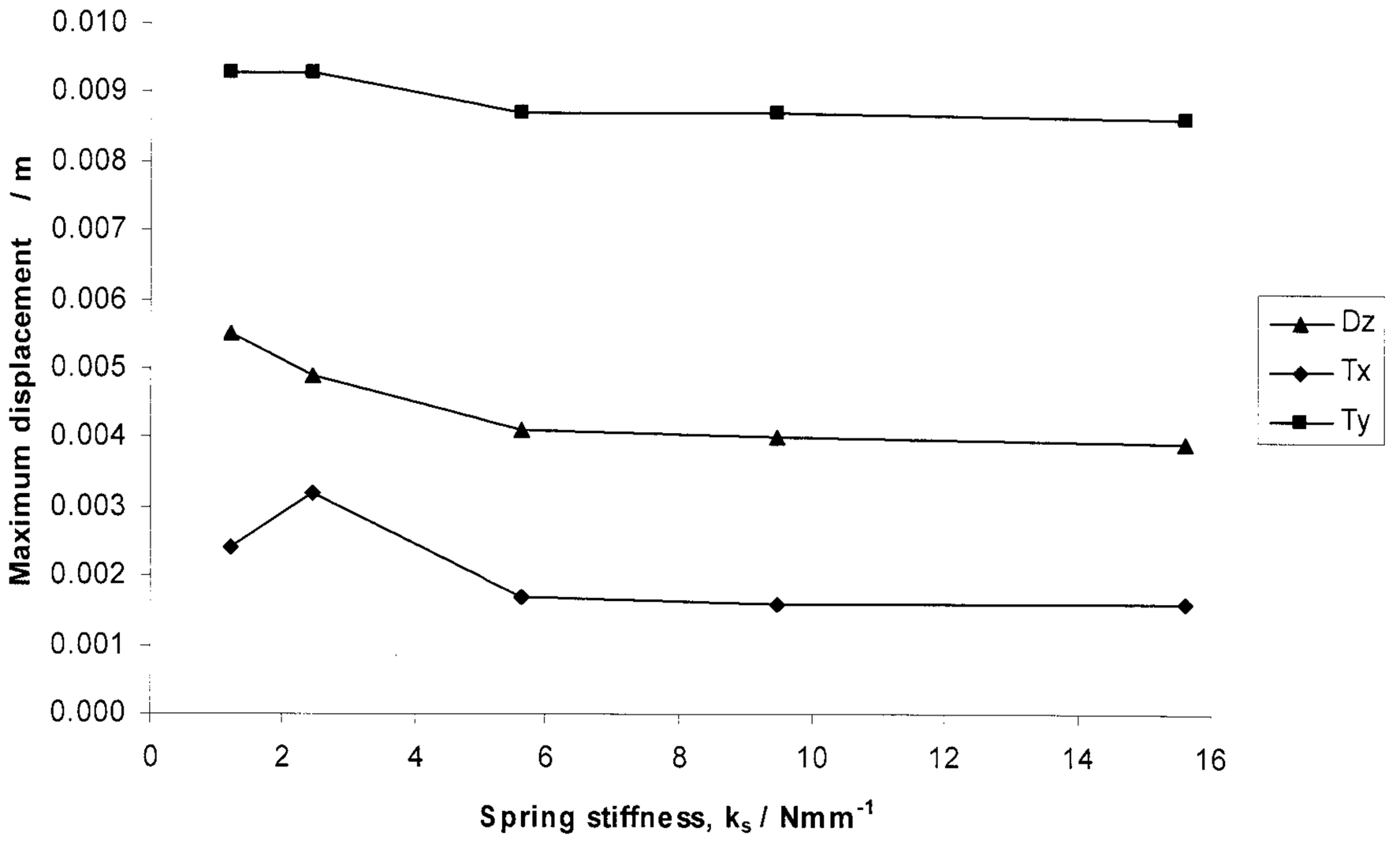

Figure 3.54 Vertical and rotational displacements

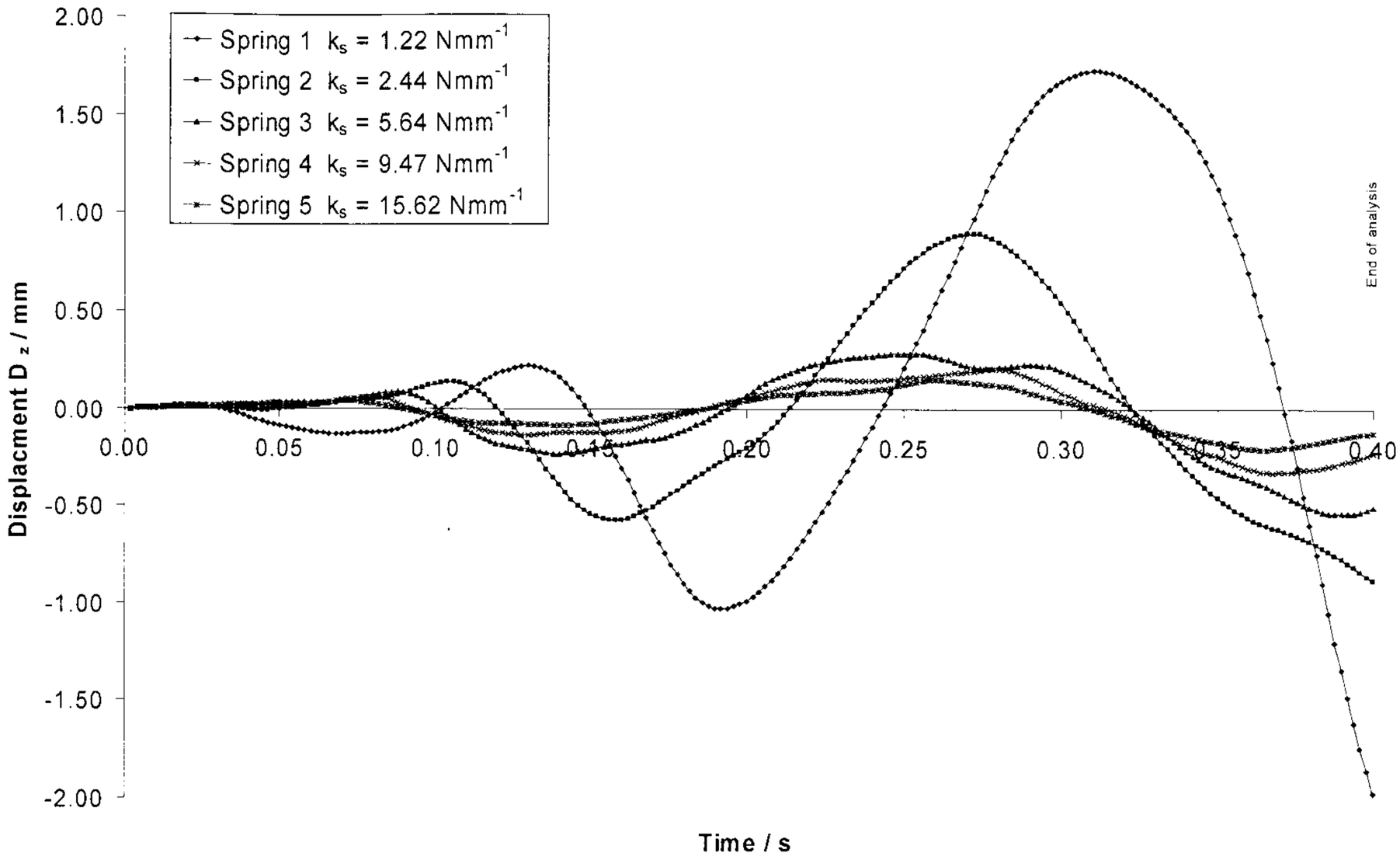

Figure 3.55 Displacement response against time at node 18

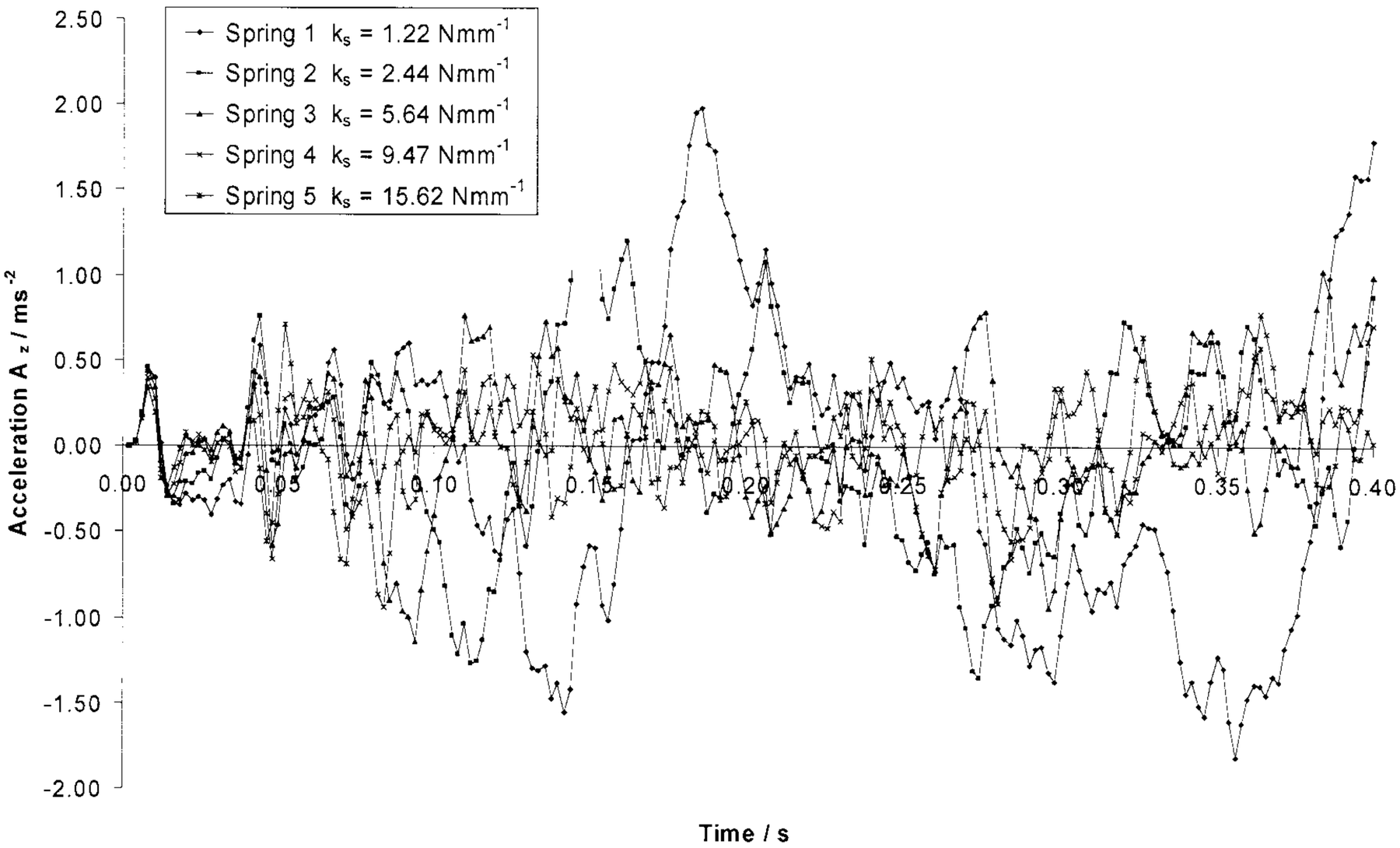

Figure 3.56 Acceleration response against time at node 18

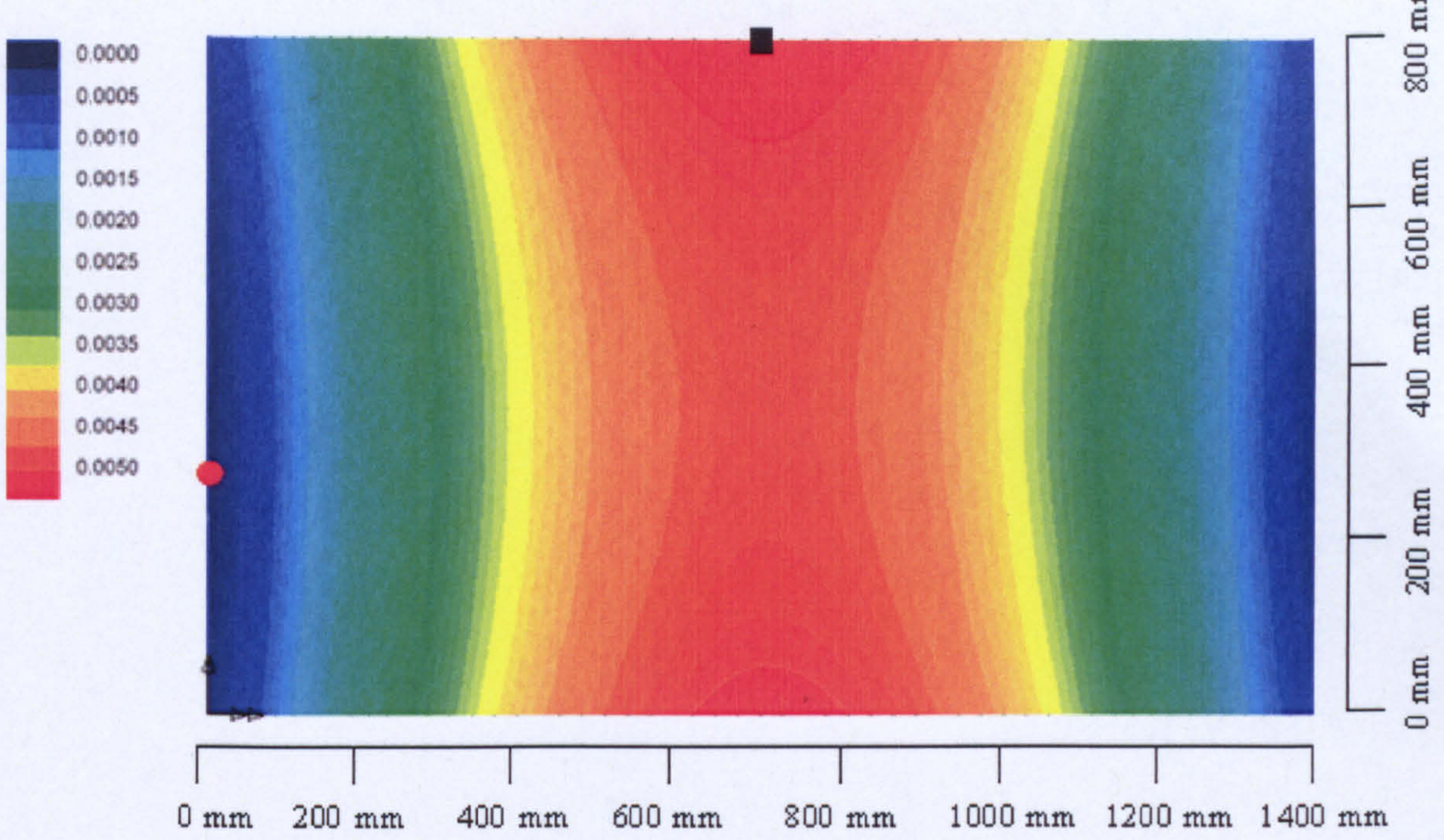

Figure 3.57 **Contour plot of displacement Dz in mm for spring stiffness 1 after one full loading cycle, 0.285 s.**
Maximum value at node 1834 is 0.0055 mm ■
Minimum value at node 597 is -0.0008 mm ●

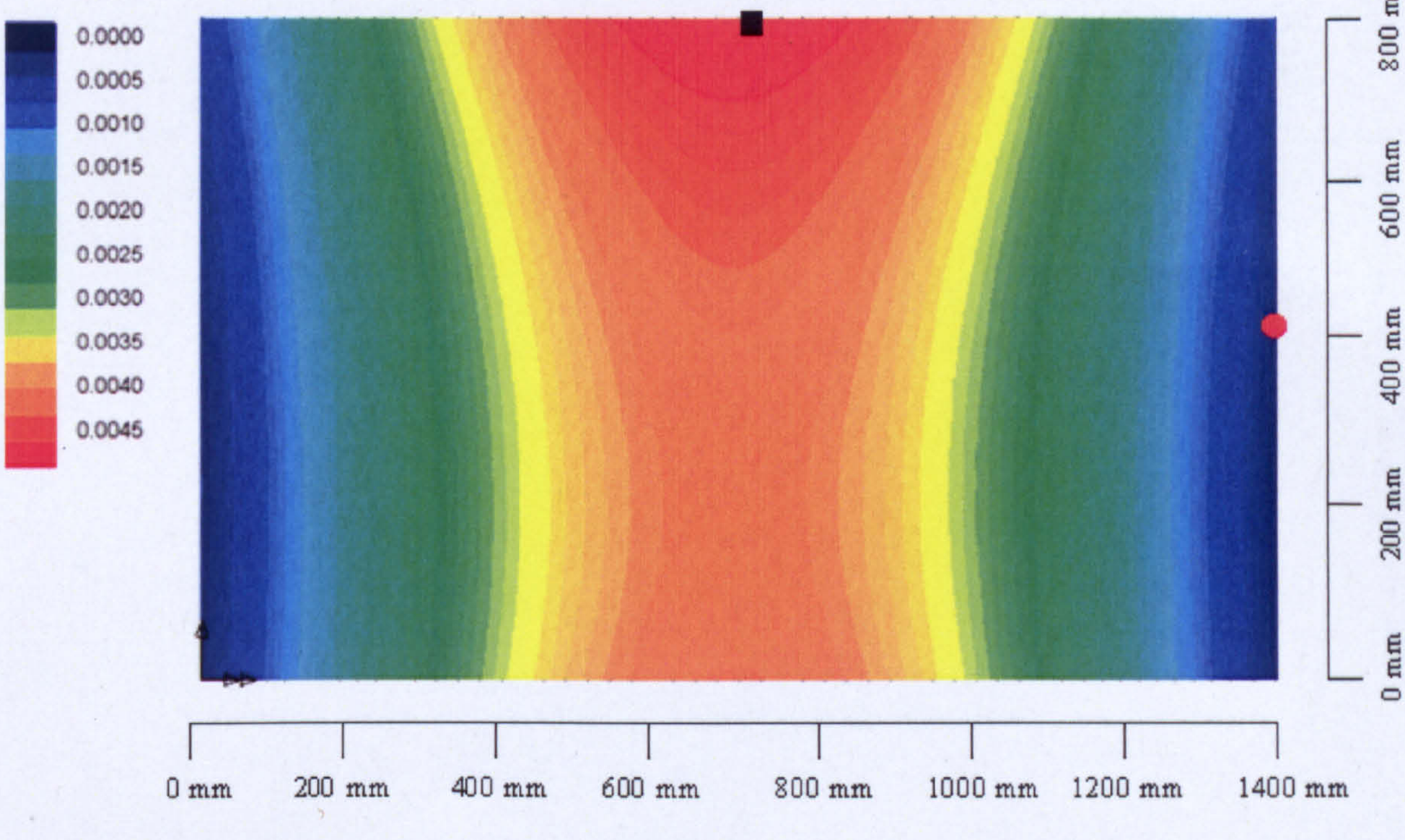

Figure 3.58 **Contour plot of displacement Dz in mm for spring stiffness 2 after one full loading cycle, 0.26 s.**
Maximum value at node 1834 is 0.0049 mm ■
Minimum value at node 4276 is -0.00016 mm ●

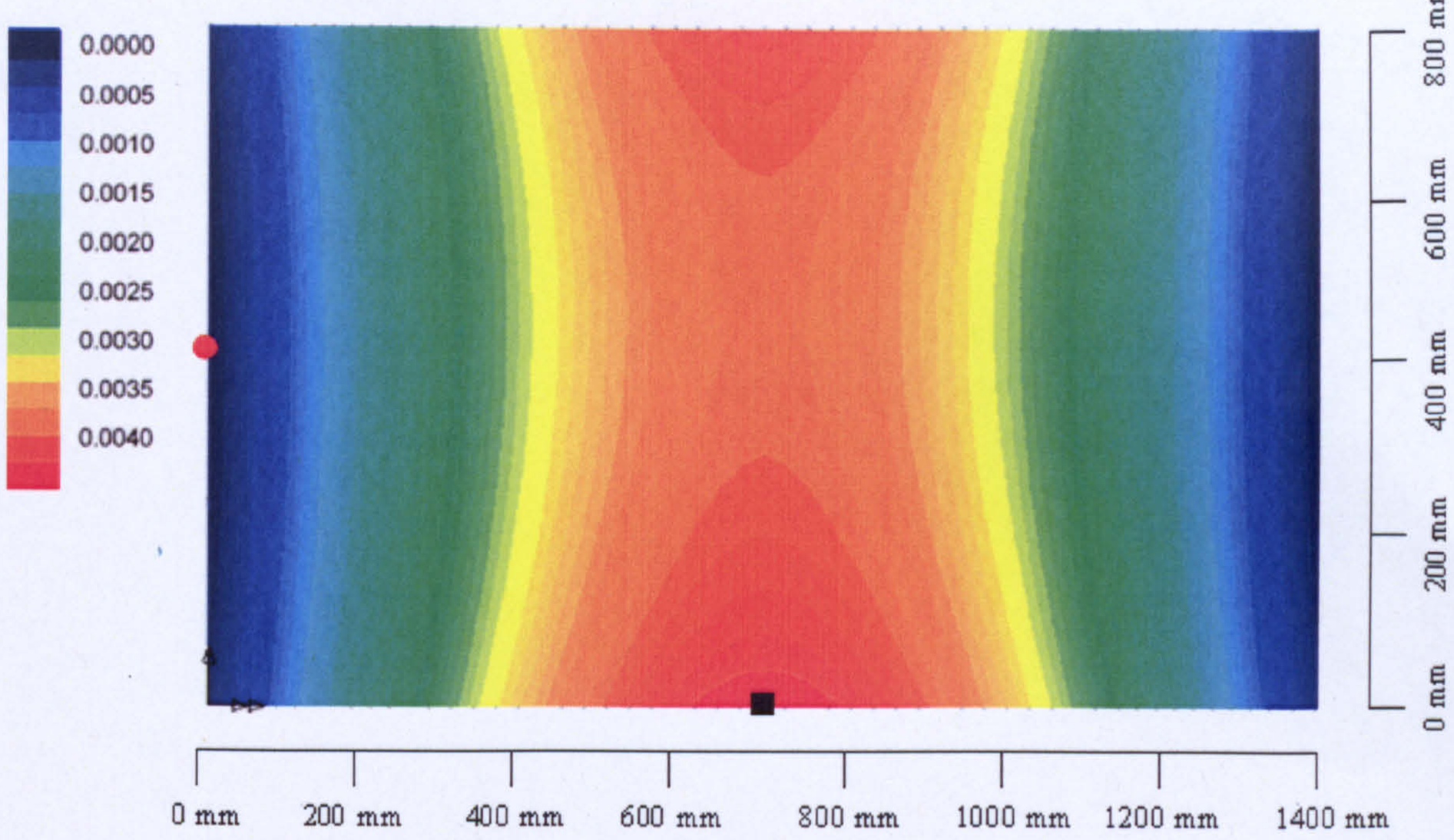

Figure 3.59 **Contour plot of displacement Dz in mm for spring stiffness 3 after one full loading cycle, 0.25 s.**
Maximum value at node 2226 is 0.0041 mm ■
Minimum value at node 445 is -0.0008 mm ●

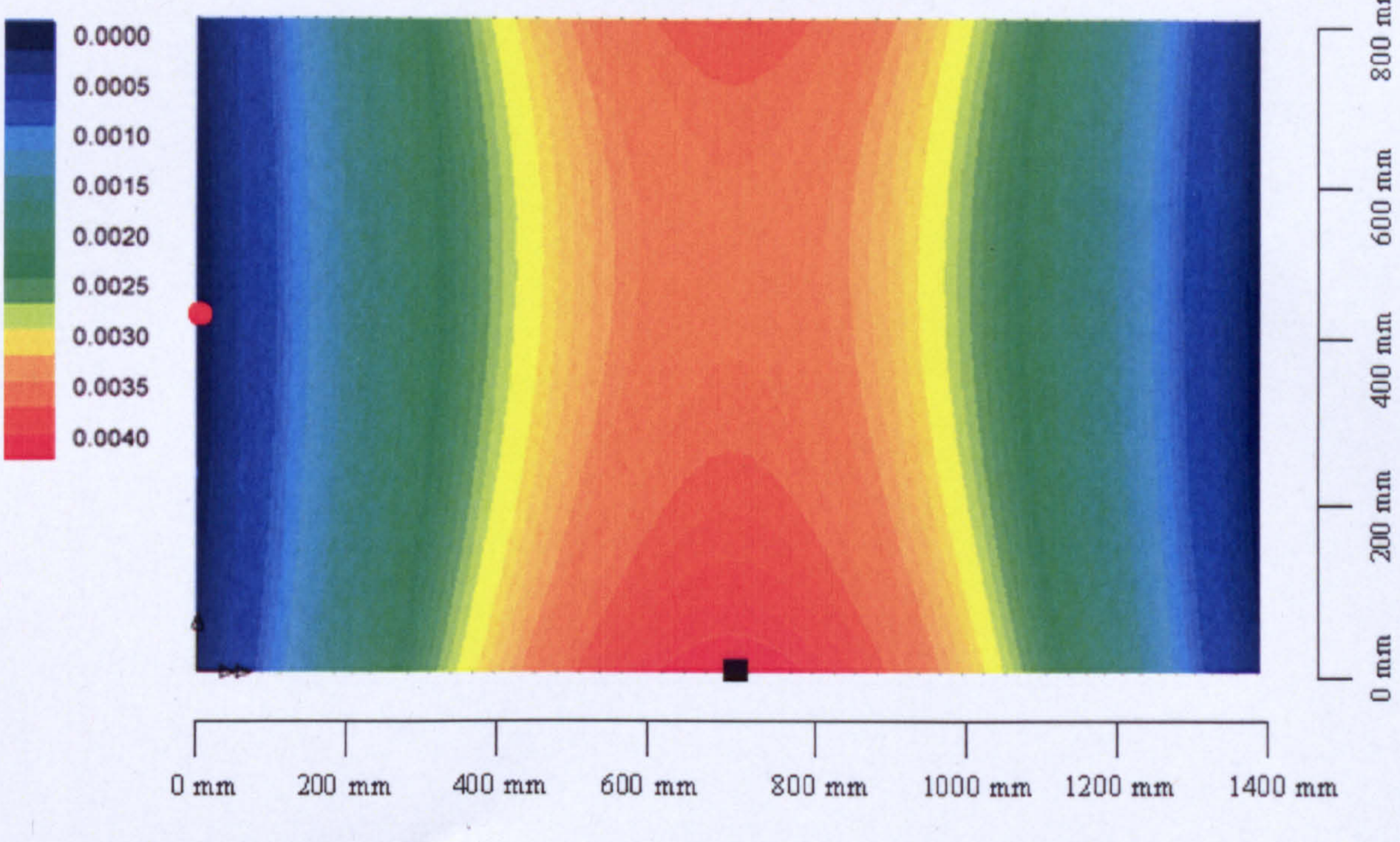

Figure 3.60 **Contour plot of displacement Dz in mm for spring stiffness 4 after one full loading cycle, 0.246 s.**
Maximum value at node 2226 is 0.0040 mm ■
Minimum value at node 445 is -0.00015 mm ●

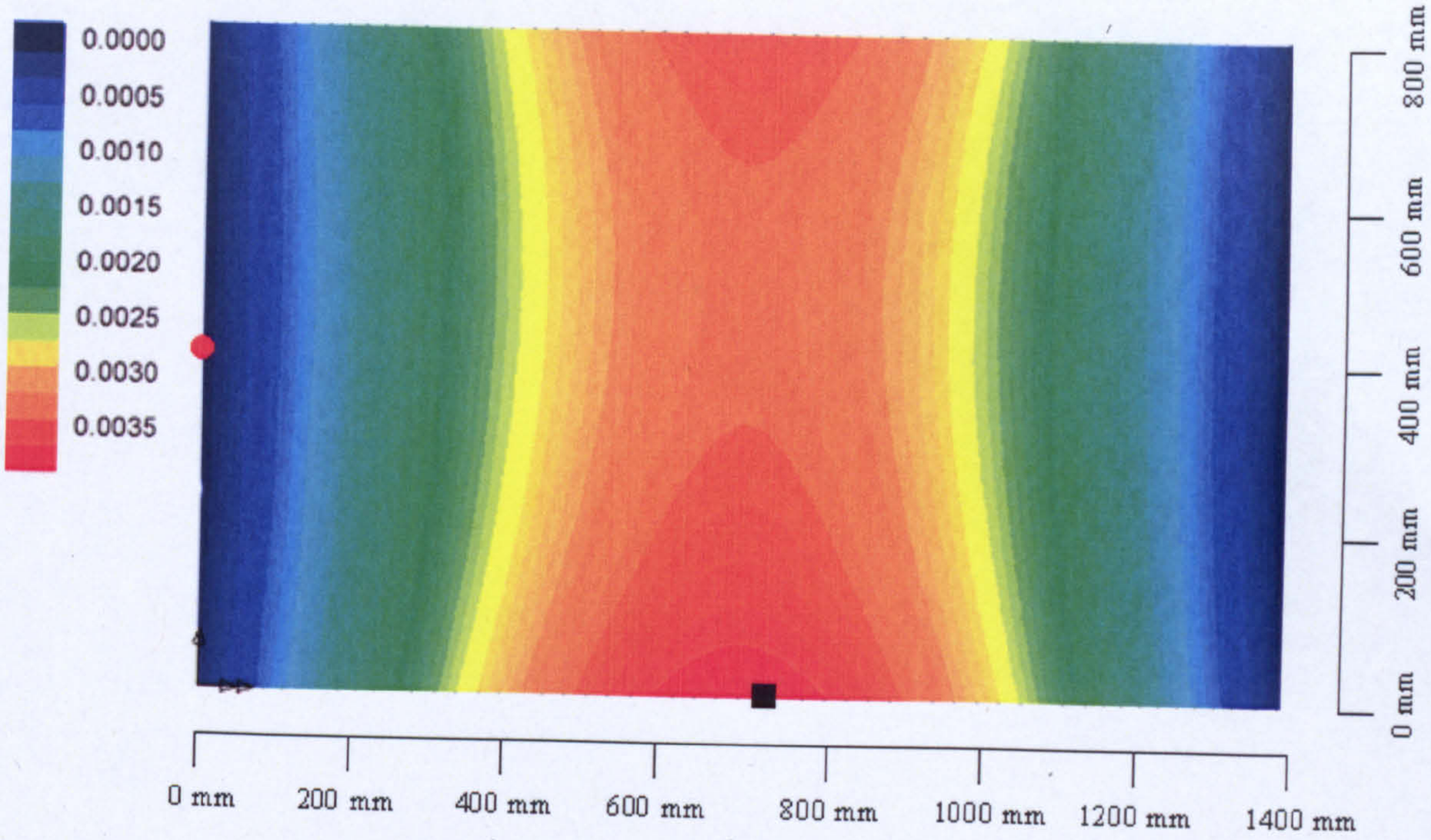

Figure 3.61 **Contour plot of displacement Dz in mm for spring stiffness 5 after one full loading cycle, 0.24 s.**
Maximum value at node 2226 is 0.0039 mm ■
Minimum value at node 445 is -0.00019 mm ●

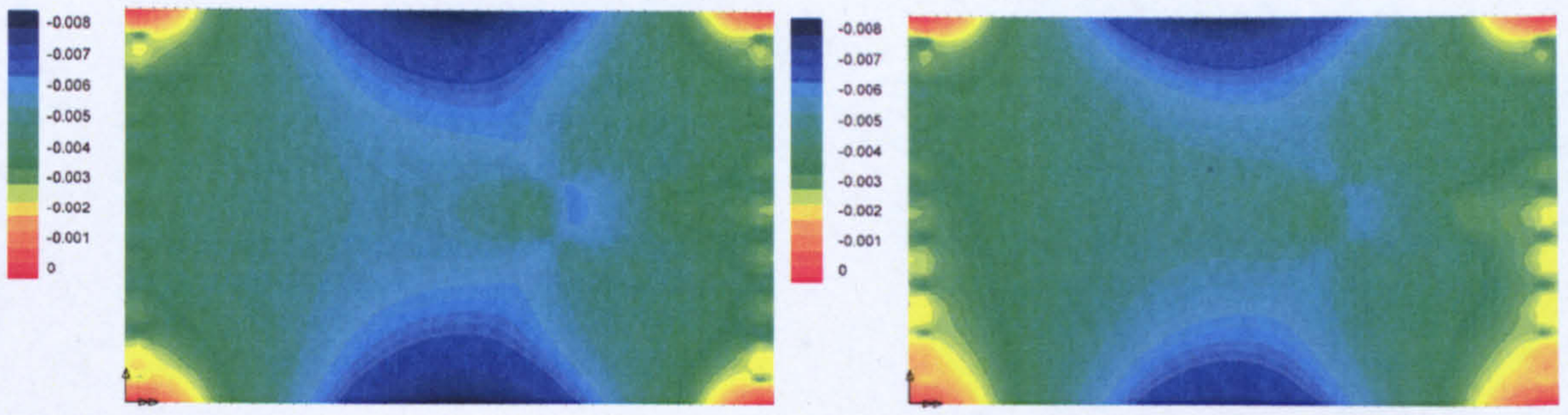

Spring 1 - $k_s = 1.22\ Nmm^{-1}$

Spring 2 - $k_s = 2.44\ Nmm^{-1}$

Spring 3 - $k_s = 5.64\ Nmm^{-1}$

Spring 4 - $k_s = 9.47\ Nmm^{-1}$

Spring 5 - $k_s = 15.6\ Nmm^{-1}$

(a)

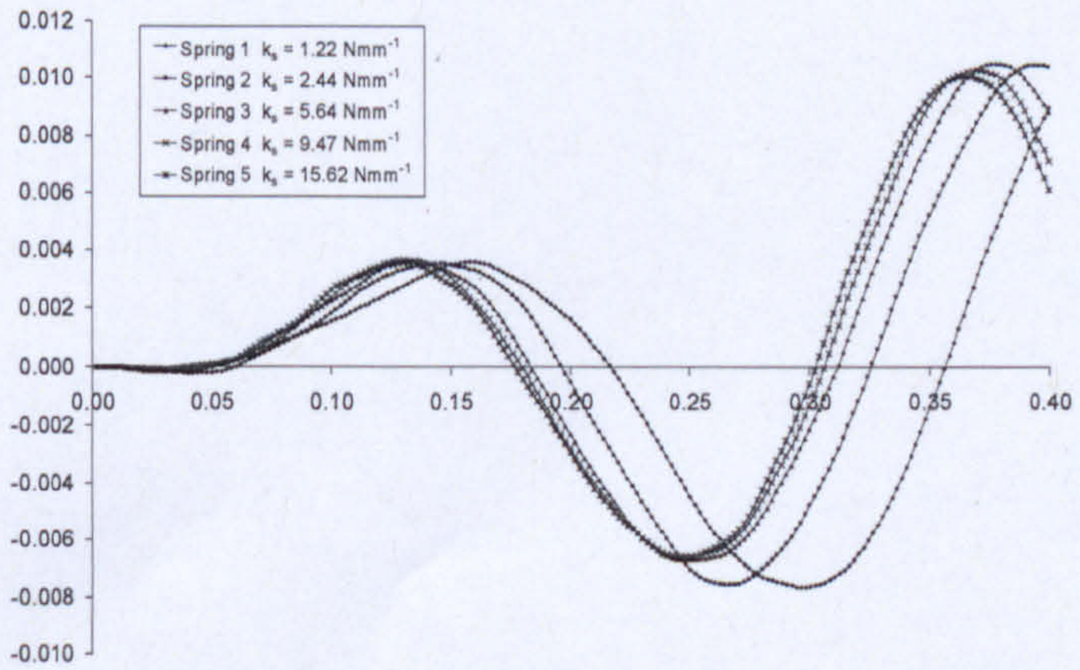

(b)

Figure 3.62 Bending strain about y axis.
Figure 3.61 (a) shows contour plots of bending strain for each spring stiffness.
Figure 3.61 (b) shows bending strain at node point 18 for each spring stiffness.

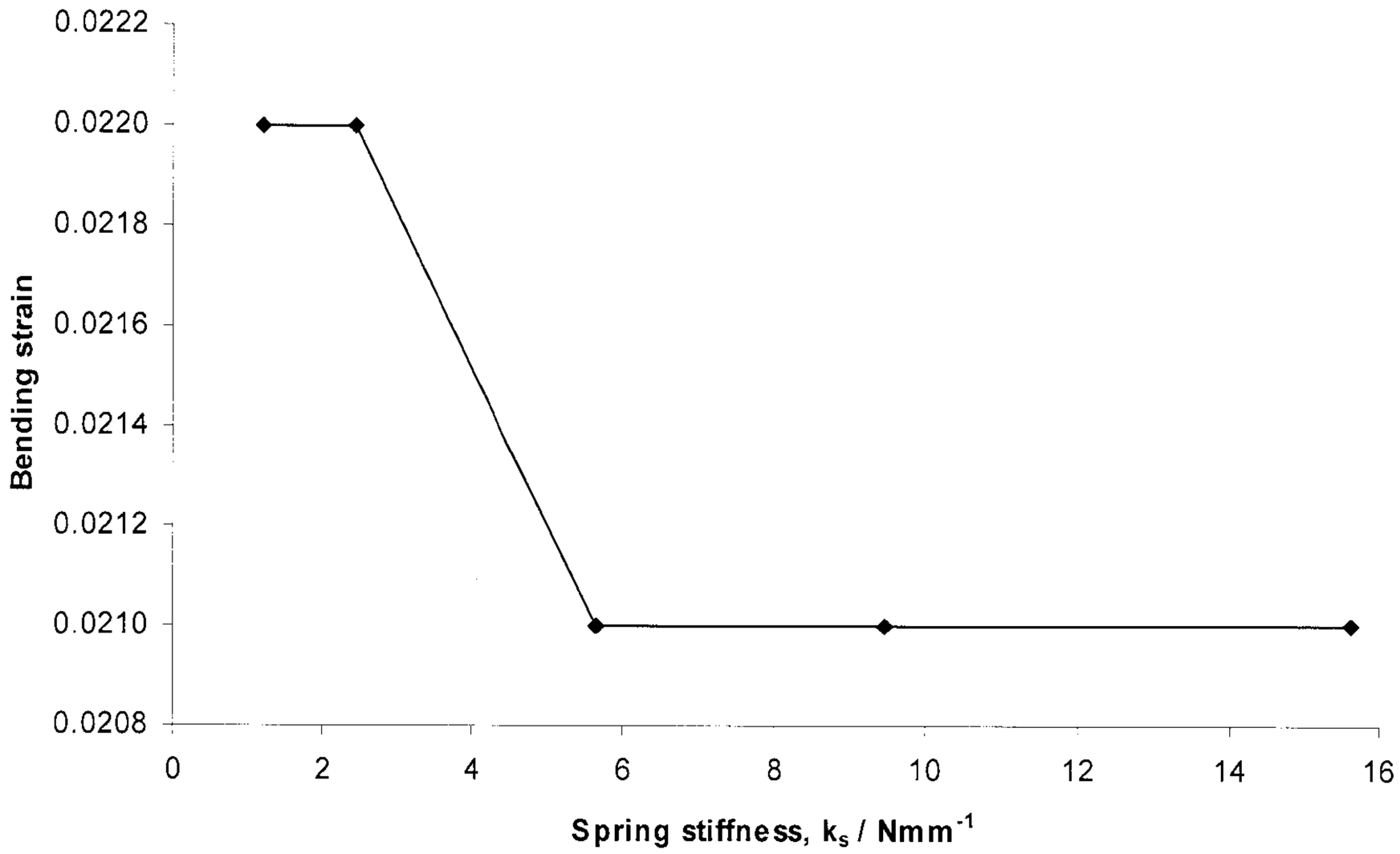

Figure 3.63 Maximum bending strain

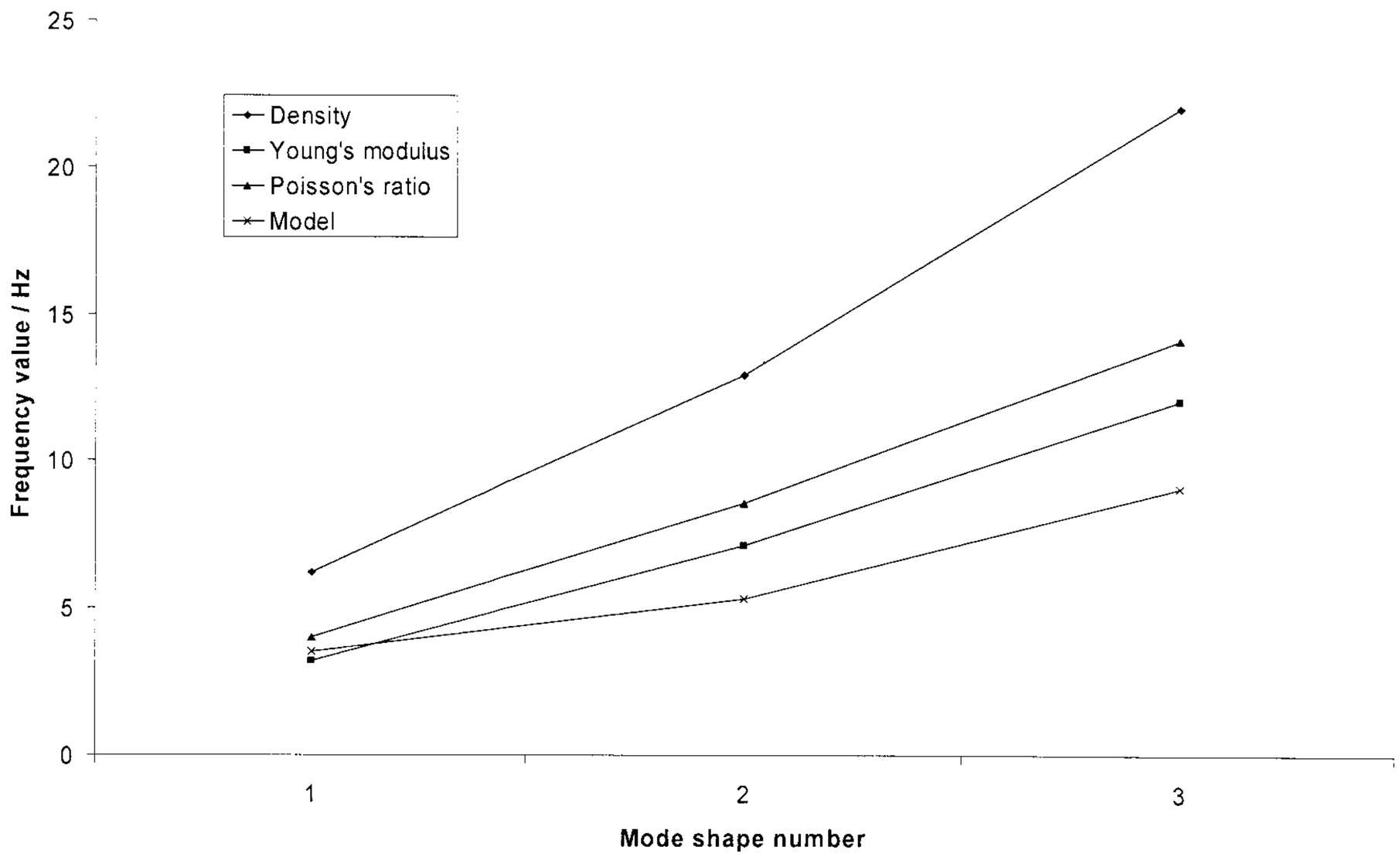

Figure 3.64 Parametric study on plate response. All values of density, E and Poisson's ratio are half the actual value used in the model.

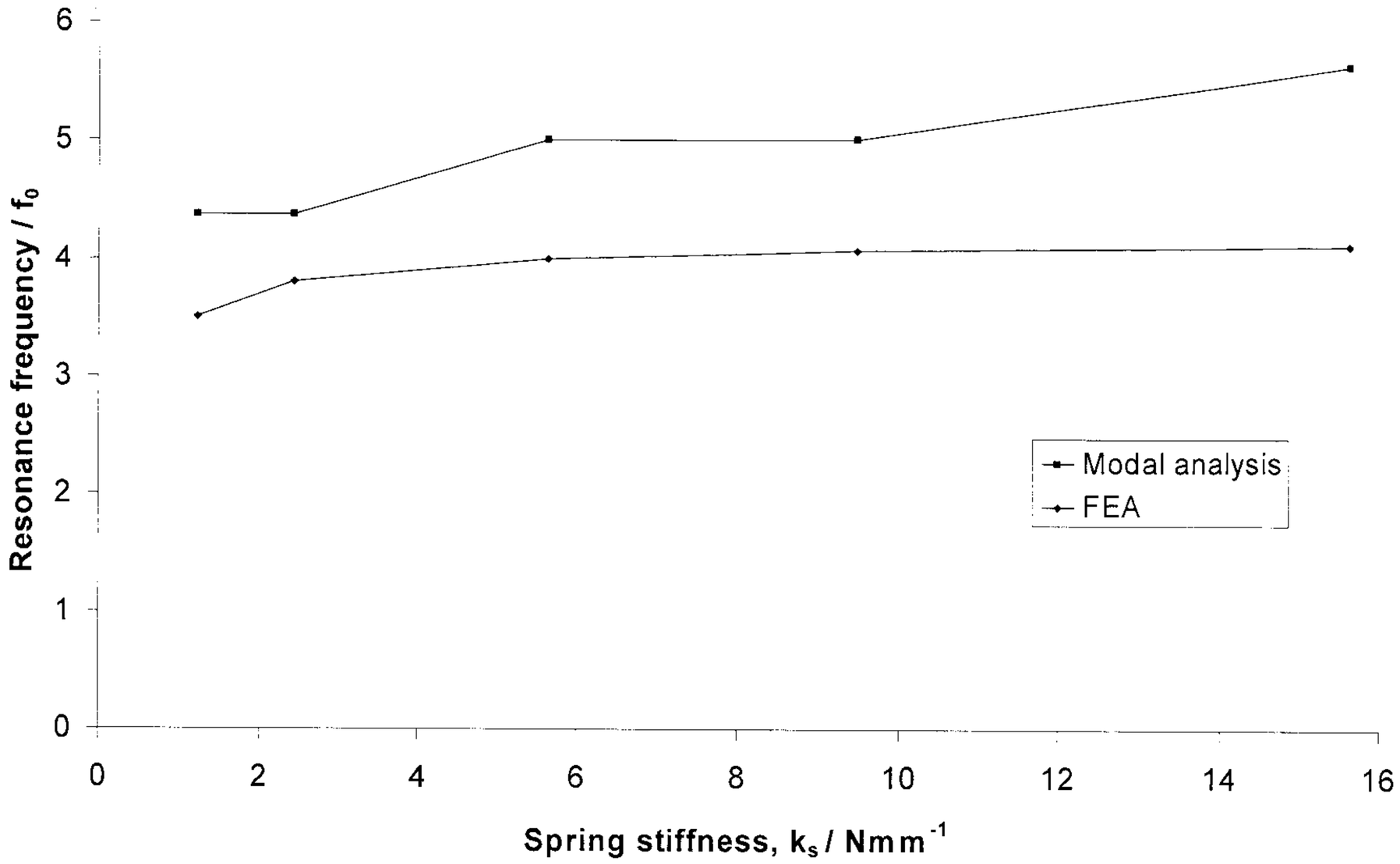

Figure 3.65 Comparison of experimental and analytical data for frequency

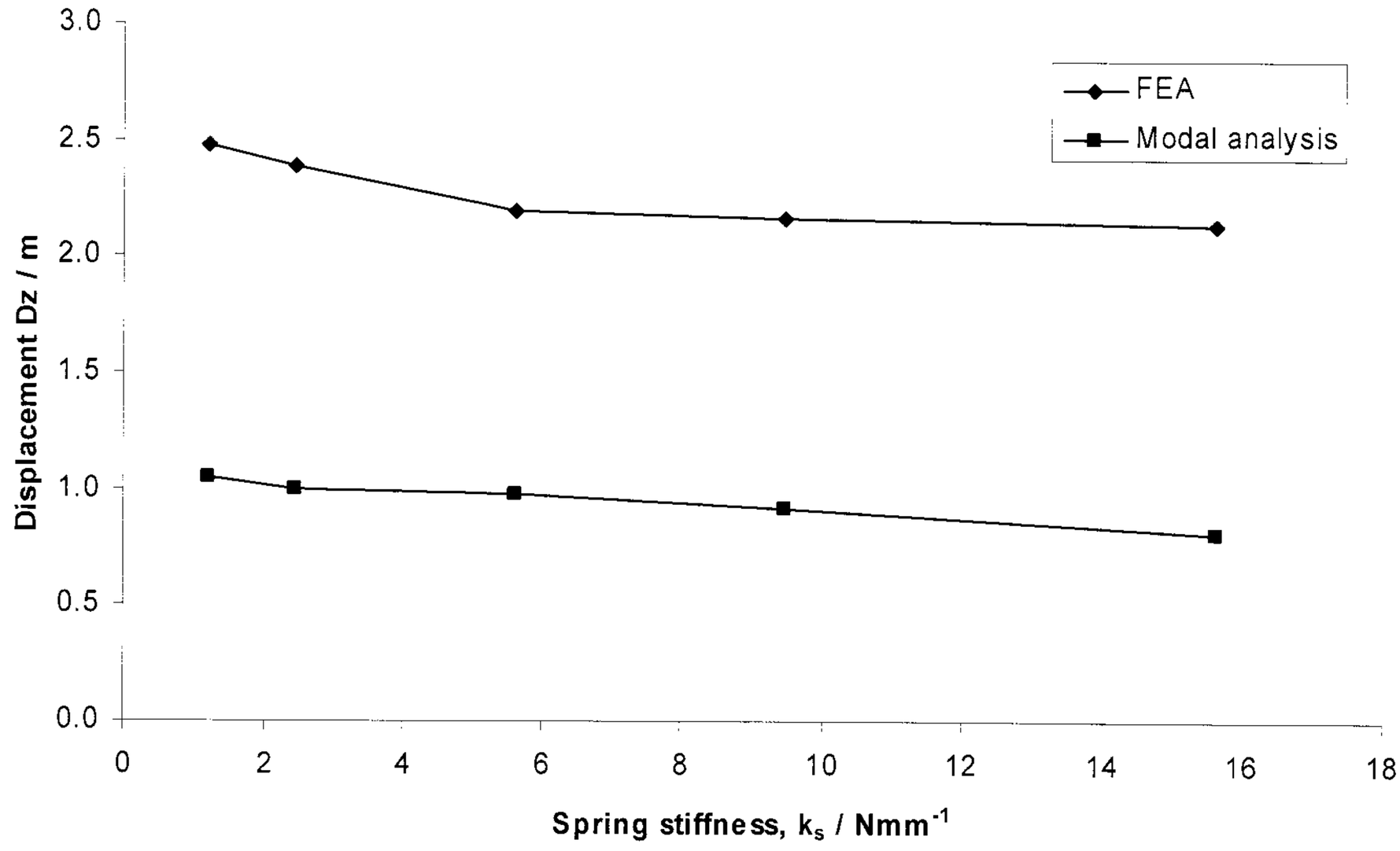

Figure 3.66 Comparison of experimental and analytical data for displacement

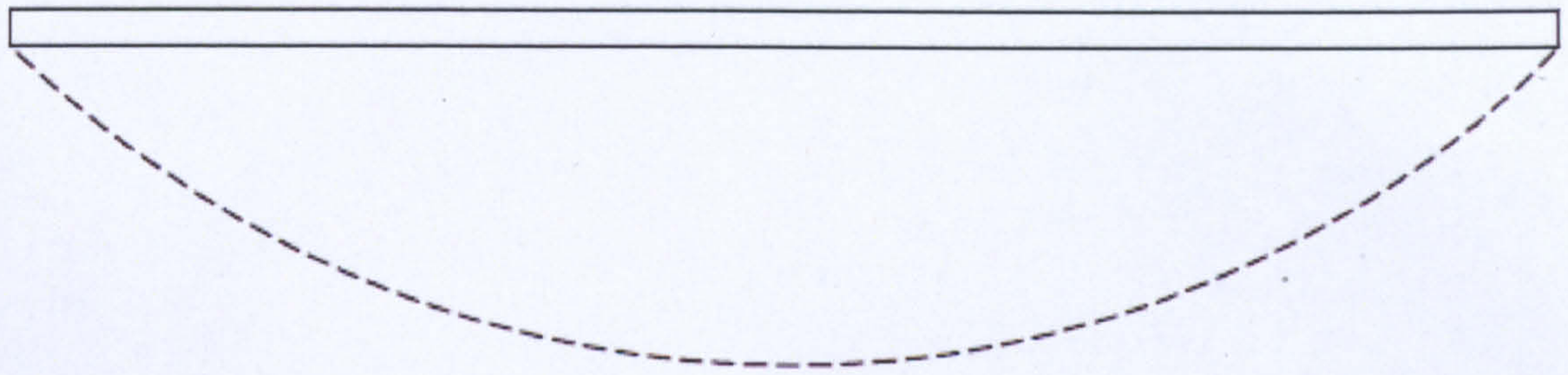

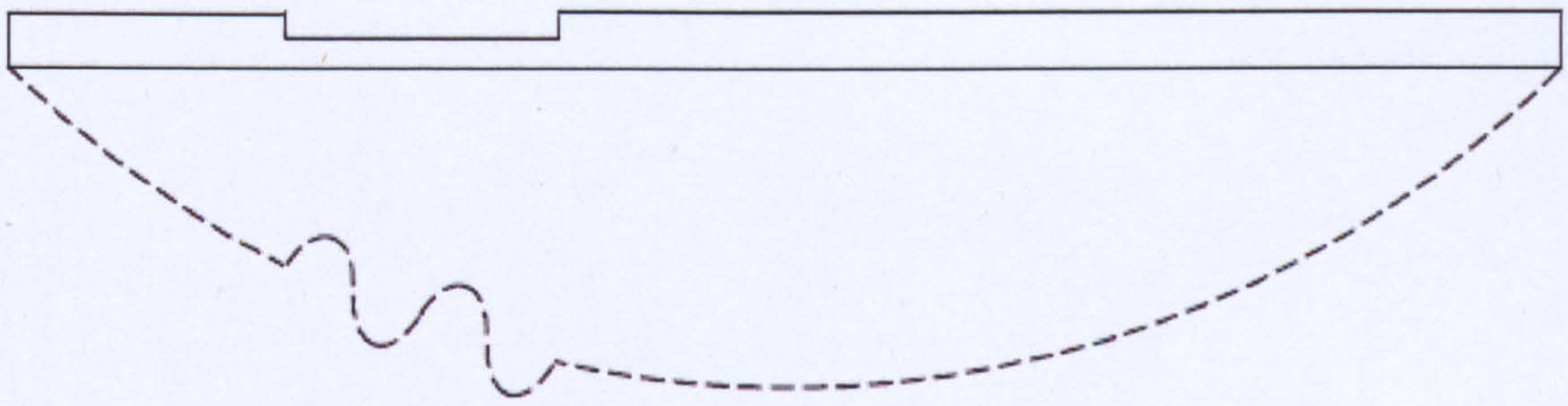

Figure 3.67 Alteration in modal response due to local damage effects

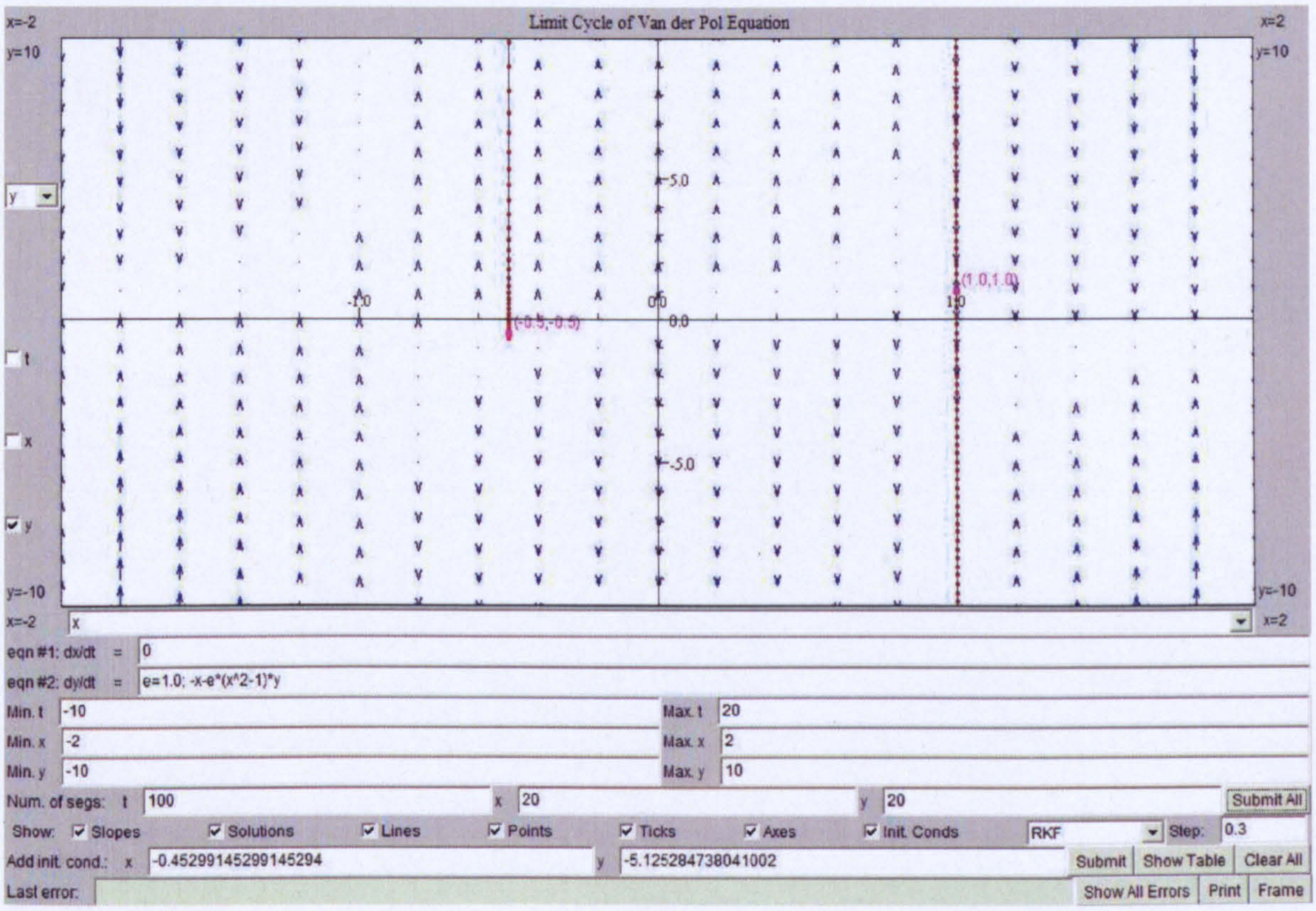

Figure 3.68 Van der Pol plot with *dx/dt* equal to zero times y

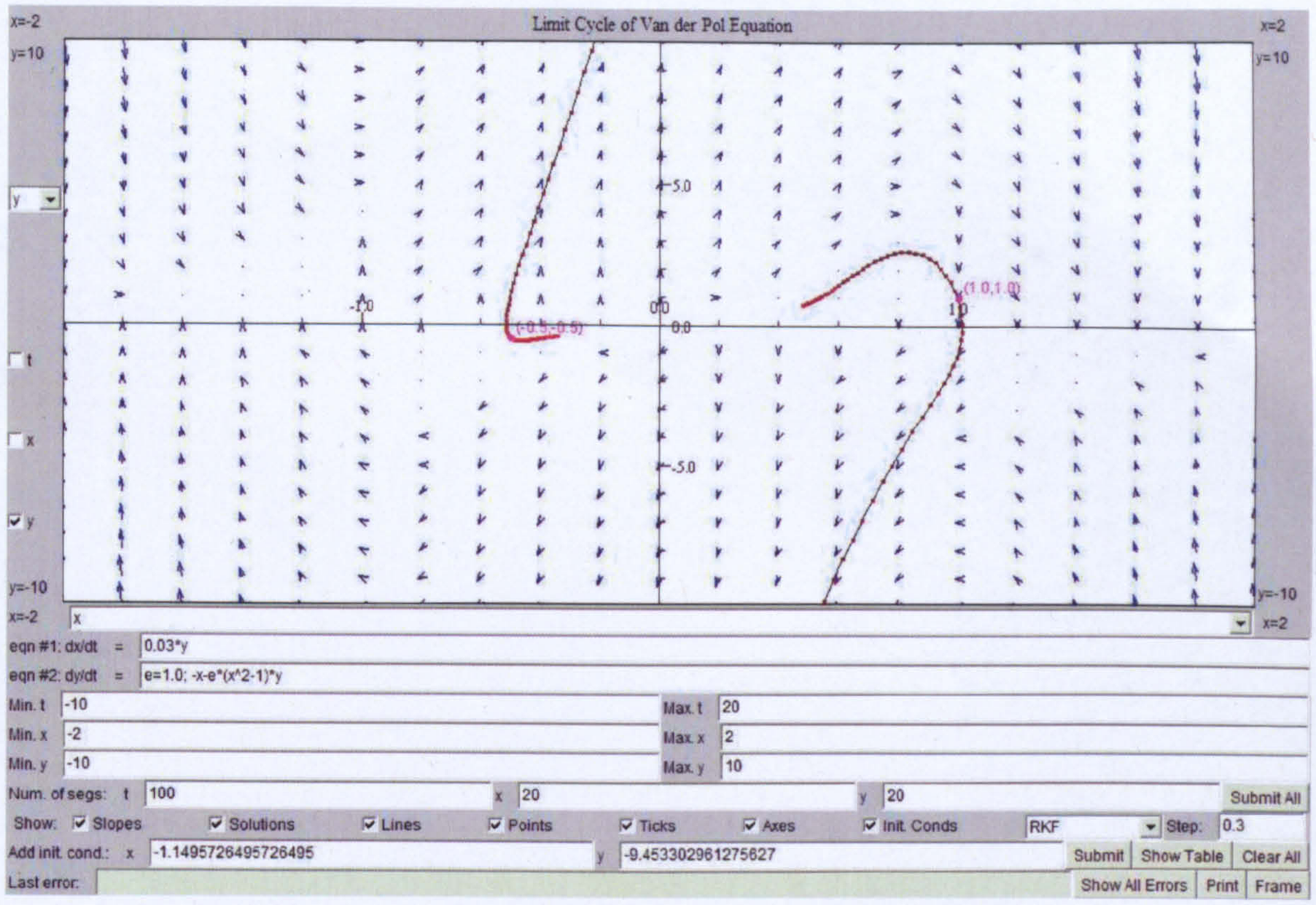

Figure 3.69 Van der Pol plot with *dx/dt* equal to 0.03 times y

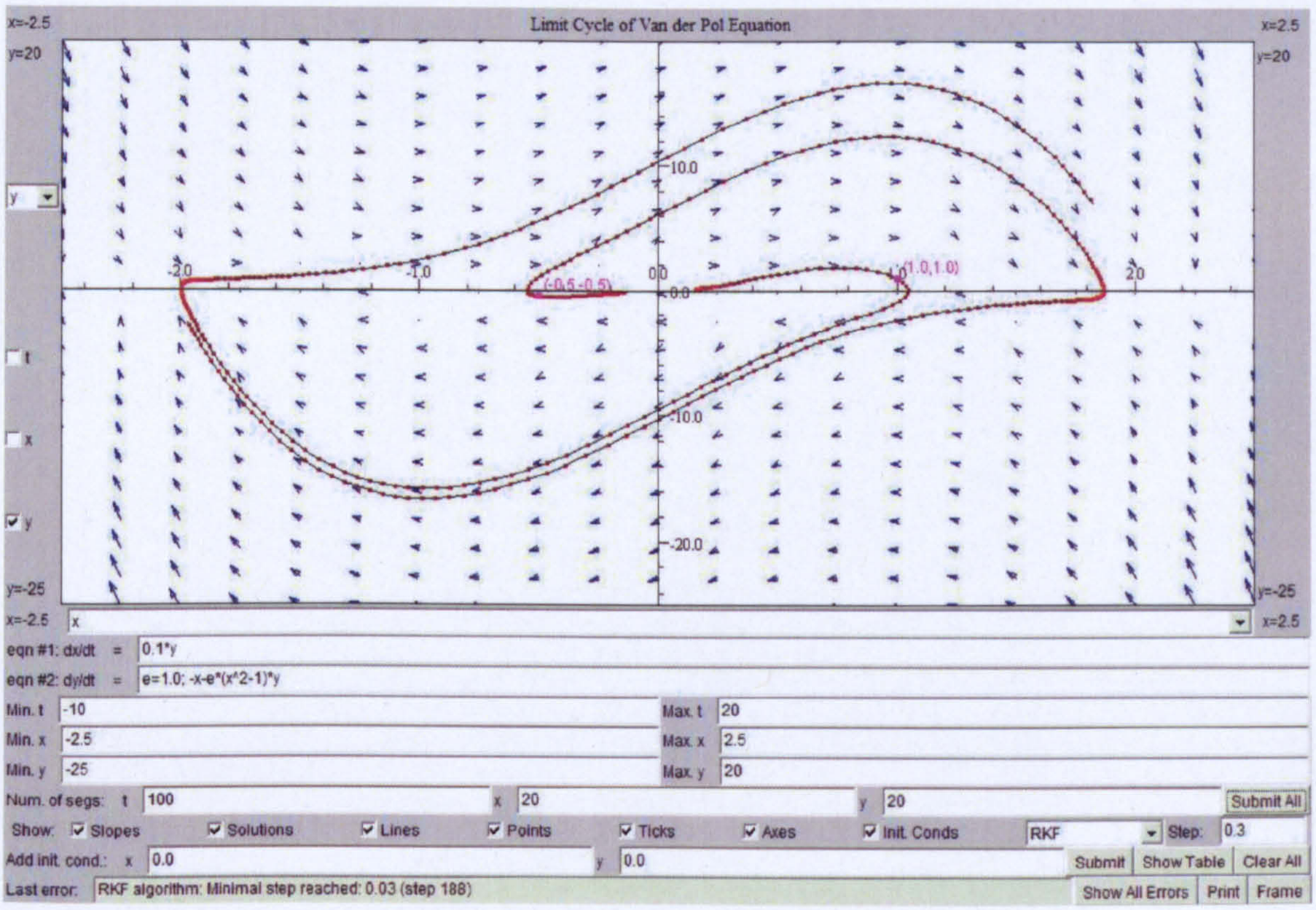

Figure 3.70 Van der Pol plot with *dx/dt* equal to 0.1 times y

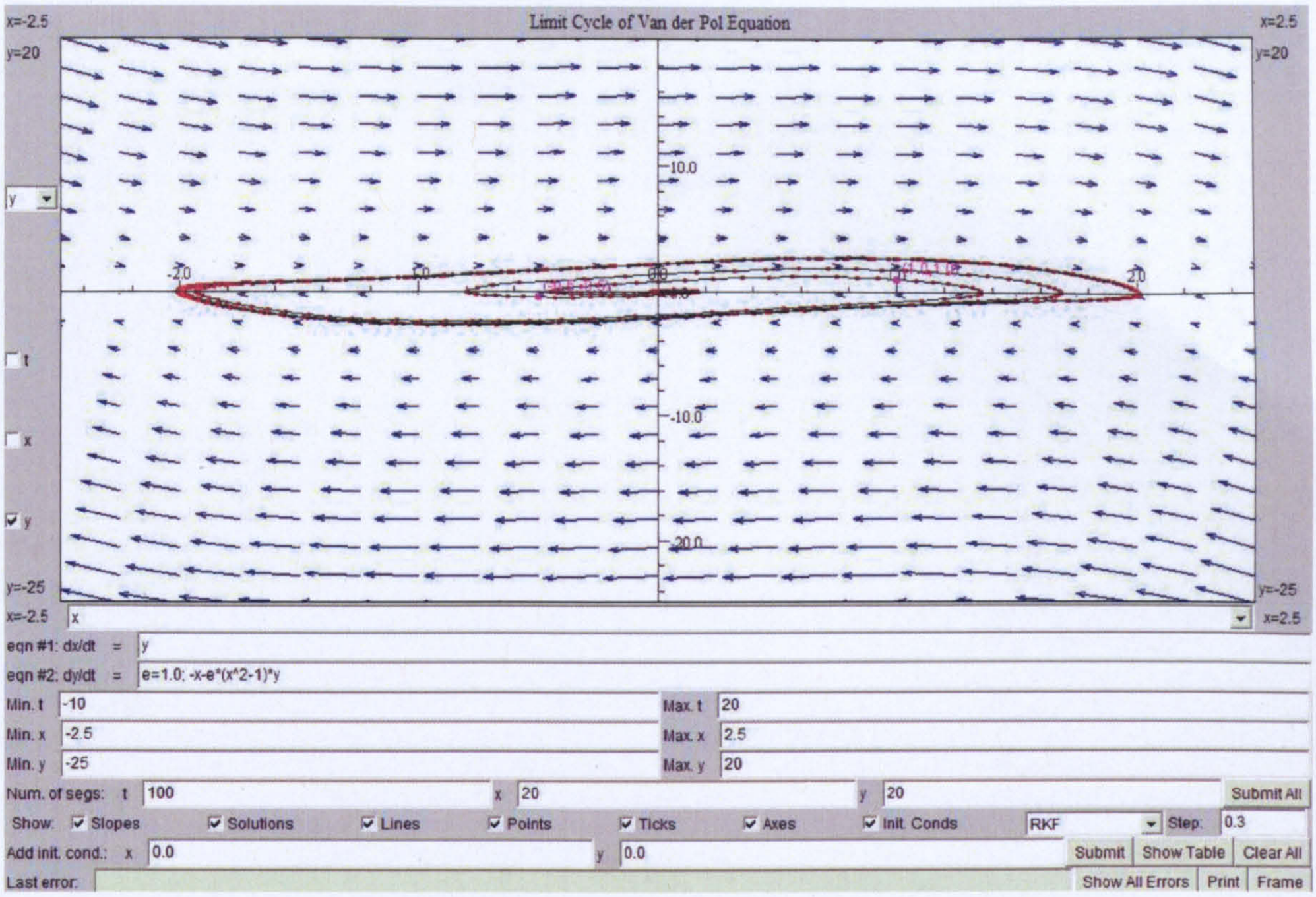

Figure 3.71 Van der Pol plot with *dx/dt* equal to one times y

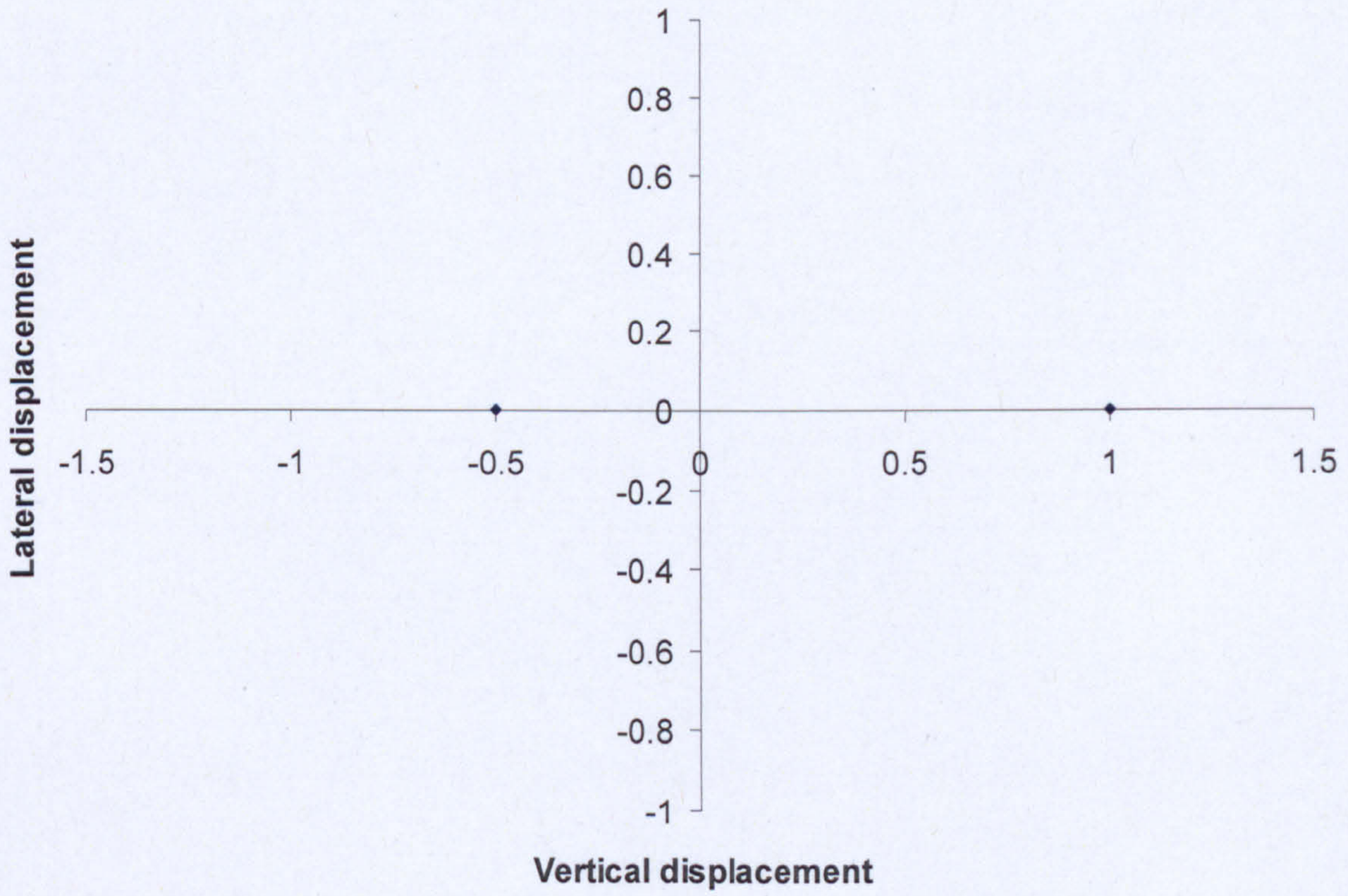

Figure 3.72 Poincaré map of the Van der Pol plot with *dx/dt* equal to zero

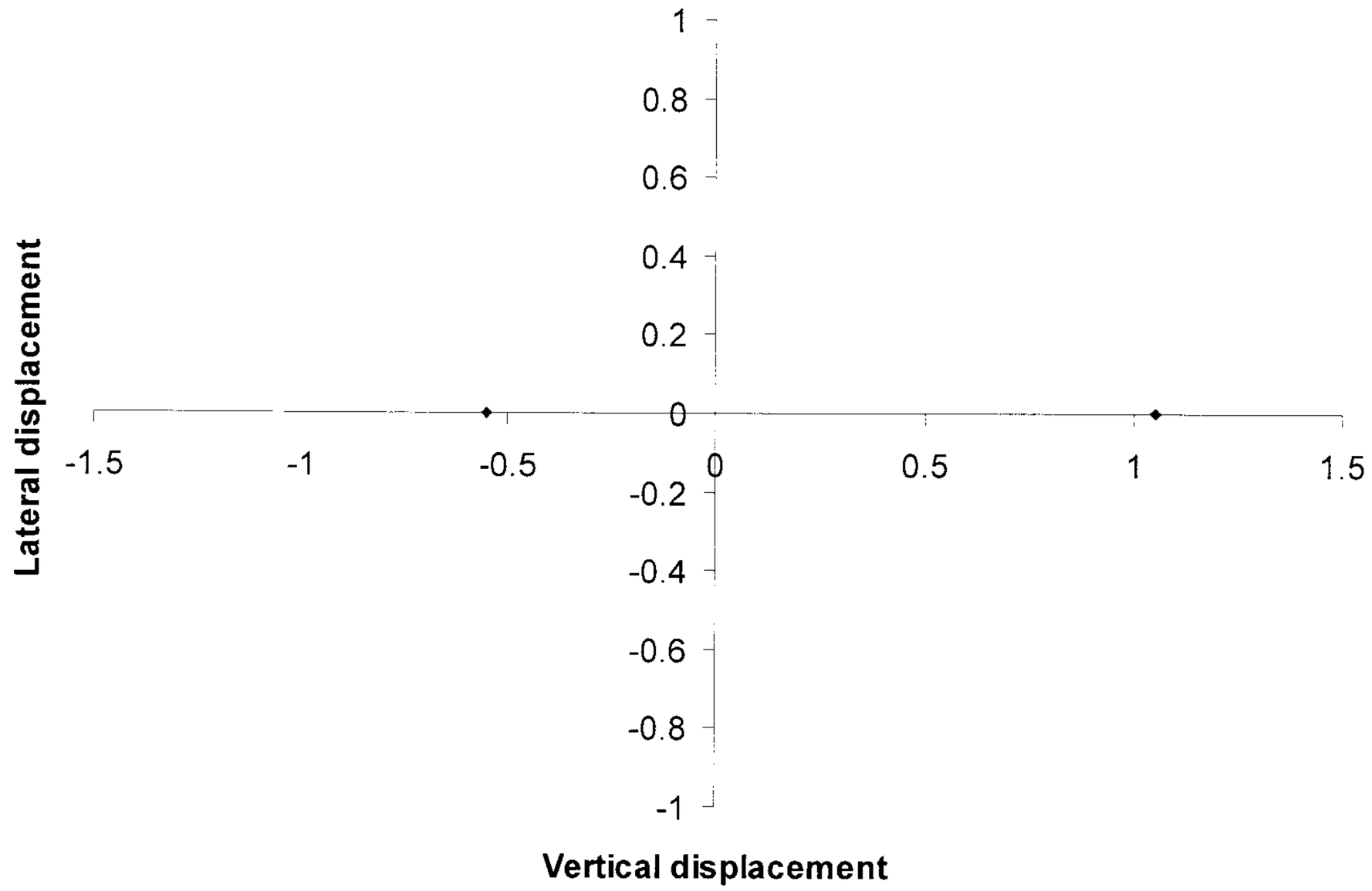

Figure 3.73 Poincaré map of the Van der Pol plot with *dx/dt* equal to 0.03 times y

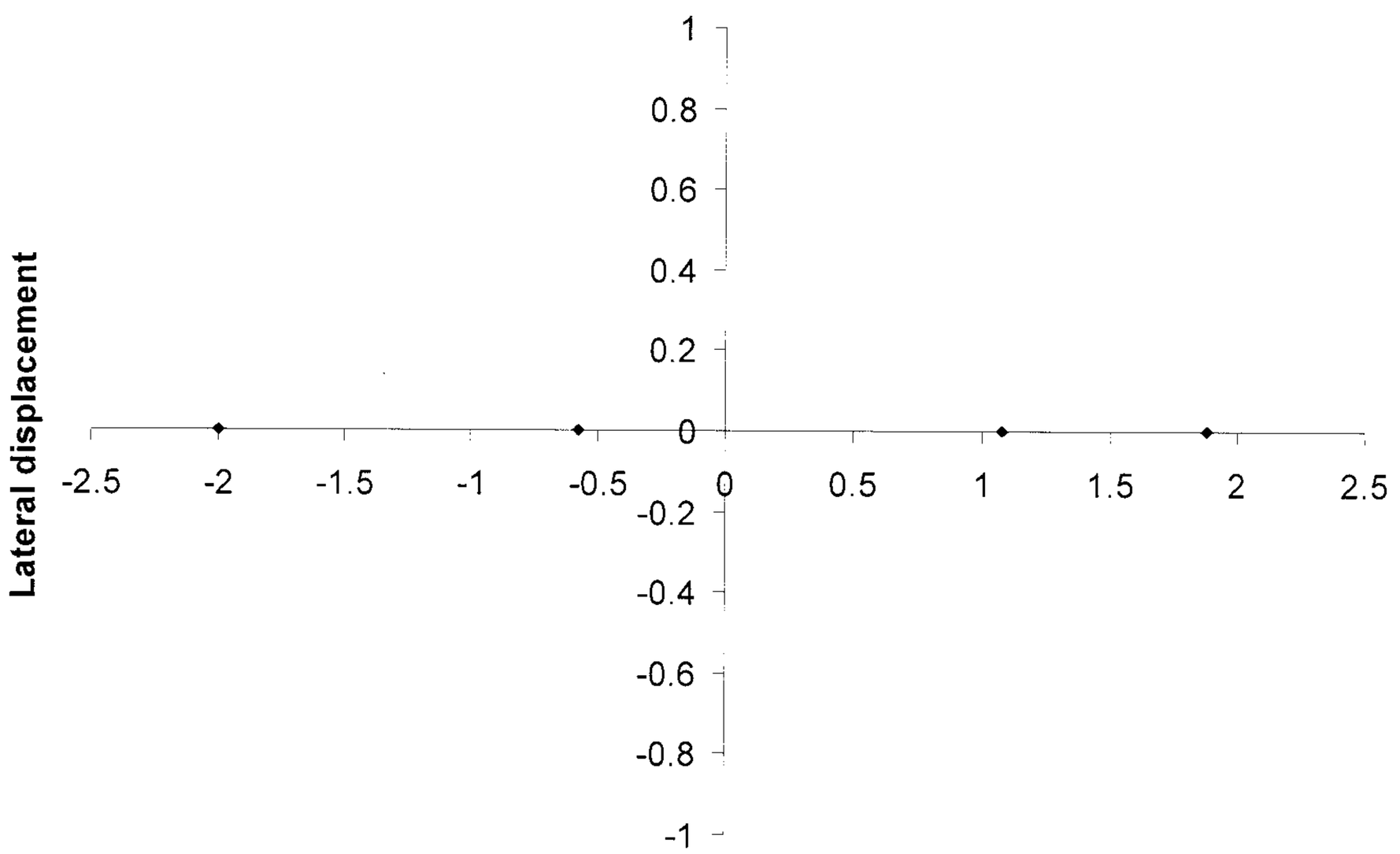

Figure 3.74 Poincaré map of the Van der Pol plot with *dx/dt* equal to 0.1 times y

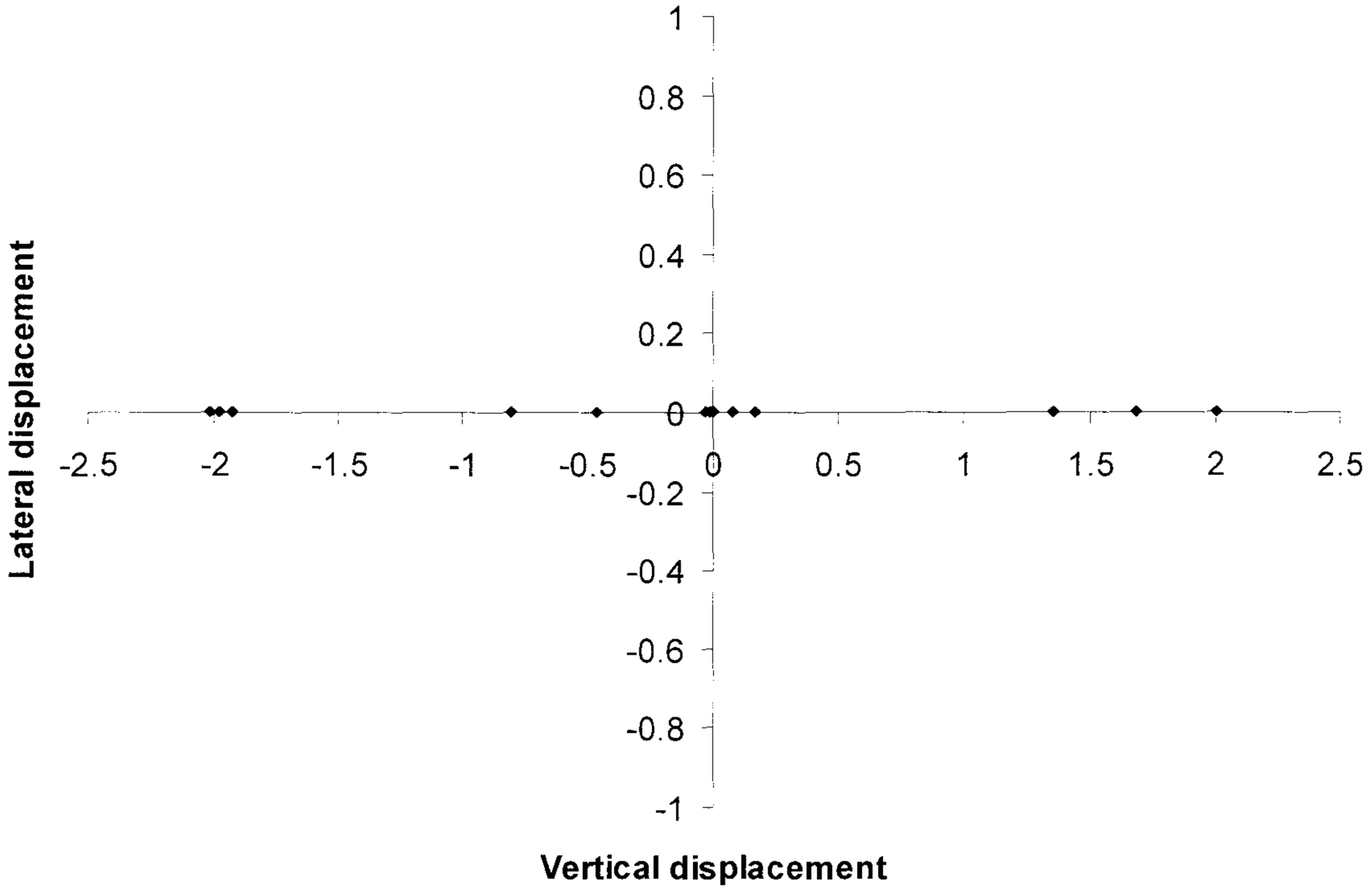

Figure 3.75 Poincaré map of the Van der Pol plot with *dx/dt* equal to one times y

Table 3.1 Stiffness values for each individual spring diameter

	Test 1, k_s Nmm^{-1}	Test 2, k_s Nmm^{-1}	Test 3, k_s Nmm^{-1}	$\overline{k_s}$ in Nmm^{-1} at $\alpha = 10°$	$\overline{k_s}$ in Nmm^{-1} at $\alpha = 20°$
Spring 1	1.23	1.22	1.21	1.13	1.05
Spring 2	2.43	2.46	2.44	2.21	1.99
Spring 3	5.55	5.66	5.71	5.09	4.92
Spring 4	9.35	9.52	9.55	8.65	8.07
Spring 5	15.6	15.6	15.7	14.9	12.1

Table 3.2 Average stiffness values for springs

	Spring 1	Spring 2	Spring 3	Spring 4	Spring 5
Average k_s, Nmm^{-1}	1.22	2.44	5.64	9.47	15.62

Table 3.3 Plate frequencies for variable support displacements (10 N load)

Primary plate resonance frequency due to 10 N load (Hz)						
V_0 / mm \ V_L / mm	0	-0.64	-1.06	-1.77	-4.10	-8.20
0	3.790	3.721	3.677	3.603	3.377	3.029
-0. 64	3.721	3.654	3.612	3.541	3.323	2.986
-1.06	3.677	3.612	3.571	3.501	3.289	2.959
-1.77	3.603	3.541	3.501	3.434	3.230	2.913
-4.10	3.377	3.323	3.289	3.230	3.052	2.770
-8.20	3.029	2.986	2.959	2.913	2.770	2.542

Table 3.4 Plate frequencies for variable support displacements (50 N load)

Primary plate resonance frequency due to 50 N load (Hz)						
V_L / mm V_L / mm	0	-3.20	-5.30	-8.90	-20.5	-41.0
0	3.790	3.461	3.268	2.975	2.281	1.591
-3.20	3.461	3.190	3.028	2.778	2.170	1.541
-5.30	3.268	3.028	2.883	2.658	2.101	1.508
-8.90	2.975	2.778	2.658	2.470	1.988	1.454
-20.5	2.281	2.170	2.101	1.988	1.679	1.293
-41.0	1.591	1.541	1.508	1.454	1.293	1.066

Table 3.5 Displacement values relating to support stiffness values

Spring stiffness, Nmm^{-1}	Force amplitude, N	Corresponding displacement at V_0 or V_L, mm	Force amplitude, N	Corresponding Displacement at V_0 or V_L, mm
Infinite	-10	0	-50	0
1.220	-10	-8.20	-50	-41.0
2.442	-10	-4.10	-50	-20.5
5.638	-10	-1.77	-50	-8.90
9.475	-10	-1.06	-50	-5.30
15.62	-10	-0.64	-50	-3.20

Table 3.6 Material and geometric properties of PMMA plate

Material or geometric property	Value
Breadth, m	0.8
Span, m	1.4
Depth, m	0.01
Density, kgm^{-3}	1194
Area in x-y plane, m^2	0.008
Second moment of area, m^4	6.667×10^{-8}
Young's modulus, GPa	3.15

Table 3.7 Accelerometer and excitation point locations for modal analysis and FEA

Accelerometer location (x , y) / mm			Excitation location (x , y) / mm				
Point 1	Point 12	Point 25	Point 4	Point 7	Point 14	Point 17	Point 24
x = 250	700	1250	x = 250	450	700	950	1250
y = 200	300	700	y = 600	600	600	600	600

Table 3.8 Resonant frequencies for modal analysis testing on PMMA plate

Support Condition	Frequency 1 (Hz)	Frequency 2 (Hz)	Frequency 3 (Hz)	Frequency 4 (Hz)	Frequency 5 (Hz)	Frequency 6 (Hz)	Frequency 7 (Hz)	Frequency 8 (Hz)
Free *	5.00	10.0	18.1	23.8	33.1	41.9	----	----
Simply Supported	5.63	15.0	22.5	34.4	----	50.6	----	----
Fixed	7.50	15.6	22.5	35.6	----	48.8	----	----
Spring 1	4.38	6.88	10.6	15.0	15.6	25.0	28.1	42.5
Spring 2	4.38	8.75	13.1	17.5	18.1	26.9	29.4	43.1
Spring 3	5.00	10.6	16.9	22.5	26.3	32.5	----	46.3
Spring 4	5.00	11.3	18.8	25.0	30.0	36.9	----	48.8
Spring 5	5.63	11.9	19.4	27.5	34.4	42.5	----	----

---- = mode not present

* Data is out of sequence. Free and fixed conditions should form the upper and lower bounds on fundamental frequency. The intermediate stiffnesses should lie between these two bounds. Anomalous results indicate the support condition was not as free as hoped.

Table 3.9 Results of eigenvalue analysis in FEA for PMMA plate

Support Condition	Frequency 1 (Hz)	Frequency 2 (Hz)	Frequency 3 (Hz)	Frequency 4 (Hz)	Frequency 5 (Hz)	Frequency 6 (Hz)	Frequency 7 (Hz)	Frequency 8 (Hz)	Frequency 9 (Hz)	Frequency 10 (Hz)
Free *	4.16	9.94	16.69	24.17	27.07	32.27	37.08	44.56	47.34	61.96
Simply Supported	4.19	10.70	17.04	25.98	34.92	38.69	48.71	52.23	68.96	77.71
Fixed	8.89	13.47	24.51	31.42	34.84	48.34	54.77	56.38	80.16	81.86
Spring 1	3.51	5.34	9.07	12.85	14.57	23.53	26.39	28.26	34.76	39.04
Spring 2	3.81	6.79	11.63	15.12	18.59	25.73	28.68	29.09	35.79	40.55
Spring 3	4.00	8.37	14.22	18.62	25.10	29.96	30.44	35.17	38.26	44.54
Spring 4	4.07	9.09	15.27	20.73	29.36	30.91	34.43	39.60	42.19	49.01
Spring 5	4.12	9.59	15.92	22.39	31.86	32.76	38.45	42.34	49.13	54.98
Variation in thickness - Spring 5 [1]	3.92	9.19	15.29	21.61	30.51	31.85	37.67	40.97	48.85	54.30

* Data is out of sequence. Free and fixed conditions should form the upper and lower bounds on fundamental frequency. The intermediate stiffnesses should lie between these two bounds. Anomalous results indicate the support condition was not as free as hoped.

1 Alteration in thickness as indicated by diagram below. $\delta_{thickness}$ is 0.0015 mm.

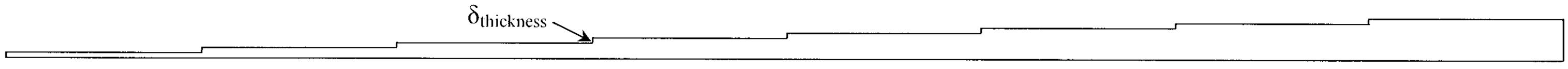

CHAPTER 4

Full-scale testing

4.1 Introduction

The data presented in this chapter relate to the highway bridge currently in use on the A1, specifically on the stretch of carriageway known as the Berwick-upon-Tweed bypass. This chapter presents details of the Principal Inspection Report (PIR), traffic count, vehicle speed, and axle weight data derived from *in situ* induction loops and weigh-in-motion (WIM) sensors, followed by data arising from the non-destructive testing of the bridge.

The research presented aims to establish the information required to determine the effects of degradation in bearing condition on the bridge response thereby setting a baseline for subsequent condition monitoring. It draws upon the key findings of Chapter 3 and illustrates the use of the recorded change in fundamental frequency for a range of support stiffnesses (f_0 = 0.09, f_1 = 0.35, and f_2 = 0.6 Hz / Nmm^{-1}) presented in Section 3.2.1.2. To assist the transition from small-scale model to full-scale field testing additional research to that presented in Chapter 2 is used. Research in the early 1990s[4.1] indicated that structural damage can cause significant changes to resonant frequencies and modeshapes. This chapter highlights this method for the structure tested. The replacement of failed bearings is expensive and potentially disruptive, in both financial and engineering terms. Bearing failure can lead to damage to the superstructure; early identification of decay could save time and money.

The dynamic response of highway bridges to the applied random traffic excitation arising from day-to-day loading has been widely researched[4.2-4.4]. Investigations into structural health monitoring[4.5-4.7] and damage detection[4.8-4.11] are also covered by existing research. The influence of bridge bearings upon the dynamic response of a bridge, in particular the effect of a gradual degradation of the bearing, has also been considered[4.12-4.14].

The testing described herein relates to traffic count, speed, and weight (strictly speaking, mass) data obtained from the WIM sensors and the induction loops incorporated in the carriageway. The vibrations measured would be meaningless unless they could be related to the traffic causing them. The bridge owner's PIR is used for information relating to the bridge's general condition: similarly, little may be meaningfully said about the measured vibrations in the absence of any assessment of the bridge's structural integrity from a broader engineering perspective.

The set of NDT results are intended to represent a baseline state for condition monitoring through further regular measurements. Although the bridge has been in use for over 20 years (it was officially opened in 1982), the bearings should be functioning as intended. The accuracy of the results for this testing is reliant upon the correct parameter identification; modal data included in the identification analysis can affect the accuracy of results. Problems with identification of modal parameters are discussed in Section 4.6.3.

To confirm the concept highlighted in Chapter 3, a full-scale dynamic modal response test of an actual highway bridge currently in use was performed. After meeting at the

Scottish Roads, Highways and Traffic Management conference (Ingliston 2004), the Department of Transport, Highways Agency, Napier University and a private company called Applied Traffic, a suitable bridge to test was made available to this *ad hoc* consortium.

4.2 Bridge location and type

The main theme of the research is to determine the dynamic response of the structure, and the effect of bearing degradation using modal analysis, which is a tool familiar to most engineers.

The bridge tested was a two-lane highway bridge and is located on the A1 (Berwick-upon-Tweed bypass) over the River Tweed (Ordnance Survey grid ref. NT 974 517). The bridge was opened in 1982 and runs approximately North-South over the River Tweed. The bridge was designed to BS 5400 and comprises twin plate girders, with a smaller central beam and K-shaped bracing sections at 6.00 m centres across the length of the structure[4.15]. A general view of the bridge is shown in Figure 4.1. The 13.5 m wide deck is a reinforced concrete slab with edge cantilevers. The bridge was designed to carry 45 units of HB loading and consists of four spans; 37 m, 56 m, 53 m and 49 m. The combinations of HA and HB loading are shown in Figure 4.2, along with the axle spacing for the HB loading vehicle. At the South abutment, the expansion joint is a Waboflex® moulded rubber segmental joint system (see Figure 4.3) and the bearing is a Freyssinet® guided sliding pot bearing (see call out from Figure 4.4). Pot bearings are designed to allow a relative rotation of up to 1/50, whilst at the same time providing the same effect as a point-contact rocker bearing as the centre of pressure does not vary by more than 4% in any axis or direction. The bearings are designed to allow the structure

to translate in the longitudinal direction due to a low coefficient of friction PTFE surface ($\mu_{kinetic} \approx 0.04$ to 0.10), and are restricted from movement in the transverse direction by two steel guide-rails. The bearings are located beneath a stiffening plate beam which connects the span beams, which are 7 m apart from centre to centre, 3.5 m either side of the centre line of the running surface. The bearings at the south abutment are 4 m apart, two metres either side of the centreline. The bearings located at the top of the three piers are steel rocker bearings, with the bridge fixed in place at the north abutment. The bridge slopes from South to North with a level change of approximately 1 m, and leads to a five arm roundabout located approximately 200 m from the South bank of the River Tweed. The plate girders are 2205 × 50 mm (web), 1000 × 50 (bottom flange), 600 × 50 mm (top flange), changing to 1000 × 50 mm over the supports. The stringer beam over the total length of the bridge is a 553 × 210 × 101 kg/m universal beam section. The stringer beam is bolted to several steel angle sections which act as transverse stiffeners, and produce a K-section shown in Figure 4.4.

The expansion joint at the south abutment is located directly above the bearings separating the head wall from the bridge superstructure. The expansion joint is considered to be faulty as it protrudes from the running surface of the bridge, when installation requires that the joint be raised no more than ± 5 mm from the running surface. As a result, impact loading from vehicles striking the expansion joint is imparted onto the structure. The installation of expansion joints greatly influences their ability to perform as intended[4.16]. In research on expansion joints, the effect of an impact loading, and hence the DAF, are shown to be important factors to consider when designing the expansion joint[4.17]. In certain cases, when the load factor is also added, the DAF can be over two. This indicates that the fault with this expansion joint is

potentially significant. Research in the 1970s outlined the major factors influencing dynamic loading caused by vehicle suspensions[4.18].

In addition to the steel superstructure, an access cage (see Figure 4.5) and walkway are located underneath the bridge running surface for maintenance purposes. The steel walkway runs the entire length of the bridge and is bolted to the steel K-sections.

4.3 Test arrangement

The main theme of the research was to use modal analysis to determine the bridge's dynamic response and the effect of bearing degradation thereon. Vibration data were collected in 15 minute runs, for a four hour period on Thursday 19th May 2005 using accelerometers connected to spectrum analysis equipment. The data were analysed by fast Fourier transform (FFT) methods.

Following initial investigations of site layout and facilities, the following testing methodology was derived for the set of tests recorded on the bridge. Access to the bridge soffit adjacent to the head wall at the south abutment was by a four metre retractable ladder attached to the access cage through a removable section in the cage floor (Figure 4.5). Accelerometers were attached to the soffit using a small, plastic mounting clip (see Figure 3.19 for detailed drawing) fixed in place using a two-part epoxy glue (Figure 4.6). The small plastic clips will remain *in situ* to ensure that subsequent measurements of bridge response will be recorded in exactly the same positions, allowing direct comparison of results.

Each of the accelerometers was connected to the analyser by a 30 m long cable, type AO 0463-K. The cables' cores are 2 mm in diameter and have a capacitance of 100 pFm^{-1}. The cable insulator is polyethylene, the cable coating is polyvinylchloride and has a working temperature range of -20°C to 70°C.

The accelerometers used for the testing were the same 4508-B type accelerometers used in the small-scale model testing. This type of transducer is robust enough to undertake this testing as it is considered a general use transducer. The analyser used in the laboratory testing was used to record and analyse the data from the bridge testing (see Figure 4.7)

For these tests there are no input values to record (traffic itself forming the excitation as opposed to a hammer) unlike in the laboratory tests. As a result, FRFs constructed are related to data obtained from traffic WIM sensors for Type 56 HGVs and not from force transducer measurements as loading from larger vehicles is considered more damaging. The damage caused by vehicle axle loads is a fourth power relationship as shown in Eq. 4.1, so the larger the axle load, the greater the damage[4.19].

$$DF = (\text{Gross vehicle mass})^4 \qquad \text{Eq. 4.1}$$

In the laboratory testing, a measurement was taken when the impact hammer was triggered at a given force. For the bridge testing, as there is no input force transducer, data were recorded over a four hour period using a data storage function in the analyser. The length of time recordings can be taken over is variable. A period of 15 mins was chosen to reduce the file size of the recordings, therefore reducing the chance of any

data being lost. A typical 15 min recording of an accelerometer signal produced a 30 MByte file with as much file space again for the duplicate, back-up, copy.

Once these data were recorded, they can be played back in the PULSE software and analysed accordingly. Specific events captured in a recording can be analysed in greater detail by zooming in and highlighting any section of the recording using signal analysis software. The highlighted section of data can then be analysed, thereby obtaining the autospectra and related graphs for that time period.

4.3.1 Location of accelerometers

To investigate various sections of the bridge structure and the overall structural response due to vehicle movements, five tests were performed. The initial test which was only a matter of seconds in length was taken to indicate the background noise level on the bridge. This test was performed with the accelerometers in the arrangement used for the first set of tests at the south abutment where the expansion joint and pot bearings are located.

The first hour of testing was carried out with a line of four accelerometers located at the headwall of the bridge superstructure, with the accelerometers numbered from left to right looking in a southward direction. Two accelerometers were located on either side of the steel stringer beam which runs the entire length of the structure. Each accelerometer was located so as to be as close as possible to the line of the wheel tracks of the vehicles traversing the running surface. The fifth accelerometer was located on the bearing plinth beneath the northbound lane (see Figure 4.8). The exact locations are shown in Figure 4.9.

The third set of tests comprises a set-up similar to that of tests 1 and 2. The four accelerometers were moved from the headwall to the first intermediate K-shaped bracing section, 6 m from the headwall. Four 15 min tests were then recorded as before. Test 4 simply saw the accelerometers moved to the next K-shaped bracing sections moving out across the span from the South. Four 15 min scans were recorded for each of Tests 2 to 4. Figure 4.4 showed the locations of accelerometers for these tests. The fifth accelerometer was not used in test 3 or 4 as there is no bearing located under the K-shaped bracing sections.

Test 5 used nine accelerometers to trace vehicle movement along the bridge, both southbound and northbound. The nine accelerometers were sited 200 mm from the centreline of the bridge, underneath the southbound carriageway. Accelerometer 1 was on the headwall and Accelerometers 2 to 9 were on the first to eighth K-shaped bracing sections counting from the South abutment; Accelerometer 7 was sited over the first set of piers housing a set of rocker bearings. Each line shown on Figure 4.10 indicates the position of an accelerometer (one *per* K-shaped bracing section) for this test arrangement. To allow each cable used to be a reasonable length, and not the full 30 m, the analyser was moved from its initial location to accelerometer location 5 which was equidistant from accelerometers 1 and 9 (see Figure 4.11).

All tests were completed on the same day, and the temperature ranged from 9°C to 16°C. This may have a bearing on the results, although recent research on concrete slabs indicates that whilst frequencies have a negative correlation with temperature, the most influential parameter is Young's modulus[4.20] which, over this 7°C temperature range, exhibits little change.

4.4 WIM Classifier

Traffic data for vehicles crossing the bridge were obtained from Applied Traffic who, in conjunction with the Highways Agency, monitor the bridge traffic with WIM sensors. These are located on the South side of the bridge, with one sensor in each lane. The sensor consists of two separate sections: the first comprising two piezoelectric devices set into the carriageway surface. These act as an on/off switch, counting the number of axles, axle loads, axle spacing and vehicle speed. The second section comprises an induction loop located between the two piezoelectric devices. The induction loop detects the overall length of the vehicle. The general instrumentation arrangement is shown in Figure 4.12, and the datalogger is shown in Figure 4.13. Speed, classification and count accuracy has been repeatedly checked and verified in association with the DTLR including the use of Home Office approved speed monitoring equipment to verify speed accuracy to within ± 1 mph. Compliance with the accepted DfT and Highways Agency standards are met by calibration tests. Three vehicles comprising a 5 or 6 axle articulated vehicle, a 3 axle rigid vehicle and a 2 axle rigid vehicle are loaded to give a spread of axle weights ranging from 1 tonne through to 10 tonnes. Ten set up passes are used to produce the calibration factor and five further passes are used to confirm the system accuracy. Under COST 323 European WIM specification recommendations, the sensor should meet the accuracy of Class B (10) which specifies GVW accuracy of ± 10 % for 95 % confidence.

The data were collected, added to a database, and each traffic event assigned a reference number. In addition to axle loads and speeds, the data included each vehicle classification number (see Table 4.1), the lane in which each vehicle was travelling, their speeds, gross vehicle weights and axle weights, and the time at which each vehicle

passed the sensors. Histograms and statistics were produced for: distributions of variables, determination of their means, variances, standard deviations and quartile points. In recent years, a system utilising this type of sensor has been developed for use in maintenance regimes for Area 14[4.21].

4.4.1 WIM theory

To produce the various types of data, the sensor uses two simple techniques using piezoelectric sensors and an inductive loop. A piezoelectric crystal is a naturally occurring material, where certain crystals, in this case quartz, emit an electrical charge when subjected to mechanical loading. This electrical charge can then be converted into a voltage, which is then related directly to a force or pressure.

The induction loop, an electric conductor, is placed into the road surface. It is activated when the large metal mass of the vehicle passes overhead, completing the circuit. The system detects the induced current as the vehicle passes over, with different vehicle types producing different currents for a constant inductance in the loop. It is often difficult to detect smaller vehicles with induction loops, but the sensitivity can be increased to compensate. This can often lead to double counting of vehicles, or vehicles not in the same lane being detected and counted (refer to p. 243 for error bounds).

The WIM senor data were intended to be used to determine which vibrations detected by the FFT analyser are related to specific vehicle types and axle loads. This was to be achieved by matching the time signatures on the set of readings taken from both the WIM and the FFT analyser. Any significant events were then to be analysed in greater detail.

4.5 Results

4.5.1 Principal inspection report

The PIR, arising from inspections performed in November 2001 and February 2002 by Northumberland County Council, was obtained and defects at various locations on the bridge were noted. In July 2003, A-one Integrated Highway Services (a 50:50 joint venture between Halcrow Group Limited and Colas Limited) assumed the role of agent from Northumberland County Council and now maintain the bridge as Managing Agent Contractor for Highways Agency Area 14. Figure 4.14 shows the countrywide separation of areas and the main routes within Area 14.

4.5.2 Traffic survey

The traffic data obtained are to be related to dynamic loading caused by shockwaves induced in the bridge by vehicles striking the expansion joint. The data obtained from the WIM sensor located on the south side of the bridge for one typical day has been arranged into 21 separate vehicle classifications shown in Table 4.1. The day chosen in this case is a Wednesday as this is considered a "neutral" day in terms of traffic movements. A "neutral" day is one where there are no extreme events on the road network. The weekend, Mondays and Fridays are considered "non-neutral" due to unusual traffic patterns. Mondays and Fridays see the network more heavily loaded due to people attending work and HGVs delivering goods at the start and end of the week.

Each vehicle classification was divided into lane number, producing two data sets for each vehicle type. Tables 4.2 and 4.3 show data obtained for vehicle speeds in the northbound and southbound lanes respectively. Tables 4.4 and 4.5 show data obtained

for overall gross vehicle weight (strictly a mass in kg) in both northbound and southbound directions for all recorded vehicles.

Tables 4.6 to 4.11 present data obtained for individual axle loads for all vehicle types recorded in both directions across the bridge. Tables 4.6 and 4.7 present the maximum and minimum axle weights recorded for each vehicle type in both directions. Tables 4.8 and 4.9 show data relating to average axle weights recorded, and Tables 4.10 and 4.11 present the standard deviations obtained for each vehicle type in both directions.

Note that in these data tables, vehicle types 5N, 6N, 7N, and 8N are not shown. This is because no vehicles of this type were recorded on the day of testing.

From the data obtained, histograms showing the spread of gross vehicle weight, axle weight and velocity were produced and are shown as Figures 4.15 to 4.30. This data was then used to determine the values of vehicle momentum, kinetic energy and vehicle damage factors. The results of these are shown as Figures 4.31 to 4.36.

4.5.3 NDT

Figure 4.37 shows acceleration *versus* time traces for each of Accelerometers 1 to 5 inclusive which were used to represent the background noise level for the subsequent testing. Figure 4.38 shows the FFT of these data, presenting the frequency spectra for background noise measurements. Figure 4.39 shows a zoomed in section over the first 50 Hz.

Figures 4.40 to 4.43 show the time traces and subsequent FFT of data for three time sections recorded during the first hour of testing at test location 2.

Figures 4.44 to 4.47 show similar data for hour two at test location 3. Figures 4.48 to 4.51 show the data for hour three at test location 4.

Figures 4.52 to 4.57 show similar data relating to test 5, where nine accelerometers were located along the centreline of the bridge.

Figures 4.58 to 4.63 show the inertance, admittance and dynamic stiffness obtained for a 92 kN HGV for data obtained in Figures 4.40 and 4.42.

4.6 Discussion

4.6.1 Principal inspection report

The PIR written between December 2001 and January 2002 highlighted several points of interest regarding the condition of the bridge. The previous PIR from December 1996 indicated that cracks were evident in certain areas of the substructure and bridge deck. Steelwork in the superstructure was showing signs of corrosion. Since the previous PIR the parapets were replaced and the steel superstructure painted.

The PIR highlighted cracking and spalling on the concrete piers and abutments. Several cracks propagating from the bearing plinths at the South, central and North piers were evident: many of these were not noted in the December 1996 PIR. The South abutment has several cracks on both internal and external walls. The abutment is hollow and houses a corroded wastewater pipe, further contributing to what is a naturally humid,

saline environment (the bridge lies 3 km from the coast). The external wall of the South abutment has some spalling with exposed reinforcement on the East face of the abutment.

The bearings at the South abutment were repainted and are considered to be in satisfactory condition although the East bearing plinth showed signs of spalling. The south, central and north pier bearings showed evidence of seepage of lubricant from the bearing housing (see Figure 4.64). This was due to their being fully packed with grease and temperature effects subsequently driving some of the lubricant out the bearing housing at locations where the lack of a sealant permits. The central and north pier bearing plinths both showed signs of cracking. The north abutment was considered to be satisfactory. The steel superstructure was considered to be in a satisfactory condition, with only minor corrosion at the North abutment due to localised water seepage. The concrete slab has numerous hairline cracks with three cracks showing evidence of salt staining. Several sections of the concrete slab showed evidence of water seepage possibly due to inadequate waterproofing, this has since been remedied. Improvements in the condition and layout of the south approach to the bridge were made in early 2006. This scheme involved the resurfacing and reconstruction of the existing carriageway from Scremerston roundabout to the River Tweed Bridge a distance of 3.5 km (2.2 miles). The works began in February 2006 and were completed in March 2006. Further remediation of the structure, including the resurfacing of the existing carriageway between the River Tweed Bridge and the A6105, utilising crack and seat treatment to existing lean mix concrete to remove faults in the structure is to be completed. This action is accompanied by replacement of the River Tweed Bridge waterproofing, surface materials and replacement deck drainage system. The works are expected to

start in August 2006 and be completed in December 2006 at an estimated cost of £2.5m[4.22]. Another point of interest is that the bridge recently failed the HA and HB loading tests with respect to displacement criteria. This failure does not necessarily mean the structure is unsafe, but does indicate that all members are working close to capacity. This could have an impact on the serviceability state of the structure more than the ultimate limit state, producing cracking across the concrete deck sections, which will in turn lead to a reduction in structural stiffness. With this in mind, identification of degradation in performance of bearings then becomes more problematic to determine accurately.

4.6.2 Traffic survey

Table 2 shows that the average speed of most vehicle types crossing the bridge in the northbound direction is approximately 40 mph (65 kmh). Data presented in Figure 4.15 and 4.16 show the spread of vehicle speeds in both lanes. These figures indicate that the vast majority of vehicles occur in the 35 to 50 mph range. The speed of vehicles is considered to be of interest for the larger vehicles, such as articulated lorries, as the dynamic loading imparted upon the bridge structure will be greater due to the larger vehicle mass. The momentum is given by Eq. 4.2 and the kinetic energy by Eq. 4.3. Typical values for a family saloon were 55252 $kgms^{-1}$ and 1.17×10^6 J, for a 44 tonne HGV were 1.62×10^6 $kgms^{-1}$ and 29.98×10^6 J, and for the maximum overloaded vehicle recorded during testing (59.9 tonnes) were 2.3×10^6 $kgms^{-1}$ and 45.6×10^6 J. Standard deviations of the data for vehicle speeds indicates that the larger vehicles have a much narrower range of speeds, again in part due to the large mass of vehicle, compared to smaller vehicles such as cars or vans.

$$p = mv \qquad \text{Eq. 4.2}$$

$$KE = \frac{1}{2}mv^2 \qquad \text{Eq. 4.3}$$

Figures 4.31 to 4.36 show the momentum, kinetic energy and damage factor results for all vehicles recorded during the period of monitoring. These figures are weighted due to the large number of cars occurring compared to the larger HGV types of vehicle which account for approximately 15 % of vehicles recorded. However, this small percentage of vehicles has a much more damaging effect on the performance of the bridge. This is shown in Figures 4.35 and 4.36 where only 10 % of vehicles in lane 1 and 5 % of vehicles in lane 2 produce significant damage factors. This damage factor, combined with the larger vehicles increased momentum and kinetic energy, imparted onto the structure through the expansion joint could result in extreme remedial action, even complete replacement, being required.

What is apparent from this data set is that the majority of HGVs are either overloaded or have the mass unevenly distributed over the axles. Table 4.1 indicates that of the 528 overloads in both lanes combined, 370 are recorded for Type 56 vehicles. This can result in greater impacts on the faulty expansion joint. Figures 4.17 and 4.18 present data obtained for gross vehicle weight, noting the relatively small number of vehicles running at over 44 tonnes in either direction which is 3 % in both directions.

The distribution of axle weights is clearly shown in Figures 4.19 to 4.30, although the data shown in Figures 4.19, 4.20, 4.25 and 4.26 are heavily weighted to the lower end of the axle weight distribution due to the higher volume of cars detected compared to HGVs. It should also be pointed out that most HGVs tend not to be overloaded on the

front two axles as these carry the loading from the vehicle cab and top section of trailer. The figures show that the most overloaded axles are more commonly the 3rd and 4th axles which tend to be located at the rear, or at least close to the rear, of the vehicle. This is case in both directions of travel.

Only the data from these particular vehicles was of particular interest as the larger vehicles generate greater dynamic loading. Another interesting point from the data is that of the 528 combined overloads, 339 vehicles were recorded as weighing more than 44 tonnes. The reason for the slight difference between numbers of vehicles overloaded and those weighing more than 44 tonnes is that the maximum load criteria is dependent on the axle spacing and vehicle suspension type as indicated by The Road Vehicles (Construction and Use) Regulations 1986[4.27]. Many modern vehicles now have load transfer bars which distribute loading evenly to each axle, reducing the likelihood of poor loading. However, the data presented in Figures 4.19 to 4.30 show a wide range of axle loads, although it should be noted that few are considered to be over the maximum axle weights permitted for each vehicle type.

Investigations into dynamic responses of bridge structures to HGV loading[4.14] have attempted to develop methods for determining the response due to a given set of vehicle loading. The information shown indicates that the spread of vehicle loading is relatively restricted, with most standard deviations of axle loading being between one and three tonnes. It is also obvious that many of the vehicles travelling across the bridge are overloaded on certain axles due to poor load distribution, some axles carrying very little weight and others overloaded, and in many cases overloaded overall.

The maximum vehicle weight recorded for the data analysed was a Type 56 vehicle running with an overall gross weight of 59.9 tonnes. No vehicles crossed the bridge with an abnormal load escort during the monitoring period. One of the other main factors that affect the vibration signal is the type of vehicle suspension. Loading from air suspension is generally lower compared to steel suspension, in the order of 10 % less in certain cases[4.23]. The number of wheels *per* axle is also considered, with twin wheels considered to produce higher dynamic load coefficients[4.24].

There were no emergency services present within 1 km of the bridge, nor were there any road traffic accidents during the monitoring period within 10 km of the bridge. No road works were underway within 10 km of the bridge during the monitoring period. The presence of any of the aforementioned factors may affect the measured vehicle speed distributions in a number of ways: luckily, this did not appear to happen here.

4.6.3 NDT

Initial testing to establish background vibrations in the absence of traffic excitation was undertaken. Figure 4.37 shows the time domain plot for a sub-sampled 6 s of recording. Figure 4.37 shows acceleration *versus* time traces for each of accelerometers 1 to 5 inclusive which were used to represent the background noise level for the subsequent testing. As with all acceleration *versus* time plots (also known as time domain plots), Figure 4.37 was analysed by FFT methods which gave rise to Figure 4.38 which presents the autospectra (or frequency domain plots). The vibration levels recorded in Figure 4.38 were insignificant with the exception of those arising around 0.25 Hz. Following consultation with the accelerometer manufacturer, the peak may be ignored as it was safely assumed to be a spectral component produced by the accelerometer, and

thankfully *not* a resonant frequency of the bridge. Various factors such as wind induced movement of the cables, triboscopic effects induced by close proximity to metal piping and high capacity power cables within the structure, and errors inherent within the equipment are all considered possible reasons for the noise to occur. As the high-pass filter was set to 0.7 Hz in any case, the peak at 0.25 Hz cannot be a recorded frequency, and was therefore filtered and removed from the data in the time domain.

Regardless of source of vibration the bridge's first three resonant frequencies rising from the fundamental frequency (f_0) through to mode 3 (f_2) were: 1 Hz $\leq f_0 \leq$ 2 Hz, 3 Hz $\leq f_1 \leq$ 4 Hz, and 10 Hz $\leq f_2 \leq$ 11 Hz. The band attributed to each mode of vibration encompasses the frequency resolution, Δf of 0.25 Hz for the system used, and allows for variability caused by thermal changes during the monitoring period. Values obtained for the resonance frequencies obtained are compared with values calculated by FEA and the modified Euler-Bernoulli method outlined in Chapter 3. These values are shown in Table 4.12 and show that the FEA and Rayleigh-Ritz method both provide close agreement for the first two resonance frequencies, but underestimate the actual frequency recorded for the third resonance by 5 Hz.

To show the effects of traffic on the bridge's dynamic response, sample acceleration *versus* time plots from Test 2 (five accelerometers on the South abutment headwall) are provided in Figures 4.40 and 4.42. From left to right (722 s $\leq t \leq$ 729 s), Figure 4.40 shows vibrations from two three axle HGVs (724.5 s $\leq t \leq$ 726 s) with a similar sized three axle HGV travelling in the opposite direction immediately afterwards, which is then followed by two larger HGVs (726 s $\leq t \leq$ 727.5 s), then a slight gap to a further three axle HGV (728 s $\leq t \leq$ 728.5 s). Figure 4.42 is taken over a longer period of time,

approximately 20 s in total. Figure 4.42 highlights the effect of vehicles travelling in both directions, striking the expansion joint at either exactly the same instant or close to each other. Nine large HGVs pass within this time period, interspersed with five cars or smaller vans.

The northbound vehicles were typified by sudden impact as they passed the expansion joint and were detected. They were then followed by a gradual decrease in measured acceleration as they moved out onto the span; increasing distance between vehicle and instrumentation resulted in attenuation of the signal. In this respect the plots may be regarded as influence lines for acceleration at a point for a rolling northbound load. FFT analysis yielded the frequency domain plots shown in Figure 4.41 and 4.43 where the vibrations were most intense at the easternmost extremity of the bridge deck (closest to the point of excitation). There then followed a gradual decay of the vibration's intensity (amplitude) as the signal propagated transversely across the deck at right angles to the direction of traffic. Also of note was the vibration signal in Accelerometer 5 which was attached to the bearing: the absence of vibration would indicate that the elastomeric bearings were working properly. These data, and the remaining data contained in Appendix 2, are offered as the baseline dynamic response of the bearings for future condition monitoring to assess long-term deterioration.

Figures 4.44 to 4.47 are the time and frequency domain plots showing sampled data from Test 3. The equivalent plots for Test 4 are shown in Figures 4.48 to 4.51 were, in all practical senses, identical to those obtained from Test 3 but shifted 6.0 m North. Test 3 and Test 4 involved the recording of vibrations at the first and second K-shaped bracing sections (Sections 2 and 3 respectively on Figure 4.10). These particular time

traces were taken over a longer period of time than those shown previously. The samples shown here typify the bridge's response to a multi-axle vehicle. The signal to noise ratio was lower by approximately 5 % due to the effects of the vehicle-induced vibrations propagating across the carriageway's surface. This resulted in the vehicle run-up and run-off manifesting itself as a more classical amplification and decay curve on both sides of the central peak acceleration. This arose because the vehicle's vibrations were now being recorded 6.0 m (Section 2 on Figures 4.10) and 12.0 m (Section 3 on Figure 4.10) away from the expansion joint in Tests 3 and 4 respectively which lead to a lag time and less of a dynamic "thump" which was recorded directly below the expansion joint itself.

The frequency domain plots (Figures 4.45, 4.47, 4.49 and 4.51) exhibiting the highest vibration amplitudes and peak accelerations were those closest to the centreline of the bridge deck. This was because there were several vehicles passing over the bridge in quick succession, as evidenced by 12 distinct events in Figure 4.45. The general trend, as the accelerometers were moved out onto the span was for individual traffic events to become less distinct as constructive and destructive interference patterns and transient vibrations combined to blur the clear rise-peak-fall event discernible directly beneath the expansion joint.

Test 5 measured the movement of traffic over the bridge from the South abutment headwall, over the first pier (Section 7 on Figure 4.10) to Section 9. The first pier is topped off by a set of rocker bearings whose condition was also subject to assessment in both the PIR and through the use of this NDT as a baseline case for condition monitoring. Figures 4.52 to 4.57 are the time and frequency domain plots for Test 5.

Accelerometer 7 (Section 7 over the first pier and rocker bearings) indicated that at the lower end of the frequency spectrum, there was less movement than at positions on each side of the bearings. The author recommends re-recording these readings upon restoration of the correct grade and/or quantity of lubricant to the bearing, rather than use this anomalous condition as a representative base line for future monitoring.

Accelerometers 1 to 9 show the passage of a northbound HGV over the bridge in Figure 4.52. The detection time at each K-shaped bracing section was slightly faster than a typical HGV's average speed (V = 26 ms^{-1}). The pulse exhibited rise-peak-decay behaviour with reduced movement over the pier and bearing. The similarity to the influence lines for deflection, shear force, or bending moment was intuitively apparent although impossible to derive from the measured accelerations alone. Influence lines of acceleration at each accelerometer location versus vehicle location (which corresponds to an accelerometer location) for the vehicle shown in Figure 4.52 are shown in Figure 4.65. This indicates that acceleration levels increase as the vehicle approaches the supports, and decrease at midspan.

Figure 4.54 shows two large 6 axle HGVs travelling in opposite directions, passing each other over accelerometer position number 5. Both vehicles are travelling at a similar velocity and are of a similar mass. Figure 4.56 shows the influence of vehicle platoons, taken over a longer period of time of 50 s, with over 30 vehicles detected within this period.

Transforming the data from the time domain to the frequency domain (see Figures 4.53, 4.55 and 4.57) indicates that vibration amplitudes recorded were much lower at the

bearing locations, accelerometer 1 at the south abutment and accelerometer 7 at the first pier housing the first set of rocker bearings.

Combining the accelerations with recorded vehicle masses allows the input force from a vehicle to be applied and the accompanying frequency response function (FRF) derived. Vehicle classification 56 (articulated 3 and 3) was used along with the average speed (39 mph or 63 kmh) and average mass (43280 kg) from Tables 1, 2 and 3 respectively. Multiplying the average vehicle mass by the average acceleration (2.13 ms^{-2}) gave a force of approximately 92 kN. Using this force, FRFs of the inertance, admittance, and dynamic stiffness were derived for all recorded time sections. As the important section under consideration is at the south abutment, data relating to the hour recorded at this location is shown. Figures 4.58 to 4.63 show FRFs relating to data for the time sections recorded in Figures 4.41 and 4.43. The inertance shown in Figures 4.58 and 4.59 is the acceleration divided by the force causing this acceleration and it is a dynamic measure (in $ms^{-2}N^{-1}$ units) of inertia, or the ease with which a body may be accelerated. Note the low inertance measured at Accelerometer 5 on the bearing at the south abutment headwall: the structure is effectively isolated as evidenced by the inertance indicating a body *c*. 100 times less easily accelerated than the more "lively" deck.

The admittance, sometimes known as either mechanical admittance or mobility, shown in Figures 4.60 and 4.61 is the velocity divided by the force causing the bridge movements (not to be confused with the traffic speeds) and it is a dynamic measure (in $ms^{-1}N^{-1}$units) of the ease with which a body may be moved at a certain velocity.

The dynamic stiffness shown in Figures 4.62 and 4.63 is the force divided by the displacement and it is a dynamic measure (in Nm^{-1} units) of the ease with which a body

may be deformed. In similar fashion to the admittance FRF, the lower frequencies ($f <$ 20 Hz) were more energetic and this should be monitored over the life of any structure of this importance. Deterioration through corrosion, cracking, delamination, degradation of bearing, and regular overloading of the bridge will manifest themselves here first. The dynamic stiffness, along with the time and frequency domain plots over the joints and bearings, will give the best early indication of progressive damage to the bridge. This is a truism for most civil and structural engineering applications: the lower frequency modes carry the most energy and unfortunately cause the most damage. Whether this will prove to be the case for any given structure will require regular monitoring and risk analysis-based maintenance.

Using the dynamic stiffness data obtained for vehicles in Figure 4.62 for accelerometer 5 (located on the bearing at the South abutment), several plots shown in Figures 4.66 to 4.68 highlight the effect of average gross vehicle weight, average axle weight and average vehicle speed on the first three resonance frequencies for the bridge. Each vehicle parameter above was divided by the dynamic stiffness values obtained in Figure 4.62, and then plotted against the salient parameter to highlight its possible effect on the dynamic stiffness recorded. These figures indicate that f_1, the second resonance frequency, is affected most by each parameter. The average gross vehicle weight is the parameter with most influence on dynamic stiffness.

The data collected from this section of work, combined with the findings of Chapter 3, give rise to Figures 4.69 and 4.70. These show the effects of a change in either displacement and stiffness or frequency and stiffness. These figures, based on data

obtained on for baseline bearing stiffness relating to displacement and frequency, indicate the values that should cause concern with respect to bearings.

It should be noted, however, that although this proposed method will indicate degradation of bearing performance, other factors that can affect the overall performance of the structure should be taken into consideration. Cracking of the concrete superstructure can have a significant effect on the frequency response of a structure, as highlighted by much of the research presented in Chapter 2. As a result, care must be taken when determining the actual cause of alteration in frequency. It is recommended that accelerometers be located at the abutments, and more specifically on the bearings, to accurately monitor the bearing performance.

A parametric study carried out by altering the FEA parameters, such as ρ, E and ν, to determine the effect of a change in structural condition on the resonance frequencies of the bridge. The values obtained are shown in Table 4.13. These values show that altering the Young's Modulus or density value has a much greater effect on the recorded frequencies than Poisson's ratio. Any change in E value cannot simply be attributed to a degradation in bearing condition, as stated in the previous paragraph. It would be good engineering practice to use this method in combination with a visual inspection and other NDT techniques to discount the effect of cracking on the E value obtained.

The next stage in result recording and analysis will come in 2008, when a 3 year inspection will be requested and comparisons made with the baseline case readings presented herein. With suitable access arrangements and hopefully, continuity in the research, monitoring over a 50 year period would be possible.

4.7 Conclusions

- The NDT method presented was worthy of inclusion in a major structure's maintenance and inspection plan. No disruption to traffic was caused, and no damage to the structure ensued.

- When matched with weigh-in-motion sensors and accurate vehicle counting and classification software, the NDT proved useful in matching vehicle events with the dynamic structural response.

- Vehicle speeds had a small distribution, most falling in the 35 to 50 mph range.

- The majority of Type 56 HGVs were overloaded.

- Axle weight distribution was poor in many HGVs.

- Gross vehicle weight had the greatest effect on dynamic stiffness response.

- The momentum, kinetic energy and damage factor were significantly larger in relation to larger vehicles.

- Larger HGVs made up a small percentage of overall vehicles recorded, but contributed a much higher proportion of damage caused to the bridge.

- Displacement and frequency were both valid measures of bearing performance and therefore state of degradation.

- The bridge bearings were performing as expected, and doing so adequately.

- The expansion joint had a more severe effect upon the measured vibrations.

- Repeat testing is needed over the rocker bearing after remedial action has been completed.

- Future testing to continue this form of condition monitoring is recommended.

- Although this proposed method will indicate degradation of bearing performance, other factors that can affect the overall performance of the structure should be taken into consideration.

- Cracking of the concrete superstructure can have a significant effect on the frequency response of a structure, care must be taken when determining the actual cause of alteration in frequency.

- It is recommended that accelerometers be located at the abutments, and more specifically on the bearings, to accurately monitor the bearing performance.

4.8 References

4.1 Mazurek D.F. and DeWolf J.T. Experimental study of bridge monitoring technique. *Proc. Am. Soc. Civ. Engnrs, J. Struct. Engng*, **116(9)**, 1990, 2532-2549.

4.2 Peeters B. and Ventura C. E. Comparative study of modal analysis techniques for bridge dynamic characteristics. *Mech. Sys. Signal Process.*, **17(5)**, 2003, 965-988.

4.3 Salawu O.S. and Williams C. Review of full-scale dynamic testing of bridge structures. *Engng Structs*, **17(2)**, 1995, 113-121.

4.4 Alampalli S. Effects of testing, analysis, damage and environment on modal parameters. *Mech. Sys. Signal Process.*, **14(1)**, 2000, 63-74.

4.5 Pajawit A. and Kanok-Nukulchai W. Health monitoring of highway bridges based on a global flexibility index. *Engng Structs*, **27(9)**, 2005, 1385-1391.

4.6 Verboven P., Parloo E., Guillaume P. and van Overmeire M. Autonomous structural health monitoring - Part I: modal parameter estimation and tracking. *Mech. Sys. Signal Process.*, **16(4)**, 2002, 637-657.

4.7 Parloo E., Verboven P., Guillaume P. and van Overmeire M. Autonomous structural health monitoring - Part II: vibration-based in-operation damage assessment. *Mech. Sys. Signal Process.*, **16(4)**, 2002, 659-675.

4.8 Salawu O.S. Detection of structural damage through changes in frequency: a review. *Engng Structs*, **19(9)**, 1997, 718-723.

4.9 Wang X., Hu N., Fukunaga H. and Yao Z.H. Structural damage identification using static test data and changes in frequencies. *Engng Structs*, **23(6)**, 2001, 610-621.

4.10 Dutta A. and Talukdar S. Damage detection in bridges using accurate modal parameters. *Finite Elements in Anal. & Design*, **40(3)**, 2004, 287-304.

4.11 Casas J. R. and Aparicio A. C. Structural damage identification from dynamic test data. *Proc. Am. Soc. Civ. Engnrs, J. Struct. Engng*, **120(8)**, 1994, 2437-2450.

4.12 Yau J. D., Wu Y.-S. and Yang Y.-B. Impact response of bridges with elastic bearings to moving loads. *J. Sound & Vib.*, **248(1)**, 2001, 9-30.

4.13 Kim C.-W., Kawatani M. and Hwang W-S. Reduction of traffic-induced vibration of two-girder steel bridge seated on elastomeric bearings. *Engng Structs*, **26(14)**, 2004, 2185-2195.

4.14 Green M. F. and Cebon D. Dynamic response of highway bridges to heavy vehicle loads: theory and experimental validation. *J. Sound & Vib.*, **170(1)**, 1994, 51-78.

4.15 British Standards Institution. *BS 5400-1:1988 Steel, concrete and composite bridges – Part 9: Bridge bearings*. BSI, London, 1983.

4.16 Price A.R. The performance in service of bridge deck expansion joints. *Laboratory Report LR1104, Transport & Road Research Laboratory,* Crowthorne, 1984.

4.17 Steenbergen M.J.M.M. Dynamic response of expansion joints to traffic loading. *Engng Structs*, **26**, 2004. 1677-1690.

4.18 Page J. A review of dynamic loading caused by vehicle suspensions. *Supplementary Report SR82UC, Transport & Road Research Laboratory,* Crowthorne, 1974.

4.19 Addis R.R. and Whitmarsh R.A. Relative damaging power of wheel loads in mixed traffic. *Laboratory report LR979*, Transport & Road Research Laboratory, Crowthorne, 1981.

4.20 Xia Y., Hao H., Zanardo G. and Deeks A. Long term vibration monitoring of an RC slab: temperature and humidity effect. *Engng Structs*, **28**, 2006, 441-452.

4.21 Masters J. Technology to drive road maintenance forward. *Transportation Professional, J. Instn Highways and Transportation*, 6, 2006, 17-18.

4.22 Jennings A. and McWharand R. Highways Agency - A1 Berwick bypass Phase II. Highways Agency, www.highways.gov.uk/roads/projects/11236.aspx, 20 June 2005.

4.23 Mitchell G.G.B. The effect of the design of goods vehicle suspensions on loads on roads and bridges. *Research Report RR115*, Transport & Roads Research Laboratory, Crowthorne, 1987.

4.24 Mace D.G.W. and Stephenson C.A. Dynamic road load measurements on a two-axle semi-trailer. *Research Report RR171*, Transport & Roads Research Laboratory, Crowthorne, 1989.

4.25 Highways Agency. Area 14 : Northumberland, Tyne and Wear, Durham and North Yorkshire. Highways Agency, www.highways.gov.uk/aboutus/2337.aspx, 2005.

4.26 British Standards Institution. *BS 5400-2:2005 Steel, concrete and composite bridges – Part 2: Specification of loads*. BSI, London, 2005.

4.27 The Roads Vehicles (Construction and Use) Regulations 1986. HMSO, London, 1986.

Figure 4.1 The A1 Bridge at Berwick-upon-Tweed: general view facing North

(2) HB vehicle straddling two notional lanes

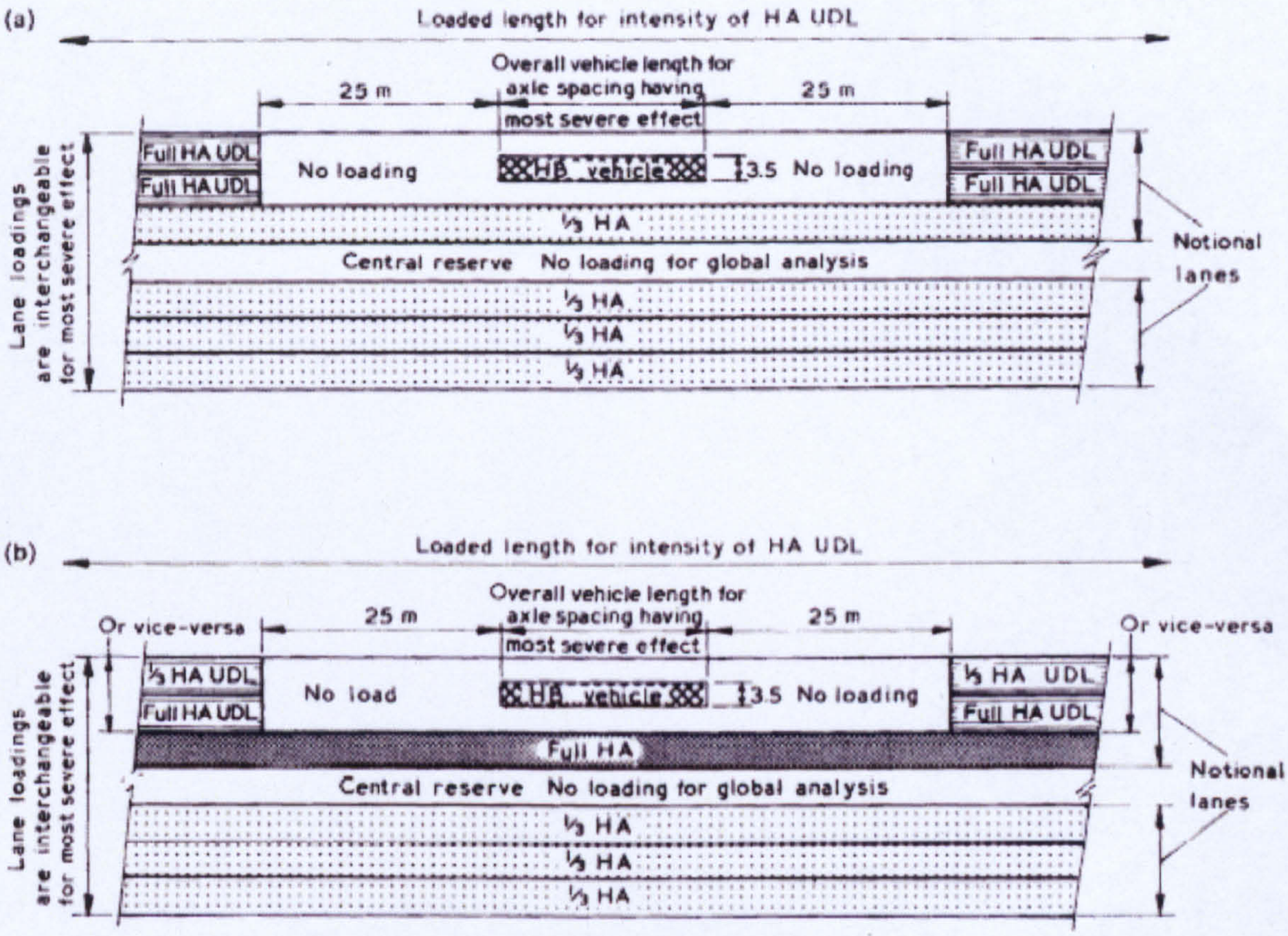

(a)

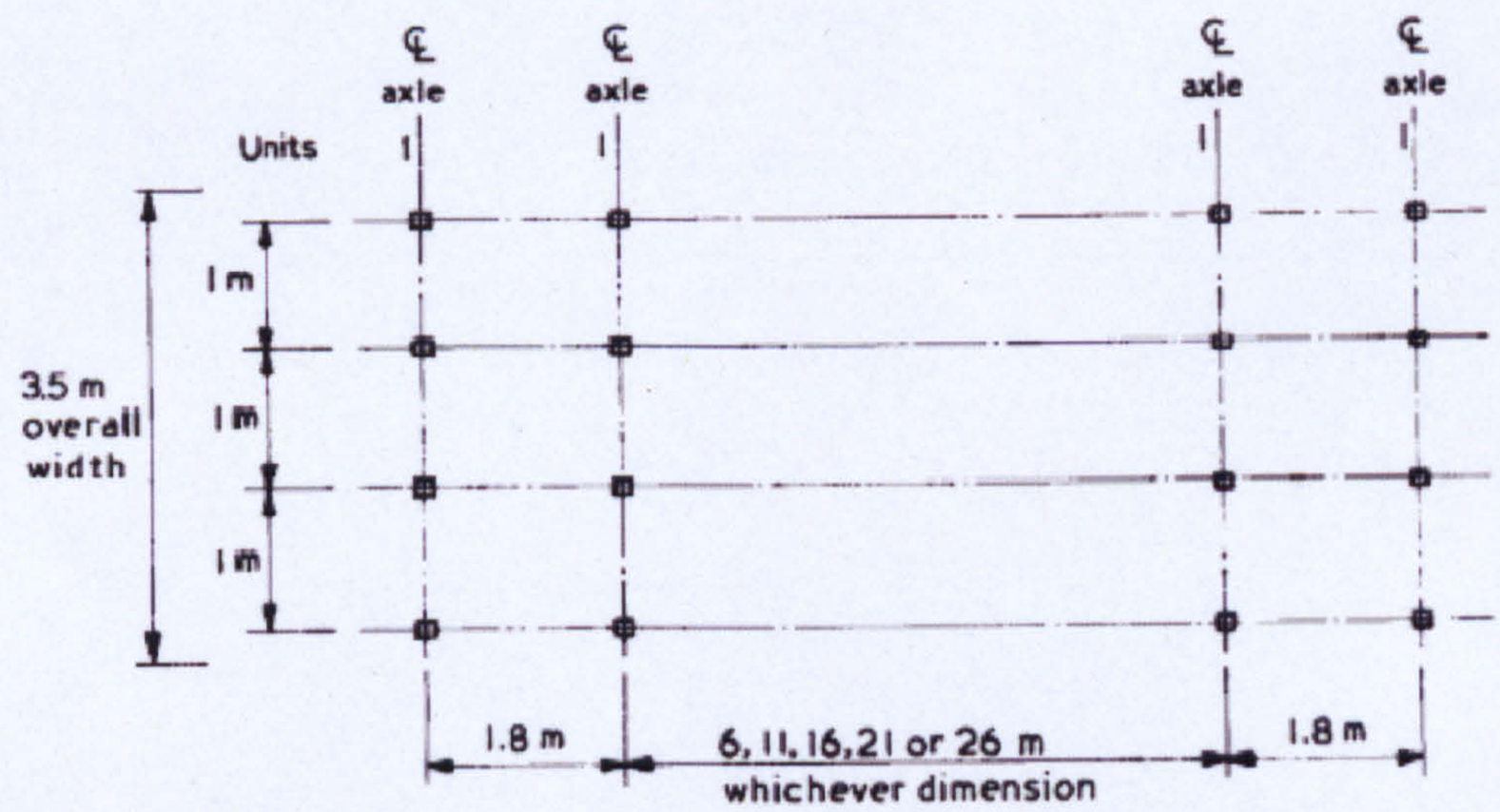

(b)

Figure 4.2 HA and HB loading diagrams[4.26]

Figure 4.2 (a) shows the possible combinations of HA and HB loading used in bridge design.

Figure 4.2 (b) shows a plan view of the HB loading vehicle giving axle spacings.

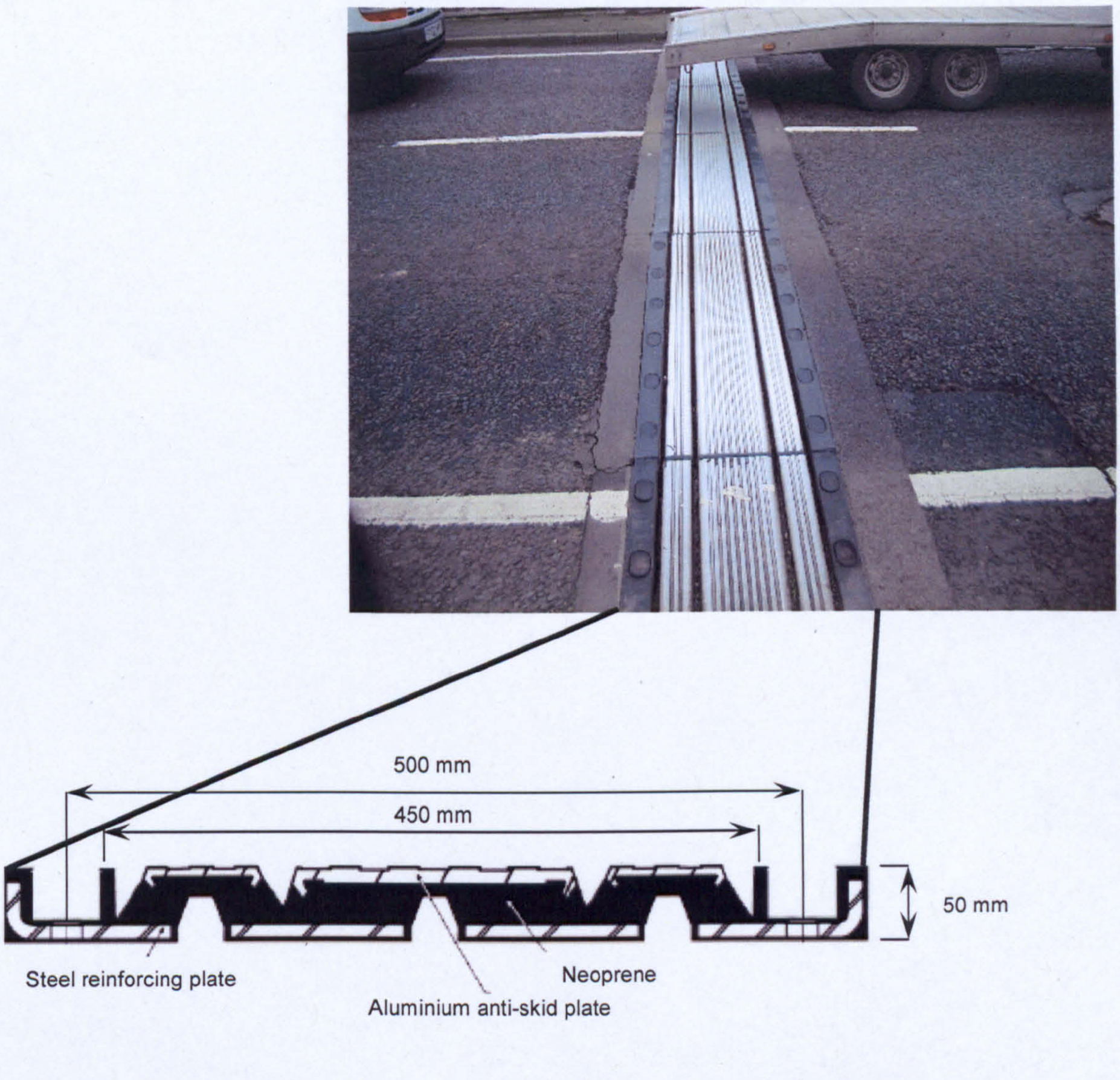

Figure 4.3 Expansion joint located at south abutment directly above bearings

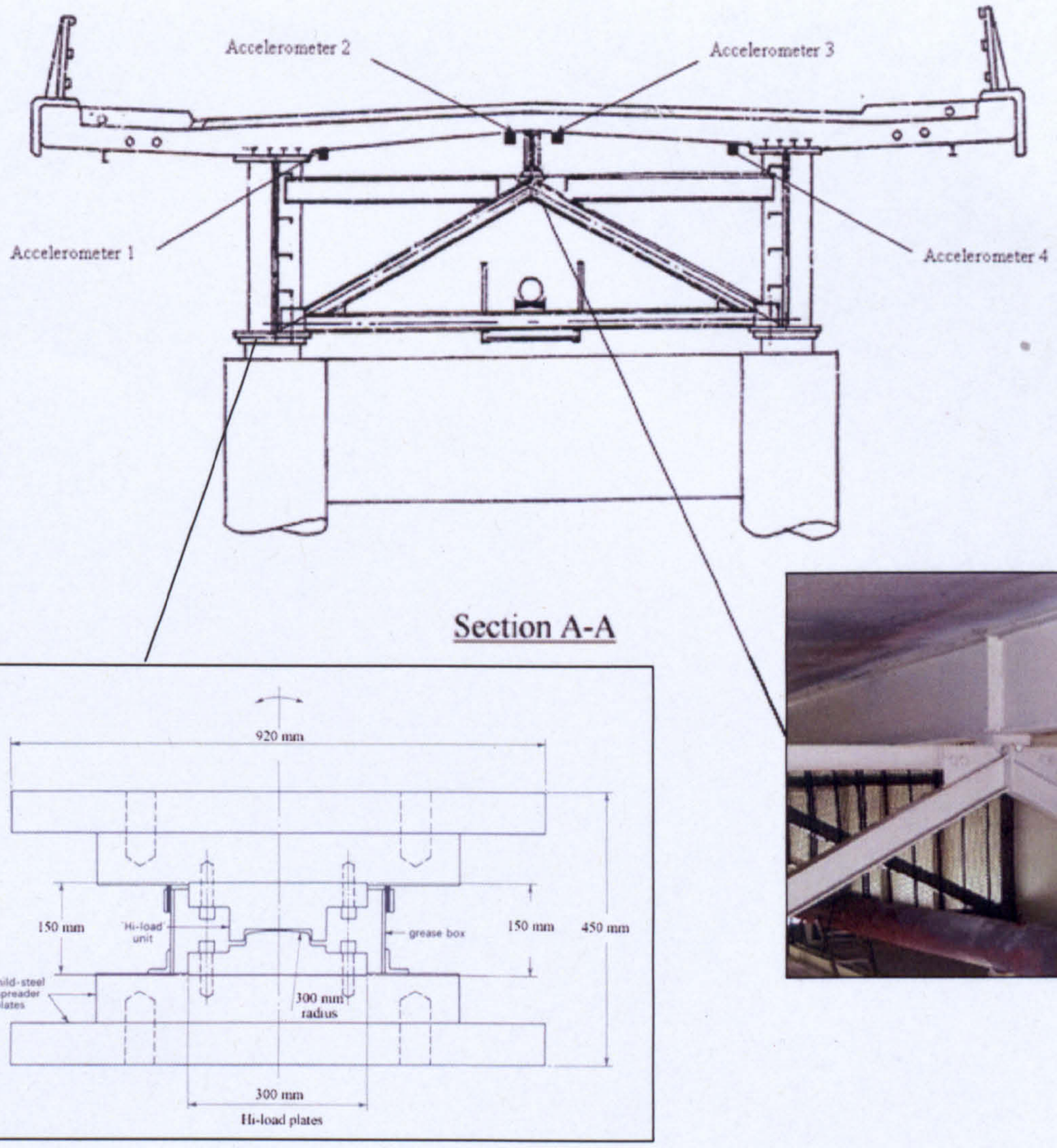

Figure 4.4 Accelerometer locations: typical K-shaped bracing (Section 2 shown)

Figure 4.5 Access cage and walkway with access ladder *in situ*

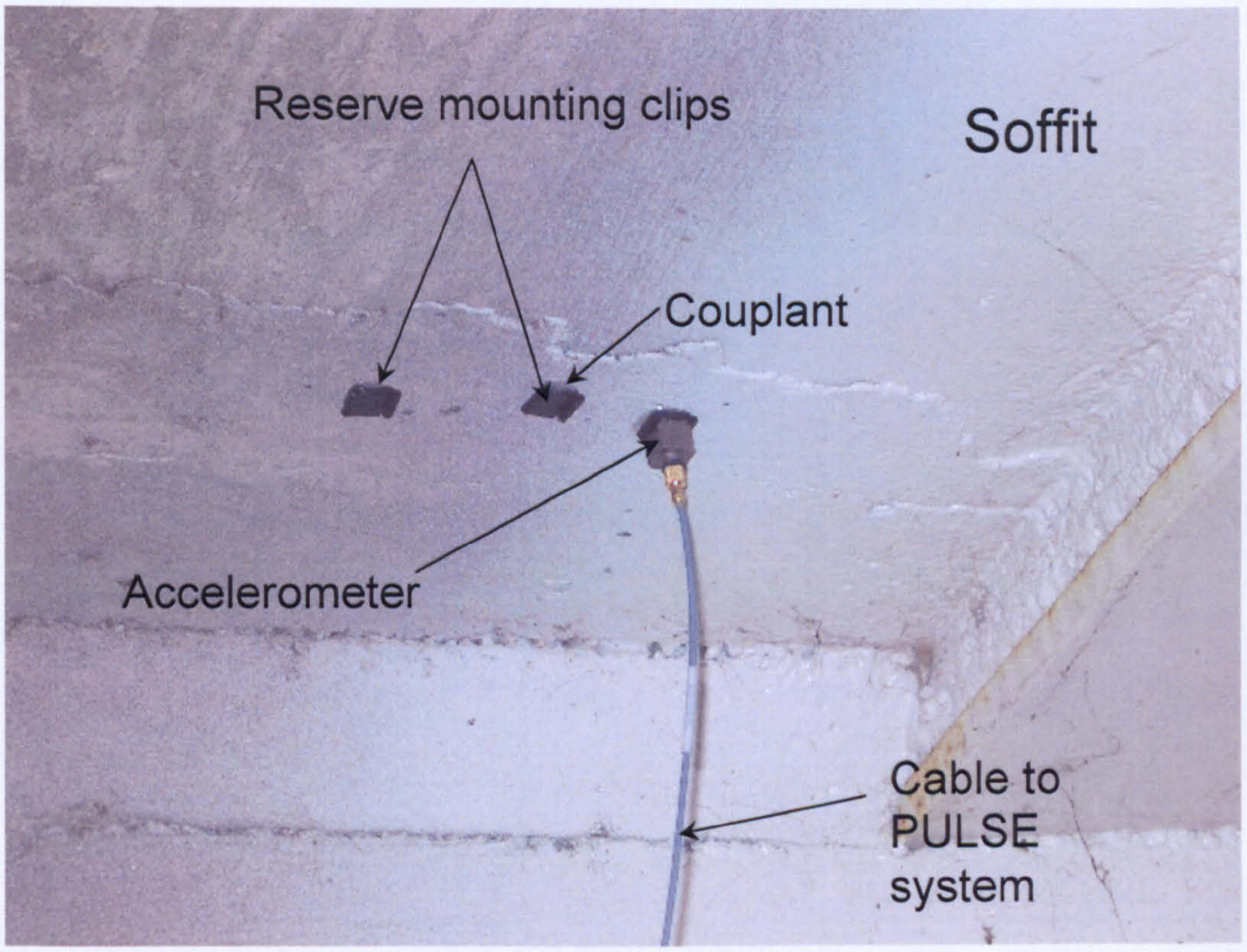

Figure 4.6 Accelerometer *in situ* with mounting clips

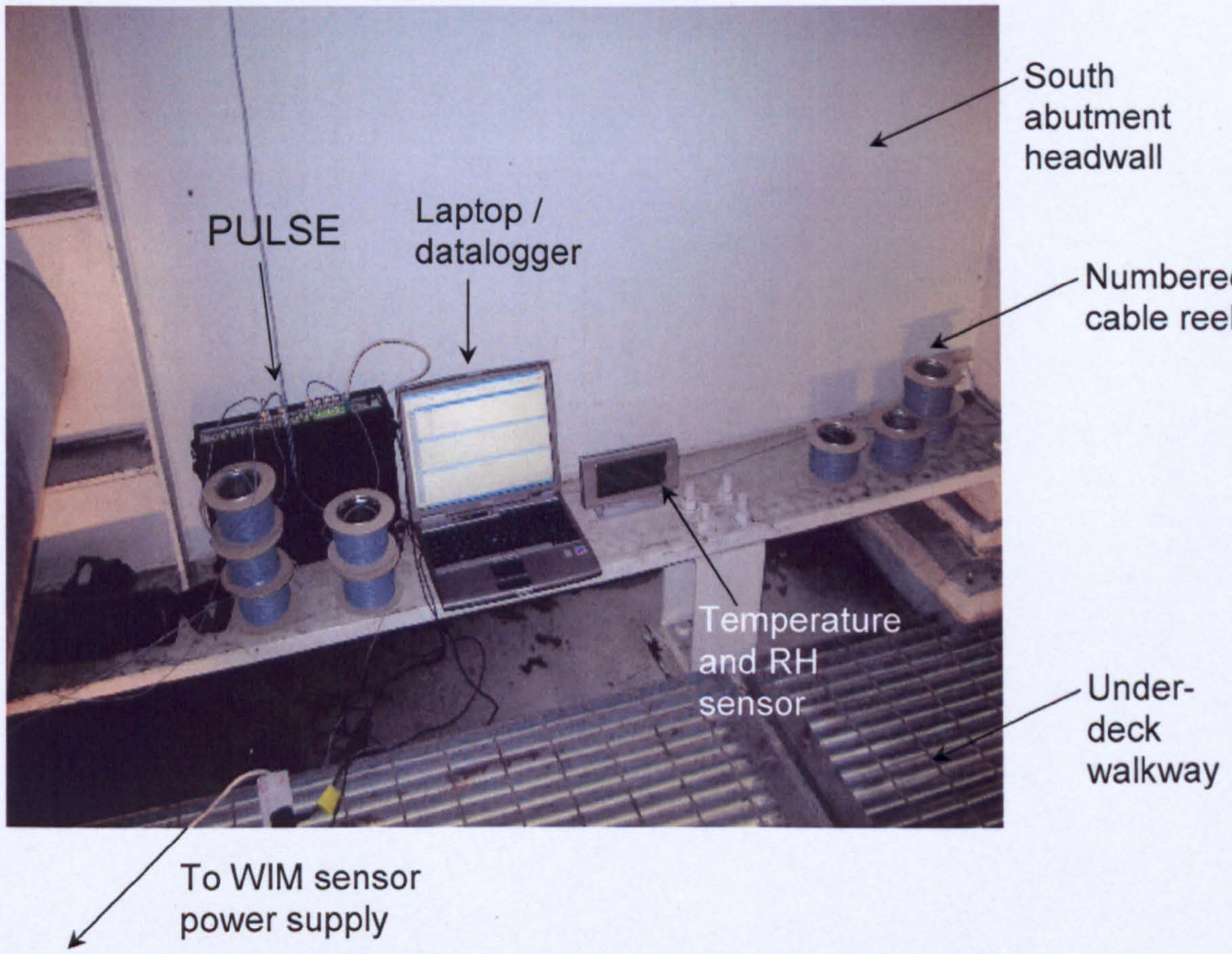

Figure 4.7 Analyser lay out for initial testing

Figure 4.8 Accelerometer 5 mounted on bearing plinth

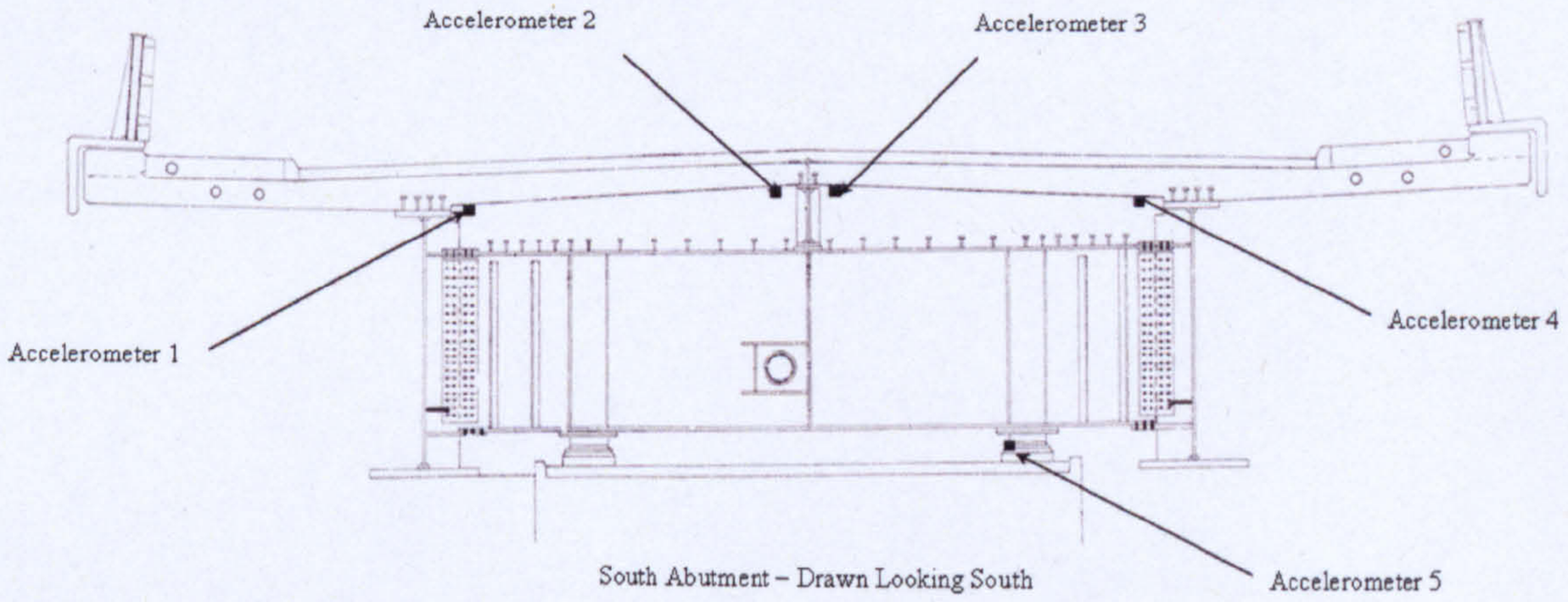

Figure 4.9 Accelerometer locations: South abutment, Section 1

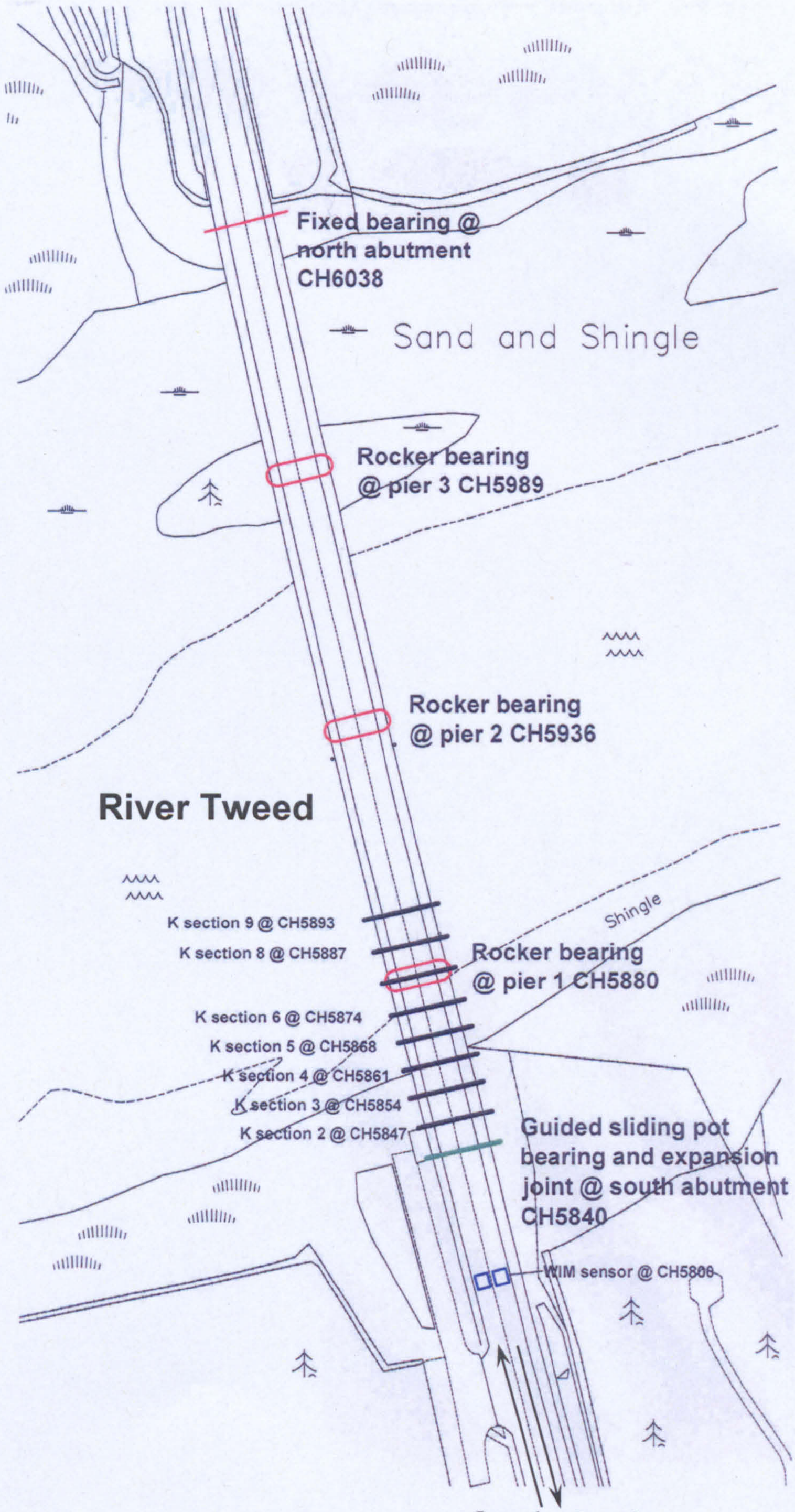

Figure 4.10 Test section location plan (Scale 1:150)

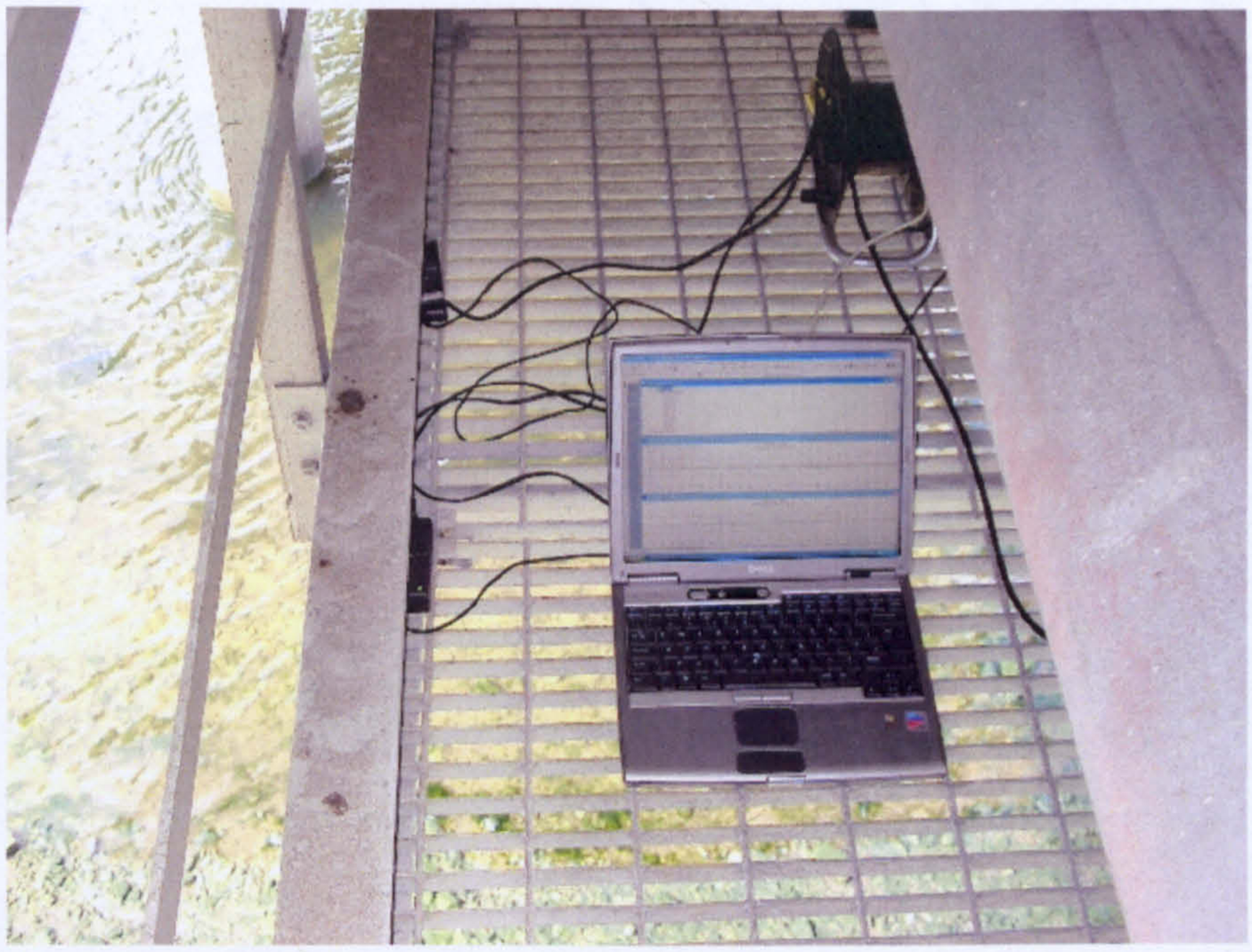

Figure 4.11 Analyser in position for final testing regime, test 5

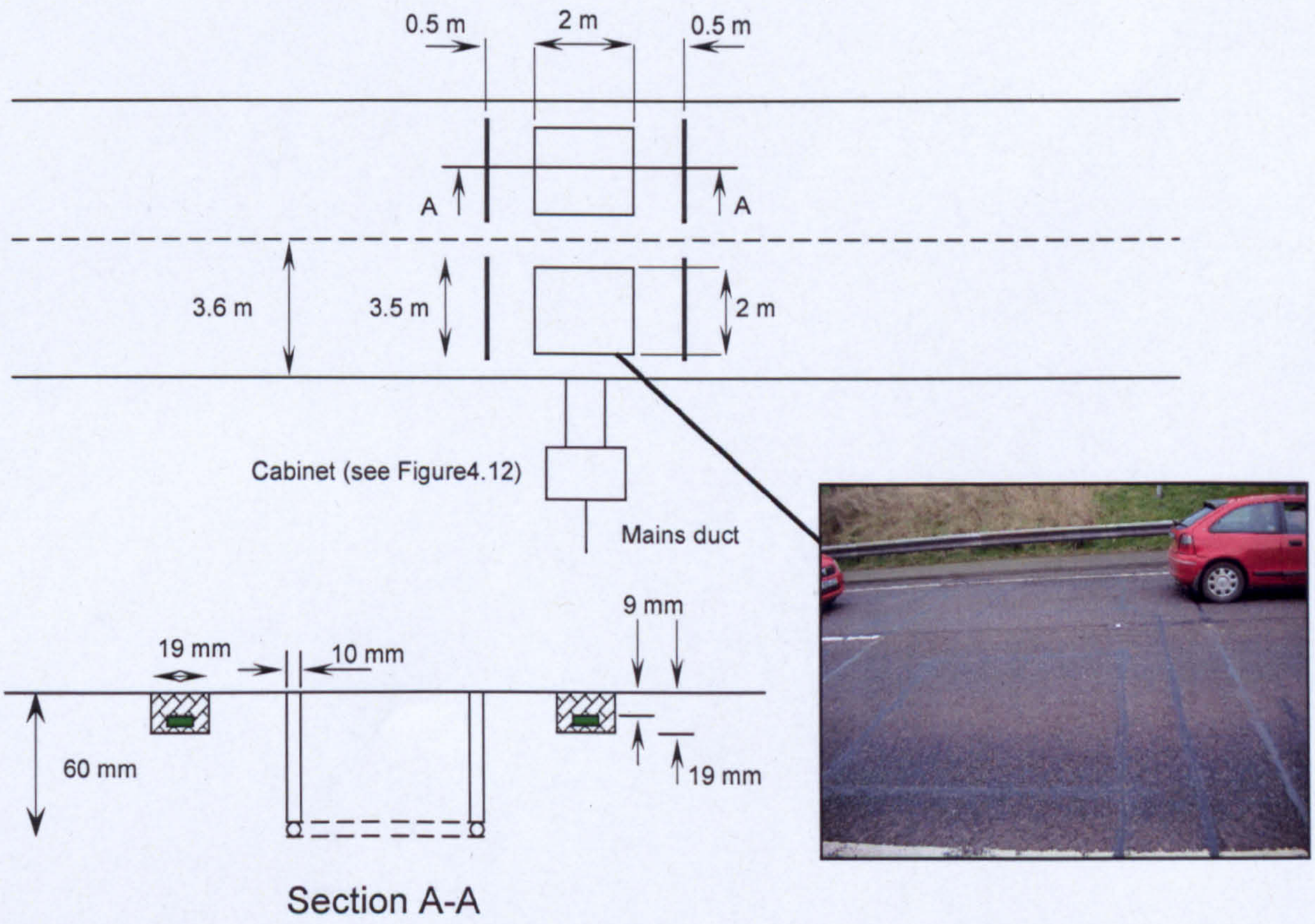

Figure 4.12 Typical instrumentation layout: weigh-in-motion sensors and induction loops

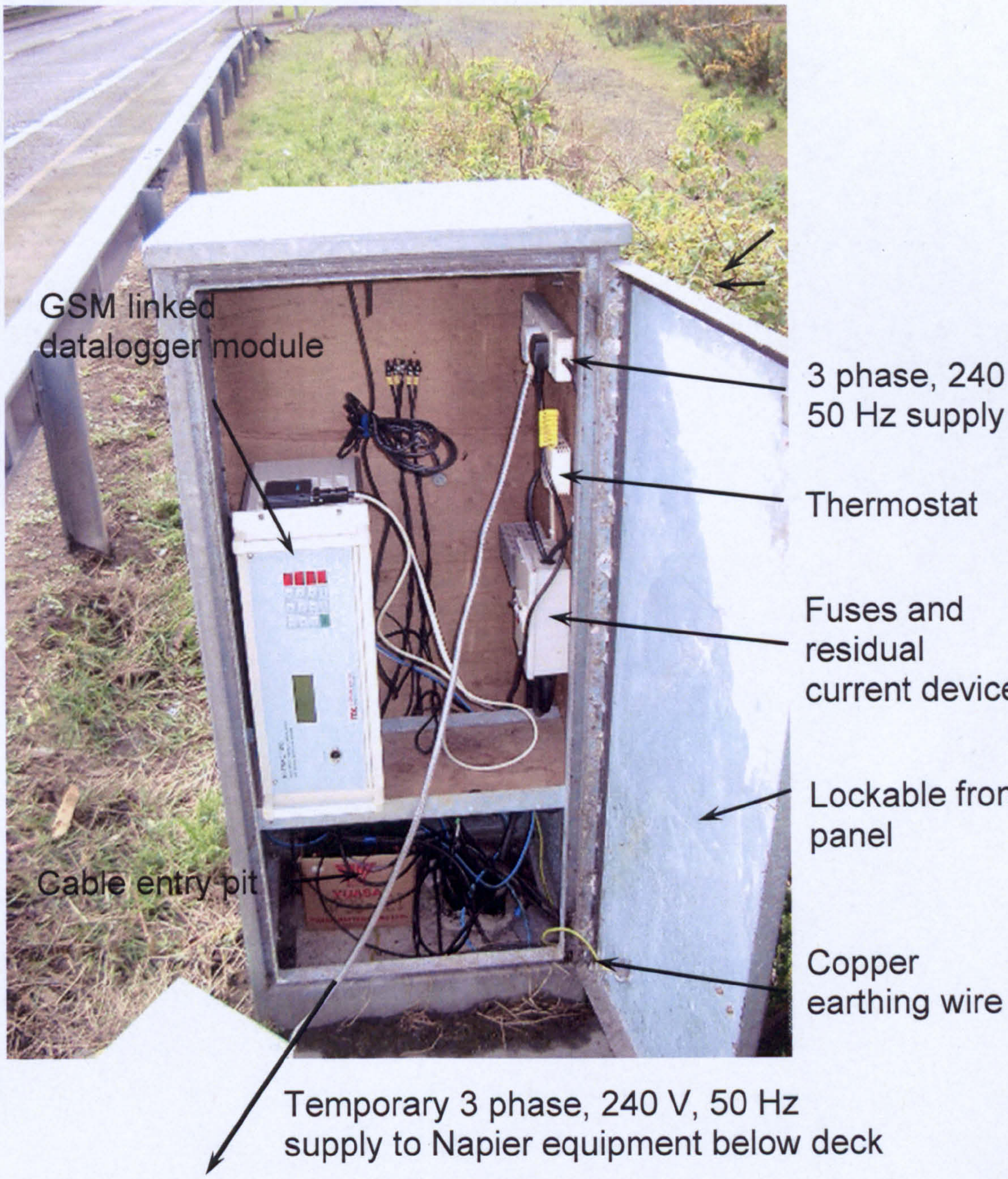

Figure 4.13 WIM data logger and housing

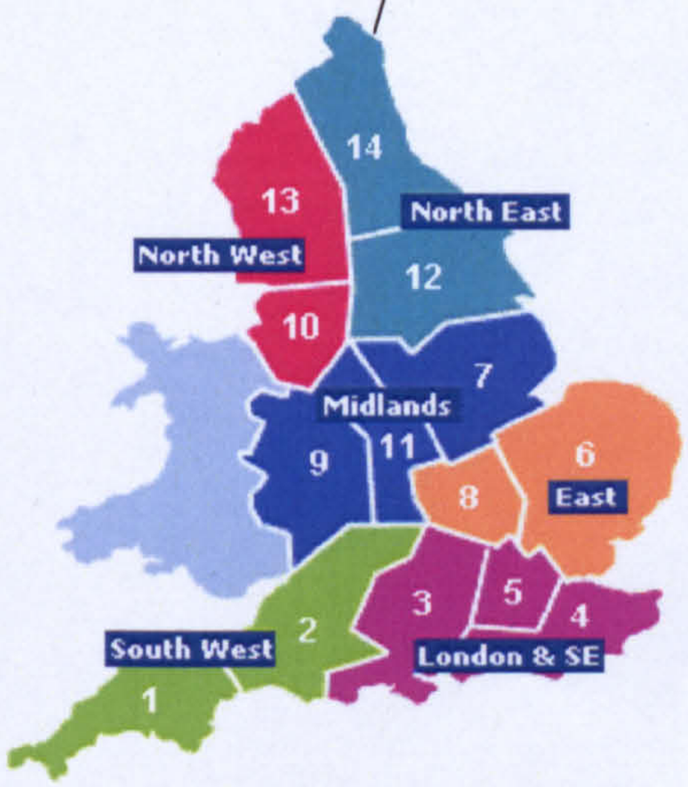

Annual budget	**£20 million**
Miles of motorway and trunk road	**185 miles (298 km)**
Number of bridges	***c.* 200**

Figure 4.14 Highways Agency Area 14

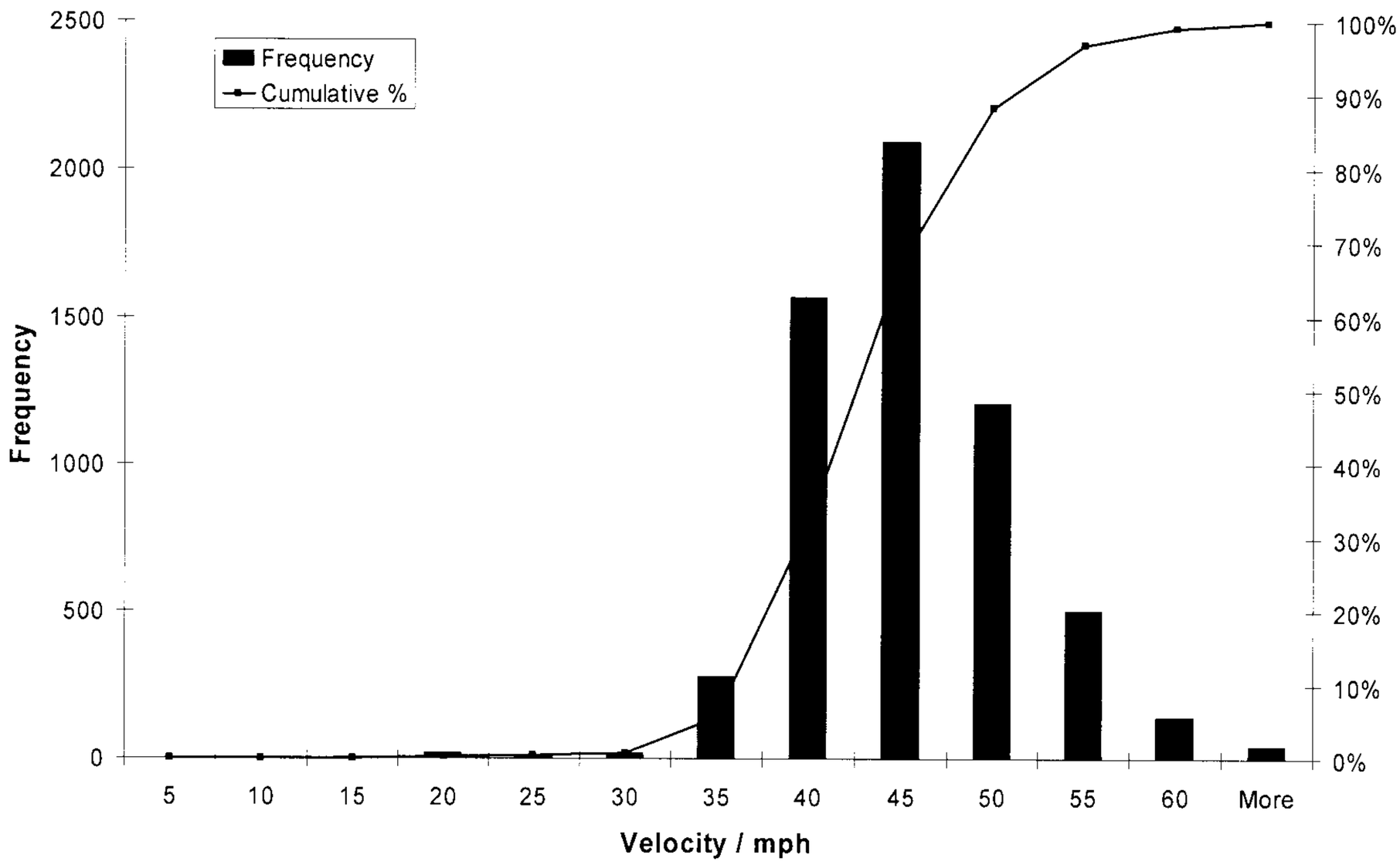

Figure 4.15 Velocity histogram for vehicles in lane 1

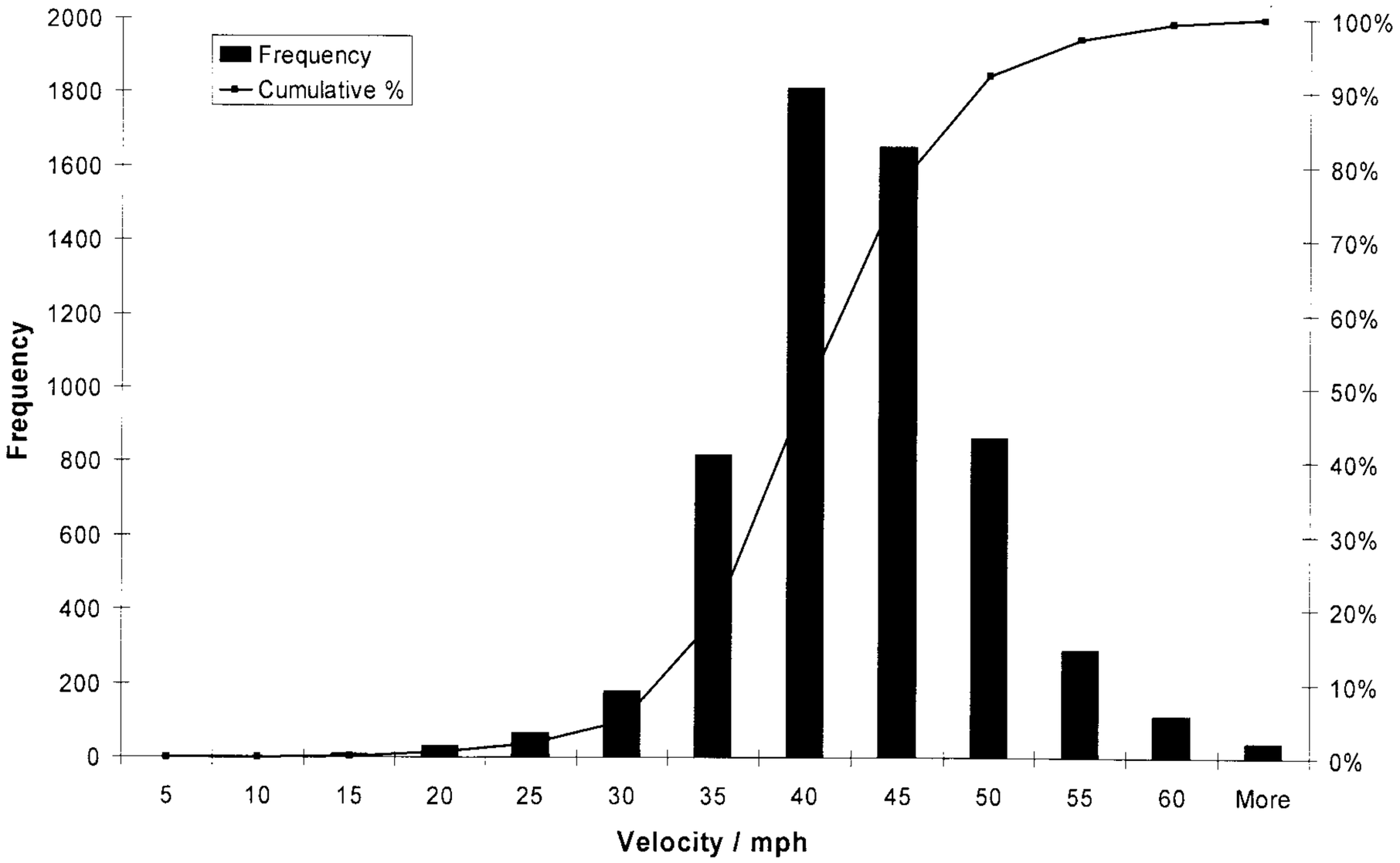

Figure 4.16 Velocity histogram for vehicles in lane 2

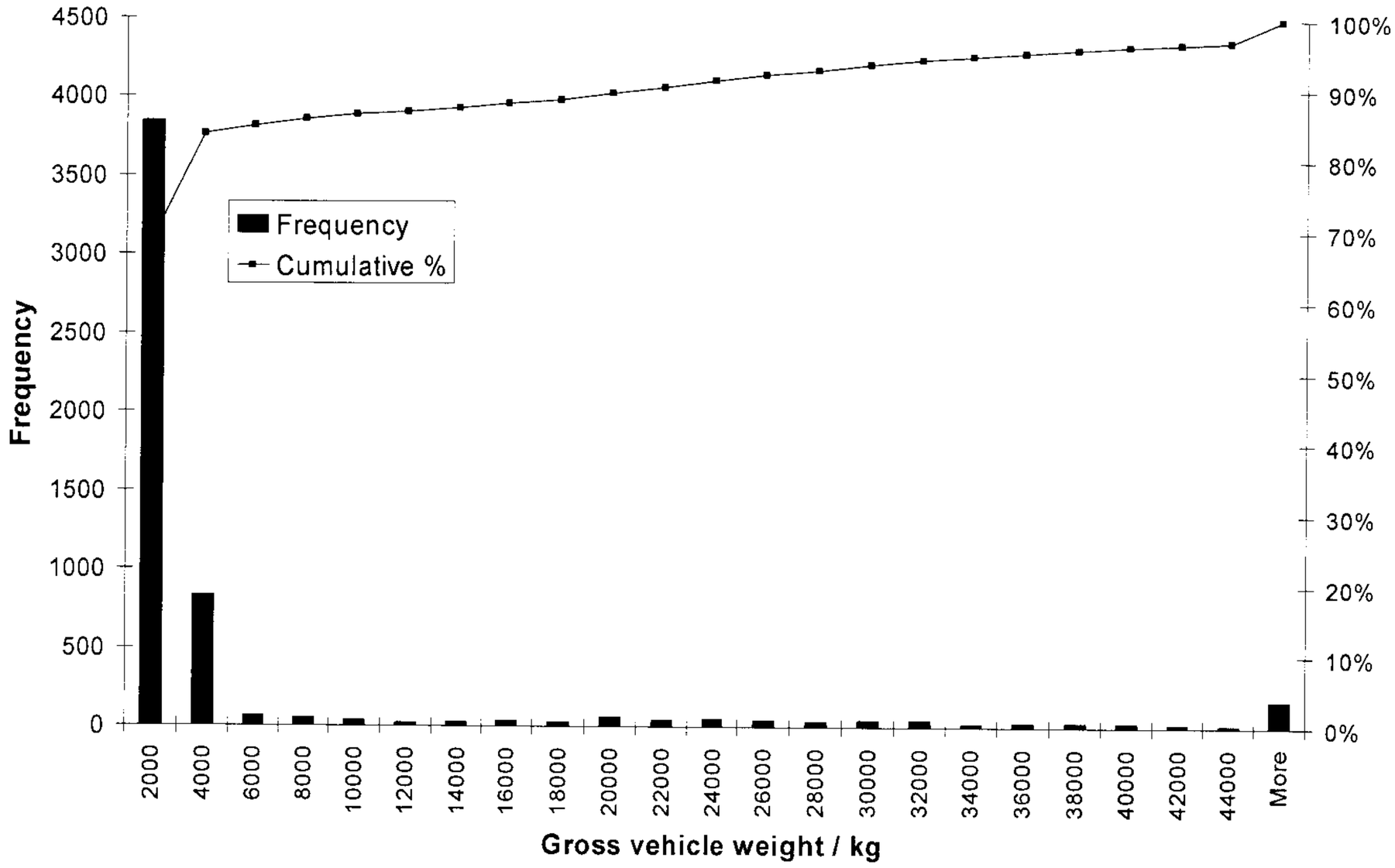

Figure 4.17 Gross vehicle weight histogram lane 1

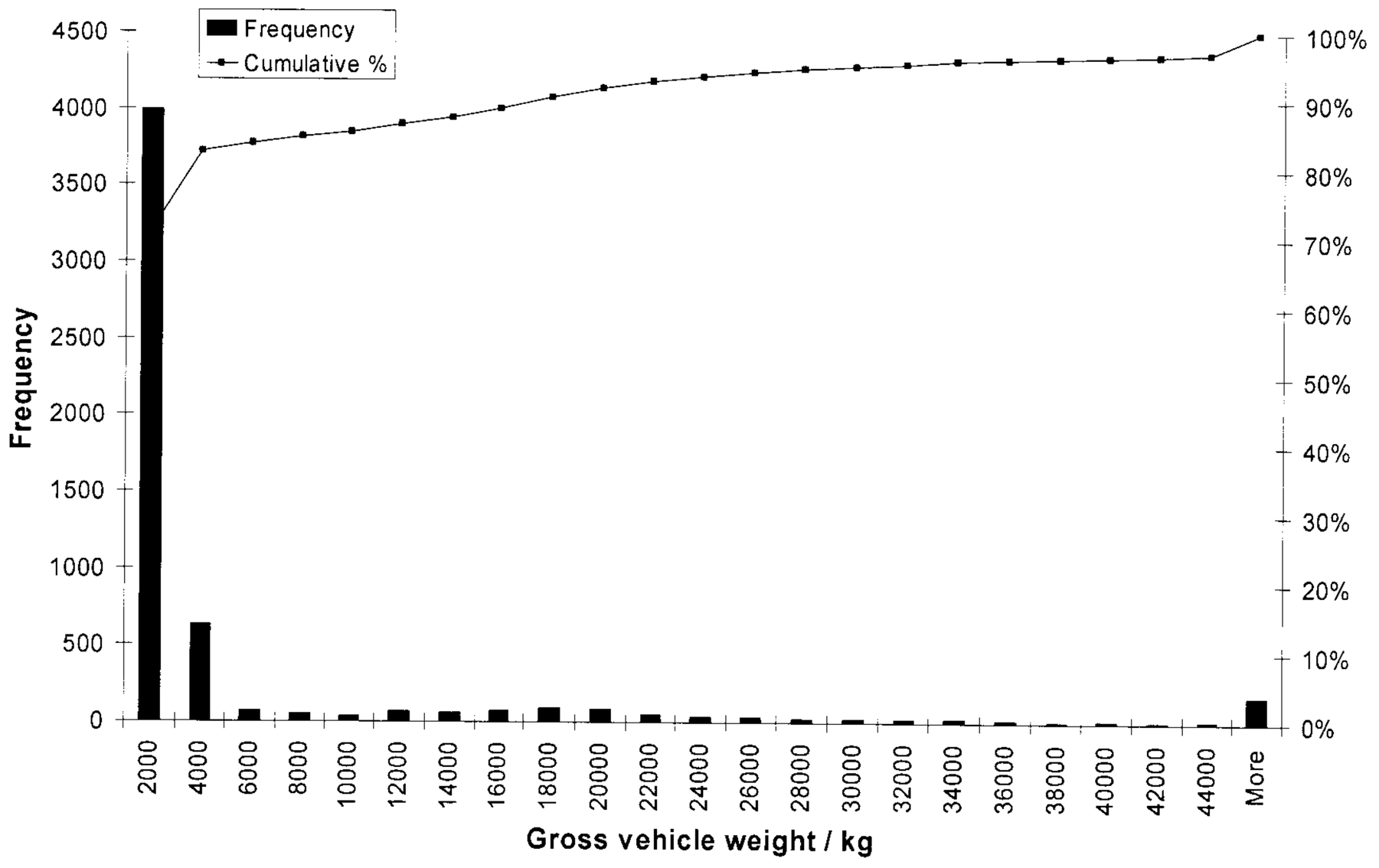

Figure 4.18 Gross vehicle weight histogram lane 2

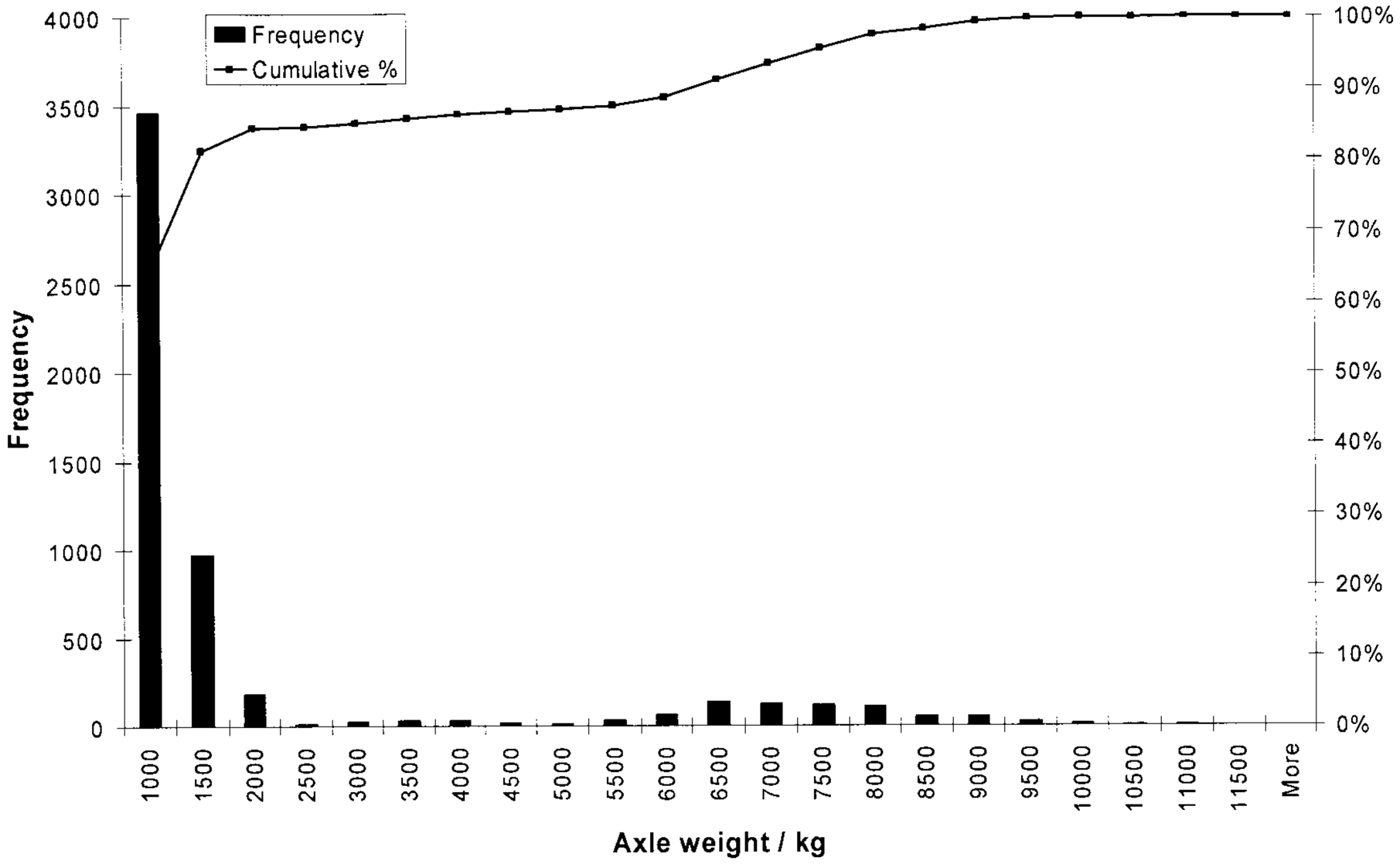

Figure 4.19 Axle 1 weight histogram lane 1

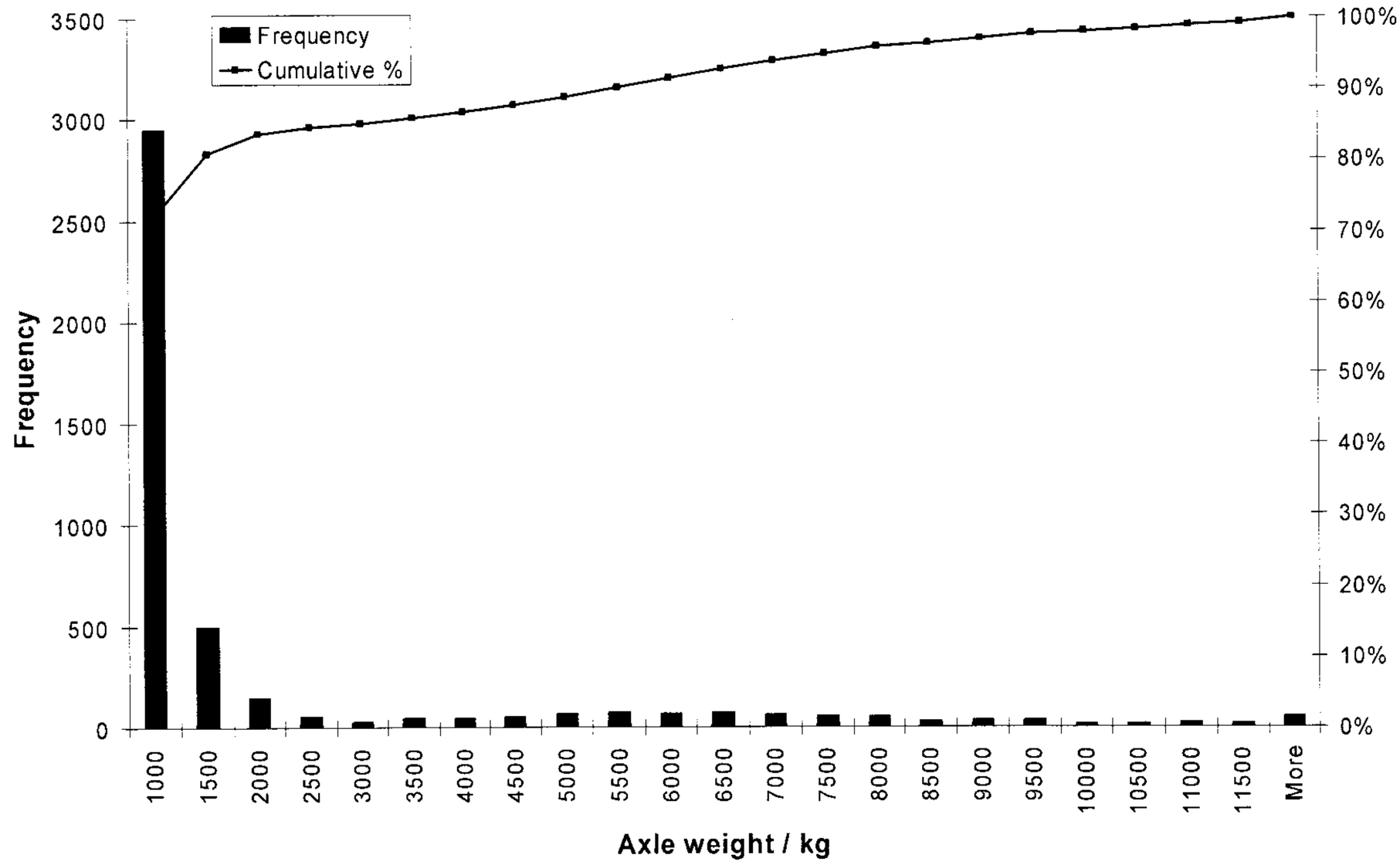

Figure 4.20 Axle 2 weight histogram lane 1

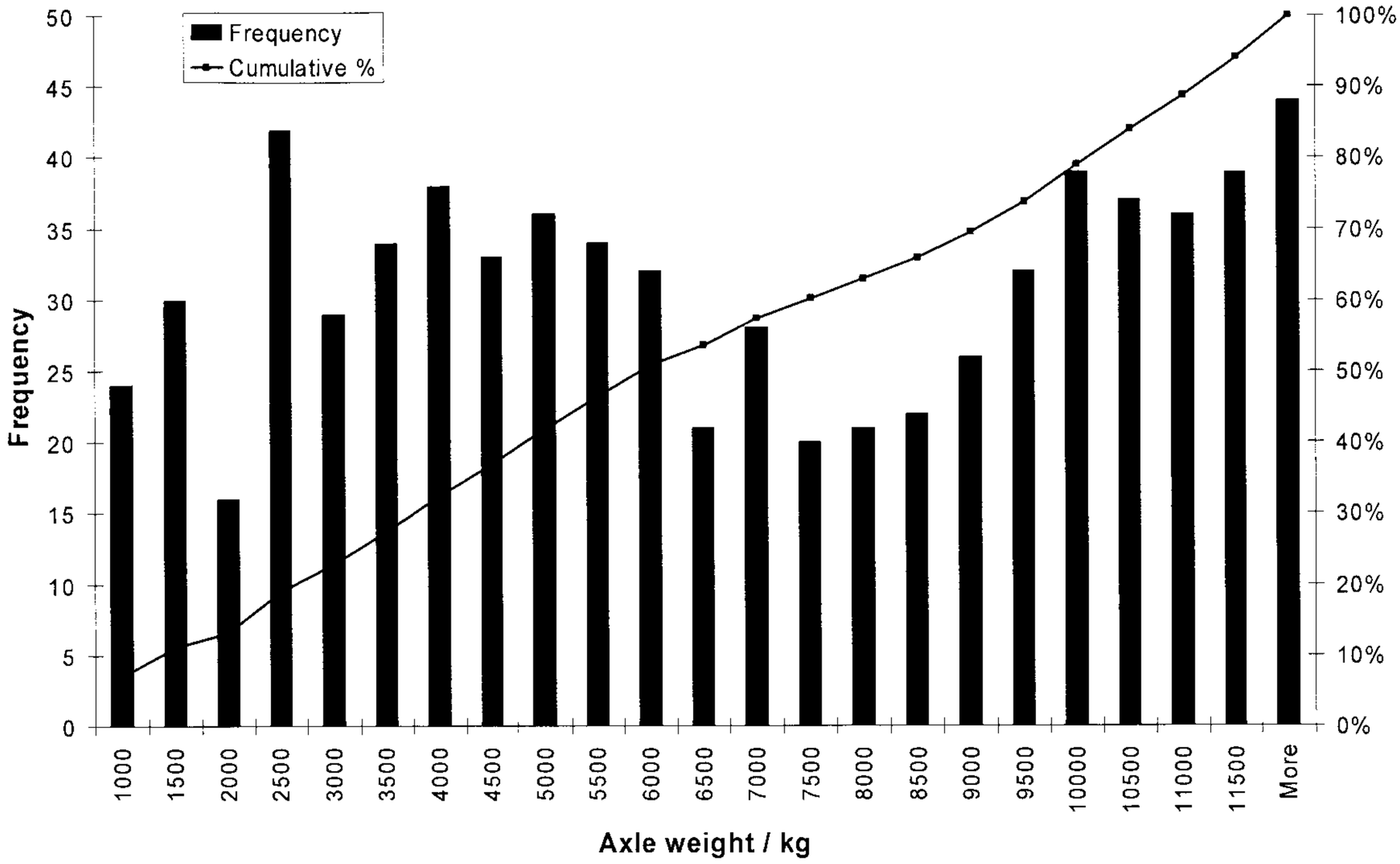

Figure 4.21 Axle 3 weight histogram lane 1

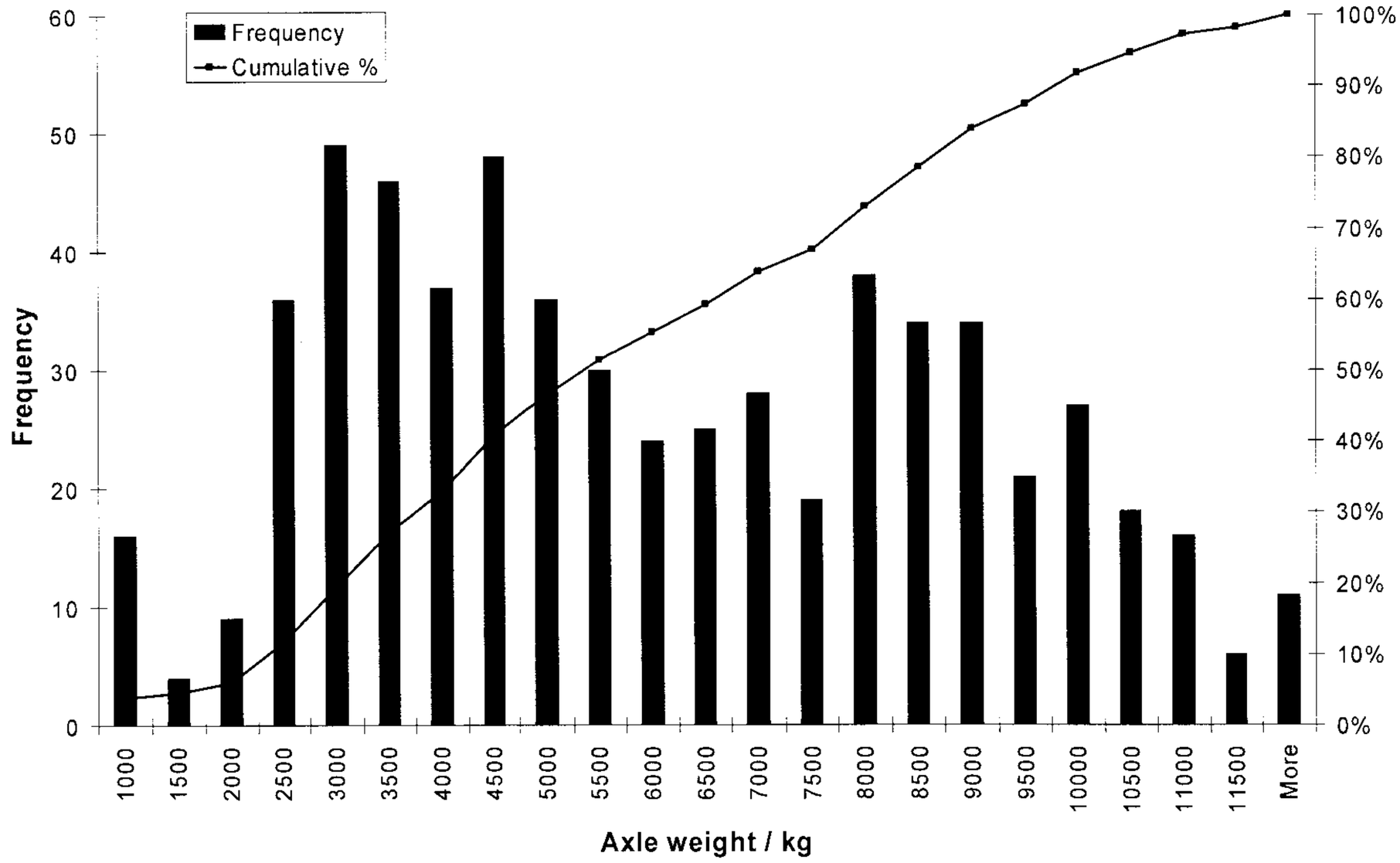

Figure 4.22 Axle 4 weight histogram lane 1

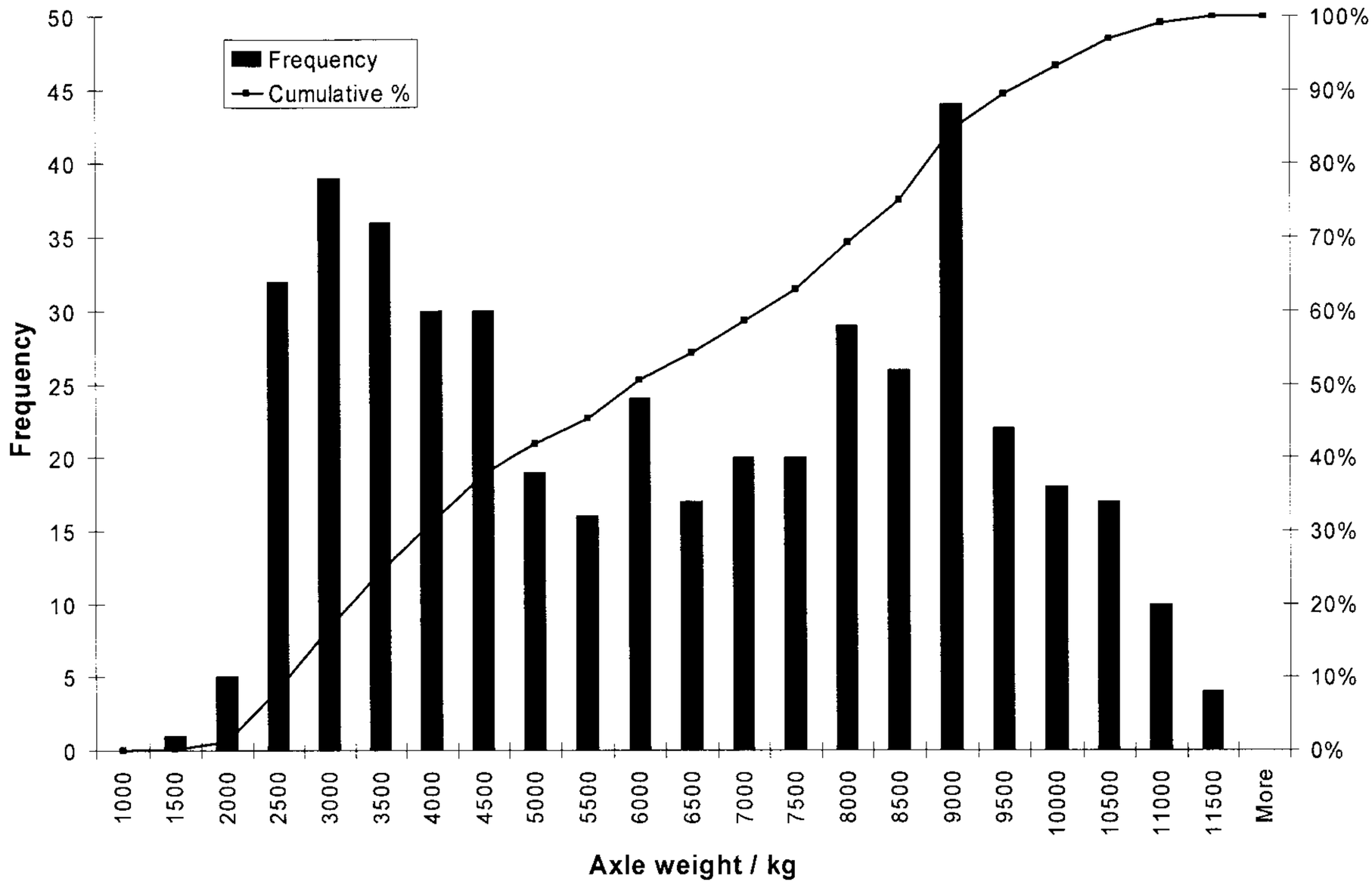

Figure 4.23 Axle 5 weight histogram lane 1

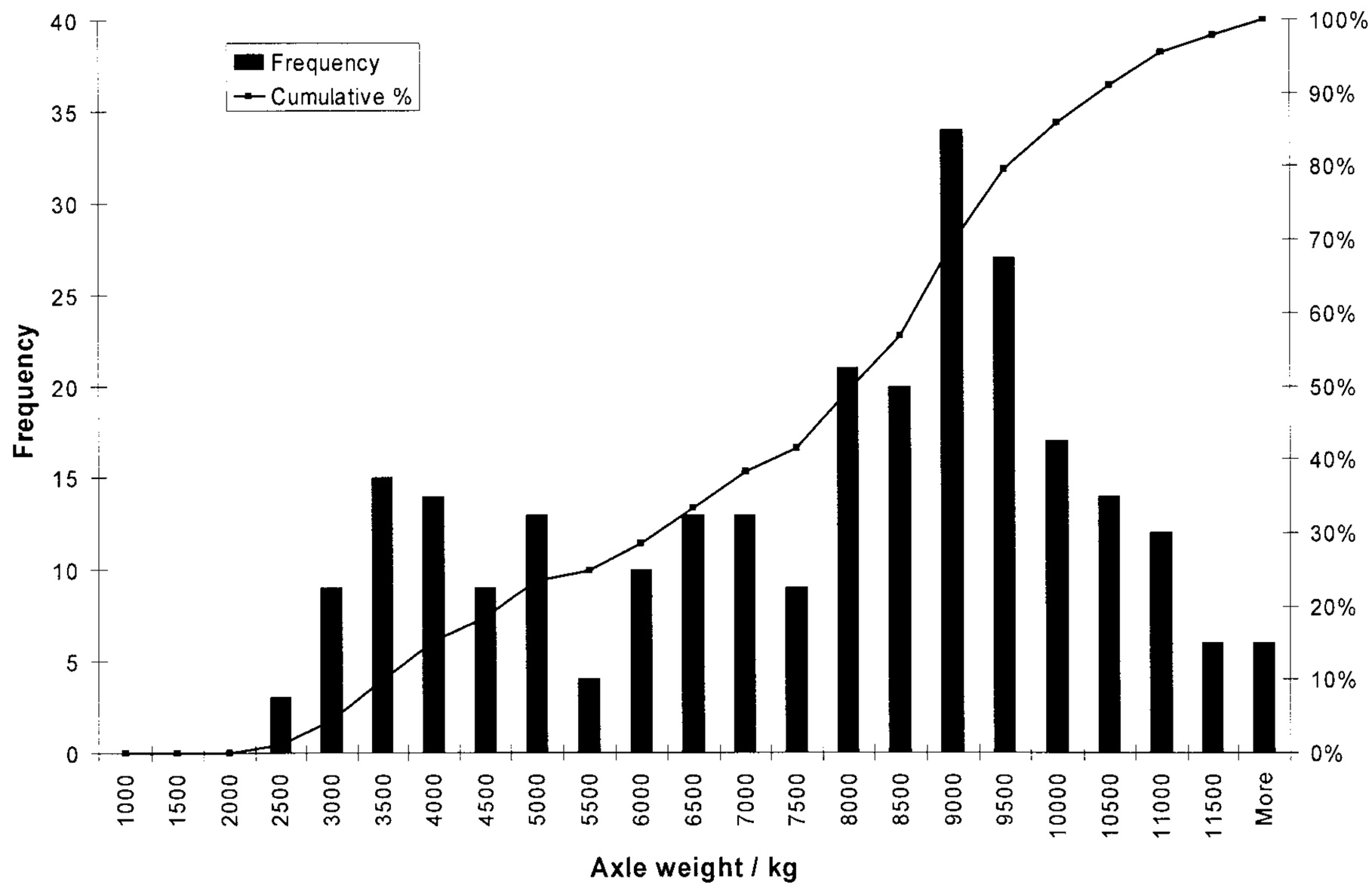

Figure 4.24 Axle 6 weight histogram lane 1

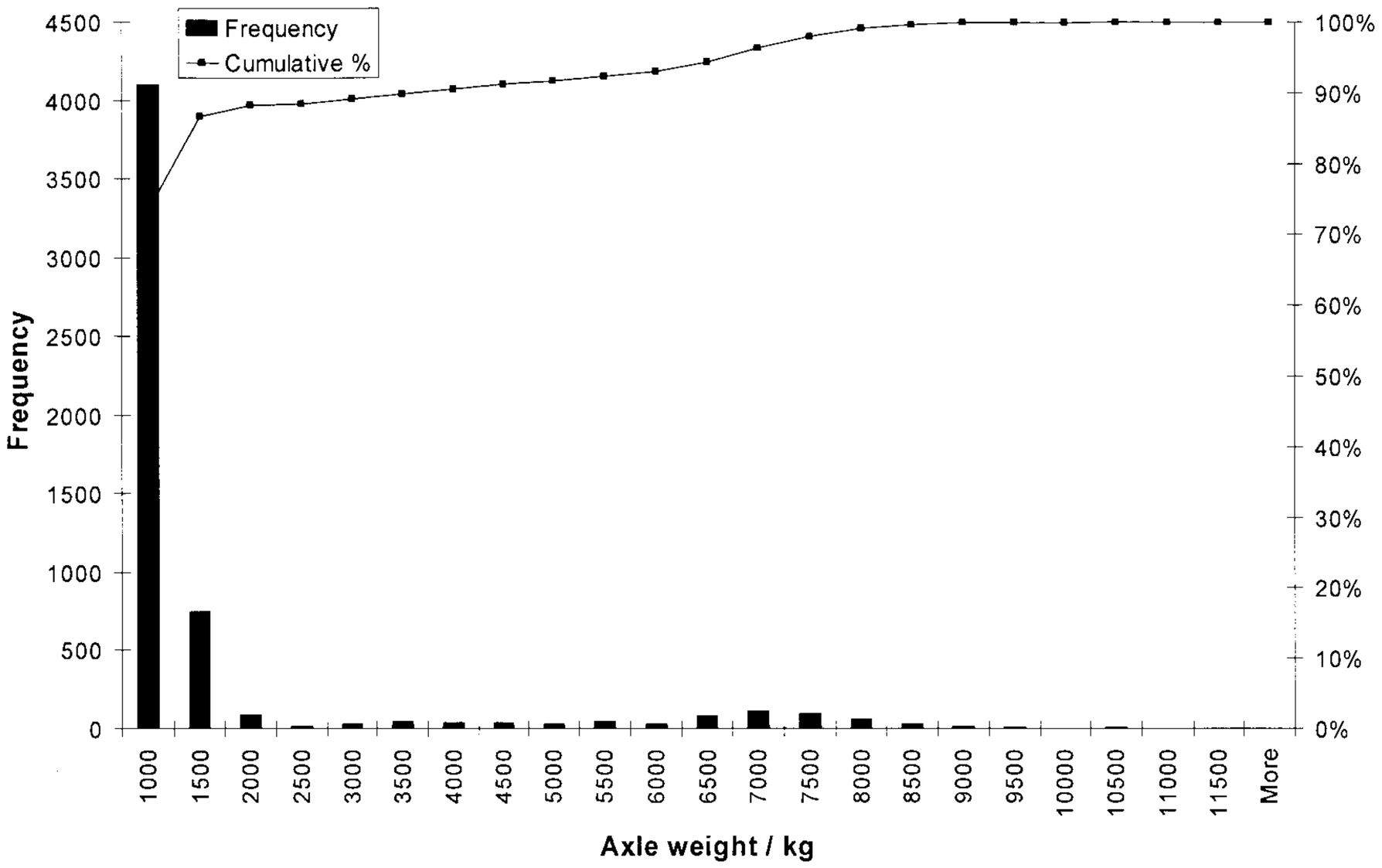

Figure 4.25 Axle 1 weight histogram lane 2

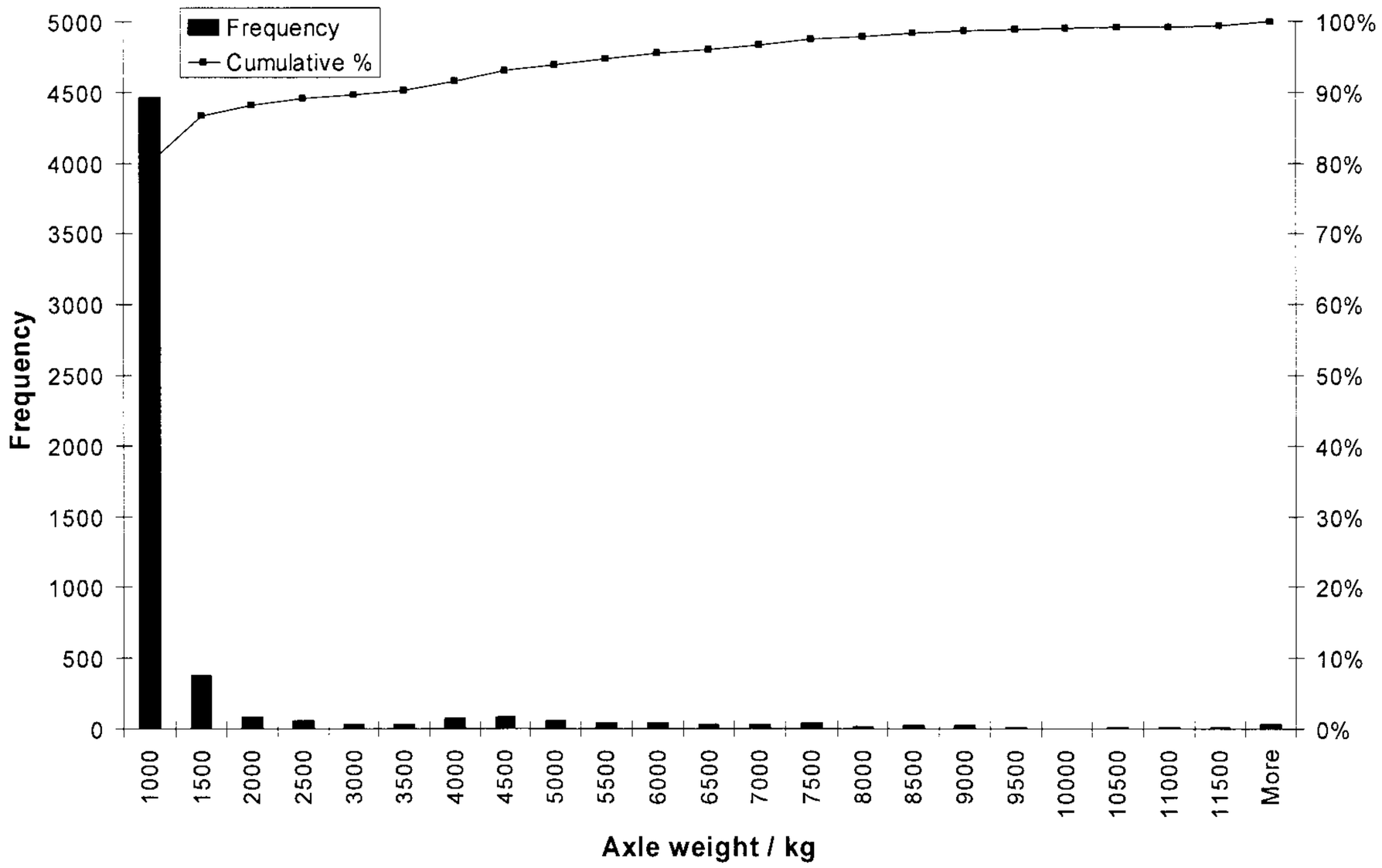

Figure 4.26 Axle 2 weight histogram lane 2

Figure 4.27 Axle 3 weight histogram lane 2

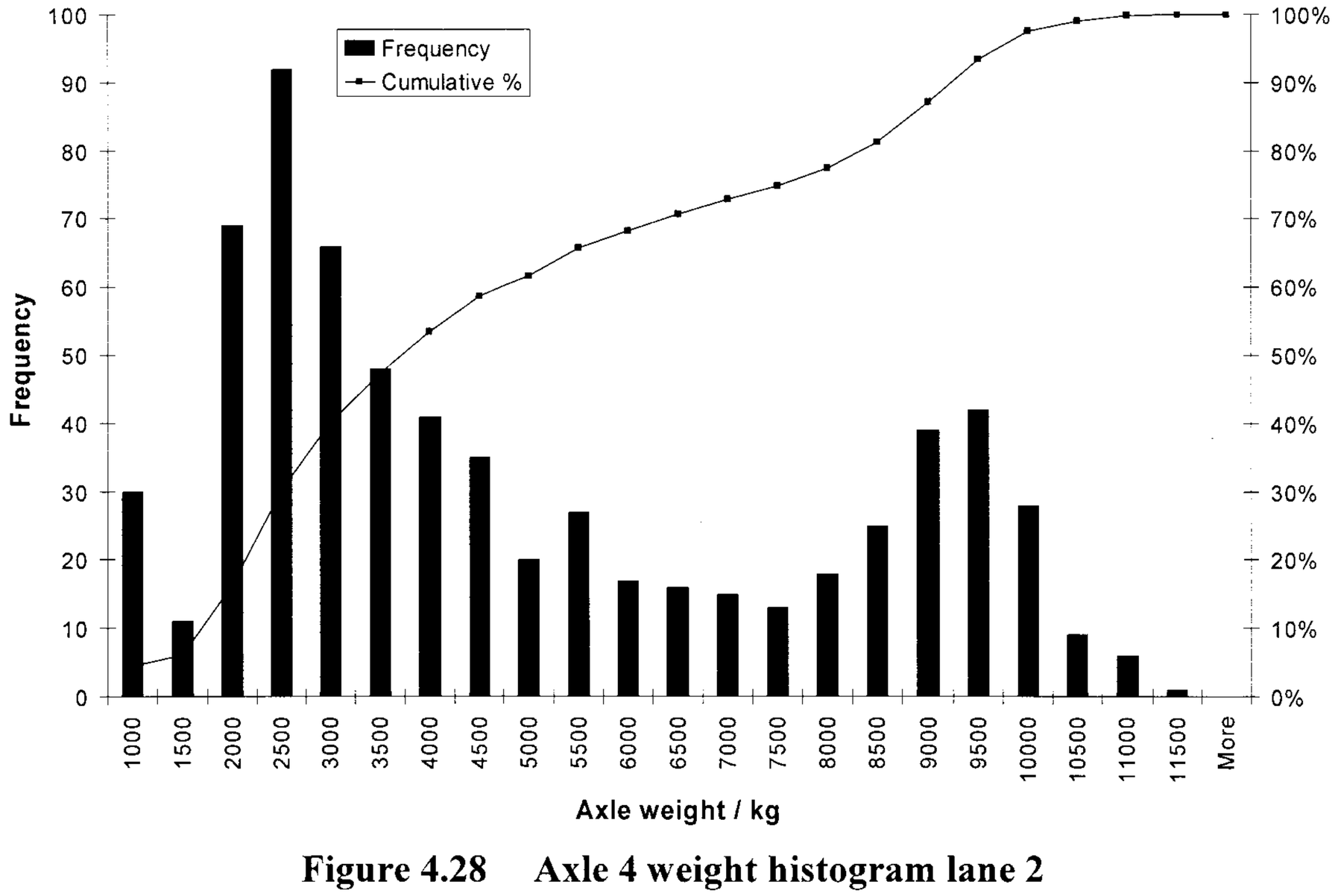

Figure 4.28 Axle 4 weight histogram lane 2

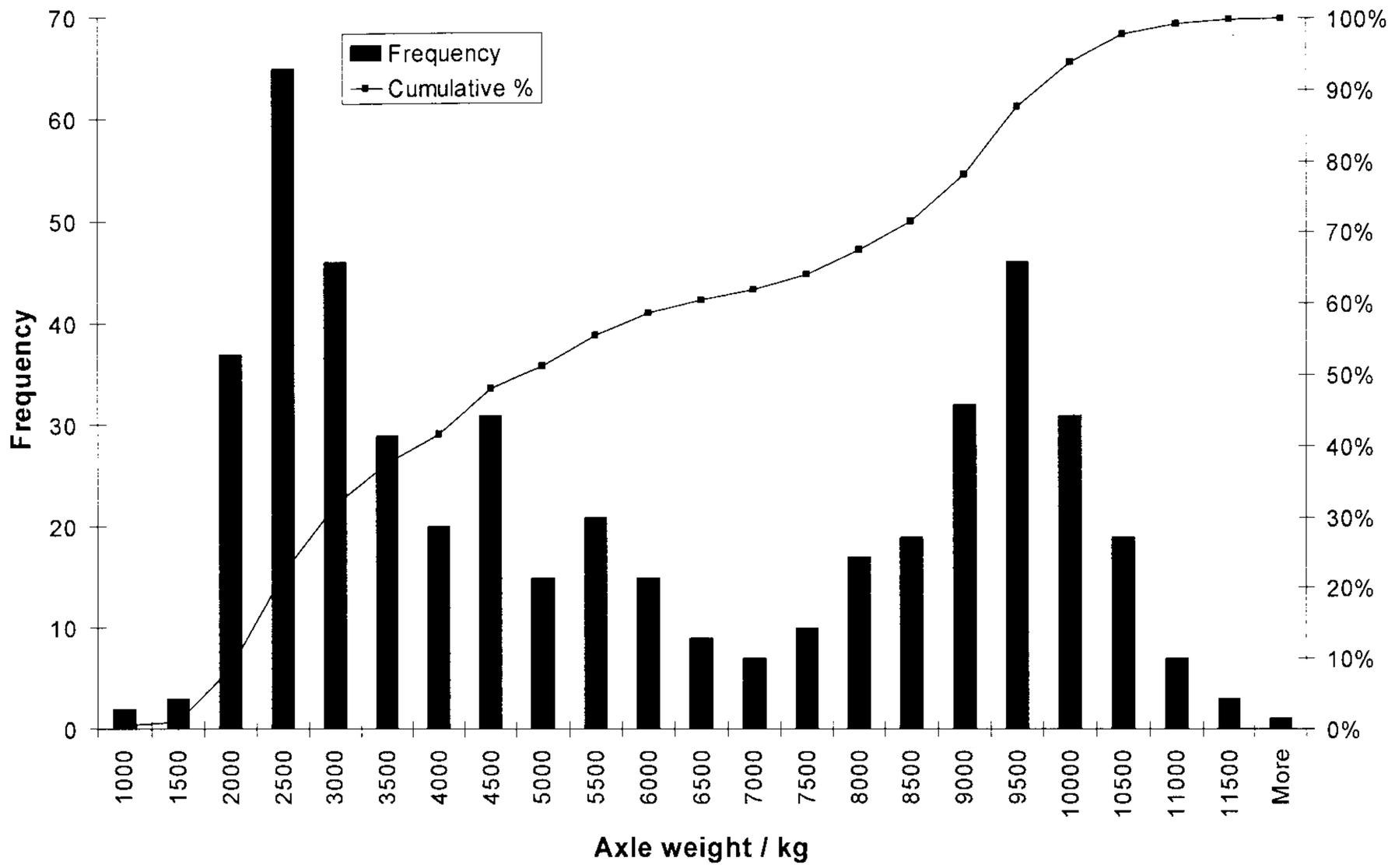

Figure 4.29 Axle 5 weight histogram lane 2

Figure 4.30 Axle 6 weight histogram lane 2

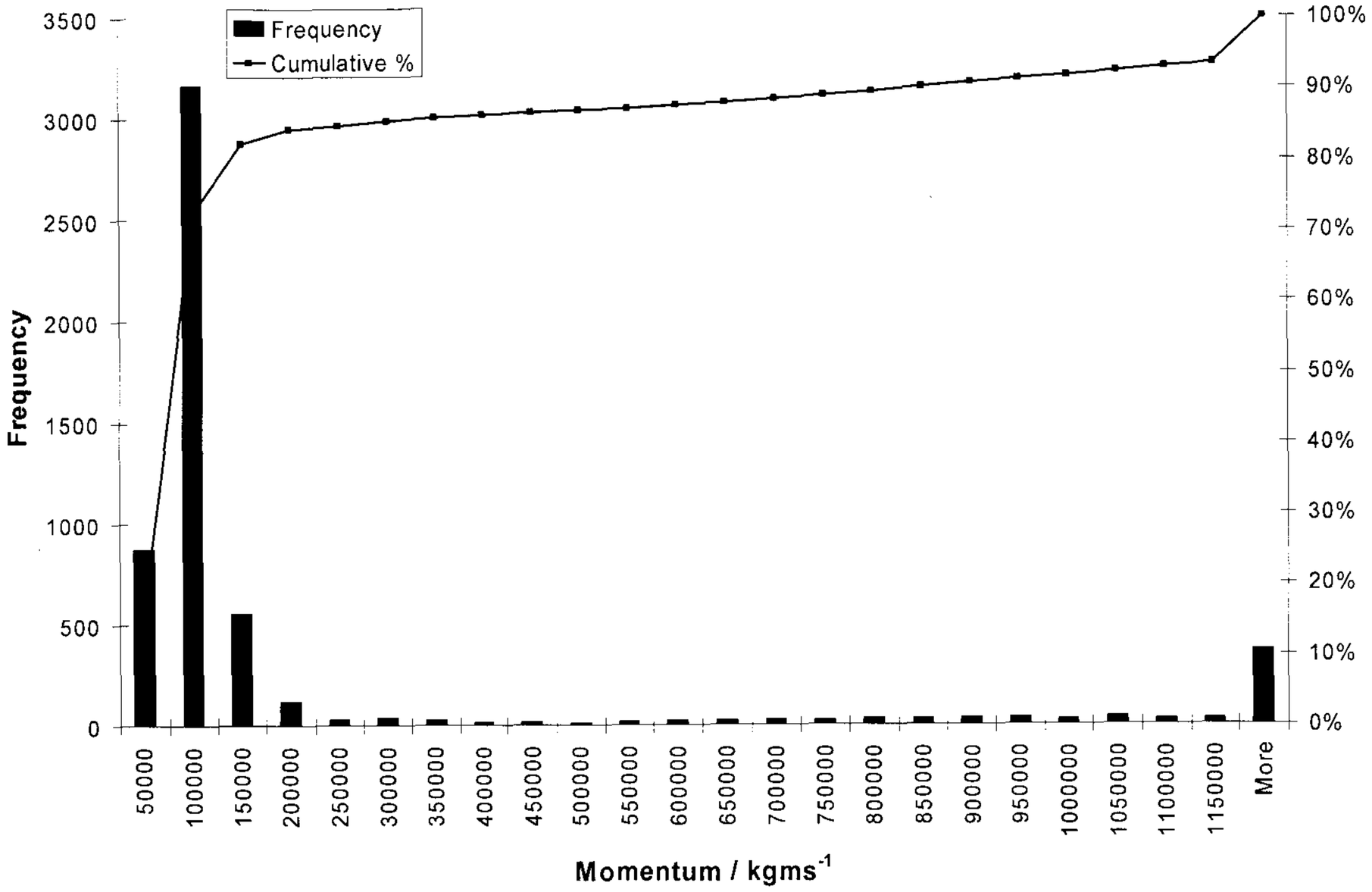

Figure 4.31 Vehicle momentum histogram lane 1

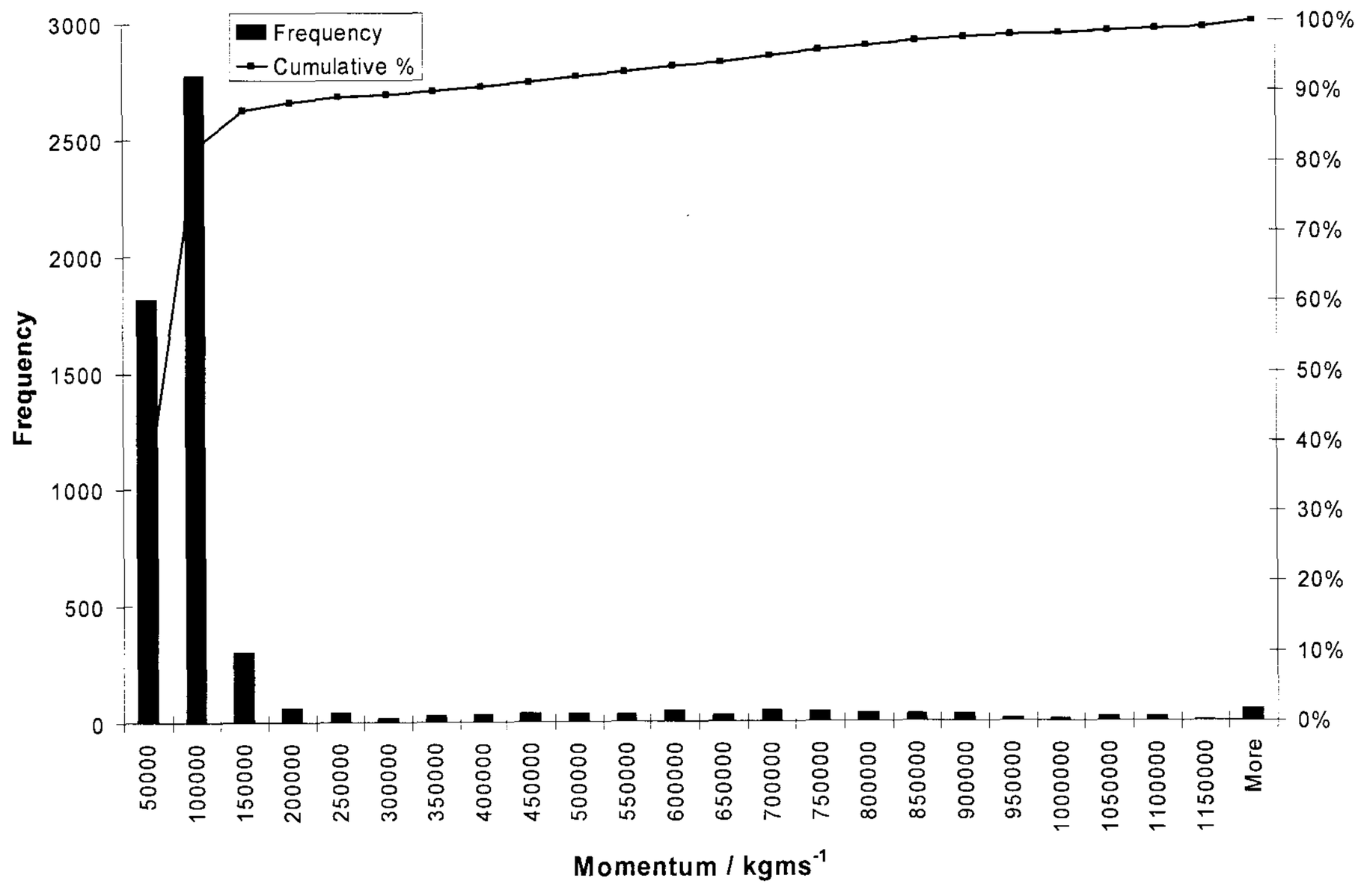

Figure 4.32 Vehicle momentum histogram lane 2

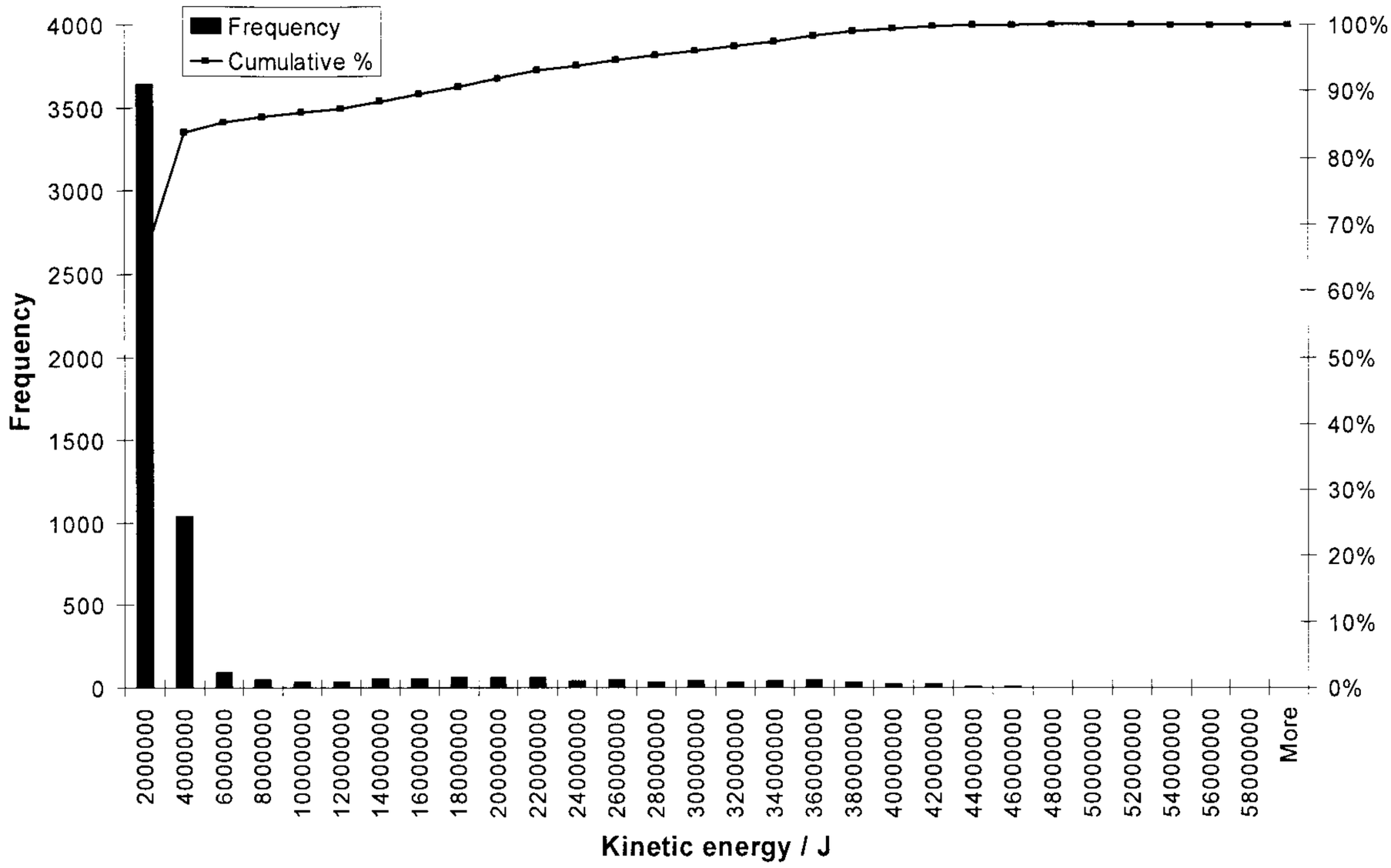

Figure 4.33 Kinetic energy histogram lane 1

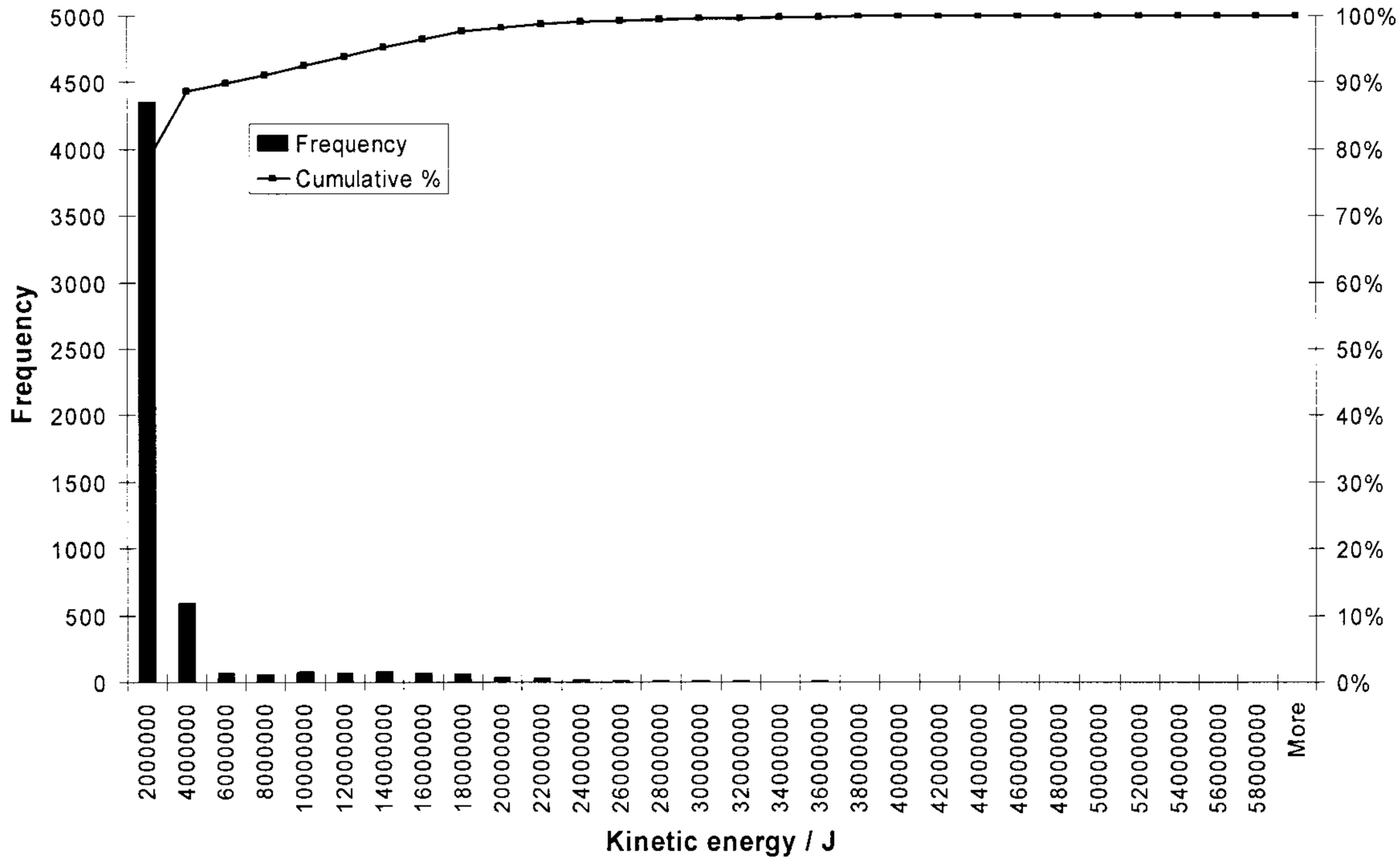

Figure 4.34 Kinetic energy histogram lane 2

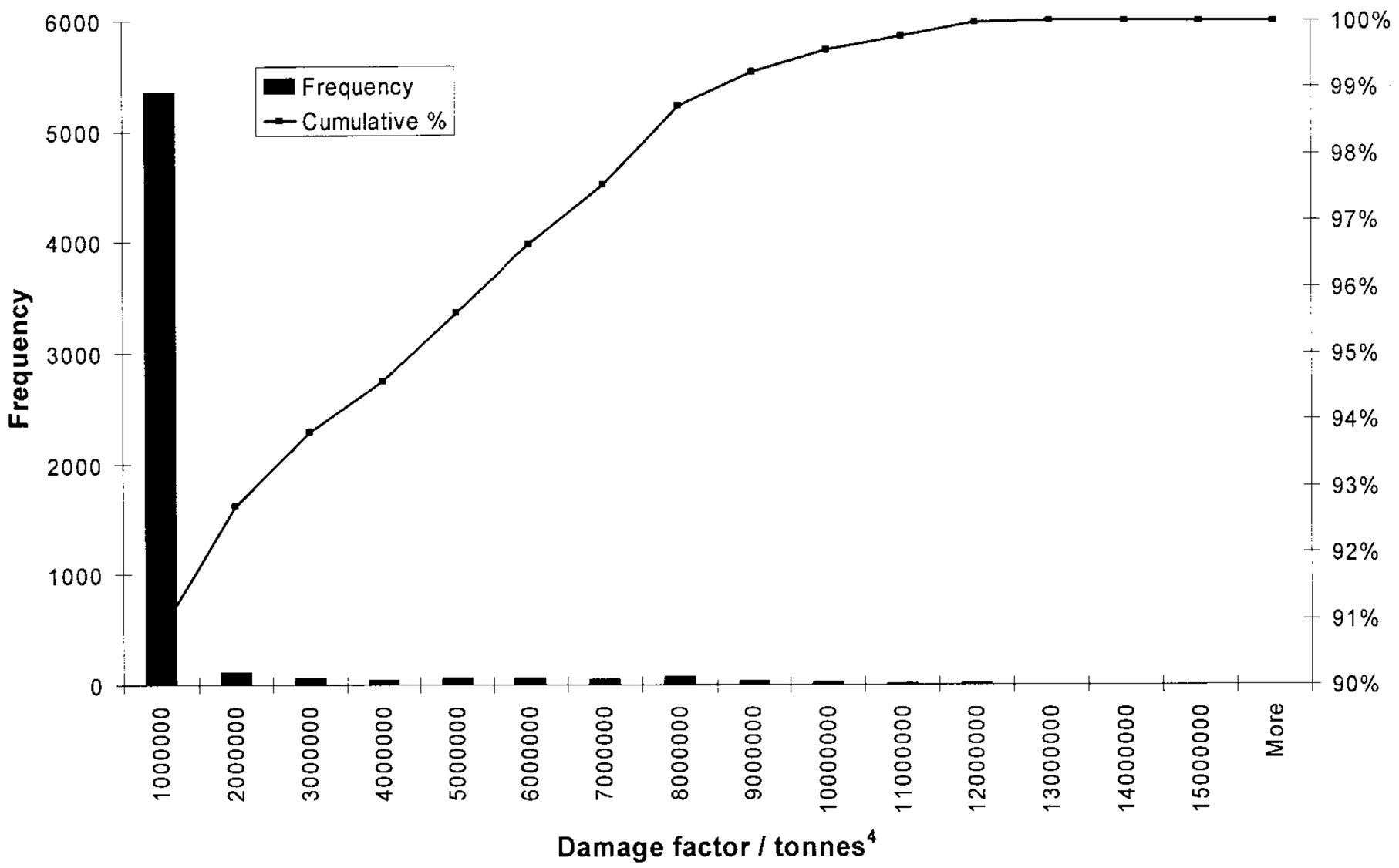

Figure 4.35 Damage factor histogram lane 1

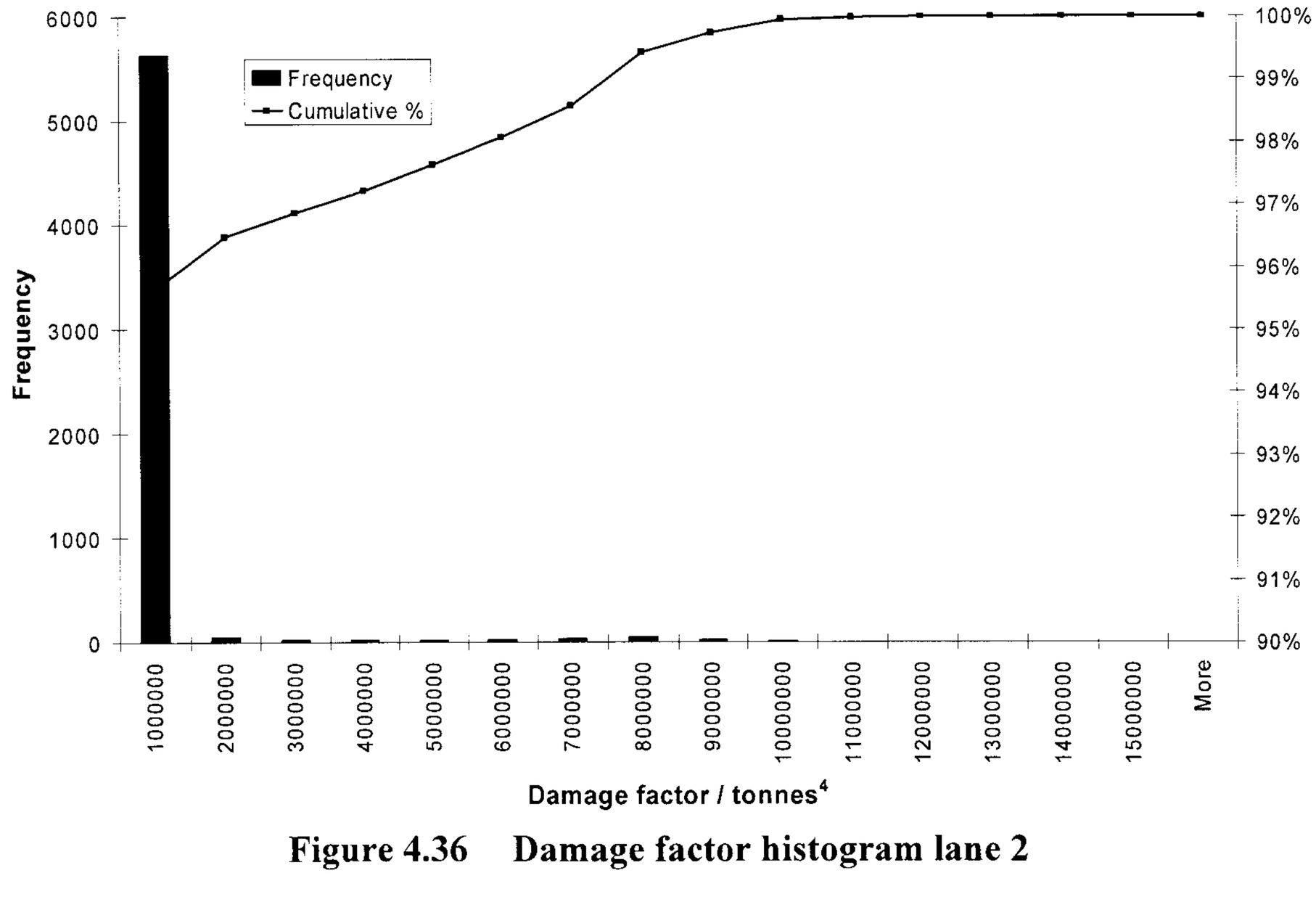

Figure 4.36 Damage factor histogram lane 2

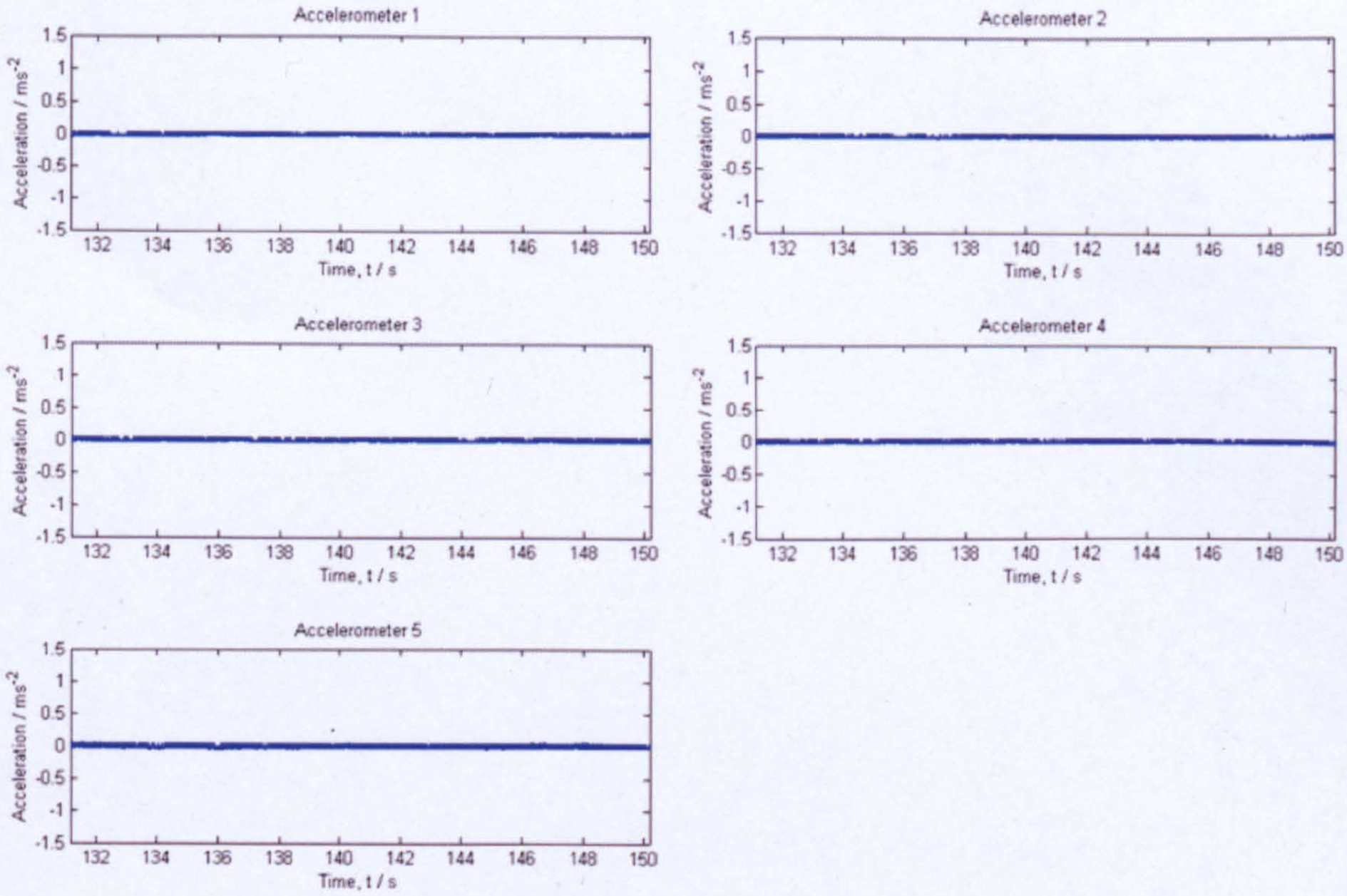

Figure 4.37 Time trace of background noise level

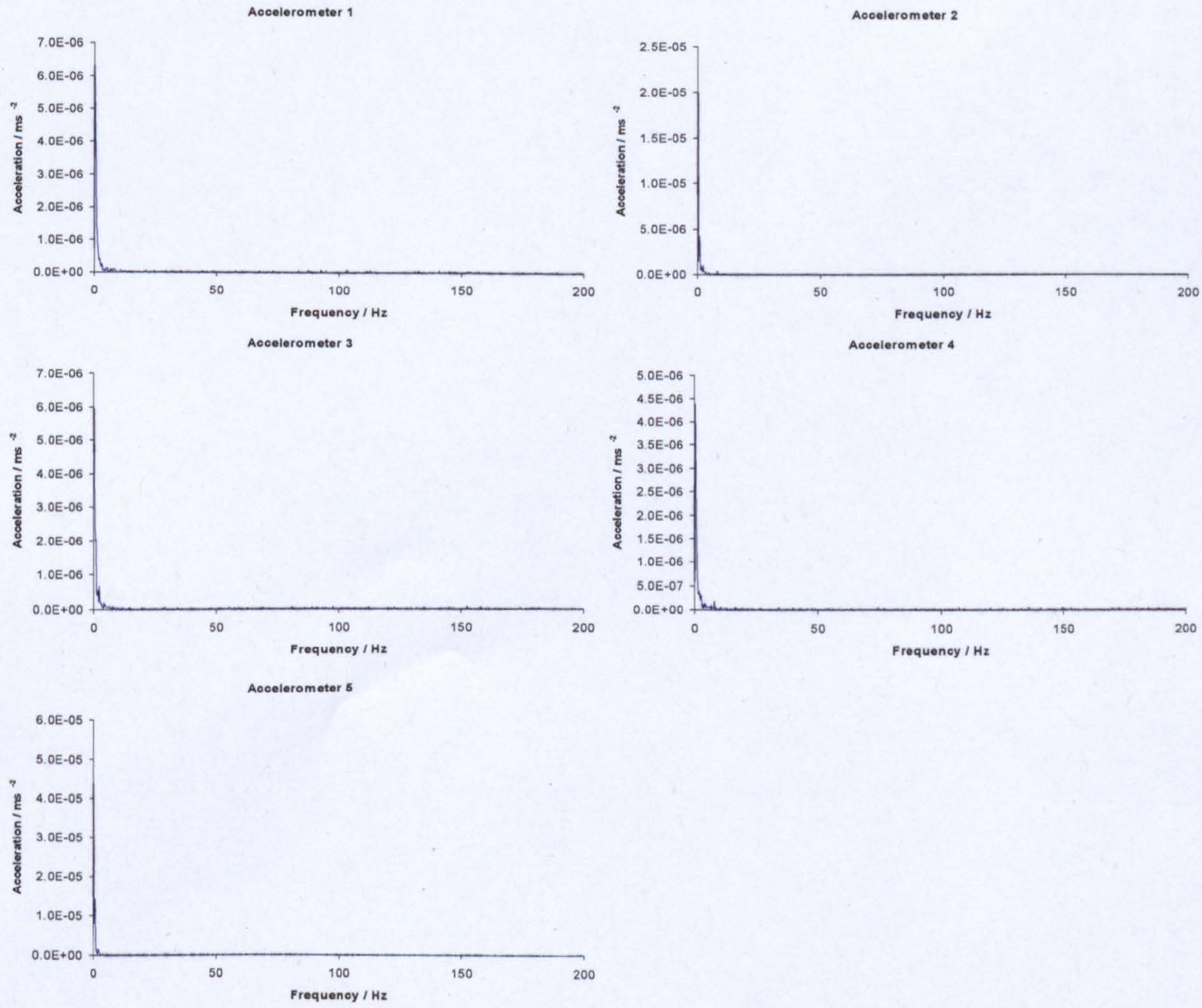

Figure 4.38 Frequency domain plot of Figure 4.14

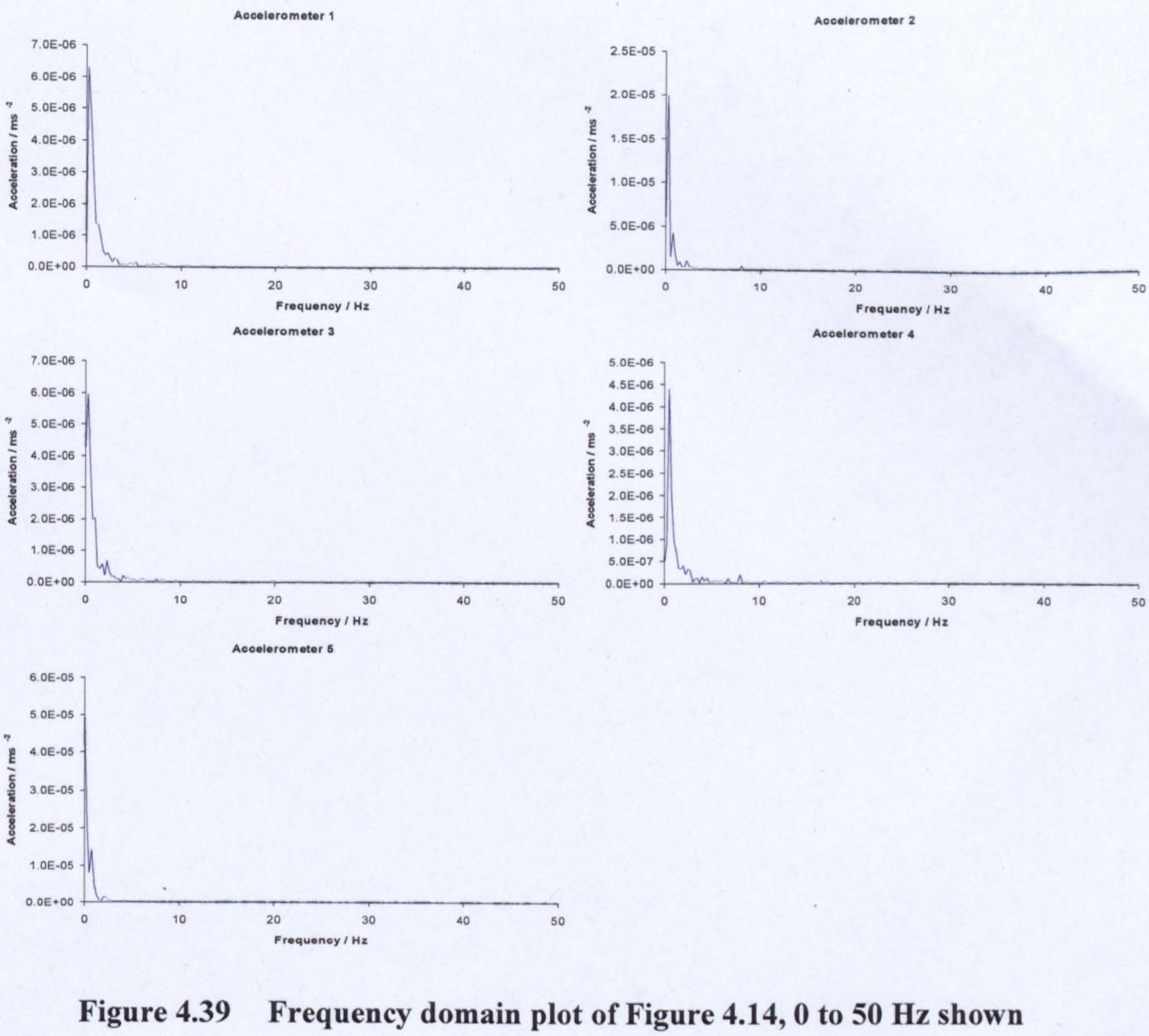

Figure 4.39 Frequency domain plot of Figure 4.14, 0 to 50 Hz shown

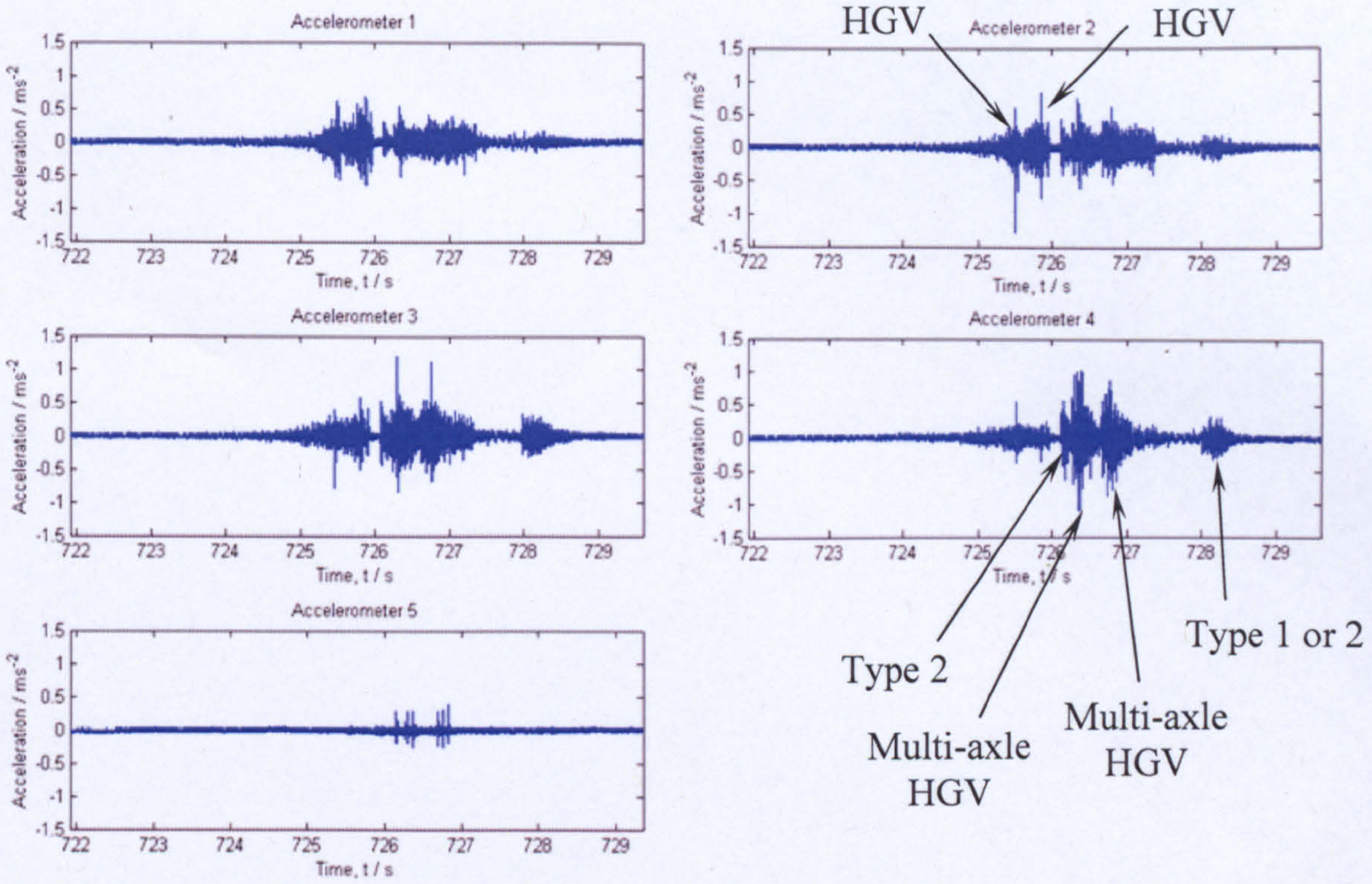

Figure 4.40 Time domain plot for test 2 (722 s -729 s) – Arrows indicate typical acceleration traces for vehicle types

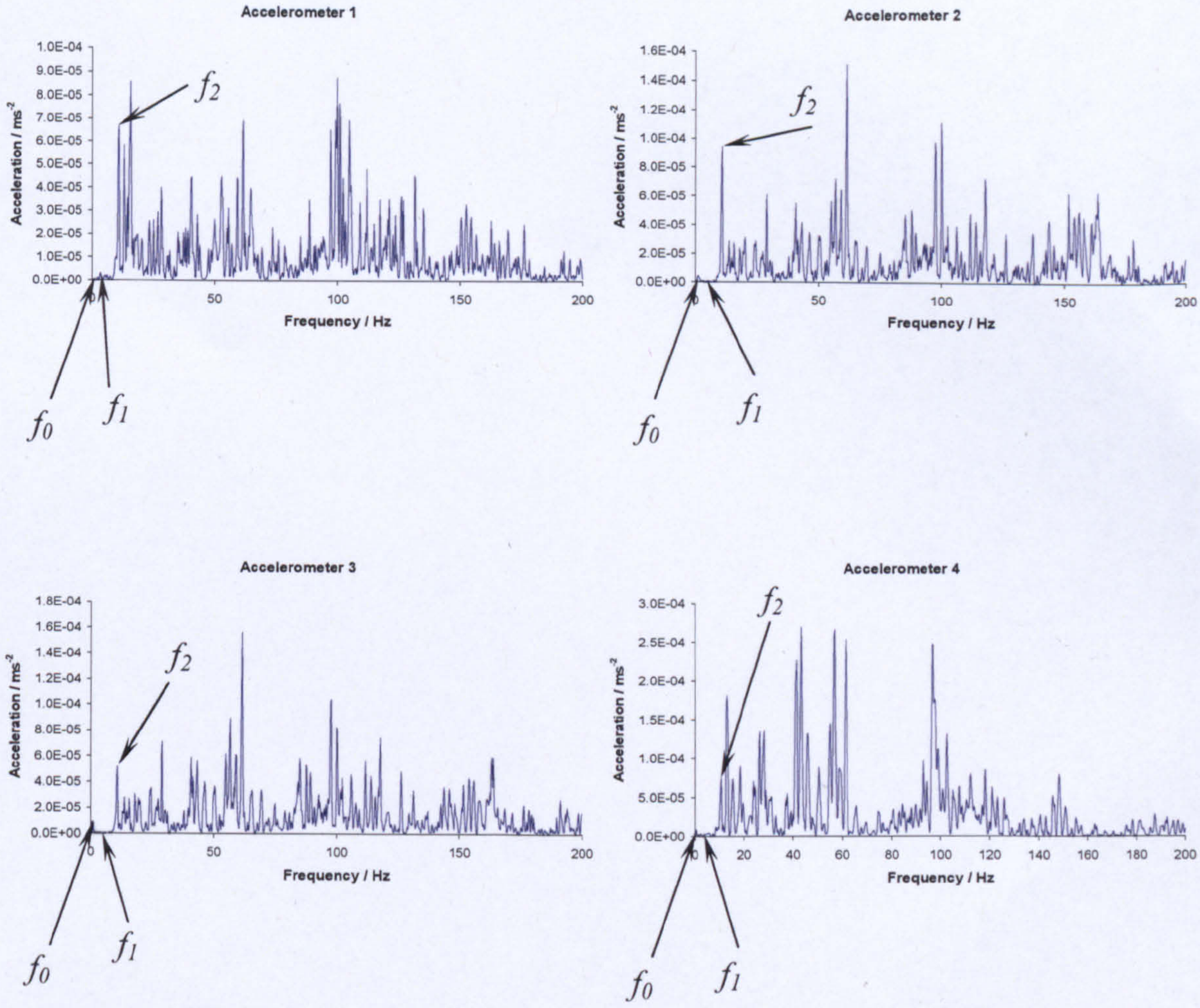

Figure 4.41 Frequency domain plots of Figure 4.40 (Arrows indicate location of 1st resonance frequency used in Figure 4.66)

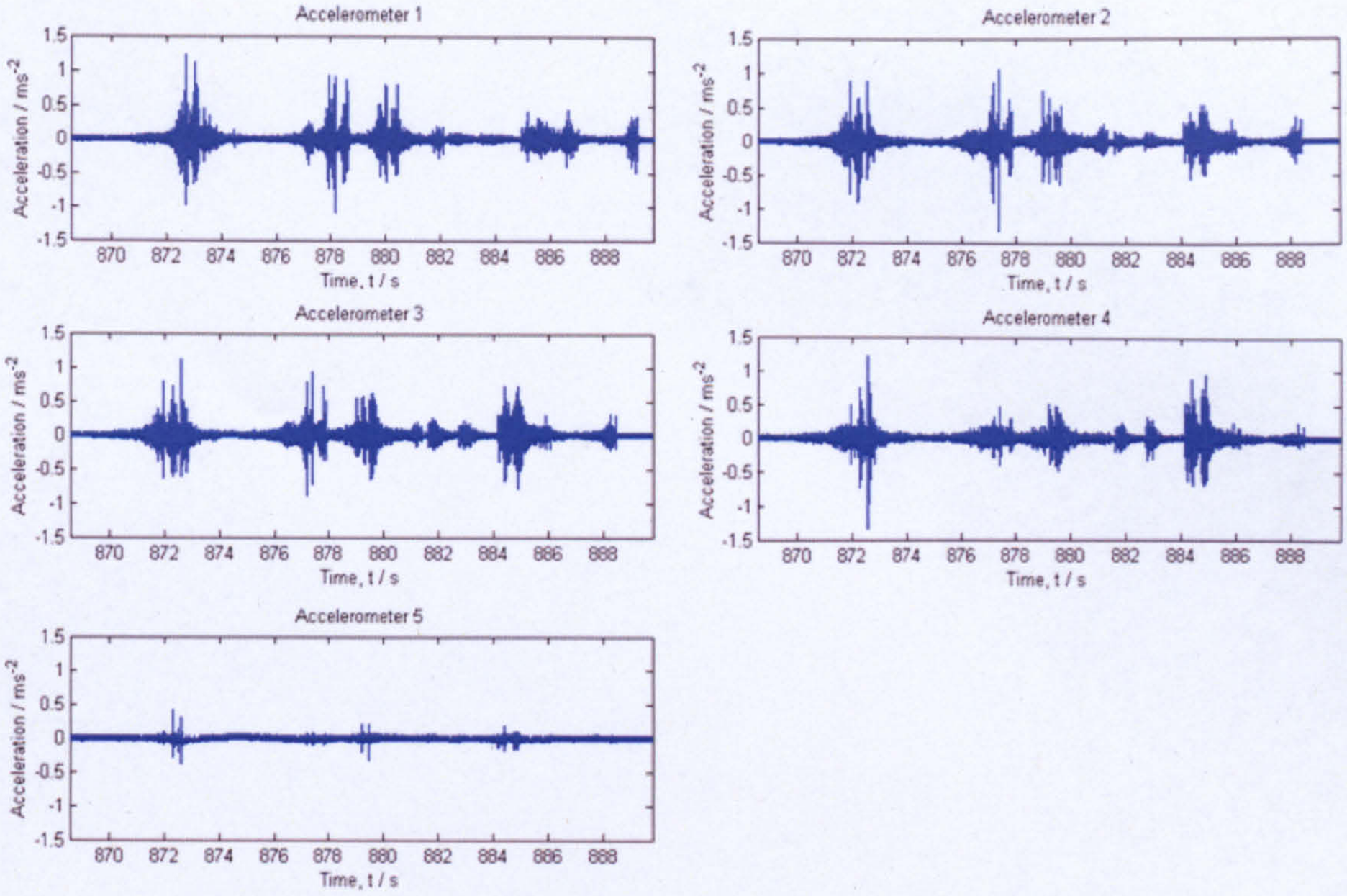

Figure 4.42 Time domain plot for test 2 (869 s - 890 s)

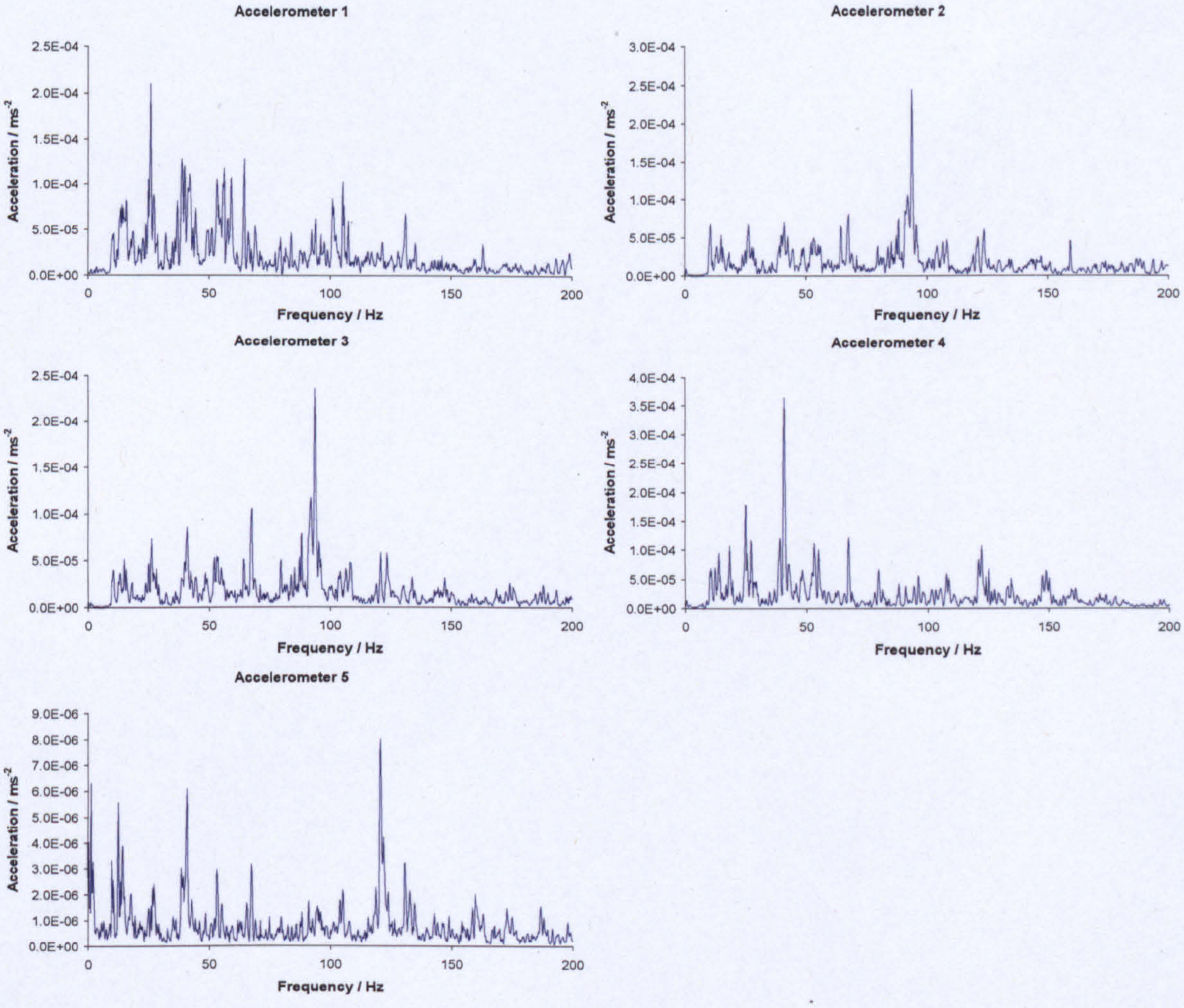

Figure 4.43 Frequency domain plot of Figure 4.42

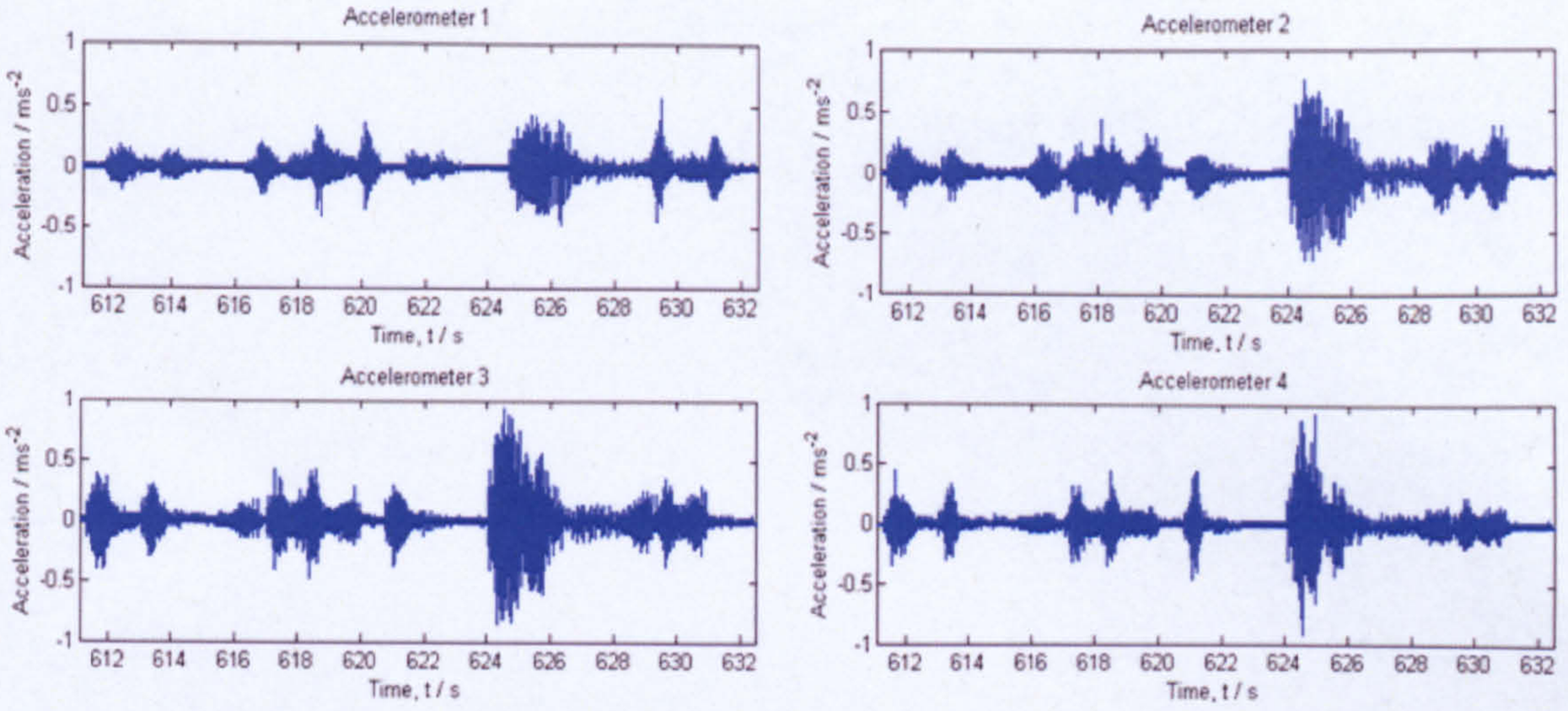

Figure 4.44 Time domain plot for test 3 (610 s - 630 s)

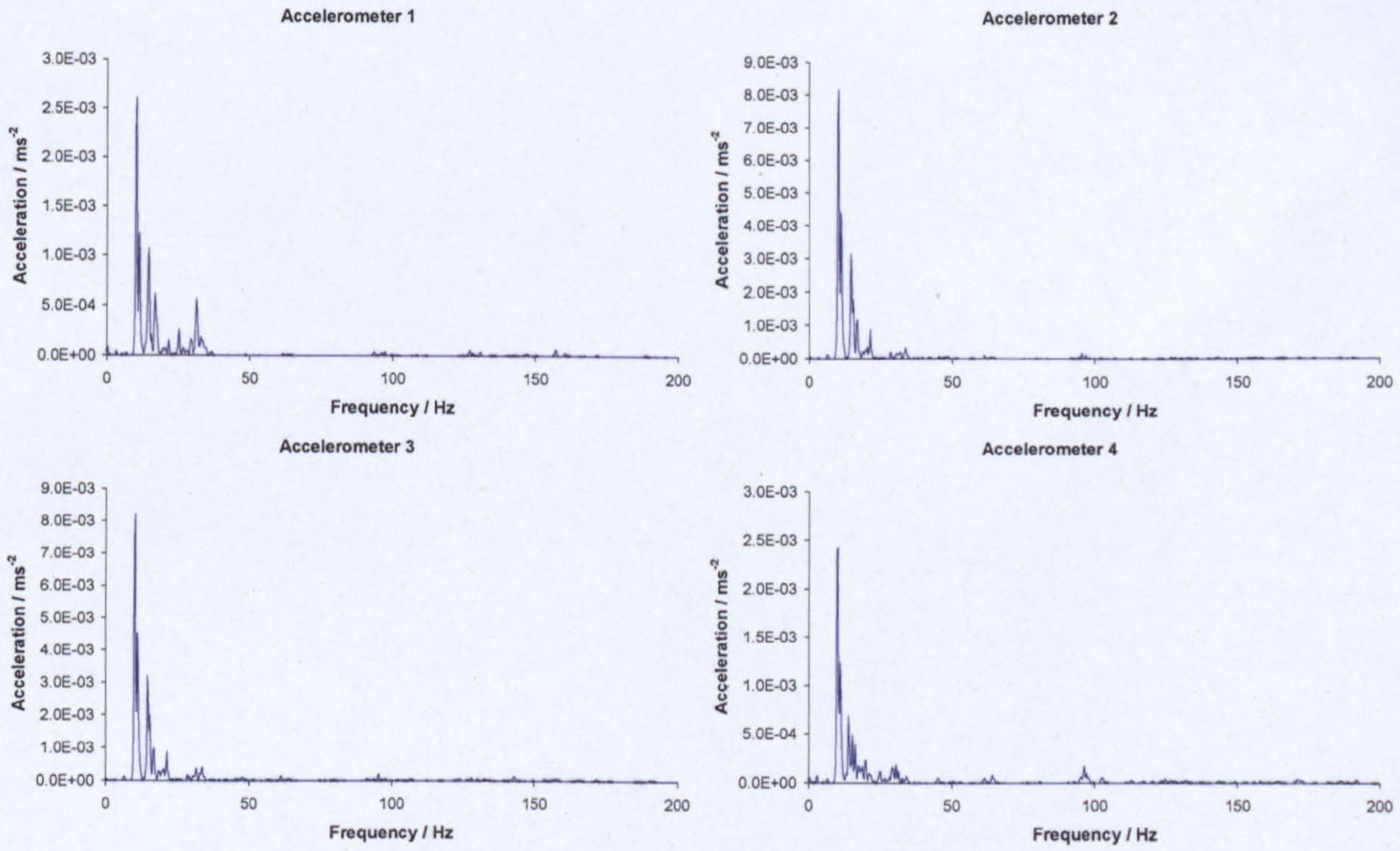

Figure 4.45 Frequency domain plot of Figure 4.44

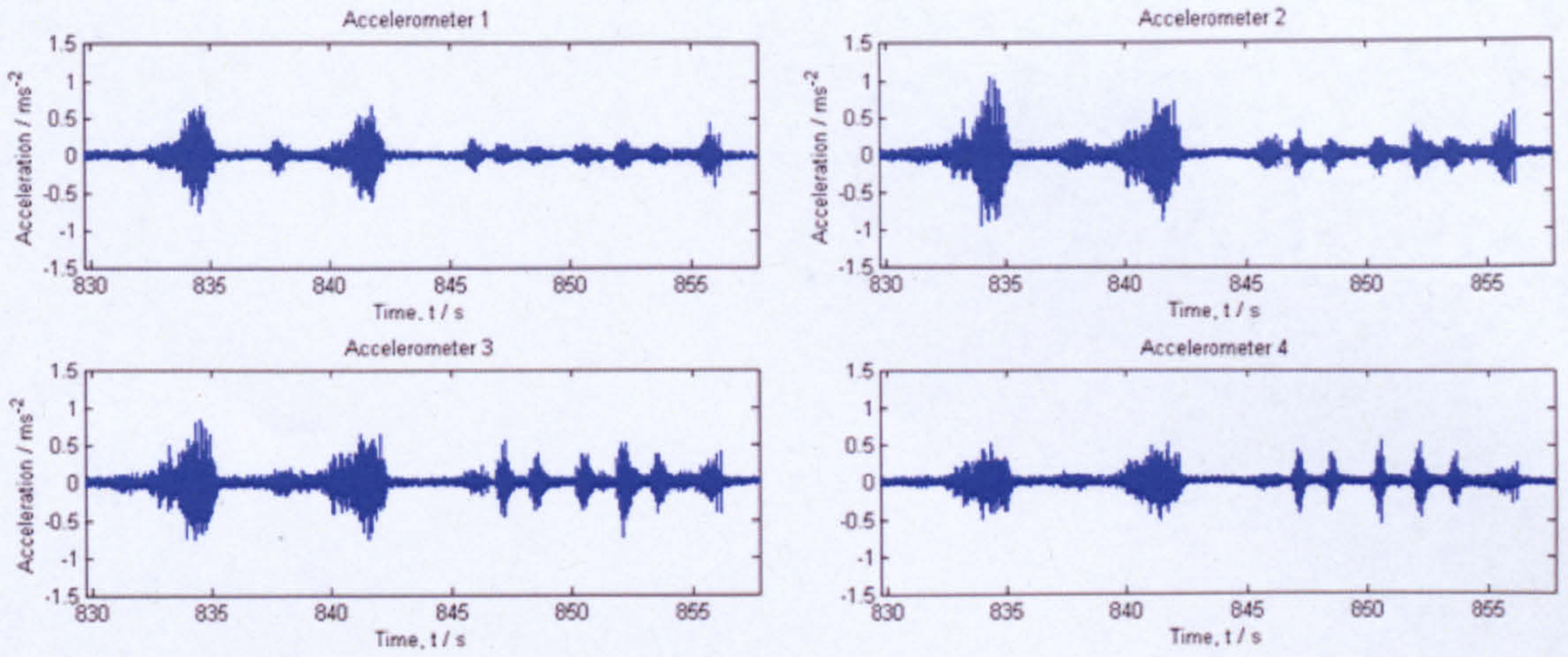

Figure 4.46 Time domain plot for test 3 (830 s - 860 s)

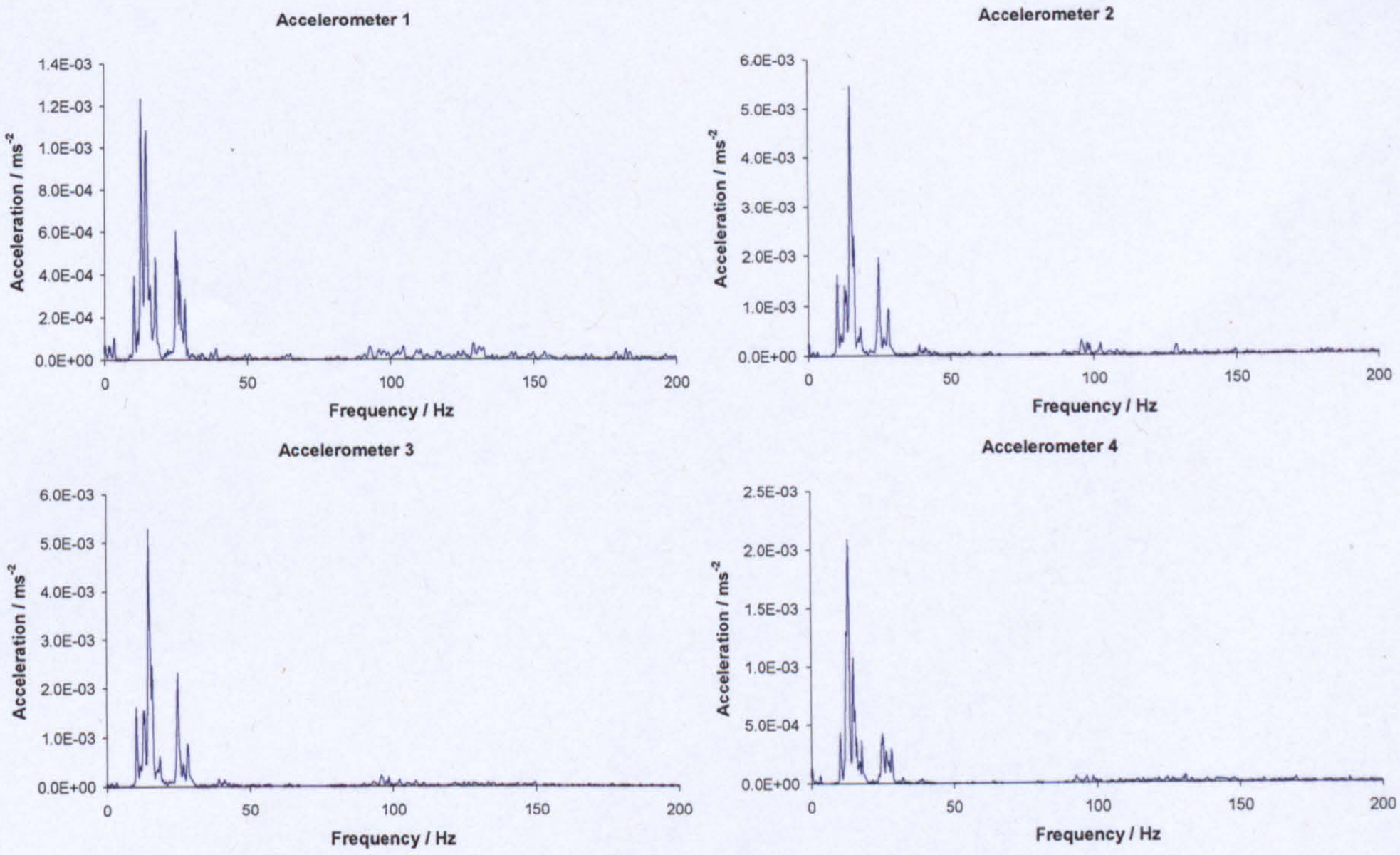

Figure 4.47 Frequency domain plot of Figure 4.46

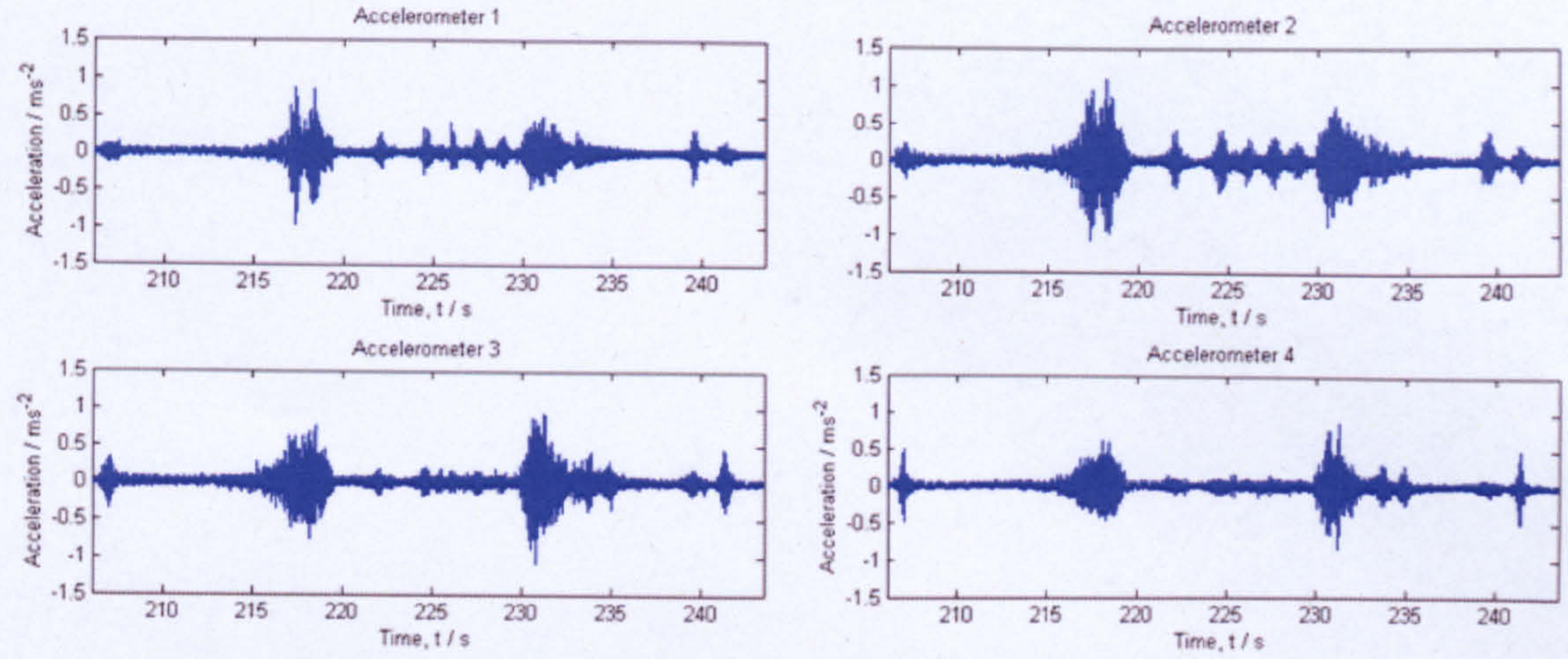

Figure 4.48 Time domain plot for test 4 (205 s - 245 s)

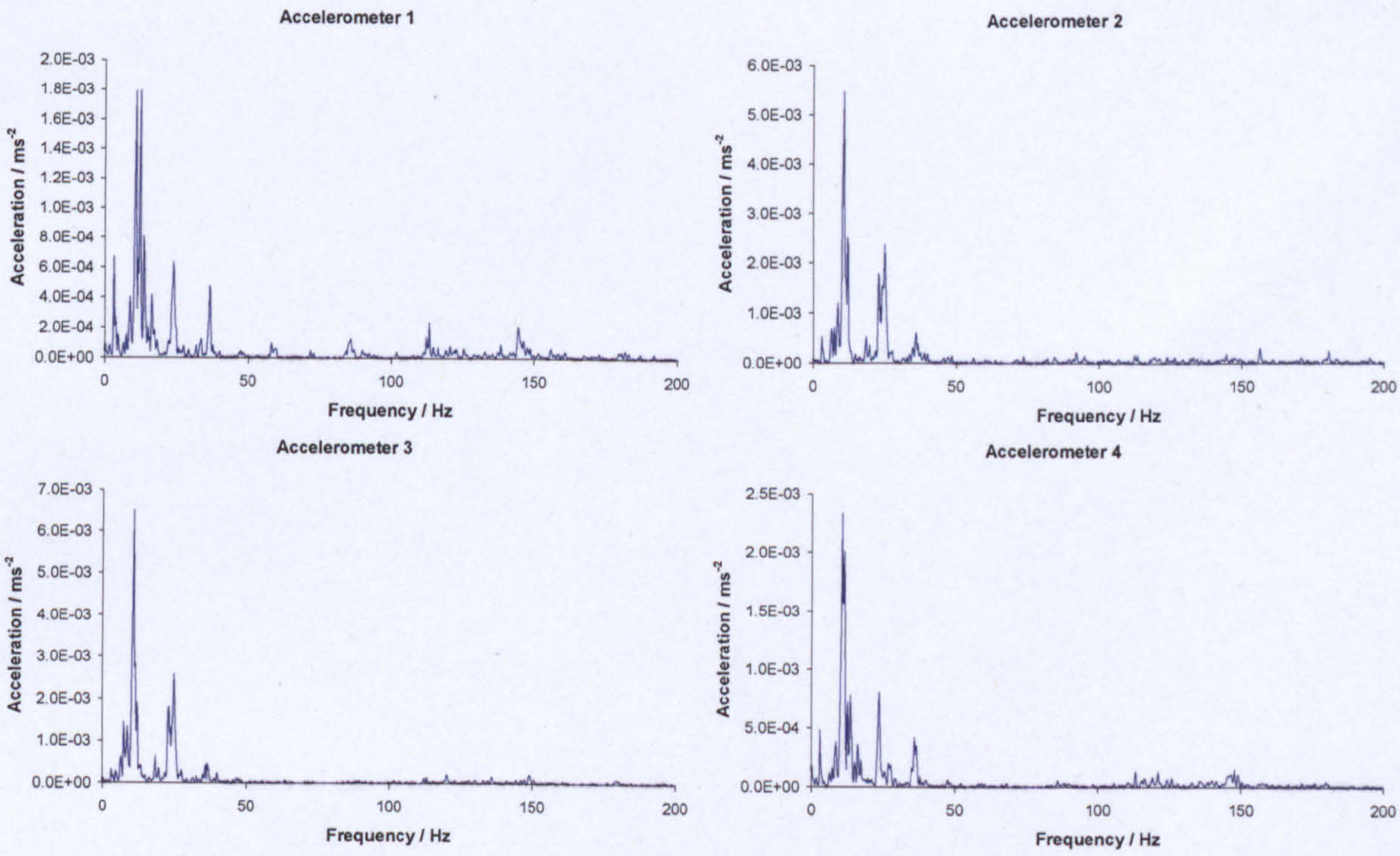

Figure 4.49 Frequency domain plot of Figure 4.48

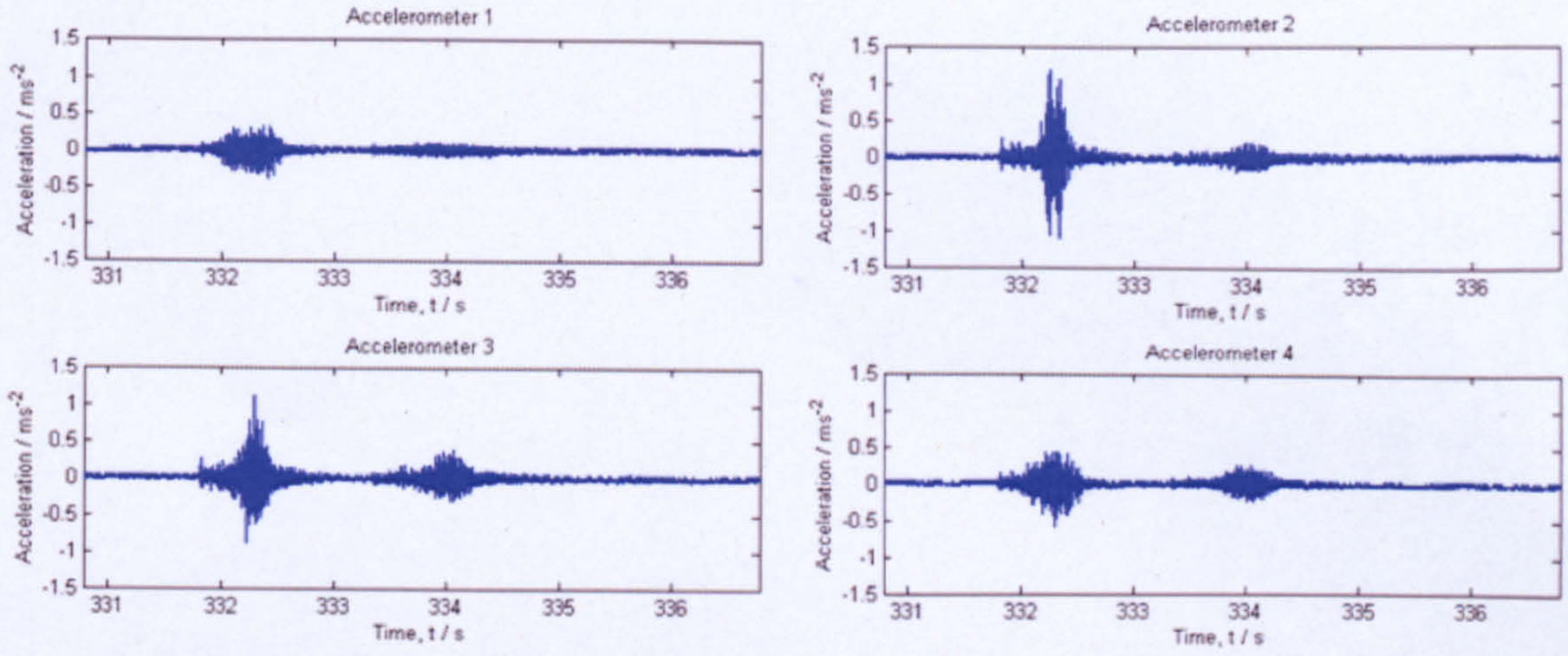

Figure 4.50 Time domain plot for test 4 (331 s -337 s)

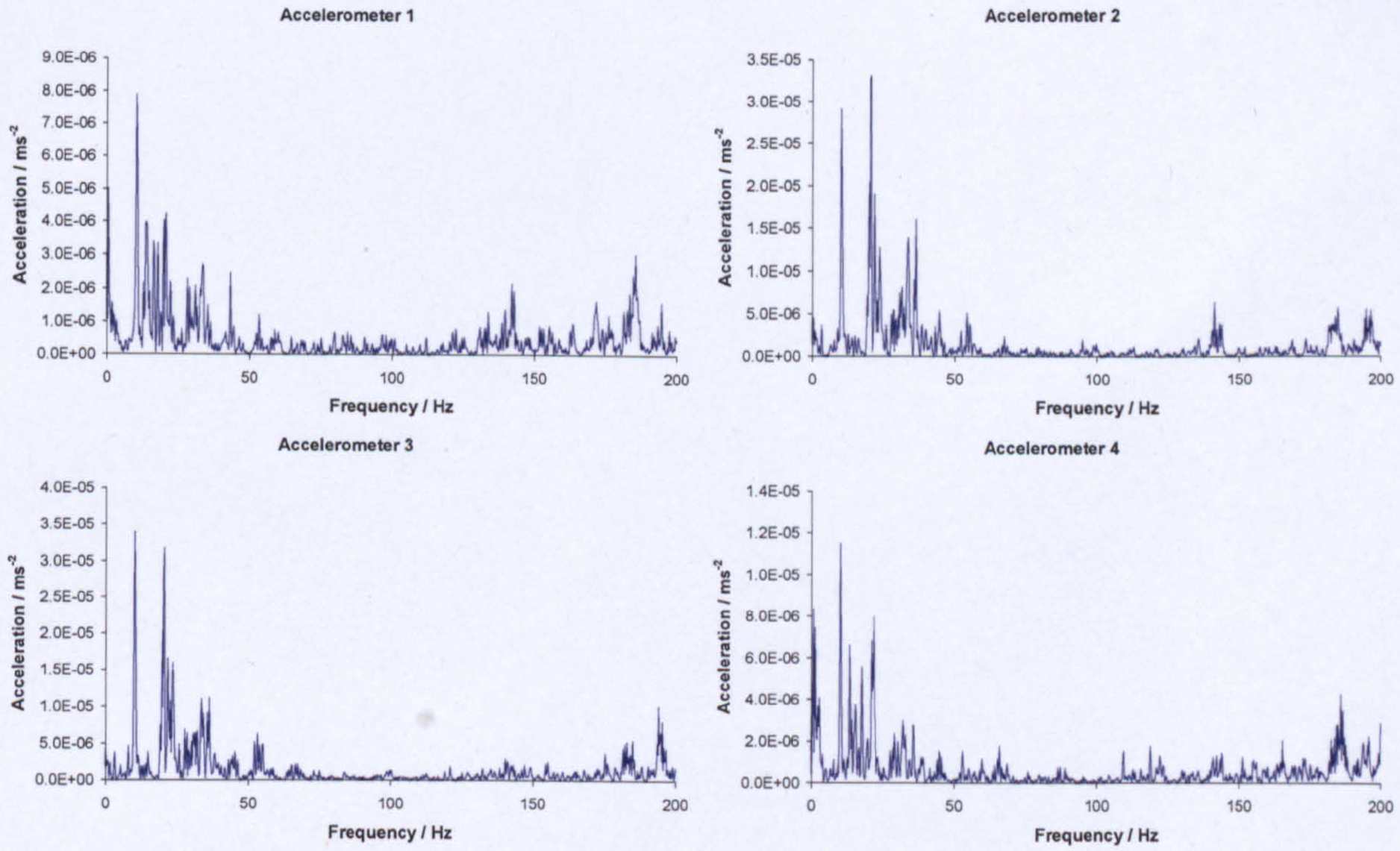

Figure 4.51 Frequency domain plot of Figure 4.50

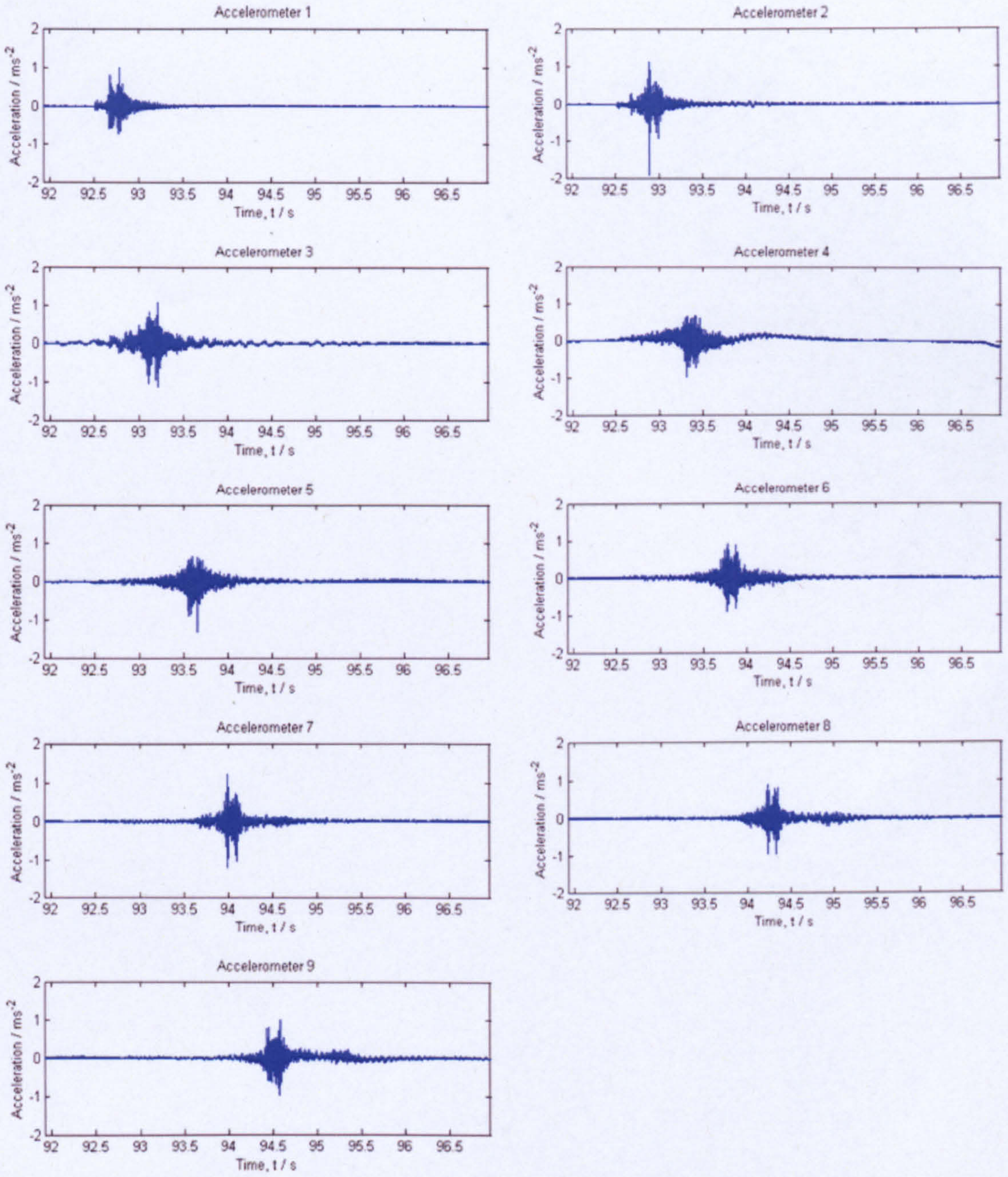

Figure 4.52 Time domain plot for test 5 (82 s - 97 s)

Figure 4.53 Time domain plot for test Figure 4.52

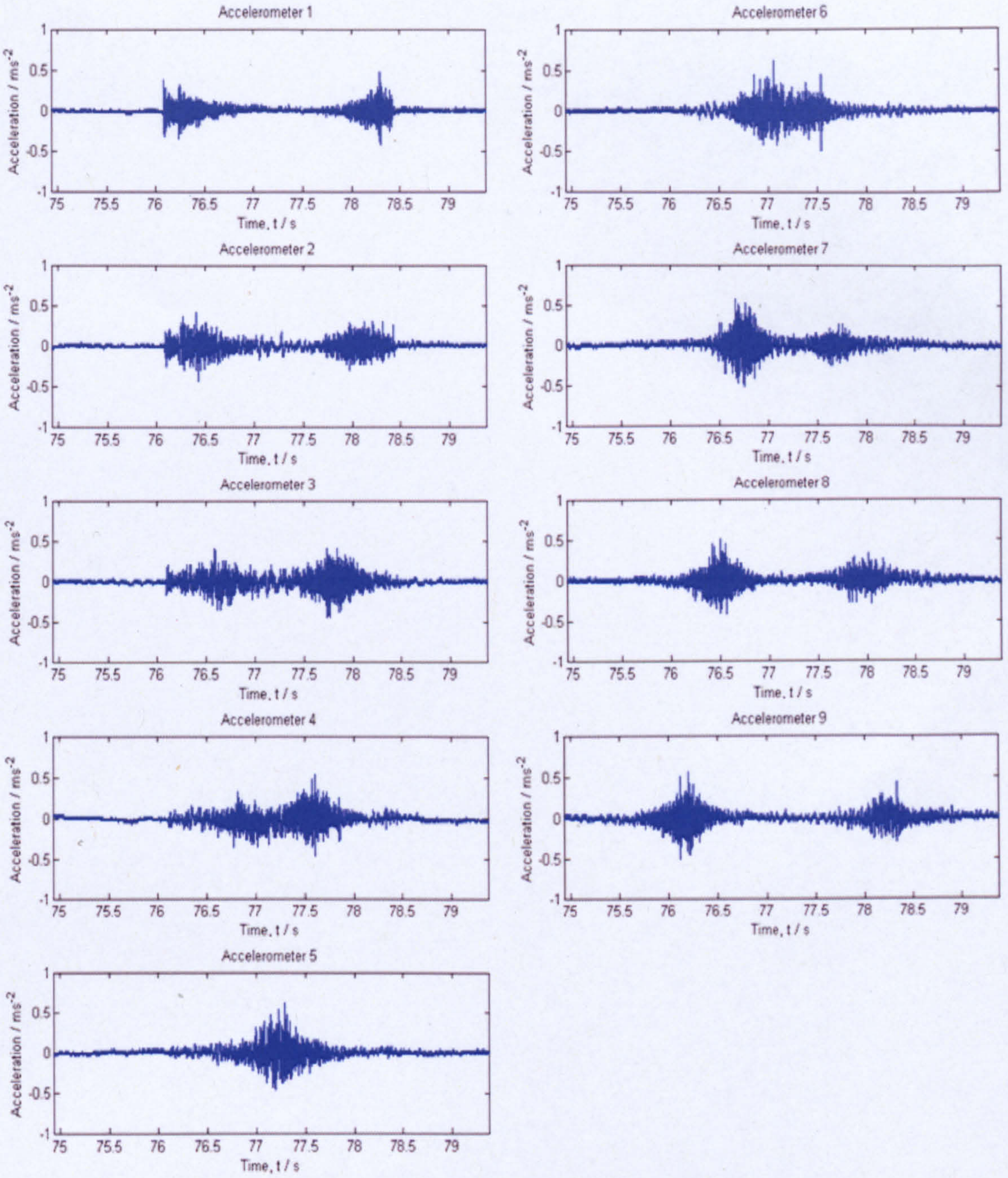

Figure 4.54 Time domain plot for test 5 (75 s - 80 s)

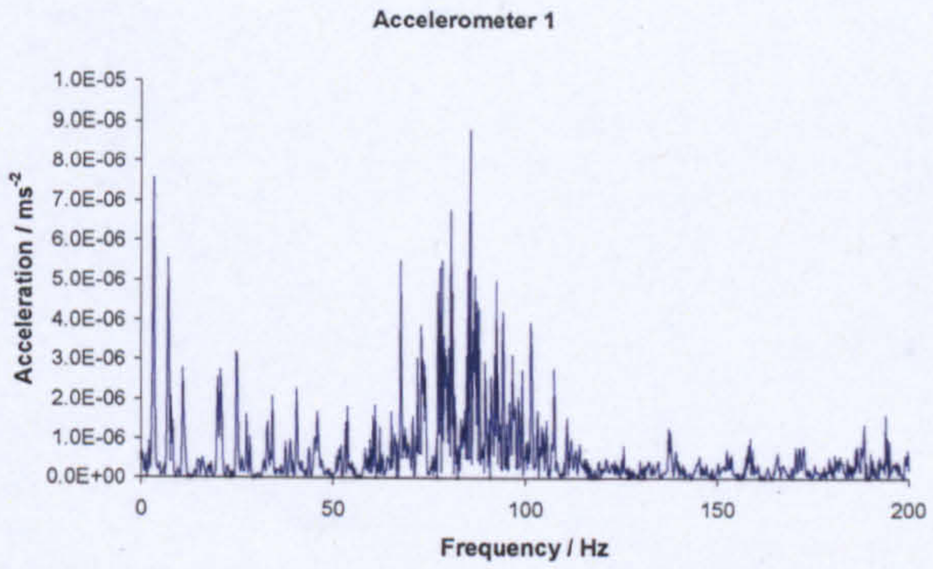

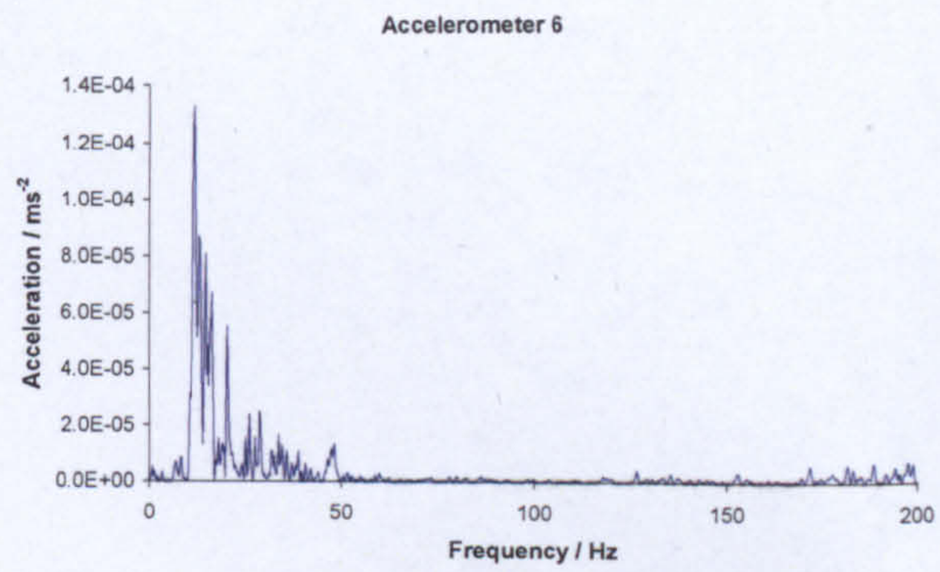

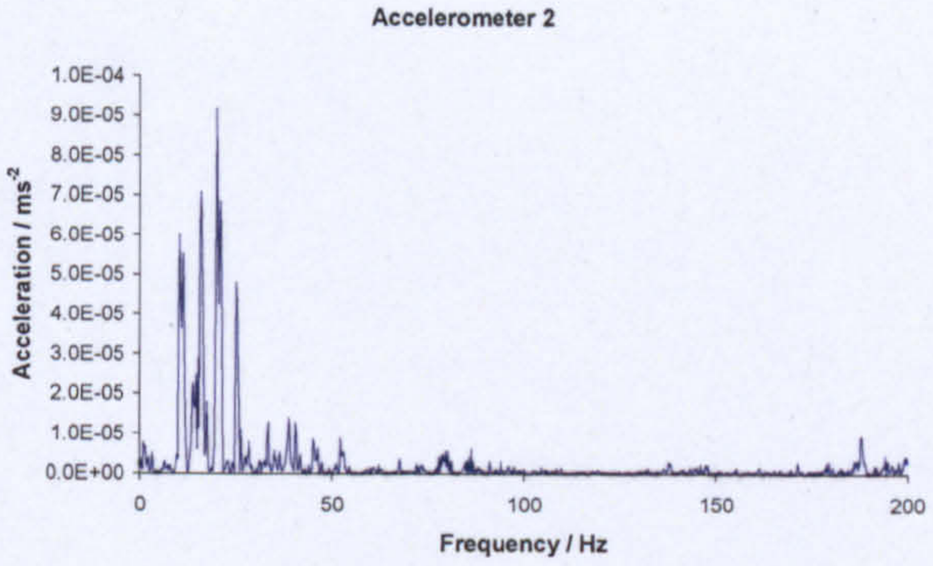

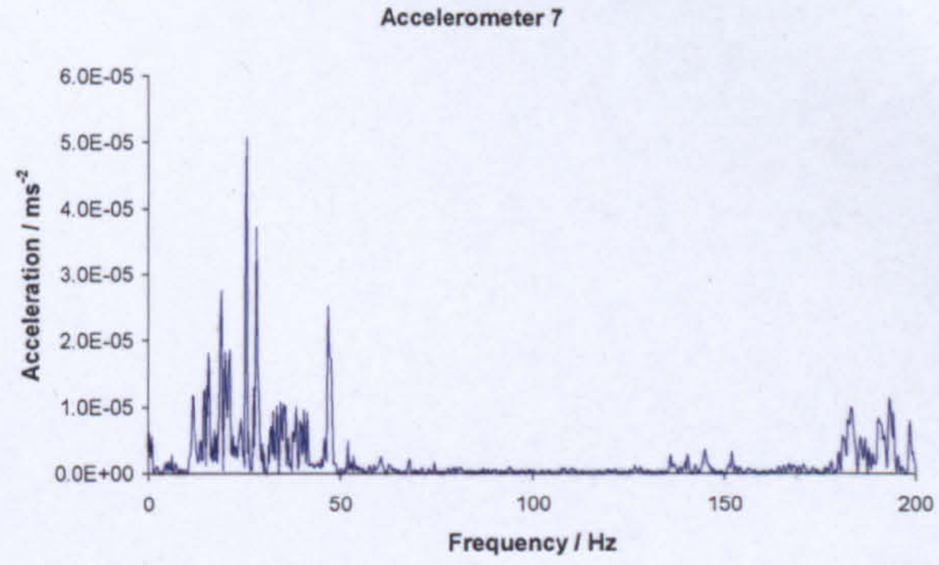

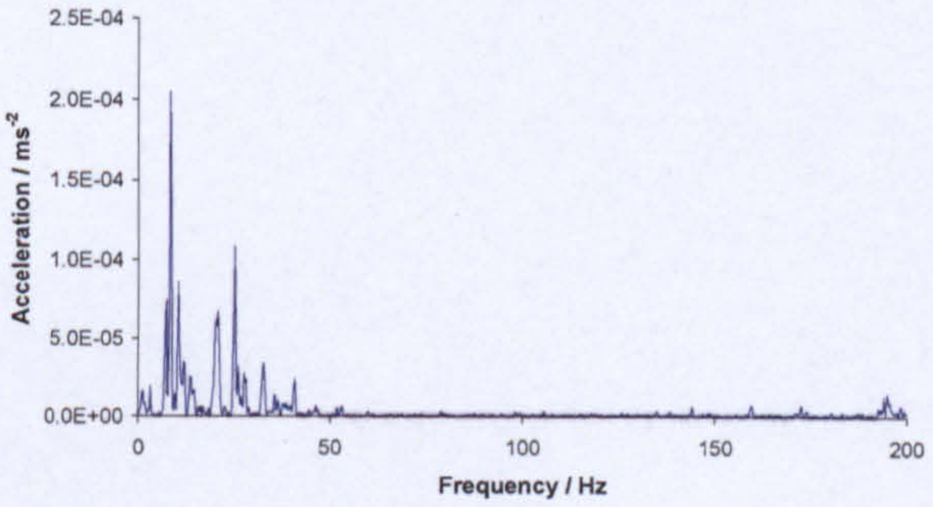

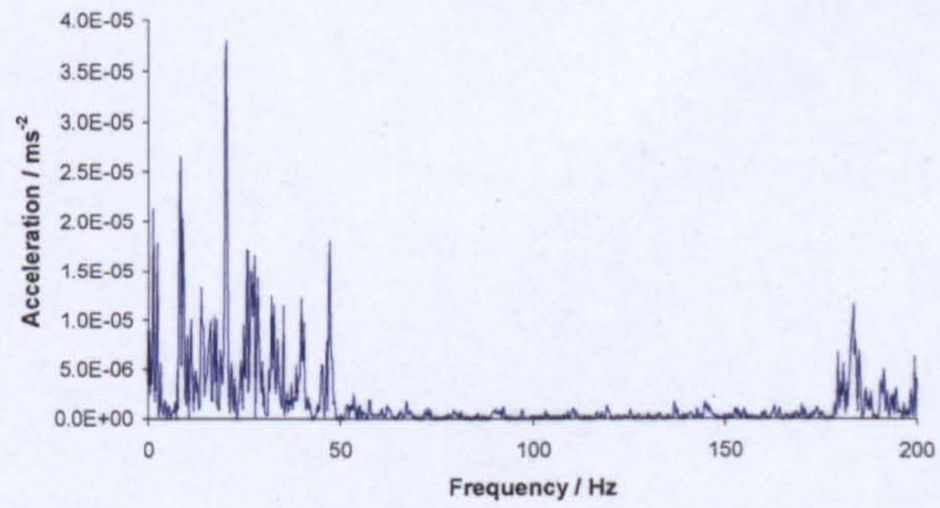

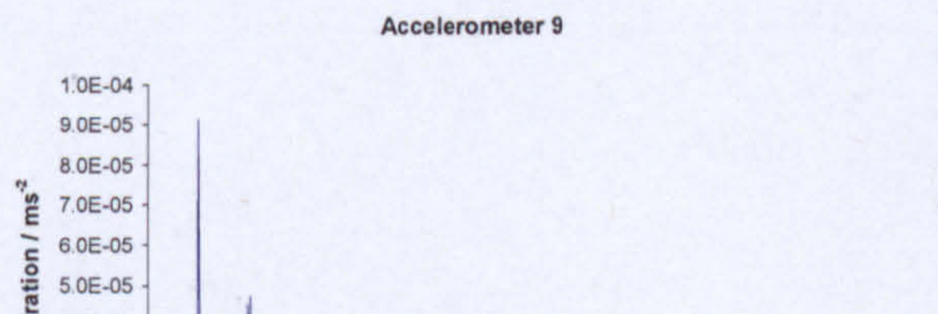

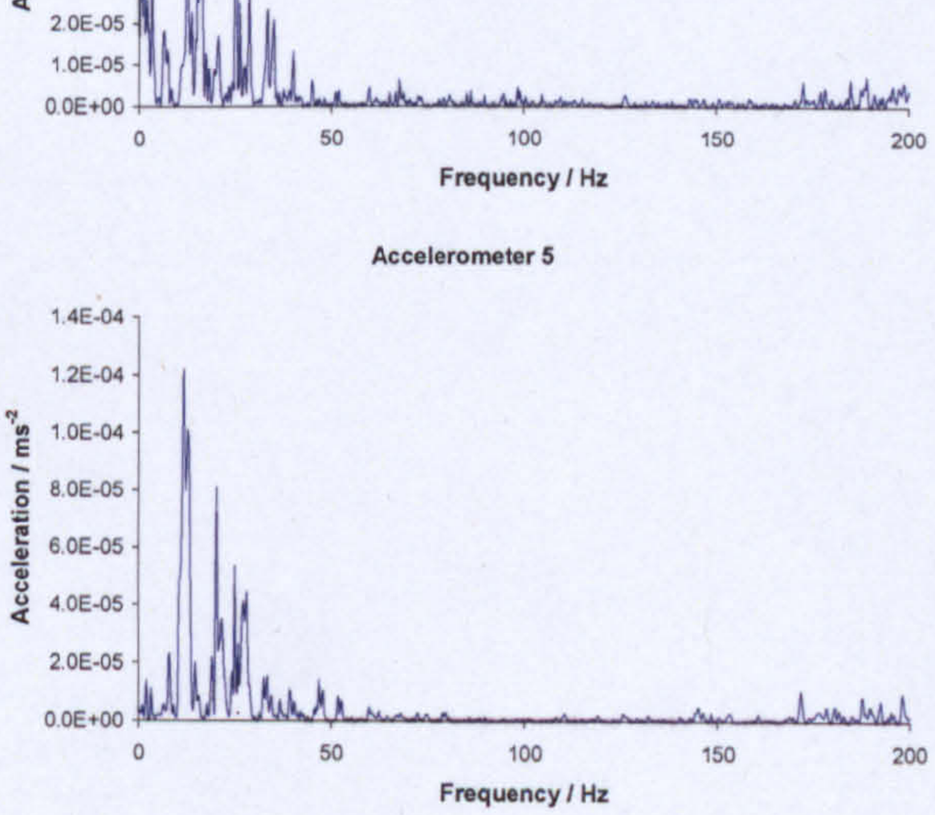

Figure 4.55 Frequency domain plot of Figure 4.54

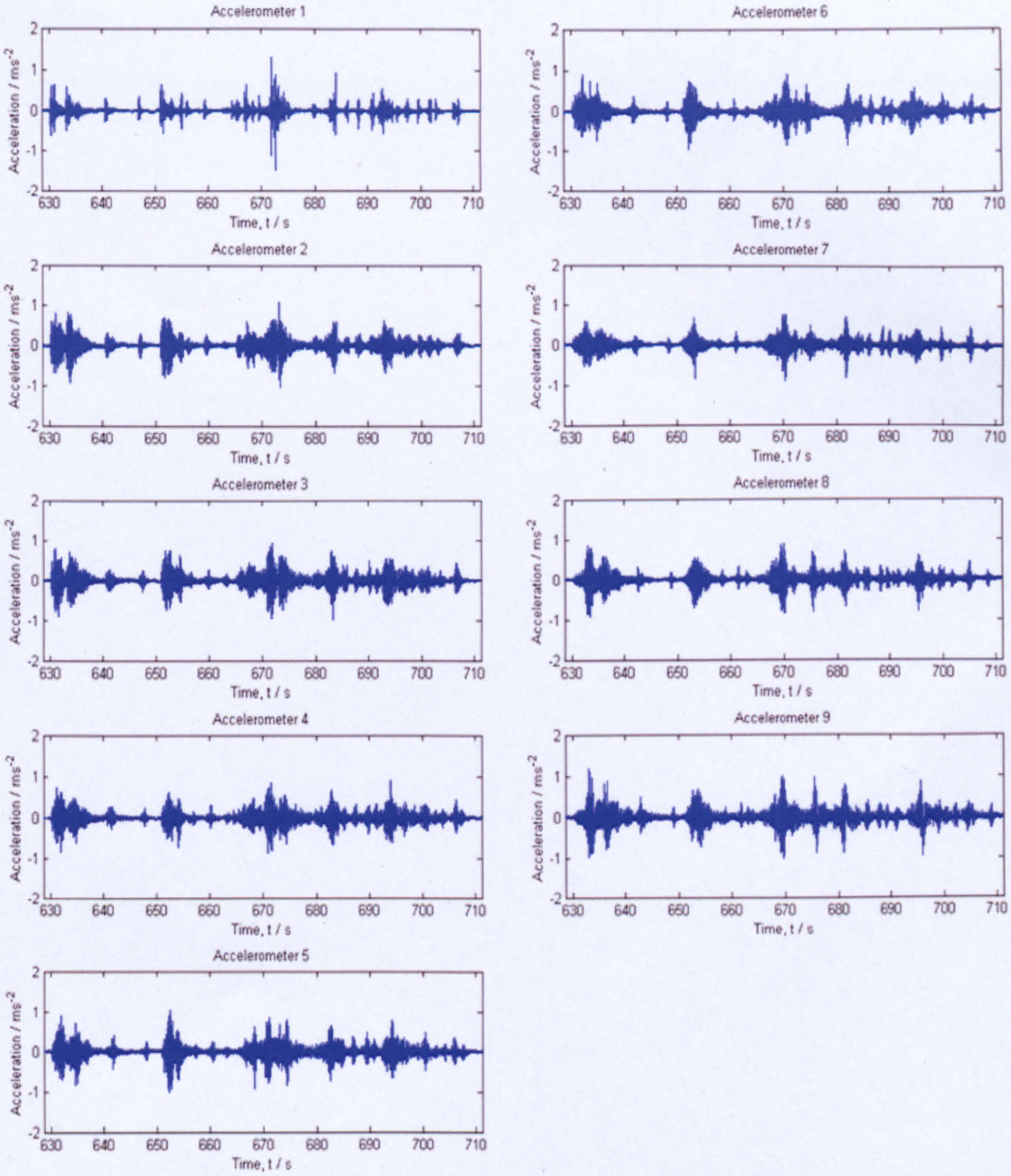

Figure 4.56 Time domain plot for test 5 (630 s - 710 s)

Figure 4.57 Frequency domain plot of Figure 4.56

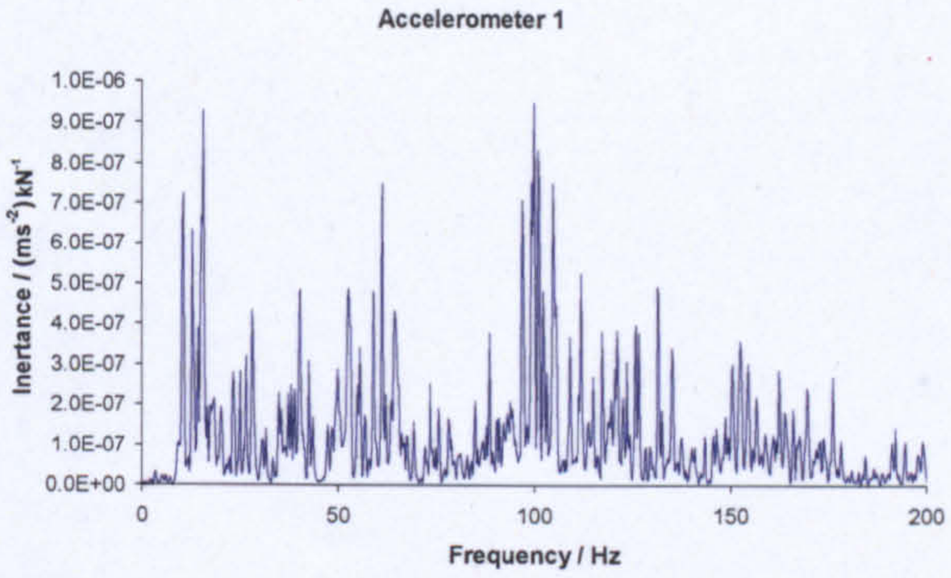

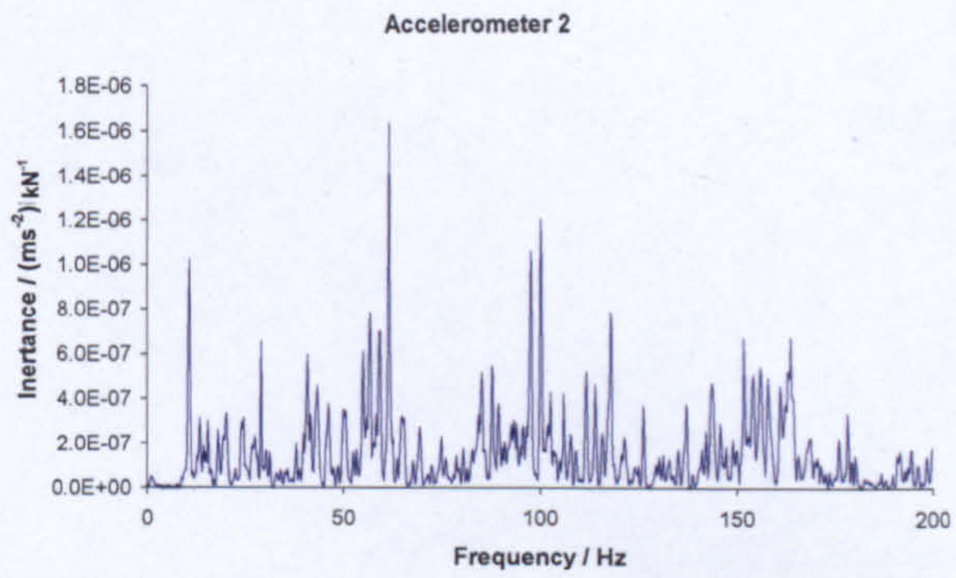

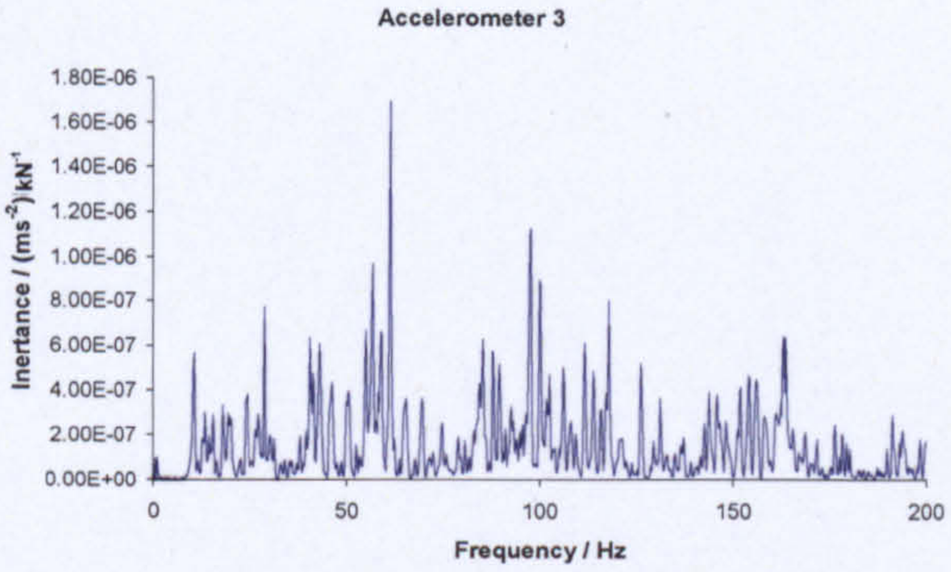

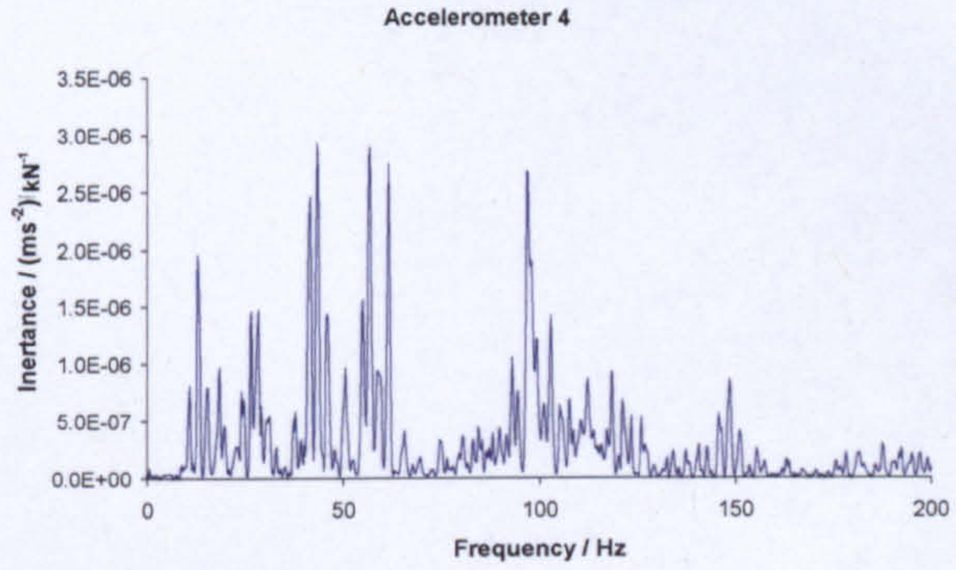

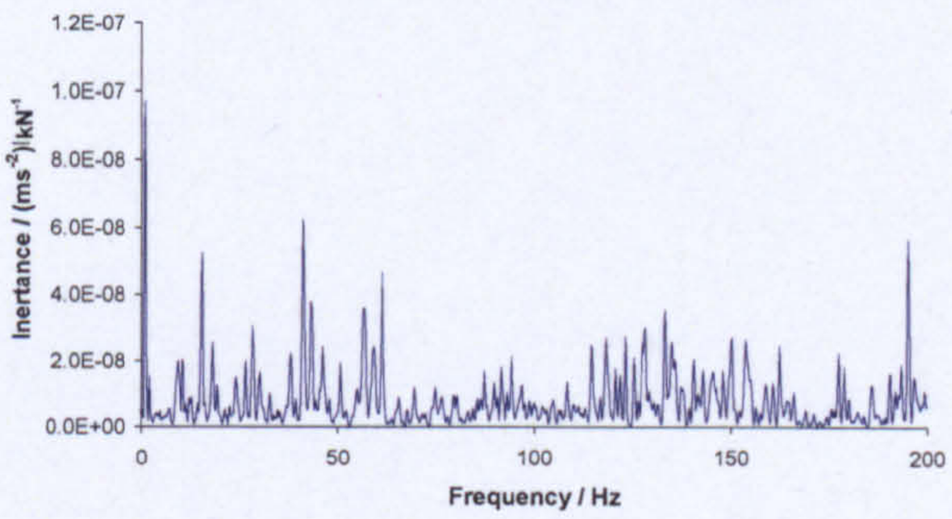

Figure 4.58 Inertance FRF under 92 kN HGV load of Figure 4.41

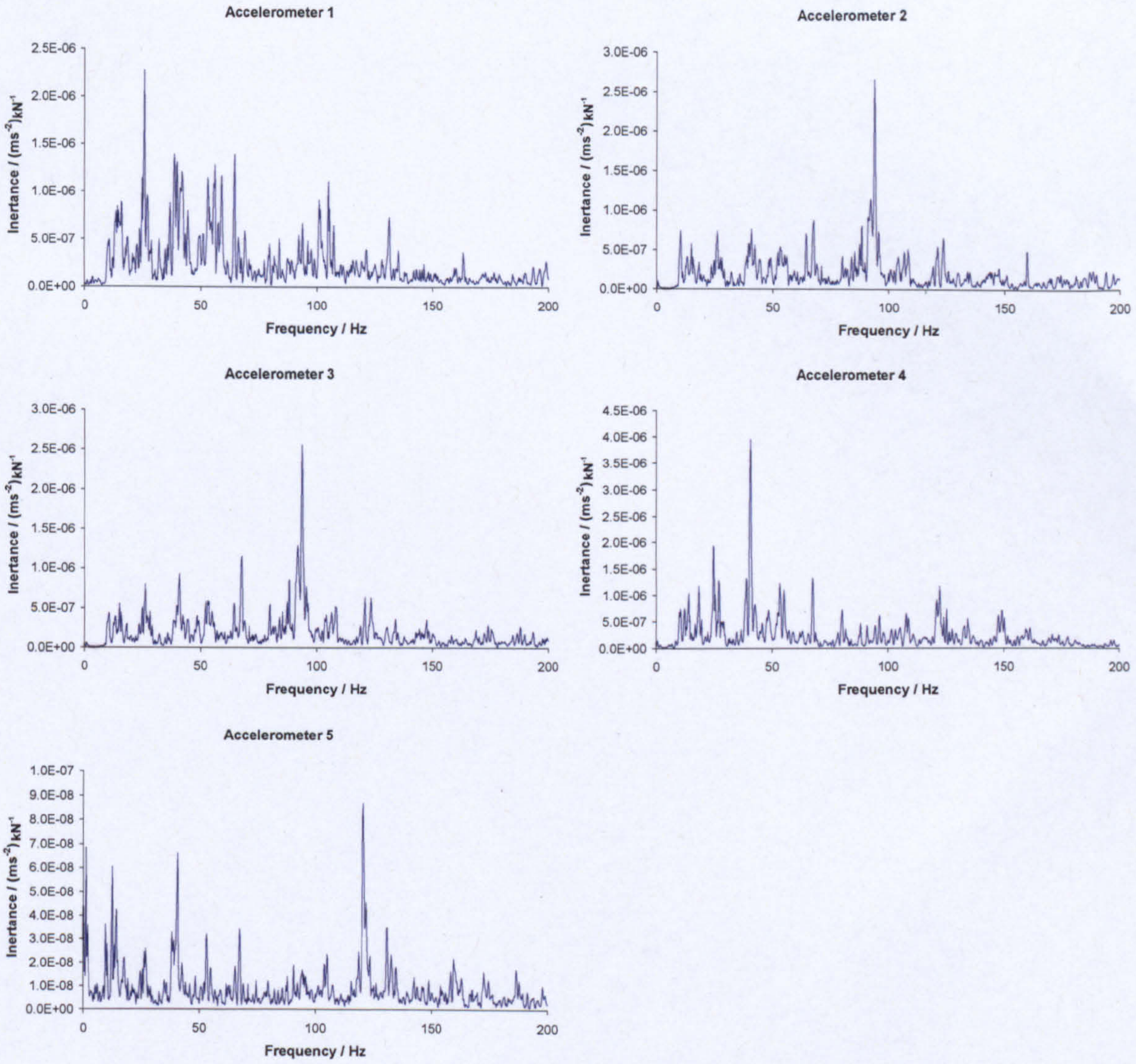

Figure 4.59 Inertance FRF under 92 kN HGV load of Figure 4.43

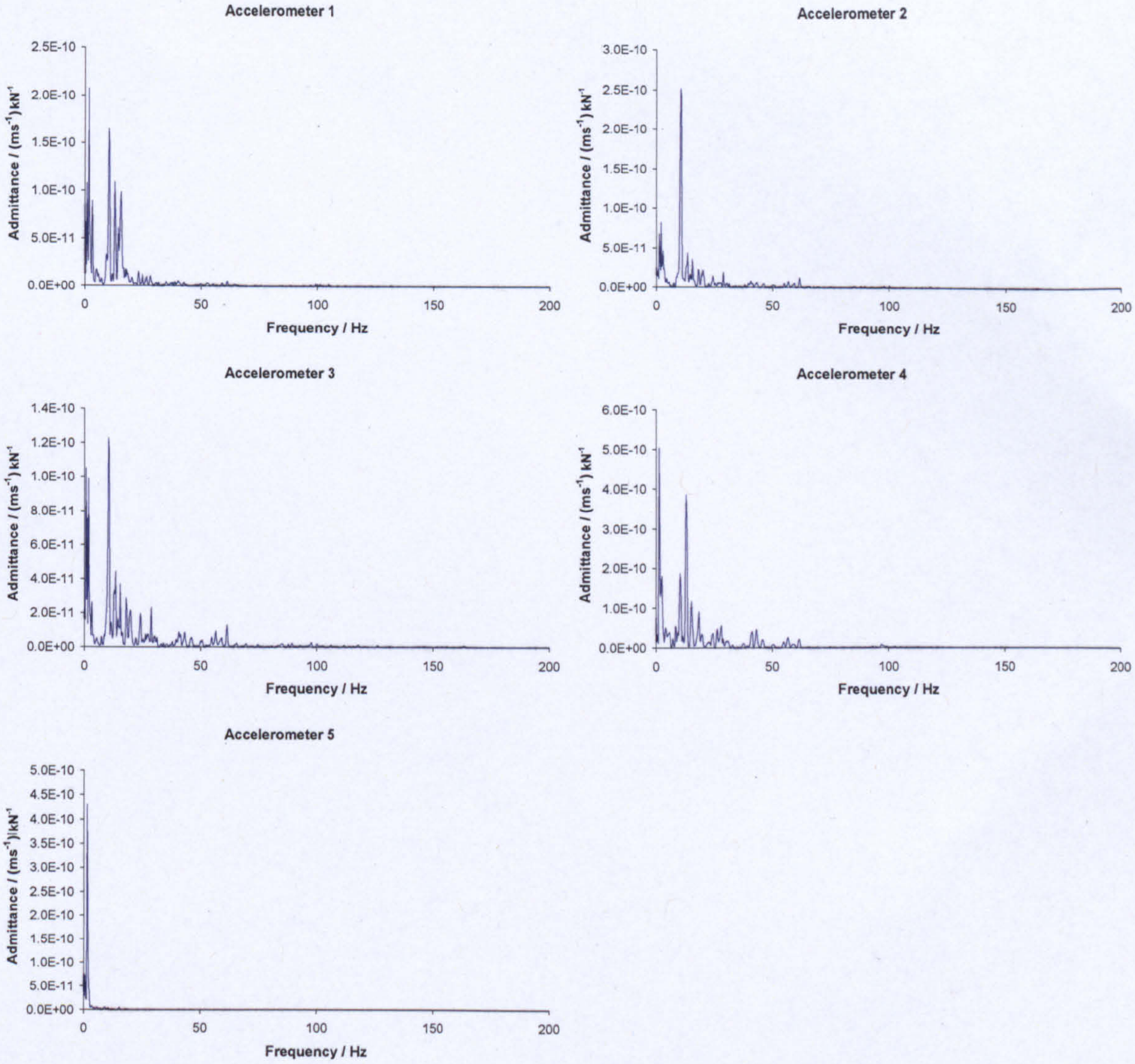

Figure 4.60 Admittance FRF under 92 kN HGV load of Figure 4.41

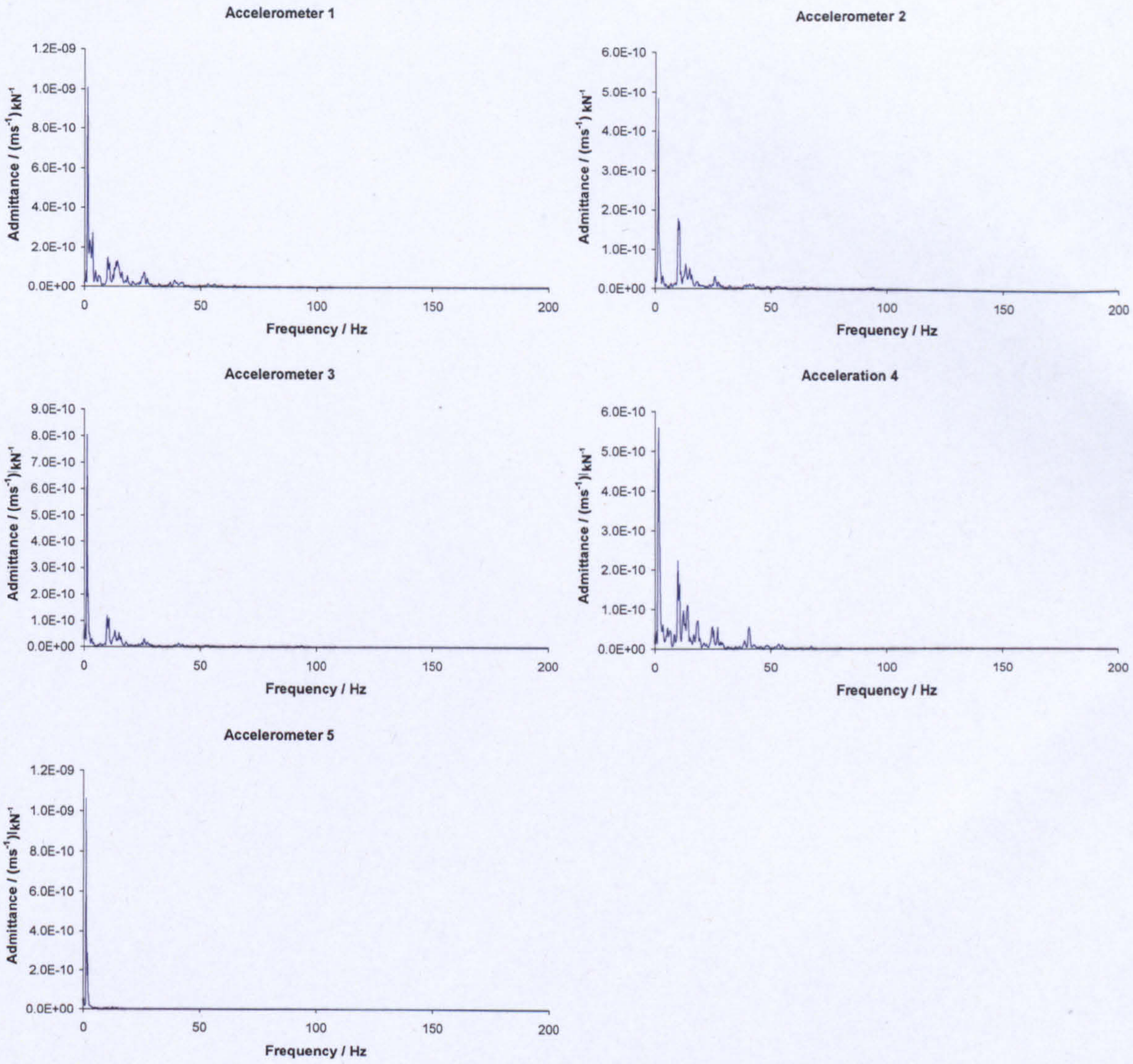

Figure 4.61 Admittance FRF under 92 kN HGV load of Figure 4.43

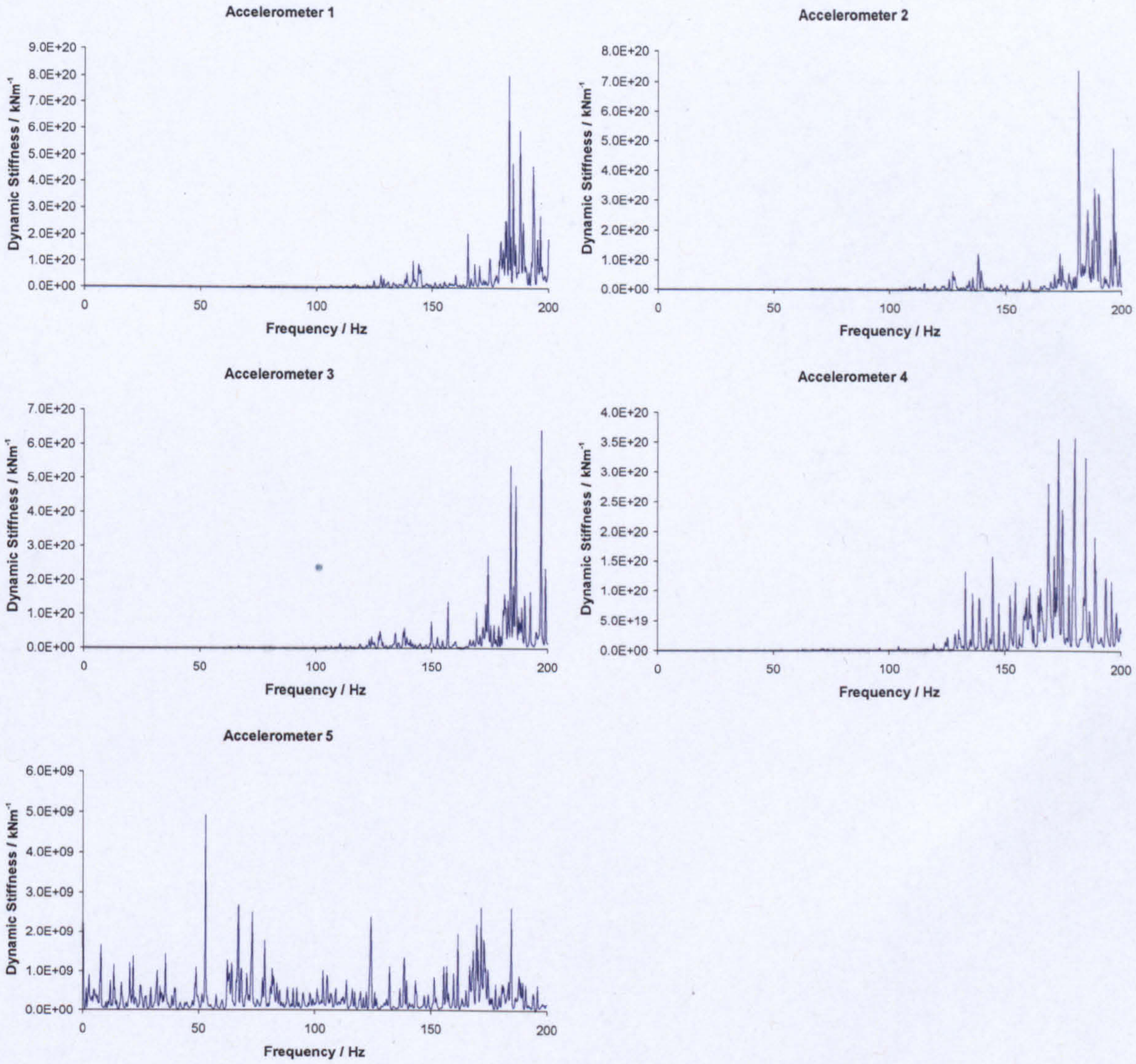

Figure 4.62 Dynamic stiffness FRF under 92 kN HGV load of Figure 4.41

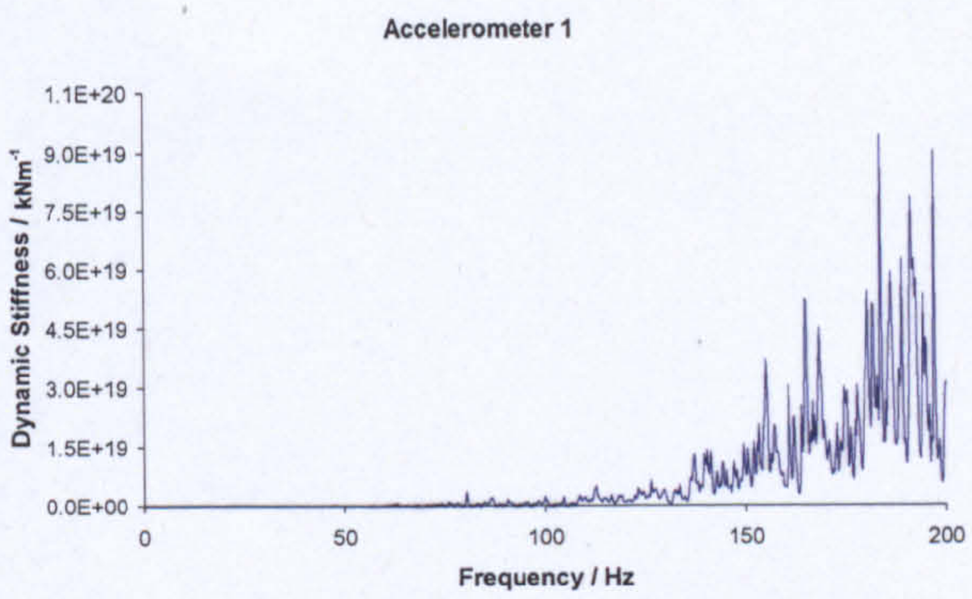

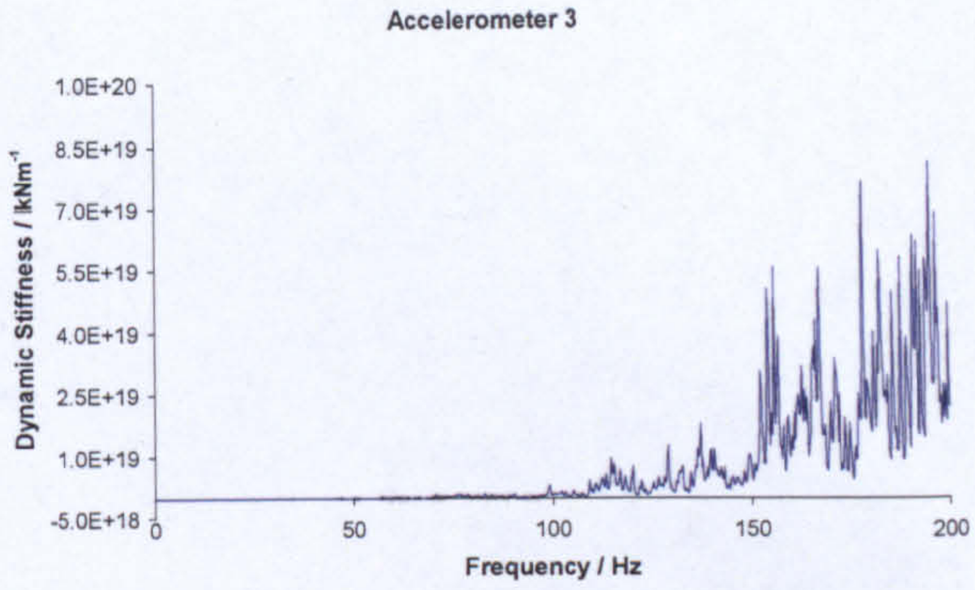

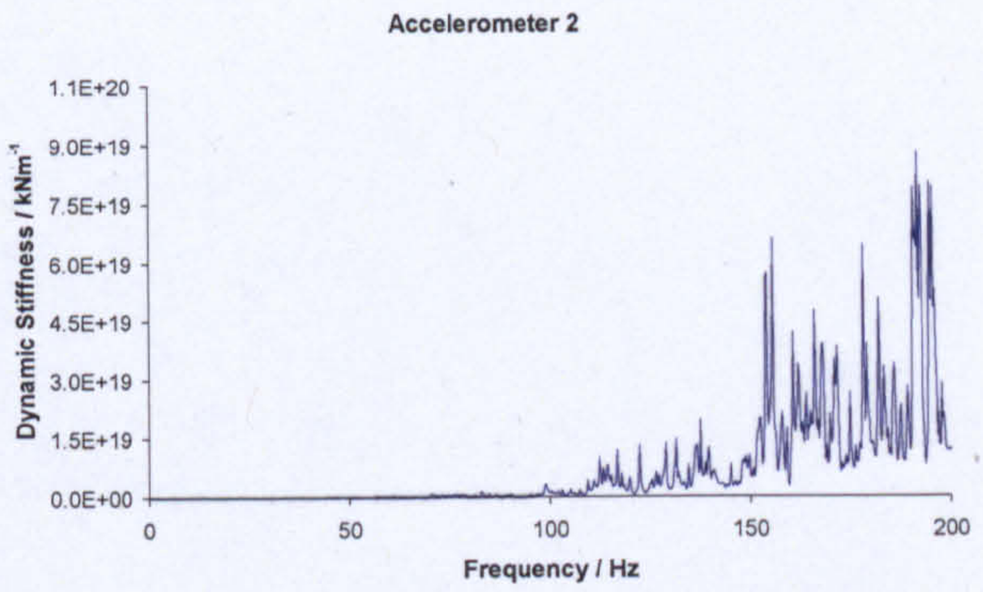

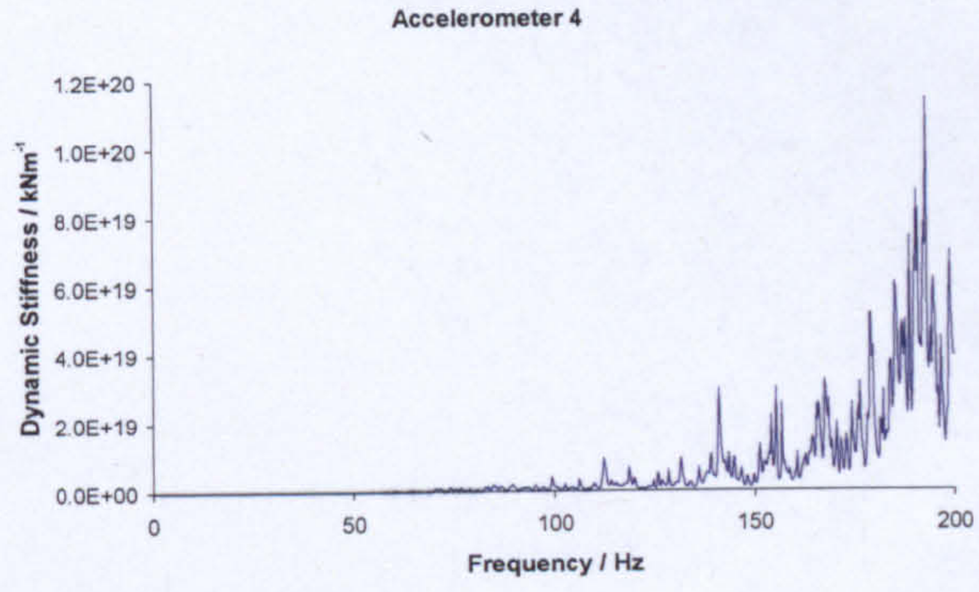

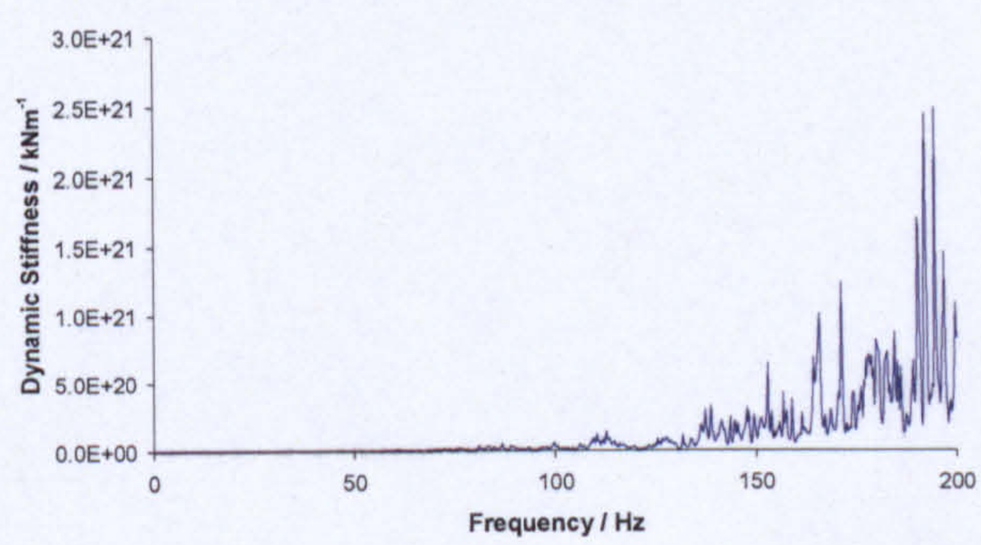

Figure 4.63 Dynamic stiffness FRF under 92 kN HGV load of Figure 4.43

Figure 4.64 Rocker bearing with grease escaping from housing

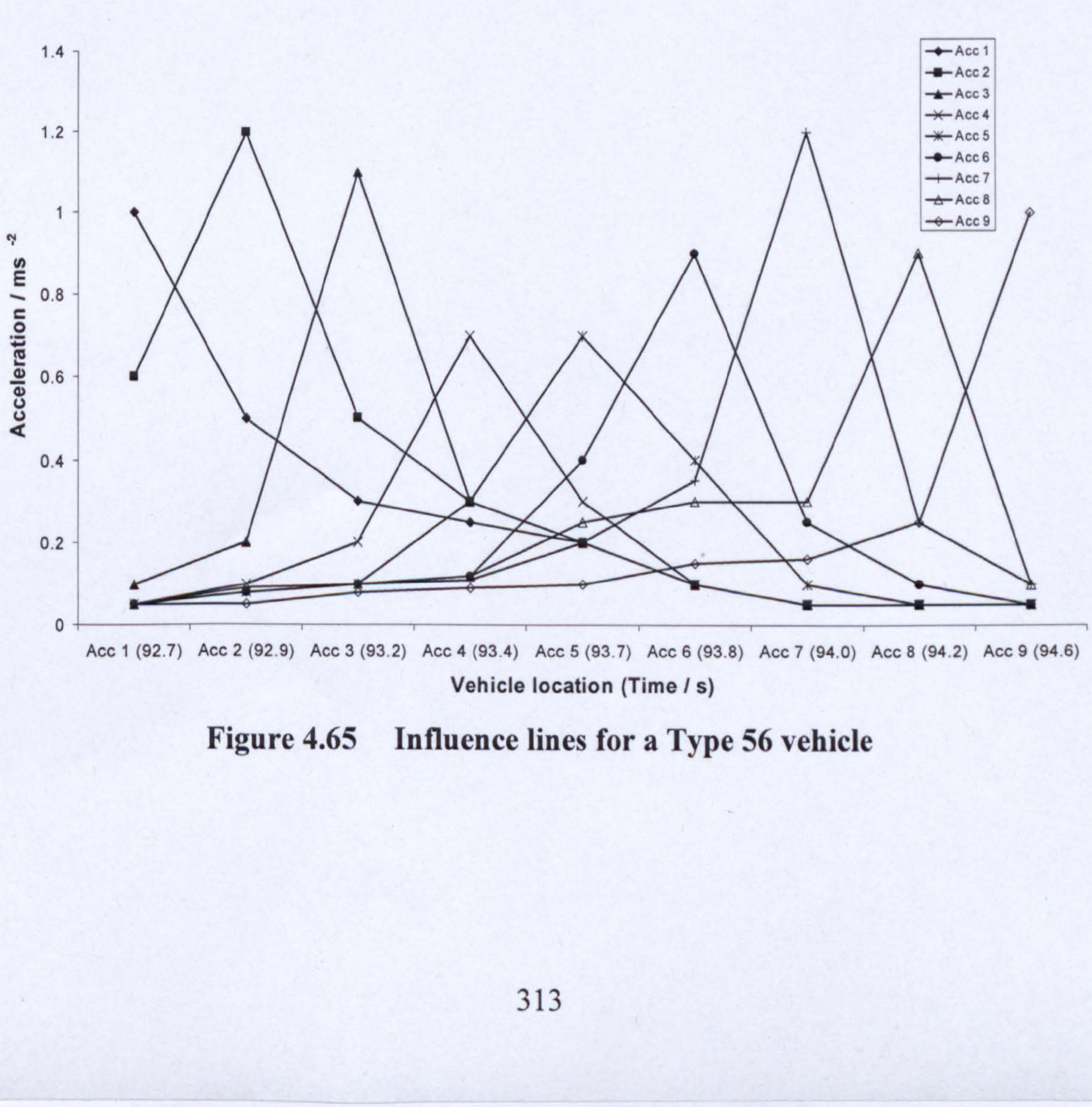

Figure 4.65 Influence lines for a Type 56 vehicle

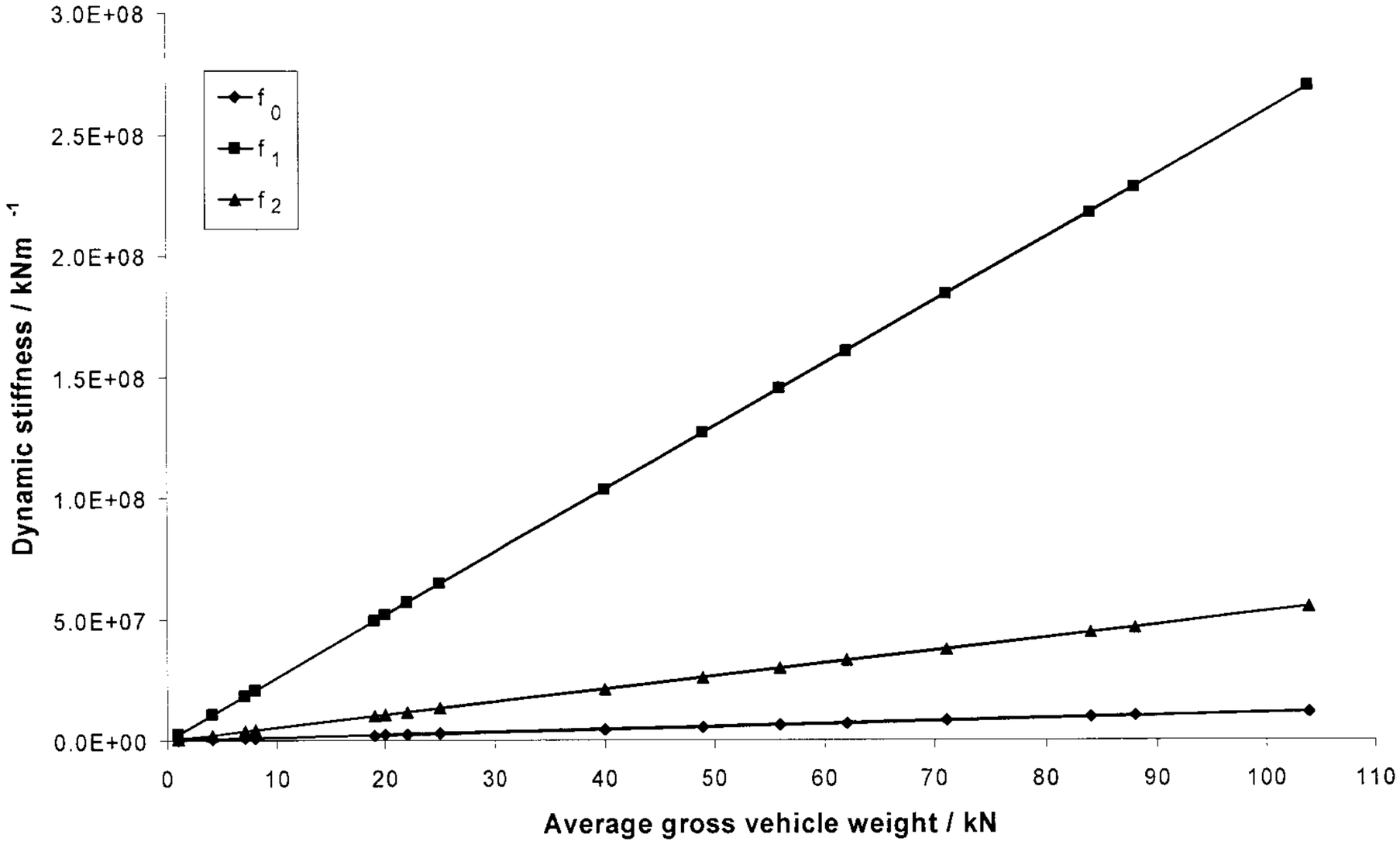

Figure 4.66 Effect of average GVW on dynamic stiffness

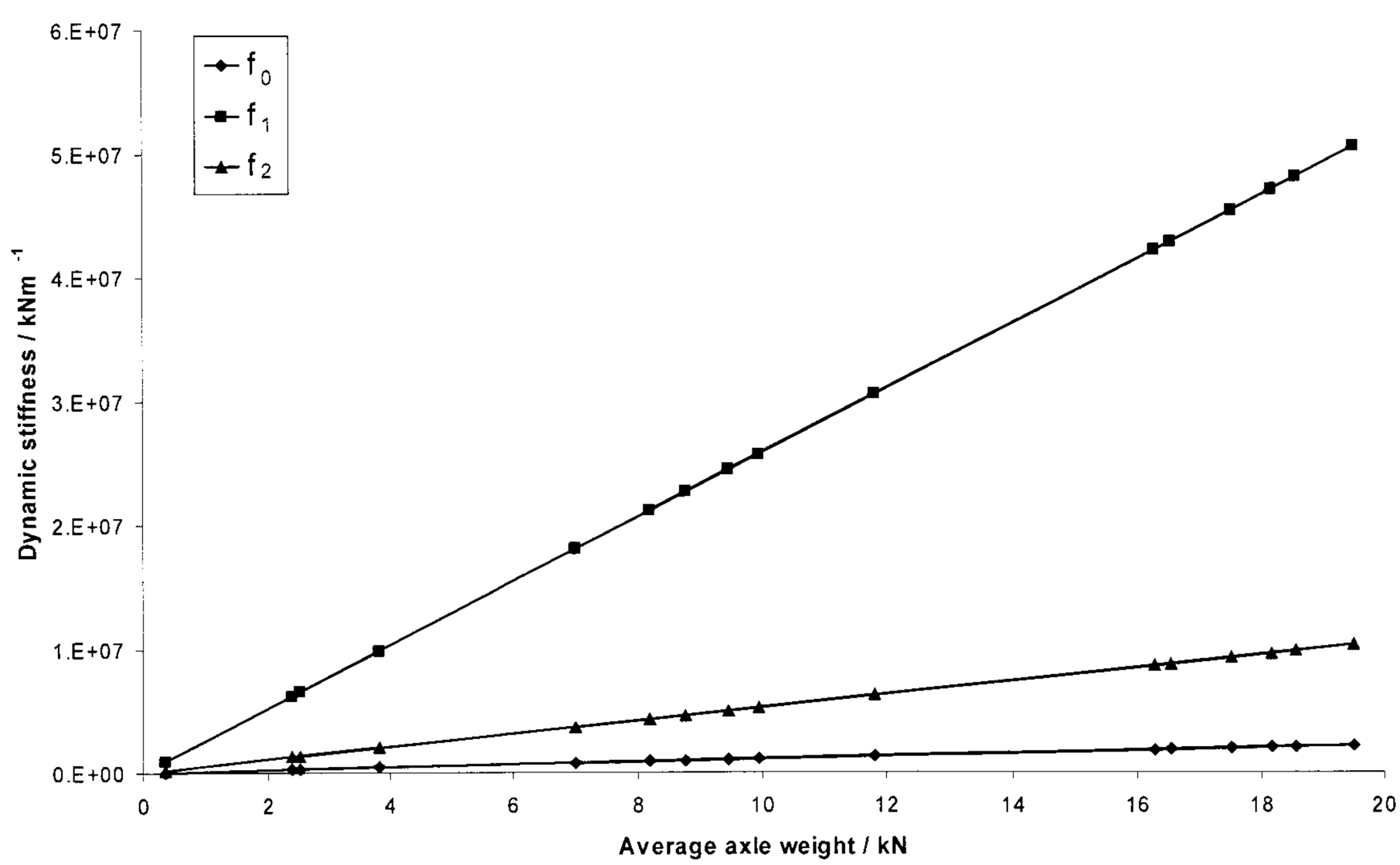

Figure 4.67 Effect of average axle weight on dynamic stiffness

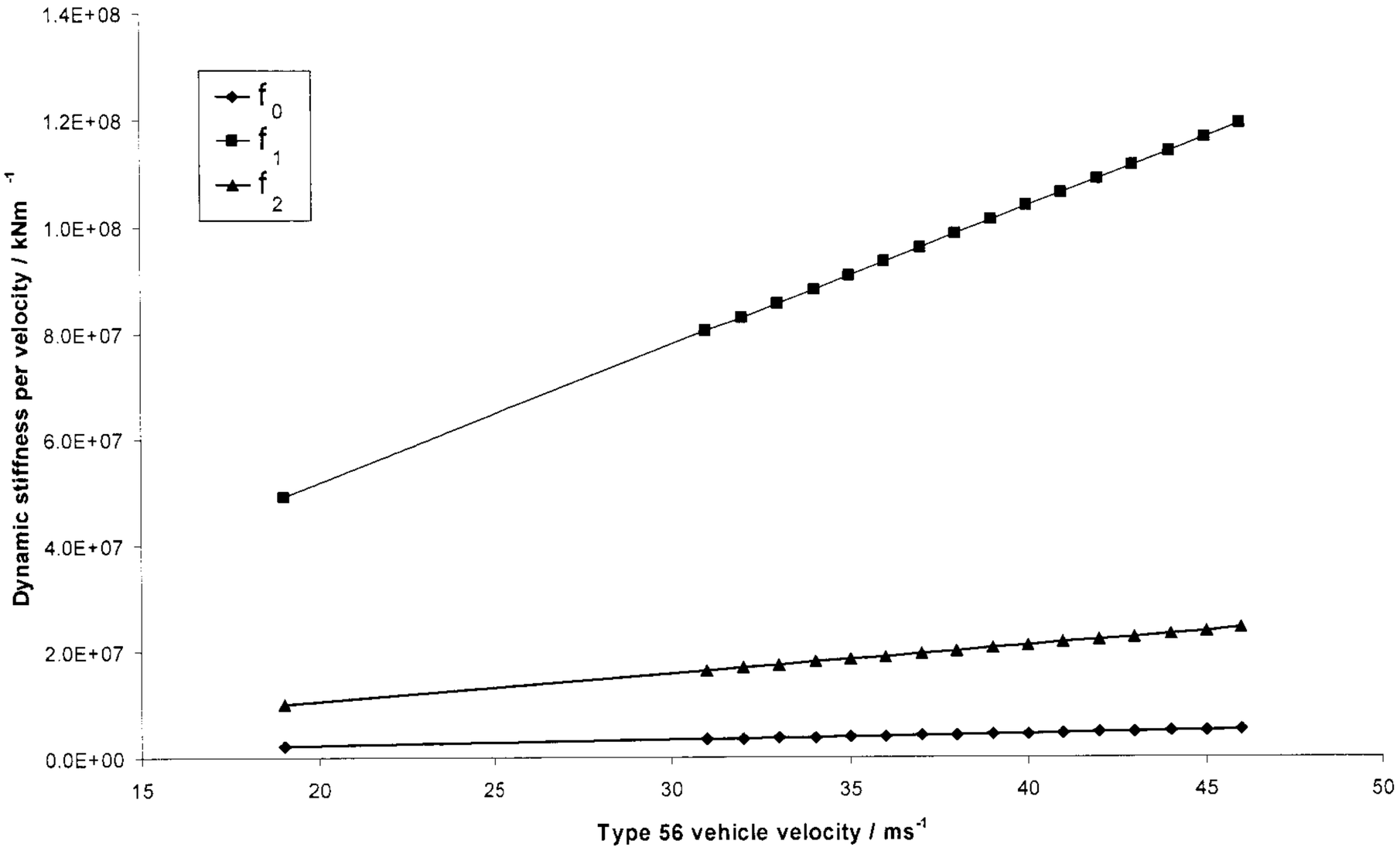

Figure 4.68 Effect of Type 56 velocity on dynamic stiffness

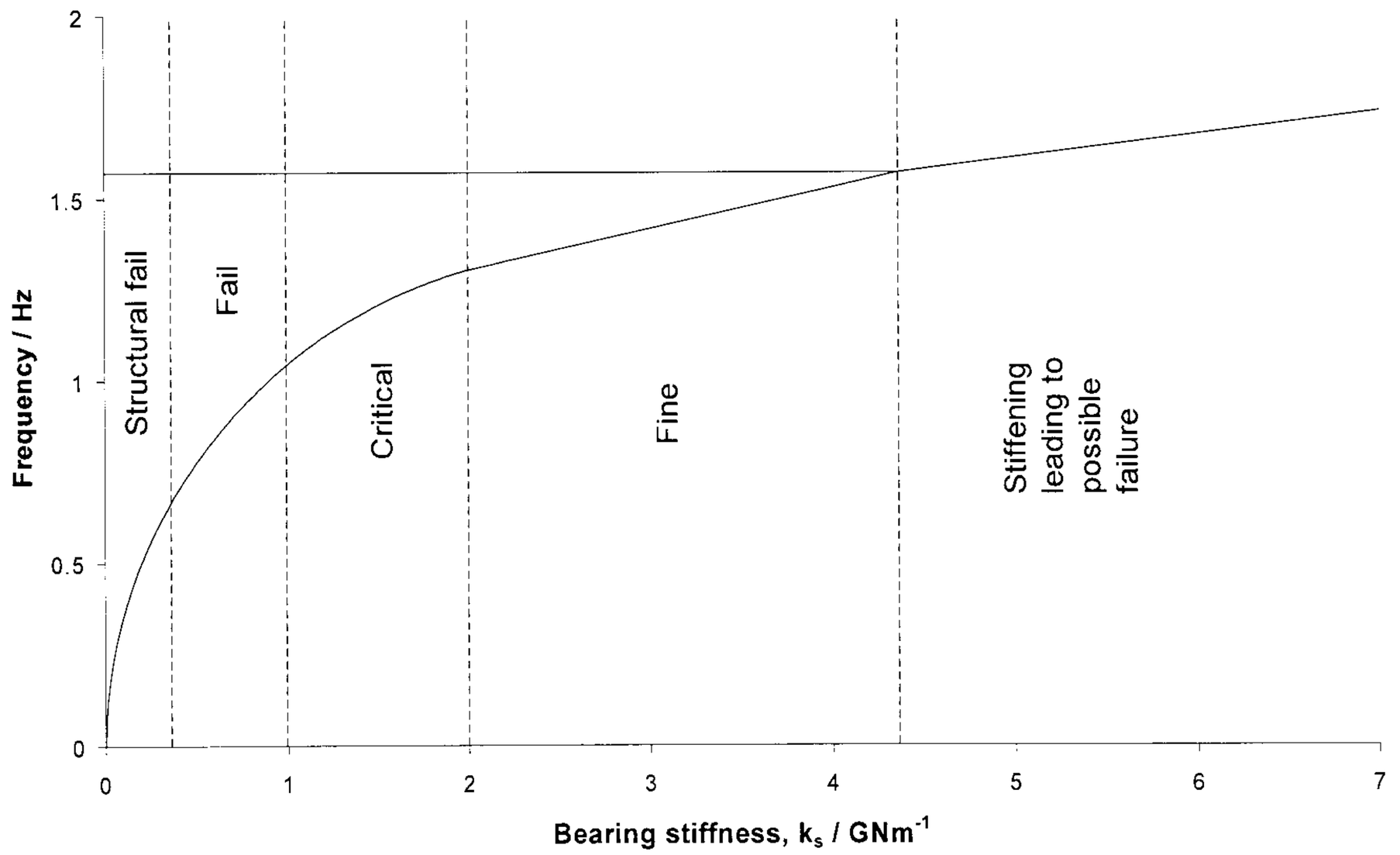

Figure 4.69 Effect of bearing stiffness on primary resonance frequency

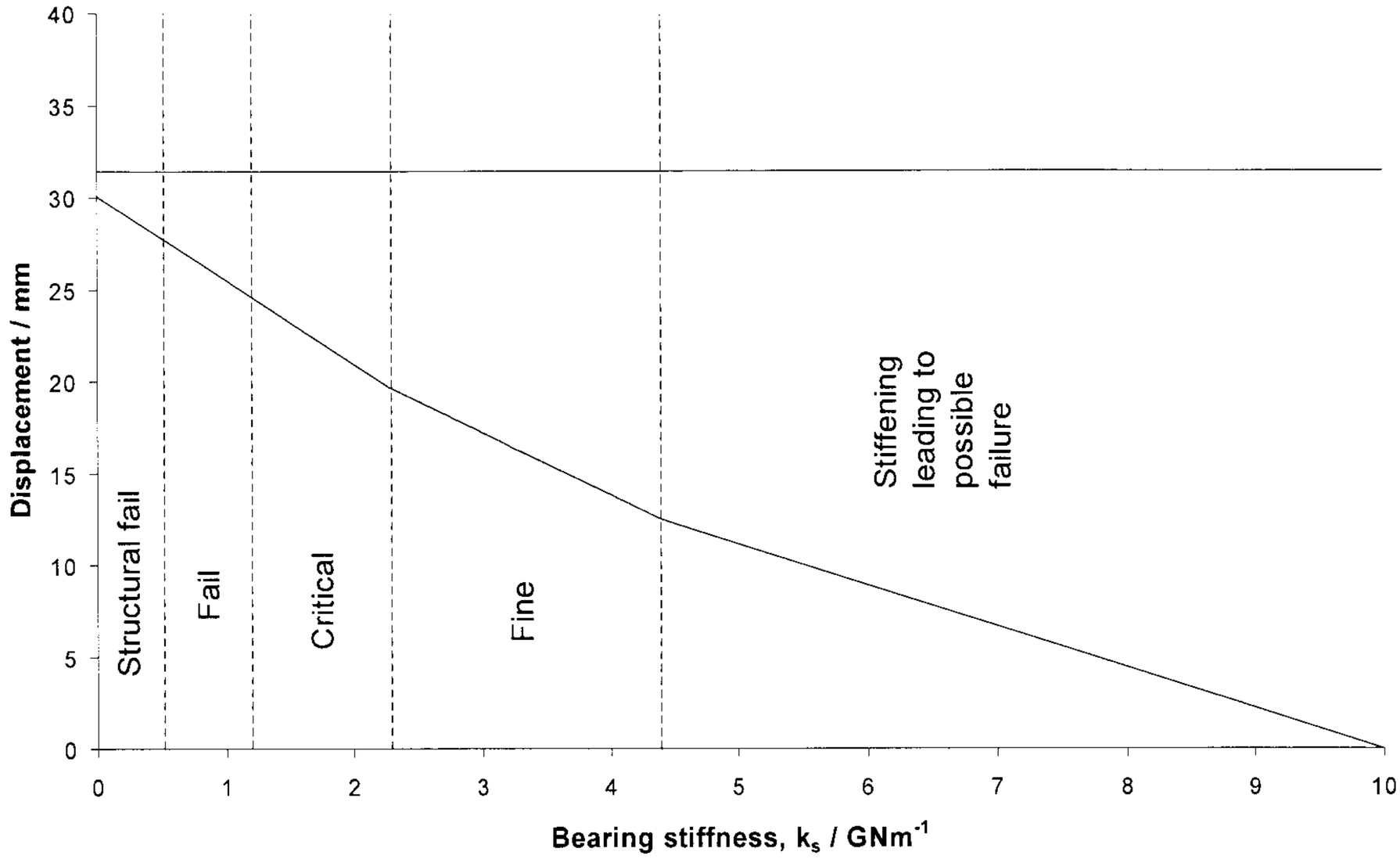

Figure 4.70 Effect of bearing stiffness on displacement

Table 4.1 Vehicle classifications

V_T	Description	Number of axles	N_1 (lane 1)	N_2 (lane 2)	*OL_1	OL_2
0	Motorcycle	2	16	13	0	0
1	Car / Light Van / Taxi / MPV	2	4337	4534	0	0
2	Van / LGV	2	423	471	0	1
21	Car or Van with Trailer	4	65	73	0	0
31	2 axle rigid	2	332	339	14	10
32	3 axle rigid	3	56	67	21	4
33	4 axle rigid	4	10	10	6	0
3N	Vehicle with 3 or more axles - unclassified	3	4	8	1	1
41	Rigid 2 axle drawing LGV with 1 or 2 axle trailer	3 or 4	26	43	3	1
42	Rigid 2 axle drawing LGV with 3 axle trailer	5	4	3	0	0
4N	Vehicle with 4 or more axles - unclassified	4	26	26	15	0
51	Articulated 2 and 1	3	10	5	0	0
52	Articulated 2 and 2	4	85	88	3	0
54	Articulated 3 and 2	5	16	8	5	1
55	Articulated 2 and 3	5	170	222	37	35
56	Articulated 3 and 3	6	269	249	193	177
5N	Vehicle with 5 or more axles - unclassified	5	0	0	0	0
61	2 or 3 axle buses / coaches	2 or 3	16	15	0	0
6N	Vehicle with 6 or more axles - unclassified	6	0	0	0	0
7N	Vehicle with 7 or more axles - unclassified	7	0	0	0	0
8N	Vehicle with 8 or more axles - unclassified	8	0	0	0	0

* OL_1 = Overloaded vehicles in lane 1

Table 4.2 Vehicle speed data for traffic in lane 1 (northbound)

V_T	V_{max}/V_{min} (mph)	$V\ ave$ (mph)	σ_S (mph)	25th %ile (mph)	50th %ile (mph)	75th %ile (mph)	85th %ile (mph)
0	32 / 52	42	5.4	40	42	44	47
1	13 / 78	44	6.0	41	44	48	50
2	14 / 60	43	5.5	40	43	46	48
21	24 / 52	40	5.2	38	41	44	45
31	32 / 61	43	4.5	39	42	45	48
32	32 / 49	39	3.1	36	38	41	42
33	34 / 53	41	4.9	39	40	41	42
3N	38 / 44	40	2.7	39	39	40	42
41	32 / 48	41	3.7	39	41	42	45
42	31 / 40	33	4.5	31	31	33	36
4N	32 / 42	38	2.4	37	39	40	41
51	16 / 46	38	8.3	38	39	40	44
52	21 / 47	39	4.0	38	40	42	42
54	36 / 46	40	2.3	38	40	41	41
55	24 / 49	40	3.5	38	40	42	44
56	19 / 46	39	2.5	38	39	40	41
61	37 / 46	42	2.9	39	42	44	45

N.B. The percentile values for several vehicle classifications are the same as average values obtained due to rounding errors.

Table 4.3 Vehicle speed data for traffic in lane 2 (southbound)

V_T	V_{max}/V_{min} (mph)	$V\,ave$ (mph)	σ_s (mph)	25th %ile (mph)	50th %ile (mph)	75th %ile (mph)	85th %ile (mph)
0	32 / 53	42	5.6	39	41	42	47
1	11 / 74	41	7.1	37	41	45	48
2	16 / 66	41	7.1	37	41	45	48
21	16 / 49	39	6.2	36	39	43	46
31	13 / 99	40	7.3	36	40	44	46
32	25 / 52	39	5.0	32	39	42	44
33	26 / 47	38	4.9	36	39	44	45
3N	34 / 55	42	7.3	37	41	46	50
41	31 / 55	41	4.7	37	41	43	45
42	29 / 32	30	1.7	29	29	31	31
4N	27 / 47	39	3.4	38	39	40	42
51	31 / 44	37	6.0	32	37	43	43
52	26 / 49	40	4.2	38	39	42	44
54	30 / 52	42	8.1	35	43	48	48
55	27 / 52	40	4.8	38	40	43	44
56	15 / 49	39	5.3	36	39	42	44
61	25 / 46	39	5.4	37	40	43	43

N.B. The percentile values for several vehicle classifications are the same as average values obtained due to rounding errors.

Table 4.4 Vehicle axle loading data for traffic in lane 1 (northbound)

V_T	VW_{min} / VW_{max} (kg)	VW_{ave} (kg)	σ_{VW} (kg)	Damage factor (tonnes^4)	Relative damage factor
0	270 / 860	441	134	0.04	0.008
1	500 / 9100	1471	399	4.68	1
2	880 / 15500	2678	1339	51.4	10.98
21	1180 / 15200	3299	2038	118	25.30
31	1330 / 23500	7753	5494	3613	771.7
32	9900 / 38400	25679	6312	434823	92867
33	11000 / 40900	34030	9370	1341059	286416
3N	4350 / 20900	9833	7711	9349	1997
41	1860 / 41100	15249	11726	54071	11548
42	21600 / 36300	27200	6332	547363	116903
4N	27100 / 41500	36604	3605	1795206	383410
51	3530 / 27200	8722	7666	5787	1236
52	10200 / 39200	23451	5522	302444	64594
54	22100 / 47600	33781	7546	1302237	278125
55	15300 / 54700	28296	8853	641062	136915
56	20200 / 60000	43275	10256	3507101	749027
61	4400 / 9600	7088	1299	2524	539.1

Table 4.5 Vehicle axle loading data for traffic in lane 2 (southbound)

V_T	VW_{min} / VW_{max} (kg)	VW_{ave} (kg)	σ_{VW} (kg)	Damage factor (tonnes^4)	Relative damage factor
0	350 / 490	466	37	0.05	0.01
1	280 / 11100	1341	362	3.23	1.00
2	800 / 19800	2397	1331	33	10.21
21	1090 / 9400	2835	1147	65	19.98
31	2030 / 21500	7335	4855	2895	895
32	9200 / 38400	17540	6315	94650	29269
33	11400 / 22400	14900	3399	49288	15242
3N	1280 / 19200	5279	5829	777	240
41	2030 / 33100	15191	7915	53253	16468
42	15400 / 28100	19700	7275	150614	46575
4N	9500 / 28400	13050	4212	29003	8969
51	3190 / 20900	10340	7945	11431	3535
52	4100 / 34200	20173	5540	165608	51211
54	17400 / 44700	27263	8812	552452	170836
55	1170 / 52300	24482	9037	359242	111089
56	7700 / 58500	43586	11054	3609010	1116022
61	4580 / 12000	6739	2157	2062	638

Table 4.6 Maximum and minimum axle weights for vehicles in lane 1 (northbound). All values shown in kg.

V_T		Axle 1	Axle 2	Axle 3	Axle 4	Axle 5	Axle 6
0	AW_{min}	30*	130				
	AW_{max}	200	790				
1	AW_{min}	200	90*				
	AW_{max}	5000	4100				
2	AW_{min}	440	440				
	AW_{max}	5900	9800				
21	AW_{min}	610	470	100*	150*		
	AW_{max}	4000	5600	5600	2300		
31	AW_{min}	640	690				
	AW_{max}	10500	1430				
32	AW_{min}	4300	2400	1500			
	AW_{max}	11000	**13400**	**14200**			
33	AW_{min}	3600	4200	2100	1100		
	AW_{max}	8900	9400	**12100**	**12300**		
3N	AW_{min}	1700	1380	500			
	AW_{max}	7100	**13300**	1460			
41	AW_{min}	1010	730	90*	400		
	AW_{max}	10100	**14700**	8200	8600		
42	AW_{min}	2700	4700	4000	4200		
	AW_{max}	9100	8800	5900	6200		
4N	AW_{min}	5100	4800	8300	8000		
	AW_{max}	9400	9300	**12400**	**12100**		
51	AW_{min}	1060	1240	400			
	AW_{max}	7400	9200	10600			
52	AW_{min}	2700	3400	1200	1300		
	AW_{max}	9200	10800	11400	10800		
54	AW_{min}	5800	3100	3800	2800	2900	
	AW_{max}	10700	8700	11000	11400	11100	
55	AW_{min}	3600	3700	1600	1700	1400	
	AW_{max}	10100	**15900**	10200	10800	10700	
56	AW_{min}	4400	700	2700	1000	2400	2300
	AW_{max}	9600	**12100**	**13900**	11000	11500	**13500**
61	AW_{min}	1990	2410				
	AW_{max}	4300	5800				

*N.B. The values marked are considered to be a result of either misclassification or miscounting events.
Values in bold font type are illegally overloaded given the absence of an abnormal load escort and the statutory notifications and permissions.

Table 4.7 Maximum and minimum axle weights for vehicles in lane 2 (southbound). All values shown in kg.

V_T		Axle 1	Axle 2	Axle 3	Axle 4	Axle 5	Axle 6
0	AW_{min}	150	190				
	AW_{max}	160	330				
1	AW_{min}	120	130				
	AW_{max}	2200	8900				
2	AW_{min}	460	290				
	AW_{max}	7500	**12300**				
21	AW_{min}	400	430	100	220		
	AW_{max}	1400	3900	1900	2200		
31	AW_{min}	1040	650				
	AW_{max}	8800	**13200**				
32	AW_{min}	4300	1400	2000			
	AW_{max}	10400	**14500**	**14500**			
33	AW_{min}	3700	4100	1300	1500		
	AW_{max}	5800	6300	5000	5300		
3N	AW_{min}	140	550	400			
	AW_{max}	6200	**12600**	1530			
41	AW_{min}	930	810	100	100		
	AW_{max}	8700	11200	6500	6700		
42	AW_{min}	2700	5600	2300	1400	1700	
	AW_{max}	10300	7300	4200	3100	3400	
4N	AW_{min}	2400	2000	900	1400		
	AW_{max}	8800	7300	7900	6300		
51	AW_{min}	1100	1200	520			
	AW_{max}	7100	6200	8000			
52	AW_{min}	1800	1640	460	200		
	AW_{max}	8100	10500	8500	8800		
54	AW_{min}	5200	800	1600	3200	3300	
	AW_{max}	7400	6900	9900	10600	11000	
55	AW_{min}	4800	2800	700	1000	1400	
	AW_{max}	10600	**16900**	9500	9600	11100	
56	AW_{min}	2700	400	2100	700	700	600
	AW_{max}	9900	11300	**16600**	11100	**11700**	**11900**
61	AW_{min}	1800	1800				
	AW_{max}	4000	8100				

*N.B. The values marked are considered to be a result of either misclassification or miscounting events.
Values in bold font type are illegally overloaded given the absence of an abnormal load escort and the statutory notifications and permissions.

Table 4.8 Average axle weights for vehicles in lane 1 (northbound). All values shown in kg.

V_T	Lane 1	Axle 1	Axle 2	Axle 3	Axle 4	Axle 5	Axle 6
0	AW_{ave}	130	311				
1	AW_{ave}	827	644				
2	AW_{ave}	1366	1312				
21	AW_{ave}	1012	1183	918	708		
31	AW_{ave}	3555	4199				
32	AW_{ave}	8127	9011	8541			
33	AW_{ave}	6990	7430	9740	9870		
3N	AW_{ave}	3788	5013	1033			
41	AW_{ave}	4545	5222	2687	3160		
42	AW_{ave}	4545	5222	2687	2439		
4N	AW_{ave}	7619	7573	10588	10823		
51	AW_{ave}	3046	3116	2560			
52	AW_{ave}	6784	6936	4835	4895		
54	AW_{ave}	7625	5519	7525	6438	6675	
55	AW_{ave}	7426	8241	4102	4236	4291	
56	AW_{ave}	6896	5655	9015	7018	7225	7467
61	AW_{ave}	3249	3838				

Table 4.9 Average axle weights for vehicles in lane 2 (southbound). All values shown in kg.

V_T		Axle 1	Axle 2	Axle 3	Axle 4	Axle 5	Axle 6
0	AW_{ave}	159	307				
1	AW_{ave}	776	565				
2	AW_{ave}	1285	1112				
21	AW_{ave}	880	944	846	469		
31	AW_{ave}	3491	3843				
32	AW_{ave}	6885	5661	4994			
33	AW_{ave}	4310	4570	3040	2980		
3N	AW_{ave}	2005	2509	765			
41	AW_{ave}	5250	4867	2503	2631		
42	AW_{ave}	5367	6667	3200	2067	2400	
4N	AW_{ave}	4365	4088	2312	2285		
51	AW_{ave}	3476	3128	3736			
52	AW_{ave}	6545	5830	3836	3961		
54	AW_{ave}	6250	3650	6175	5413	5775	
55	AW_{ave}	7327	6775	3298	3423	3660	
56	AW_{ave}	7104	5359	8718	7238	7425	7743
61	AW_{ave}	3015	3724				

Table 4.10 **Standard deviations of axle weights for vehicles in lane 1 (northbound). All values shown in kg.**

V_T	Axle 1	Axle 2	Axle 3	Axle 4	Axle 5	Axle 6
0	34	153				
1	196	224				
2	572	827				
21	460	949	750	492		
31	2384	3240				
32	1432	2564	3233			
33	1744	1731	2999	3389		
3N	2591	5633	424			
41	3252	3892	2362	2439		
42	3077	1741	874	903	835	
4N	1031	931	1106	1011		
51	2574	2500	3109			
52	1093	1560	1786	1826		
54	1395	1980	2451	2484	2558	
55	1048	2777	1915	1974	2062	
56	935	2024	2310	2382	2369	2518
61	583	946				

Table 4.11 Standard deviations of axle weights for vehicles in lane 2 (southbound). All values shown in kg.

V_T	Axle 1	Axle 2	Axle 3	Axle 4	Axle 5	Axle 6
0	3	36				
1	164	230				
2	641	756				
21	179	486	448	469		
31	2118	2915				
32	1533	2913	2569			
33	748	685	1280	1088		
3N	1817	4106	550			
41	2599	2761	1581	1632		
42	4277	929	954	907	889	
4N	1314	945	1669	908		
51	3130	2086	3011			
52	1010	1926	1702	1664		
54	735	2099	2998	2425	2543	
55	836	3072	1905	1936	2082	
56	885	1850	2235	2605	2655	2754
61	682	1799				

Table 4.12 Resonance frequencies of bridge structure

Method	f_0 (Hz)	f_1 (Hz)	f_2 (Hz)
NDT	1 - 2	3 - 4	10 - 11
FEA	2.0	3.0	4.3
Rayleigh-Ritz	1.603	3.2	4.8

Table 4.13 Parametric study of FEA model for bridge structure

Altered parameter	f_0 (Hz)	f_1 (Hz)	f_2 (Hz)
Original baseline	2.0	3.0	4.4
0.5 times Young's modulus	1.5	2.1	3.1
0.5 times Poisson's ratio	2.1	3.0	4.3
0.5 times density	2.9	4.2	6.2
All	2.0	3.0	4.3

CHAPTER 5

Conclusions and recommendations for future research

5.1 Executive summary

Although health monitoring of bridge structures is relatively advanced, the scope for further research is wide. The study presented in this thesis contained research on plate structures; ranging from a simple Euler-Bernoulli method to determine natural frequencies; modal analysis of a plate structure in the laboratory; FEA of the plate structure; modal analysis on a full-scale structure subjected to vehicle loading; and FEA of a simplified model representing the full-scale structure. A combination of these methods has allowed the conclusions highlighted herein to be drawn with respect to the effects of support degradation, and the consequent effect on structural performance.

5.2 Conclusions

5.2.1 Chapter 2

Theoretical and experimental works are still being carried out on plate structures, bearings and full-scale highway bridge structures. Although plates with more conventional boundary conditions have been investigated thoroughly, the current investigations are concerned with the effects of moving loads or variable boundary conditions on the dynamic performance of plate structures.

In recent years, with the increase in computational power available, researchers have employed OMA techniques to extract natural frequencies and material properties from full-scale structures excited by ambient vibration, as opposed to the more conventional classic modal analysis techniques used in this thesis.

Few researchers, in terms of damage location, have investigated the effect of support condition on the dynamic response of a structure, and this is one area that provides further scope for research. At present, the available literature on bearings is mostly concerned with the material properties or performance of the bearings under either compressive or shearing loading. Research in America currently involves investigations into the performance of *in situ* bearings are restricted to the behaviour in cold temperatures, and the effects of bearing walking.

5.2.2 Chapter 3

The modified Euler-Bernoulli method for plate structures provided a simple method to determine the fundamental resonant frequency when support conditions were variable at each end of the plate. An alteration of support stiffness in the model can have a marked effect on the resonant frequency of the plate (approx. 23 % frequency change between spring 1 (1.22 Nmm^{-1}) and 5 (15.62 Nmm^{-1})). However, the proposed method did underestimate the exact resonant frequency value by almost 13%. This difference is due to idealised conditions assumed for the analytical models, compared to the actual conditions for modal testing. It is considered that improvement of the method is possible if consideration is given to rotational and translational restraint in the constituent equations. The method only produced the first resonant frequency, but could be extended to higher order modes with application of higher order polynomial assumed mode shape functions in the general equation.

Simple modal analysis testing protocols, such as the single input-multiple output test used herein, were adequate for routine inspection purposes. Modal analysis allowed the effect of stiffness to be visualised through waterfall plots of FRFs.

Forced vibration testing indicated that bending modes were of more use for detection of the effect of alteration in bearing support stiffness. Torsional modes provide no real discernable pattern. Identification of the mode shapes was essential if accelerometer locations are not to coincide with nodal points, resulting in possible missed modeshapes. Finite element analyses may offer some useful guidance, albeit at some cost (both direct and time-based), as to the mode shapes likely in a deck slab.

In terms of damage detection or quantification, considering individual resonant frequency values was not considered to be a viable option, rather the mode shapes relating to each frequency which can be matched were of significance.

The structural support conditions, with reference to their stiffness in particular, were effective in influencing the FRF measured on a model bridge deck. Continual monitoring over time would be required if this method were to have any basis as a condition monitoring, or degradation assessment, tool. Indeed, the FRF may be used as an accurate general indication of the overall state of a bridge deck's stiffness. Support changes affected wave propagation across the model deck slab.

Displacement and acceleration values in the vertical direction provided accurate information as to the response of the plate when subjected to forced vibration with variable support stiffness, although velocity response was not a viable diagnostic tool in this case. Of particular interest was that the relative displacements observed at the mid-span due to loading at plate edges were higher than those subjected to loading at the centre nodes. The plate response and propagation of waves was therefore dependent on the location of excitation. Excitation data relating to a non-resonant frequency did not

provide any insight into the effects of support stiffness, although data presented from modal analysis testing showed the effect of approaching or receding from a resonant frequency in the higher spring stiffnesses. The baseline frequency used in any full-scale condition assessment should be chosen to avoid proximity to a natural frequency of the bridge deck.

Strain values provided no indication of the effect of support stiffness on wave propagation or dynamic response.

5.2.3 Chapter 4

The NDT method presented was worthy of inclusion in a major structure's maintenance and inspection plan. No disruption to traffic was caused, and no damage to the structure ensued.

When matched with weigh-in-motion sensors and accurate vehicle counting and classification software, the NDT proved useful in matching vehicle events with the dynamic structural response. Vehicle speeds had a small distribution, most falling in the 35 to 50 mph range over the whole spectrum of vehicle types, meaning gross vehicle weight had the greatest effect on dynamic stiffness response.

Larger HGVs made up a small percentage of overall vehicles recorded, but contribute a much higher proportion of damage caused to the bridge. The majority of Type 56 HGVs were overloaded, with axle weight distribution poor in many HGVs. The momentum, kinetic energy and damage factor was significantly larger in relation to larger vehicles.

From results obtained, displacement and frequency were both valid measures of bearing performance and therefore state of degradation.

The bridge bearings were performing as expected, and doing so adequately, and the faulty expansion joint had a more severe effect upon the measured vibrations. It is recommended that accelerometers be located at the abutments, and more specifically on the bearings, to accurately monitor the bearing performance. Repeat testing over the faulty rocker bearings are required after remedial action has been completed. This would then be assumed as the baseline reading.

Future testing to continue this form of condition monitoring is recommended. Although this proposed method will indicate degradation of bearing performance, other factors that can affect the overall performance of the structure should be taken into consideration. Cracking of the concrete superstructure can have a significant effect on the frequency response of a structure, care must be taken when determining the actual cause of alteration in frequency.

5.3 Recommendations for future work

Recommendations for further research are outlined in this section to continue the research outlined in this thesis. Several aspects of this research could be explored in greater detail: the finite element analysis, further full-scale field testing, laboratory based experimentation and investigations into plate behaviour using the simplified method outlined and possible refinements to the method. The recommendations are not claimed to be any less important than the work completed by the author. The

recommendations do represent clearly defined steps forward from the author's current findings and as such provide potentially years of future analysis.

The data collected and presented within this thesis are intended to be considered as a baseline reading for the bridge dynamic response. Further testing in 5 years on the bridge at Berwick-Upon-Tweed is recommended in order to compare the response now to the future response, thus hopefully indicating any change in response due to the possible degradation of the bearings, or perhaps other factors such as cracking, corrosion, spalling, walking, or indeed overloading.

One possible line of future investigation is the analysis of bearing performance on a large scale by damaging bearings and testing the response of small scale structures. Many researchers have carried out testing to determine the ultimate shear and compressive loading capacity of bearings. However, these bearings have not been tested in a structure after damage, or stressing, has been completed. Bearings, or sections of bearings, could be artificially aged by either cyclical shear tests, compressive tests or through subjecting bearings to alterations in ambient temperature. The bearings could then be tested in scaled down models of structures, and the response due to impact loading recorded.

In addition to the laboratory testing, stiffness values of bearings after ageing effects have been applied could be obtained and used in finite element models to accurately predict the effects of bearing degradation. The research presented within Chapter 2 describes the effect of bearing pads on the performance of highway bridges, taking into consideration the pad-bridge interface which defines the support boundary conditions.

Further investigations into the response of plate structures with elastic edge constraints are recommended. Of interest are the effects of skew on the dynamic response, and the concentration and dissipation of transverse wave acceleration.

Use of FEA to update the condition of bearings, in accordance with the modal analysis results obtained from testing, could aid evaluation of the projected performance of the structure in future states of disrepair.

5.4 Summary

The author has presented various recommendations for future research on the dynamic response of highway bridges and the effect of bearing degradation. This concludes the author's recommendations for future research and the thesis proper; what follows are the Appendices containing copies of the author's publications and analysed data files.